

50
LET/YEARS

MATERIALI
MATERIALS AND TECHNOLOGY
IN TEHNOLOGIJE

1

MATER.
TEHNOLOGIJE

LETNIK
VOLUME

51

ŠTEV.
NO.

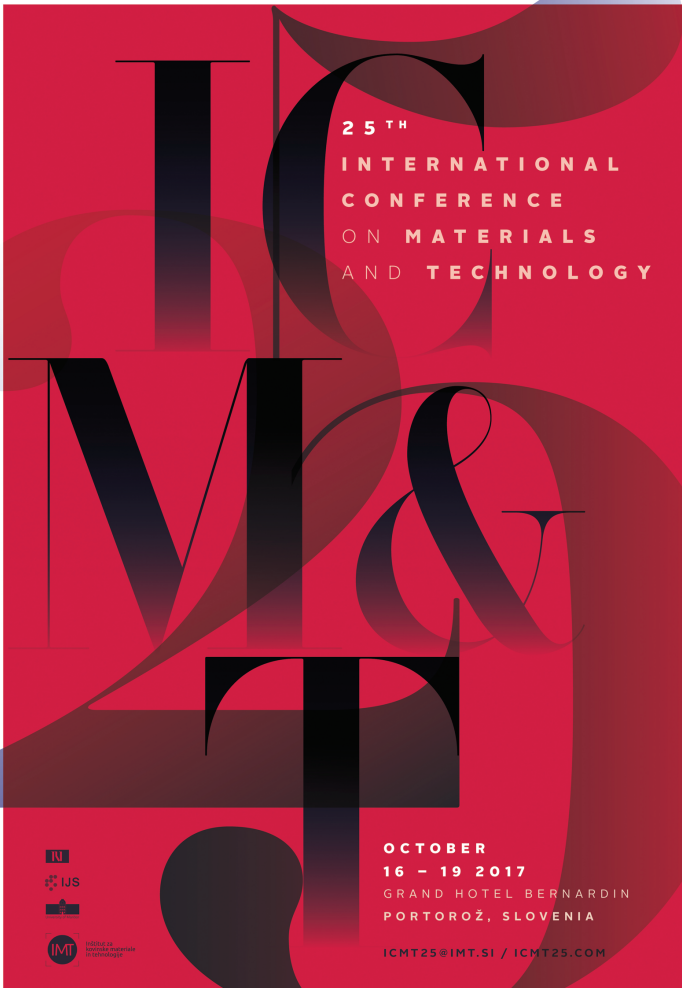
1

STR.
P.

1-177

LJUBLJANA
SLOVENIJA

JAN.-FEB.
2017



ICMT
25TH
INTERNATIONAL
CONFERENCE
ON MATERIALS
AND TECHNOLOGY

OCTOBER
16 - 19 2017
GRAND HOTEL BERNARDIN
PORTOROŽ, SLOVENIA

ICMT25@IMT.SI / ICMT25.COM

Logos: IRI, IJS, IMT, and others.

ISSN: 1580-2949

UDK: 669+666+678+53

MATERIALI IN TEHNOLOGIJE

MATERIALS AND TECHNOLOGY

1

MATER.
TEHNOLOGIJE

LETNIK
VOLUME
51

ŠTEV.
NO.
1

STR.
P.

1-177

LJUBLJANA
SLOVENIJA

JAN.-FEB.
2017

MATERIALI IN TEHNOLOGIJE / MATERIALS AND TECHNOLOGY so znanstvena serijska publikacija, ki objavlja izvirne in tudi pregledne znanstvene članke ter tehnične novice, ki obravnavajo teoretična in praktična vprašanja naravoslovnih ved in tehnologije na področjih kovinskih in anorganskih materialov, polimerov, vakuumske tehnike in v zadnjem času tudi nanomaterialov.

The journal MATERIALI IN TEHNOLOGIJE / MATERIALS AND TECHNOLOGY is a scientific journal, devoted to original scientific papers, reviewed scientific papers and technical news concerned with the areas of fundamental and applied science and technology. Topics of particular interest include metallic materials, inorganic materials, polymers, vacuum technique and lately nanomaterials.

© MATERIALI IN TEHNOLOGIJE

Izdajatelj (Published for):

Inštitut za kovinske materiale in tehnologije Ljubljana (IMT)

Soizdajatelji (Associated Publishers):

IMPOL Slovenska Bistrica, METAL Ravne, TALUM Kidričevo

Izdajanje **MATERIALI IN TEHNOLOGIJE** sofinancira: Javna agencija za raziskovalno dejavnost Republike Slovenije (ARRS) (Journal **MATERIALS AND TECHNOLOGY** is financially supported by Slovenian Research Agency (ARRS))

Glavni in odgovorni urednik (Editor-in-Chief): Paul John McGuiness

Pomočnik glavnega urednika (Associate Editor-in-Chief): Matjaž Godec

Častna glavna urednika (Honorary Editors-in-Chief): Franc Vodopivec, Matjaž Torkar

Souredniki (Co-Editors):

Igor Belič (IMT), Jaka Burja (IMT), Aleksandra Kocijan (IMT), Djordje Mandrino (IMT), Boštjan Markoli (NTF), Irena Paulin (IMT), Danijela A. Skobir Balantič (IMT), Darja Steiner Petrovič (IMT), Bojan Podgornik (IMT), Srečo Škapin (IJS), Rok Zaplotnik (IJS), Ema Žagar (KI)

Tehnični urednik (Technical Editor): Erika Nared (IMT)

Lektorji (Linguistic Advisers): Erika Nared (IMT) (slovenski jezik), Paul John McGuiness (IMT) (angleški jezik)

Mednarodni pridruženi člani uredniškega odbora (International Advisory Board):

Thomas Bell, The University of Birmingham, Birmingham, UK • Ugur Esme, Mersin University, Tarsus, Turkey • Leonid B. Getsov, NPO CKT, St. Petersburg, Russia • Peter Jurči, Faculty of Materials Science and Technology of the STU, Trnava, Slovakia • V. Lupinc, Istituto per la Tecnologia dei Materiali Metallici non Tradizionali, Milano, Italia • Ilija Mamuzić, Sveučilište u Zagrebu, Hrvatska • David Nolan, Bluescope Steel Limited and University of Wollongong, Wollongong, Australia • Hans-Eckart Oechsner, Universität Darmstadt, Darmstadt, Deutschland • Günther Petzow, Max-Planck-Institut für Metallforschung, Stuttgart, Deutschland • Karlo T. Raić, Belgrade University, Belgrade, Serbia • Jozef Zrník, Technická Univerzita, Košice, Slovakia

Uredniški odbor (Editorial Board):

Igor Belič (IMT), Jaka Burja (IMT), Monika Jenko, Varužan Kevorkijan (IMPOL), Aleksandra Kocijan (IMT), Andraž Legat (ZAG), Vojteh Leskovešek (IMT), Matjaž Godec (IMT), Paul McGuiness (IMT), Djordje Mandrino (IMT), Boštjan Markoli (NTF), Jožef Medved (NTF), Peter Panjan (IJS), Irena Paulin (IMT), Danijela A. Skobir Balantič (IMT), Darja Steiner Petrovič (IMT), Tatjana Večko Pirtovšek (METAL Ravne), Bojan Podgornik (IMT), Božidar Sarler (IMT), Janez Šetina (IMT), Avgust Šibila (TALUM), Srečo Škapin (IJS), Borivoj Šuštaršič, Rok Zaplotnik (IJS), Ema Žagar (KI)

Izdajateljski svet (Editorial Advisory Board):

Matjaž Godec (Inštitut za kovinske materiale in tehnologije), Edvard Slaček (IMPOL), Marko Drobnič (TALUM), Andrej Gradišnik (METAL Ravne)

Članki revije **Materiali in tehnologije** so indeksirani v/Articles published in **Materials and Technology** are indexed in: SCIENCE CITATION INDEX EXPANDED, MATERIALS SCIENCE CITATION INDEX® AND JOURNAL CITATION REPORTS/ SCIENCE EDITION.

Po bazi podatkov JCR15 ima **Materiali in Tehnologije** dejavnik vpliva 0,439. / In JCR15 Database Mater. Tehnol. has an impact factor of 0.439.

Članki objavljeni v periodični publikaciji **MATERIALI IN TEHNOLOGIJE** so indeksirani v mednarodnih sekundarnih virih: (Articles published in journal are indexed in international secondary periodicals and databases):

- DOAJ (Directory of Open Access Journals)
- Google Scholar
- SCIRUS
- CA SEARCH® – Chemical Abstracts®
- METADEX®
- TEME – Technology and management
- Inside Conferences
- Engineered Materials Abstracts®
- Aluminium Industry Abstracts
- SCOPUS
- Civil Engineering Abstracts
- Ceramic Abstracts/World Ceramic Abstracts
- Corrosion Abstracts
- Mechanical & Transportation Engineering Abstracts
- CSA Aerospace & High Technology Database
- Solid State and Superconductivity Abstracts
- Materials Business File
- Referativnyj žurnal: Metallurgija
- COBIB

Izhajanje: 6 števil letno / Published: 6 issues per year

Naročnina / Subscription: 42 EUR – tujina / abroad: 85 EUR

Naslov uredništva (Editorial Address):

MATERIALI IN TEHNOLOGIJE
IMT Ljubljana
Lepi pot 11
1000 Ljubljana, Slovenija
Telefon: +386 1 470 18 60
Telefax: +386 1 470 19 39
Podračun pri UJP št. 01100-6030344339

Na INTERNET-u je revija **MATERIALI IN TEHNOLOGIJE** dosegljiva na naslovu (ELECTRONIC ACCESS): <http://mit.imt.si>

Elektronska pošta (E-mail): mit@imt.si

Oblikovanje ovitka (Design): Ignac Kofol
Računalniški prelom in tisk (Prepress and Printed by): NONPAREL grafične storitve d.o.o., Medvode
Naklada (Circulation): 400 izvodov/issues

UDK: 669+666+678+53

ISSN: 1580-2949

MATER. TEHNOL.	LETNIK VOLUME	51	ŠTEV. NO.	1	STR. P.	1–177	LJUBLJANA SLOVENIJA	JAN.–FEB. 2017
-------------------	------------------	----	--------------	---	------------	-------	------------------------	----------------

VSEBINA – CONTENTS

Editorial preface/Predgovor urednika

P. McGuiness	3
--------------------	---

*IZVIRNI ZNANSTVENI ČLANKI – ORIGINAL SCIENTIFIC ARTICLES***Developing a friction-stir welding window for joining the dissimilar aluminum alloys AA6351 and AA5083**

Iskanje varilnega okna za tornu vrtilno varjenje pri spajanju različnih aluminijevih zlitin AA6351 in AA5083 R. Palanivel, R. F. Laubscher, I. Dinaharan, N. Murugan	5
---	---

Rock burst dependency on the type of steel arch support in the Velenje mine

Hribinski udari v odvisnosti od vrste jeklenih podpornih lokov v premogovniku Velenje G. Vižintin, J. Mayer, B. Lajlar, Ž. Vukelić	11
---	----

Effect of cutting parameters on the drilling of AlSi₇ metallic foams

Vpliv parametrov rezanja pri vrtnju kovinskih pen iz AlSi ₇ G. Uzun, U. Gokmen, H. Cinici, M. Turker	19
--	----

A metamaterial-embedded wide-band antenna for the microwave C-band

Širokopasovna antena v vgrajenim metamaterialom za mikrovalovni C-pas Md. I. Hossain, M. R. I. Faruque, M. T. Islam, A. Rahman	25
---	----

Erosion wear resistance of titanium-matrix composite Ti/TiN produced by diode-laser gas nitriding

Odpornost kompozita proti erozijski obrabi Ti/TiN, izdelanega s plinskim nitriranjem s pomočjo diodnega laserja A. Lisiecki, A. Kurc-Lisiecka	29
--	----

Miswak (Salvadora Persica Roots): discovery of a new biomaterial for removing heavy metals from water in Saudi Arabia

Miswak (korenine <i>Salvadora Persica</i>): odkritje novega biomateriala za odstranjevanje težkih kovin iz vode v Saudski Arabiji S. A. Aljlil	35
--	----

Poly(vinyl alcohol): formulation of a polymer ink for the patterning of substrates with a drop-on-demand inkjet printer

Poli(vinil alkohol): sestavljanje polimernega črnila za tiskanje podlag z brizgalnim tiskalnikom P. Šuly, P. Krčmář, J. Mašlík, P. Urbánek, I. Kuřitka	41
---	----

Influence of chemical additives and curing conditions on the mechanical properties and carbonation resistance of alkali-activated slag composites

Vpliv kemijskih dodatkov in pogojev sušenja na mehanske lastnosti in odpornost na karbonacijo z alkalijami aktiviranih kompozitov žlindre P. Bulejko, V. Bílek Jr.	49
--	----

Effect of holding time on the production of Nb-NbAl₃ intermetallic composites via electric-current-activated sintering

Vpliv časa zadržanja na izdelavo Nb-NbAl ₃ intermetalnih kompozitov z električnim tokom aktiviranih s sintranjem M. Aybey, T. Yener, M. Ipek, S. Zeytin	55
---	----

Analysis of the fiber distribution, size, and volume ratio of unidirectional composite plates with different thicknesses

Analiza razporeditve vlaken, velikosti in volumskega deleža v enosmernih, različno debelih kompozitnih ploščah R. Zemčík, H. Srbová, K. Ekštejn, I. Pirner, R. Medlín	59
--	----

The use of natural sepiolite fiber in concrete

Uporaba naravnega sepiolitnega vlakna v betonu S. Koltka, T. Uygunoğlu, E. Sabah, M. Fatih Can	65
---	----

Nano-indentation investigations of the mechanical properties of thin TiO₂, WO₃ and their composites layers, deposited by spray pyrolysis

Preiskave mehanskih lastnosti z nanotrdo tankih TiO ₂ , WO ₃ in njunih kompozitnih plasti, nanešenih s pršilno pirolizo S. Cherneva, R. Iankov, N. Radic, B. Grbic, M. Datcheva, D. Stoychev	75
---	----

Corrosion determination of reinforcement using the electrical resistance method

Določanje korozije palice v armiranem betonu s pomočjo metode električne upornosti M. Brodňan, P. Koteš, J. Vaněrek, R. Drochytka	85
--	----

Effect of quenching parameters on the mechanical properties of the 7A04 aluminium alloy

Vpliv parametrov gašenja na mehanske lastnosti aluminijeve zlitine 7A04 D. Shi, K. Kang, G. Gao	95
--	----

Bio-plastic composite substrate material based microstrip-fed printed antenna for wireless communications Tiskana antena za brezžično komunikacijo iz bioplastičnega kompozita z mikrotrakom za napajanje T. Alam, M. R. I. Faruque, M. S. Alam, Md. M. Islam, Md. Z. Mahmud, M. T. Islam	101
The growth of beta phase in the gamma-brass–copper diffusion couple Rast beta faze v difuzijskem paru gama medenina – baker A. Hoxha, D. Heger	105
Investigation of the geometrical accuracy and thickness distribution using 3D laser scanning of AA2024-T3 sheets formed by SPIF Preiskava geometrijske natančnosti in razporeditev debeline s tridimenzionalnim laserskim skeniranjem pločevine iz AA2024-T3, preoblikovane s stopnjujočim preoblikovanjem kovine H. Bayram, N. S. Köksal	111
Formation of a corrosion-resistant alumina coating on a 6061 aluminum alloy using a combination of micro-arc oxidation and sealing treatments Tvorba korozijsko obstojne Al ₂ O ₃ prevleke na zlitini aluminija 6061 s kombinacijo oksidacije v mikroobloku in postopka tesnjenja A. Hilmi Paksoy, F. Muhaffel, M. Koca, O. Gokce, S. Mohammadzadeh, H. Cimenoglu	117
Classification of surface defects on steel sheet using convolutional neural networks Klasifikacija površinskih napak z uporabo konvolucijske nevronske mreže S. Zhou, Y. Chen, D. Zhang, J. Xie, Y. Zhou	123
Optimization of the machining parameters for the turning of 15-5 PH stainless steels using the Taguchi method Uporaba Taguchi metode za optimizacijo parametrov obdelave pri struženju nerjavnega jekla 15-5 PH Ş. Çetin, T. Kivak	133
Powder-metallurgy preparation of NiTi shape-memory alloy using mechanical alloying and spark-plasma sintering Uporaba metalurgije prahov za pripravo NiTi zlitine s spominom s pomočjo mehanskega legiranja in sintranja z iskrilno plazmo P. Novák, H. Moravec, V. Vojtěch, A. Knaislová, A. Školáková, T. F. Kubatík, J. Kopeček	141
Lacunarity properties of nanophotonic materials based on poly(methyl methacrylate) for contact lenses Razporeditev praznin nanofotoničnega materiala na osnovi poli(metil metakrilata) za kontaktne leče M. Tomić, B. Bojović, D. Stamenković, I. Mileusnić, D. Koruga	145
Molecular dynamics simulations of plastic deformation of metallic surfaces Simulacije plastične deformacije kovinskih površin z metodo molekularne dinamike N. Pukšič, M. Jenko, M. Godec	153
STROKOVNI ČLANKI – PROFESSIONAL ARTICLES	
The influence of an isothermal annealing process on the structure and magnetic properties of the bulk amorphous alloy FeCoBYMo Vpliv izotermnega žarjenja na strukturo in magnetne lastnosti masivne amorfnе zlitine FeCoBYMo P. Pietrusiewicz, M. Nabiafek, J. Olszewski, S. Lesz	157
Rheological properties of feedstocks and the structure of injection moulders for sintering composite tool materials based on MMCS Reološke lastnosti mešanic in struktura vbrizganih rezkarjev za sintranе kompozitne orodne materiale na osnovi MMCS K. Gołombek, G. Matula, J. Mikuła, M. Soković	163
Grain-refining ability of ultra-rapid annealing for low-carbon steel: severe plastic deformation Sposobnost udrobnjenja zrn pri zelo hitrem žarjenju maloogljičnega jekla po veliki plastični deformaciji M. A. Mostafaei, M. Kazeminezhad	173

EDITORIAL PREFACE

Fifty years of publishing scientific papers is an impressive record – one that we at the journal *Materials and Technology* are not unreasonably proud. I like to think that our success is down to an ability to adapt, to move with the times, but not always to follow convention. Since I took over the job of the Editor in Chief last year we have introduced some important changes, most notable an end to publishing purely technical papers. Such papers, while both interesting and useful to a small number of specialists, tend not to appeal to a wider audience of materials and technology researchers and so reduce the impact of the journal on its target audience.

In keeping with the ethos of my predecessor Matjaž Torkar, who was Editor in Chief from 2012 to 2016, I will be trying to publish exciting papers from scientists who are making a mark with new research techniques, new applications and new materials. A good example in this latest issue is the paper entitled *Molecular dynamics simulations of plastic deformation of metallic surfaces* by Nuša Pukšič and her colleagues, who are reporting on the behavior of surfaces at the atomic level. Of course, the journal will continue to publish more conventional, high-quality research on metallic materials, polymers, biomaterials and relevant technologies. However, we will not be acting a repository for stale research that lacks relevance and fails to attract the interest of researchers.

It is very likely that as we raise standards the number of rejected manuscripts will increase, and I understand it is not a pleasant experience to have your paper rejected by a journal. But authors have to understand that the journal cannot publish every article that it receives, and the fairest way to select the articles for publication is through a review process that considers factors like relevance, excellence, innovation, and wider impact. We also consider how well previous publications by the authors have been cited, and use this as a guideline for the relevance of their research.

Starting next year, the first issue of *Materials and Technology* will publish the best papers presented at the annual (this year it is the 25th Anniversary) ICM&T Conference, which in 2017 will be held in Portorož from the 16th to the 19th of October. In previous years we spread these papers throughout all 6 issues, but in order to highlight the work presented at this important materials-related event we have decided to showcase the best of the conference in a single issue.

Dr. Paul McGuiness

PREDGOVOR UREDNIKA

Petdeset let izdavanja znanstvenih člankov je zelo lepo obdobje, na kar smo pri reviji *Materiali in tehnologije* lahko upravičeno ponosni. Sam sem mnenja, da je uspeh revije ta, da je sposobna prilagajanja, da gre v korak s časom na področju, ki ga pokriva. Odkar sem lansko leto prevzel urednikovanje revije, smo predstavili nekatere pomembne spremembe, med drugim tudi ukinitvev objavljanja strokovnih člankov. Tovrstni članki so sicer zanimivi in koristni manjšemu številu strokovnjakov, ne dosežejo pa širše skupine raziskovalcev na področju materialov in tehnologij ter tako vplivajo na zmanjševanje faktorja vpliva pri ciljni skupini.

Pri ohranjanju etike mojega predhodnika na tem mestu, dr. Matjaža Torkarja, ki je bil urednik revije med 2012 in 2016, si bom prizadeval, da bodo v reviji objavljeni zanimivi članki raziskovalcev, ki s svojim delom predstavljajo nove raziskovalne tehnike, nove aplikacije in nove materiale. Dober primer takšnega je članek Nuše Pukšič in njenih sodelavcev v tej številki revije z naslovom *Molecular dynamics simulations of plastic deformation of metallic surfaces*, ki poročajo o obnašanju površin na atomskem nivoju. Seveda bo revija tudi v prihodnje stremela k objavljanju bolj konvencionalnih, visokokvalitetnih raziskav na področju kovinskih materialov, polimerov, biomaterialov in sorodnih tehnologij. Skratka, revija ne bo zbirala člankov z zastarelimi raziskavami, ki niso primerni in ne dosegajo zanimanja raziskovalcev današnjega časa.

Zelo verjetno je, da ko bomo dvignili standard, se bo število zavrženih rokopisov še povečalo. Razumemo tudi, da ni prijetno, ko je članek pri kakšni reviji zavržen. Avtorji morajo razumeti, da revija ne bo objavljala vseh prejetih člankov. Najboljši in najbolj korekten način izbire člankov za objavo je recenziranje člankov, kjer se upošteva ustreznost, odličnost in širši vpliv, ki ga ima članek na širšo publiko. Upošteevamo pa tudi, kako pogosto so bila predhodna objavljanja avtorjev citirana in to uporabimo kot smernico za pomembnost njihovih raziskav.

S pričetkom v naslednjem letu bodo v prvi številki revije *Materiali in tehnologije* objavljeni najboljše članki, predstavljeni na letni konferenci o Materialih in tehnologijah, ki bo v letu 2017 od 16. do 17. oktobra potekala v Portorožu. V prejšnjih letih smo članke objavljali od številke do številke, ker pa želimo poudariti dela predstavljena na tem pomembnem dogodku, ki bo letos že 25. po vrsti, smo se odločili predstaviti najboljše iz konference v eni številki.

Dr. Paul McGuiness

DEVELOPING A FRICTION-STIR WELDING WINDOW FOR JOINING THE DISSIMILAR ALUMINUM ALLOYS AA6351 AND AA5083

ISKANJE VARILNEGA OKNA ZA TORNO VRTILNO VARJENJE PRI SPAJANJU RAZLIČNIH ALUMINIJEVIH ZLITIN AA6351 IN AA5083

Ramaswamy Palanivel¹, Rudolf Frans Laubscher¹, Isaac Dinaharan¹,
Nadarajan Murugan²

¹University of Johannesburg, Department of Mechanical Engineering Science, Johannesburg 2006, South Africa

²Coimbatore Institute of Technology, Department of Mechanical Engineering, Coimbatore 641014, Tamil Nadu, India
rpelmech@yahoo.co.in

Prejem rokopisa – received: 2015-03-04; sprejem za objavo – accepted for publication: 2015-12-21

doi:10.17222/mit.2015.049

In this study a welding window was constructed for the relatively new welding process of friction-stir welding (FSW) to join the 6-mm-thick dissimilar aluminium alloys AA5083-H111 and AA6351-T6. The dissimilar joints were fabricated using different combinations of tool rotational speeds and welding speeds. The effect of the process parameters on the macrostructure of the joints was analysed and reported. Established along with the macrostructural analysis, a welding window was made. These windows will act as reference maps for selecting the appropriate FSW process parameters to produce defect-free welds of dissimilar aluminium alloys.

Keywords: friction stir welding, dissimilar joints, welding window, macrostructure

V študiji je bilo postavljeno varilno okno, za relativno nov postopek tornu vrtilnega varjenja (FSW), za spajanje različnih aluminijevih zlitin AA5083-H111 in AA6351-T6 debeline 6 mm. Zvari so bili izdelani s pomočjo različne kombinacije rotacijskih hitrosti orodja in hitrosti varjenja. Analiziran je bil vpliv procesnega parametra na mikrostrukturo zvarov. Na podlagi analize makro strukture je bilo postavljeno okno za varjenje. Ta okna služijo kot referenčna pri izbiri ustreznih parametrov tornu rotacijskega varjenja različnih aluminijevih zlitin, za izdelavo zvarov brez napak.

Ključne besede: tornu vrtilno varjenje, spoji različnih materialov, varilno okno, makrostruktura

1 INTRODUCTION

Environment friendly friction stir welding (FSW) is a solid-state welding process invented by the The Welding Institute (TWI) in 1991 in the UK to join metals, more specifically aluminum alloys, which are used in transportation industries, having a low melting point and difficult to join with conventional techniques. FSW uses a rotating tool with a pin travelling along the weld path and plastically deforming the surrounding material to make the weld. The warmth created by the rubbing between the rotating tool and the plates encourages a local increase in the temperature and softens the materials underneath the tool shoulder and simultaneously the plunged rotating tool pin moves and mixes the softened materials by intense plastic deformation, joining both in a solid-state weld. Attractive benefits of the FSW of aluminum alloys compared to fusion-welding processes are less distortion, lower residual stresses, fewer weld defects, no hot cracking and execution without a shielding gas.¹⁻³ The fine microstructure in friction-stir welds produces good mechanical and metallurgical properties. By developing such technology, one of the most important facts is the possibility of joining different alumi-

num alloys.⁴ The joining of dissimilar aluminum alloys offers the potential to give the advantages of different materials, often providing unique solutions to engineering-industry requirements.

The foremost FSW process parameters that determine the joint strength and microstructure are the tool rotational speed, welding speed, axial force and tool pin profile.² The effects of the tool rotational speed and welding speed were investigated by various researchers⁵⁻⁸ in order to obtain better mechanical and metallurgical properties of the welded joints. S. A. Khodir et al.⁹ studied the FSW of 2024 Al alloy plate to 7075 Al alloy plate and observed that the rise in welding speed tended to the formation of a kissing bond and pores. A. Steuwer et al.¹⁰ quantified the effect of the tool rotational speed and traverse speed on the residual stress of 3-mm-thick AA5083 and AA6082 joints. They reasoned that the tool rotational speed was a useful process variable to optimize the residual stress. The welding speed determines the exposure time of this frictional heat per unit length of weld and subsequently affects the grain growth.¹¹ M. J. Peel et al.¹² noticed a 35 % drop in microhardness in the HAZ of the AA5083 side of the

dissimilar joint consisting of the aluminum alloys AA5083 and AA6062. N. Shanmugasundaram and N. Murugan¹³ developed a mathematical model to study the effect of FSW parameters on the tensile strength and elongation of dissimilar AA2024–AA5083 joints. S. Rajakumar et al.¹⁴ optimized the developed models using the software expert to maximize the tensile strength of the joints.

Despite the great quantity of published literature about the FSW, insufficient information exists in the selection of working ranges of the process parameters based on macrostructural observations. Hence in this investigation an attempt has been made in developing a welding window based on the macrostructural observation to produce defect-free welds.

2 EXPERIMENTAL PART

Rolled aluminum-alloy AA6351 and AA 5083 plates of size 100 mm × 50 mm × 6 mm were used in this study. AA5083 and AA6351 were kept along the retreating side and advancing side of the joint line, respectively. Due to better tensile properties¹⁵ the straight square tool pin having a shoulder diameter of 18 mm, a pin diameter of 6 mm and a pin length of 5.6 mm was used to fabricate the joints. The manufactured FSW tool is shown in **Figure 1**. The FSW line was parallel to the rolling direction of AA5083-H111 and perpendicular to the rolling direction of AA6351-T6. The dissimilar butt welding was carried out on an in-house built FSW machine (M/s RV Machine Tools, Coimbatore, INDIA) by combinations of rotational speed (800 min⁻¹ to 1200 min⁻¹) and welding speed (45 mm/min to 85 mm/min). Axial force (15 kN) and tool tilt angle (01) were maintained constant for all the joints. The single-pass welding procedure was followed to weld the joints. The specimens were made as per standard metallography procedures and etched with concentric Keller reagent. The digital image of the ma-



Figure 1: Photograph of manufactured FSW tool
Slika 1: Posnetek izdelanega orodja za FSW

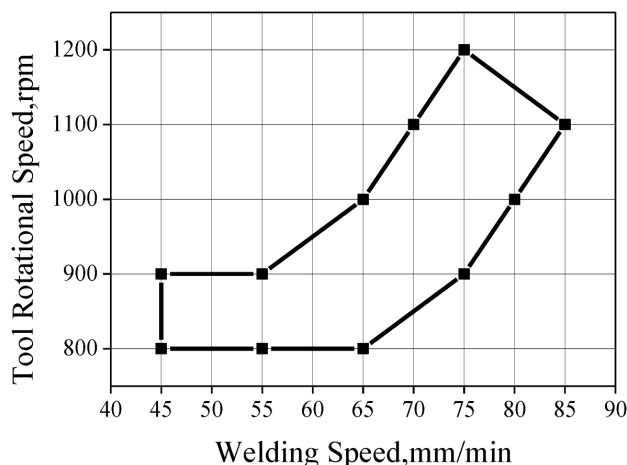


Figure 2: Welding window for dissimilar aluminium alloys
Slika 2: Varilno okno za različne aluminijeve zlitine

crostructure of the etched specimens was captured utilizing a digital optical scanner to read the quality of the dissimilar joints produced by the various combinations of FSW process parameters. The welding window was made based on a macrostructural analysis for the joining of dissimilar aluminum alloy by different combinations of rotational speed and welding speed. Stoppage of material flow due to defects was observed using a scanning electron microscope. A verification test was made within the welding window region to validate the results.

3 RESULTS

Effects of the process parameters on the macrostructure of dissimilar joints are presented in **Table 1**, with the probable reason. **Figure 2** shows the welding window of joining dissimilar aluminium alloys based on a macrostructural analysis. The tool rotational speed and

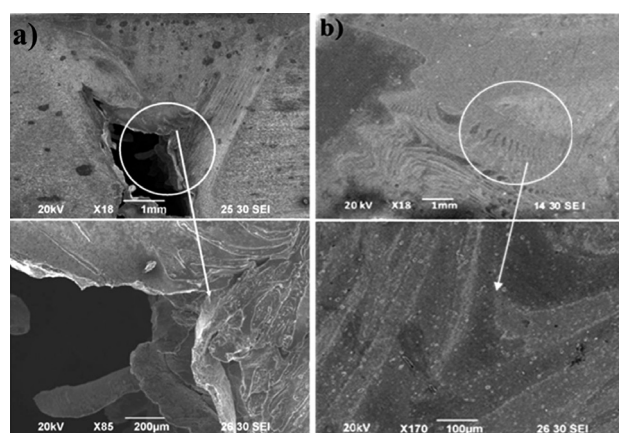
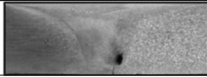
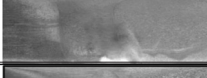
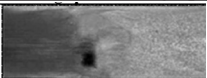
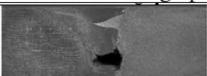
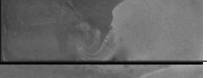
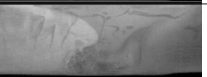


Figure 3: SEM images: a) defects of the joints and material flow clogged due to the defects, b) macrostructure without defects and proper material flow

Slika 3: SEM-posnetki: a) napake v spoju in preprečen tok materiala zaradi napak, b) makrostruktura brez napak in ustrezen tok materiala

Table 1: Effect of process parameter on the macrostructure of dissimilar joints

Tabela 1: Vpliv procesnega parametra na makrostrukturo spojev različnih materialov

S.no	Parameter	Macrostructure	Name of the defects	Probable reason
Welding speed of 45 mm/min				
	Rotational speed, min ⁻¹	RS AS		
1	700		Pinhole at advancing side of the weld zone	Insufficient stirring action of tool
2	800		No defects	Sufficient heat generation and interaction of tool
3	900		No defects	Sufficient heat generation and stirring action of the tool
4	1000		Tunnel at the bottom, of weld zone	High heat generation
Welding speed of 55 mm/min				
5	700		Pinhole at retreating side	Insufficient stirring action of tool
6	800		No defects	Sufficient heat generation and interaction of tool
7	900		No defects	Sufficient heat generation and interaction of tool
8	1000		Pinhole At advancing side	High heat generation
Welding speed of 65 mm/min				
9	700		Tunnel defects at weld zone collapse	Insufficient heat and stirring action of the tool
10	800		No defects	Sufficient pulsating stirring action and flow of plasticized material
11	900		No defects	Sufficient pulsating stirring action and flow of plasticized material
12	1000		No defects	Sufficient pulsating stirring action and flow of plasticized material
13	1100		Tunnel defects at the bottom of weld zone	High heat generation
Welding speed of 75 mm/min				
14	800		Tunnel defects at retreating side of the weld zone	Insufficient stirring action of tool
15	900		No defects	Sufficient heat generation
16	1000		No defects	Sufficient heat generation
17	1100		No defects	Sufficient heat generation
18	1200		No defects	Sufficient heat generation
19	1300		Tunnel defects at the bottom of the weld zone	High heat generation

Welding speed of 85 mm/min				
20	1000		Pinhole at advancing side	Insufficient heat generation
21	1100		No defects	Sufficient heat generation
22	1200		Tunnel defects at nugget collapse	Insufficient stirring action of tool

the welding speed that are considered, which contribute remarkably to the generation of frictional heat during the welding. During welding the combination of process parameters that are having too high or too low heat input produces defects due to improper material flow. The rotational speed of 800 min^{-1} to 1200 min^{-1} yielded defect-free joints depending on the welding speed used and the welding speed in the range of 45 mm/min to 85 mm/min yielded defect-free joints depending on the rotational speed used.

4 DISCUSSION

Joining of aluminium alloys by fusion welding produces defects like hot cracking, porosity, slag inclusion, etc. with the mechanical and metallurgical properties. Usually, the friction stir welded joints are free from these defects since the absence of melting during welding; metals are joined in the solid state due to the heat generated by the friction and flow of metal by the stirring action. However, FSW joints are likely to have other defects like pinhole, tunnel defect, piping defect, kissing bond, cracks, etc. due to the improper flow of metal and insufficient consolidation of the metal in the weld zone.

A low welding speed and a high tool rotational speed increases the frictional heat due to the increased residing time of tool. Tool rotational speed results in stirring and mixing of the material about the rotating pin, which in turn increases the temperature of the metal. It seems to be the most important process variable since it is given to influence the weld speed. A low rotational speed to produce a low heat input. This low heat input results in lack of stirring and yields defects. It is clear that in FSW, as the rotational speed increases the heat input also increases. **Figure 3** shows SEM images of the macrograph and mixing of the material of the joints. The material flow of the FSW joint from advancing side to retreating side and vertical movement (bottom to top) is collaged due to the defects formation as shown in **Figure 3a**. Proper mixing of the material due to the absence of defects is shown in **Figure 3b**. More heat input destroys the regular flow behaviour of plasticized material and a higher rotational speed causes the excessive release of stirred materials to the upper surface, which leaves voids in the weld zone.^{16,17} The lowest and highest welding speed produces defects due to the increased frictional heat and insufficient frictional heat generated, respectively.¹⁸ In general FSW at higher welding speeds results in a short exposure time in the weld area with insufficient heat and poor plastic flow of the metal and causes some voids, like defects, in the joints. Higher welding speeds are associated with low heat inputs, which result in faster cooling rates of the welded joint and hence yields defects. The developed welding window was validated with verification tests and the results are presented in **Figure 4**, having no defects within the welding-window regions.

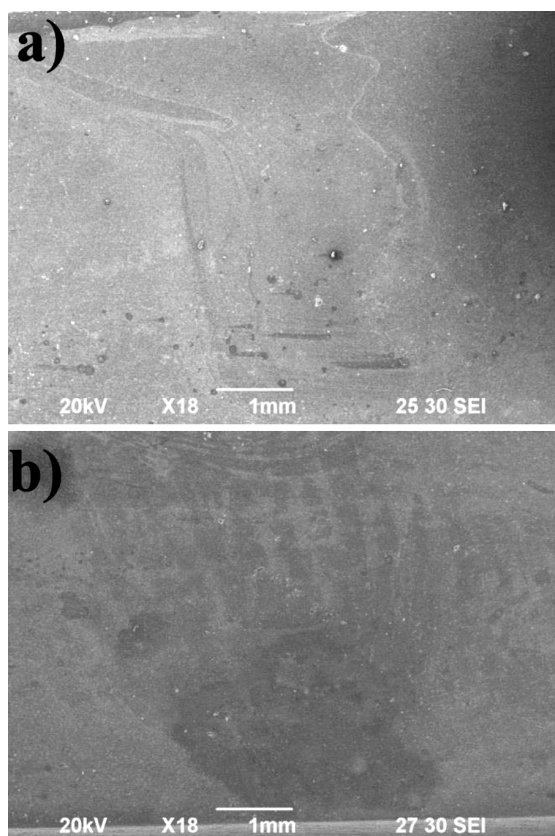


Figure 4: SEM image of the macro images of the dissimilar FSW joints with in the welding window region: a) 70 mm/min and 900 min^{-1} , b) 80 mm/min and 1100 min^{-1}

Slika 4: SEM-posnetek makro izgleda FSW-spoja različnih materialov, na področju varilnega okna: a) 70 mm/min in 900 min^{-1} , b) 80 mm/min in 1100 min^{-1}

5 CONCLUSION

Defect-free dissimilar FSW joints were produced under a wide range of rotational speeds and welding speeds. The friction stir welding window was developed to obtain defect-free welds.

The developed welding window will be applied as a ready reference to select the appropriate rotational and welding speeds to manufacture the defect-free joints.

6 REFERENCES

- ¹ R. S. Mishraa, Z. Y. Ma, Frictions stir welding and processing, *Materials Science and Engineering R*, 50 (2005) 1–2, 1–78, doi:10.1016/j.mser.2005.07.001
- ² R. Nandan, T. DebRoy, H. K. D. H Bhadeshia, Recent advances in friction-stir welding process, weldment structure and properties, *Progress in Material Science*, 53 (2008) 6, 980–1023, doi:10.1016/j.pmatsci.2008.05.001
- ³ Y. Uematsu, K. Tokaji, H. Shibata, Y. Tozaki, T. Ohmune, Fatigue behavior of friction stir welds without neither welding flash nor flaw in several aluminium alloys, *International Journal of Fatigue*, 31 (2009) 10, 1443–1453, doi:10.1016/j.ijfatigue.2009.06.015
- ⁴ T. Saeid, A. Abdollah-Zadeh, B. Sazgari, Weldability and mechanical properties of dissimilar aluminum–copper lap joints made by friction stir welding, *Journal of Alloys and Compounds*, 490 (2010) 1–2, 652–655, doi:10.1016/j.jallcom.2009.10.127
- ⁵ M. Ericsson, R. Sandstrom, Influence of welding speed on the fatigue of friction stir welds and comparison with MIG and TIG, *International Journal of Fatigue*, 25 (2003) 12, 1379–1387, doi:10.1016/S0142-1123(03)00059-8
- ⁶ P. Cavaliere, G. Campanile, F. W. Panella, A. Squillace, Effect of welding parameters on mechanical and microstructural properties of AA6056 joints produced by friction stir welding, *Journal of Material Processing Technology*, 180 (2006) 1–3, 263–270, doi:10.1016/j.jmatprotec.2006.06.015
- ⁷ C. Leitao, R. M. Leal, D. M. Rodrigues, A. Loureiro, P. Vilaca, Mechanical behaviour of similar and dissimilar AA5182-H111 and AA6016-T4 thin friction stir welds, *Materials and Design*, 30 (2009) 1, 101–108, doi:10.1016/j.matdes.2008.04.045
- ⁸ H. J. Aval, S. Serajzadeh, A. H. Kokabi, Evolution of microstructures and mechanical properties in similar and dissimilar friction stir welding of AA5086 and AA6061, *Materials Science and Engineering A*, 528 (2011) 28, 8071–8083, doi:10.1016/j.msea.2011.07.056
- ⁹ S. A. Khodir, T. Shibayanagi, Friction stir welding of dissimilar AA2024 and AA7075 aluminum alloys, *Materials Science and Engineering B*, 148 (2008) 1–3, 82–87, doi:10.1016/j.mseb.2007.09.024
- ¹⁰ A. Stewart, M. J. Peel, P. J. Withers, Dissimilar friction stir welds in AA5083–AA6082: The effect of process parameters on residual stress, *Materials Science and Engineering A*, 441 (2006) 1–2, 187–196, doi:10.1016/j.msea.2006.08.012
- ¹¹ T. Sakthivel, G. S. Sengar, J. Mukhopadhyay, Effect of welding speed on microstructure and mechanical properties of friction stir welded aluminum, *International Journal of Advanced Manufacturing Technology*, 43 (2009) 5–6, 468–473, doi:10.1007/s00170-008-1727-7
- ¹² M. J. Peel, A. Stewart, P. J. Withers, Dissimilar friction stir welds in AA5083–AA6082 Part II: Process parameter effects on microstructure, *Metallurgical and Materials Transactions A*, 37 (2006) 7, 2195–2206, doi:10.1007/BF02586139
- ¹³ N. Shanmugasundaram, N. Murugan, Tensile behavior of dissimilar friction stir welded joints of aluminum alloys, *Materials and Design*, 31 (2010) 9, 4184–4193, doi:10.1016/j.matdes.2010.04.035
- ¹⁴ S. Rajakumar, C. Muralidharan, V. Balasubramanian, Predicting tensile strength, hardness and corrosion rate of friction stir welded AA6061-T6 aluminium alloy joints, *Materials and Design*, 32 (2011) 5, 2878–2890, doi:10.1016/j.matdes.2010.12.025
- ¹⁵ R. Palanivel, P. Koshy Mathews, The tensile behavior of friction-stir welded dissimilar aluminium alloys, *Mater. Tehnol.*, 45 (2011) 6, 623–626
- ¹⁶ K. Elangovan, V. Balasubramanian, Influences of tool pin profile and welding speed of the formation of friction stir processing zone in AA2219 aluminium alloy, *Journal of Materials Processing Technology*, 200 (2008) 1–3, 163–175, doi:10.1016/j.jmatprotec.2007.09.019
- ¹⁷ K. Elangovan, V. Balasubramanian, Influences of pin profile and rotational speed of the tool on the formation of friction stir processing zone in AA2219 aluminum alloy, *Materials Science and Engineering A*, 459 (2007) 1–2, 7–18, doi:10.1016/j.msea.2006.12.124
- ¹⁸ R. Palanivel, P. Koshy Mathews, I. Dinakaran, N. Murugan, Mechanical and metallurgical properties of dissimilar friction stir welded AA5083-H111 and AA6351-T6 aluminum alloys, *Transaction of the Non Ferrous Metal Society China*, 24 (2014) 1, 58–65, doi:10.1016/S1003-6326(14)63028-4

ROCK BURST DEPENDENCY ON THE TYPE OF STEEL ARCH
SUPPORT IN THE VELENJE MINEHRIBINSKI UDARI V ODVISNOSTI OD VRSTE JEKLENIH
PODPORNIH LOKOV V PREMOGOVIKU VELENJEGoran Vižintin¹, Janez Mayer², Bojan Lajlar², Željko Vukelić¹¹University of Ljubljana, Faculty of Natural Sciences and Engineering, Aškerčeva Street 12, SI-1000 Ljubljana, Slovenia²Velenje Colliery, Partizanska 78, 3320 Velenje, Slovenia
goran.vizintin@guest.arnes.si*Prejem rokopisa – received: 2016-05-11; sprejem za objavo – accepted for publication: 2016-07-01*

doi:10.17222/mit.2016.084

The Velenje Colliery is operating in the largest coal deposit in Slovenia and at the same time in one of the thickest known coal seams in the world. The lignite seam is at one point up to 165 m thick. Until now more than 220 million tons of lignite coal were extracted from this seam. The colliery is situated in the so-called Velenje depression, which is a component part of the Southern Karawanke geotectonic unit. Considering the coal mining we can claim that rock bursts are a kind of constant that accompany the mining activities and represent occasional difficulties during production and at the same time disturb the local inhabitants. Based on complaints and at the same time because of the need for a thorough understanding of the causes of ground shaking, the Velenje Colliery decided for a systematic monitoring and evaluation of the seismic events. Based on these measurements the seismic events were precisely located and correlated to the technological process itself. Seismic events analysis indicates that these events are instantaneous stress relaxations piled up for a longer time because of the lignite extraction. This last statement can be confirmed by an analysis of the longitudinal seismic waving first arrivals (P) to seismological stations of the state monitoring network of Slovenia, Austria and Italy, even though such events are rare because of their weakness. The same analysis showed that the magnitudes rarely reach over 1.5 of local magnitude after Richter. Simultaneously with the seismic events analysis we analyzed the way of support relaxation. Tests on the existing support type K24 showed that this support is capable of withstanding large stresses without deformation. From these tests we found that the stress relaxation at currently used support type K24 can occur over relatively large deformations. The relatively simple stress-relaxation analysis at existing support shows it surprisingly well match to the energy relaxed at rock bursts in Velenje Colliery. Based on research done between 2003 in 2012 it is possible to conclude that the existing support type must be replaced with one that can relax the stress more frequently and with less deformation, consequently reducing rock bursts and increasing safety at work.

Keywords: rock burst, steel arch, induced seismicity

Premogovnik Velenje deluje na največjem nahajališču premoga v Sloveniji, ki je hkrati eno takih, ki ima najbolj debele plasti premoga na svetu. Plast lignita je na enem mestu debela tudi do 165 m. Do sedaj je bilo izkoriščenih 220 milijonov ton lignita iz te plasti. Premogovnik se nahaja v velenjski depresiji, ki je sestavni del geotektonskega dela Južnih Karavank. Pri rudarjenju premoga so hribinski udari konstanta, ki spremlja rudarske aktivnosti in občasno predstavlja težave pri proizvodnji ter istočasno moti lokalno prebivalstvo. Zaradi pritožb in hkrati zaradi potrebe po razumevanju vzrokov tresenja tal, so se v Rudniku Velenje odločili za sistematično registriranje in oceno seizmičnih pojavov. Na osnovi teh meritev so bili seizmični dogodki natančno locirani in povezani s samim tehnološkim procesom. Analiza seizmičnih dogodkov kaže, da gre za trenutne sprostitve napetosti, ki so se nakopičile v daljšem času zaradi ekstrakcije lignita. To trditev je mogoče potrditi z analizo longitudinalnih seizmičnih valovanj (P), ki pridejo prva do seizmoloških postaj državne kontrolne mreže v Sloveniji, Avstriji in Italiji, čeprav so taki dogodki redki zaradi šibkosti valov. Analiza je pokazala, da lokalna magnituda redko preseže 1,5 po Richterju. Istočasno z analizo seizmičnih pojavov smo analizirali način relaksacije podporja. Preizkusi na obstoječem podporju vrste K24 so pokazali, da to podporje lahko prenese večje napetosti brez deformacije. Iz teh preizkusov sledi, da se pri trenutni uporabljeni podpori vrste K24 lahko pojavijo sprostitve napetosti preko relativno velikih deformacij. Relativno preprosta analiza sproščanja napetosti je pokazala dobro ujemanje z energijo sproščeno pri hribinskem udaru v premogovniku Velenje. Na osnovi raziskav, opravljenih med 2003 in 2012, je mogoče zaključiti, da je obstoječo vrsto podporja potrebno zamenjati s tako, ki lahko bolj pogosto sprošča napetosti in z manj deformacije, kar omogoča manj hribinskih udarov in poveča varnost pri delu.

Ključne besede: hribinski udari, jekleni lok, povzročena seizmičnost

1 INTRODUCTION

Velenje Colliery is situated in the northern part of Slovenia in the so-called Velenje depression, which is a component part of the Southern Karawanke geotectonic unit. Southern Karawanke form the northern part of the Velenje depression and the northern part of its basement reaching from the Smrekovec fault in the north to the Velenje fault in the south. On the northern margins of the depression the layers of Triassic dolomite are slightly folded, but from the depression margin the Triassic dolo-

mite is steeply inclined towards the southeast. North of Topolšica we can find the outcrops of Upper Carboniferous and Lower Permian age. The black shale, the quartz sandstone and conglomerate and the grey limestone are typical. In the vicinity of the Velenje fault there is a minor parallel fault along which the zone of Paleozoic husks is present. This zone consists of quartz conglomerate, shale and limestone.¹ The Velenje depression is a component part of a larger Velenje–Dobrna depression. The depression is placed between the Velenje fault in the north and the Šoštanj fault on the southern

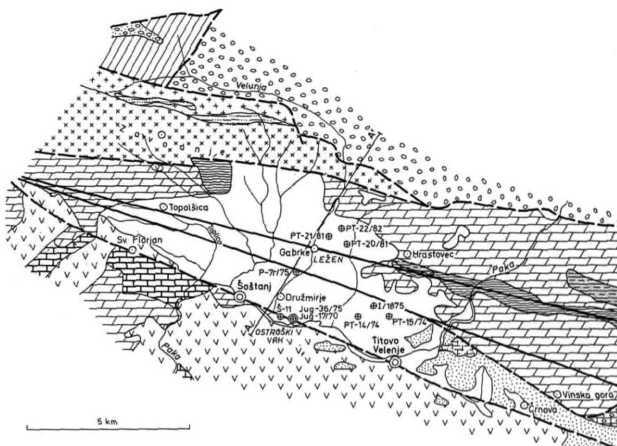


Figure 1: Geologic map of the Velenje depression and the surroundings¹

Slika 1: Geološka mapa velenjske depresije in okolice¹

edge following the quite right shape of the depression or a basin. The origin of the depression dates into the Styrian orogenic phase (Lower Miocene). At that time of general uplift of the territory, the Badenian lithotamnic limestone was sedimented upon the Egerian and Eggenburgian basement made of andesitic tuff and marly clay. North of the Velenje fault the Karawanke were ashore yet. At the end of Badenian period the sea withdraws. In the terrestrial phase in the Athic orogenic phase (lower Pliocene) the majority of Miocene sediments were eroded. The depression started to sink in the Rodian tectonic phase (middle Pliocene) as the upper Pliocene strata are proved yet in the roof of the coal seam.² As shown by boreholes that were bored through the Pliocene coal-bearing strata, the depression continued to sink through the complete Upper Pliocene.¹ The Gorenje–Šoštanj block is situated south of Šoštanj fault.

This block is built mostly of Oligocene andesitic tuffs and marly clay. Nearby these volcanic and clastic sediments there are some outcrops of Triassic dolomite and upper Permian black limestone found western and northwestern from Šoštanj¹ (Figures 1 and 2).

The coal seam of Pliocene age is syncline shaped and as such adapted to the paleomorphological and geological characteristics of the observed area. Along the Šoštanj fault the coal seam is thicker, but gets thinner towards the northeast. The thickening is also attributed to major sinking in the area around the Šoštanj fault. The deposit, represented with this single coal seam is 8.3 km long and round 1.5 km wide. In some areas around the Šalek valley there can be found other coal appearances in the shape of high ash coal layers, black organic clays, brown organic silt and clay. The depression is filled up with the sediments of Pliocene and Pleistocene age. The component parts of the depression fill are alternating layers of clays, silts, sands, pebbles, claystones, siltstones, marls and conglomerates. In-between the Velenje coal seam is placed.³ The sedimentary fill of the depression represents the complete sedimentation cycle, reaching from the terrestrial phase over marshy phase to the lacustrine phase. The floor strata are of Pliocene age and up to 400 m thick. In the lower part the floor is made of particles from surrounding rocks but higher the clay, silt and sands are present. These materials represent the first, lacustrine fill of the depression, but further on the sinking continued much more slowly and in the marshy environment a lot of organic substance has been deposited. Above the floor strata there are organic clays and high ash coal that pass into more pure coal. The coal seam thickness reaches up to 165 m at one point, but is on average around 60 m. After the marshy phase the sinking of the depression continued in the way that the

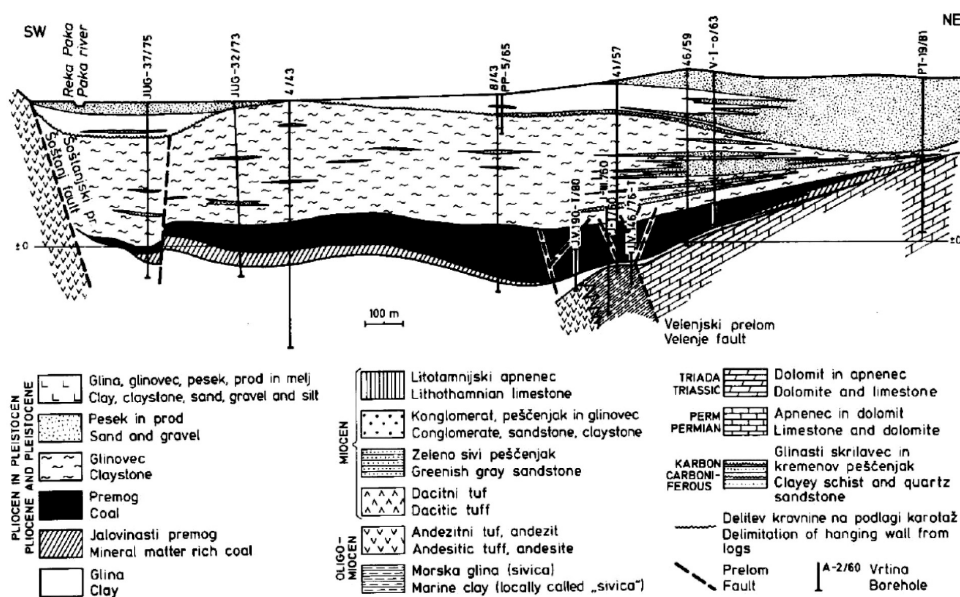


Figure 2: Cross-section through the Velenje depression oriented NE-SW, with underground outline of the coal seam³

Slika 2: Presek skozi velenjsko depresijo, orientirano SV-JZ s podzemnim prikazom ležišča premoga³

lake formed again and the roof sediments slowly filled the lake. Also above the coal there are Pliocene and Pleistocene sediments represented mainly by clays, sandy clays, mudstones and sands (Figure 2).

2 THE MINING METHOD

After 1970 the specially adapted longwall mining method has been developed in the Velenje Colliery. This method is tailored to great seam thickness and coal seam geometry, using a mechanized hydraulic shield roof support. Besides coal extraction the fill-in and hardening of the goaf behind the support is enabled. The coal is extracted in levels that follow each below other from the roof towards the floor. The longwall face is kind of divided into the upper and lower sectors. Longwall faces in the Velenje Colliery are 160 m to 200 m wide. The mine design imposes the extraction from edge of the seam towards the centre in slices that are from 400 m to 800 m long and from 3 m to 15 m high. The working process is completely mechanized using the hydraulic shield support and the shearer that cuts the coal. There is a chain conveyor installed to transport the coal from the

lower and the upper sector of the face. Coal extraction follows the retreating method where the designed block is developed to its boundary first and then mined back. Development means to elaborate the supply roadway (travel road or main gate or head gate) and the haulage roadway (belt road or tail gate), make the connection between them with the face roadway and enable the ventilation. As the chocks are installed the face advances and the shearer and shield support move forward and the goaf increases. This goaf collapses under the weight of the overlying strata. The upper sector of the face is won by slow movements of the canopy as the stress crushes the coal. The working cycle is complete when all the coal from the upper sector comes down. The working height of the face can be limited by calculation involving the thickness of the isolating clay layer above the coal seam. This clay layer protects the face against intrusions of water bearing sands.⁴ Considering the Velenje mining method the most important parameters are fractures in the rock and a roof strata collapse. This has to do with excavation principles and advancing techniques of mining. Because of the use of natural forces in the mining process the upper sector is a basis of high productivity of the face (Figures 3 and 4). Subsidence of

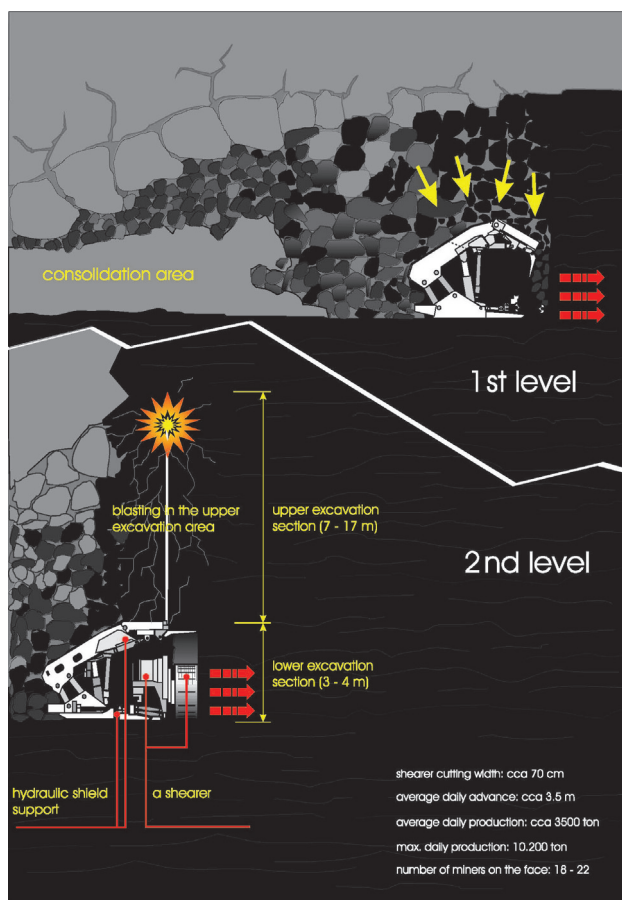


Figure 3: Cross-section of the hydraulic shield support with the principle of mining in the Velenje Colliery⁴

Slika 3: Presek hidravlične varovalne podpore z načinom izkopavanja v rudniku Velenje⁴

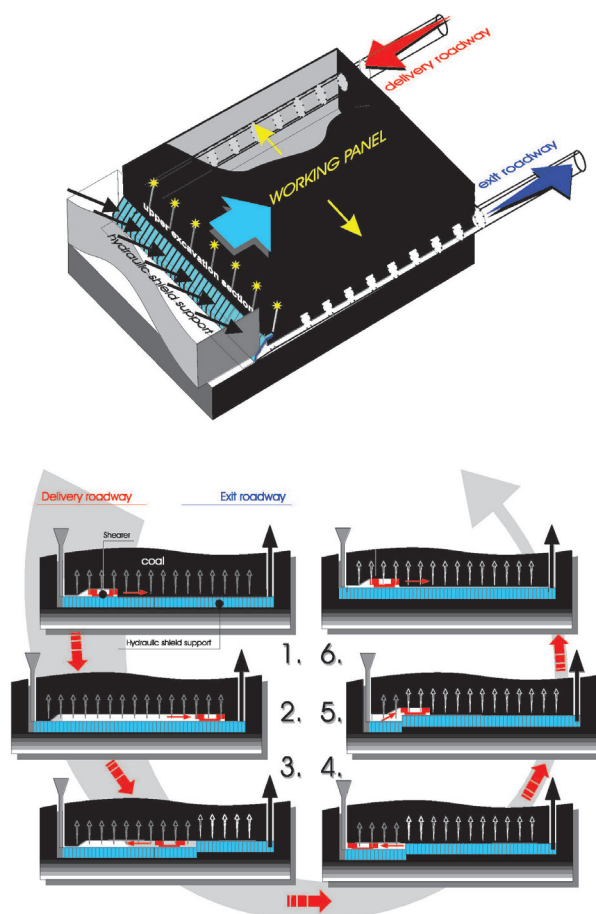


Figure 4: Layout of the longwall face with separate phases of coal extraction⁴

Slika 4: Izgled širokega čela z ločenimi fazami izkopavanja premoga⁴

the surface above excavated longwall faces resulted in formation of three subsidence lakes.

3 INDUCED SEISMICITY

Each change of natural stress condition in the Earth’s interior can result in a rock relaxation. The most common are the natural changes of the stress-state conditions, but starting with the extraction of raw materials the induced seismic events can be very frequent too. Seismicity in mines depends on mining depth and mining geometry, production percentage, geological anomalies (faults, dykes) and tectonic pressures. In an underground roadway the deformation and stress energy rise with depth and at the same time the possibility of a rock burst rises too, applied to all the roadway cross-section shapes.⁵ Rock burst by definition is a powerful collapse of the rock, occurring quite periodically in underground mining. Rapid excavation is followed by sudden rock collapse parallel to the face, inducing rock bursting. Most often the rock bursts are observed in hard and deformable rocks⁶, at processes of space enlargements caused by rapid excavation in mines and collieries. The development of better excavation methods of raw materials enabled the rise of production, but also caused rapid adjacent rock instability and seismic events occurrence. Due to seismic events increase, the systematic monitoring begun and resulted the finding of rock bursts mechanisms. J. C. Johnston and H. H. Einstein⁷ suggested six of them:

- Ore excavation at high vertical roof pressure;
- Roof collapse in underground roadway;
- Slipping along existing fault;
- Rock collapse in front of the advancing face;
- Fractured rock at the active face and on the opposite side of the face due to pressure growth;
- Bearing pillar collapse.

Based on further geological research and seismic record analyses, J. C. Johnston and H. H. Einstein⁷ defined two rock burst types shown in **Table 1**. Relation at Type I depends primarily on mining, longwall face rating and blasting schedule. Upper magnitude limit of the

Type I depends on the rock strength, but the epicenter location depends on the position of the mining site and its geometry. Rock burst intensity at Type II depends on the interaction between induced stress in mine area, tectonic stress area and fault possibility. Excavation depth is another one of the important criteria. Shallow mining can induce seismicity, but it is depending on a large number of parameters, like face depth, face rate, face geometry, tectonic stress, mining stress, fault zone proximity regarding face position⁷ (**Table 1**).

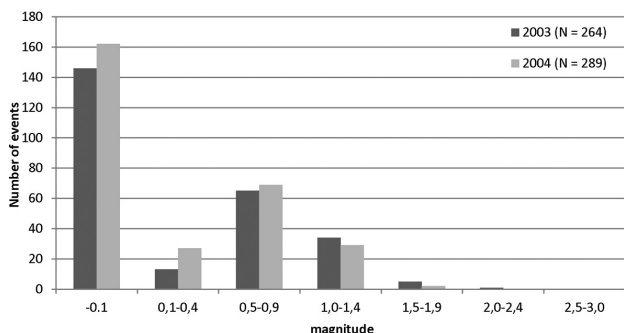
Table 1: Rock burst types⁷

Tabela 1: Vrste drobljenja kamenine⁷

TYPE I	TYPE II
In general the relation is a function of mining activity.	There are not enough data to define the relationship to mining relations.
Location is round 100 m inside of the face or inside existing weakness zone or the geological anomaly is close to the mine.	Location is set on the existing fault plane that can be up to 3 km away from the mine.
The rock can crack as the induced mining stresses exceed the shear strength of the rock. Crack planes can be variously oriented.	Occurs on existing tectonic faults. Mining can induce the events on faults with advantageous orientation.
High stress drops are often observed.	Stress drop is similar to natural earthquakes.
Magnitudes are low to medium.	High magnitudes are very likely.

4 SEISMICITY IN THE COLLIERY AREA

In 1999 the Velenje Colliery decided to set up a local observation site network in the Šalek valley. The decision was taken because of rock burst events in the mine and with the goal to locate the hypocenters of quakes better. The strongest quake reached intensity of IV–V after EMS-98⁸. Until then such measurements were only made in the state-owned observational network. The measurements in mine’s local network enable us to locate the weak seismic events in Šalek valley, but only in a range of the coal deposit dimensions. Underground observation sites system setup and calibration has been done by company K-UTEC Sondershausen.⁹ This digital seismic observation sites system for monitoring of rock bursts at longwall faces enables a precise location of seismic wave’s source and intensity.^{9,10,11} The surface system setup has been constructed by the Velenje Colliery staff.^{9,10,11} Such a network setup with regular sensor layout can ensure the systems accuracy from ±1 m to ±10 m.⁹ Based on such a network setup we recorded 289 seismic events, which were also recorded on the state network in 2004. Considering the underground and the surface system of Velenje Colliery there were 106 matches that undoubtedly belong to the Velenje Colliery area. Only four stronger seismic events met the requirements for kinematic analysis of focal quake mecha-



Graph 1: Number of events of specific magnitudes in the years 2003 and 2004

Graf 1: Število dogodkov s specifično magnitudo v letih 2003 in 2004

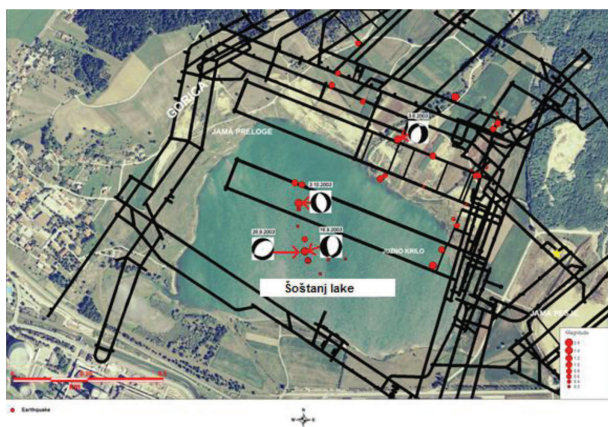


Figure 5: Focal mechanisms of four seismic events of which the signals could be interpreted for first moves

Slika 5: Žariščni mehanizmi štirih seizmičnih dogodkov, katerih signal je mogoče razlagati za prve premike

nism.¹² Figure 5 shows a certain part of localized events and the four analyzed too.

From analysis of four focal mechanisms in Figure 5, taking into consideration the classification¹³ shown in Figure 6, we can conclude that in all four events it is about the predominant normal component of the fault. We can explain this with sudden stress relaxation together with displacement in a crushed zone corresponding to subsidence due to mining.

The magnitude measurements showed practically insignificant magnitudes between 0 and 0.1 for most events. The next most frequent magnitudes were between 0.5 and 0.9 in 2004 and 2005. The highest magnitude

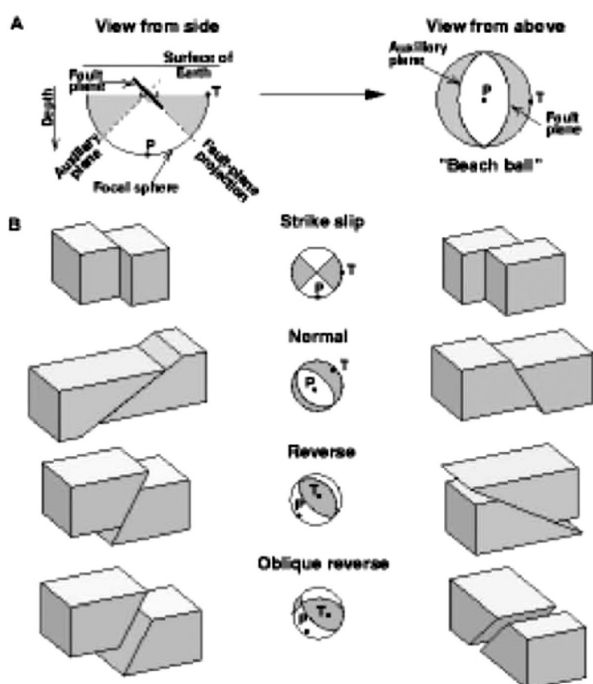


Figure 6: Faults with the corresponding focal mechanisms¹³

Slika 6: Poškodbe z ustreznim žariščnim mehanizmom¹³

was 2.4 in 2003 and 1.6 in 2004. From Graph 1 we can conclude that the majority of the seismic events are not detected by the Šoštanj inhabitants. In the Šalek valley area the state seismic observational network did record one larger event not recorded by the local colliery network. We are not able to locate this event precisely enough without data from local network. Many recorded events in both networks have the dominant event frequency larger than 3 Hz. According to the size and localities of seismic event occurrences it is possible to conclude that all of them are Type-I rock bursts. The only event that could be classified as Type II is the larger one, but there are not enough data to localize it more precisely.

5 STEEL ARCH SUPPORT AND ROCK BURSTS

At the moment of rock burst occurrence a powerful collapse of the rock takes place. Rapid excavation is followed by sudden rock collapse parallel to the face, inducing rock bursting.⁶ From experience we know the support damages occur as a consequence of rock bursts (Figure 7). Rock burst reduction can be achieved through some specific measures, one of these being slowdown of the coal production speed, but such a measure is a very undesirable one as the production speed is one of the key parameters of the colliery's economics.^{14,15}

Following the reports made in department for safety at work we can find that support damages in the mine rarely exceed 50 m. In the case of shorter damage segments the displacement at joints is larger, but in case of longer damage segments the displacement at joints is smaller. Observations show the possibility of combinations at damage sections up to 50 m where certain joints get larger and others get smaller deformations or somewhere deformations are not noticeable at all. Figure 7 shows deformations after the rock burst where at the middle two joints the shift is 0.37 m while the other two



Figure 7: Damages on K24 support after a rock burst

Slika 7: Poškodbe na podporju K24 po hribinskem udaru

joints remained practically without any deformation. In case of this specific rock outburst the damaged section reached 50 m in length but not all of the joints were equally damaged. Resulting from the Velenje Colliery local seismic network and seismic stations in Slovenia, Italy, Austria, Hungary and Croatia measurements we know that such events rarely exceed 1,5 magnitude after Richter.

In 2011 and 2012 the mechanic characteristics of existing support have been analyzed in context of rock burst exploration. The K24-type steel arch support is currently in use in the Velenje Colliery. This support type is thermally treated (hardened) meaning the arch is more flexible. In cases where larger pressure acts on steel arch support K24 this support reacts in a discontinuous yielding manner (sudden relaxation). The support has been sent to a certified laboratory in Oprava, Czech Republic for a comparative test. For comparison the support type TH29 has been chosen while relaxing the stress in significantly shorter deformation intervals.¹⁶ Results of the loaded support joint deformations comparative tests are shown in **Graph 2**. As seen from **Graph 2** the majority of TH29 support joints relax the stress in short deformation intervals while this is not the case for joints of the K24 support. Also seen from **Graph 2**, that compares clamp samples of K24 and TH29 support, the K24 clamp yields at 380 kN load resulting in deformation of 0,031 m momentary displacement. Knowing the deformation displacement on the clamp at given force we can calculate the deformation work with the following Equation (1):

$$W_{\text{def}} = F \times s \quad (1)$$

where W_{def} – deformation work (J), F – force of load (N) and s – deformation displacement (m), resulting for one clamp 11.78 kJ. Following the reports made in department for safety at work we can find that support damages in the mine rarely exceed 50 m. Considering the fact that each frame has got seven joints and three frames are installed per one meter of the underground

roadway we can calculate the number of joints that yield on the length of 50 m with the next Equation (2):

$$S_{\text{tot}} = (L \times (N - 1) + 1) \times S \quad (2)$$

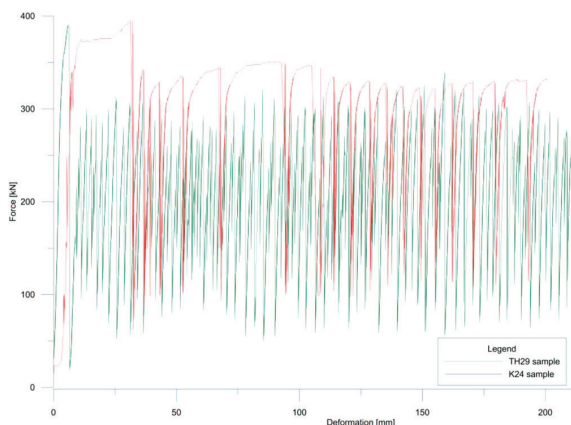
where S_{tot} – number of all support joints, L – length in meters, N number of frames per meter and S number of clamps. In case of rock burst in length of 50 m the number of clamps is 707. We can make a calculation of common deformation energy needed for deformation of 707 clamps by multiplication of number of clamps and deformation work: 707 clamps \times 11.78 kJ/clamp results: 8.34 MJ. Regarding the Equation (3):¹⁷

$$M_L = (\lg(W_{\text{def}} \times 10^7) - 11.8)/1.5 \quad (3)$$

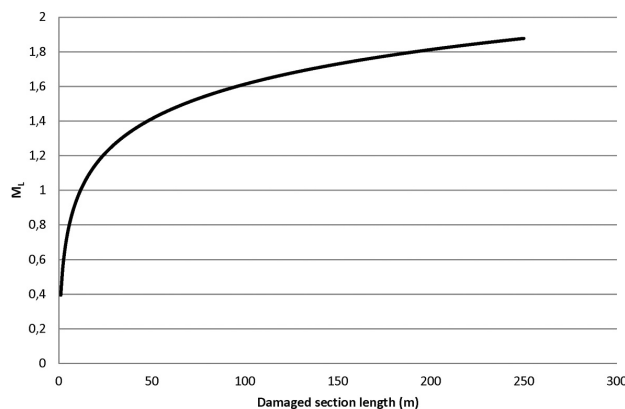
where M_L – local magnitude of seismic waving, this energy is equivalent to Richter local magnitude $M_L = 1.41$. **Graph 3** shows relation between support deformation length and local magnitude M_L . From **Graph 3** taking into account **Graph 1** follows that sudden support yielding rarely exceeds 50 m length and this complies with rock burst observation experience.

6 DISCUSSION

Results of our multiannual research show that it is possible to relate the seismic events and the activities in the Velenje Colliery. Majority of seismic events is very weak and therefore not detectable and do not represent any disturbance to local inhabitants. In spite of the previous fact such events are uncomfortable or even fatal for miners or other workers in the mine. In 1970 the specially adapted longwall mining method was developed that is tailored to great seam thickness and coal seam geometry using mechanized hydraulic shield roof support. This method significantly improved the economics of underground coal production. From the other side, the excavation speed increases the imbalance in the stress state of the fractured and damaged rock behind the longwall face. As a consequence of that inside the rock the stress is accumulated and can be suddenly relaxed,



Graph 2: Comparison of stress relaxation on K24 and TH29 support
Graf 2: Primerjava sproščanja napetosti na K24 in TH29 podporju



Graph 3: Local magnitude M_L size in dependence of damaged section length

Graf 3: Velikost lokalne magnitude M_L v odvisnosti od dolžine poškodovanega odseka

causing a rock burst. The coal production speed is economically very important and therefore not to be decreased, but there are some other specific measures that can help to reduce the stress relaxation in the zone of the fractured and damaged rock. Seismic events analysis indicates the possibility to determine the focal points of the most seismic events. It is also possible to establish that most seismic events are under the $M_L = 1.5$ value. Regarding their dynamics and localities of seismic events occurrences, it is possible to conclude that all of them are Type-I rock bursts. Until now, the events of Type II were not recorded with the local Velenje Colliery seismic system. Some larger events recorded only in the state network of seismological observation stations indicate the possibility of their presence but without any detection in the local network the precise localization is not possible. Further analysis of satisfactory recorded seismic events in both networks indicates the probability of these seismic events to be a consequence of stress relaxation in fractured rock. As well, from the other side, based on underground observation we know that during rock bursts the deformation of steel arch support is usually not longer than 50 m. In terms of energy this corresponds to measured seismic events in the Velenje Colliery area. It is also true that rock bursts leave effects on shorter distances too but we have to bear in mind that in such cases deformations in clamp areas are larger. In spite of the fact that these statements are initial findings of multiannual research, in our opinion the way of joint deformation on steel arch support is the reason for rock burst occurrence in the Velenje Colliery. Therefore, we suggest that Velenje Colliery as a measure for rock burst reduction starts to substitute the existing K24 support with another one which enables the gradual stress relaxation together with gradual deformation as for example the TH29 support.

Our next suggestion to Velenje Colliery is to consider activities for stress relaxation in spots more exposed to rock bursts. One of these activities might be blasting in flank boreholes filled with minor explosive amounts. Before boring the flank boreholes a very precise micro locations map of potential rock bursts is required. Elaboration of such map requires a fixed underground monitoring system so the existing mobile system needs to be replaced. In addition to improved monitoring system the stress measurements on steel arch support need to start. In case of reaching the limit yield values, a clear danger of rock burst is indicated. Based on better localization and monitoring of stress increase at joints, the precise procedure of preventive blasting will be prescribed.

7 CONCLUSIONS

From the research we can see the connection between support type and rock bursts. Support type that blocks continuous stress relaxation in form of minor deforma-

tions can cause stress accumulation and in case of overburden the support deformation is large. Such event results the rock burst, hurting people and damaging mine facilities. In order to reduce the rock bursts we suggest to Velenje Colliery the following:

- Start to introduce the steel arch support capable of stress relaxation in form of constant short deformations.
- Set up a fixed rock burst occurrence monitoring system.
- Develop in-seam stress monitoring system (pressure cells installed in rock).
- Test the loaded arch support frames for in-arch stress measurements development.
- Develop relaxation blasting procedures using boreholes.
- Set up rock burst description database.

Ongoing research should be directed into possibility of rock burst Type-II occurrence. These rock bursts can cause more severe seismic events along otherwise stable fault structures that become active because of excavation conditioned disturbed spatial geophysical equilibrium.

Acknowledgments

This study was financially supported by the research project L1-5451 funded by Slovenian Research Agency (ARRS).

8 REFERENCES

- ¹ A. Brezigar, B. Ogorelec, L. Rijavec, P. Mioč, *Geološka zgradba predpliocenske podlage Velenjske udorine in okolice*, Ljubljana, *Geologija*, (1987) 30, 31–65
- ² A. Brezigar, A. Šercelj, F. Velkoverh, D. Vrhovšek, G. Kosi, *Paleontološke raziskave pliokvartarne skladovnice Velenjske udorine*, Ljubljana, *Geološki zbornik*, (1983) 3, 31–33
- ³ A. Brezigar, *Premogova plast Rudnika lignita*, Velenje, Ljubljana, *Geologija*, (1985/86) 28/29, 319–336
- ⁴ F. Žerdin, E. Dervarič, *The velenje mining method: a system of longwall sub-level caving extraction*, *Glückauf*, 134 (1998) 7/8, 383–392
- ⁵ K. S. Guha, *Induced Earthquake*, Dordrecht: Kluwer Academic Publishers, 2000, 314
- ⁶ P. J. Bardet, *Finite Element Analysis of Rockburst as Surface Instability*, Elsevier Science Publishers, *Computers and Geotechnics*, (1989) 8, 177–193, doi:10.1016/0266-352X(89)90042-6
- ⁷ J. C. Johnston, H. H. Einstein, *A survey of mining associated rockbursts*, *Proc. 2nd Int. Symp. On Rockburst and Seismicity in Mines*, Rotterdam, Balkema 1990, 121–128
- ⁸ J. Bajc, M. Živčič, M. Gostinčar, *Seizmična aktivnost v Šaleški dolini spomladi 2002*, *Potresi*, (2004) 2002, 55–70
- ⁹ J. Mayer, M. Mavec, I. Zadnik, R. Lah, *Spremljanje rudarsko induciranih seizmičnih pojavov v Premogovniku Velenje*, *RMZ-mater. geoenviron.*, (2002) 1, 51–60
- ¹⁰ J. Likar, E. Dervarič, M. Medved, J. Mayer, G. Vižintin, *Monitoring and analyses of seismic events at the Velenje coal mine*, *Acta geotech. Slov.*, (2008) 5, 20–28
- ¹¹ M. Medved, E. Dervarič, G. Vižintin, J. Likar, J. Mayer, *Analysis of seismic events at the Velenje Coal mine*, *RMZ-mater. geoenviron.*, (2008) 4, 464–475

G. VIŽINTIN et al.: ROCK BURST DEPENDENCY ON THE TYPE OF STEEL ARCH SUPPORT IN THE VELENJE MINE

- ¹² T. Živec, Analiza potresne dejavnosti na območju premogovnika Velenje, diplomsko delo, Ljubljana, 2005, 69
- ¹³ A. V. Cronin, A Draft Primer on Focal Mechanism Solution for Geologists, Baylor University, 2004
- ¹⁴ M. Medved, I. Ristović, J. Rošar, M. Vulić, An overview of two years of continuous energy optimization at the Velenje coal mine, *Energies (Basel)*, **(2012)** 5, 2017–2029, doi:10.3390/en5062017
- ¹⁵ I. Ristović, M. Stojaković, M. Vulić, Recultivation and sustainable development of coal mining in Kolubara basin. *Therm. sci.*, **(2010)** 3, 759–772, doi:10.2298/TSCI091123002R
- ¹⁶ R. Podjatke, H. Witthaus, J. Breedlove, Development in Steel Roadway Support – A Track Record, 27th International Conference on Ground Control in Mining, **(2008)**, 358–365
- ¹⁷ B. Gutenberg, F. C. Richter, Magnitude and Energy of Earthquakes, *Science*, **(1936)** 83, 183–185

EFFECT OF CUTTING PARAMETERS ON THE DRILLING OF
AlSi₇ METALLIC FOAMSVPLIV PARAMETROV REZANJA PRI VRTANJU KOVINSKIH PEN
IZ AlSi₇Gultekin Uzun¹, Ugur Gokmen², Hanifi Cinici¹, Mehmet Turker¹¹Gazi University, Faculty of Technology, 06500 Ankara, Turkey²Gazi University, Vocational School of Technical Sciences, 06500 Ankara, Turkey
uzun.gultekin@gazi.edu.tr*Prejem rokopisa – received: 2015-05-27; sprejem za objavo – accepted for publication: 2015-12-17*

doi:10.17222/mit.2015.106

In this study, the behaviors of Al matrix metallic foams, produced by the powder-metallurgy method, against the hole-drilling operation were examined. The stirred Al, 7 % Si and 1 % TiH₂ powders were pressed in a mould under uniaxial pressure (600 MPa) and then deformed, and in this way foamable block samples were obtained. The block samples were subjected to a foaming process at 710 °C. The obtained samples were drilled at different cutting speeds (10, 30, 50, 70) mm/min and feed rates (0.15, 0.225, 0.30) mm/r with drill tips of different diameters (4, 5 and 6) mm. It was observed that the foam affected the chip breakings and chip adhesions increased in proportion to the cutting speed. In the deviation from circularity, the feed rate turned out to be a more effective parameter than the cutting speed.

Keywords: foams, cutting, machining, tooling

V študiji je bilo preiskovano obnašanje kovinskih pen na osnovi Al, izdelanih po metodi metalurgije prahov, pri vrtanju luknje. Mešanica Al, 7 % Si in 1 % TiH₂ prahov je bila stisnjena v orodju z enosnim tlakom (600 MPa) in potem deformirana, da so bili dobljeni vzorci sposobni za penjenje. Vzorci so bili izpostavljeni procesu penjenja pri temperaturi 710 °C. Dobljeni vzorci so bili vrtani pri različnih hitrostih rezanja (10, 30, 50, 70) mm/min in hitrostih podajanja (0,15, 0,225, 0,30) mm/r, s svedri z različnimi premeri (4, 5, 6) mm. Ugotovljeno je, da pena vpliva na lomljenje ostružkov, oprijemanje ostružkov pa se povečuje proporcionalno s hitrostjo rezanja. Pokazalo se je, da na odstopanja od kroga bolj vpliva hitrost podajanja kot pa hitrost rezanja.

Ključne besede: pene, rezanje, strojna obdelava, orodja

1 INTRODUCTION

Foams of cellular structure and materials having high porosity are materials on which intensive studies are made due to their combination of mechanical and physical properties.¹ Maintaining the high-temperature strength and structure of metallic foams with respect to porous polymer materials is one of their important characteristics.² Al has a great importance among the metallic foams.³ Nowadays, these materials are used in engineering applications and attract a lot of attention.⁴ Al foams are known with their thermal strength, acoustic insulation, and sound- and energy-absorbency properties.⁵ They can be used as a filling material in profiles for energy absorption.⁶ Among their areas of usage, automotive and space industry lead, especially where a lower density is needed.⁷ The machines that are being used in industrial applications are subjected to vibration and dynamic loads during running. These vibration and dynamic loads cause high noise and wear in the moulds. For the purpose of minimizing these problems aluminum foams are preferred in the machine manufacturing because of their low- and high-energy damping abilities.⁸ In the industrial applications, metallic foams can be joined with bolts and rivets because of their porous struc-

tures. During the drilling of foams, cutting and feed speeds cause the breakdown or plastic deformation of porosities. Besides the chip formation that occurred the during drilling operation, it also affects the cutting speed and cutting temperature. For this reason the surface quality and gauge accuracy of the hole change.⁹⁻¹³

In this study, Al matrix metallic foams were produced by the powder-metallurgy (PM) method. For the purpose of examining the effect of the foaming time period on the porosity morphology, foaming was carried out for different periods (8, 10, 12, 14 and 16) min. After determining a suitable foaming period, depending on the porosity structure, foam samples of 25×40×120 mm were produced. Al foams of high porosity were subjected to drilling at different cutting speeds (10, 30, 50, 70) m/min and feed rates (0.15, 0.225, 0.30) mm/r with drill tips of different diameters (4, 5, and 6 mm). During the drilling operation, effects of the cutting parameters on the cutting force were examined by measuring the cutting forces. After the drilling operation, measurements of the deviation from circularity were made and the samples were compared, depending on the process parameters.

2 MATERIALS AND METHOD

2.1 Material

In the experimental studies, Al powders and Si powders with 99.9 % purity were used as the matrix material and 98 % pure TiH₂ powders as the foaming agent. The physical properties of the used powders are given in **Table 1**.

Table 1: Physical properties and production methods of the powders used in the tests

Tabela 1: Fizikalne lastnosti in metode izdelave prahov, uporabljenih pri preizkusih

Materials	Physical properties			
	Production method	Melting temperature (°C)	Density (g/cm ³)	Powder size (µm)
Aluminum	Gas atomization	660	2.7	<160
Si	Gas atomization	1410	2.34	<10
TiH ₂	–	<400	3.91	<45

2.2 Method

2.2.1 Aluminum foam production

7 % Si and 1 % TiH₂ (both by weight) were added to 99.9 % pure Al powder and stirred for 1 h. The powder mixture was pressed one-way in a mould under 600 MPa pressure and block samples were obtained. The obtained samples were subjected to preheating at 550 °C for 1 h. Then, the samples were 50 % deformed and cut for foam production in (10 × 40 × 120) mm sizes (**Figure 1**). Foamable block samples were subjected to the foaming process at 710 °C and Al foams of (25 × 40 × 120) mm were obtained.

2.2.2 Drilling operation

Drilling tests were made at the Johnford VMC 550 CNC vertical machining center. As the cutting tool, uncoated HSS (DIN 338) drills (manufactured by the WERKO cutting tool company) having (4, 5, and 6) mm diameter were employed. The technical characteristics and cutting parameters of the HSS drills used in the tests are given in **Table 2**.

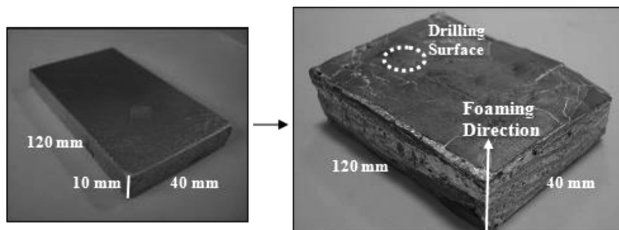


Figure 1: Sample picture before and after foaming process
Slika 1: Posnetek vzorca pred in po postopku penjenja

Table 2: Cutting-tool characteristics and cutting parameters

Tabela 2: Značilnosti rezilnega orodja in parametri rezanja

Cutting tool materials	HSS
Standard	DIN 338
Cutter geometry	Ø4, Ø5, Ø6, mm 118°
Cutting speed	10, 30, 50, 70 m/min
Feed rate	0.15, 0.225, 0.30 mm/r
Cutter type	Cylindrical shank drill

Drilling tests were made under dry cutting conditions and 15 mm deep longitudinal holes were drilled. Taking into consideration the heat distribution around the drilled hole, the distance between the hole axes was specified to be 8 mm.

In the drilling operation, among the three force constituents, since the radial and cutting forces are relatively small, the third force constituent which is axial force (feed force, F_z) and torque (M_z) values are taken into consideration. In this study, three cutting-force constituents were measured, but only the axial force (F_z) was evaluated. Because of the porous structure of the material, variations occurred in the axial force. For this reason the maximum-cutting force values were taken as a reference for the axial force. Cutting-force measurements were made with a Kistler 9257A type dynamometer attached to the vertical machining center worktop. An attachment mould was designed and manufactured for better attachment of the samples to the dynamometer. In **Figure 2** the test set-up is given. For the purpose of eliminating the twisting effect on the drill, the dislocation distance of drill tip from the tool holder was kept to a minimum. This value remained constant in all of the tests to determine the comparison accuracy in the obtained data.

Deviation from circularity is defined as the difference between the biggest and smallest radius measured from a certain center point (**Figure 3a**). However, there are several ways of determining a hole center. There are widely used methods such as the minimum radial deviation (MRD), in which the point of the smallest radial deviation is assumed to be the center and the least-squares circle (LSC). In the measurements of deviation from circularity of the holes using CMM, the

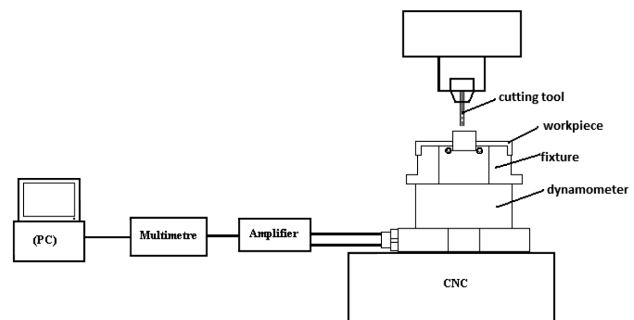


Figure 2: Test set-up
Slika 2: Eksperimentalni sestav

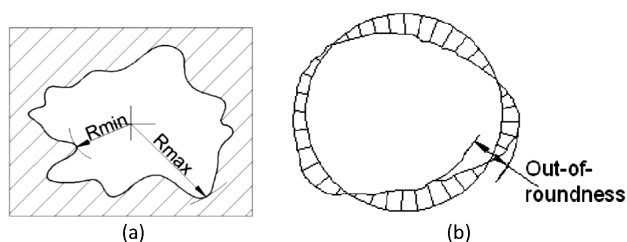


Figure 3: Circularity measurements: a) DFC-deviation from circularity, b) LSC-least squares circle.¹²

Slika 3: Merjenja krožnosti: a) DFC-odstopanja od krožnosti, b) LSC-krog najmanjših kvadratov.¹²

LSC method was employed for the determination of the center point. The LSC method center point expresses the center of the circle, having the sum of least squares of the radial coordinates (**Figure 3b**).

The measurements of DFC of the drilled holes were carried out with a Mitutoyo CMM (Coordinate Measuring Machine). The deviation from circularity and from the hole diameter were determined by taking coordinates from at least three separate points in each hole by using a $\varnothing 4$ mm prop.

3 EXPERIMENTAL RESULTS AND DISCUSSION

3.1 Pore morphology and density

In the foam production by pore morphology (PM) method the parameters must be selected properly and the process must be controlled.¹⁴ Banhart, in his study, examined the linear expansion of Al/TiH₂ mixture that was subjected to the foaming process at 750 °C and stated that linear expansion varied with respect to the time and in the case of exceeding the maximum expansion duration, the adhesion of pores and then breakdowns started.¹⁵ In the case of suitable foaming duration it is

possible to produce a homogeneous structured foam with high porosity. The pore morphologies of Al foams obtained in the experimental studies are given in **Figure 4**. In the produced foams, the highest density value (1.01 g/cm³) was obtained in the foaming processes lasting for 8 min, whereas the lowest value (0.58 g/cm³) was obtained in the foaming processes for 16 min. When the pore morphology (**Figure 4a**) obtained in the foaming process for 8 min is examined, it is clearly seen that certain areas remained without foaming. This is attributed to the insufficient foaming duration. The porosity structure of the 16 min foaming process is shown in **Figure 4c**. With the increasing of the foaming duration thinning on the pore walls and partial adhesions of pores were observed. It is thought that adhesion of the pores is leading to pore coarsening and causing a decrease in density. It can be said that parallel to the pore structure and the obtained density (10 min – 0.88 g/cm³) the ideal foaming duration is 10 and 12 min (**Figure 4b**). When time saving is considered, it is thought that 10 min foaming duration will be sufficient.

Mechanical characteristics of metallic foams may vary depending on the shape size and surface area of the pores in the structure. Mechanical characteristics of the foam structure are mostly affected by the density and metal matrix specification.¹⁶ The mechanical performance of Al matrix foams is evaluated depending on the microstructural properties and the pore geometry. Pore wall thickness and side geometry involve microstructural variables. Geometrical characteristics involve pore shape, pore size and the distribution and defects in the pore structure.¹⁷ During 10 min of foaming duration in which the homogeneous distribution of pore structures were observed, drilling (with different diameters) was applied to the obtained foams (**Figure 5**). When the sec-

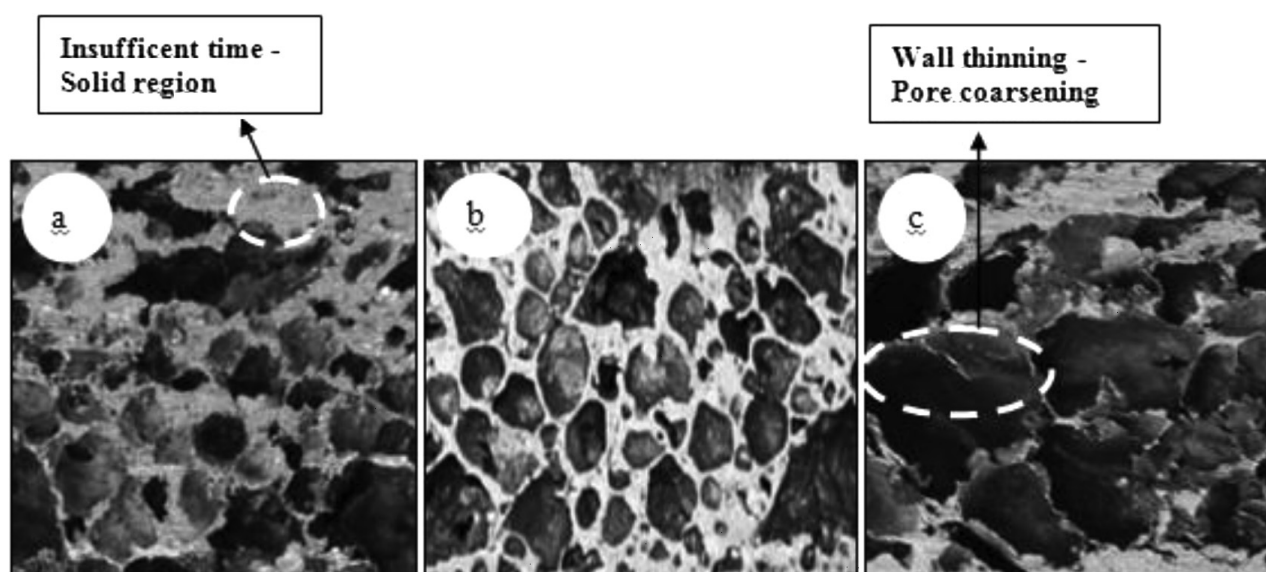


Figure 4: Effect of foaming duration on pore morphology: a) 8 min, b) 10 min, c) 16 min

Slika 4: Vpliv trajanja penjenja na morfologijo por: a) 8 min, b) 10 min, c) 16 min

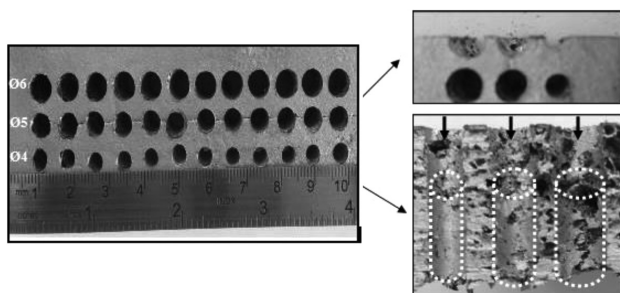


Figure 5: Pictures of drilling surface and holes section of Al foam sample

Slika 5: Posnetek vrtane površine in presek lukenj na vzorcu Al pene

tional pictures of drilled surfaces given in **Figure 5** were examined, closure and regional concentrations were located on the pores, depending on the effect of the drilling force. H. Bart-Smith et al.¹⁸, in a study on the energy-damping capacity of Al foams, mentioned the distribution of regional deformation bands and accumulation depending on the compression deformation. In their study, during drilling, it is thought that the pores around the drill tip joined partially (depending on the applied pressure) and regional concentrations were created.

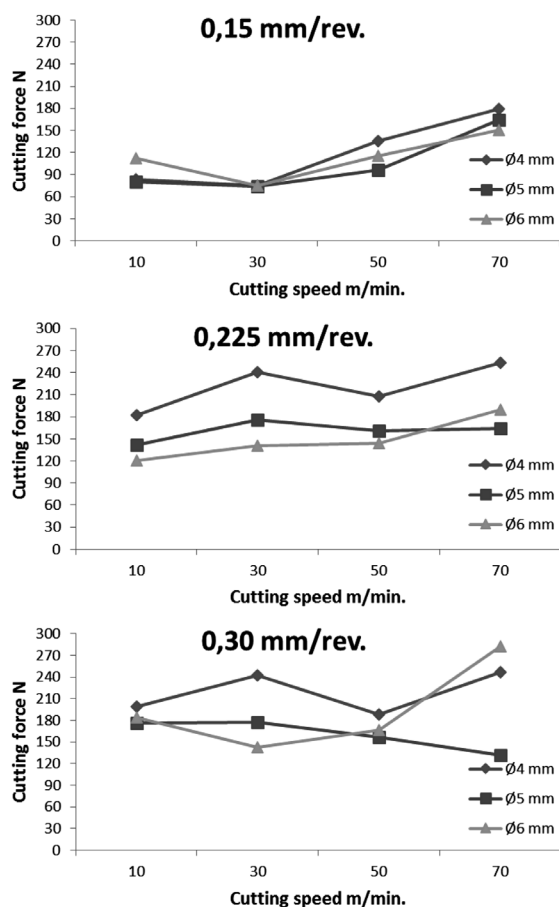


Figure 6: Variation in feed force depending on the cutting speeds, feed amount and drill diameter

Slika 6: Spreminjanje sile podajanja v odvisnosti od hitrosti rezanja, podajanja in premera svreda

3.2 Evaluation of cutting forces

The variation of feed force (F_z) values with respect to the cutting force, feed and tool type of the holes obtained after the drilling operations is given in **Figure 6**. From this figure it is clear that for all three cutting types, the obtained feed force values increased with the increasing cutting speed and feed. The increased feed values caused the chip volume removed per unit time to increase and consequently growing of cutting forces.^{19,20} With the increasing feed amount, the feed force increased in the interval of 200–500 %. From the graphs it was observed that feed force was 80–164 N at the 0.15 mm/r feed amount, 120–254 N at 0.225 mm/r and 132–282 N at 0.30 mm/r. The feed force increased for all feed rates with the increasing cutting speed. This was attributed to the higher adhesion tendency of the Al material on the cutting tool. The adhesion criteria on the cutting tool are clearly seen in **Figure 7**.

In **Figure 7** it is clearly seen that the chip adhesions increase with increasing cutting speed. During machining of aluminum and some aluminum alloys, the chip is continuous, quite thick, strong and is not broken easily. An increase was observed in the cutting forces with the increasing difficulty of the hard chip discharge. Difficulties in the chip discharge depending on drilling length, which is the most important problem in drilling operations, cause the chips to squeeze in the hole, to increase the cutting forces and even to break the tool.^{21–23} It was seen that due to the porous structure in the foam material, chip breakings failed with the increasing cutting speed and more material adhered on the cutting tool. Chips were broken at lower cutting speeds and fewer adhesions were observed. With the increasing feed amount, formation of more chip caused higher feed

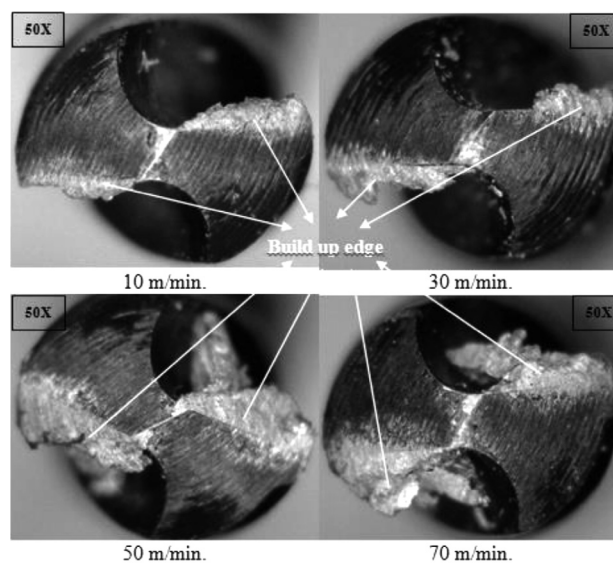


Figure 7: Built-up edge on the cutting tool with the increasing cutting speed

Slika 7: Nastajanje roba na rezilnem orodju pri naraščanju hitrosti rezanja

force, whereas at lower feed rates less feed force was created. In all feed rates and cutting speeds the highest cutting force was obtained with Ø4 mm drills. This can be explained with the cutting tool of small diameter causing extensive squeezing of the chips. The lowest feed forces were obtained with Ø6 mm drill.

3.3 Evaluation of hole diameters

In the literature it is stated that the diameter in the hole inlet and deviation from circularity (*DFC*) values are higher with respect to the hole outlet because of the dynamic instability of cutting tool in the first entry to the hole. It is said that there are decreases in these values along the hole inlet and outlet and this is due to guidance of the hole to the drill till the hole outlet.¹² For the purpose of providing a comparison accuracy, deviation values in the hole diameter were obtained by the measurements made at the hole inlet. Variations in the diameter values of the holes drilled under different cutting conditions and cutting parameters are given in **Figure 8**.

From the **Figure 8** it was observed that at 0.15 and 0.225 mm/r feed rate, the hole diameter values decreased with the increase of cutting speed, whereas at 0.30 mm/r feed rate, hole diameter values increased. At 0.15 and 0.225 mm/r feed rate, increasing of cutting speed caused decreases of 11 % in hole diameters for all drills. The increasing tendency in the hole diameters depending on cutting speed at the highest feed rate (0.30 mm/r) was measured to be 16 % in the Ø4 mm drill, 23 % in the Ø5 mm drill and 7 % in the Ø6 mm drill. It is thought that the increasing cutting and feed speeds caused the hole diameters to get bigger by increasing the vibrations.²⁴ It was decided that fewer deviations in the hole diameters

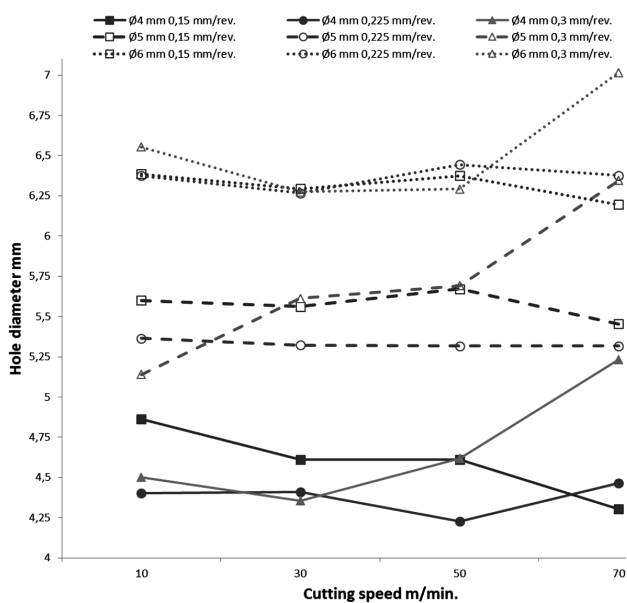


Figure 8: Variations in the hole diameters depending on the cutting parameters and cutting conditions

Slika 8: Spreminjanje premera luknje v odvisnosti od parametrov rezanja in pogojev pri rezanju

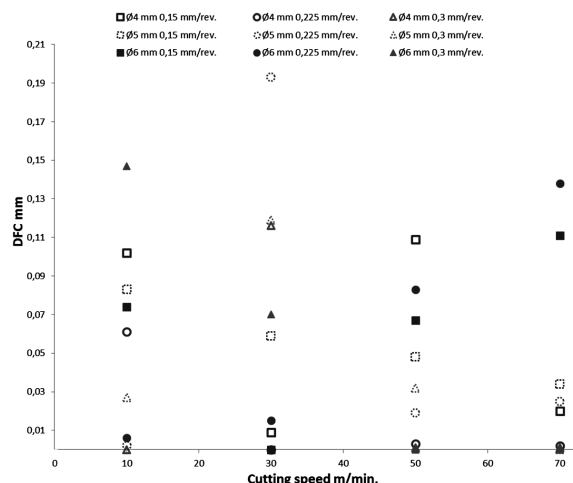


Figure 9: Variations of *DFC* depending on cutting parameters and cutting conditions

Slika 9: Spreminjanje *DFC* od parametrov rezanja in pogojev pri rezanju

are due to less vibration at lower feed rate and slower penetration into the pieces. During the cutting operation, bending and shape variations occur in the material at the feed direction due to its porous structure. This can be more clearly seen at higher feed rates. For this reason, higher deviations from the diameter were determined at higher feed rates. It can be said that the feed rate is more effective than the cutting speed for the increase in the hole diameters.

When the *DFC* graph (**Figure 9**) was examined, a maximum *DFC* value of 0.2 mm was recorded. Decreases were observed in the *DFC* values with the increases in cutting speed. Especially at 70 m/min cutting speed and 0.3 mm/r feed rate, the lowest *DFC* values were obtained. The effect of feed rate on the *DFC* value at 50 m/min cutting speed is seen more clearly. Decreases were observed in the *DFC* values with the increase in the feed rate. This can be explained with the more rapid penetration and less distortion on the surface. At lower feed rates, overcontact of drill to the hole walls caused the *DFC* value to increase. As far as the *DFC* is concerned, the feed rate was more effective than the cutting speed.

4 CONCLUSION

In this study, the effect of different foaming durations on the pore structure of Al foam material was examined and the foaming duration for homogenous pore distribution was determined. The obtained samples were drilled with drills of different diameters at different feed rates and cutting speeds. The behaviors of the Al foam structure were evaluated during the drilling operation, depending on the drilling parameters. The obtained data as a result of the experimental study is given below.

Feed forces increased with the increase in cutting speed. This can be explained by the increasingly harder chip discharge.

Feed force exhibited increases in the interval 200–500 % with the increase in feed amount.

Foamed structure affected the chip breakings causing an increase in chip adhesions proportionally with the cutting speed.

The highest feed forces were measured with Ø4 mm drills, whereas the lowest ones were determined with Ø6 mm drills.

The lowest *DFC* values were obtained with Ø6 mm drills by using the tool on which the lowest feed forces occurred.

Feed rate turned out to be a more effective parameter than the cutting speed for *DFC*.

In all of the cutting tools, *DFC* was less at the higher cutting speed and higher feed rate combinations.

5 REFERENCES

- ¹ J. Banhart, Manufacture, characterization and application of cellular metals and metal foams, *Progress in Materials Science*, 46 (2001), 559–632, PII: S0079-6425(00)00002-5
- ² P. S. Liu, K. M. Liang, Functional materials of porous metals made by P/M, electroplating and some other techniques, *Journal of Materials Science*, 36 (2001) 21, 5059–5072, doi:10.1023/A:1012483920628
- ³ P. R. Onck, R. Merkerk, J. T. M. De Hosson, I. Schmidt, Fracture of metal foams: In-situ testing and numerical modeling, *Advanced Engineering Materials*, 6 (2004) 6, 429–431, doi:10.1002/adem.200405156
- ⁴ A. Kim, M. A. Hasan, S. H. Nahm, S. S. Cho, Evaluation of compressive mechanical properties of Al-foams using electrical conductivity, *Composite Structures*, 71 (2005) 2, 191–198, doi:10.1016/j.compstruct.2004.10.016
- ⁵ Y. Y. Zhao, D. X. Sun, A novel sintering-dissolution process for manufacturing Al foams, *Scripta Mater.*, 44 (2001), 105–110
- ⁶ L. E. G. Cambroner, J. M. Ruiz-Roman, F. A. Corpas, J. M. Ruiz Prieto, Manufacturing of Al-Mg-Si alloy foam using calcium carbonate as foaming agent, *Journal of Materials Processing Technology*, 209 (2009), 1803–1809, doi:10.1016/j.jmatprotec.2008.04.032
- ⁷ J. Banhart, J. Baumeister, Deformation characteristics of metal foams, *Journal of Materials Science*, 33 (1998), 1431–1440, doi:10.1023/A:1004383222228
- ⁸ R. Neugebauer C. Lies, J. Hohlfield, T. Hipke, Adhesion in sandwiches with aluminum foam core, *Production Engineering*, 1 (2007) 3, 271–278, doi:10.1007/s11740-007-0046-4
- ⁹ S. Kalidas, R. E. DeVor, S. G. Kapoor, Experimental investigation of the effect of drill coatings on hole quality under dry and wet drilling conditions, *Surface and Coatings Technology*, 148 (2001) 2–3, 117–128, doi:10.1016/S0257-8972(01)01349-4
- ¹⁰ R. P. Zeilmann, W. L. Weingaertner, Analysis of temperature during drilling of Ti6Al4V with minimal quantity of lubricant, *Journal of Materials Processing Technology*, 179 (2006) 1–3, 18–23, doi:10.1016/j.jmatprotec.2006.03.077
- ¹¹ S. Yağmur, A. Acır, U. Şeker, M. Günay, An Experimental Investigation of Effect of Cutting Parameters on Cutting Zone Temperature in Drilling, *Journal of the Faculty of Engineering and Architecture of Gazi University*, 28 (2013) 1, 1–6
- ¹² T. H. Mohammed, Hole quality in deep hole drilling, *Materials and Manufacturing Processes*, 16 (2001) 2, 147–164, doi:10.1081/AMP-100104297
- ¹³ S. Mohan, H. S. Shan, Analysis of Roundness Error and Surface Roughness in the Electro Jet Drilling Process, *Materials and Manufacturing Processes*, 21 (2006) 1, 1–9, doi:10.1081/AMP-200060398
- ¹⁴ U. Gökmen, M. Türker, Effect of Al₂O₃ Addition on the Foamability Behaviour of Aluminum And Alumix 231 Based Metallic Foam, *Journal of the Faculty of Engineering and Architecture of Gazi University*, 27 (2012) 3, 651–658
- ¹⁵ J. Banhart, Manufacture, characterization and application of cellular metals and metal foams, *Progress in Materials Science*, 46 (2001), 559–632, PII: S0079-6425(00)00002-5
- ¹⁶ A. Uzun, U. Gökmen, H. Cinici, H. Koruk, M. Türker, Investigation of modal properties of AISi₇ foam produced by powder metallurgy technique, *Material Testing*, 55 (2013) 7–8, 598–601, doi:10.3139/120.110475
- ¹⁷ A. H. Benouali, L. Froyen, J. F. Delerue, M. Wevers, Mechanical analysis and microstructural characterisation of metal foams, *Materials Science and Technology*, 18 (2002) 5, 489–494, doi:10.1179/026708302225002056
- ¹⁸ H. Bart-Smith, A. F. Bastawros, D. R. Mumm, A. G. Evans, D. J. Sypeck, H. N. G. Wadley, Compressive deformation and yielding mechanisms in cellular Al alloys determined using X-Ray tomography and surface strain mapping, *Acta Materialia*, 46 (1998) 10, 3583–3592, doi:10.1016/S1359-6454(98)00025-1
- ¹⁹ Sandvik Coromant, *Modern Metal Cutting*, Sandvikens Tryckeri, Sweden, 1994, 2–61
- ²⁰ G. Uzun, I. Korkut, The effect of cryogenic treatment on tapping, *The International Journal of Advanced Manufacturing Technology*, 67 (2013) 1–4, 857–864, doi:10.1007/s00170-012-4529-x
- ²¹ K. W. Kim, T. K. Ahn, Force prediction and stress analysis of a twist drill from tool geometry and cutting conditions, *International Journal of Precision Engineering and Manufacturing*, 6 (2005) 1, 65–72, http://www.dbpia.co.kr/Article/686491
- ²² M. Pirtini, I. Lazoglu, Forces and hole quality in drilling, *International Journal of Machine Tools & Manufacture*, 45 (2005) 11, 1271–1281, doi:10.1016/j.ijmactools.2005.01.004
- ²³ L. J. Wang, X. Wang, H. F. Zhao, Effect of the cutting ratio on cutting forces and the drill life in vibration drilling, *The International Journal of Advanced Manufacturing Technology*, 24 (2004) 11–12, 865–872, doi:10.1007/s00170-003-1803-y
- ²⁴ M. Kurt, Y. Kaynak, E. Bağcı, Evaluation of drilled hole quality in Al 2024 alloy, *The International Journal of Advanced Manufacturing Technology*, 37 (2008) 11–12, 1051–1060, doi:10.1007/s00170-007-1049-1

A METAMATERIAL-EMBEDDED WIDE-BAND ANTENNA FOR THE MICROWAVE C-BAND

ŠIROKOPASOVNA ANTENA Z VGRAJENIM METAMATERIALOM ZA MIKROVALOVNI C-PAS

Md. Ikbal Hossain¹, Mohammad Rashed Iqbal Faruque¹, Mohammad Tariqul Islam², Atiqur Rahman¹

¹Space Science Center (ANGKASA), 43600 UKM, Bangi, Selangor, Malaysia

²University Kebangsaan Malaysia, Department of Electrical, Electronic and Systems Engineering, 43600 UKM, Bangi, Selangor, Malaysia
ipk_eee@yahoo.com

Prejem rokopisa – received: 2015-06-30; sprejem za objavo – accepted for publication: 2015-12-15

doi:10.17222/mit.2015.145

In this paper a metamaterial-embedded, compact microstrip-fed patch antenna is introduced for microwave C-band applications. The proposed antenna is composed of a rectangular metamaterial-embedded patch, microstrip-fed line and a partial ground plane. The finite-integration technique (FIT) based on Computer Simulation Technology (CST) Microwave Studio is utilized in this study. The measurements of antenna performances are conducted in a near-field measurement laboratory. The antenna performance parameters comprising the reflection coefficient, radiation efficiency, gain, and radiation pattern are studied to validate the antenna performance. The measured results show that the proposed metamaterial-embedded antenna exhibits a wide impedance bandwidth over the C band (from 3.77 GHz to 6.58 GHz). The results also indicate good radiation efficiency and antenna gain with a nearly omni-directional radiation pattern at the frequencies of interest.

Keywords: antenna, head model, substrate material

V članku je predstavljena kompaktna mikrotrakasta antena v obliki obliža, z vgrajenim metamaterialom za uporabo v mikrovalovnem C-pasu. Predlagana antena je sestavljena iz v obliž vgrajenega metamateriala pravokotne oblike, iz linije iz mikrovlakna za napajanje in z delno ozemljeno površino. V študiji je uporabljena tehnika končne integracije (FIT), ki temelji na tehnologiji računalniške simulacije (CST) Microwave Studio. Meritve zmogljivosti antene so bile izvedene v gluhi sobi merilnega laboratorija. Za oceno zmogljivosti antene so bili izmerjeni parametri zmogljivosti, ki obsegajo koeficient refleksije, učinkovitost sevanja, izkoristek in sevalni diagram. Izmerjeni rezultati kažejo, da ima antena z vgrajenim metamaterialom širok impedenčni pas v C pasu (od 3,77 GHz do 6,58 GHz). Rezultati kažejo tudi na dobro učinkovitost sevanja antene in izkoristek antene s skoraj vsesmernim diagramom sevanja na frekvencah interesa.

Ključne besede: antena, glava modela, material podlage

1 INTRODUCTION

With the exponentially increasing need for electronic communications, interest in designing a broadband antenna with a wide frequency coverage is increasing. The microstrip antenna offers a low-profile, conformal design, ease of manufacture and integration, and it is low cost and lightweight.¹ Although the microstrip patch antennas have a low profile and compact size characteristics, they suffer from a narrow bandwidth and low gain, and a poor polarization purity and tolerance problem.²⁻³ In the past decade, various techniques have been proposed to enhance the bandwidth of microstrip antennas with an increasing substrate thickness⁴, using slots on radiating patches⁵, using magneto dielectric substrates⁶, and stacking different radiating elements.⁷

A wide-band antenna of wide-slot belonging to a microstrip line was designed using a fork-like tuning stub to increase the bandwidth.⁸ This design approach successfully showed a wide bandwidth but an antenna gain changing below 1.5 dBi over the complete operational frequency bands. A slotted microstrip antenna was

proposed for enhancing the bandwidth printed on an FR-4 substrate with about 2.01 dBi antenna gain.⁹ Nowadays, metamaterials are being used in antenna engineering to enhance the antenna's performance and reduce the antenna's sizes. However, the electromagnetic band gap (EBG) or metamaterial can also be used to enhance the antenna performance, such as the antenna gain and impedance bandwidth.¹⁰ The bandwidth enhancement of a microstrip patch antenna was performed using planar artificial magnetic conductor (AMC) surface.¹¹ A compact wide-band microstrip antenna was proposed with a modified patch and ground plane using a metamaterial.¹²

In this paper, a wide-band microstrip-fed patch antenna is proposed for microwave C-band radar applications. For the antenna-bandwidth enhancement, the metamaterial structure is incorporated with the antenna patch. Moreover, the antenna performance in terms of radiation efficiency, gain, and gain radiation pattern are analyzed in this study.

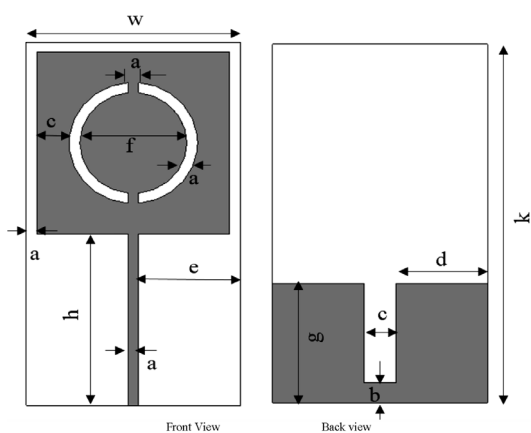


Figure 1: Proposed antenna geometry
Slika 1: Predlagana geometrija antene

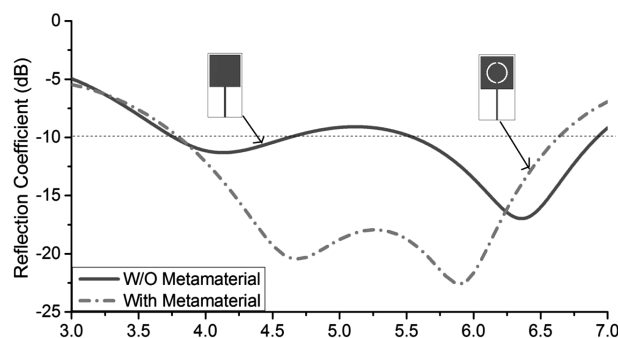


Figure 3: Reflection coefficient of proposed antenna with and without metamaterial

Slika 3: Koeficient sevanja predlagane antene, z in brez metamateriala

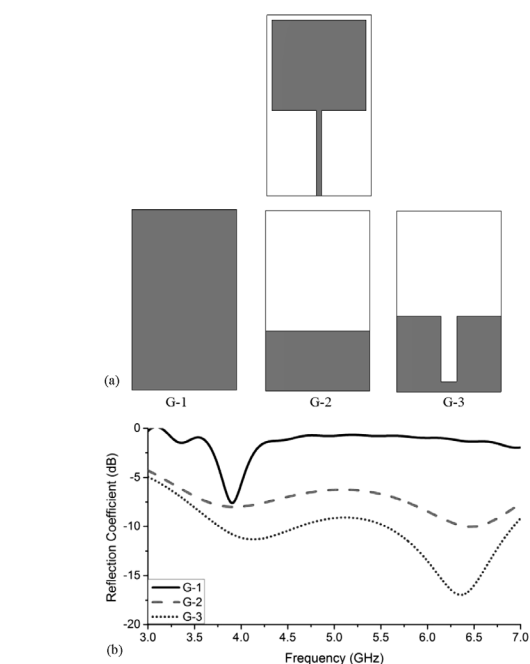


Figure 2: Antenna design phases: a) ground plane configurations and b) reflection coefficient for different configurations

Slika 2: Faze sestavljanja antene: a) konfiguracija osnovne plošče in b) koeficient odseva pri različnih konfiguracijah

2 ANTENNA DESIGN

Figure 1 shows the geometry of the proposed microstrip antenna. The antenna consists of a rectangular patch with metamaterial, a partial ground plane and a printed microstrip line. A circular split-ring resonator with two slots is used as a metamaterial structure. The excitation is fed between the microstrip line and the ground using an SMA connector of 50Ω normalized impedance. A 0.8-mm-thick, FR-4 sheet with a 4.6 relative permittivity is used as the substrate.

Table 1: Antenna design specifications

Tabela 1: Specifikacija zgradbe antene

Parameter	Value (mm)	Parameter	Value (mm)
a	1	f	10
b	2	g	12
c	3	h	17
d	8.5	k	36
e	9.5	w	20

The antenna specifications are listed in **Table 1**. The antenna design investigation was based on the finite-investigation technique (FIT) of the CST microwave studio. A prototype of the proposed antenna is fabricated using

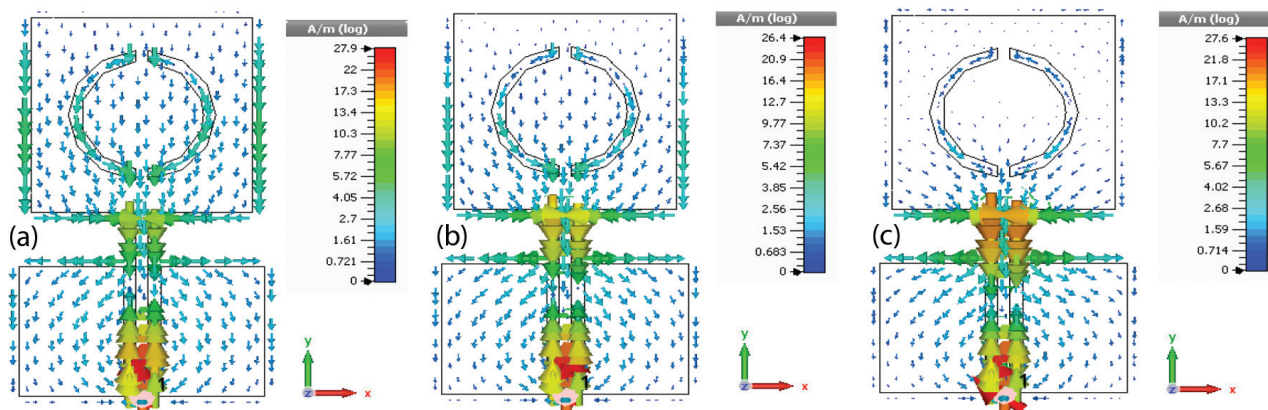


Figure 4: Surface current distribution of proposed antenna at: a) 4.5 GHz, b) 5 GHz and c) 5.5 GHz

Slika 4: Razporeditev toka po površini predlagane antene pri: a) 4,5 GHz, b) 5 GHz in c) 5,5 GHz

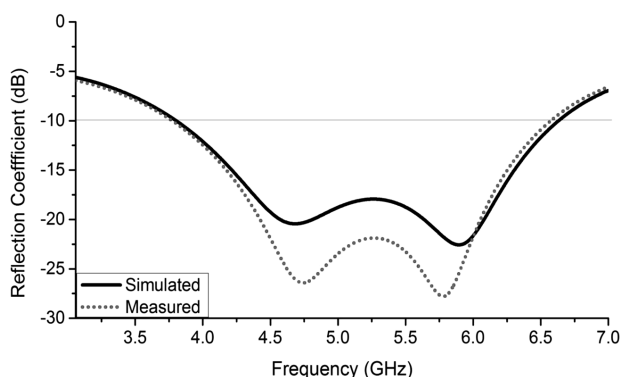


Figure 5: Simulated and measured reflection coefficient of the proposed antenna

Slika 5: Simuliran in izmerjen koeficient odseva predlagane antene

the printed-circuit technique for measurement in an anechoic chamber. The total antenna dimensions are $36 \times 20 \times 0.8$ mm. At first, the proposed antenna is considered as a simple microstrip patch antenna with full ground plane (g-1), as indicated in **Figure 2a**. Secondly, a partial ground plane (g-2) is used to get a wide bandwidth. Finally, a slotted partial ground plane (g-3) is taken for the least back reflections. The reflection coefficient of the antenna with three different ground plane configurations is plotted in **Figure 2b**. The reflection coefficients of the proposed antenna with and without the metamaterial are plotted in **Figure 3**. The results indicate that the incorporation of the proposed metamaterial with an antenna leads to a dramatically wider antenna impedance bandwidth. The surface current distributions of the proposed metamaterial antenna are given in **Figure 4** comprising frequencies at 4.5 GHz, 5 GHz, and 5.5 GHz considering a zero phase of the input signal. The results show that the lower frequency response of the antenna depends significantly on the antenna patch. On the other hand, the antenna patch length does not affect the response of the antenna at the upper frequencies.

3 ANALYSIS AND RESULTS

According to **Figure 5**, the proposed antenna exhibits a wide bandwidth 2.81 GHz (from 3.77 GHz to 6.58

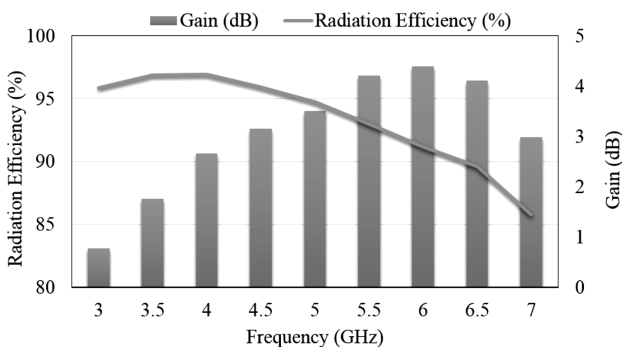


Figure 6: Peak gain and radiation efficiencies of the proposed antenna
Slika 6: Največji izkoristek in učinkovitost sevanja predlagane antene

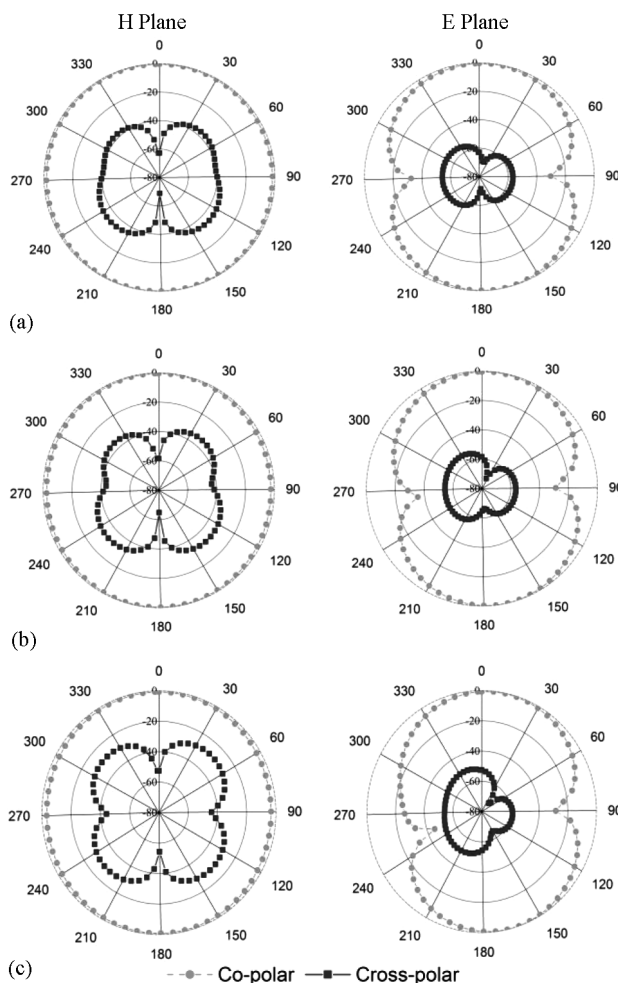


Figure 7: Radiation pattern at: a) 4.5 GHz, b) 5 GHz, and c) 5.5 GHz
Slika 7: Diagram sevanja pri: a) 4,5 GHz, b) 5 GHz in c) 5,5 GHz

GHz). Very good agreement is observed between the measured and simulated results, indicating an almost identical bandwidth. According to the measured reflection coefficient, the antenna's fractional bandwidth is 54.97 % at the central frequency. The measured results of the peak gain and radiation efficiency of the proposed antenna are plotted in **Figure 6**. The antenna radiation efficiency varies from 85 % to 97 % for different frequencies.

On the other hand, the proposed antenna exhibits an antenna peak gain from 1 dB to 4.5 dB for different frequencies. However, the proposed antenna shows very good radiation efficiency and gain over the operating frequency range of the antenna. **Figure 7** indicates the measured gain radiation pattern of the proposed antenna at 4.5 GHz, 5 GHz, and 5.5 GHz. The results show near omni-directional radiation patterns in the H plane. The results at other frequencies of the C band exhibit very similar patterns as plotted, indicating stable radiation patterns are obtained. The radiation patterns of the proposed antenna are quite similar to the planar quarter-wavelength mono-pole antenna.¹³

4 CONCLUSIONS

In this paper, a wide-band antenna for microwave C-band application is proposed. The bandwidth enhancement is obtained using metamaterial incorporation with an antenna patch. The results indicate that the proposed antenna exhibits a wide impedance bandwidth from 3.77 GHz to 6.58 GHz. The results also indicate good radiation efficiency and antenna gain with a nearly omnidirectional radiation pattern at the frequencies of interest. This antenna can be used in long-distance radar communication systems.

5 REFERENCES

- ¹ H. Elsadek, *Microstrip Antennas for Mobile Wireless Communication Systems*, INTECH Open Access Publisher, 2010, doi:10.5772/7705
- ² D. M. Pozar, *Microstrip antennas*, *The Proceedings of IEEE*, 80 (1992) 1, 79–91, doi:10.1109/5.119568
- ³ T. Alam, M. R. I. Faruque, M. T. Islam, N. Misran, *Composite-material printed antenna for a multi-standard wireless application*, *Mater. Tehnol.*, 49 (2015) 5, 745–749, doi:10.17222/mit.2014.232
- ⁴ R. Garg, *Microstrip antenna design handbook*, Artech House, 2001
- ⁵ J. Lao, R. Jin, J. Geng, Q. Wu, *An ultra-wideband microstrip elliptical slot antenna excited by a circular patch*, *Microwave and Optical Technology Letters*, 50 (2008) 4, 845–846, doi:10.1002/mop.23240
- ⁶ L. Yousefi, B. Mohajer-Iravani, O. M. Ramahi, *Enhanced bandwidth artificial magnetic ground plane for low-profile antennas*, *IEEE Antennas and Wireless Propagation Letters*, 6 (2007), 289–292, doi:10.1109/LAWP.2007.895282
- ⁷ B. L. Ooi, S. Qin, M. S. Leong, *Novel design of broad-band stacked patch antenna*, *IEEE Transactions on Antennas and Propagation*, 50 (2002) 10, 1391–1395, doi:10.1109/TAP.2002.802087
- ⁸ J. Y. Sze, K. L. Wong, *Bandwidth enhancement of a microstrip-line-fed printed wide-slot antenna*, *IEEE Transactions on Antennas and Propagation*, 49 (2001) 7, 1020–1024, doi:10.1109/8.933480
- ⁹ J. Y. Jan, J. W. Su, *Bandwidth enhancement of a printed wide-slot antenna with a rotated slot*, *IEEE Transactions on Antennas and Propagation*, 53 (2005) 6, 2111–2114, doi:10.1109/TAP.2005.848518
- ¹⁰ N. Engheta, Nader, Richard W. Ziolkowski, eds. *Metamaterials: physics and engineering explorations*, John Wiley & Sons, (2006), ISBN: 978-0-471-76102-0
- ¹¹ R. C. Hadarig, M. E. De Cos, F. Las-Heras, *Microstrip patch antenna bandwidth enhancement using AMC/EBG structures*, *International Journal of Antennas and Propagation*, 2012 (2011), doi:10.1155/2012/843754
- ¹² H. Xiong, H. O. N. G. Jing-Song, T. A. N. Ming-Tao, L. I. Bing, *Compact microstrip antenna with metamaterial for wideband applications*, *Turkish Journal of Electrical Engineering and Computer Science*, 21 (2013) 2, 2233–2238, doi:10.3906/elk-1204-6
- ¹³ M. R. I. Faruque, M. I. Hossain, M. T. Islam, *Low specific absorption rate microstrip patch antenna for cellular phone applications*, *IET Microwaves, Antennas & Propagation*, 9 (2015) 14, 1540–1546, doi:10.1049/iet-map.2014.0861

EROSION WEAR RESISTANCE OF TITANIUM-MATRIX COMPOSITE Ti/TiN PRODUCED BY DIODE-LASER GAS NITRIDING

ODPORNOST KOMPOZITA PROTI EROZIJSKI OBRABI Ti/TiN IZDELANEGA S PLINSKIM NITRIRANJEM S POMOČJO DIODNEGA LASERJA

Aleksander Lisiecki¹, Agnieszka Kurc-Lisiecka²

¹Silesian University of Technology, Faculty of Mechanical Engineering, Welding Department, Konarskiego 18A, 44-100 Gliwice, Poland

²University of Dąbrowa Górnicza, Rail Transport Department, Cieplaka 1c, 41-300 Dąbrowa Górnicza, Poland
aleksander.lisiecki@polsl.pl

Prejem rokopisa – received: 2015-06-30; sprejem za objavo – accepted for publication: 2016-02-05

doi:10.17222/mit.2015.160

A prototype experimental stand equipped with a novel high-power direct diode laser (HPDDL), characterized by unique properties of the laser beam, was applied for producing titanium-matrix composite (TMC) surface layers during the laser gas nitriding (LGN) of the titanium alloy Ti6Al4V in the liquid state. The erosion wear characteristic of the substrate and nitrided surface layers was investigated. It was found that the erosion wear resistance of the composite surface layers is significantly higher than the substrate of titanium alloy Ti6Al4V. The erosion wear resistance depends on the angle of incidence. Reducing the angle of incidence decreases the weight loss of the composite surface layers and simultaneously increases the weight loss of the Ti6Al4V. It was found that the weight loss of the composite surface layer with the highest resistance is over six times lower compared to the Ti6Al4V, at an incident angle of 15°.

Keywords: laser nitriding, titanium alloy, diode laser, erosion wear, composite

Prototipno eksperimentalno stojalo opremljeno z novim diodnim laserjem velike moči (HPDDL), značilnem po edinstvenih lastnostih laserskega žarka, je bilo uporabljeno za izdelavo površinske plasti kompozita na osnovi titana (TMC), med plinskim nitriranjem z laserjem (LGN) titanove zlitine Ti6Al4V, v staljenem stanju. Preiskovane so bile značilnosti erozijske obrabe podlage in nitrirane površine. Ugotovljeno je bilo, da je odpornost na erozijsko obrabo kompozitne površinske plasti občutno večja v primerjavi s podlago iz titanove zlitine Ti6Al4V. Odpornost na erozijsko obrabo je odvisna od vpadnega kota. Zmanjšanje vpadnega kota zmanjšuje izgubo teže površinske kompozitne plasti in hkrati poveča izgubo teže Ti6Al4V. Ugotovljeno je, da je izguba teže kompozitne površinske plasti, z največjo odpornostjo, pri vpadnem kotu 15°, več kot šestkrat manjša v primerjavi z Ti6Al4V.

Ključne besede: nitriranje z laserjem, titanova zlitina, diodni laser, erozijska obraba, kompozit

1 INTRODUCTION

Titanium alloys, thanks to their excellent strength-to-weight ratio and excellent corrosion resistance, are widely used in aerospace, automotive, power plant, maritime, and many other industries.¹⁻⁶ The most commonly used titanium alloy is Ti6Al4V (Grade 5 according to ASTM). Light metals and alloys are of particular importance in aerospace. For example, more than half of the rotating parts of a modern turbofan aircraft engine are made of titanium alloys, including the rotors and fan blades.⁷⁻⁹ Similarly, the blades made of titanium alloys are commonly used in the steam turbines of high-power generators.¹⁰⁻¹³ Titanium alloys are also used for manufacturing parts for turbochargers, air and hydraulic pumps, turbines and impellers, etc.¹⁴⁻¹⁶ In each of the above cases, the working surfaces are exposed to wear, mainly by erosion or cavitation erosion.^{1,17} For example, the engines of planes, helicopters, and other aircraft, as well as rocket engines are often subjected to severe erosion from sand and dust particles, drops of

rain, or other solid and hard particles in flight and also during manoeuvres at the airport or landing pad.¹⁸⁻²⁰

However, titanium alloys, and particularly pure titanium, do not possess high resistance to erosive wear because of the relatively low surface hardness.¹⁻⁶ Therefore, various methods to modify the surface of the titanium alloys are used in industry, and also new methods and techniques are being developed.^{1-6,21}

Among the many methods of surface modification of titanium alloys, one of the most efficient is laser gas nitriding (LGN).² Y. Fu et al.² have studied different methods for improving the erosion resistance of pure titanium. They have found that the laser surface treatment of titanium in a nitrogen atmosphere provides the best results and a significant improvement of the erosion resistance compared to other methods of surface treatment and the deposition of surface layers.²

Although the LGN method was invented in 1983, it is still being developed. The reason for this is the continuous development of laser devices and associated with this advances in laser technology.^{1,4} The LGN process for

titanium and titanium alloys has been widely studied by scientists, and also there are plenty of articles in this field. However, most of the articles concern the structure, morphology, corrosion resistance, tribology and mechanical properties of the surfaced layers produced by gaseous CO₂ and solid-state YAG lasers.^{4,22} There are only a few publications on the application of high-power diode lasers (HPDLs) in the process of titanium nitriding and also there is no information on the erosion wear resistance of surface layers nitrided by HPDLs.^{23–25}

In the present work, a novel continuous wave (CW) HPDL emitted in the near-infra-red band at 808 nm, with a rectangular laser beam spot and a uniform energy distribution across the spot was applied for producing surface layers on the titanium alloy Ti6Al4V during LGN. The erosion wear resistance of the Ti6Al4V alloy before and after the LGN process at different angles of incidence was investigated.

2 EXPERIMENTAL PART

The titanium alloy Ti6Al4V (Grade 5 according to ASTM B265) with the nominal chemical composition 6.29 Al, 4.12 V, 0.14 C, 0.18 Fe in % of mass fractions and balance Ti was chosen for investigations of the nitriding process. The specimens of titanium alloy for the nitriding tests and for the erosion tests were cut into coupons 50.0×100.0 mm from a hot-rolled sheet having a thickness of 3.0 mm. The specimens of titanium alloy used for the erosion tests were mechanically ground by 180-grit SiC paper and cleaned. In turn, the specimens for LGN tests were mechanically ground and degreased with acetone prior to the nitriding tests.

The trials of LGN were carried out by means of a fully automated prototype stand equipped with a novel high-power direct diode laser (HPDDL) characterized by direct emission of the laser beam, rectangular laser-beam spot with a width of 1.8 mm and a length of 6.8 mm at a given configuration of optics and a short wavelength of 808 nm.

The short wavelength is advantageous because of the efficiency of the heat transfer to the metal surface as a result of Fresnel absorption. In this case the absorption coefficient on the surface of the titanium alloy for the 808 nm wavelength is significantly higher compared to the wavelength of gaseous CO₂ lasers and even compared to the solid-state lasers. Additionally, the multi-mode and even energy distribution of the laser radiation along the longer side of the beam spot ensures the uniform irradiation of the laser-treated surface and a uniform temperature distribution across the processing track.⁴ In order to ensure the full control of the processing atmosphere, the samples were placed in a nitrogen-filled chamber. The pure nitrogen (99.999 % purity) was supplied into the chamber at flow rate of 10.0 L/min and a pressure of 1.0 atm. The nitrogen flow was switched in advance of about 90 s to remove the air from the

chamber. The laser beam was delivered into the chamber through a transparent cover made of tempered glass. The rectangular beam was focused on the top surface of the specimens and the beam spot was set transversely to the scanning direction. The test surface layers were produced as single stringer beads during linear scanning of the surface by the laser beam in a pure nitrogen atmosphere. The test surface layers were produced at different processing parameters, and thus a different heat input of nitriding. The processing parameters are given in **Table 1**.

Table 1: Parameters of the laser gas nitriding of the titanium alloy Ti6Al4V by the HPDDL

Tabela 1: Parametri plinskega nitriranja z laserjem titanove zlitine Ti6Al4V z HPDDL

No. of surface layer	Scanning speed, mm/min	Laser output power, W	Heat input, J/mm	Power density, kW/cm ²
S1	200	1000	300	8.17
S2	200	800	240	6.54
S3	200	600	180	4.90

The erosion tests were performed in accordance with the ASTM G76 standard for a determination of the erosion rate by solid particles' impingement in a gas stream. The apparatus used to carry out the erosion tests was built strictly in accordance with the requirements of the standard. The solid particles used for the erosion tests were natural angular alumina sands with a size of 50 μm. The erodent particles were fed from a disk powder feeder and accelerated from a nozzle by pressured dry air. The pressured air was supplied from a cylinder and the pressure was stabilized by a two-stage pressure reducer. The air pressure was adjusted to provide the particle velocity of 70 m/s. The feed rate of the abrasive sand was set at 2.0 g/min. The distance from the nozzle tip to the tested surface was kept at 10.0±0.5 mm. A nozzle having an inner diameter of 1.5 mm and a length of 50 mm was applied. A rotary sample holder allowed for a change in the angle of the particles' impingement on the surface from 15° to 90°. Prior to the erosion test of the surface layers and the base metal, a calibration of the particles' velocity was performed according to the procedure given in the ASTM G76 standard. The material used for the calibration was C22 annealed steel, according to EN 10250-2 (1020 steel according to AISI).

All the erosion tests were performed under ambient conditions with a temperature of about 25 °C and a relative humidity of 45–50 %.

The base metal Ti6Al4V titanium alloy and the surface layers were eroded for 5 and 10 minutes at impact angles of 15°, 30°, 45° and 90°.

The weight of the samples was measured before and after the erosion test using a laboratory scale with an accuracy of ±0.01 mg. Prior to the measurements of weight, each sample was cleaned with compressed air and the weight was measured three times in order to

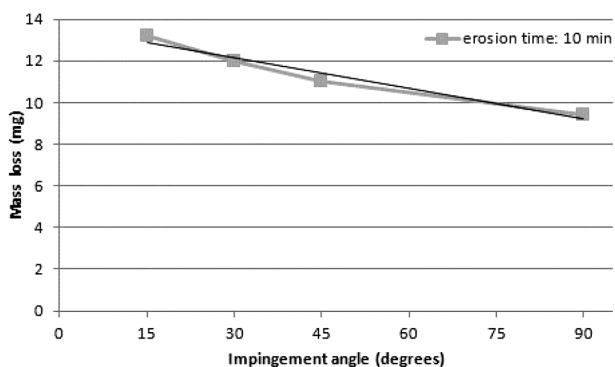


Figure 1: Relationship between the mass loss and impingement angle for erosion of the base metal Ti6Al4V

Slika 1: Odvisnosti med izgubo mase in vpadnim kotom pri eroziji osnovne kovine Ti6Al4V

determine the mean value and to provide the high accuracy of the measurement.

Subsequently, the eroded surfaces were analysed with a scanning electron microscope (SEM) to identify the mechanisms of wear and mass loss.

3 RESULTS AND DISCUSSION

The relationship between the mass loss and the impingement angle after 10 min of erosion test of the base metal Ti6Al4V is shown in **Figure 1**. As can be seen, the mass loss of the base metal is clearly dependent on the angle of alumina particles' impact (impingement angle), and the mass loss increases with a decreasing the angle. Such dependence is typical for ductile materials, as indicated in the literature.¹⁻³

On the other hand, in the case of the laser gas nitrided surface layers the relationship between the mass loss and impingement angle is different, as can be seen in **Figure 2**. For all of the nitrided surface layers the lowest mass loss occurred at the lowest impingement angle of 15°, while increasing of the angle resulted in increasing of the mass loss, reaching the maximum at an angle of 90°, as shown in **Figure 2**. Thus in general, the nitrided surface layers exhibited brittle-type behaviour, characteristic for hard and brittle materials.¹⁻³ The obtained results are different from those presented by J. R. Laguna-Camacho et al.³ in the case of TiN coatings deposited by PVD on the substrate of steel. In addition, the data in **Figure 2** indicate a clear relationship between the laser processing parameters and the erosion behaviour of the nitrided surface layers. For example, the surface layer produced at the lowest laser output power of 600 W (Sample S3) and so the lowest heat input of 180 J/mm exhibited the lowest mass loss so the best erosion resistance (R_e) at the highest angle of 90°, as can be seen in **Figure 2a**. In this case the mass loss was about 5 mg. In contrast, the surface layer produced at the highest heat input of 300 J/mm (laser power 1000 W, Sample S1) exhibited the highest mass loss of about 8 mg, (**Figure 2c**). For comparison, the surface layer produced at the medium heat

input of 240 J/mm (Sample S2) also showed a medium mass loss below 7 mg, (**Figure 2b**). Here, it is possible to conclude that in the range of the investigated parameters the erosion resistance of the laser nitrided surface layers at the impingement angle of 90° is almost directly proportional to the heat input of the LGN process. This phenomenon can be explained by the differences in the microstructure of the surface layers nitrided at different parameters (heat inputs). At a high impingement angle (e.g., 90°) the particles impact both the hard TiN nitrides and the softer metallic matrix. So in this case the mass loss, thus the erosion resistance R_e , is dependent on the properties of the titanium nitrides' precipitations (brittle material type), but equally on the properties of the metallic matrix (a rather ductile material type). SEM micro-

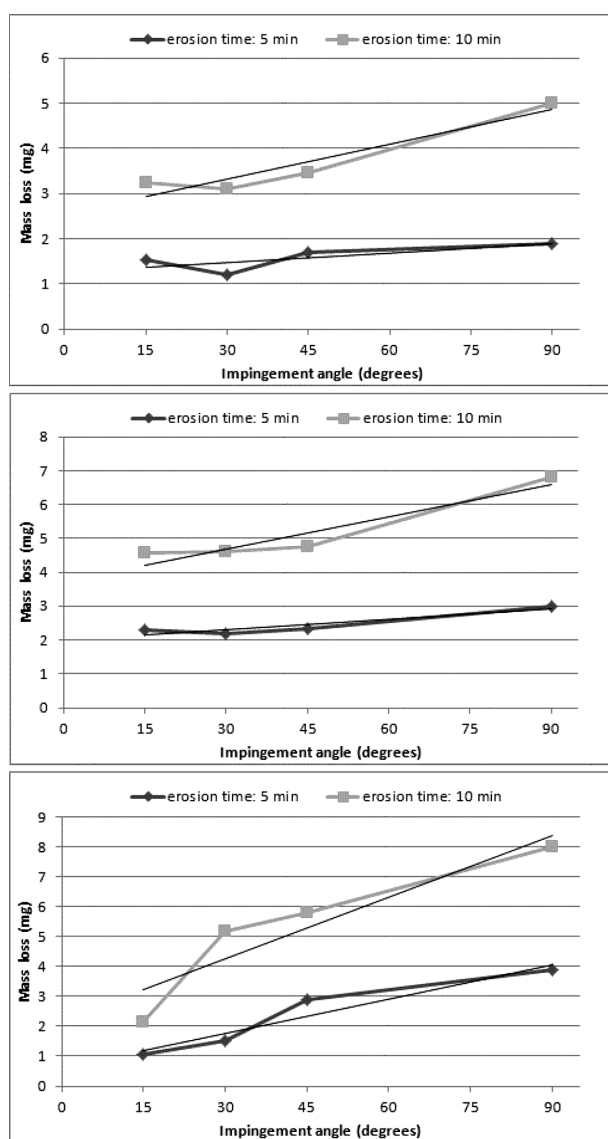


Figure 2: Relationship between the mass loss and impingement angle for different erosion times of the nitrided surface layers: a) S3, b) S2 and c) S1

Slika 2: Odvisnost med izgubo mase in vpadnim kotom pri različnih časih erozije nitrirane površinske plasti: a) S3, b) S2 in c) S1

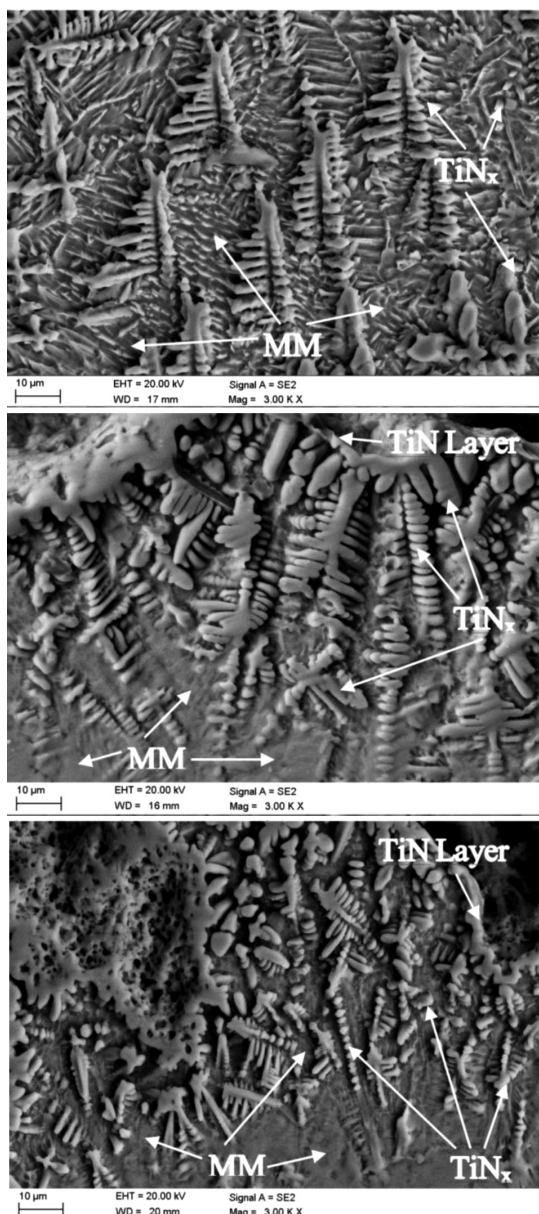


Figure 3: SEM micrographs of the nitrated surface layers, showing the composite structure consisting of TiN_x dendrites in a metallic matrix of samples: a) S1, b) S2 and c) S3; TiN Layer – a homogenous layer of titanium nitrides on the top surface, MM – metal matrix of $Ti\alpha(N)$, TiN_x – titanium nitrides precipitation with various stoichiometric concentration ($\delta-TiN$, $\epsilon-Ti_2N$)

Slika 3: SEM-posnetek nitrirane površinske plasti, ki kaže kompozitno strukturo, ki sestoji iz TiN_x dendritov v kovinski osnovi vzorcev: a) S1, b) S2 in c) S3; TiN plast – homogena plast titanovih nitridov na površini, MM – kovinska osnova $Ti\alpha(N)$, TiN_x – izločanje titanovih nitridov z različno stehiometrično koncentracijo ($\delta-TiN$, $\epsilon-Ti_2N$)

graphs of the nitrated surface layers at the same magnification are presented in **Figure 3**. As can be seen, the morphology and size of the TiN dendrites, as well as the proportion between the nitrides (population) and the metallic matrix, are different for every surface layer. The microstructure and morphology of every single surface layer correlate with the microhardness profile on the

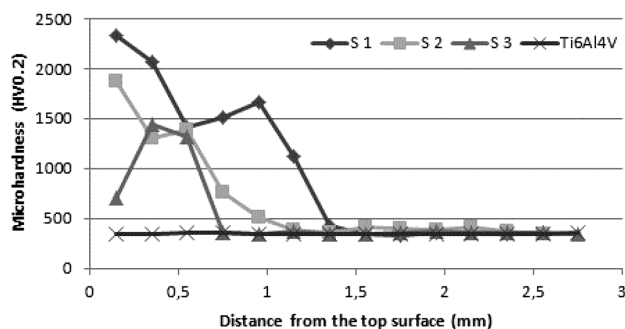


Figure 4: Microhardness distribution on the cross-section of nitrated surface layers and the base metal of titanium alloy Ti6Al4V

Slika 4: Razporeditev mikrotvrdote na preseku nitrirane površinske plasti in osnovne kovine, titanove zlitine Ti6Al4V

cross-section, (**Figure 4**). The surface layer produced at the highest heat input of 300 J/mm is composed of long and densely packed TiN dendrite precipitations with a relatively small amount of metallic matrix (**Figure 3a**). Therefore, the microhardness in this case reaches the maximum value and remains at a high level to a depth of about 1.4 mm, (**Figure 4**). The high amount of TiN dendrites characterized by a very high microhardness is responsible for the erosion behaviour of the surface layer at the angle of 90° . In turn, the nitrated surface layers produced at lower heat inputs have fewer TiN dendrite precipitations (**Figure 3b, c**). Additionally, these surface layers are thinner and also the size of the TiN dendrites is smaller and the share of metallic matrix is significantly higher. These differences in the structure and morphology of the surface layers cause a change in the microhardness distribution as well as in the erosion behaviour (**Figure 2, 4**). In this case, the softer metallic matrix has a greater influence on the erosion wear mechanism (erosion behaviour).

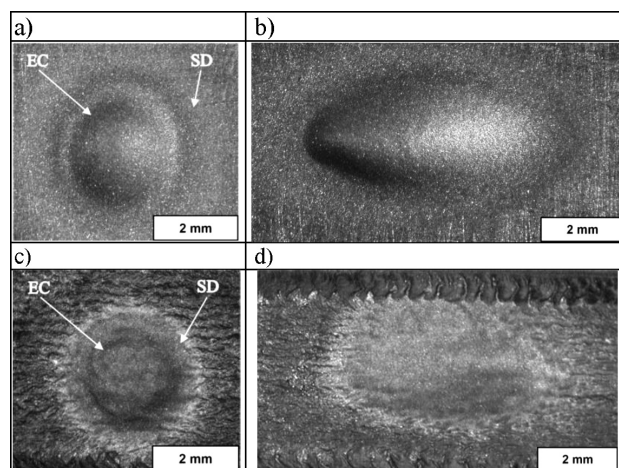


Figure 5: A view of eroded surfaces of titanium alloy Ti6Al4V at the incident angle of: a) 90° and b) 15° and nitrated surface layer S1 eroded at the incident angle of c) 90° and d) 15° ; EC – erosion crater, SD – secondary damage ("halo effect")

Slika 5: Izgled erodirane površine titanove zlitine Ti6Al4V pri vpadnem kotu: a) 90° in b) 15° in nitrirana površinska plast S1, erodirana pri vpadnem kotu c) 90° in d) 15° ; EC – erozijski krater, SD – sekundarne poškodbe ("halo efekt")

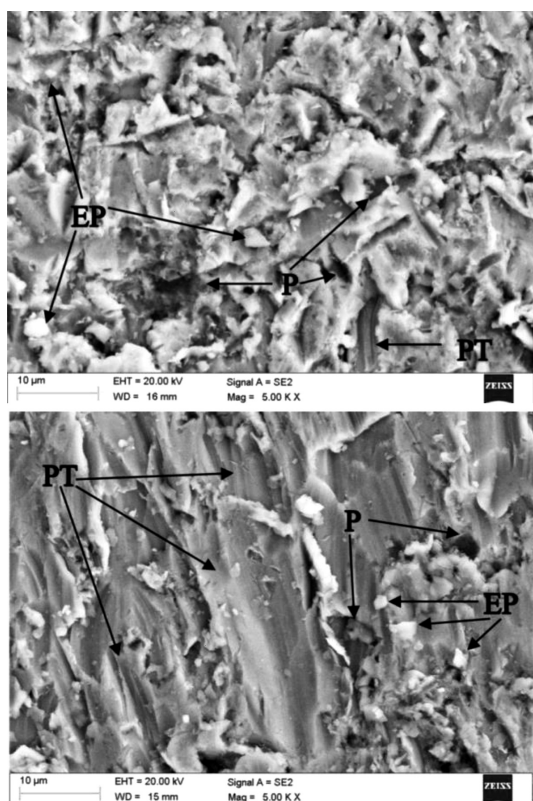


Figure 6: SEM morphology of the bottom surface of eroded craters of titanium alloy Ti6Al4V at the incident angle of: a) 45° and b) 15°; P – pits, PT – ploughing trenches, EP – erodent particles

Slika 6: SEM morfolologija površine dna kraterja titanove zlitine Ti6Al4V, pri vpadnem kotu, a) 45° in b) 15°; P – jamice, PT – brazde, EP – delci nastali pri eroziji

On the other hand, in the case of the lowest impingement angle of 15°, the surface layer produced at the maximum heat input, having the maximum depth and maximum microhardness, exhibited the lowest mass loss, and thus the highest erosion resistance R_e , (**Figure 2c**). However, the relationship between the mass loss at the angle of 15° and the processing parameters of the LGN process (in general, the heat input) is not as clear and simple as in the case of the angle 90°. The reason for this is the different way of impacting the surface by the alumina erodent particles. When the erosive stream impacts the surface at a low angle of 15°, the alumina particles are partially bounced and slide on the top surface. In such conditions the erosive wear of the composite surface layer is limited by the erosion rate of the hard and wear-resistant titanium nitride precipitations, and the softer metal matrix is not exposed to such strong erosion as at high angles of impact. Thus, the amount of metallic matrix has less effect on the overall erosion rate at a low angle of impact. The eroded craters produced at different incident angles on the surface of the titanium alloy Ti6Al4V and on the nitrided surface layers are shown in **Figure 5**. The shape and area of the craters depend on the incident angle. The circular craters characterized by the smallest area were produced at an angle of 90°. The increase in the erosion angle changes the shape of the

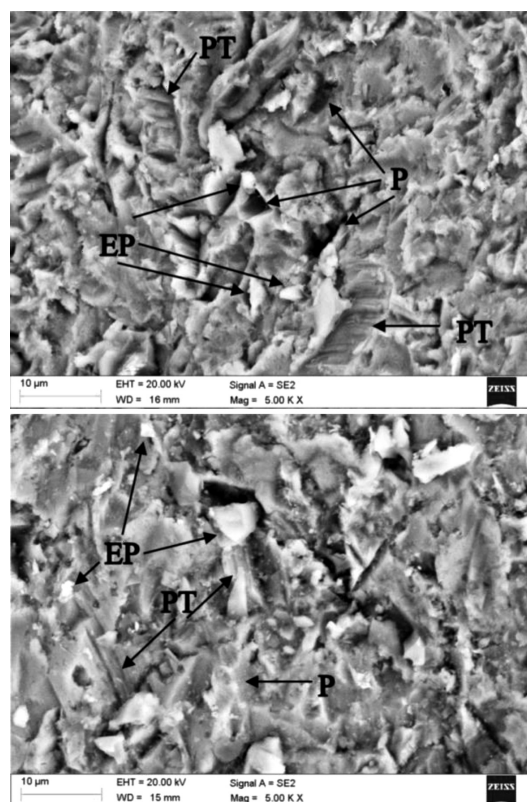


Figure 7: SEM morphology of the bottom surface of eroded craters of nitrided surface layer S1 at the incident angle of 90° a) and 15° b); P – pits, PT – ploughing trenches, EP – erodent particles

Figure 7: SEM morfolologija površine dna erozijskega kraterja na nitrirani površinski plasti S1, pri vpadnem kotu a) 90° in b) 15°; P – jamice, PT – brazde, EP – delci nastali pri eroziji

crater to an elliptical shape and simultaneously increases the wear area. The secondary erosion damage zone can be observed around the deep eroded craters (**Figure 5**). This secondary damage is caused by the scattered particles of the erodent stream. This phenomenon is called, in the literature, the "halo effect".³

The SEM morphology of the bottom surface of the eroded craters is shown in **Figure 6, 7**. The worn surfaces of the titanium alloy Ti6Al4V eroded at high incident angles show irregular indentations, craters and deep pits (**Figure 6a**). Additionally, fragments of erodent particles embedded in the surface were identified in the bottom of the eroded craters (**Figure 6a**). On the other hand, the worn surfaces eroded at low incident angles show deep and long scratches and plastically deformed ploughing trenches (**Figure 6b**). Besides the fragments of erodent particles embedded in the surface, also some wear debris inside the trenches were found. The appearance of the eroded surfaces and traces of wear indicate two different mechanisms of wear during erosion at low and high incident angles. At low incident angles the material loss is mainly caused by the abrasive wear by plastic deformation of the material, cutting and ploughing the surface by the angular erodent particles. In turn, at high incident angles, the material loss is mainly caused by plastic deformation and extrusion of the ma-

material. The worn surface morphology of the nitrided surface layer eroded at a low incident angle is clearly different compared to the base metal of titanium alloy, as can be seen in **Figure 7b**. In this case the ploughing trenches are shorter because the erodent particles rebound from the hard surface. Large erodent particles embedded in the surface were also found. The worn surface of the nitrided surface layer eroded at a high angle were more roughened with pits and craters, but without traces of cracks (**Figure 7a**). The erodent particles embedded in the surface were found also. In this case the material loss is caused by brittle ruptures of the composite layer, especially the hard TiN precipitations.

4 CONCLUSIONS

The base metal of titanium alloy Ti6Al4V exhibited ductile-type behaviour, reaching the maximum erosion rate at the lowest angle of 15° of the alumina particles' impact. Unlike the titanium alloy, the nitrided surface layers exhibited brittle-type behaviour, reaching the maximum erosion rate at the high angle of 90°. Nevertheless, the erosion resistance (R_c) of the nitrided surface layers is higher for all the angles of impingement compared to the base metal of titanium alloy. Additionally, in the range of the investigated processing parameters, the heat input of the LGN process has a strong influence on the microstructure, morphology and microhardness distribution across the surface layers, and also on the erosion behaviour, especially at the angle of 90°. It was found that the erosion rate of the composite surface layers at an angle of 90° depends on the properties of hard nitrides and the softer metal matrix equally. In turn, the erosion rate of the composite surface layers at a low angle of 15° depends mainly on the properties of the hard nitride precipitations. In this case the amount and properties of the metallic matrix has less effect on the overall erosion rate.

5 REFERENCES

- H. C. Man, Z. D. Cui, T. M. Yue, F. T. Cheng, Cavitation erosion behavior of laser gas nitrided Ti and Ti6Al4V, *Mat. Sci. Eng. A*, 355 (2003), 167–173, doi:10.1016/S0921-5093(03)00062-5
- Y. Fu, H. Du, Y. Gu, Improvement of Erosion Resistance of Titanium with Different Surface Treatments, *J. Mater. Eng. Perf.*, 9 (2000), 571–579
- J. R. Laguna-Camacho, J. E. Escalante-Martínez, R. Cruz-Vicencio, J. V. Méndez-Méndez, I. Arzate-Vázquez, I. Hernández-Romero, M. Vite-Torres, Solid Particle Erosion Behaviour of TiN Coating on AISI 4140 Steel, *J. Surf. Eng. Mat. Adv. Tech.*, 4 (2014), 1–8, doi:10.4236/jsemat.2014.41001
- A. Lisiecki, Titanium Matrix Composite Ti/TiN Produced by Diode Laser Gas Nitriding, *Metals*, 5 (2015), 54–69, doi:10.3390/met5010054
- I. Mitelea, E. Dimian, I. Bordeasă, C. Crăciunescu, Cavitation Erosion of Laser-Nitrided Ti–6Al–4V Alloys with the Energy Controlled by the Pulse Duration, *Tribol. Lett.*, 59:31 (2015), 1–9, doi:10.1007/s11249-015-0558-6
- M. Dhanda, B. Haldar, P. Saha, Development and Characterization of Hard and Wear Resistant MMC Coating on Ti-6Al-4V Substrate by Laser Cladding, *Proceed. Mater. Sci.*, 6 (2014), 1226–1232
- A. Lisiecki, Welding of titanium alloy by Disk laser, *Proc. of SPIE Vol. 8703, Laser Technology 2012: Applications of Lasers*, 87030T (January 22, 2013), doi:10.1117/12.2013431
- A. Lisiecki, Welding of thermomechanically rolled fine-grain steel by different types of lasers, *Arch. Metall. Mater.*, 59 (2014), 1625–1631, doi:10.2478/amm-2014-0276
- A. Kurc-Lisiecka, Wojciech Ozgowicz, Wiktoria Ratuszek, Joanna Kowalska, Analysis of deformation texture in AISI 304 steel sheets, *Sol. St. Phenom.*, 203–204 (2013), 105–110, doi:10.4028/www.scientific.net/SSP.203-204.105
- R. Burdzik, L. Konieczny, Z. Stanik, P. Folega, A. Smalcerz, A. Lisiecki, Analysis of impact of chosen parameters on the wear of camshaft, *Arch. Metall. Mater.*, 59 (2014), 957–963, doi:10.2478/amm-2014-0161
- J. Kusiński, S. Kac, A. Kopia, A. Radziszewska, M. Rozmus-Górnkowska, B. Major, L. Major, J. Marczak, A. Lisiecki, Laser modification of the materials surface layer – a review paper, *Bull. Pol. Acad. Sci. Tech. Sci.*, 60 (2012), 711–728, doi:10.2478/v10175-012-0083-9
- J. Górka, Weldability of thermomechanically treated steels having a high yield point, *Arch. Metall. Mater.*, 60 (2015), 469–475
- R. Burdzik, T. Węgrzyn, Ł. Konieczny, A. Lisiecki, Research on influence of fatigue metal damage of the inner race of bearing on vibration in different frequencies, *Arch. Metall. Mater.*, 59 (2014), 1275–1281, doi:10.2478/amm-2014-0218
- A. Grajcar, M. Rożański, S. Stano, A. Kowalski, Microstructure characterization of laser-welded Nb-microalloyed silicaluminum TRIP steel, *J. Mater. Eng. Perform.*, 23 (2014), 3400–3406
- J. Górka, Changes in the structure and properties of the steel S700MC by heat treatment, *Adv. Mat. Res.*, 1036 (2014), 111–116
- T. Węgrzyn, J. Piwnik, D. Hadryś, R. Wieszała, Car body welding with micro-jet cooling, *J. Arch. Mater. Sci. Eng.*, 49 (2011), 90–94
- A. Grajcar, M. Rożański, S. Stano, A. Kowalski, B. Grzegorzczak, Effect of Heat Input on Microstructure and Hardness Distribution of Laser Welded Si-Al TRIP-Type Steel, *Adv. Mater. Sci. Eng.*, 2014 (2014), doi.org/10.1155/2014/658947
- B. Oleksiak, G. Siwiec, A. Blacha-Grzechnik, J. Wieczorek, The obtained of concentrates containing precious metals for pyrometallurgical processing, *Metalurgija* 53 (2014), 605–608
- D. Janicki, High power diode laser cladding of wear resistant metal matrix composite coatings, *Sol. St. Phenom.*, 99 (2013), 587–592
- J. Słania, Influence of phase transformations in the temperature ranges of 1250-1000 °C and 650-350 °C on the ferrite content in austenitic welds made with T 23 12 LRM3 tubular electrode, *Arch. Metall. Mater.*, 50 (2005), 757–767
- Z. Brytan, M. Bonek, L. A. Dobrzański, W. Pakielna, Surface Layer Properties of Sintered Ferritic Stainless Steel Remelted and Alloyed with FeNi and Ni by HPDL Laser, *Adv. Mat. Res.*, 291-294 (2011), 1425–1428, doi:10.4028/www.scientific.net/AMR.291-294.1425
- M. Muszyfaga-Staszuk, L.A. Dobrzański, S. Rusz, M. Staszuk, Application examples for the different measurement modes of electrical properties of the solar cells, *Arch. Metall. Mater.*, 59 (2014), 247–252
- D. Janicki, Disk Laser Welding of Armor Steel, *Arch. Metall. Mater.*, 59 (2014), 1641–1646, doi:10.2478/amm-2014-0279
- B. Słazak, J. Słania, T. Węgrzyn, A. P. Silva, Process Stability Evaluation of Manual Metal Arc Welding Using Digital Signals, *Mater. Sci. Forum*, 730-732 (2013), 847–852
- M. Staszuk, L. A. Dobrzański, T. Tański, W. Kwaśny, M. Muszyfaga-Staszuk, The effect of PVD and CVD coating structures on the durability of sintered cutting edges, *Arch. Metall. Mater.*, 59 (2014), 269–274

MISWAK (SALVADORA PERSICA ROOTS): DISCOVERY OF A NEW BIOMATERIAL FOR REMOVING HEAVY METALS FROM WATER IN SAUDI ARABIA

MISWAK (KORENINE SALVADORA PERSICA): ODKRITJE NOVEGA BIOMATERIALA ZA ODSTRANJEVANJE TEŽKIH KOVIN IZ VODE V SAUDSKI ARABIJI

Saad A. Aljlil

National Center for Membrane Technology (NCMT), King Abdulaziz City for Science and Technology (KACST),
P. O. Box 6086 Riyadh, Kingdom of Saudi Arabia
saljlil@kacst.edu.sa

Prejem rokopisa – received: 2015-07-01; sprejem za objavo – accepted for publication: 2015-12-17

doi:10.17222/mit.2015.183

The aim of this study was to evaluate Miswak (Salvadora Persica Roots Powder, SPRP) as a natural bio-adsorbent from Saudi Arabia for water treatment. The adsorption capacity of the SPRP increased with an increasing concentration of heavy-metal ions and the temperature of the experimental solution. The maximum adsorption capacity of the SPRP was 18.2 mg g⁻¹ and 20.79 mg g⁻¹ for lead at 25 °C and 45 °C, respectively. Of the two isotherm models (Langmuir and Freundlich), the Langmuir model fitted the experimental data well at 45 °C, while the Freundlich model correlated well with the experimental data at 25 °C.

Keywords: Miswak (Salvadora Persica Roots), Miswak powder, lead, Langmuir, Freundlich isotherm model, contaminated water, adsorption capacity

Namen te študije je bila oceniti Miswaka (prah iz korenin Salvadora Persica, SPRP) kot naravnega bioadsorbenta iz Saudske arabije, za obdelavo vode. Zmogljivost absorpcije SPRP se povečuje z naraščanjem koncentracije ionov težkih kovin in temperature eksperimentalnih raztopin. Maksimalna zmogljivost absorpcije svinca s SPRP je bila 18,2 mg g⁻¹ in 20,79 mg g⁻¹ pri 25 °C oziroma pri 45 °C. Med dvema izotermnima modeloma (Langmuir in Freundlich), se je Langmuir model dobro skladal z eksperimentalnimi podatki pri 45 °C, medtem ko je bila korelacija Freundlich modela z eksperimentalnim podatki dobra pri 25 °C.

Ključne besede: Miswak (korenine Salvadora Persica), Miswak prah, svinec, Langmuir, Freundlichov izometrični model, kontaminirana voda, zmogljivost absorpcije

1 INTRODUCTION

Lead (Pb) is one of the toxic metals present in different types of waters as a pollutant. It is a potential source of human health hazards such as heart failure, thyroid and liver damage when its concentration in water is above the permissible limits for various uses. Currently, many conventional water-treatment techniques such as membrane processes, chemical precipitation, ion-exchange processes and adsorption are used for the removal of heavy metals such as lead. Existing technologies for heavy metals' removal from waters and wastewaters are often ineffective, expensive, time consuming and unavailable in developing countries. Therefore, the use of Miswak (SPRP) as a low-cost adsorbent seems a viable approach for removing the lead ions from waters and or wastewater through an adsorption process.

Among the different water-treatment techniques, the adsorption of heavy metal by miswak (SPRP) is considered as cheap and cost effective compared to more expensive process such as ion exchange. Many natural local materials such as clay, charcoal, solid waste from

water-treatment plants and different agricultural wastes (biomaterials) are available for wastewater purification. Saudi Arabia is one of the largest producers of Miswak stick (roots of Salvadora persica tree) in the world and this is mainly used for cleaning teeth instead of using chemically produced tooth pastes.

Many industries use aqueous solutions of heavy metals such as lead for manufacturing batteries. Unfortunately, the removal of heavy metals such as Pb, Zn, Co and Cr from aqueous solutions is both difficult and expensive. Previously, different types of adsorbents, such as activated carbon, activated sludge, various types of natural clays, carbon aerogels, coirpith carbon, natural zeolites and date-pits powder were used for water treatment. Similarly, heavy-metal removal was achieved by expensive ion-exchange resins (U.S. Patent No. 4,133,755). These investigators used various adsorbents, mainly a dithiocarbamate bond-containing low-molecular-weight compound, amorphous silica and activated carbon powder, granulated with a vinyl acetate polymer binder and clay as a thixotropic excipient for removing heavy metals. However, Cody (U.S. Patent No. 5,667,694) used granulated materials for treating mer-

cury-contaminated wastewater for removing heavy metals such as lead and the radioactive contaminants from contaminated aqueous systems including aqueous soil systems. They used organically modified smectite clay or organoclay to treat these systems. This product removes heavy-metal ions by flotation and air sparging (U.S. Patent No. 5,256,615). According to this patent, a granular inorganic ion exchanger was obtained by firing at 400 °C or above, a granular molded product of a mixture of a metal alkoxide such as Si(OMe)₄ or hydrolyzate, a clay mineral such as sepiolite and an inorganic ion exchanger such as antimony pentoxide having mechanical strength and heat resistance without losing its inherent ion exchangeability (World Patent Publication No. WO 00/72958). M. Minamisawa et al.¹ investigated the adsorption of Cd(II) and Pb(II) at pH 2–6.7 on different biomaterials and inorganic adsorbents. They also stated that biomaterials prepared from plant materials are promising for the development of novel and low-cost adsorbents. Also, bio-adsorbents proved to be potential remediation materials for the removal of heavy metals and organic materials.² Rice husk (RH), fly ash and similar other low-cost (agricultural by-product) bio-adsorbents were used for the removal of various heavy metals and metalloids (such as Pb, Cd, Zn, Ni and As) from both groundwater and surface water.³ In another study, agricultural waste-based biosorbents (AWBs) showed equal or even greater adsorption capacities compared to conventional adsorbents for removing heavy metals from contaminated waters.⁴ Recently, a wide range of low-cost modified adsorbents including activated carbon, natural source adsorbents (clay, bentonite, zeolite, etc.), biosorbents (black gram husk, sugar-beet pectin gels, citrus peels, banana and orange peels, carrot residues, cassava waste, algae, algal, marine green macroalgae, etc.), and byproduct adsorbents (sawdust, lignin, rice husk, rice husk ash, coal fly ash, Snail Shells, *Melanoides tuberculata* Muller etc.) were examined for the removal of some heavy metals from water.^{5,6} The reported the highest adsorption capacities for Zn²⁺ were 168 mg g⁻¹ on powdered waste sludge, 128.8 mg g⁻¹ dried marine green macroalgae, 73.2 mg g⁻¹ lignin, 55.82 mg g⁻¹ cassava waste, and 52.91 mg g⁻¹ bentonite. Some investigators utilized *Portulaca oleracea* plant biomass (dried leaves and stem) and dried leaves of water hyacinth along with the effect of pH, contact time and adsorbent dose on biosorption and removing some heavy metals such as Cd, Pb, Zn and Cr from the aqueous solutions and wastewaters.⁷ They reported a maximum removal of Pb at pH of 5 with 120 min of contact time and 3 g of adsorbent dose.

A review on the use of *Salvadora persica* roots powder (SPRP) as a bioadsorbent for the removal of heavy metals from waters did not refer to any study relating to this material. However, in the water- or wastewater-treatment sector dealing with polluted groundwater, waste effluents from industrial, domestic, agriculture, potable drinking water in the markets and health facilities, it is imperative to remove highly toxic

heavy metals from the available water and waste effluents for its safe reuse in agriculture and other purposes. In Saudi Arabia, Miswak (roots of *Salvadora persica* tree) is abundant and is a cost effective biomaterial. Therefore, a study on the use of Miswak powder as an adsorbent for removing heavy metals may determine it as an appropriate biomaterial substitute for commercial activated-carbon and other adsorbents. The main aim of this study was to explore the possibility of using Miswak (SPRP) as a new natural biomaterial and low-cost adsorbent for removing toxic heavy metals such as lead from waters and wastewaters.

2 MATERIALS AND METHODS

2.1 Materials

The adsorbate is a lead-ion solution prepared from lead (II) nitrate purified LR and supplied by VWR International SAS 201.

Salvadora persica is a tree naturally growing in Jazan, Saudi Arabia from which the miswak (root portion of tree) was prepared and is commonly known as Arak tree. The miswak samples were collected, dried, crushed and milled to a particle size less than 125 mesh (particles sized between about 0.125 mm to 0.25 mm). Then, the powder was used as an adsorbent for removing heavy metals from waters and wastewater. The inherent ion-exchange capacity of this powder is in the pH range between 3 and 5. For example, the miswak powder contains many functional groups such as carboxylic groups as found by FT-IR analysis (**Table 1**). As the pH of the solution affects the charge on the functional groups, therefore the functional groups such as carboxylate are protonated at low pH values.⁸ The surface area and pore characteristics of miswak powder as an adsorbent are given in **Table 2**. The chemical analysis of miswak powder was carried by XRF and presented in **Table 3**.

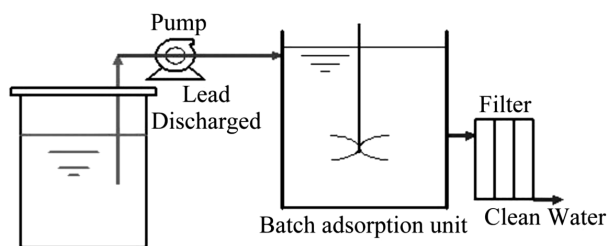
Table 1: Some of the main functional groups in Saudi miswak powder
Tabela 1: Nekaj glavnih funkcionalnih skupin v savdskem miswak prahu

Observed band (cm ⁻¹)	Functional group
3488- 3100	O-H
	N-H
2800-2900	C-H
1600-1740	C=O
	Carbonyl
1000-1200	C-O

Table 2: Surface area and pore characteristics of Saudi miswak powder

Tabela 2: Površina in značilnosti por v savdskem miswak prahu

Element	Miswak stick powder
BET surface area (m ² g ⁻¹)	0.6933
Pore volume (<i>p/po</i> =0.97) (cm ³ g ⁻¹)	0.001788
Average pore width (nm)	10.3144



Lead Waste Water Tank

Figure 1: Experimental setup for heavy-metal adsorption
Slika 1: Eksperimentalni sestav za adsorpcijo težke kovine

Table 3: Chemical analysis of Saudi miswak powder by XRF

Tabela 3: XRF kemijska analiza savdskega miswak prahu

Element	Composition (%)
S	23.0752
Cl	11.195
K	10.02
Ca	55
Fe	0.492
Zn	0.108
Br	0.0998

The experimental set up showing the adsorption system including a batch adsorption unit for removing heavy metals from contaminated wastewater is presented in **Figure 1**.

2.2 Equilibrium experiments

Equilibrium isotherm experiments for the miswak powder were carried out by placing 0.25 g of powder with 50 mL lead solution in a batch adsorption unit. The concentration of lead ion solution ranged from 50 to 800 ppm. The particle size of the miswak powder was 0.125 mm. The equilibrium experiments were run for a total period of 3 h to ensure that the adsorption process is in a state of equilibrium. After termination of the experiment, samples were collected, filtered and the concentration of Pb was measured by atomic absorption spectroscopy. The amount of Pb ion adsorbed on the surface of miswak powder was calculated using the following Equation (1):

$$q_e = \frac{v(C_0 - C_e)}{M} \quad (1)$$

where M is the mass of miswak powder in g, V is the volume of the solution in liters, q_e is the amount of ion adsorbed mg g^{-1} , C_0 is the initial concentration of lead ion solution as mg/L and C_e is concentration of Pb ion at equilibrium in mg/L . The equilibrium adsorption isotherm curves were prepared from the amount of lead ion adsorbed on the surface of the miswak powder and the Pb concentration in solution.

3 RESULTS AND DISCUSSION

3.1 Ion removal efficiency of Miswak powder

The Pb ion concentration in the solution after treatment was less than 285.17 ppm and the removal efficiency of Pb ion by miswak powder was more than 58.81 %.

3.2 Initial concentration vs. Pb ion adsorption

The data in **Figure 2** shows that the adsorption capacity of the sPb ion increased with increasing the initial concentration. The maximum adsorption capacity of the miswak powder was 18.2 mg g^{-1} and 20.79 mg g^{-1} at $25 \text{ }^\circ\text{C}$ and $45 \text{ }^\circ\text{C}$, respectively. The process of Pb-ion adsorption on the negative sites of the miswak powder is due to the electrostatic attraction between these negative sites and the lead ions. Furthermore, the formation and number of negative sites on the surface of the miswak powder are mainly due to the presence of a carboxyl group. The miswak powder has chemical functional groups such as carboxylic acid (COOH), as shown by FT-IR analysis (**Table 1**). The study's findings agree with many researchers who reported that the metal uptake capacity of the root for different metals was in the order of: $\text{Ni} > \text{Cd} > \text{Pb} > \text{Cu} > \text{Cr}$; stem $\text{Ni} > \text{Pb} > \text{Cu} > \text{Cd} > \text{Cr}$; and leaf $\text{Ni} > \text{Cd} > \text{Cu} > \text{Pb} > \text{Cr}$. They also reported that Ni adsorption was the highest in the root and its concentration was 428.4 ng/g dry wt. Also the trend of adsorption of the phytomass was similar for Ni and Cd, i.e., $\text{root} > \text{leaf} > \text{stem}$.⁹⁻¹²

3.3 Temperature vs. adsorption capacity of Miswak powder

The adsorption capacity of miswak powder increased with increasing temperature (**Figure 2**), thus indicating that the adsorption process of Pb ions on miswak powder is an endothermic process. Therefore, the adsorption of Pb ions on the surface of the miswak powder is favorable. The results agree with those of S. A. Aljlil et al.¹³

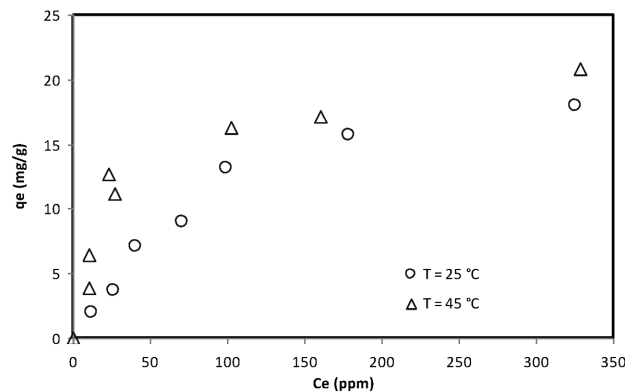


Figure 2: Equilibrium isotherm for lead ions adsorption on miswak powder

Slika 2: Ravnotežna izoterma za adsorpcijo ionov svinca na miswak prahu

who reported similar behavior when increasing the solution temperature.

4 SAUDI MISWAK STICK POWDER VS. COMMERCIAL ADSORBENTS

The maximum adsorption capacities of miswak powder, activated carbon and silica were taken from the equilibrium isotherm experimental data for comparing the ion-removal efficiency among these different adsorbents (Table 4). The results in Table 4 indicated that miswak powder proved to be the best bio-adsorbent compared to other similar adsorbents. Because it seems cheaper, has a relatively high saturation capacity, a natural biomaterial and easily available locally.

Table 4: Comparison between miswak powder and other commercially available adsorbents for the adsorption of lead ions

Tabela 4: Primerjava med miswak prahom in drugimi komercialno dostopnimi adsorbenti za adsorpcijo ionov svinca

Adsorbent	Saturation (maximum) capacity, (mg g ⁻¹)
Activated carbon	7.49
Miswak powder	18
Silica	5.15

5 ANALYSIS OF THE EQUILIBRIUM EXPERIMENTAL RESULTS

Two types of equilibrium isotherm models were used in this paper, i.e., the Langmuir and Freundlich models.

5.1 Langmuir isotherm model

The Langmuir isotherm model assumes that a monolayer of lead ions is adsorbed on the miswak powder particles and is also used to estimate the maximum capacity. The Langmuir isotherm Equation (2) is written as follows:

$$q_e = \frac{KC_e}{1+bC_e} \quad (2)$$

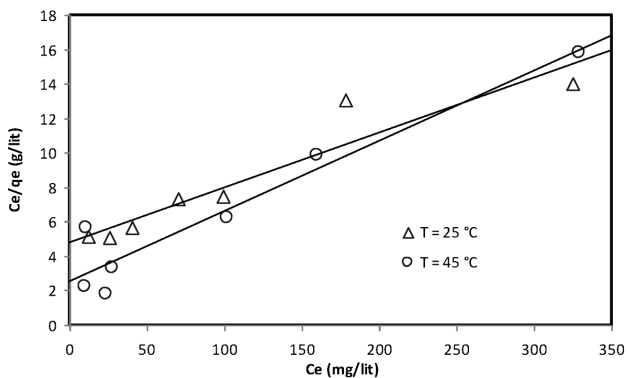


Figure 3: Langmuir equilibrium isotherm for lead adsorption on Miswak powder

Slika 3: Langmuir ravnotežna izoterma za adsorpcijo svinca na Miswak prahu

The Langmuir model in the linear form is:

$$\frac{C_e}{q_e} = \frac{1}{K} + \left(\frac{b}{K}\right)C_e \quad (3)$$

The equilibrium parameters, K and b , can be determined by using the non-linear regression method with Equation (3).

Figure 3 shows the relationship between C_e and q_e at $T = 25\text{ °C}$ and $T = 45\text{ °C}$. The equilibrium constants, K and b , were estimated using the nonlinear regression method and are tabulated in Table 5. As shown in Figure 3, the Langmuir model fits the experimental data well at $T = 45\text{ °C}$.

Table 5: Langmuir equilibrium parameters for lead ions adsorption on Miswak powder

Tabela 5: Parametri Langmuir ravnotežja za adsorpcijo ionov svinca na Miswak prahu

Temperature	K (L/g)	b (L/mg)	R^2
$T = 25\text{ °C}$	0.2024	0.00644	0.8895
$T = 45\text{ °C}$	0.3758	0.01529	0.9230

5.2 Freundlich isotherm model

The Freundlich isotherm model was applied to describe the data from equilibrium adsorption experiments for a heterogeneous surface. The Freundlich model is written as follows in Equation (4):

$$q_e = K_F C_e^{1/n} \quad (4)$$

The equilibrium parameters, K_F and n , can be calculated by using the non-linear regression method with Equation (4). The adsorption of metal ions on miswak powder is favorable when the values of n are greater than one¹⁴.

The Freundlich model in the linear form is:

$$\lg(q_e) = \lg(k_F) + \frac{1}{n} \cdot \lg(C_e) \quad (5)$$

Figure 4 shows the relationship between C_e and q_e at $T = 25\text{ °C}$ and $T = 45\text{ °C}$. The equilibrium constants were

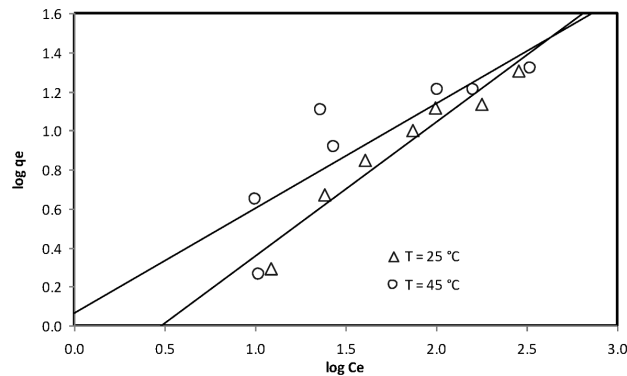


Figure 4: Freundlich equilibrium isotherm for lead adsorption on Miswak powder

Slika 4: Freundlich ravnotežna izoterma za adsorpcijo svinca na Miswak prahu

estimated using the nonlinear regression method and are tabulated in **Table 6**. As shown in **Figure 4**, the Freundlich model also correlates the experimental data well at $T = 25\text{ }^{\circ}\text{C}$.

Table 6: Freundlich equilibrium parameters for lead ions adsorption on Miswak powder

Tabela 6: Freundlich ravnotežni parametri za adsorpcijo ionov svinca na Miswak prahu

Temperature	K (L/g)	b (L/mg)	R^2
$T = 25\text{ }^{\circ}\text{C}$	0.7207	1.457	0.941
$T = 45\text{ }^{\circ}\text{C}$	1.0690	1.862	0.720

6 CONCLUSIONS

The adsorption of lead ions on the surface of miswak powder was studied. The study on the influence of the initial concentrations on the adsorption capacity of the Saudi miswak powder indicated that the saturation capacity increased with increasing the initial solution concentration. The maximum adsorption capacity of miswak powder (SPRP) for lead ions was $18.2\text{ (mg g}^{-1}\text{)}$ and $(0.79\text{ (mg g}^{-1}\text{)})$ at $25\text{ }^{\circ}\text{C}$ and $45\text{ }^{\circ}\text{C}$, respectively. The application of Langmuir and Freundlich models showed that this model fitted the experimental data well at $T = 45\text{ }^{\circ}\text{C}$, while, the Freundlich model correlated the experimental data well at $T = 25\text{ }^{\circ}\text{C}$.

Acknowledgements

The author would like to thank King Abdulaziz City for Science and Technology (KACST) for the support and encouragement to carry out the study.

7 REFERENCES

- ¹ M. Minamisawa, H. Minamisawa, S. Yoshida, N. Takai, Adsorption behavior of heavy metals on biomaterials, *J. Agric. Food Chem.*, 52 (2004) 18, 5606–5611, doi:10.1021/jf0496402
- ² M. Ahmaruzzaman, V. K. Gupta, Rice Husk and Its Ash as Low-Cost Adsorbents in Water and Wastewater Treatment, *Ind. Eng. Chem. Res.*, 50 (2011) 24, 13589–13613, doi:10.1021/ie201477c
- ³ H. A. Hegazi, Removal of heavy metals from wastewater using agricultural and industrial wastes as adsorbents, *HBRC Journal*, 9 (2013) 3, 276–282, doi:10.1016/j.hbrj.2013.08.004
- ⁴ T. A. H. Nguyen, H. H. Ngo, W. S. Guo, J. Zhang, S. Liang, Q. Y. Yue, Q. Li, T. V. Nguyen, Applicability of agricultural waste and by-products for adsorptive removal of heavy metals from wastewater, *Bioresource Technology*, 148 (2013), 574–585, doi:10.1016/j.biortech.2013.08.124
- ⁵ M. Castañeda, M. S. Mirasol, L. A. Raymundo, J. Solidum, Biosorption and Desorption of Lead (Pb^{2+}) from Simulated WasteWater Using Freshwater Snail Shells, *Melanoides tuberculata* Muller (Family Thiaridae), 2nd International Conference on Environment and BioScience, IACSIT Press, Singapore, 44 (2012), 54–59, doi:10.7763/IPCBE.2012.V44.12
- ⁶ H. M. Zwain, M. Vakili, I. Dahlan, Waste Material Adsorbents for Zinc Removal from Wastewater: A Comprehensive Review, *International Journal of Chemical Engineering*, 2014 (2014), 1–13, doi:10.1155/2014/347912
- ⁷ C. Mahamadi, Water hyacinth as a biosorbent: A review, *African Journal of Environmental Science and Technology*, 5 (2011) 13, 1137–1145, doi:10.5897/AJESTX11.007
- ⁸ S. A. Al-Jlil, Equilibrium Study of Adsorption of Cobalt ions from Wastewater using Saudi Roasted Date Pits, *Research Journal of Environmental Toxicology*, 1 (2010) 4, 1–12, doi:10.3923/rjet.2010.1.12
- ⁹ M. N. V. Prasad, H. Freitas, Removal of toxic metals from solution by leaf, stem and root phytomass of *Quercus ilex* L. (holly oak), *Environmental Pollution*, 110 (2000) 2, 277–283, doi:10.1016/S0269-7491(99)00306-1
- ¹⁰ S. S. Ahluwalia, D. Goyal, Microbial and plant derived biomass for removal of heavy metals from wastewater, *Bioresource Technology*, 98 (2007) 12, 2243–2257, doi:10.1016/j.biortech.2005.12.006
- ¹¹ R. Ginn, J. S. Szymanowski, J. B. Fein, Metal and proton binding onto the roots of *Fescue rubra*, *Chemical Geology*, 253 (2008), 130–135, doi:10.1016/j.chemgeo.2008.05.001
- ¹² A. Dubey, A. Mishra, S. Singhal, Application of dried plant biomass as novel low-cost adsorbent for removal of cadmium from aqueous solution, *International Journal of Environmental Science & Technology*, 11 (2014) 4, 1043, doi:10.1007/s13762-013-0278-0
- ¹³ S. A. Al-Jlil, F. D. Alsewailam, Lead Uptake by Natural Clay, *Journal of Applied Sciences*, 22 (2009) 9, 4026–4031, doi:10.3923/jas.2009.4026.4031
- ¹⁴ O. E. Abdel Salam, N. A. Reiad, M. M. ElShafei, A study of the removal characteristics of heavy metals from wastewater by low-cost adsorbents, *Journal of Advanced Research Journal of Advanced Research*, 2 (2011) 4, 297–303, doi:10.1016/j.jare.2011.01.008

POLY(VINYL ALCOHOL): FORMULATION OF A POLYMER INK FOR THE PATTERNING OF SUBSTRATES WITH A DROP-ON-DEMAND INKJET PRINTER

POLI(VINIL ALKOHOL): SESTAVLJANJE POLIMERNEGA ČRNILA ZA TISKANJE PODLAG Z BRIZGALNIM TISKALNIKOM

Pavol Šuly, Petr Krčmář, Jan Mašlík, Pavel Urbánek, Ivo Kuřitka

Tomas Bata University, Centre of Polymer Systems, Tr. Tomase Bati 5678, 760 01 Zlín, Czech Republic
suly@ft.utb.cz

Prejem rokopisa – received: 2015-07-01; sprejem za objavo – accepted for publication: 2016-01-19

doi:10.17222/mit.2015.180

Nowadays, inkjet-printing technology is considered one of the most promising deposition techniques. It allows the highly precise deposition of functional materials to the required place on a substrate and a cost-saving printing process, especially when the drop-on-demand manner is used. Moreover, it represents the perfect technique for the controlled deposition of polymer material, especially for polymer solutions, because of their low viscosity and better process ability. Poly(vinyl alcohol) was chosen because of its versatile application potential; moreover, its compatibility with the human body only increases its usability in bio-applications. The main purpose of this research was to find the appropriate solvent system for poly(vinyl alcohol) and its printability. Solutions with the best properties were printed in pre-defined patterns and personally defined motifs and the printing conditions were optimized in order to obtain patterns with the best possible shape and resolution, which were analysed by optical microscopy.

Keywords: inkjet ink, poly(vinyl alcohol), printed patterns, viscosity, surface tension

Dandanes tehnologija tiskanja z brizganjem predstavlja eno najobetavnejših tehnik za nanašanje. Omogoča zelo natančen nanos funkcionalnih materialov na določeno mesto na podlago, je cenovno ugoden proces, še posebno pri zahtevnem posebnem načinu tiskanja. Poleg tega predstavlja odlično tehniko za kontroliran nanos polimerne materiala, še posebno raztopine polimera, zaradi nizke viskoznosti in boljše sposobnosti procesa. Zaradi vsestranske možnosti uporabe je bil izbran poli(vinil alkohol), poleg tega pa njegova kompatibilnost s človeškim telesom povečuje možnosti biuporabe. Glavni namen te raziskave je bil poiskati primeren sistem raztapljanja poli(vinil alkohola) s sposobnostjo za tiskanje. Raztopine z najboljšimi lastnostmi so bile uporabljene pri tiskanju določenih vzorcev in osebno opredeljenih motivov. Pogoji tiskanja so bili optimirani za doseganje vzorcev z največjo možno obliko in ločljivostjo, kar je bilo analizirano s svetlobno mikroskopijo.

Ključne besede: črnilo za brizganje, poli(vinil alkohol), tiskani vzorci, viskoznost, površinska napetost

1 INTRODUCTION

Inkjet printing (IJP) can be considered as an ideal manufacturing tool for the preparation of thin films or various shape patterns at required places. This technique is also suitable for patterning fragile as well as flexible substrates. In principle, the ink is converted into droplets that are ejected through nozzles and delivered onto the required place according to a predefined pattern controlled by a computer unit.

The droplets are supplied either continuously or on demand, which describes the two basic forms of IJP. The first type, continuous inkjet printing, is mainly used for coding; the stream of liquid is broken up into stream of droplets that are charged electrically. The required droplets are deflected during the flight through the deflection plate and delivered to the substrate; the non-deflected droplets are collected in a gutter, passed through the filter and reused (depending on the arrangement of the apparatus). On the other hand, the droplets are formed only when needed by a heater or piezo-element in drop-on-demand (DOD) manner of inkjet printing, resulting in

smaller drop size generation and higher placement accuracy in comparison with continuous IJP.¹ Inkjet printing technology is used as a manufacturing tool in different industrial fields. There are numerous application examples of IJP, for instance, the technique is used to prepare organic light-emitting diodes (OLED) and polymer light-emitting diodes (PLED); printed electronics including sensors, solar cell, circuits; rapid prototyping; life science application including enzyme-based sensors, tissue engineering; and the other application such as flexible displays, magnetic and memory applications, and thin-film transistors.²⁻⁴ Moreover, the potential of IJP was successfully demonstrated in biological and pharmaceutical applications, as in ^{1,5}.

The IJP can be considered for a relative simple process, if all requirements are fulfilled. The requirements can be divided into four groups, namely: ink materials, substrate properties, droplet formation and the printing algorithm. Each element plays an important role in the whole printing system. The viscosity, surface tension and particles size represent the ink material group; for substrate, the crucial parameters are wettability, surface

energy and surface structure. Other properties are related to printing conditions, such as drop generation, platform, and algorithm. These parameters include the type of used actuator, droplet size, printing procedure and others.⁶

In a polymer system the viscosity of the solutions or dilute solutions is defined by polymer concentration. In general, the viscosity of the solution increases with increasing content of the polymer at the same temperature, and opposite, the viscosity decreases with increasing temperature independently on the polymer concentration. A similar effect of temperature can be observed for the surface tension, but in this case, the overall change of surface tension is not as significant as in the case of the viscosity. Surface tension influences both the drop formation during the flight from nozzle to substrate and the wettability of printed substrate.

The shapes and quality of the printed patterns or motives depend on the required resolution and other parameters. N. Perinka et al.⁷ investigated the quality and morphology of printed motives using different print-head volumes, substrate temperatures, and firing voltages. They observed that each parameter significantly affects the final quality and uniformity of printed motives. The quantity of deposited material can be affected by firing voltage as well as the print-head volumes. The substrate temperature showed an important influence on the final morphology of the prepared layer.

IJP is ideal manufacturing tool for material deposition. There are a lot of articles focused on printing of dispersion and polymers used mainly in printed electronics; however, only few of them are focused on printability of water-soluble polymers (for example poly(vinyl alcohol), polyvinylpyrrolidone, polyacrylic acid, polyacrylamides and other).

In this work, the poly(vinyl alcohol) solutions were prepared in various polar solvents and their mixtures. The viscosity and surface tension of each solution were determined and adjusted so that the optimal values were achieved. The solutions with the best properties were then printed with a piezoelectric drop-on-demand material printer on a flexible substrate made from polyethylene terephthalate. Finally, the printed patterns were analysed microscopically. The main purpose of this research is finding the ideal solvent system for PVA and its printability.

2 EXPERIMENTAL PART

2.1 Materials

Two commercial poly(vinyl alcohols) (PVA) that represent water-soluble polymers, and Dimethyl sulphoxide (DMSO) for UV spectroscopy grade, $\geq 99.8\%$ (GC), were purchased from Sigma-Aldrich. The main PVA characteristics are listed in **Table 1**. Distilled water was used as a major solvent. A food colorant was used for better visibility of printed layer onto polymer flexible substrate made from coated polyethylene terephthalate.

Table 1: The basic characteristics of poly(vinyl alcohols)

Tabela 1: Osnovne značilnosti poli(vinil alkoholov)

Sample	PD*	DH*	M _w *
Mowiol® 6-98	1000	98.0–98.8 mol.%	~47,000
Mowiol® 4-98	600	98.0–98.8 mol.%	~27,000

* where PD is polymerization degree, DH is degree of hydrolysis, and M_w is weight average molecular weight

The pure PVA solutions at different concentrations were prepared by dissolving of granulated PVA in distilled water at 85 ± 2 °C and continual stirring. Then, the different surfactants were added to solutions to decrease the surface tension. Later, the PVA was dissolved in a mixture of distilled water/DMSO in the volume ratio 2:1. DMSO has two roles in the used system, firstly as a co-solvent that has higher boiling point than water; secondly as a surfactant to decrease the surface tension of PVA solutions. All solutions were passed through a syringe filter (LUT Syringe Filters PTFE (Labicom s.r.o.) with pore size 0.24 μm) to eliminate the insoluble particles and other impurities.

2.2 Methods

The crucial parameters of each inkjet ink are viscosity, surface tension and conductivity at the jetting conditions (temperature, shear rate and others). Therefore, the viscosity and surface tension (SFT) measurements were determined with the highest precision. The viscosity measurements of the prepared solutions were carried out using a capillary Ubbelohde viscometer, type 0a and Ia depending upon the solutions' compositions and the expected viscosity at laboratory temperature. The density was determined by pycnometers. The final dynamic viscosity was calculated from the determined kinetic viscosity. The surface tension was carried out using a force tensiometer K100 from KRÜSS (GmbH Germany) using the plate method (also called the Wilhelmy plate method). In this assessment, the plate is oriented perpendicular to the interface, and the force exerted on it is measured.

Solution with suitable properties were filled into cartridges (type: piezo-driven jetting device with integrated reservoir and heater) and printed by Dimatix Materials Printer DMP-2800 series (Fujifilm Dimatix) on the coated PET foil. The printed patterns were analysed with an optical microscope LEICA DVM2500 Digital Camera (Leica Microsystems).

3 RESULTS AND DISCUSSION

3.1 Polymer-solvent system

Poly(vinyl alcohol) is a synthetic polymer that contains polar -OH side groups attached to the main carbon backbone. These polar groups prefer an interaction with the other group of the same affinity. In the other words, polar polymer is more soluble in polar solvents

and conversely. Therefore, PVA is often dissolved in polar solvents such as water, dimethyl sulphoxide, ethylene glycol, and primary alcohols and others. It can also be expected that water will be the dominant solvent in all cases.

The properties of PVA, such as solubility, solvent resistance, flexibility, crystallinity, and viscosity, are affected mainly by its degree of hydrolysis (DH) and polymerization degree (DP). A higher dissolving temperature is necessary for more hydrolysed PVA. Similar behaviour occurred in the case of the comparison of two PVA with same degree of hydrolysis, but different DP. Moreover, these parameters also affect the viscosity of the solutions. The higher viscosity is observed for PVA with a higher DP or molecular weight and concentration due to presence of long chains that enhance the formation intra- and inter-hydrogen bonds.^{8,9}

The first problem is dissolving the temperature associated with almost fully hydrolysed PVA used in this work because; the dissolving process is performed around 85 °C, at which the water evaporation process has begun. Therefore, the dissolving was carried out using a beaker covered by watch glass and a Petri dish; this arrangement was also helpful to maintain a stable dissolving temperature. This problem could be also partially solved by using any co-solvent with a higher boiling point, whereby a higher boiling point of the solvent mixture will be achieved. The high dissolving temperature also avoids using the commonly primary alcohols as a separate solvent because their boiling point does not exceed 100 °C; for illustration, the following boiling points are noted, methanol ~65 °C, ethanol ~78 °C and propan-1-ol ~97 °C.¹⁰ But, they could be used as surfactants due to their miscibility with water and low surface tension.

Finally, the PVA 6-98 was dissolved in pure water and water with the addition of ethanol. Ethanol was added to the solution after cooling to ambient temperature in various mass fractions. The PVA 4 – 98 was dissolved in pure water and in a mixture of water/dimethyl sulphoxide (volume ratio 2:1). It represents a good ratio between the DMSO consumption and the needed value of SFT for the solution. The selected ratio was chosen after SFT measurements of mixtures water/DMSO in different ratios (1:1, 2:1, 3:1 and 4:1) without any polymer content.

3.2 Viscosity and surface tension

The basic characteristics of the solutions are listed and discussed in this section. However, the reasons for the used methods must be clarified. There are two main groups for the classification of fluids according their viscosity behaviour with respect to shear rate; Newtonian and non-Newtonian that involves pseudo-plastic (shear-thinning) and dilatant (shear-thickening) fluids. The viscosity is independent over whole range of shear rate for the Newtonian. In contrast, the viscosity is changed

within the shear rate in the case of non-Newtonian fluids. The change of viscosity according to the shear rate is typical for polymer solutions and the polymer concentration has an important role.¹¹

If the print-head nozzle is considered as a long capillary with a small diameter, then an apparent shear rate could be calculated using the following Equation (1):

$$\dot{\gamma}_A = \frac{4 \cdot \dot{Q}}{\pi \cdot R^3} \quad (1)$$

Where \dot{Q} is the volumetric flow rate ($\dot{Q} = S \cdot v$), R is the capillary radius, S is the nozzle area, and v is the velocity of the droplets (detected by drop-watcher camera). In the results, the apparent shear rate must be corrected to the true shear rate (using Rabinowitz correction), but the value of the shear rate is above $1 \times 10^5 \text{ s}^{-1}$ in IJP.¹²

There are many studies in which the prepared inkjet inks are characterized by simple methods, for example, by a rolling balls AMVn viscometer¹³, a Brookfield viscometer¹⁴, or by changing the geometry of conventional rheometers. H. Dakhil and A. Wierschem¹⁵ reported the possibility to measure low viscosities at high shear rate by modification of a gap width in a commercial rotational rheometer. L. Pan and P. E. Arratia¹⁶ presented a PDMS-based microfluidic rheometer that can be used for the measurement of fluids with a Reynolds number (Re) below 1, and in range of shear rates up to 10^4 s^{-1} .

The Re number is defined as the relative importance of the inertia forces to viscous forces:

$$Re = \frac{\rho \cdot v \cdot L}{\eta} \quad (2)$$

Where ρ and η are the solution density and viscosity, v is the mean fluid velocity and L is a characteristic length scale.¹⁶ In our case, we consider L as the nozzle diameter and v as the droplet velocity during jetting.

Based on the observed data that are listed later, the calculated values of the prepared solution according to Equation (2) will be in the range 18.5–102.2, 22.0–39.7, 35.4–98.5, and 14.4–40.3 for aqueous PVA 6-98, PVA 6-98+ethanol, aqueous PVA 4-98, and PVA 4-98 in a water/DMSO mixture, respectively. These values of the Reynolds number correspond to a laminar flow for all the prepared solutions inside of the nozzle.

The most important dynamic parameters of inkjet inks are viscosity and surface tension. The measurements of viscosity and SFT have been performed by static methods due to both being impossible to measure at a high shear rate and the basic characterisation of the prepared solution for scientific purposes. However, based on the above-mentioned references, the obtained results hold up even for such high shear rate systems as IJP and the data can be successfully used in ink-formulation development. **Tables 2 to 5** show the density, dynamic viscosity and surface tension of the prepared PVA solutions in different solvent systems at the laboratory tem-

perature. The dynamic viscosity, η , values were calculated by using following Equation (3):

$$\eta = \rho \cdot \nu \quad (3)$$

Table 2: Density, dynamic viscosity and surface tension of PVA 6-98 aqueous solutions

Tabela 2: Gostota, dinamična viskoznost in površinska napetost vodne raztopine PVA 6-98

Concentration of PVA 6-98 solutions (w/%)	Density (kg·m ⁻³)	Dynamic viscosity (10 ⁻³ Pa·s)	Surface tension (10 ⁻³ N·m ⁻¹)
0.5	998	1.26	55.2
1.5	1001	2.06	55.8
2	1018	2.31	53.5
2.5	1003	3.14	50.9
3.5	1021	4.28	55.7
5	1058	7.35	53.9

Table 3: Density, dynamic viscosity and surface tension of PVA 6-98 aqueous solutions with ethanol

Tabela 3: Gostota, dinamična viskoznost in površinska napetost PVA 6-98 vodne raztopine z alkoholom

Origin PVA 6-98 conc. (w/%)	Content of ethanol (w/%)	New conc. (w/%)	Density (kg·m ⁻³)	Dynamic viscosity (10 ⁻³ Pa·s)	Surface tension (10 ⁻³ N·m ⁻¹)
2.5	7.9	2.32	1007	3.27	48.2
2.5	11.8	2.24	1003	3.46	46.0
2.5	15.8	2.16	998	3.95	43.8
3.5	11.8	3.13	1004	5.41	47.2
3.5	15.8	3.02	1000	5.57	44.6
3.5	19.7	2.92	995	5.83	41.1

Table 4: Density, dynamic viscosity and surface tension of PVA 4-98 aqueous solutions

Tabela 4: Gostota, dinamična viskoznost in površinska napetost vodne raztopine PVA 4-98

Concentration of PVA 4-98 solutions (w/%)	Density (kg·m ⁻³)	Dynamic viscosity (10 ⁻³ Pa·s)	Surface tension (10 ⁻³ N·m ⁻¹)
1	1016	1.33	60.0
1.5	1017	1.67	58.8
2	1018	1.97	61.1
2.5	1020	2.43	59.4
3	1021	2.64	60.2
4	1023	3.73	60.7

Table 5: Density, dynamic viscosity and surface tension of PVA 4-98 solutions in water/DMSO mixture

Tabela 5: Gostota, dinamična viskoznost in površinska napetost raztopine PVA 4-98 v mešanici voda/DMSO

Concentration of PVA 4-98 solutions (w/%)	Density (kg·m ⁻³)	Dynamic viscosity (10 ⁻³ Pa·s)	Surface tension (10 ⁻³ N·m ⁻¹)
1	1069	3.42	53.8
1.5	1069	3.98	52.8
2	1071	5.19	53.8
2.5	1070	5.66	56.7
3	1073	7.25	56.3
4	1072	9.61	56.4

where ν is kinematic viscosity and ρ is the density of solutions.

As can be seen, at the higher polymer concentration the higher viscosity was observed for both cases of PVA aqueous solutions, as for PVA 6-98 as for PVA 4-98. However, the PVA 6-98 aqueous solutions show higher viscosity values in comparison with the second one. This difference is caused by the higher polymerization degree (higher molecular weight), in which the presence of long chains enhances the formation of intra- and inter-hydrogen bonding, as were discussed previously and notified in ^{8,9}.

Similar behaviour was also observed for the surface tension. The SFT could be considered as a constant in both cases, because the SFT oscillates around the mean values 53 mN·m⁻¹ for PVA 6-98 and 60 mN·m⁻¹ for PVA 4-98, respectively. Although small differences are seen, no upward or downward trend was recorded.

There are recommended values of viscosity and SFT for inkjet inks enabling the preparation of functional layers (or patterns) by the used material printer. The values for viscosity are in range of 10–12 mPa·s, and 28–42 mN·m⁻¹ for the surface tension, of course, at a certain jetting temperature.¹⁷ The obtained values of the SFT were higher than the recommended limits, thus, the SFT was decreased by using miscible additives. The available surfactant Triton X-100 and BYK-348 were added at the beginning, but decreasing of SFT was not observed. Moreover, Triton X-100 precipitated in the PVA solution. Therefore, the SFT was decreased by using the co-solvent. The different mass fraction of ethanol was added to PVA 6-98 solutions; the new concentration of solutions was calculated by using following Equation (4):

$$w_1 \cdot M_1 + w_2 \cdot M_2 = w_3 \cdot (M_1 + M_2) \quad (4)$$

where w_x is the weight fraction of polymer in solution and M_x is the weight of solution.

As can be seen, the addition of ethanol resulted in a small increase of the solution viscosity and lowers the SFT (**Table 3**). The effect of ethanol content on density, viscosity, and surface tension of binary water+ethanol mixtures at different temperature was investigated in ¹⁸. They determined a limit for the mole fraction of ethanol at around 0.3; up to this limit the viscosity and density of mixture water + ethanol increase significantly, they reached maximum values at the mentioned value, and then decrease up to characteristic values for pure ethanol. For SFT, the simple downward trend was observed without any anomaly or unexpected deflections.

In short, the addition of 20 % of mass fractions of ethanol taken on the mass of solution, (corresponding to ~0.08 mole fraction of ethanol), resulted in a decrease of SFT from 55 mN·m⁻¹ to 41 mN·m⁻¹ and an increase of viscosity from 4 mPa·s to 6 mPa·s. A similar effect was observed for each other solution with a defined amount of ethanol.

DMSO was chosen as a co-solvent for PVA 4-98. The DMSO, polar solvent with higher boiling point than water, was a mixture with water at certain ratio before the dissolving process. In comparison with pure PVA 4-98 aqueous solutions, the solutions show lower surface tension, but higher density and viscosity at the same concentration of polymer (**Table 4** and **5**). The density was slightly increased (about 1.05 times), but the viscosity was increased by 3 times. The mean value of SFT decreased by $5 \text{ mN}\cdot\text{m}^{-1}$ from $60 \text{ mN}\cdot\text{m}^{-1}$ to $55 \text{ mN}\cdot\text{m}^{-1}$. The mean value of SFT of the PVA 4-98 solutions is similar to the mean SFT value of PVA 6-98 aqueous solution. The viscosities of PVA 4-98 solutions prepared in water/DMSO are nearer to the recommended ink properties than other ones.

3.3 Printing process

The solutions showed the best properties from each polymer-solvent system were printed on flexible PET foil. There was also proposed a pulse waveform that consists of several stages that are defined by the slew rate, duration, and magnitude of pulse voltage. A uniform droplet velocity was achieved by adjusting the voltage at each nozzle. **Figure 1** and **Figure 2** show the droplets formation and ejection from the nozzle. As can be seen, the droplets velocity (about $6 \text{ m}\cdot\text{s}^{-1}$) was very similar in both cases. The mixture with ethanol did not show a significant long-tail formation in comparison with the next one. This long-tails disappeared several microseconds later during the airborne stage.

The printing of the PVA 6-98 aqueous solution at any concentration was impossible, probably due to the high DP and its effects. The same results were obtained in the case of the PVA 6-98 solution containing ethanol after printing several lines. Approximately a half of cartridge volume was consumed before clogging the nozzles that could be associated with the content of ethanol because of its low boiling point. Also, the relatively high temperatures of both cartridge and substrate ($33 \text{ }^\circ\text{C}$ and $45 \text{ }^\circ\text{C}$, respectively) support the evaporation process that occurs before the printing process itself. The cleaning cycles were performed more often than for PVA 4-98 in

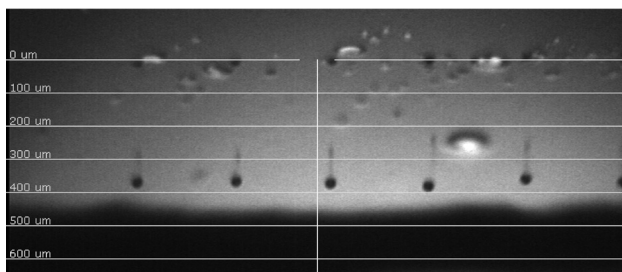


Figure 1: Droplets generation and their velocity, PVA concentration 2.5 % of mass fractions in water with ethanol (15.8 % of mass fractions), firing voltage 28–32 V, temperature of cartridge $33 \text{ }^\circ\text{C}$

Slika 1: Nastajanje kapljic in njihova hitrost, koncentracija PVA 2,5 % masnega deleža v vodi z etanolom (15,8 % masnega deleža), napetost pri brizganju 28 ~ 32 V, temperatura kartuše $33 \text{ }^\circ\text{C}$

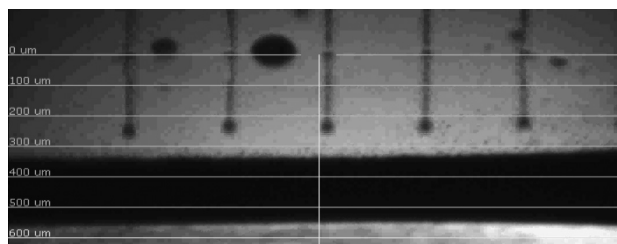


Figure 2: Droplets generation and their velocity, PVA concentration 2.5 % of mass fractions in water/DMSO mixture, firing voltage 33 V, temperature of cartridge $33 \text{ }^\circ\text{C}$

Slika 2: Nastajanje kapljic in njihova hitrost, koncentracija PVA 2,5 % masnega deleža v mešanici voda/DMSO, napetost pri brizganju 33 V, temperatura kartuše $33 \text{ }^\circ\text{C}$

mixture water/DMSO. A similar effect was also obtained for the PVA 4-98 aqueous solution.

The four basic groups of requirements important for ink formulation that have been mentioned in theory (materials – ink properties, substrate properties, droplet formation and the printing algorithm) are important; however, this work is focused on the preparation of an appropriate formula of polymer ink for specific substrate (coated PET foil). Thus, the modification of the substrate surface and the properties were not considered. Also, the printing algorithm (waveform) and its subgroups were used in the same way in all experiments once they had been optimized for the preparation of all the patterns. The last important group (droplet generation) was important, because the voltage waveform was prepared and applied for all solutions. Moreover, the uniform droplet velocity was reached by modification of the voltage for the needed nozzles. This voltage was different for each prepared polymer-solvent system.

3.4 Analysis of printed patterns

Well-defined patterns were printed after optimization of the printing conditions. The patterns include pre-defined and personally proposed patterns (single dots or

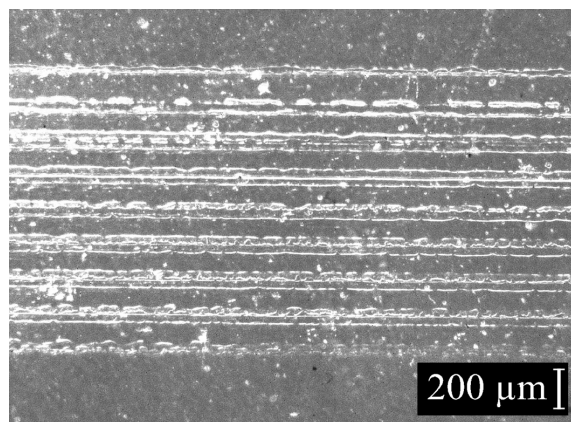


Figure 3: Magnified area of rectangle-shape pattern prepared from PVA 6-98 solution with 15.8 % of mass fractions of ethanol

Slika 3: Povečano področje štirioglate oblike, pripravljene z raztopino s 15,8 % masnim deležem PVA 6-98 v etanolu

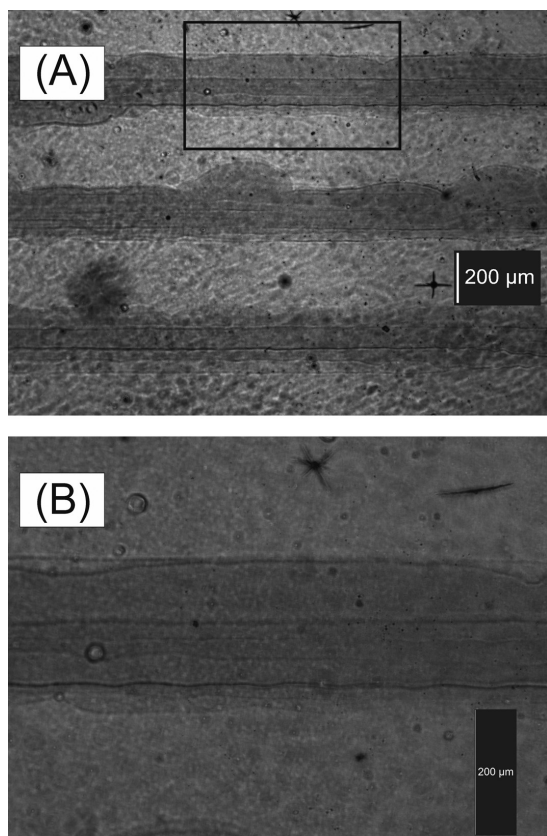


Figure 4: The set of lines of 3 % of mass fractions of aqueous polymer solution PVA 4-98, magnified: a) 40 times, and b) 100 times, respectively

Slika 4: Množica linij s 3 % masnega deleža raztopine polimera PVA 4-98, povečano: a) 40 × in b) 100 ×

dots array, rectangle-shape pattern with variation in resolution, and other motives). In this work, only fractions of prepared patterns are shown. Firstly, the simple rectangular-shape pattern was printed from the PVA 6-98 solution with the addition of ethanol. The pattern is shown in **Figure 3**. As can be seen, the pattern is not uniform; there are places where the particular printed lines affected each other (the left top corner), and in contrast, there are places where the solution ink is either missing or exists in an insufficient amount (the right bottom corner).

Depending on the observed results, the solution of PVA 4-98 was used to prepare a single-lines pattern. Based on the obtained results, the polymers with lower molecular weight are more suitable for the IJP process in comparison with a polymer with a high DP. This proposal can be supported by the following series of pictures. **Figure 4** shows the printed lines of PVA aqueous solution with a lower DP. As can be seen, the edges of printed lines are not smooth, moreover, the bulging effect was observed in a random part of the lines. It suggested that the energy of the prepared ink was sufficient for drop formation, but the delay time was insufficient to eliminate this instability effect (bulging). The widths of the printed layers are about 200 μm. The food colorant

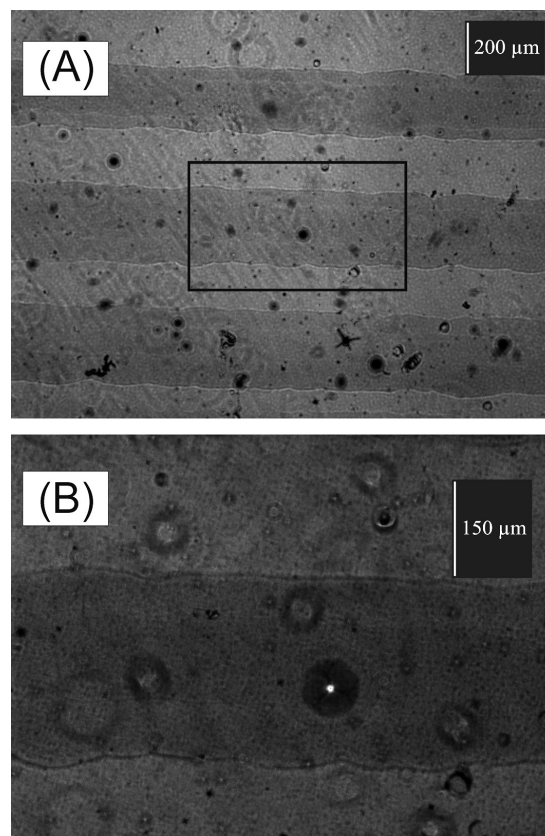


Figure 5: The set of lines of 2.5 % of mass fractions of polymer solution PVA 4-98 in water/DMSO mixture, magnified: a) 40 times, and b) 100 times, respectively

Slika 5: Množica linij z 2,5 % masnega deleža raztopine polimera PVA 4-98 v mešanici voda/DMSO, povečano: a) 40 × in b) 100 ×

was added to the solution to improve the visibility of the patterns (the amount of colorant was 0.5 % of the mass fractions given to the amount of solution). It was found that the addition of colorant up to 1 % of mass fractions has no influence on the structure of the printed patterns;

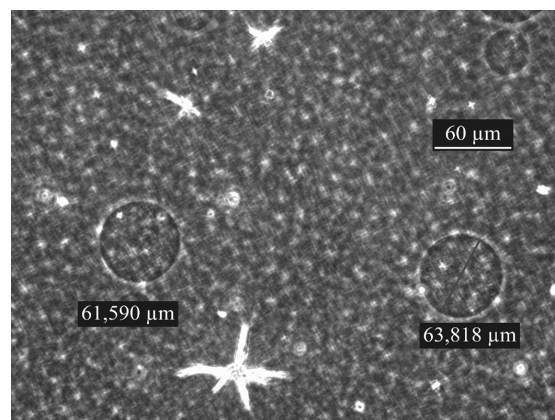


Figure 6: Single droplets prepared from 2.5 % of mass fractions of polymer solution PVA 4-98 in water/DMSO mixture, magnified 200 times, 254 μm drop spacing

Slika 6: Posamezne kapljice pripravljene iz 2,5 % masnega deleža polimera PVA 4-98 v mešanici voda/DMSO, povečano 200 ×, razdalja med kapljicama 254 μm

however, the larger amount of colorant together with the pattern's resolution can lead to the formation of crystalline structures. Tube-like shape structures were randomly situated on the surfaces of the patterns with a diameter in the range of 0.5 μm up to 5 μm . The formation of the crystalline structure also depends on the drying condition.

The same pattern was also prepared from solution of PVA 4-98 in a water/DMSO mixture (**Figure 5**). The patterns are smoother, with good visible edges. The width of these lines is about 250 μm and larger, which could be caused by the better wettability of the substrate by ink with a lower surface tension. Additionally, the last mentioned ink was used to prepare patterns based on single drops at accurate positions. The drop lines or drop arrays were prepared at various drop spacings. The results are shown in **Figure 6**. The distance between two neighbouring droplets is 254 μm . The droplet diameter is in the range 60–65 μm . The droplets show an almost perfect circular shape, but their height is uneven. This effect could be controlled by adjusting the evaporation profile. In general, the effect is more visible at higher temperatures of the substrate.^{7,19}

4 CONCLUSION

Several solutions of PVA 6-98 and PVA 4-98 were prepared to find the optimal composition formula for the preparation of a polymer inkjet ink. The viscosity and surface tension were determined. The PVA 6-98 aqueous solutions were not suitable for the printing process at any polymer concentration. Next, the defined amount of ethanol was added to the solutions to decrease their surface tensions. This effect was observed, but ethanol probably caused the clogging of the print head nozzles because of its vapours at printing temperatures. The PVA 4-98 with a lower molecular weight was used in the next series of experiments. The pure PVA 4-98 aqueous solution at a certain concentration shows suitable properties for IJP processing. Several patterns were prepared, but the formation of the droplet and their jetting velocity were not uniform during the whole printing process, which led to the preparation of less accurate patterns. The best results were obtained for solutions of PVA 4-98 prepared in a water/DMSO (2:1 v/v) solvent mixture. The prepared ink showed the best properties for the preparation of single drop patterns as well as other patterns such as grid, lines, rectangles, and other. The preparation of water-resistant patterns from PVA will be the goal of future work as well as the preparation of more sophisticated patterns. From a practical point of view, let us note that the results could extend the potential of PVA based formulations in the biological and medical sciences.

Acknowledgements

This work was supported by the Ministry of Education, Youth and Sports of the Czech Republic – Program NPU I (LO1504). We also acknowledge the support of the Internal Grant Agency of Tomas Bata University in Zlín (number: IGA/CPS/2015/006).

5 REFERENCES

- J. Li, F. Rossignol, J. Macdonald, Inkjet printing for biosensor fabrication: combining chemistry and technology for advanced manufacturing, *Lab Chip*, 15 (2015) 12, 2538–2558, doi:10.1039/C5LC00235D
- A. Hudd, Inkjet Printing Technologies, The Chemistry of Inkjet Inks, S. Magdassi (Ed.), Singapore, World Scientific Publishing, 2010, 3–18
- B. Derby, Inkjet printing of functional and structural materials: fluid property requirements, feature stability, and resolution, *Annual Review of Materials Research*, 40 (2010) 1, 395–414, doi:10.1146/annurev-matsci-070909-104502
- M. Singh, H. M. Haverinen, P. Dhagat, G. E. Jabbour, Inkjet printing-process and its applications, *Advanced Materials*, 22 (2010) 6, 673–685, doi:10.1002/adma.200901141
- Q. Zheng, J. Lu, H. Chen, L. Huang, J. Cai, and Z. Xu, Application of inkjet printing technique for biological material delivery and antimicrobial assays, *Analytical Biochemistry*, 410 (2011) 2, 171–176. doi:10.1016/j.ab.2010.10.024
- C.-T. Chen, Inkjet Printing of Microcomponents: Theory, Design, Characteristics and Applications, Features of Liquid Crystal Display Materials and Processes, N. V. Kamanina, (Ed.), Rijeka, Croatia, InTech, 2011, 43–60
- N. Perinka, C. H. Kim, M. Kaplanova, Y. Bonnassieux, Preparation and Characterization of Thin Conductive Polymer Films on the base of PEDOT:PSS by Ink-Jet Printing, *Physics Procedia*, 44 (2013), 120–129, doi:10.1016/j.phpro.2013.04.016
- J. Tao: Effects of Molecular Weight and Solution Concentration on Electrospinning of PVA. M.S. thesis, Mechanical Engineering Department, Worcester Polytechnic Institute, Worcester, MA, 2003 <http://www.wpi.edu/Pubs/ETD/Available/etd-0613103-130015/unrestricted/jtao.pdf>, 20.6.2015
- H. J. Endres, A. Siebert-Raths, *Engineering Biopolymers: Markets, Manufacturing, Properties and Applications*, Carl Hanser Verlag, Munich, 2011, 149–224
- J. Vohlřídál, A. Julák, K. Štulík, *Chemické a analytické tabulky*, Praha: Grada Publishing, 1999, 177, 276, 369
- T. Sochi, Flow of non-newtonian fluids in porous media, *Journal of Polymer Science Part B: Polymer Physics*, 48 (2010) 23, 2437–2767, doi:10.1002/polb.22144
- X. Wang, W. W. Carr, D. G. Bucknall, J. F. Morris, High-shear-rate capillary viscometer for inkjet inks, *Review of Scientific Instruments*, 81 (2010) 6, 065106–, doi:10.1063/1.3449478
- C. A. Lamont, T. M. Eggenhuisen, M. J. J. Coenen, T. W.L. Slaats, R. Andriessen, P. Groen, Tuning the viscosity of halogen free bulk heterojunction inks for inkjet printed organic solar cells, *Organic Electronics*, 17 (2015), 107–114, doi:10.1016/j.orgel.2014.10.052
- X. Nie, H. Wang, J. Zou, Inkjet printing of silver citrate conductive ink on PET substrate, *Applied Surface Science*, 261 (2012), 554–560, doi:10.1016/j.apsusc.2012.08.054
- H. Dakhil, A. Wierschem, Measuring low viscosities and high shear rates with a rotational rheometer in a thin-gap parallel-disk configuration, *Applied Rheology*, 24 (2014) 6, 63795–, doi:10.3933/AppRheol-24-63795
- L. Pan, P. E. Arratia, A high-shear, low Reynolds number microfluidic rheometer, *Microfluidics and Nanofluidics*, 14 (2013) 5, 885–894, doi:10.1007/s10404-012-1124-2

P. ŠULY et al.: POLY(VINYL ALCOHOL): FORMULATION OF A POLYMER INK FOR THE PATTERNING OF SUBSTRATES ...

¹⁷ FUJIFILM Dimatix 2010, Fujifilm Dimatix Materials Printer DMP-2800 series: User Manual, Document no. PM000040 Rev. 05, <http://www.lilliu.co.uk/resources/DMP/DMP2800GuideVersion2.0.pdf>, 20.6.2015

¹⁸ I. S. Khattab, F. Bandarkar, M. A. A. Fakhree, A. Jouyban, Density, viscosity, and surface tension of water+ethanol mixtures from 293 to 323 K, *Korean Journal of Chemical Engineering*, 29 (2012) 6, 812–817, doi:10.1007/s11814-011-0239-6

¹⁹ Y. H. Yun, J. D. Kim, B. K. Lee, Y. W. Cho, H. Y. Lee, Polymer inkjet printing: construction of three-dimensional structures at micro-scale by repeated lamination, *Macromolecular Research*, 17 (2009) 3, 197–202, doi:10.1007/BF03218679

INFLUENCE OF CHEMICAL ADDITIVES AND CURING CONDITIONS ON THE MECHANICAL PROPERTIES AND CARBONATION RESISTANCE OF ALKALI-ACTIVATED SLAG COMPOSITES

VPLIV KEMIJSKIH DODATKOV IN POGOJEV SUŠENJA NA MEHANSKE LASTNOSTI IN ODPORNOST NA KARBONACIJO Z ALKALIAMI AKTIVIRANIH KOMPOZITOV ŽLINDRE

Pavel Bulejko¹, Vlastimil Bílek Jr.²

¹Brno University of Technology, Faculty of Mechanical Engineering, Heat Transfer and Fluid Flow Laboratory, Technická 2896/2, 616 69 Brno, Czech Republic

²Brno University of Technology, Faculty of Chemistry, Material Research Centre, Purkyňova 118, 612 00 Brno, Czech Republic
pavel.bulejko@vut.cz

Prejem rokopisa – received: 2015-07-01; sprejem za objavo – accepted for publication: 2016-01-27

doi:10.17222/mit.2015.185

The main aim of the presented work is to investigate the effect of the addition of air-entraining (AEA) and shrinkage-reducing agents (SRA) on the mechanical properties and carbonation resistance of alkali-activated slag (AAS). The materials used for the sample preparation were blast-furnace slag activated using sodium silicate and AEA or SRA in various amounts. The samples were cured in various conditions (air curing under laboratory conditions and water curing at the same temperature) and the influence of these was also studied. The prepared samples (specimens with dimensions of 100 mm × 20 mm × 20 mm) were tested for compressive and bending strengths. The experimental results show that the addition of AEA did not have a significant influence on the mechanical properties, while the addition of SRA had a negative effect. However, the carbonation resistance markedly decreases with an increase of both agents. The same is true for air curing, as mechanical strengths are lower compared to those samples cured in water, and the ratio of the strength of the air-cured composite and that of the water-cured composite decreases with an increase in the content of SRA.

Keywords: alkali-activated slag, carbonation resistance, chemical additives, mechanical properties

Glavni namen tega dela je preiskava vpliva dodatka za zmanjšanje vsebnosti zraka (angl. AEA) in dodatka za zmanjšanje krčenja (angl. SRA) na mehanske lastnosti in odpornost na karbonacijo z alkalijami aktivirane žlindre (angl. AAS). Materiali za pripravo vzorcev so bili plavžna žlindra, aktivirana z natrijevim silikatom in različnim dodatkom AEA ali SRA. Vzorci so bili strjeni pri različnih pogojih (strjevanje na zraku v laboratorijskih pogojih in strjevanje v vodi pri enaki temperaturi) in študiran je bil njihov vpliv. Pripravljeni vzorci, z merami 100 mm × 20 mm × 20 mm, so bili preizkušeni na tlačno in upogibno trdnost. Rezultati preiskav kažejo, da dodatek AEA ni imel pomembnega vpliva na mehanske lastnosti, medtem ko je dodatek SRA nanje vplival negativno. Vendar pa se je odpornost na karbonacijo močno zmanjšala z večanjem vsebnosti obeh dodatkov. Enako velja za strjevanje na zraku, saj so mehanske lastnosti slabše v primerjavi z vzorci, strjenimi v vodi in se razmerje trdnosti vzorcev strjenih v vodi in razmerje trdnosti na zraku strjenih kompozitov, zmanjša s povečanjem vsebnosti SRA.

Ključne besede: z alkalijami aktivirana žlindra, odpornost na karbonacijo, kemijski dodatki, mehanske lastnosti

1 INTRODUCTION

AAS has received increasing attention as a potential alternative to Portland cement (PC) due to its high strength, durability and low environmental impact.¹⁻³ Many studies have been carried out on AAS to determine its microstructure characterization,^{4,5} reaction kinetics,^{6,7} and chemical resistance.^{8,9} Additionally, the thermodynamic modelling of AAS cements¹⁰ and the phenomenon of AAS composite shrinkage¹¹⁻¹⁴ have been studied. The latter has a negative effect on AAS properties, especially in terms of mechanical strength.^{15,16} Therefore, many chemical and mineral admixtures have recently been introduced to this area.

Chemical additives, especially those that are organic based, have recently been added to PC concrete with positive results. In addition to the commonly known

application of superplasticizers, shrinkage-reducing agents (SRA) and air-entraining agents (AEA) have recently been gaining interest. SRAs are able to decrease the surface tension of water in concrete pores, which decreases the capillary tension within the pore structure. This is why shrinkage is reduced when water evaporates. Such SRAs are primarily based on polypropylene glycol.¹⁷ The main reason for introducing an AEA is to produce air bubbles dispersed throughout the concrete. This provides durability to the hardened concrete during frost-thaw cycling. The AEA is a surfactant with a structure consisting of hydrophilic and hydrophobic groups,¹⁸ based on a soluble salt of an alkyl aryl sulphonate.^{19,20} After adding AEA into a cement paste, AEA molecules are quickly adsorbed into the interface of the cement-water-air system. The adsorption of surfactant causes a significant reduction of the free energy from the system,

thus making a large number of small, closed, uniform bubbles. As the cement particles are now separated, the frictional resistance among them is reduced, thus increasing the workability of the mixture. Conversely, a higher amount (generally more than 0.004 % of mass fractions) of AEA cannot improve the fluidity of the mixture because the free water content in the unit volume paste decreases, causing a workability loss.¹⁸ SRAs and AEAs do not only influence the aforementioned properties, as most of these agents are primarily determined to be used in PC-based systems. These agents may increase the porosity²¹ and thus influence the compressive and bending strengths. Another important issue is the carbonation of AAS composites. Together with various curing conditions, the final material behaviour may be completely different. The main aim of this work is to study the influence of additives and curing conditions on the mechanical properties and the ability to resist the carbonation of an AAS composite.

2 EXPERIMENTAL PART

2.1 Materials

Ground, granulated blast-furnace slag with a specific surface of $380 \text{ m}^2 \text{ kg}^{-1}$ was used as a raw material. A liquid sodium silicate was used as an alkaline activator. The activator consisted of 47 % of dry matter, i.e., 16.8 % of Na_2O and 30.2 % of SiO_2 , thus providing an $\text{SiO}_2/\text{Na}_2\text{O}$ molar ratio of 1.85. The phase composition of the slag was determined using a PANalytical Empyrean X-ray diffraction (XRD) spectrometer. The slag consists predominantly of an amorphous phase with a smaller amount of crystalline mellilite and merwinite. Granulometric measurements to determine the particle size distribution were performed with a Sympatec HELOS KR laser analyser with a measurement range between $0.1 \mu\text{m}$ and $1.500 \mu\text{m}$. The particle-size distribution is shown in **Figure 1**. The median particle size is $8.45 \mu\text{m}$.

Chryso®Air A was used as an AEA. It is a commercially available chemical agent based on sulphonic acids and coconut oil, with the reaction products diethanolamine and sodium thiocyanate. Chryso®Serenis was

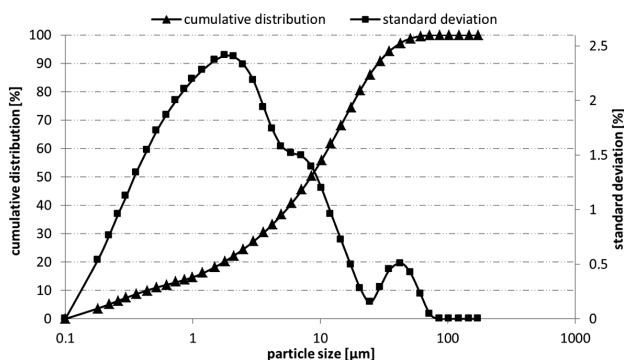


Figure 1: Particle size distribution of blast-furnace slag
Slika 1: Razporeditev velikosti delcev plavžne žilindre

used as a shrinkage inhibitor (SRA). This additive is based on 2-methyl-2,4-pentanediol. Both are generally used for PC-based systems.

2.2 Composition of mortars and specimens preparation

Mortars were prepared by mixing the blast-furnace slag with an activating solution and sand. The amount of sodium silicate was 4.2 % by weight of slag. Standard fine sand as defined by CSN EN 196 1²² was used as an aggregate. The slag-to-sand ratio and water-to-slag ratio of all the prepared mortars were 0.50 and 0.40, respectively. The mortars were subsequently modified by the addition of SRA in the amount of 0.25 %, 0.50 %, 1.00 % and 2.00 % by weight of slag. Finally, two mixtures were also modified with AEA in the amounts of 0.10 % and 0.50 % by mass of slag. The mortars were then cast into steel molds, demolded after 24 h, submerged in water for 3 d and then stored in air under ambient conditions until the 28th day. They were then tested. The other samples (with the same composition) were cured and submerged in water for the entire time. These were then compared with those cured in air.

2.3 Strength testing, carbonation and morphology

Compressive and bending strengths were tested on mortar specimens, with measurements of $20 \text{ mm} \times 20 \text{ mm} \times 100 \text{ mm}$, after 28 days. At least three samples of each composition were taken for a three-point bending test and the remaining parts of broken specimens were used for measurements of the compressive strength.

The depth of carbonation was determined on freshly broken specimens by spraying 1.0 % phenolphthalein solution on the fracture surface of the prism. The carbonation depth was measured and the sprayed cross-section surface photographed.

The microstructure of the selected AAS pastes was investigated using a ZEISS EVO LS 10 scanning electron microscope in the secondary-electron mode at a magnification of $1000\times$ and an accelerating voltage of 10 kV. Gold sputter-coated fracture surfaces of air-cured Ref. and SRA1.00 pastes at the age of 28 d were examined using this technique.

3 RESULTS AND DISCUSSION

The flexural and compressive strengths of tested samples with various amounts of additives are shown in **Figure 2**. In **Figure 3**, the strengths are displayed relative to the strengths of the samples cured for 28 d submerged in water (samples submerged in water = 100 % strength, e.g. the reference water-cured mortar had approximately 121 MPa.²³ Generally, the curing of samples submerged in water led to higher values of compressive and bending strengths, which corresponds to the work of F. Collins and J. G. Sanjayan.²⁴ This is why the plotted values of air-cured samples are also

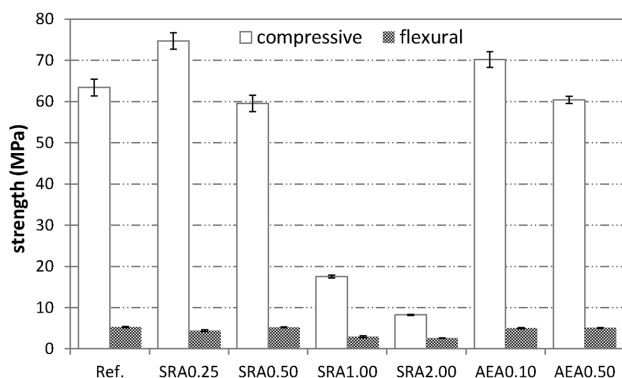


Figure 2: Compressive and flexural strengths of the prepared air-cured mortars

Slika 2: Tlačna in upogibna trdnost pripravljenih, na zraku sušenih malt

displayed relative to those cured in water. The curing of the specimens submerged in water permits their flexural and compressive strength development. It is also likely that surface cracking, which is often visible on AAS specimens, could serve as a crack initiator, leading to the propagation of major shrinkage cracks. Consequently, this significantly contributes to the decrease in flexural strengths.

The reduction of flexural strength is highest in the samples with 1 % and 2 % of SRA. The same is true for compressive strengths. With a lower content of SRA (0.25 % and 0.50 %), the reduction of strengths is lower than that of the reference sample without additives. In all the samples with SRA, the decrease of flexural strengths is lower compared to the compressive strengths, except for the sample with 0.25 % of SRA. This can be related to shrinkage. With a higher SRA content, the shrinkage and cracking during sample aging in air is reduced. However, a larger amount of SRA (in this study higher than 0.50 %) has a negative effect on the compressive strength. Therefore, sample SRA0.25 has a higher relative compressive strength than bending because the amount of SRA is such that it has no effect on the shrinkage and does not negatively influence the com-

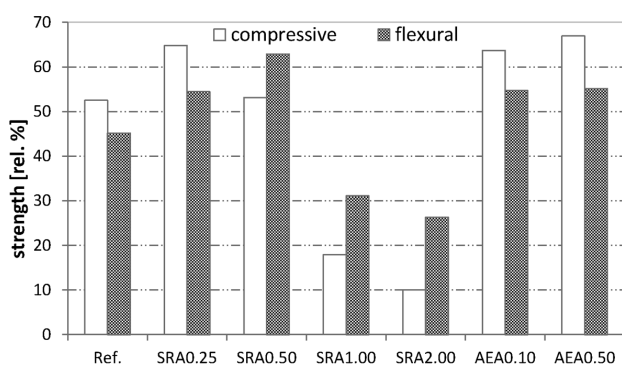


Figure 3: Relative compressive and flexural strengths (mortars cured in water = 100%)

Slika 3: Relativne tlačne in upogibne trdnosti (malta strjena v vodi = 100 %)

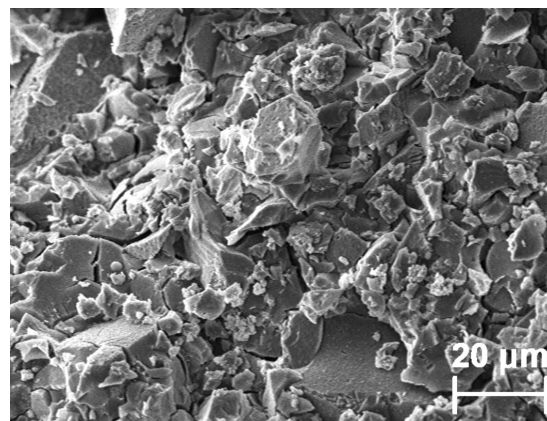


Figure 4: SEM picture of air-cured reference pastes

Slika 4: SEM-posnetek na zraku strjene referenčne paste

pressive strengths at the same time. The rapid reduction of strengths with the addition of SRA of 1 % and higher is further explained by the SEM images. **Figure 4** and **Figure 5** show the SEM picture of the fracture surface of the reference sample and the sample with 1 % of SRA, respectively. A dense matrix among the grains of slag is obvious in **Figure 4**, whereas in **Figure 5**, more porous matter among the grains of slag is observed. This also conforms to the study by V. Bílek et al.²³, where the authors investigated the influence of commercially available admixtures on the drying shrinkage of AAS in relation to the mechanical properties. Finally, the samples containing AEA had the highest relative compressive strengths (with AEA0.50 as the highest).

The carbonation depth reached 2.19 mm for SRA0.5 (Figure 7a) while SRA1.00 and SRA2.00 were completely carbonated (Figure 7b) after 28 d. Therefore the carbonation depths for SRA1.00 and SRA2.00 are not shown in Figure 6. According to V. Bílek et al.,²³ SRA likely acts as a hydration retardant. When the samples with a higher amount of SRA are cured in air, they lose significant amounts of water before they mature. Therefore, they contain a lower amount of binding phase, which is associated with higher porosity and

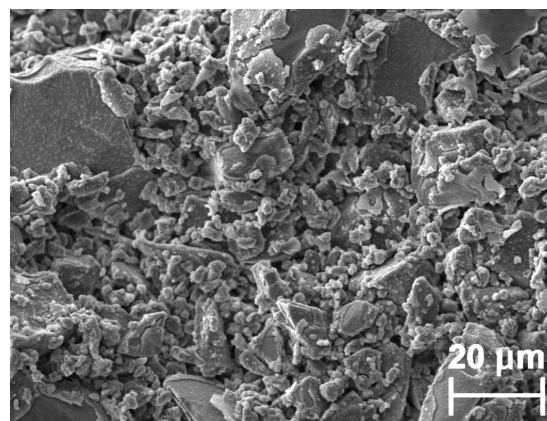


Figure 5: SEM picture of air-cured SRA1.00 paste

Slika 5: SEM-posnetek na zraku strjene SRA1.00 paste

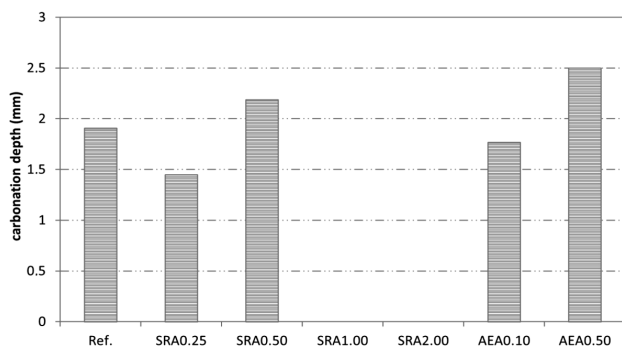


Figure 6: Carbonation depth of the prepared mortars

Slika 6: Globina karbonacije pripravljenih malt

thus faster carbonation. This is another reason for their low strengths.

Some of the results obtained, especially those for carbonation resistance, are inconsistent with those reported earlier. C. Bilim et al.²⁵ did not observe a significant difference in the carbonation depth of the samples with and without SRA activated by solid sodium silicate. When C. Bilim et al.²⁶ used liquid sodium silicate, the carbonation resistance of AAS mortars was even better in the presence of SRA. These differences are caused by the different composition of the mixtures (particularly the SiO_2 to Na_2O ratio of the activator) and are most likely due to the different origins of the additives used. Bilim et al. used SRA based on polypropylene glycol in both aforementioned studies^{25,26}, while the SRA used in the present study was based on 2-methyl-2,4-pentanediol. This indicates a strong dependence in the behaviour of AAS on the composition of commercially

available SRAs originally developed for PC-based systems.

4 CONCLUSION

Based on the results above, the conclusions can be summarized as follows:

- It was confirmed that curing by submerging in water is better for AAS than air curing in ambient laboratory conditions. The compressive and flexural strengths significantly decreased in all samples.
- When the content of admixtures was low, the reduction in strengths was slightly lower compared to the reference sample with no additive, while with a higher amount of SRA, the reduction in strengths was significantly higher.
- The incorporation of more than 0.5 % of SRA led to a rapid carbonation of AAS, which is likely related to the negative effect of SRA on AAS hydration and the resulting porous matrix.

Acknowledgement

This work is an output of the research and scientific activities of project LO1202 and the project Materials Research Centre at FCH BUT – Sustainability and Development, REG LO1211, with financial support of the MEYS under the programme NPU I.

5 REFERENCES

- ¹ M. Chi, Effects of dosage of alkali-activated solution and curing conditions on the properties and durability of alkali-activated slag concrete, *Construction and Building Materials*, 35 (2012), 240–245, doi:10.1016/j.conbuildmat.2012.04.005
- ² W. Zhang, Y. Hama, S. H. Na, Drying shrinkage and microstructure characteristics of mortar incorporating ground granulated blast furnace slag and shrinkage reducing admixture, *Construction And Building Materials*, 93 (2015), 267–277, doi:10.1016/j.conbuildmat.2015.05.103
- ³ E. Crossin, The greenhouse gas implications of using ground granulated blast furnace slag as a cement substitute, *Journal of Cleaner Production*, 95 (2015), 101–108, doi:10.1016/j.jclepro.2015.02.082
- ⁴ Y. Gu, Y. Fang, D. You, Y. Gong, C. Zhu, Properties and microstructure of alkali-activated slag cement cured at below- and about-normal temperature, *Construction and Building Materials*, 79 (2015), 1–8, doi:10.1016/j.conbuildmat.2014.12.068
- ⁵ L. Y. Yang, Z. J. Jia, Y. M. Zhang, J. G. Dai, Effects of nano-TiO₂ on strength, shrinkage and microstructure of alkali activated slag pastes, *Cement and Concrete Composites*, 57 (2015), 1–7, doi:10.1016/j.cemconcomp.2014.11.009
- ⁶ B. S. Gebregziabihier, R. Thomas, S. Peethamparan, Very early-age reaction kinetics and microstructural development in alkali-activated slag, *Cement and Concrete Composites*, 55 (2015), 91–102, doi:10.1016/j.cemconcomp.2014.09.001
- ⁷ X. Gao, Q. L. Yu, H. J. H. Brouwers, Reaction kinetics, gel character and strength of ambient temperature cured alkali activated slag-fly ash blends, *Construction and Building Materials*, 80 (2015), 105–115, doi:10.1016/j.conbuildmat.2015.01.065
- ⁸ M. Komljenović, Z. Baščarević, N. Marjanović, V. Nikolić, External sulfate attack on alkali-activated slag, *Construction and Building Materials*, 49 (2013), 31–39, doi:10.1016/j.conbuildmat.2013.08.013

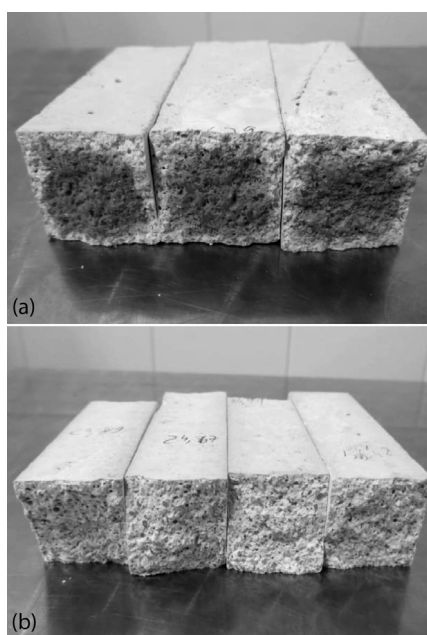


Figure 7: Carbonation of sample: a) SRA0.5 with carbonation depth of 2.19 mm and b) SRA1.0 completely carbonated

Slika 7: Karbonacija vzorcev: a) SRA0.5, z globino karbonacije 2,19 mm in b) SRA1.0 popolnoma karboniran

- ⁹ I. Ismail, S. A. Bernal, J. L. Provis, R. San Nicolas, D. G. Brice, A. R. Kilcullen, S. Hamdan, J. S. J. van Deventer, Influence of fly ash on the water and chloride permeability of alkali-activated slag mortars and concretes, *Construction and Building Materials*, 48 (2013), 1187–1201, doi:10.1016/j.conbuildmat.2013.07.106
- ¹⁰ R. J. Myers, B. Lothenbach, S. A. Bernal, J. L. Provis, Thermodynamic modelling of alkali-activated slag cements, *Applied Geochemistry*, 61 (2015), 233–247, doi:10.1016/j.apgeochem.2015.06.006
- ¹¹ J. J. Thomas, A. J. Allen, H. M. Jennings, Density and water content of nanoscale solid C-S-H formed in alkali-activated slag (AAS) paste and implications for chemical shrinkage, *Cement and Concrete Research*, 42 (2012), 377–383, doi:10.1016/j.cemconres.2011.11.003
- ¹² X. Yuan, W. Chen, Z. Lu, H. Chen, Shrinkage compensation of alkali-activated slag concrete and microstructural analysis, *Construction and Building Materials*, 66 (2014), 422–428, doi:10.1016/j.conbuildmat.2014.05.085
- ¹³ N. K. Lee, J. G. Jang, H. K. Lee, Shrinkage characteristics of alkali-activated fly ash/slag paste and mortar at early ages, *Cement and Concrete Composites*, 53 (2014), 239–248, doi:10.1016/j.cemconcomp.2014.07.007
- ¹⁴ C. D. Atiş, C. Bilim, Ö. Çelik, O. Karahan, Influence of activator on the strength and drying shrinkage of alkali-activated slag mortar, *Construction and Building Materials*, 23 (2009), 548–555, doi:10.1016/j.conbuildmat.2007.10.011
- ¹⁵ F. Collins, J. G. Sanjayan, Strength and shrinkage properties of alkali-activated slag concrete placed into a large column, *Cement and Concrete Research*, 29 (1999), 659–666, doi:10.1016/S0008-8846(99)00011-3
- ¹⁶ F. Jin, K. Gu, A. Al-Tabbaa, Strength and drying shrinkage of reactive MgO modified alkali-activated slag paste, *Construction and Building Materials*, 51 (2014), 395–404, doi:10.1016/j.conbuildmat.2013.10.081
- ¹⁷ M. Palacios, F. Puertas, Effect of superplasticizer and shrinkage-reducing admixtures on alkali-activated slag pastes and mortars, *Cement and Concrete Research*, 35 (2005), 1358–1367, doi:10.1016/j.cemconres.2004.10.014
- ¹⁸ B. Ma, W. Huixian., Rheological properties of self-compacting concrete paste containing chemical admixtures, *Journal Of Wuhan University Of Technology-Mater. Sci. Ed.* 28 (2013), 291–297, doi:10.1007/s11595-013-0681-x
- ¹⁹ T. Bakharev, J. G. Sanjayan, Y. B. Cheng, Effect of admixtures on properties of alkali-activated slag concrete, *Cement and Concrete Research*, 30 (2000), 1367–1374, doi:10.1016/j.cemconres.2004.10.014
- ²⁰ A. M. Rashad, A comprehensive overview about the influence of different additives on the properties of alkali-activated slag – A guide for Civil Engineer, *Construction and Building Materials*, 47 (2013), 29–55, doi:10.1016/j.conbuildmat.2013.04.011
- ²¹ J. Saliba, E. Rozière, F. Grondin, A. Loukili, Influence of shrinkage-reducing admixtures on plastic and long-term shrinkage, *Cement and Concrete Composites*, 33 (2011), 209–217, doi:10.1016/j.cemconcomp.2010.10.006
- ²² ČSN EN 196-1:2005, Methods of testing cement – Part 1: Determination of strength 2005
- ²³ V. Bílek Jr., L. Kalina, J. Koplík, R. Novotný, M. Hajdúchová, T. Opravil, Influence of chemical admixture on properties of alkali-activated slag-based mortars, *Advanced Materials Research*, 1124 (2015), 37–42, doi:10.4028/www.scientific.net/AMR.1124.37
- ²⁴ F. Collins, J. G. Sanjayan, Cracking tendency of alkali-activated slag concrete subjected to restrained shrinkage, *Cement and Concrete Research*, 30 (2000), 791–798, doi:10.1016/S0008-8846(00)00243-X
- ²⁵ C. Bilim, O. Karahan, C.D. Atiş, S. İlkentapar, Effects of chemical admixture and curing conditions on some properties of alkali-activated cementless slag mixtures, *KSCE Journal of Civil Engineering*, 19 (2015), 733–741, doi:10.1007/s12205-015-0629-0
- ²⁶ C. Bilim, O. Karahan, C.D. Atiş, S. İlkentapar, Influence of admixtures on the properties of alkali-activated slag mortars subjected to different curing conditions, *Materials and Design*, 44 (2013), 540–547, doi:10.1016/j.matdes.2012.08.049

EFFECT OF HOLDING TIME ON THE PRODUCTION OF Nb-NbAl₃
INTERMETALLIC COMPOSITES VIA
ELECTRIC-CURRENT-ACTIVATED SINTERINGVPLIV ČASA ZADRŽANJA NA IZDELAVO Nb-NbAl₃
INTERMETALNIH KOMPOZITOV Z ELEKTRIČNIM TOKOM
AKTIVIRANIH S SINTRANJEM

Muhammed Aybey, Tuba Yener, Mediha Ipek, Sakin Zeytin

Sakarya University, Engineering Faculty, Department of Metallurgy and Materials Engineering, Esentepe Campus, 54187, Adapazari,
Sakarya, Turkey
tcerezci@sakarya.edu.tr

Prejem rokopisa – received: 2015-07-01; sprejem za objavo – accepted for publication: 2016-02-05

doi:10.17222/mit.2015.179

A recently developed powder metallurgy processing technique – Electric Current Activated (Assisted) Sintering (ECAS) was employed to produce intermetallic Nb-NbAl₃ composites. In this study, to produce Nb-NbAl₃ in-situ intermetallic composites, Nb (99.8 % purity, less than 44 μm) and Al (99.5 % purity, less than 44 μm) elemental powders were mixed in the stoichiometric ratio corresponding to the Nb-Al phase diagram. The effect of different processing times, for (10, 30, 60) s, under maximum of 2000 A and 1.5-2.0 V, was investigated. Scanning electron microscopy and X-ray diffraction analysis were used to characterize the produced samples. X-ray diffraction studies revealed that the dominant phases are NbAl₃ and Nb. Scanning electron microscopy examinations showed a dense microstructure with a very low amount of porosity and also a trace amount of residual aluminium. The microhardness of the test materials sintered for 60 s via electric-current-activated sintering was about 405 HV±46 HV0,05.

Keywords: in situ composites, NbAl₃ aluminides, electric current activated sintering (ECAS)

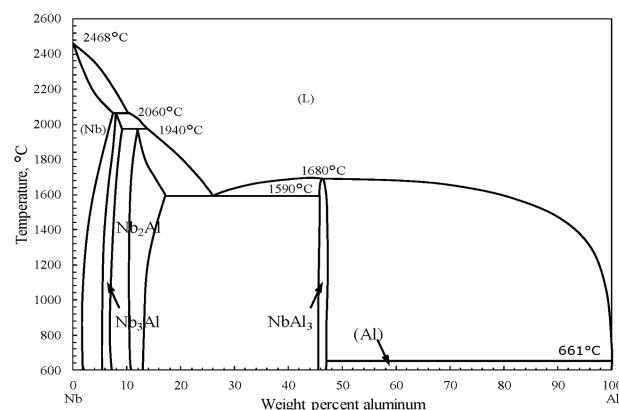
Pred kratkim razvita tehnika v metalurgiji prahov: sintranje, aktivirano z električnim tokom (ECAS), je bilo uporabljeno za in situ izdelavo intermetalnega kompozita Nb-NbAl₃. V študiji sta bila za in situ proizvodnjo Nb-NbAl₃ intermetalnega kompozita zmešana elementna prahova Nb (99.8 % čistost, delci manjši od 44 μm) in Al (99.5 % čistost, delci manjši od 44 μm), zmešana v stehiometričnem razmerju, skladno s faznim diagramom Nb-Al. Preiskovan je bil vpliv različnih časov izdelave: (10, 30, 60) s pri toku maksimalno 2000 A in napetosti 1,5-2,0 V. Izdelani vzorci so bili karakterizirani z vrstično elektronsko mikroskopijo in rentgensko difrakcijo. Rentgenska difrakcija je odkrila, da sta prevladujoči fazi NbAl₃ in Nb. Vrstična elektronska mikroskopija je pokazala gosto mikrostrukturo z majhnim deležem poroznosti in sledovi preostalega aluminija. Mikrotrodota preizkusnega materiala, sintranega 60 s, s sintranjem aktiviranim z električnim tokom, je bila okrog 405 HV±46 HV0,05.

Ključne besede: in situ kompoziti, NbAl₃ aluminidi, sintranje aktivirano z električnim tokom (ECAS)

1 INTRODUCTION

Intermetallic compounds have been the focus of significant research and development efforts during recent years. Among intermetallic compounds, niobium aluminides are very important and attractive.¹⁻³ Three intermetallic compounds are present in the Nb–Al binary system including Nb₃Al (A15 structure), Nb₂Al (D8b structure) and NbAl₃ (DO22 structure, TiAl₃ type).⁴⁻⁷ Among the various compounds in the Nb–Al system (Figure 1), NbAl₃ with its high melting point (1680 °C), low density (4.54 g/cm³), is attractive as a potential material for high-temperature applications.^{6,8} The applications of NbAl₃ include its use in turbine blades in aircraft engines or in stationary gas turbines.^{1,9} However, despite its attractive features, its usage is limited by inadequate ductility at room temperature. So, for optimization of room-temperature toughness, microstructural modifications are required.^{1,6,10} In-situ toughening is an alternative technique to enable a combination of brittle intermetallic phase with a ductile metallic phase in one

step production.^{11,12} Some conventional methods such as melting, casting and mechanical alloying techniques or self-propagating high-temperature synthesis (SHS)⁷⁻⁹ can be used for manufacturing intermetallics. A recently

Figure 1: Nb-Al phase diagram⁷Slika 1: Fazni diagram Nb-Al⁷

developed electric current activated/assisted sintering (ECAS) technique has been used in this study. This system enables the cold formed compact obtained from uniaxial compression to be inserted into a container, which is heated by passing an electrical current. In the present paper we prefer to apply the direct current resistive sintering technique to the Nb+3Al powder mixture in order to investigate a new route to determine the effect of holding time on the production of Nb-NbAl₃ in-situ composites.

2 EXPERIMENTAL PART

2.1 Materials and methods

Al and Nb elemental powders with 35–44 µm grain size and purity of 99.5 % and 99.8 %, respectively, were mixed to give the nominal composition of Nb₄₀Al₆₀ (w/%) for the formation of a NbAl₃ intermetallic based metallic Nb reinforced in-situ composite. The powder mixture was ball milled for 15 min then cold-pressed before sintering to form a cylindrical compact in a metallic die under a uniaxial pressure of 200 MPa. The dimensions of the compact were 15–16 mm diameter and 3–4 mm thickness. The production of Nb aluminide-based intermetallic compound was performed via the electric current activated sintering technique in an open atmosphere at 2000 A for (10, 30, 60) s. They are denoted as C1 and C2 and C3 in the following section, respectively. The process parameters are listed in **Table 1**.

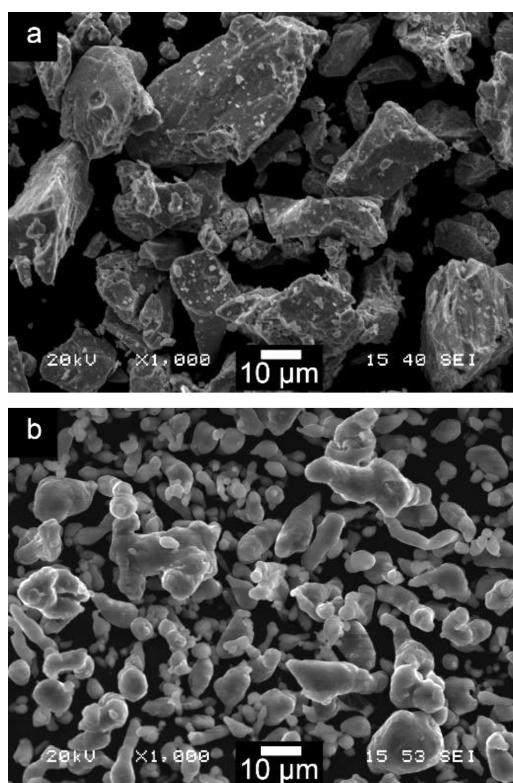


Figure 2: SEM micrographs of: a) Nb, b) Al powder
Slika 2: SEM-posnetka: a) Nb in b) Al prahu

Table 1: Process parameters for the samples

Tabela 1: Procesni parametri vzorcev

Sample code	w/%	Current (A)	Holding time (s)
C1	40Nb-60Al	2000	10
C2	40Nb-60Al	2000	30
C3	40Nb-60Al	2000	60

2.2 Characterization

The morphologies of the samples were examined by scanning electron microscopy (SEM-EDS) in terms of the resulting phases. X-ray diffraction (XRD) analyses were carried out using Cu-K α radiation with a wavelength of 0.15418 nm over a 2 θ range of 10–80°. The microhardness of the test materials was measured using a Vickers indentation technique with a load of 0.98 N using Leica WMHT-Mod model Vickers hardness instrument.

3 RESULTS AND DISCUSSION

3.1 SEM-EDS Analysis

Figure 2 shows SEM micrographs of the elemental Nb and Al powder particles. As seen in **Figure 2** the Al particles are rounded and Nb particles are angular and sharp cornered in shape.

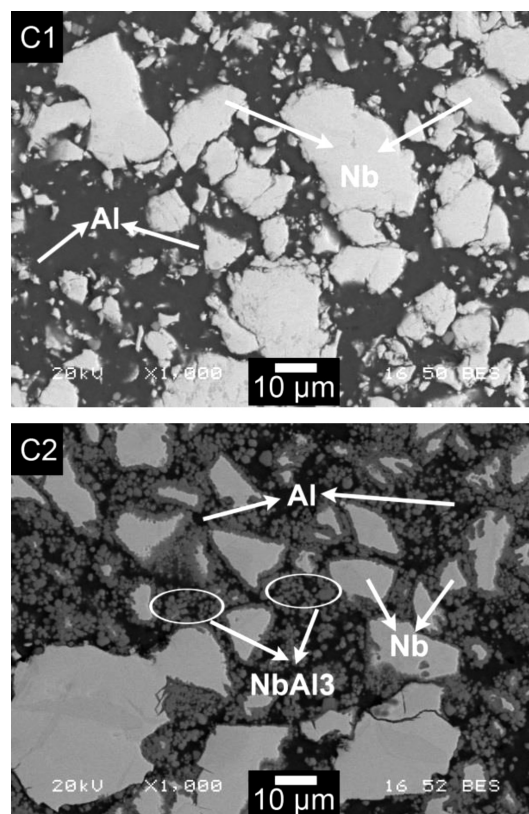


Figure 3: SEM micrographs of: a) C1 and b) C2 samples
Slika 3: SEM-posnetka vzorcev a) C1 in b) C2

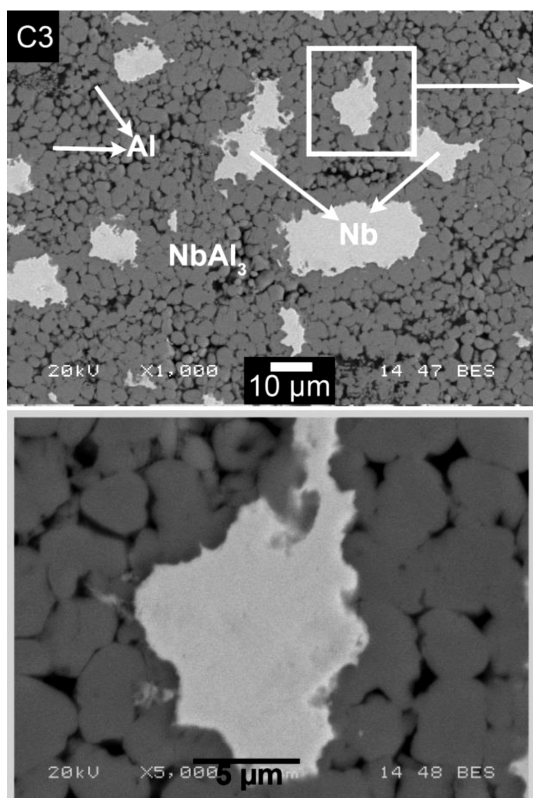


Figure 4: SEM micrographs of C3 Sample: a) 1000 ×, b) 5000 ×
Slika 4: SEM-posnetka vzorca C3: a) 1000 ×, b) 5000 ×

SEM-EDS analyses of C1, C2 and C3 intermetallic compounds are shown in **Figure 3**. The microstructure in **Figure 3a** shows that the low holding time results in separately formed Nb and Al areas. Increasing the processing time from 10 s to 30 s in C2, (**Figure 3b**), it starts to form a new phase like NbAl₃, but these microstructures are still far from the desired stoichiometric composition of the main NbAl₃ phase.

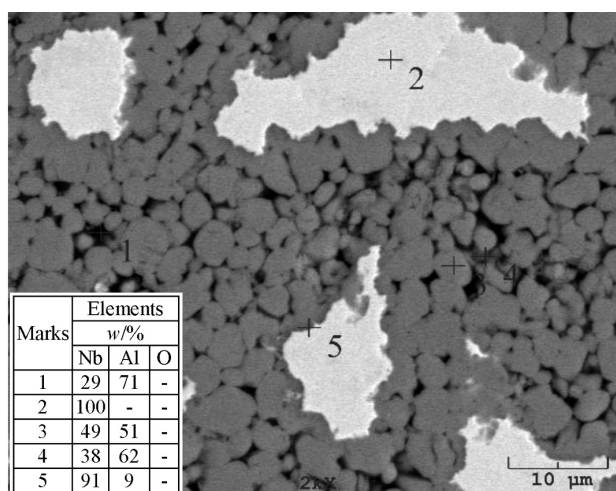


Figure 5: SEM-EDS analyses of C3 samples
Slika 5: SEM-EDS-analize na vzorcu C3

When it comes to the C3 sample, as seen in **Figure 4**, increasing the process holding time to 60 s, the main phase in the microstructure is Nb and NbAl₃. Besides this, there is also a little amount of residual Al phase and a little oxidation problem because of the open atmosphere sintering in ECAS. But that was not detected in the XRD analyses for being a small amount. In addition to that, a nearly fully dense microstructure was obtained after just a minute of holding process time, thanks to the electric current resistive sintering system.

As can be seen in the SEM-EDS analyses in **Figure 5**, the reaction was also not completed in the C3 compound. It is assumed that the applied voltage or current is insufficient for the complete transformation of the NbAl₃ phases in the sintering.

3.2 XRD Analysis

The XRD analysis, **Figure 6**, shows that the main phase of the composite is NbAl₃. The Nb phase is also seen in the XRD analyses, as desired. These results support the observations from the SEM-EDS analysis (**Figure 5**). This can be inferred from this result: Nb-NbAl₃ in-situ composites can be obtained for one minute and one step electric current activated system; however, for eliminating the residual aluminium in the compact. It is obvious that, it can be optimized with some other parameters such as voltage or current.

3.3 Hardness

The hardness values HV_{0.05} of the C1, C2 and C3 samples were measured as 165±20, 250±27, 405±46 respectively. The hardness of the intermetallic composites increases from 165±20 HV to 405±46 HV by increasing the holding time in the process due to the formation of a higher proportion of intermetallic phases. The hardness results for the NbAl₃ composite is in agreement with the literature.¹³

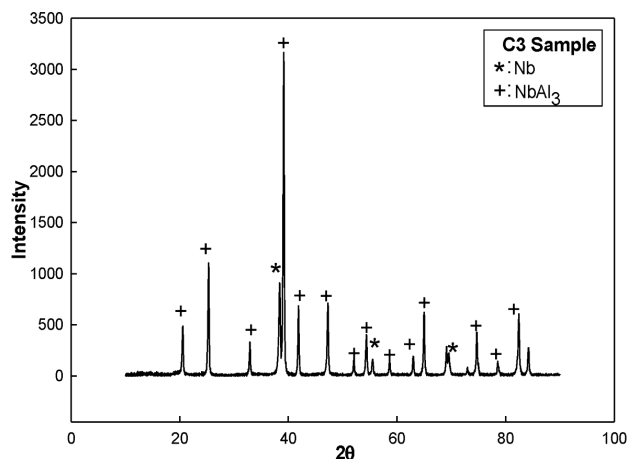


Figure 6: XRD Analyses of C3 sample (Nb-NbAl₃)
Slika 6: Rentgenogram vzorca C3 (Nb-NbAl₃)

4 CONCLUSIONS

Some of the results obtained from this study can be summarized as follows:

- Niobium aluminide-based composites were fabricated by electric current activated/assisted sintering at 2000 A in only 60 s.
- Under such conditions, the reaction is nearly completed within a very short period of time and the end-product is consolidated to a nearly fully dense microstructure.
- SEM-EDS and XRD analyses showed that 60 s are sufficient for obtaining Nb-NbAl₃ phases. However, for eliminating the residual aluminium in the compact it can be optimized some other parameters such as voltage or current.
- Hardness of the intermetallic composites increases from 165±20 HV to 405±46 HV by increasing the holding time in the process by ensuring the formation of a higher proportion of intermetallic phases

Acknowledgement

This work was supported by Sakarya University Research Foundation (Project Number: 2013-01-08-034)

5 REFERENCES

- ¹ V. Gauthier, F. Bernard, E. Gaffet, D. Vrel, M. Gailhanou, J. Larpin, Investigations of the formation mechanism of nanostructured NbAl₃ via MASHS reaction, *Intermetallics*, 10 (2002), 377–389, doi:10.1016/S0966-9795(02)00010-9
- ² L. Muruges, K. V. Rao, R. Ritchie, Powder processing of ductile-phase-toughened Nb- Nb₃Al in situ composites, *Materials Science and Engineering A*, 189 (1994), 201–208, doi:10.1016/0921-5093(94)90416-2
- ³ V. Gauthier, C. Josse, F. Bernard, E. Gaffet, J. Larpin, Synthesis of niobium aluminides using mechanically activated self-propagating high-temperature synthesis and mechanically activated annealing process, *Materials Science and Engineering A*, 265 (1999), 117–128, doi:10.1016/S0921-5093(98)01141-1
- ⁴ X. Y. Yan, D. J. Fray, Synthesis of niobium aluminides by electro-deoxidation of oxides, *Journal of Alloys and Compounds*, 486 (2009), 154–161, doi:10.1016/j.jallcom.2009.06.176
- ⁵ L. M. Peng, Synthesis and mechanical properties of niobium aluminide-based composites, *Materials Science and Engineering A*, 480 (2008), 232–236, doi:10.1016/j.msea.2007.07.046
- ⁶ W. Miao, K. Tao, B. Liu, B. Li, Formation of NbAl₃ by Nb ion implantation using metal vapor vacuum arc ion source, *Nuclear Instruments and Methods in Physics Research Section B: Beam Interactions with Materials and Atoms*, 160 (2000), 343–348, doi:10.1016/S0168-583X(99)00600-X
- ⁷ C. L. Yeh, H. J. Wang, Effects of sample stoichiometry of thermite-based SHS reactions on formation of Nb–Al intermetallics, *Journal of Alloys and Compounds*, 485 (2009), 280–284, doi:10.1016/j.jallcom.2009.06.098
- ⁸ H. Sina, S. Iyengar, Studies on the formation of aluminides in heated Nb–Al powder mixtures, *Journal of Alloys and Compounds*, 628 (2015), 9–19, doi:10.1016/j.jallcom.2014.12.151
- ⁹ N. Wang, C. Du, J. Hou, Y. Zhang, K. Huang, S. Jiao, et al., Direct synthesis of Nb–Al intermetallic nanoparticles by sodiothermic homogeneous reduction in molten salts, *Intermetallics*, 43 (2013), 45–52, doi:10.1016/j.intermet.2013.07.005
- ¹⁰ H. Chung, M. Jilavi, T. Duffey, M. Shannon, W. Kriven, J. Mazumder, NbAl₃/Al microlaminated thin films deposited by UV laser ablation, *Thin solid films*, 388 (2001), 101–106, doi:10.1016/S0040-6090(01)00833-1
- ¹¹ T. Yener, S. Okumus, S. Zeytin, In Situ Formation of Ti-TiAl₃ Metallic-Intermetallic Composite by Electric Current Activated Sintering Method, *Acta Physica Polonica A*, 127 (2015), 917–920, doi:10.12693/APhysPolA.127.917
- ¹² T. Yener, S. Zeytin, Synthesis And Characterization Of Metallic-Intermetallic Ti-TiAl₃, Nb-Ti-TiAl₃ Composites Produced With Electric-Current-Activated Sintering (ECAS), *Mater. Tehnol.*, 48 (2014), 847–850
- ¹³ D. Totten, S. Mackenzie, *Handbook of Aluminum vol. 2, Alloy Production and Materials Manufacturing*: Markel, Decker, 2003

ANALYSIS OF THE FIBER DISTRIBUTION, SIZE, AND VOLUME RATIO OF UNIDIRECTIONAL COMPOSITE PLATES WITH DIFFERENT THICKNESSES

ANALIZA RAZPOREDITVE VLAKEN, VELIKOSTI IN VOLUMSKEGA DELEŽA V ENOSMERNIH, RAZLIČNO DEBELIH KOMPOZITNIH PLOŠČAH

Robert Zemčík¹, Hana Srbová², Kamil Ekštein³, Ivan Pirner⁴, Rostislav Medlín⁵

¹University of West Bohemia in Pilsen, NTIS – New Technologies for the Information Society, Univerzitní 22, 301 00 Pilsen, Czech Republic

²University of West Bohemia in Pilsen, Department of Mechanics, Univerzitní 22, 301 00 Pilsen, Czech Republic

³University of West Bohemia in Pilsen, Department of Computer Science and Engineering, Univerzitní 22, 301 00 Pilsen, Czech Republic

⁴University of West Bohemia in Pilsen, Department of Cybernetics, Univerzitní 22, 301 00 Pilsen, Czech Republic

⁵University of West Bohemia in Pilsen, New Technologies – Research Centre in the West Bohemian Region, Univerzitní 22, 301 00 Pilsen, Czech Republic
zemcik@kme.zcu.cz

Prejem rokopisa – received: 2015-07-02; sprejem za objavo – accepted for publication: 2015-12-18

doi:10.17222/mit.2015.195

This work focuses on an assessment of the real fiber and matrix volume ratios of unidirectional fiber composites that can be used for the design of corresponding numerical models on the micro-scale. Samples with polished cross-sections were prepared from three composite plates and they were previously analyzed using scanning electron microscopy (SEM). All the plates were manufactured from the same prepreg material using autoclave technology. Each plate consisted of a different number of plies. Images of the various parts of the composite cross-sections obtained with SEM are analyzed using several image-processing techniques programmed in Matlab, its Image Processing Toolbox, and C code. The results of this analysis are the center positions and radii of all fibers within the image. The fiber and matrix volume ratios are determined subsequently and mutually compared for different locations across the plates' thicknesses.

Keywords: composite, unidirectional, micromechanics, constituents, image, detection, microscopy, cross-section

Delo je osredotočeno na oceno realnih vlaken in volumskega deleža v osnovi, v enosmernih kompozitih iz vlaken, ki jih je mogoče uporabiti za postavitev ustreznih numeričnih modelov na mikropodročju. Pripravljeni vzorci, s poliranim presekom, iz treh kompozitnih plošč, so bili pregledani s pomočjo vrstičnega elektronskega mikroskopa (SEM). Vse plošče so bile izdelane iz enakega, v avtoklavih izdelanega, predimpregniranega materiala. Vsaka plošča je bila sestavljena iz različnega števila plasti. Posnetki različnih delov preseka kompozita, dobljeni s SEM, so bili analizirani z več tehnikami za obdelavo slik, programiranimi v Matlab, Image Processing Toolbox in C-kodo. Rezultati teh analiz so pozicije sredine in radiji vseh vlaken na posnetku. Pozneje so bili določeni, in medsebojno primerjani, volumenski deleži vlaken na različnih lokacijah preko debeline plošče.

Ključne besede: kompozit, enosmeren, mikromehanika, gradniki, posnetek, odkrivanje, mikroskopija, prečni presek

1 INTRODUCTION

All methods of fabricating unidirectional fiber-reinforced composites result in a non-uniform distribution of fibers in the matrix. The fiber distribution affects the mechanical properties of the composite. In ¹ the local stress fields and damage initiation in dependence on the fiber distribution are investigated. Although the fiber volume ratio (usually designated as v_f) determines the geometry of composite micromodels and subsequently the identified homogenized material properties², it is a problem to determine it precisely. For example, a fiber composite structure manufactured by transfer molding method typically ranges between approximately $v_f = 0.5$ and $v_f = 0.6$.³ The actual value can be different in various parts of the structure and it can significantly influence the local properties, such as the stiffness, strength, or durability.

2 EXPERIMENTAL PART

Three specimens were cut out from three different carbon/epoxy plates (designated as A, B, and C) using a water jet. Each plate was made of a different number (1, 2, and 4) of similar autoclaved prepreg layers. The specimens were fixed in epoxy resin and their cross-sections were polished on a low-speed polishing machine.

Gray-scale images of various parts of the cross-sections were obtained using scanning electron microscopy (SEM). The images were obtained using a magnification factor of 4000 with 15.9 px/μm (pixels per micrometer), as shown in **Figure 1**. They were taken at the top, middle and bottom regions of the plate's thickness. An example of the image in **Figure 2** with a full thickness view (obtained using magnification factor of 150) shows the layers and approximate position of the three investigated areas.

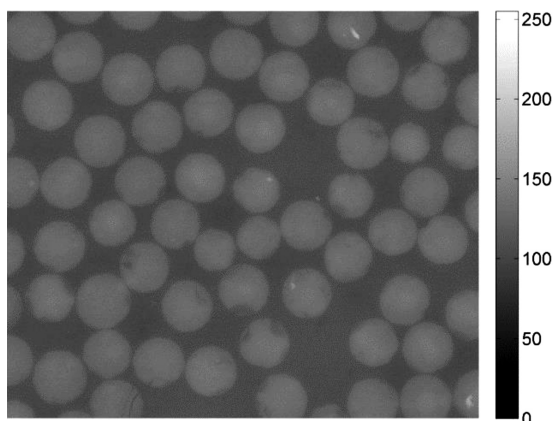


Figure 1: Original image of bottom area of plate C, intensity values range from 82 to 201

Slika 1: Originalni posnetek spodnjega dela plošče C, vrednosti intenzitete so med 82 in 201

In general, the quality of the obtained SEM images is quite low and the contrast varies between the different areas and samples. Therefore, the following automated image analysis includes several quality-improving steps.

3 IMAGE PROCESSING

The design stage of the image-processing algorithm was preceded by a thorough analysis of the obtained gray-scale microscopic images of the material cuts. Each image is a matrix $f(x,y)$ with pixel intensity values ranging from 0 to 255 and x and y being the pixel coordinates ($x = 1..M$, $y = 1..N$, where $M \times N$ defines the image size). All these images demonstrated a substantial, strong

common trait, which is a rather small contrast gradient over the whole image. Thus, the standard computer vision methods for both edge detection and binarization provide poor results or fail completely, which makes the object detection impossible.

The analysis of the image collection proved that the tonal distribution of the gray-scale images (represented by a histogram of pixel values) is of a bimodal nature. It clearly indicates that the image can be successfully segmented so that two global regions are identified: a background and the desired set of foreground objects, in this case the fibers of the composite material.

However, due to the small contrast gradient the bimodal histogram – or rather its region of the highest interest where the binarization threshold is located – is very narrow and even a minor inaccuracy in the position of the threshold can spoil the binarization. Unfortunately, the traditional reliable techniques for threshold detection, like, e.g., the Otsu method, set the binarization threshold in this case completely incorrectly. The Otsu method is a robust efficient technique for binarization-threshold estimation used in most of the computer-vision toolboxes. It is used, for instance, by MATLAB's `im2bw` function for image binarization.⁴

Thus, a new robust method for threshold estimation on images with bimodal histograms was needed.

4 THRESHOLD ESTIMATION

Before computing the threshold estimate the original image $f(x,y)$ is filtered by a median filter over a 3×3 neighborhood. Then, a histogram $h(i)$ of pixel intensities $i = 0..255$ is computed. The obtained histogram must be weighted before further processing as it has usually rather extreme values at both ends, i.e., both very low and very high intensities are contained heavily in the image (mostly due to the black-and-white state information added by the microscope software). The weighting is performed by a Hann window. The weighted histogram is then smoothed by Gaussian smoothing, a convolution filtering with a Gaussian kernel. The neighborhood used for the discrete convolution is an odd ceiling of 2.5 % of the whole histogram length, i.e., for the 256-bin histogram seven neighboring values are used. The value of the variance is set to 1.

The weighted smoothed histogram is numerically differentiated in order to get an estimate of the first derivative dh/di with respect to the intensity. The derivative is smoothed by the same Gaussian filter as mentioned above. In the next step, the histogram derivative is gated.

A list of threshold position candidates is assembled by searching for zero values of the histogram. Since the histogram is discrete a zero-crossing detection algorithm is applied.

Depending on the character of the input image, the candidate list should have 2 or 3 items (although under real conditions, it might have more than three and the

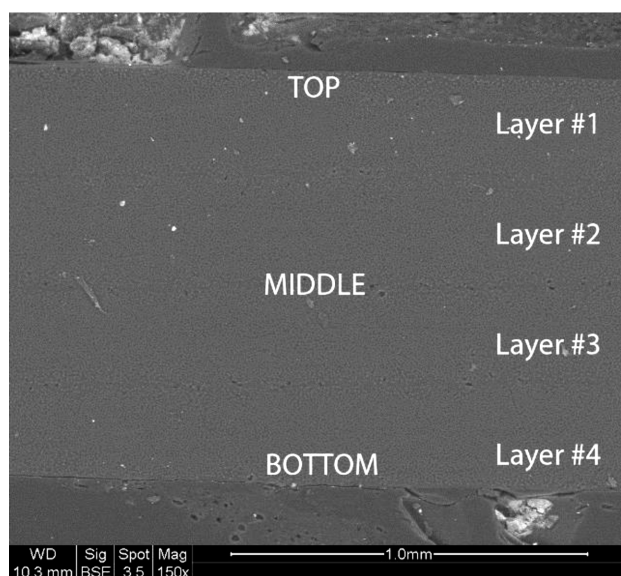


Figure 2: Cross-section of unidirectional composite plate (C) made of 4 prepregs obtained using SEM, approximate locations of investigated areas (top, middle, and bottom) are marked

Slika 2: SEM-posnetek preseka enosmerne kompozitne plošče (C), izdelane iz 4 predimpregniranih plasti, označeni so približni položaji preiskovanega področja (vrh, sredina, dno)

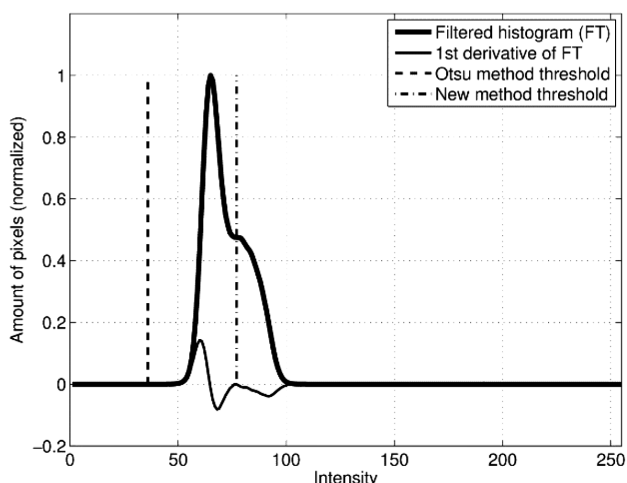


Figure 3: Threshold estimation from histogram
Slika 3: Prag, določen iz histograma

algorithm is robust to this case). One of the candidate items is always equal to the position of the maximum value in the histogram. Then, the threshold position t is set to the next candidate in the direction towards the side where there is more remaining candidates – in the case with three or more candidates in the list. If there are only two candidates, the threshold position is set to the candidate not equal to the maximum position (such situation is depicted in **Figure 3**).

5 FIBER CENTER DETECTION

The original gray-scale image f is binarized to f_{bin} (**Figure 4**) using the threshold value t obtained above:

$$f_{\text{bin}}(x, y) = \begin{cases} 0, & f(x, y) < t \\ 1, & f(x, y) \geq t \end{cases} \quad (1)$$

and then processed by dilation.⁵ The dilated image (**Figure 5**) is obtained as:

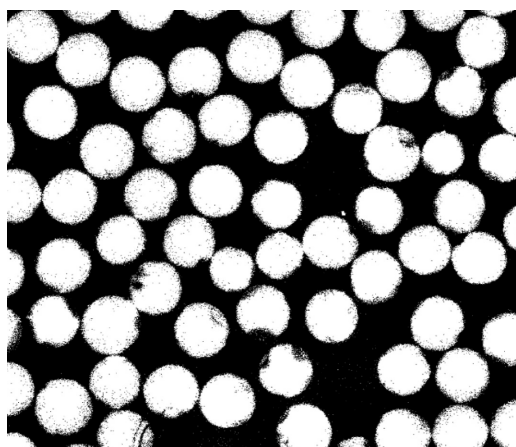


Figure 4: Binary image of bottom area of plate C, threshold intensity was determined to be $i = 118$

Slika 4: Binarna slika spodnjega dela plošče C, intenziteta praga je bila določena kot $i = 118$

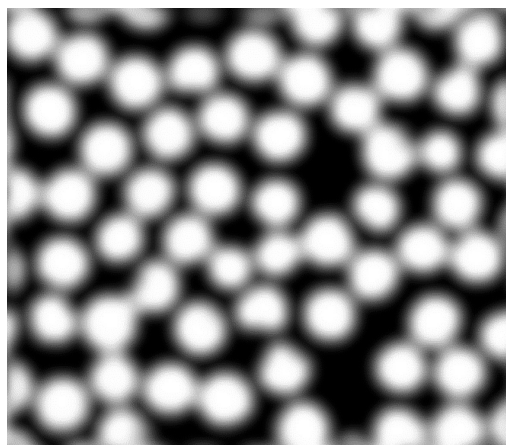


Figure 5: Dilated image of bottom area of plate C
Slika 5: Razširjena slika spodnjega dela plošče C

$$\bar{f}(x, y) = (f_{\text{bin}} \oplus g)(x, y) = \max\{f(x-x', y-y') + g(x', y') \mid (x', y') \in D_B\} \quad (2)$$

where g is binary structuring matrix (5×5) of ones, with rectangular domain D_B .⁴

The preprocessed image, a circle binary mask of the minimum fiber cross-section size and a discrete spatial matrix⁶ are then transformed with two-dimensional discrete Fourier transform:

$$F(u, v) = \sum_{n=0}^{N-1} \sum_{m=0}^{M-1} f(x, y) \cdot e^{-2\pi i \left(\frac{nx}{N} + \frac{my}{M} \right)} \quad (3)$$

where F is the image matrix in spatial frequencies u and v . Matrix G in spatial frequencies is obtained by discrete convolution:

$$G(u, v) = F(u, v) * (H(u, v) \cdot Q(u, v)) \quad (4)$$

where H is a binary mask and Q is the matrix transformed by the Fourier transform (3). Its local maxima are considered as the fiber center positions (x_j, y_j) .^{4,6}

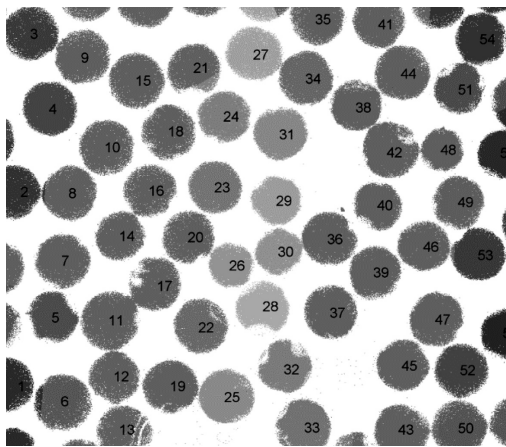


Figure 6: Clustered image of bottom area of plate C, in total, 56 clusters were detected

Slika 6: Slika gruč v spodnjem delu plošče C, skupaj je bilo odkritih 56 gruč

6 RADIUS AND AREA DETECTION

Further, a cluster analysis was applied to the binary image f_{bin} . The cluster analysis is an iterative process where a set of similar objects (pixels with similar intensity) is assigned to a group (cluster). The center positions. In this case a hierarchical clustering method was used. Each cluster belongs to one of the center positions (x_j, y_j) . The fiber area S_j is calculated as the number of pixels assigned to each cluster j (Figure 6) and the corresponding fiber radius r_j is then approximated by Equation (5):

$$r_j = \sqrt{\frac{S_j}{\pi}} \quad (5)$$

The fiber volume ratio v_f is then calculated as the ratio of pixels corresponding to all the fibers and the total number of pixels (in the selected rectangular area).

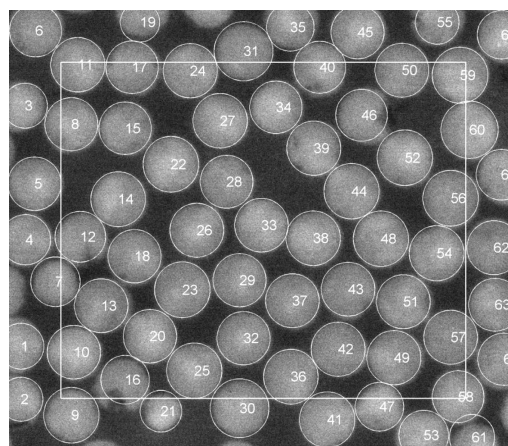


Figure 9: Analyzed bottom area of plate A, gray-scale from SEM with maximized contrast, circles denote detected fibers (position and size)
Slika 9: Analiziran spodnji del plošče A, SEM-posnetek s povečanim kontrastom, krogi označujejo odkrita vlakna (pozicijo in velikost)

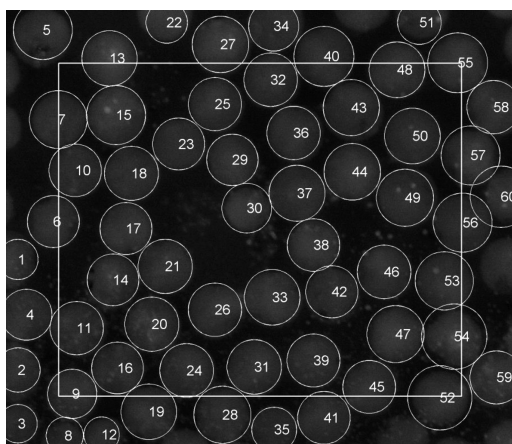


Figure 7: Analyzed top area of plate A, gray-scale from SEM with maximized contrast; circles denote detected fibers (position and size)
Slika 7: Analiziran vrhnji del plošče A, SEM-posnetek s povečanim kontrastom; krogi označujejo odkrita vlakna (pozicijo in velikost)

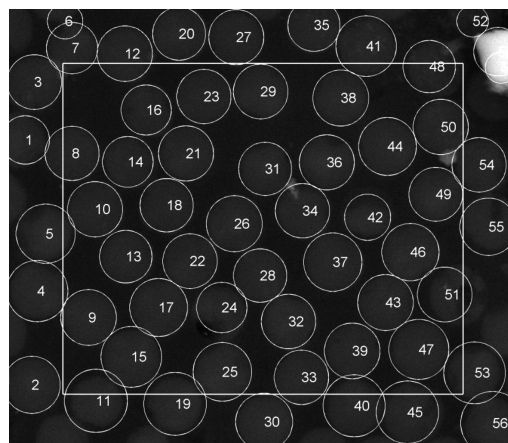


Figure 10: Analyzed top area of plate B, gray-scale from SEM with maximized contrast, circles denote detected fibers (position and size)
Slika 10: Analiziran zgornji del plošče B, SEM posnetek s povečanim kontrastom, krogi označujejo odkrita vlakna (pozicijo in velikost)

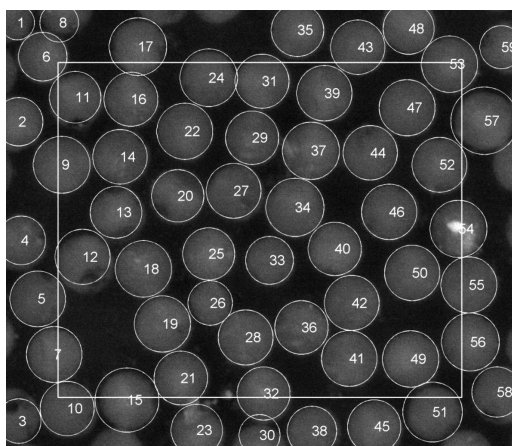


Figure 8: Analyzed middle area of plate A, gray-scale from SEM with maximized contrast, circles denote detected fibers (position and size)
Slika 8: Analizirano srednje področje plošče A, SEM-posnetek s povečanim kontrastom, krogi označujejo odkrita vlakna (pozicijo in velikost)

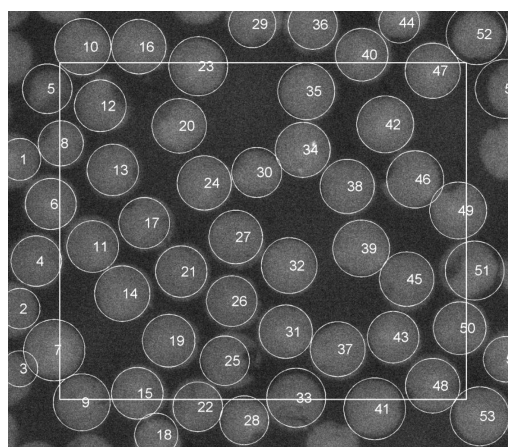


Figure 11: Analyzed middle area of plate B, gray-scale from SEM with maximized contrast, circles denote detected fibers (position and size)
Slika 11: Analiziran srednji del plošče B, SEM-posnetek s povečanim kontrastom, krogi označujejo odkrita vlakna (pozicijo in velikost)

7 RESULTS

All the images were analyzed using the above-described process. The positions and sizes of the detected fibers (cyan circles with cluster IDs) are shown in **Figures 7 to 15**. The gray-scale images are shown with maximized contrast. The yellow rectangle denotes an area for which the fiber volume ratio and the average fiber radius were calculated. The calculated values (together with standard deviation "SD") are summarized in **Table 1**. It was found that the volume ratio is slightly larger in the top and bottom areas in all the plates. The average fiber radius in all the plates was found to be 54.5276 px, which corresponds to 3.4294 μm.

Table 1: Properties obtained from images

Tabela 1: Lastnosti, dobljene iz posnetkov

Image / area	Fiber volume ratio	Averaged fiber radius	Fiber radius
	v_f	(r)	$sd(r)$
	(-)	(px)	(px)
A-top	0.62378	55.4685	3.3918
A-middle	0.61156	55.2918	3.5781
A-bottom	0.65256	53.8739	2.6742
B-top	0.63991	56.2806	3.6586
B-middle	0.53645	54.2127	3.6388
B-bottom	0.60706	58.3071	4.7778
C-top	0.58752	53.1380	4.1013
C-middle	0.43809	52.6896	4.1948
C-bottom	0.54454	51.4864	3.6767

8 CONCLUSIONS

A new approach was proposed for an accurate estimation of the threshold value that is necessary for the creation of a proper binary map and subsequent clustering of the objects in images. The method was used for the detection of fibers in images of cross-sections of unidirectional composite plates obtained by SEM. The

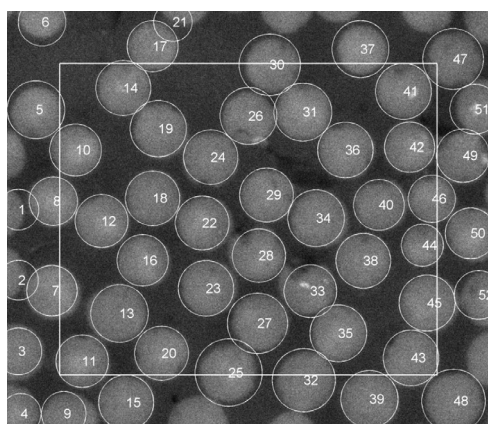


Figure 12: Analyzed bottom area of plate B, gray-scale from SEM with maximized contrast, circles denote detected fibers (position and size)

Slika 12: Analiziran spodnji del plošče, SEM-posnetek s povečanim kontrastom, krogi označujejo odkrita vlakna (pozicijo in velikost)

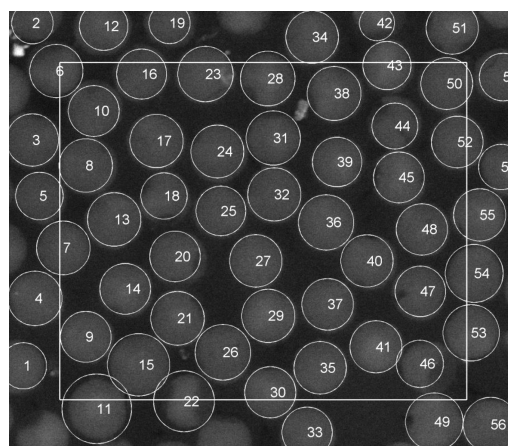


Figure 13: Analyzed top area of plate C, gray-scale from SEM with maximized contrast, circles denote detected fibers (position and size)

Slika 13: Analiziran zgornji del plošče C, SEM-posnetek s povečanim kontrastom, krogi označujejo odkrita vlakna (pozicijo in velikost)

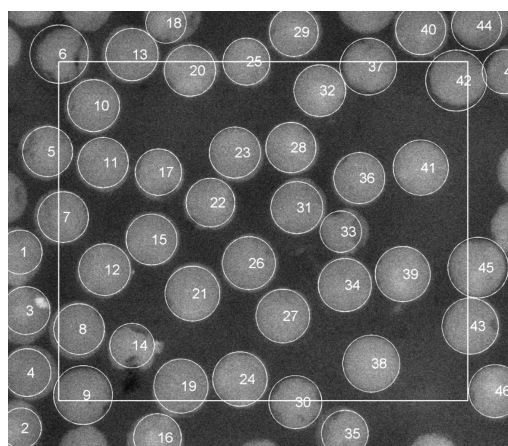


Figure 14: Analyzed middle area of plate C, gray-scale from SEM with maximized contrast, circles denote detected fibers (position and size)

Slika 14: Analiziran srednji del plošče C, SEM-posnetek s povečanim kontrastom, krogi označujejo odkrita vlakna (pozicijo in velikost)

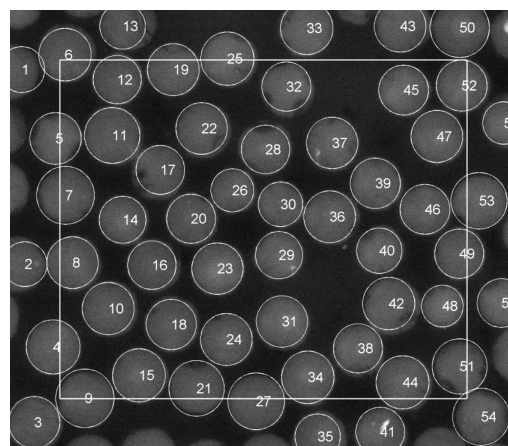


Figure 15: Analyzed bottom area of plate C, gray-scale from SEM with maximized contrast, circles denote detected fibers (position and size)

Slika 15: Analiziran spodnji del plošče C, SEM-posnetek s povečanim kontrastom, krogi označujejo odkrita vlakna (pozicijo in velikost)

method provided acceptable results, even in the case of relatively low-quality (low-contrast) images. The analysis also showed that the fiber volume ratio tends to have larger values at the surfaces of the composite, rather than in the center of the plates. Such data are important for reliable micromechanical models.⁷

Acknowledgement

The work was supported by the European Regional Development Fund (ERDF), through project "NTIS – New Technologies for Information Society", European Centre of Excellence, CZ.1.05/1.1.00/02.0090, by project LO1506 PUNTIS, and by the student research project of Ministry of Education of Czech Republic SGS-2013-036.

9 REFERENCES

- ¹ B. F. Sorenson, R. Tarleja, Effects of nonuniformity of fiber distribution on thermally-induced residual stresses and cracking in ceramic matrix composites, *Mechanics of Materials*, 16 (1993), 351–363
- ² V. Laš, *Mechanics of Composite Materials*, University of West Bohemia, Pilsen 2008
- ³ R. T. Reavely, W. Kim, Method of fabricating fiber reinforced composite articles by resin transfer molding, United States Patent, Patent no. 4988469, Jan. 29, 1991
- ⁴ User's Guide (R2013a), Mathworks, 2013, <http://www.mathworks.com/help/>
- ⁵ M. Železný, Digital image processing, Lectures, Department of Cybernetics, Faculty of Applied Sciences, University of West Bohemia, http://www.kky.zcu.cz/uploads/courses/zdo/ZDO_aktual_130215.pdf
- ⁶ H. Srbová, I. Pirner, R. Zemčík, R. Medlín, Analysis of fiber distribution and volume ratio of unidirectional composite for micromodels, *Transactions of the VŠB – Technical University of Ostrava, Mechanical Series*, LIX (2013) 3
- ⁷ T. Kroupa, H. Srbová, R. Zemčík, Identification of the initial failure and damage of substituents of a unidirectional fiber-reinforced composite using an micromodel, *Mater. Tehnol.*, 48 (2014) 4, 549–553

THE USE OF NATURAL SEPIOLITE FIBER IN CONCRETE

UPORABA NARAVNEGA SEPIOLITNEGA VLAKNA V BETONU

Selçuk Koltka¹, Tayfun Uygunoğlu², Eyüp Sabah¹, Muhammed Fatih Can¹¹Afyon Kocatepe University, Department of Mining Engineering, 03200 Afyonkarahisar, Turkey²Afyon Kocatepe University, Department of Civil Engineering, 03000 Afyonkarahisar, Turkey
uygunoglu@aku.edu.tr*Prejem rokopisa – received: 2015-07-08; sprejem za objavo – accepted for publication: 2015-12-23*

doi:10.17222/mit.2015.210

To determine the effect of sepiolitic fibers on the characteristics of fresh and hardened concrete, i.e., slumping, density, air content, ultrasonic pulse velocity, freeze-thaw, compressive strength, bending and splitting, tensile strength tests were conducted by the addition of de-fibered sepiolite to the cement in ratios of 0.5 %, 1 %, 2 % and 3 % of mass fractions. The fibers support higher slumping for fresh concrete and increased workability. Samples with 1 % and 3 % addition have similar compressive strength values to the reference series after 28 d. The bending strength of the 2 % added sample is closer to the bending strength of the 28-days reference concretes; however, it is reduced for 0.5 %, 1 % and 3 %. For all the reinforcement ratios the splitting strength increased. The highest impact strength performed for a 3 % reinforcement sample increased by 29 % and scanning electron microscopy (SEM) investigations reveal that the white sepiolite fibers are dispersed homogeneously in the concrete, and therefore it, reinforce especially at the interface of the aggregate cement paste by increasing durability.

Keywords: sepiolite fiber, mechanical activation, fiber reinforced concrete.

Za določitev vpliva sepiolitnih vlaken na značilnosti svežega in strjenega betona so bili izvedeni; razlivanje pri padcu, gostota, vsebnost zraka, hitrost ultrazvočnega impulza, zmrznjenost in odtajanje, tlačna trdnost, upogibanje in cepilno natezna trdnost z dodatkom razvlaknjene sepiolita betonu v masnih deležih 0,5 %, 1 %, 2 % in 3 %. Vlakna pospešujejo razlivanje svežega betona in izboljšajo njegovo oblikovalnost. Vzorca z dodatkom 1 % in 3 % sta pokazala podobno tlačno trdnost kot referenčna serija po 28 d. Upogibna trdnost pri vzorcu z 2 % dodatka je zelo blizu upogibni trdnosti referenčnega betona po 28 d; vendar je manjša pri dodatkih 0,5 %, 1 % in 3 %. Pri vseh dodatkih pa je cepilna trdnost narasla. Najvišja udarna žilavost izvedena pri vzorcu s 3 % dodatkom je narasla za 29 % in preiskava z vrstičnim elektronskim mikroskopom (SEM) je odkrila, da so bela sepiolitna vlakna homogeno razpršena v betonu, zato ojačajo stik agregata s cementno pasto in povečajo trajnost betona.

Ključne besede: sepiolitna vlakna, mehanska aktivacija, z vlaknom ojačan beton

1 INTRODUCTION

The term fiber reinforced concrete (FRC) is defined by the American Concrete Institute (ACI) Committee 544¹ as a concrete made of hydraulic cements containing fine or fine and coarse aggregates and discontinuous discrete fibers. Inherently, concrete is brittle under tensile loading. The mechanical properties of concrete can be improved by reinforcement with randomly oriented short discrete fibers, which prevent and control the initiation, propagation, or coalescence of cracks.^{2,3} The character and performance of FRC changes depending on the matrix properties as well as the fiber material, fiber concentration, fiber geometry, fiber orientation, and fiber distribution.^{4,5}

In the construction industry, which has undergone a very rapid development period since the 1980s, fiber-reinforced precast concrete products have been fulfilling an important role for both designers and contractors by offering technical and aesthetic convenience. Because of the health problems it caused, asbestos, once widely used as a provider of fibrous structure, left its place to fibrous synthetic materials.⁶ Straw was used to reinforce sun-baked bricks, and horsehair was used to reinforce masonry mortar and plaster. Human beings have always

been remarkably adaptable, working with the materials around them to make whatever is required. A wide variety of fibers have thus been used with cement-based matrices. They include metallic fibers, polymeric fibers, mineral fibers and vegetable fibers. In recent years, a great deal of interest has been created worldwide in the potential applications of natural fiber-reinforced, cement-based composites^{7,8}. Wood, grasses, clay and stone have all been used as they occur naturally, but man's ability to process natural resources has improved in parallel with man's own development. In modern times, a wide range of engineering materials (including ceramics, plastics, cement, and gypsum products) incorporate fibers to enhance the composite properties.^{1,9} F. O. Slate¹⁰ investigated the compressive and flexural strength of coconut-fiber-reinforced mortar. Two cement-sand ratios by weight, 1:2.75 with a water cement ratio of 0.54 and 1:4 with a water cement ratio of 0.82 were considered. The fibre content was 0.08 %, 0.16 % and 0.32 % by total weight of cement, sand and water. The mortar specimens were cured for 8 d only. It was found that, compared to that of plain mortar of both mix designs, all the strengths were increased in the case of fiber-reinforced mortar with all the considered fiber contents. However, a decrease in the strength of the

mortar with an increase of the fiber content was also observed. Z. Li et al.¹¹ studied the fiber-volume fraction and the fiber-surface treatment with a wetting agent for coir-mesh-reinforced mortar using non-woven coir mesh matting. They performed a four-point bending test and concluded that cementitious composites, reinforced by three layers of coir mesh with a low fiber content of 1.8 %, resulted in a 40 % improvement in the maximum flexural strength. The composites were 25 times stronger in flexural toughness and about 20 times higher in flexural ductility when compared to plain composites. R. Siddique¹² used the natural san fibers (its botanical name is *Crotalaria juncea*) having a length of 25 mm and three percentages by volume of concrete (0.25 %, 0.50 % and 0.75 %) in concrete. The author investigated the fresh and hardened concrete properties such as slump, Vebe time, compressive strength, splitting tensile strength, flexural strength and impact strength. As result, it was found that the slump flow and compressive strength decreased with an increase in the percentage of san fibers when the flexural and impact strengths increased. However, some fibers can negatively affect the mechanical properties of composites. For example, the addition of sisal fibers to cement mortar matrices reduced the compressive strength by 18.4 % to 32 %, the elastic modulus by 1.3 % to 15 %, the longitudinal strain capacity at ultimate stress by 15.2 % to 32.9 %, and the lateral strain capacity by 4.2 % to 24.9 %. S. K. Al-Oraimi and A. C. Seibi¹³ compared to natural and glass-fiber-reinforced concrete properties. They also report that strength is generally marginally decreased by the addition of glass and natural fibres. New types of fibers, new methods of fabrication and different types of applications are continuously being developed. One of them is sepiolite.⁸

Sepiolite is a natural clay mineral with a formula of magnesium hydrosilicate $\text{Si}_{12}\text{Mg}_8\text{O}_{30}(\text{OH})_6(\text{OH}_2)_4 \cdot 8\text{H}_2\text{O}$ characterized by its fibrous morphology and intra-crystalline channels, extending in the fiber direction (c-axis).¹⁴ It has a fibrous structure formed by the alternation of blocks and channels that grow in the fiber direction. Each structural block is composed of two inverted tetrahedral silica sheets and a central octahedral sheet containing Mg. In the inner blocks, all the corners of the silica tetrahedral are connected to adjacent blocks, but in the outer blocks, some of the corners are Si atoms bound to hydroxyls (Si–OH).¹⁵ This unique structure imparts sepiolite with a fibrous matrix with channels (3.6×10^5 nm) oriented in the longitudinal direction of the fibers. The fibrous structure of sepiolite induces sorptive, colloidal/rheological and catalytic properties, which find a variety of diverse applications. The fiber length, width and thickness of layered sepiolite as bundles of fiber can range between 10 nm and 5 μm , between 10 and 30 nm and between 5 and 10 nm, respectively. However, the length of the fibers in sepiolite varies according to the source of sepiolite.¹⁶ For example, the length of Ampan-dranda and China sepiolites reaches up to a few milli-

meters, and sometimes even a centimeter. While the fiber dimensions of Vallecas (Spain) sepiolite are $800 \text{ nm} \times 25 \text{ nm} \times 4 \text{ nm}$,¹⁷ the fiber length of the original brown sepiolite from the Türktaciri region of Turkey is determined as 5–10 μm .¹⁸

The sepiolite was used in the production of cement as natural clay (raw material) by Kavas et al.⁶ Sepiolite was replaced with clinker in proportions of (3, 5, 10, 15, 20 and 30) % by weight. Mortar specimens were prepared with sepiolite-blended cement at a water to cement ratio of 0.5. The addition of 10 % sepiolite is found to increase both the compressive and bending strengths of the mortar. However, there is very limited study in the literature on the performance of sepiolite as fiber in concrete. Therefore, in this study, it was decided to use sepiolite fibers in order to prevent micro-cracks occurring in the concrete matrix under load so that it improve the physico-mechanical properties of concrete, such as compressive, bending, and splitting strengths.

2 EXPERIMENTAL PART

2.1 Materials

2.1.1 Aggregate

The maximum 22 mm nominal size of crushed aggregate from Afyonkarahisar, Turkey was used. The coarse aggregates were calcareous stone as crushed stone I in 4–11 mm; and crushed stone II in 11–22 mm. The fine aggregates were crushed stone dusty in 0–4 mm. The characteristic properties of the aggregates are given in **Table 1** according to standards.

Table 1: Aggregate properties

Tabela 1: Lastnosti agregata

Particle size (mm)	Specific gravity (Mg/m^3)	Water adsorption (%)	Particle shape (%)	Los Angeles (%)	Ultra fine material
22.4-11.2	2.69	0.13	13.4	30	0.56
11.2-4	2.69	0.28	14.7		0.31
4-0	2.69	0.93			5.58

2.1.2 Cement

Ordinary Portland cement (OPC) was used in the experiments with a minimum strength of 45 MPa at 28 d (CEM I 42.5 R). It complies with the requirement of European Standards EN 197-1.¹⁹ The characteristic properties of cement are given in **Table 2**.

2.1.3 Sepiolite

The dolomitic sepiolite samples taken from the Eskisehir–Sivrihisar Region (purity grade is 40 %) are subject to reinforcement procedure, and the sepiolite samples with fibers uncoupled by a mechanical activation (**Figure 1**) are used in the manufacture of the fiber-reinforced concrete. After the dolomitic sepiolite having a 10,000 mPa·s times 10 % (poor quality) is reinforced by gravitational methods, its viscosity increases

Table 2: Characteristic properties of CEM I 42.5R cement
Tabela 2: Značilne lastnosti cementa CEM I 42,5R

Component	Content, %	
CaO	63.56	
SiO ₂	19.3	
Al ₂ O ₃	5.50	
Fe ₂ O ₃	3.46	
MgO	0.86	
SO ₃	2.96	
K ₂ O	0.80	
Na ₂ O	0.13	
A.K.	1.15	
Physical properties		
Initial setting time, h	2.52	
Final setting time, h	4.36	
Volume expansion, mm	3.00	
Blaine surface area, cm ² /g	3212	
Specific weight, g/cm ³	3.07	
Mechanical properties		
Compressive strength, MPa	7 d	38.7
	28 d	46.0

up to 19,000 mPa·s. The sepiolite to be used as a fiber in a concrete is a reinforced white sepiolite having uncoupled fibers and a viscosity of 19,000 mPa·s. A blender was used to disperse the fiber bundles that form the structure of the sepiolite and provide the gelation at

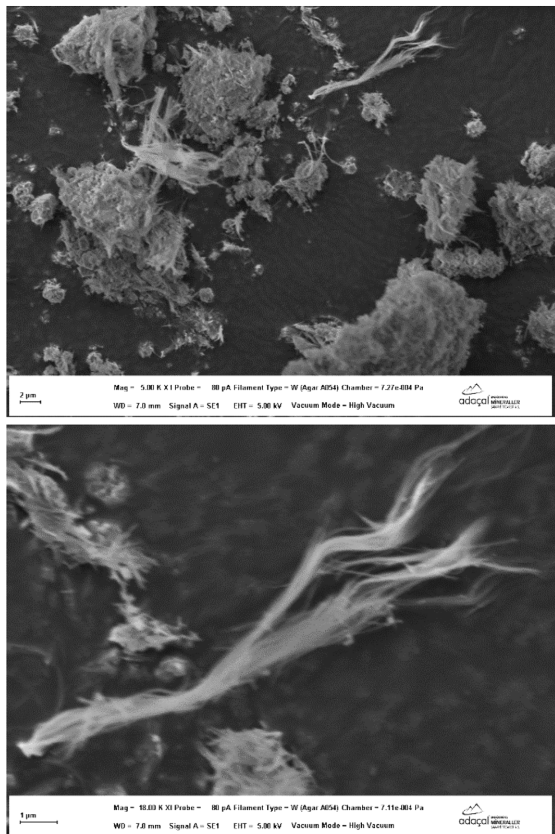


Figure 1: SEM images of sepiolite fibers
Slika 1: SEM-posnetka sepiolitnih vlaken

high speed (max 20,000 min⁻¹). Sepiolite suspensions prepared in the 2000 mL steel cup of a blender.

2.1.4 Superplasticizer

A polycarboxylic-based new generation superplasticizer admixture was used to obtain a good workability for the fresh SEPRC mixture. Its specific gravity was 1.2 kg/dm³.

2.2. Preparation of SEPRC specimens

Several series of samples were prepared to test the influential variables on the mechanical and physical properties of fresh and hardened concretes with sepiolite. The cement dosage, water to cement ratio and chemical admixture content were 350 kg/m³, 0.55 % and 1.5 % (by weight of cement), respectively, in the mixtures. The volume of aggregate was determined for the reference Portland cement concrete by assuming that approximately 1.5 % of air is trapped in the fresh concrete. The sixteen different series were designed by using fiber contents as 0 % (control), 0.5 %, 1 %, 2 % and 3 % by weight of cement. The mixing of concrete batches was carried out using a small drum mixer. The concrete dried components were mixed for 2 min. Then, to encourage a uniform distribution of fibers throughout of the concrete, fibers were added to the mixing water slowly (with diluted admixture). The mixing water was poured into a drum; the aggregates and cement were fully mixed. The fresh concrete was mixed for 3 min (**Figure 2**). The mixture proportion per cubic meter of sepiolite-fiber-rein-

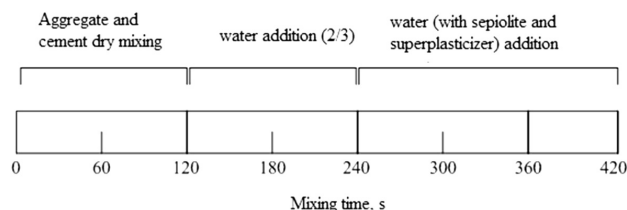


Figure 2: Concrete mixing procedure depends on the time
Slika 2: Mešanje betona je odvisno od časa

Table 3: Physico-mechanical tests on SEPRC
Tabela 3: Fizikalno-mehanski preizkusi na SEPRC

Experiments	Specimen Size	Standard
<i>Fresh concrete</i>		
Slump test ²⁰	6 dm ³	EN 206-1 (2000)
Unit weight ²¹	7 dm ³	EN 12350-6 (2009)
Air content ²²	7 dm ³	EN 12350-7 (2009)
<i>Hardened concrete</i>		
Compressive strength ²³	(150×150×150) mm	EN 12390-3 (2009)
Splitting strength ²⁴	(Ø150×300) mm	EN 12390-6 (2009)
Flexural strength ²⁵	(100×100×350) mm	EN 12390-5 (2009)
Ultrasonic pulse velocity ²⁶	(150×150×150) mm	EN 13791 (2007)
Freezing-thawing test ²⁷	(100×100×150) mm	EN 1367-1 (2007)

forced concrete (SEPRC) is given in **Table 2**. The fresh concrete was placed in the moulds with a shaker and they were de-molded after 24 h. The specimens were cured in water at 20 °C for 7 d and 28 d. The experiments that are carried out on the SEPRC series are summarized in **Table 3** according to the related standard.^{21–28}

For the SEPRC specimens, compressive strength was defined according to the EN 12390-3²³ standard using a 2000 kN compressive machine with a rate of loading controller on cubic specimens (**Table 4**) aged for 7 d and 28 d, respectively. Flexural strength was defined on the prismatic specimens under the mid-point loading with 200 kN manual controlling bending test machine. For the freeze–thaw testing, the SEPRCs were exposed to ASTM C666²⁸ Procedure A conditions: the specimens were kept in a fully saturated condition with temperature cycling between –17 °C and +20 °C, each cycle took 6 h. The climatic chamber used consisted of cooling and heating equipment producing continuous freeze–thaw cycles with chamber temperatures ranging from –20 °C to +20 °C. The specimens were frozen for 1 h in air at –17 °C, and then they were immersed into the water to thaw for 2 h at +20 °C. In total, 30 freeze–thaw cycles were performed on each of the SEPRCs.

Table 4: Quality of concrete with ultrasonic testing²⁹

Tabela 4: Ocena kvalitete betona z ultrazvočnim preizkušanjem²⁹

Wave velocity (km/s)	Quality of concrete
> 4.5	Perfect
3.5 – 4.5	Best
3.0 – 3.5	Suspect
2.0 – 3.0	Weak
< 2.0	Very weak

Moreover, freshly fractured surfaces of the SEPRC chips were coated with gold in a vacuum evaporator. They were examined using a Zeiss EVO LS 10 scanning electron microscope (SEM) to determine the morphological and mineralogical features.

3 RESULTS AND DISCUSSIONS

3.1 Fresh concrete tests

The slump test that makes it possible to determine the inspection of viscosity of the fresh concrete easily and properly is the slump test. The slump value of 0.5 %, 1 %, 2 % and 3 % of the SEPRC are 17, 16.3, 17 and 6 respectively, while the slump value of the reference concrete (0 % sepiolite) is 16. In 3 % SEPRC fiber-reinforced concrete, critical reason of a reduction in the slump value is that the sepiolite fibers have large surface areas and a capability to retain water particles²⁹. Thus, the concrete containing 3 % sepiolite has almost no consistency because of high viscosity and becomes unworkable. However, it is behind the limits specified in the EN 206-1²⁰ standard for slump values. In lower sepiolite reinforcement ratios, the slump values are within acceptable limits for concrete manufacture. For

instance, 0.5 %, 1 % and 2 % sepiolite-reinforced concretes are S3 grade, while the inspection series are S4 grade, in accordance with the EN 206-1²⁰ standard for slump values. In the SEPRC, workability of the concretes increases up to a fiber use at 2 % and their slump values increase by approximately 6 % with respect to the inspection series. But, as the fiber amount increases more, the slump value decreases significantly. The inspection series and SEPRCs up to a 2 % fiber addition are S4 grade, in accordance with the EN 206-1²⁰ standard for slump values, and the final series are S1 grade.

In **Figure 3** it is clear that because slump value of SEPRC 0.5 % and SEPRC 2 % is 17 cm, while slump value of the reference concrete 16 cm, workability of the concrete is much better than SEPRC 0. In other words, sepiolite fibers increase the workability of plain concrete. R. Jarabo et al.³⁰ also reported that sepiolite modifies the rheological properties of cement when used as an additive. This is an important result, because almost all the fiber types that were used to improve the mechanical properties, generally reduced the workability. However, 3 % fiber added to the concrete absorbs water and cement and creates a powerful mesh structure. Therefore, an increase in viscosity restricts the flow and gives a lower slump value (6 cm)^{31,32}. Thus, J. Edgington et al.³³ recommend a 2 % steel fiber content maximum and show that as polypropylene fibers are added more than 1 %, they cause a large decrease in workability. In this study, it is determined that a 3 % fiber addition reduces the workability.

A gap remains absolutely in fresh concrete during the pouring of concretes in molds. Concretes are compressed and placed by vibration or other methods in their molds and thus such gaps are minimized. Gaps trapped in the concrete both reduce the strength of the concrete and cause the concrete to contain more gaps, and thus to become more instable against any exterior environmental effects while the concrete is hardened. **Figure 3** shows the air content in the white sepiolitic fiber-reinforced concrete. Except in particular circumstances (such as concretes subject to freeze-thaw), it is not assumed that a fresh concrete contains a gap between 2–3 % and a hard-

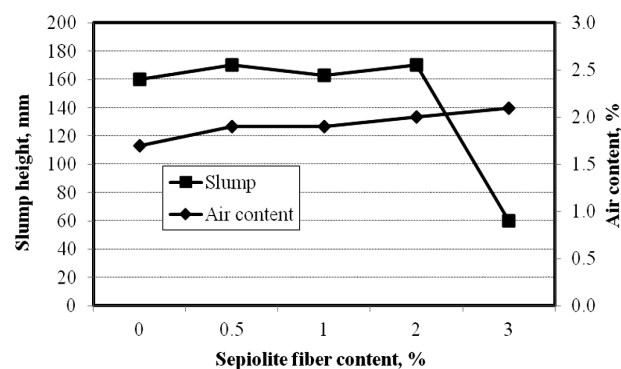


Figure 3: Slump and air content of sepiolite-reinforced concrete
Slika 3: Razledenje in vsebnost zraka v betonu ojačanem s sepiolitom

ened concrete contains a gap more than 6–8 %. It can be seen that the air content of SEPRC fibers is between 1.5 % and 2.1 %. Therefore, air content of the concretes containing SEPRC is within the proposed range.

Unit weights of fresh SEPRCs are presented in **Figure 4**. There is no change in the unit weight values of fresh concrete depending on an increase in sepiolite ratios added to concrete and such values of around 2360–2400 kg/m³.

3.2 Hardened concrete

3.2.1 Compressive strength

The cube samples manufactured in the sepiolite-reinforced concretes are subject to the compressive strength. 7- and 28-day strengths are determined for the time-dependent strength of the samples. The age of the samples in all concrete series gets along, depending on the strength development and thus their compressive strength increases depending on the development of any hydration products. While their compressive strength reduces by 5 % when the sepiolite fibers are used at 0.5 %, as shown in **Figure 5**, their strength remains the same as the reference series, when they are at 1 % and 3 % at 28 d. The probable reason for this behavior includes poor zones occurring due to poor homogeneity of the concrete, a high water ratio or an excessive amount of fibers. Similar results were observed on natural coconut-fiber-reinforced concrete by M. Ali et al.³⁴. The mechanical properties such as the static modulus of elasticity, compressive strength, compressive toughness, splitting tensile strength, modulus of rupture, total toughness index and density were investigated by the authors. They reported that the properties can increase or decrease depending on fiber length and content.

3.2.2 Flexural strength

In concrete series containing SEPRC, the results that are closest to the reference series are obtained in the concretes containing 1 % SEPRC. Upon the addition of 3 % fiber, the bending strength values are increased by approximately 22.9 % (**Figure 6**). However, it is deter-

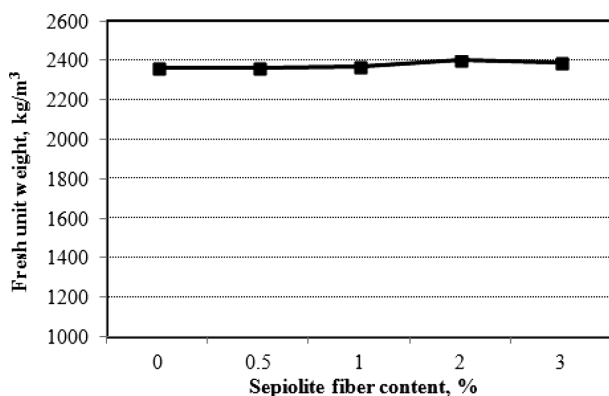


Figure 4: Fresh unit weight of sepiolite fiber-reinforced concrete
Slika 4: Enota sveže mase betona ojačanega s sepiolitnimi vlakni

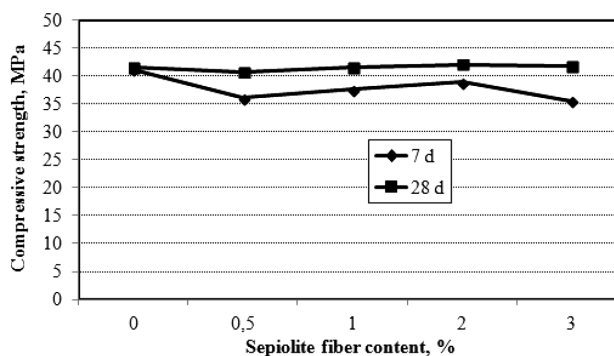


Figure 5: Compressive strength of SEP-reinforced concrete
Slika 5: Tlačna trdnost betona utrjenega s SEP

mined that the bending strength of the concretes was reduced due to difficulties in mixture and molding of the 3 % sepiolitic fiber-reinforced concrete when compared to 2 % of fiber content. It is reported by M. Emiroğlu³⁵ that, upon addition of sepiolite to the concrete, it reduces the workability and there is a reduction in the bending and compressive strengths due to its ability to retain an excessive amount of water. It is determined that a large number of micro acicular sepiolite fibers are dispersed between the matrix and the aggregates, while the sepiolitic fiber addition is 2 %. An increase in workability of the SEPRC concretes confirms the homogeneity in the microstructure. Its effects on rupture behavior are clearer than an increase in the bending strengths of the sepiolitic fibers.

3.2.3 Splitting strength

The weakest properties of the structural materials such as cement-based concrete include a lower tensile strength. Therefore, a different type and nature of fibers are added to the concrete to increase or improve its tensile strength. One of the tests, where the tensile strength is determined, is the splitting strength that gives the tensile strength indirectly in a real-like way. Aggregate dispersion of the SEPRC3 sample in the concrete that gives a high splitting strength is homogenous. Furthermore, the concrete is not separated from its matrix, but it is ruptured and broken into two parts during the force applied in the splitting of the concrete. The reason for this

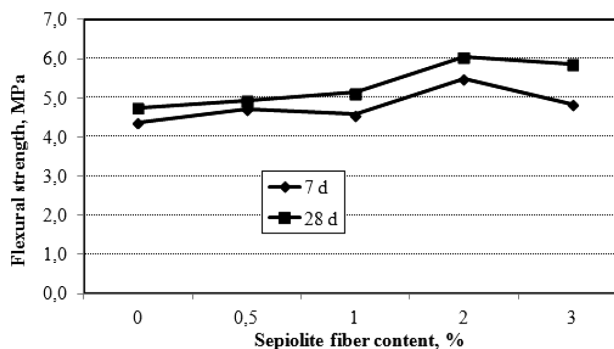


Figure 6: Flexural strength of SEP-reinforced concrete
Slika 6: Upogibna trdnost betona utrjenega s SEP

S. KOLTKA et al.: THE USE OF NATURAL SEPIOLITE FIBER IN CONCRETE

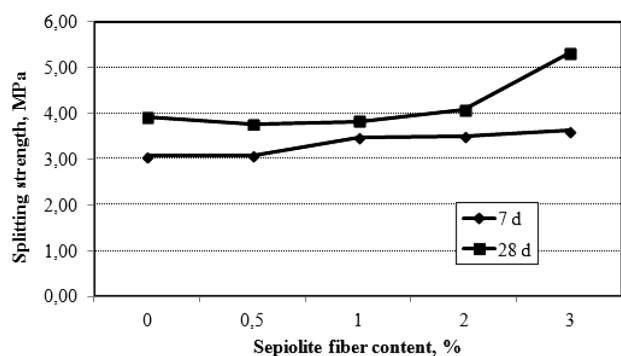


Figure 7: Splitting strength of SEP-reinforced concrete versus fiber content

Slika 7: Cepilna trdnost betona ojačanega s SEP glede na vsebnost vlaken

is that the matrix and the interface of the aggregate and matrix are reinforced by the sepiolite fibers. In the concrete samples that give a low splitting strength, the aggregate is ruptured and separated from the cement paste due to the poor interface of the cement paste and aggregate.³⁶ It was observed that the sepiolitic fibers increase the adherence of the aggregate and cement paste and the splitting strength of the concrete (**Figure 7**). In the samples containing SEPRC, their splitting tensile strength increases by 6 % and 33 %, respectively, upon the addition of 2 % and 3 % fiber, while their tensile strength never changes significantly upon the addition of 0.5 % and 1 % fiber.

3.2.1 Microstructure

In **Figure 8a** to **8e**, it was seen in the concrete sample that the hydrate cement matrix and the aggregate inter-

face have a fairly dense structure. When a crack in this aggregate is observed by 20000× magnification, an anti-crack effect of the sepiolitic fibers (A) is observed clearly. Upon an increase of the sepiolitic fibers, it contributes positively for the cement paste to become more stable and the gaps in the concrete to reduce. The dense calcium hydroxide hydrate (C-S-H) gels in the concrete and micro sepiolite fibers between these gels makes it possible to reduce the gap and to make the concrete denser. **Figure 8**, A, B and C show calcium hydroxide (CH), C-S-H gel and the ettringite needles, respectively. Since it is a binder final product in a concrete, the C-S-H gel is a critical component, and consequently it contributes mostly to the strength. It is clear that strength development is fairly fast in the inspection series. It is very effective for any chemical additive used on these dispersed cement particles and react better with water. S. Kakooei et al.³⁷ show that the macro fibers ($L = 4$ mm) reduce the crack formation and development and increase the compressive strength. But, a large majority of studies conducted on polypropylene-reinforced concretes show that there is no or very little compressive strength.^{31,38} When the SEM image of the SEPRC0.5 concrete is analyzed in **Figure 7**, the nano-sepiolite fibers contribute the adherence of the interfaces of the aggregates. Also, the nano-fibers in the surface of the even aggregates improve the weakness in interface of the aggregate cement paste. In concretes, the interfaces of the aggregate cement paste have a critical effect on the mechanical properties of the concrete as much as the component features.³⁹

It is determined that there is a film layer formed by calcium hydroxide on the aggregate surface in contact

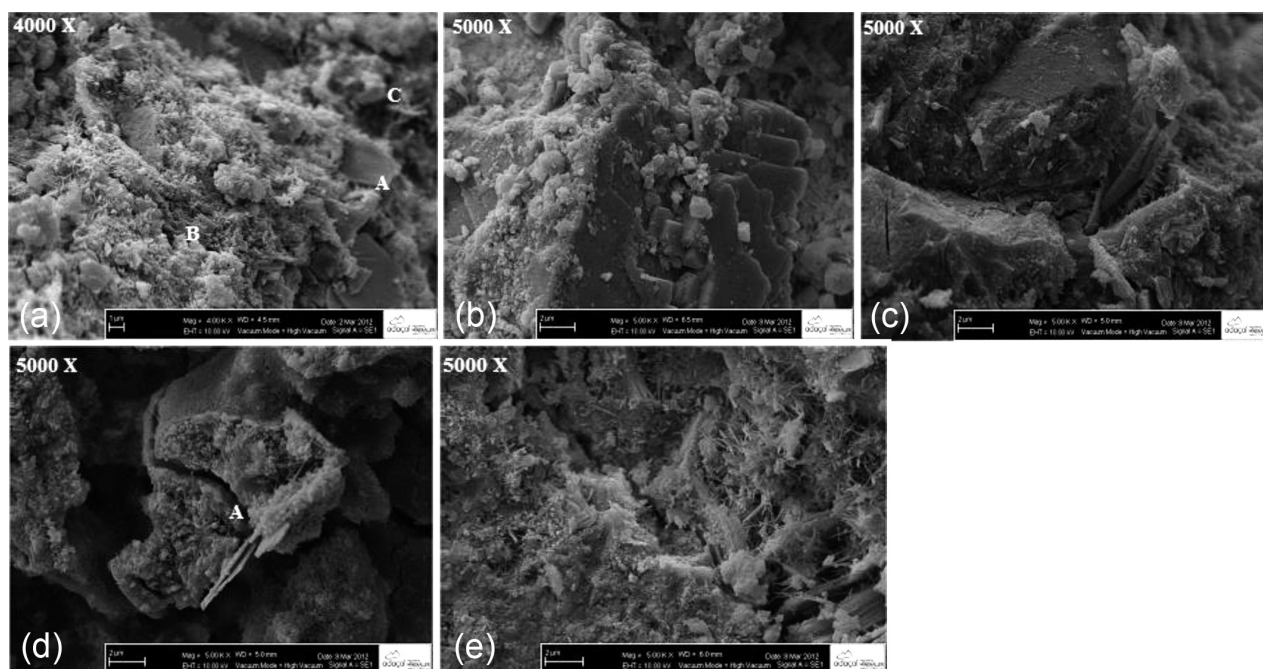


Figure 8: Distribution of sepiolite fibers in hydrated concrete: a) 0 %, b) 0.5 %, c) 1 %, d) 2 %, e) 3 %)

Slika 8: Razporeditev vlaken sepiolita v hidriranem betonu: a) 0 %, b) 0.5 %, c) 1 %, d) 2 %, e) 3 %)

with the transition zone and such a film is coated by another layer in a thin C-S-H (tobermorite) form. It is observed that such a double coat of film layer is also coated by a calcium hydroxide later in its interface.⁴⁰

3.2.5 Ultrasonic pulse velocity

Although it is difficult to find the compressive strength of any concrete by the ultrasonic test method in a sufficiently accurate way, because the ultrasonic wave velocity passing through any concrete is associated closely with amount (and density) of the gap in that concrete, it may be possible to establish a relation based on the resultant ultrasonic velocity and concrete grade. If the ultrasonic velocity is determined as a result of the experimental studies conducted on the concrete with a density of 2400 kg/m³, the results on the concrete grade are shown in **Table 4**.⁴¹ When the inspection series are compared in terms of ultrasonic pulse velocities in **Figure 9**, the ultrasonic velocity is obtained as 3.9 km/s, 4.3 km/s, 4.5 km/s and 4.4 km/s for the 0.5 %, 1 %, 2 % and 3 % fiber contents in 28-day concretes. Since their ultrasonic pulse velocity is very close to 4.5 km/s, the concretes are in good and high-quality concrete grade. The concrete series with 0.5 % fiber content are in a good concrete grade. It is recommended that fibers are used at a ratio of 2 % and more for high-quality concrete manufacture in terms of ultrasonic pulse velocity.

3.2.6 Modulus of elasticity

The modulus of elasticity of concrete is a key factor for estimating the stiffness and deformation of the buildings and members. The precise determination of the modulus of elasticity of concrete is very important for structures that require strict control of the deformability. In order to make full use of the compressive strength potential, the structures using high-strength concrete tend to be slimmer and require a higher elastic modulus so as to maintain its stiffness. Therefore, knowledge of the modulus of elasticity of high-strength concrete is very important in avoiding excessive deformation, providing satisfactory serviceability, and avoiding the most cost-effective designs.^{42,43} In the codes and standards related to the design of concrete structures, the modulus of elasticity of concrete is usually proposed by empirical equations depending on a function of the compressive strength of the concrete. Therefore, the E-moduli values were obtained with ACI codes and Turkish standards (TS) depending on the compressive strength, and it was observed that they are relatively similar when comparing them with the recommendations found in ACI 318⁴⁴, ACI 363⁴⁵ and TS 500. The following equations are recommended by ACI 318³⁶ and TS 500⁴⁶ for the relationships between compressive strength (f_c) and the E-moduli is as follows for concretes:

$$(ACI 318)^{44} \quad E_c = 4730 \times (f_c)^{1/2} \quad (1)$$

$$(ACI 363)^{45} \quad E_c = \left(\frac{g}{2.346} \right)^{1.5} (10500 \sqrt{f_c} + 70000) \quad (2)$$

$$(TS 500)^{46} \quad E_c = 14000 + 3250 \times (f_c)^{1/2} \quad (3)$$

Where f_c , E_c , and γ represent the compressive strength (mPa) elastic modulus of concrete (mPa), and unit weight (kg/dm³) of sepiolite reinforced fiber concrete, respectively.

A comparison of static modulus of elasticity obtained from the empirical expressions given by the various design codes for both plain concrete and sepiolite fiber reinforced concrete is presented in **Figure 10**. It shows the modulus of elasticity predicted by TS 500⁴⁶ is higher than compare to other code prediction. Values of elasticity modulus vary from 28 to 27 GPa for ACI codes when it was 33 GPa according to the TS 500⁴⁶ standard. A slight decrease in the results is observed for ACI codes with an increasing addition of sepiolite volume fraction. However, there was no change for the power function of the TS 500⁴⁶ standard. The modulus of elasticity of the concrete depends upon the modulus of elasticity of the hydrated cement matrix, type and content of aggregates, the water to binder ratio, and the volume of the cement⁴¹. The E-moduli of fiber-reinforced concretes may decrease or increase depending on the orientation or distribution of the fibers in the concrete. This is because the concrete can be assumed to be a highly heterogeneous material due to its composite structure. As the orientations and distributions of the fibers in the concrete mixture are random, the fiber-reinforced concrete is considered more heterogeneous than the plain concrete. Therefore, the E-moduli of sepiolite-fiber-reinforced concretes under compression have very similar changes depending on the distribution of sepiolite in concrete. The principal role of sepiolite fibers is resisting the formation and growth of cracks by providing pinching forces at the crack tips.

3.2.7 Freezing-thawing test

An expedited freeze-thaw test consisting of 30 periods is conducted for the purposes of revealing the durability properties of the sepiolite-fiber-reinforced concretes under freeze-thaw circumstances, under which they may be subject to, and then weight loss, density loss, a variation in water-absorption ratios and compres-

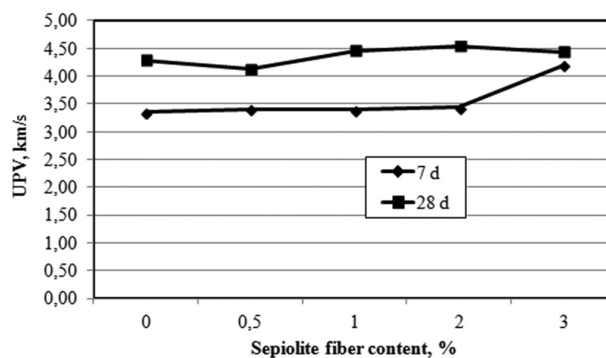


Figure 9: UPV values of sepiolite fiber-reinforced concrete versus fiber content

Slika 9: UPV vrednosti pri betonu ojačenem z vlakni sepiolita v odvisnosti od vsebnosti vlaken

S. KOLTKA et al.: THE USE OF NATURAL SEPIOLITE FIBER IN CONCRETE

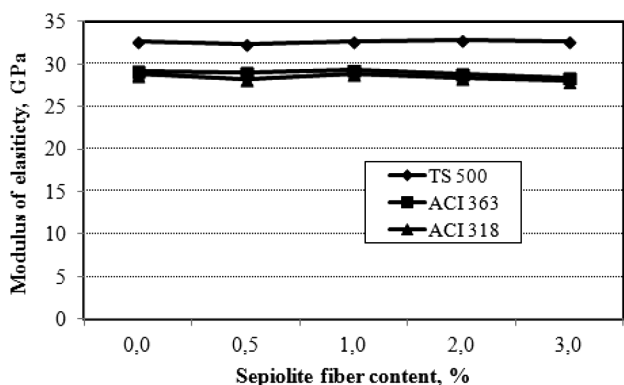


Figure 10: Modulus of elasticity of sepiolite fiber-reinforced concrete
Slika 10: Modul elastičnosti betona, ojačanega z vlakni sepiolita

sive strength are determined. In Figure 11, the density loss of 0.5%, 1 %, 2 % and 3 % fiber contents is respectively 1.28 %, 1.17 %, 1.15 % and 1.39 %, while the density loss of the reference concrete is 1.09 %. There is no significant change in the density loss of the white sepiolitic-fiber-reinforced concrete with regards to the reference concrete. Any observations similar to weight loss are conducted in the density of the concretes. However, density loss represents an increase of 7 %, 6 % and 28 %, respectively, upon the addition of 1 %, 2 % and 3 % fiber. A decrease in weight loss and density loss shows that there is a concrete more resistant against any freeze-thaw effects.

In Figure 12, it is determined that the compressive strength of the 3 % concrete sample obtained from the sepiolite-fiber-reinforced concretes is very close to the reference concrete before and after the freeze-thaw cycle. A maximum difference between the compressive strength values are obtained in the sepiolitic concretes upon the addition of 0.5 % and 1 % fibers with respect to the reference series. Fibers as high as 2 % and 3 % are used in both types of fiber, upon an increase in the strength of the interface of the aggregate-cement paste of the manufactured concretes and also of the cement paste under stresses, the strength losses of the concretes under a freeze-thaw effect are similar to the inspection series.

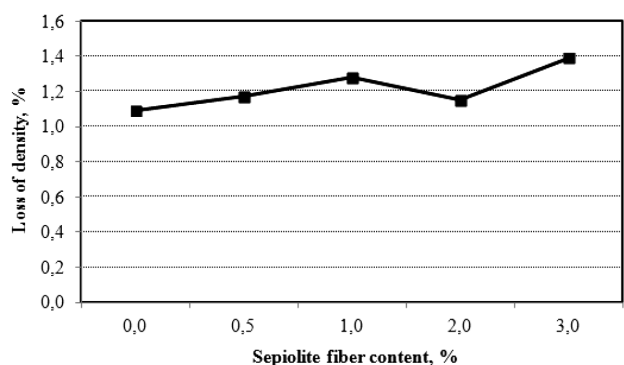


Figure 11: Loss of density of sepiolite reinforced concrete depending on freeze-thaw test

Slika 11: Zmanjšanje gostote betona, ojačanega z vlakni sepiolita, v odvisnosti od preizkusa zmrznjeno-odtaljeno

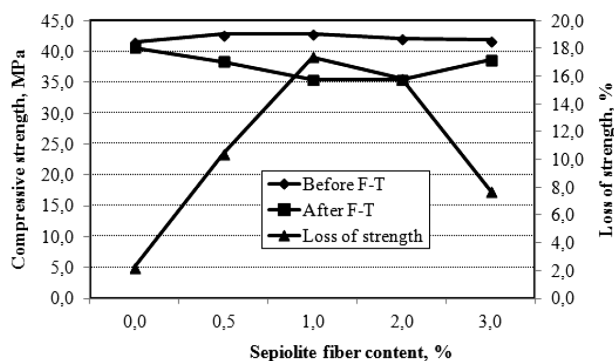


Figure 12: Change of strength of sepiolite reinforced concrete depending on freeze-thaw test

Slika 12: Spreminjanje trdnosti betona, ojačanega z vlakni sepiolita, v odvisnosti od preizkusa zmrznjeno-odtaljeno

In the inspection series, the strength loss is 2 %. In the concrete series containing SEPRC, in which 2 % and 3 % fibers are used, the strength losses are determined as 8 % and 5 %. Internal stresses occur as a result of the water in the concrete subject to freeze-thaw. Therefore, any cracks tend to occur previously in the cement paste. The sepiolitic fibers make it possible to overcome such internal stresses caused by the frozen water and prevent the concrete from being cracked. Since short fiber types greatly increase the number of fibers used in the concrete, they are used to decrease cracking and increase durability depending on the properties of the materials used; whereas, long fibers aim more often to increase the mechanical properties of the concrete.⁴⁷

Upon use of the white fibers at 0.5 %, 1 % and 3 %, a reduction of 3 % occurs in the 2 % fiber content, increases of 3 %, 97 % and 44 % are observed with regard to the reference concrete (Figure 12). As a result of such a freeze-thaw procedure, it is shown that dispersion in the white sepiolitic fiber-reinforced concrete is more. In Figure 13, water absorption values are 0.69 %, 2.33 %, 1.23 % and 0.97 %, respectively, in 0.5 %, 1 %, 2 % and 3 % fiber contents, while the water absorption value of the reference concrete is 0.63 % after the freeze-thaw cycle. Porous structural materials such as concrete have a capability to absorb water as much as open and semi-

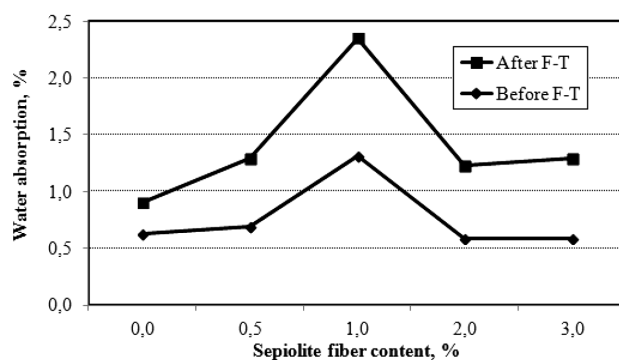


Figure 13: Change of water absorption of sepiolite reinforced concrete depending on freeze-thaw test

Slika 13: Spreminjanje absorpcije vode v betonu, ojačanem z vlakni sepiolita, v odvisnosti od preizkusa zmrznjeno-odtaljeno

open gaps included in them. If the gap diameter increases after the internal stress caused by concrete around the frozen water in its gaps before and after freeze-thaw cycle, their water absorption capability increases accordingly. Thus, since mixture and molding of the concretes become difficult upon use of fiber content over 1 %, they contain gaps more according to other fiber ratios and consequently the free water in gaps freezes and its volume increases in the freeze-thaw cycles, gaps in the concrete increase and cause absorption of more water.⁴⁸ In the concrete series containing SEPRC, it is observed that there is a smaller increase than the others with respect to water absorption in the inspection and 0.5 % fiber contents.

4 CONCLUSIONS

In the manufacture of sepiolite fiber-reinforced concrete, fiber is added to the concrete at 0.5 %, 1 %, 2 % and 3 % by weight of the cement added by fiber. In the concrete tests, it is ensured that, upon settlement of the fresh concrete, the sepiolite fibers increase the workability of the concrete and more settlement is obtained. Furthermore, although the white sepiolitic fibers trap more air in the concrete, such an amount is within an acceptable limit (approximately 0.5 %). The sepiolitic fibers have no effect unit weight of the concrete in fresh state. In the hardened concrete tests, it is determined that the white sepiolitic fibers reduce the compressive strength in comparison to the reference concrete. But, upon addition of the white sepiolitic fibers at 1% and 3% to the concrete, the compressive strength gives a value similar to 28-day reference concretes. The bending strength of the white sepiolitic fibers added at 2 % is fairly close of the bending strength of 28-day reference concretes. However, the bending strength reduces at content ratios of 0.5 %, 1 % and 3 %.

In the white sepiolitic fibers, all the content ratios increase the splitting strength. In particular, the splitting strength in the 3 % white sepiolitic fiber content increases by 29 %, and as a result of that the interface of the aggregate and cement paste becomes more stable.

The 28-day concretes manufactured with the white sepiolitic fiber according to the ultrasonic pulse velocities are located in a high-quality concrete grade. From SEM studies, it was observed that the white sepiolite fibers are dispersed homogeneously and reinforce especially the interface of the aggregate and cement paste.

In general, it was seen that the sepiolitic fibers have an effect on the fresh concrete. However, it was determined that a 2 % white sepiolitic fiber content gives more positive effects on the tensile strength among the concrete characteristics. Although any chemical additives are used in the concrete upon the addition of 3 % fiber, it is suggested that concrete is used up to 2 % complete with such chemical additives due to difficulties in the mixture.

Acknowledgement

The investigation was funded by the R&D Support Program (SAN-TEZ) of Ministry of Science, Industry and Technology with the project number 00523.STZ.2010-1, Republic of Turkey. The authors are grateful for the financial support provided by SAN-TEZ.

5 REFERENCES

- ACI 544.1R-96, State of The-Art Report on Fiber Reinforced Concrete, 66 (2002)
- N. Banthia, N. Nandakumar, Crack growth resistance of hybrid fiber reinforced cement composites, *Cement Concrete Comp.*, 25 (2003), 3–9
- A. Yan, K. Wu, X. Zhang, A quantitative study on the surface crack pattern of concrete with high content of steel fiber, *Cement and Concrete Research*, 3 (2002) 2, 1371–1375
- A. S. Ezeldin, P. N. Balaguru, Normal and high-strength fiber-reinforced concrete under compression, *Mat. Civil Eng.*, 4 (1992), 415–427
- S. P. Shah, B. V. Rangan, Fibre reinforced concrete properties, *ACI J.* 68 (1971), 126–135
- T. Kavas, E. Sabah, M. S. Çelik, Structural properties of sepiolite-reinforced cement composite, *Cement and Concrete Research*, 34 (2004), 2135–39
- E. M. Bezerra, A. P. Joaquim, H. Savastano Jr, V. M. John, V. Agopyan, The effect of different mineral additions and synthetic fiber contents on properties of cement based composites, *Cement Concrete Comp.*, 28 (2006), 555–563
- R. D. T. Filho, K. Joseph, K. Ghavami, G. L. England, The use of sisal fibre as reinforcement in cement based composites, *Rev. Bras. Eng. Agríc Ambient*, 3 (1999), 245–256
- J. M. L. Reis, Fracture and flexural characterization of natural fiber-reinforced polymer concrete, *Construction Building Materials*, 20 (2006), 673–678
- F. O. Slate, Coconut fibers in concrete, *Eng. J. Singapore*, 3 (1976), 51–54
- Z. Li, L. Wang, X. Wang, Cement composites reinforced with surface modified coir fibers, *J. Compos. Mater.*, 41 (2007), 1445–1457
- R. Siddique, Properties of concrete incorporating high volumes of class F fly ash and san fibers, *Cement and Concrete Research*, 34 (2004), 37–42
- S. K. Al-Oraimi, A. C. Seibi, Mechanical characterisation and impact behaviour of concrete reinforced with natural fibres, *Compos Struct*, 32 (1995), 165–171
- K. Brauner, A. Preisinger, Struktur und Entstehung des Sepioliths, *Tschermaks Miner Petrogr. Mitt.*, 6 (1956), 120–140
- M. Shirvani, H. Shariatmadari, M. Kalbasi, F. Nourbakhsh, B. Najafi, Sorption of cadmium on palygorskite, sepiolite and calcite; Equilibria and organic ligand affected kinetics, *Colloid Surf A*. 287 (2006), 182–190
- A. Alvarez, Sepiolite: properties and uses. *Palygorskite-Sepiolite: Occurrences, Genesis and Uses*, ed. A. Singer and E. Galan, Amsterdam, (1984) 253–287, Elsevier
- B. F. Jones, E. Galan, Hydrous phyllosilicates (exclusive of micas). *Sepiolite and Palygorskite, Reviews in Mineralogy*, ed. S.W. Bailey, Mineralogical Society of America, 19 (1988), 631–667
- H. Arik, S. Kadir, S. Saritaş, Investigation of the structural transformation and refractory properties of the brown sepiolite due to the heating at various temperatures, *Turk. J. Eng. Environ. Sci.* 20 (1996), 233–244
- EN 197-1, Cement – Part 1: Composition, specifications and conformity criteria for common cements, 2011

S. KOLTKA et al.: THE USE OF NATURAL SEPIOLITE FIBER IN CONCRETE

- ²⁰ EN 206-1, Concrete – Part 1: Specification, performance, production and conformity, 2000
- ²¹ EN 12350-6, Testing fresh concrete – Part 6: Density, 2009
- ²² EN 12350-7, Testing fresh concrete – Part 7: Air content – Pressure methods, 2009
- ²³ EN 12390-3, Testing hardened concrete – Part 3: Compressive strength of test specimens, 2009
- ²⁴ EN 12390-6, Testing hardened concrete – Part 6: Tensile splitting strength of test specimens, 2009
- ²⁵ EN 12390-5, Testing hardened concrete – Part 5: Flexural strength of test specimens, 2009
- ²⁶ EN 13791, Assessment of in-situ compressive strength in structures and precast concrete components, 2007
- ²⁷ EN 1367-1, Tests for thermal and weathering properties of aggregates – Part 1: Determination of resistance to freezing and thawing, 2007
- ²⁸ ASTM C 666, Standard test method for resistance of concrete to rapid freezing and thawing, American Society for Testing and Materials, 1997
- ²⁹ F. Wang, J. Liang, Q. Tang, J. Meng, Z. Wu, G. Li, Microstructure of sepiolite and its adsorbing properties to dodecanol, *Trans Nonferrous Metal Soc. Ch.* 16 (2006), 406–410
- ³⁰ R. Jarabo, E. Fuente, A. Moral, Á. Blanco, L. Izquierdo, C. Negro, Effect of sepiolite on the flocculation of suspensions of fibre-reinforced cement, *Cement and Concrete Research*, 40 (2010), 1524–30
- ³¹ B. Chen, J. Liu, Contribution of hybrid fibers on the properties of the high-strength lightweight concrete having good workability, *Cement Concrete Res.* 35 (2005), 913–917
- ³² M. Hsieh, C. Tu, P. S. Song, Mechanical properties of polypropylene hybrid fiber-reinforced concrete, *Mat Sci Eng A.* 494 (2008), 153–157
- ³³ J. Edgington, D. J. Hannant, R. I. T. Williams, Steel fiber reinforced concrete, *Building Research Establishment*. 17 (1974), 64–69
- ³⁴ M. Ali, A. Liu, H. Sou, N. Chouh, Mechanical and dynamic properties of coconut fibre reinforced concrete, *Construction Building Materials*, 3 (2012) 0, 814–825
- ³⁵ M. Emiroğlu, Investigation of sepiolite's effects to the mortar and concrete properties, Master's Thesis, Osmangazi University Institute of Science, Eskişehir, 2008
- ³⁶ Ç. Yalçinkaya, An Investigation on the mechanical, durability and microstructure properties of fiber reinforced self-compacting concrete with mineral powders, Master's thesis, Dokuz Eylül University, Institute of Science, İzmir, 2009
- ³⁷ S. Kakooei, H.M. Akil, M. Jamshidi, J. Rouhi, The effects of polypropylene fibers on the properties of reinforced concrete structures, *Construction Building Materials*, 27 (2012), 73–77
- ³⁸ K. Bendjillalia, M. S. Goual, M. Chemrouk, Z. Damene, Study of the reinforcement of limestone mortars by polypropylene fibers waste. Seventh international conference on material science, (2011), Beirut (Lebanon)
- ³⁹ T. Uygunoğlu, Investigation of microstructure and flexural behavior of steel-fiber reinforced concrete, *Materials and Structures*, 41 (2008), 1441–1449
- ⁴⁰ A. Uğurlu, About aggregate-cement bonds, 2. National crushed stone symposium, Istanbul (Turkey), 2008, 213–228
- ⁴¹ T.Y. Erdoğan, Concrete, ODTÜ Publisher, 2007, Turkey
- ⁴² T. Uygunoğlu, S. Özgüven, Prediction of Modulus of Elasticity in Steel-Fiber Reinforced Concrete by Composite Modeling El-Cezeri, *Journal of Science and Engineering*, 1 (2014), 19–28
- ⁴³ M. Gul, A. Bashir, J. A. Naqash, Study of Modulus of Elasticity of Steel Fiber Reinforced Concrete, *International Journal of Engineering and Advanced Technology (IJEAT)*, 3 (2014), 304–309
- ⁴⁴ ACI 318.RM-02, Building Code Requirements for Structural Concrete. ACI Committee 318, American Concrete Institute, 2002
- ⁴⁵ ACI 363.R-92, State-of-art-report on high strength concrete. ACI Committee 363, American Concrete Institute, 1997
- ⁴⁶ TS 500, Requirements for design and construction of reinforced concrete structures, Turkish Standard Institute, Ankara, Turkey, 2000
- ⁴⁷ CX. Qian, P. Stroeven, Development of hybrid polypropylene-steel fibre reinforced concrete. *Cement and Concrete Research*, 30 (2000), 63–69
- ⁴⁸ S. Hamoush, M. Picornell-Darder, T. Abu-Lebdeh, A. Mohamed, Freezing and thawing durability of very high strength concrete. *Am. J. Eng. Appl. Sci.* 4 (2011), 42–51

NANO-INDENTATION INVESTIGATIONS OF THE MECHANICAL PROPERTIES OF THIN TiO₂, WO₃ AND THEIR COMPOSITES LAYERS, DEPOSITED BY SPRAY PYROLYSIS

PREISKAVE MEHANSKIH LASTNOSTI Z NANOTRDOTO TANKIH TiO₂, WO₃ IN NJUNIH KOMPOZITNIH PLASTI, NANEŠENIH S PRŠILNO PIROLIZO

Sabina Cherneva¹, Roumen Iankov¹, Nenad Radic², Bosko Grbic²,
Maria Datcheva¹, Dimitar Stoychev³

¹Bulgarian Academy of Sciences, Institute of Mechanics, Acad. G. Bonchev str., bl.4, 1113 Sofia, Bulgaria

²ChTM, University of Belgrade, Department of Catalysis and Chemical Engineering, Njegoseva 12, 11000 Belgrade, Serbia

³Bulgarian Academy of Sciences, Institute of Physical Chemistry, Acad. G. Bonchev str., bl.11,1113 Sofia, Bulgaria
stoychev@ipc.bas.bg

Prejem rokopisa – received: 2015-07-10; sprejem za objavo – accepted for publication: 2016-01-05

doi:10.17222/mit.2015.216

The aim of the present work is to determine the indentation hardness (H_{IT}) and indentation modulus (E_{IT}) of pure TiO₂ and WO₃ thin films, as well as thin films composed of different TiO₂ and WO₃ proportions and deposited by spray pyrolysis on a stainless-steel (OC 404) substrate. Since the H_{IT} and E_{IT} of the films are properties expected to depend on the phase-chemical composition, morphology, structure and their changes when increasing the WO₃ content in the TiO₂-WO₃ composite film, the correlation between the mechanical and structural properties is also addressed. The obtained results show that H_{IT} and E_{IT} strongly depend on the concentration of the co-deposited WO₃. The determined values of H_{IT} and E_{IT} noticeably decrease (in comparison with H_{IT} and E_{IT} of the pure (100 %) TiO₂ layer) when very low concentrations of WO₃ (up to 2.5 % of W) are co-deposited. At higher concentrations of the co-deposited WO₃ (more than 2.5 % of W), the H_{IT} and E_{IT} values increase almost linearly with an increase of the WO₃ in the precursor. The observed non-proportional behavior of H_{IT} and E_{IT} is associated with specific changes of the structure and a development of defects in the deposited TiO₂-WO₃ composite phase, as well as with the increase in the amount of the formed separate WO₃ phase (with increasing of WO₃ (H₂W₃O₁₂) in the working solution) surrounded by solitary TiO₂ particles.

Keywords: inorganic compounds, chemical synthesis, electron microscopy, elastic properties

Namen predstavljenega dela je določiti trdoto vtiska (H_{IT}) in modul vtiska (E_{IT}) v tankih filmih iz čistega TiO₂ in WO₃, kot tudi tankih filmov, sestavljenih iz različnih delov TiO₂ in WO₃, nanešenih s pršilno pirolizo na podlago iz nerjavnega jekla (OC 404). Ker se pričakuje, da sta lastnosti filma H_{IT} in E_{IT} odvisni od kemijske sestave faz, morfologije, strukture in njenih sprememb, ko povečujemo delež WO₃ v TiO₂-WO₃ kompozitnem filmu, se to nanaša tudi na odvisnost med mehanskimi lastnostmi in lastnostmi strukture. Dobljeni rezultati kažejo, da sta H_{IT} in E_{IT} močno odvisna od koncentracije nanešenega WO₃. Določene vrednosti H_{IT} in E_{IT} se opazno zmanjšajo (v primerjavi z H_{IT} in E_{IT} plasti iz čistega (100 %) TiO₂) ko se nanese WO₃ z nizko koncentracijo (do 2,5 % delež W). Pri nanosih WO₃ z višjo koncentracijo (nad 2,5 % delež W), vrednosti H_{IT} in E_{IT} naraščata skoraj linearno z povečevanjem deleža WO₃ v osnovi. Opaženo neproporcionalno obnašanje H_{IT} in E_{IT} je povezano s specifičnimi spremembami v strukturi in z razvojem napak v nanešeni TiO₂-WO₃ kompozitni fazi, kot tudi s povečanjem količine nastale WO₃ faze (pri povečevanju WO₃ (H₂W₃O₁₂) v delovni raztopini), ki jo obkrožajo posamezni TiO₂ delci.

Ključne besede: neorganske spojine, kemijska sinteza, elektronska mikroskopija, elastične lastnosti

1 INTRODUCTION

The multi-functionality of titanium dioxide is of great interest for both contemporary science and technology.¹ It is the most widely used metal oxide for environmental applications², paints, electronic devices³, gas sensors⁴ and solar cells.⁵ Due to the broad range of applications and the importance of nano-sized titanium a large number of preparative methods for its synthesis have been reported, including: high-temperature processes⁶, sol-gel techniques⁷, chemical vapor deposition⁸, solvothermal processes⁹, reverse micelles¹⁰, hydrothermal methods¹¹, ball milling¹², plasma evaporation¹³, sonochemical reactions¹⁴, etc. Unlike many other techniques, spray pyrolysis represents a simple and cost-effective processing

method, which employs precursor solutions to form different types of dense or porous mono- and multiphase layers with a wide range of thicknesses. This method is also extremely versatile due to the large number of adjustable process parameters such as: substrate temperature, composition and concentration of the precursor, atomization technique, spray geometry, liquid- and gas-flow rates, etc.¹⁵

In this regard, extensive research has been carried out over the past few decades for characterizing the chemical, physical-chemical and surface/bulk-structural properties of these layers synthesized by spray-pyrolysis.^{16–22} However, investigations of their mechanical properties (such as microhardness and indentation hardness, wear resistance, indentation modulus, adhesion,

cohesion, etc.) which are very important in functional and operation exploitation aspects are practically absent.

As a very important addition it has to be pointed out that the anatase nanocrystalline form of titanium dioxide is of particular interest, because it has the highest reactivity in photocatalysis and the best antimicrobial activity.^{23–27} However, there is still a problem with the ability of TiO₂ to respond only to a small portion of the solar spectrum (<5 %) due to its relatively wide band gap (~3.2 eV).²⁸ This invokes the necessity to create a new generation of nano-sized photocatalysts based on TiO₂, being capable of utilising effectively both components (UV and visible) of the sunlight.^{29,30} It is established that doping TiO₂ with different metals or nonmetals (such as SnO₂³¹, WO₃³², ZrO₂³³ and V₂O₅³⁴) is a modification approach, used to extend the absorption range of TiO₂ to the visible region of solar light. The different dopant ions introduce electron energy levels narrowing the TiO₂ band gap. In this aspect the TiO₂-WO₃ composite material^{35,36} seems promising for visible-region-induced photocatalysis, due to the suitable combination of the energy band gaps for anatase and for WO₃. That is why several investigations were focused on the synthesis and characterization of TiO₂-WO₃ composites.^{37–41} The energy band gap of WO₃ is ~2.4–2.8 eV and both the upper edge of the valence band and the lower edge of the conduction band of WO₃ are lower than those of TiO₂. Thus, the TiO₂-WO₃ composite has a narrower energy band gap (compared to that of TiO₂) and shows enhanced photocatalytic activity with respect to its single components. This coupling of TiO₂ and WO₃ favors the transition of electrons from the valence to the conduction band and hole transfers between the bands in the opposite direction. This also reduces the electron-hole recombination rate in both semiconductors.⁴²

It was also recently shown that the unique optical and electric properties of TiO₂ unveil the possibility for its use also as photo-catalytic anticorrosion protection of steels.^{43–49} Considering the investigation of T. Tsai and co-authors⁵⁰ it is expected that deposited on steel, TiO₂ layers will create photocathode protection under the influence of UV irradiation. This protection property is based on the transfer of photo-generated electrons to the metal substrate, as a result of which its electrode potential becomes more electronegative than its corrosion potential. Consequently, the titanium oxide (in the system TiO₂/steel) will act as a non-soluble anode, providing cathode protection of the steel. Obviously, the protective layer of pure TiO₂ cannot act as photo-generated cathodic protector in the dark. However, it can be expected that doping TiO₂ with WO₃, SnO₂, MoO₃, etc., could solve this problem. These semiconductors (WO₃, SnO₂, MoO₃, etc.), which are characterized with a different energy level from those of TiO₂, can store excess electrons during UV irradiation and the stored electrons can be later released in the dark period of the corrosion attack.

Going back to the considered TiO₂-WO₃ system here, it should be pointed out that the methods of preparation of TiO₂-WO₃ systems and the characterization of their catalytic and physicochemical properties are extensively studied and discussed in the literature. Nevertheless, the data for their physical-mechanical properties are very few. Generally, the available data is obtained indirectly using the reference data of chemically or metallurgically synthesized powders that may not be proper for a determination of the properties of the materials deposited as layers/coatings (by other methods) on a specific substrate like metal, alloy, ceramics, etc.⁵¹ And to the best of our knowledge, there are no studies of thin layers obtained by spray-pyrolysis on foreign substrates. For this reason, it is essential to perform studies characterizing the mechanical properties of TiO₂, WO₃, as well as of layers composed of TiO₂-WO₃ mixtures. A knowledge about the mechanical properties is important from the exploitation point of view. The layers of TiO₂, WO₃, and TiO₂-WO₃ mixtures are exposed to a wide range of static and dynamical mechanical loads, temperature variations as well as corrosion, and other factors that lead to the degradation of their strength characteristics.⁵² The interaction of the layers with the substrate should also be investigated. Exceptionally, it is important to consider the formation of composite TiO₂-WO₃ layers on a steel substrate by spray-pyrolysis, because the process is taking place at high temperatures and it is possible to have chemical or structural interactions in the volume of the layer, as well as diffusion transitions on the TiO₂-WO₃/Substrate interface. Therefore, it is highly likely that the mechanical properties of the layer and those of the interface may differ significantly.

The objective of this investigation was to determine the indentation hardness (H_{IT}) and indentation modulus (E_{IT}) of the layers of TiO₂ and WO₃ deposited by spray-pyrolysis on stainless steel (OC 404), as well as to study the influence of the process parameter concentration of the co-deposited WO₃ in the mixed TiO₂-WO₃ layers. Since H_{IT} and E_{IT} are properties that depend on the structure, the structural and morphological changes and phase-chemical content/composition of the layers were carefully investigated, especially with regard to the increase in the WO₃ content (from 1 % to 75 % of mass fractions) in the working solution and in the deposited composite TiO₂-WO₃ layers, respectively.

2 THEORETICAL ASPECTS OF NANO-INDENTATION AS A METHOD FOR THE MECHANICAL CHARACTERIZATION OF THIN FILMS

Instrumented-indentation testing (IIT or so-called nano-indentation) has been developed over the past decade for the purpose of probing the mechanical properties of very small volumes.^{53–57} IIT is ideal for mechanically characterizing thin films, coatings, and surface layers. In addition IIT is an attractive method to

characterize the mechanical properties, because in most cases it requires little sample preparation efforts and has high measurement precision.

Basically, IIT uses a high-resolution actuator to control the penetration into the test surface by the indenter and a high-resolution sensor to continuously measure the penetration depth. One of the benefits of this method is that the contact area under load can be calculated in most cases from the load-displacement data alone, meaning that the residual impression does not have to be viewed directly using complicated imaging techniques, thus making it far easier to measure properties on the sub-micron scale. Indentation hardness (H_{IT}) and indentation modulus (E_{IT}) are the properties most frequently determined by IIT.⁵⁸

The fundamental relation from which the elastic modulus E_{IT} can be estimated is the well-known relation between the true projected contact area A_c , the initial unloading slope S and the reduced elastic modulus E_r .^{59,53}

$$E_r = \frac{\sqrt{\pi}}{2\beta} \frac{S}{\sqrt{A_c}} \quad (1)$$

where β is a constant that depends on the geometry of the indenter tip. For indenters with a triangular cross-section like the Berkovich tip $\beta = 1.034$. The true projected area is determined using the true contact depth h_c and employing the approximation given below with coefficients obtained after calibration using indentation data from a standard fused-silica sample:

$$A_c \approx C_0 h_c^2 + C_1 h_c + C_2 h_c^{1/2} + C_3 h_c^{1/4} + C_4 h_c^{1/8} + C_5 h_c^{1/16}$$

The indentation hardness is defined through the ratio of the applied load P and the corresponding true projected contact area:

$$H_{IT} = \frac{P}{A_c} \quad (2)$$

The indentation (elastic) modulus E_{IT} of the test material is calculated using the relation:

$$E_{IT} = (1-\nu^2) \left[\frac{1}{E_r} - \frac{1-\nu_i^2}{E_i} \right]^{-1} \quad (3)$$

where ν is the Poisson's ratio for the test material, and E_i and ν_i are the indenter's elastic modulus and Poisson's ratio, respectively.⁵⁴ In our case we used the elastic constants for diamond $E_i = 1141$ GPa and $\nu_i = 0.07$.

3 EXPERIMENTAL PART

3.1 Preparation of the samples

The spray-pyrolysis method has been applied for the synthesis of TiO₂-WO₃ composite coatings on foils of Sandvik OC 404 stainless steel (SS). A homemade spray-pyrolysis apparatus for the synthesis of these composites is presented in previously published studies.⁶⁰ As

precursors, a 0.02-M TiO₂ colloidal solution and 0.02-M H₂W₃O₁₂ were used. A colloidal solution containing TiO₂ nanoparticles ($d \approx 4.5$ nm) was synthesized in the manner previously described by T. Rajh et al.⁶¹ A solution of H₂W₃O₁₂ was prepared by dissolving the metal W in H₂O₂ at 60 °C. These two precursor solutions are mixed in different weight ratios in order to vary the contents of WO₃ and TiO₂ in the composites. The stainless-steel specimens (foil thickness 35 μm, 1.5 cm × 10 cm), prior to depositions of the oxide layer, were subjected to standard procedures of degreasing and ultrasonic cleaning.

The typical twin-fluid spray pyrolysis system, using a nozzle made of Pyrex glass, diameter of 0.2 mm, was applied within a homemade computer-controlled device that enabled nozzle movement with adjustable speed and direction. The key preparation parameters of the synthesized samples are presented in **Table 1**.

Table 1: Key preparation parameters of spray pyrolysis

Tabela 1: Ključni parametri pri pršilni pirolizi

Initial temperature of substrate (°C)	460
Nozzle to substrate distance (cm)	4
Nozzle speed (mm/s)	1
Diameter of spraying spot on the substrate (cm)	2
Concentration in precursor solutions (M)	0.02 (TiO ₂ colloidal solution) 0.02 (H ₂ W ₃ O ₁₂)
Air-flow rate (L/h)	300
Precursor solution flow rate (mL/h)	44
Number of nozzle passes	200
Duration of spraying (min)	50

The synthesized samples were named: TiO₂(100), TiO₂(99)-WO₃(1), TiO₂(95)-WO₃(5), TiO₂(90)-WO₃(10), TiO₂(75)-WO₃(25), TiO₂(50)-WO₃(50), TiO₂(25)-WO₃(75), and WO₃(100), according to the content (w/%) of single component in the working solution.

The thicknesses of the coatings were determined according to the relation in Equation (4):

$$T = \frac{M}{A\rho} \quad (4)$$

where A is the geometric area of the coated surface, the mass (M) and the bulk density (ρ) of the coatings. The mass of the coating (M) was determined by weighing the foil before and after the spray pyrolysis.

The coating bulk density is calculated according to Equation (5) and using the true density of anatase ($\rho_A = 3.9$ g/cm³) and WO₃ phase ($\rho_B = 5.4$ g/cm³), the percentage of anatase (k_A) and WO₃ phase (k_B) in the precursor solution, and the powder sample porosity (P) obtained by mercury intrusion porosimetry:⁶²

$$\rho = (\rho_A k_A + \rho_B k_B)(1-P) \quad (5)$$

Although the characteristics of these powders were not entirely the same as that of the films, the porosity of these powders should be considered valuable for an evaluation of the properties of pure TiO₂ and WO₃ coatings as well as of TiO₂-WO₃ composites, such as bulk density, thickness and surface area.

3.2 Structural characterization

The surface morphology, structure and elemental microanalysis of the samples were characterized by scanning electron microscopy (SEM) using a JEOL JSM 6390 electron microscope (Japan) equipped with an ultra-high-resolution scanning system in a regime of secondary-electron image (SEI), back-scattered electrons (BEI) and an INCA energy-dispersive X-ray spectrometer (EDS). The accelerating voltage was 25 kV, I ~ 65 mA. The vacuum was 10⁻⁶ mm Hg.

3.3 Mechanical characterization

The indentation modulus E_{IT} and hardness H_{IT} of the deposited TiO₂, composite TiO₂-WO₃ and WO₃ films were determined via the instrumented indentation technique. The tests were performed using NanoIndenter G200 (Agilent Technologies) equipped with a Berkovich three-sided diamond pyramid with centerline-to-face angle of 65.3° and a 20 nm radius at the tip.⁶³

The particular indentation method employed here is described in ⁶⁴. It prescribes a series of 10 loading/unloading cycles in a single-indentation experiment. The maximum prescribed load is 0.49 N with 20 s peak hold time at the maximum load for each loading-unloading cycle. As a result of the nano-indentation experiments, load-displacement curves are obtained and H_{IT} and E_{IT} are calculated as explained above using the Oliver & Pharr approximation method⁵³ and Equations 1 to 3. Within this study the indentation hardness and modulus were determined using the stiffness calculated by employing 50 % of the upper portion of the load-displacement curve during each unloading cycle. Each sample

Table 2: Estimated surface area, bulk density and thickness of TiO₂-WO₃ samples

Tabela 2: Površina, gostota in debelina vzorcev TiO₂-WO₃

Sample	Deposited mass, mg	Specific surface area, m ² /g	Bulk density, g/cm ³	Thickness, μm
TiO ₂ (100)	3.25	32.3 (5)*	2.27	0.95 (5.8)**
TiO ₂ (99)-WO ₃ (1)	3.40	32.1 (6)	2.30	0.98 (5.6)
TiO ₂ (95)-WO ₃ (5)	3.90	31.1 (7)	2.42	1.07 (5.1)
TiO ₂ (90)-WO ₃ (10)	4.05	30.0 (7)	2.58	1.04 (5.3)
TiO ₂ (75)-WO ₃ (25)	4.80	26.7 (8)	3.04	1.05 (5.2)
TiO ₂ (50)-WO ₃ (50)	5.15	21.1 (10)	3.81	0.90 (6.1)
TiO ₂ (25)-WO ₃ (75)	7.05	15.5 (12)	4.58	1.02 (5.4)
WO ₃ (100)	8.10	9.9 (15)	5.36	1.01 (5.4)

*Standard deviation of specific surface area (%)

**Standard deviation of thickness (%)

was subject to 25 indentation tests in order to have better statistics.

For the realization of an adequate and correct assessment of the mechanical properties of the considered thin deposited layers, it is necessary to guarantee a very good adhesion of the layers to the substrate, reduce the uncertainty in the determination of the layer thickness as well as to have a previous knowledge about the material's internal structure and the existing defects in the layers. The quality of the adhesion of the coatings deposited on the SS substrate was examined by observing whether there is a detachment of the coating from the substrate after a repeated bending of the foil at angle of 180° (EN ISO 2819-1994:2.9 "Bending test").

4 RESULTS AND DISCUSSION

4.1 Analytical and structural characterization of the specimens

The coatings' thicknesses, calculated according to Equation (4), are about 1 μm for all the samples, as presented in **Table 2**.

More details about the porous structure for pure TiO₂ and WO₃ powders, which are constituent parts of all the composites, are given in ⁶².

XRD data obtained for the same systems in our previous investigation confirm the formation of only the anatase phase of TiO₂, no reflections corresponding to the rutile TiO₂ phase were observed.⁶² The composites with WO₃ content greater than 10 % of mass fractions exhibits diffraction peaks of monoclinic tungsten oxide. The absence of reflections corresponding to WO₃ for samples with WO₃ content below 10 % of mass fractions reveals that clusters of WO₃ are present either in the highly dispersed form or in a concentration below the detection limit of the XRD apparatus.

For confirmation of the presence of WO₃ in the layers deposited from the working solutions with a WO₃ content below 10 % of mass fractions, which may not be detected by XRD analysis, we realized the investigation of all the TiO₂-WO₃ composite layers by EDX analysis for sufficient time of exposure (120 s). The results from the EDX analysis are shown in **Tables 3** and **4**.

Table 3: Estimated by EDX analysis percent concentration (at%) of O, Ti and W in deposited by spray-pyrolysis thin TiO₂-WO₃ layers

Tabela 3: EDX-koncentracija (at%) O, Ti in W v tankih TiO₂-WO₃ plasteh, nanešenih s pršilno pirolizo

Sample	O at%	Ti at%	W at%	Total
100 % TiO ₂	80.44	19.56	0	100
TiO ₂ (99)-WO ₃ (1)	81.16	18.22	0.62	100
TiO ₂ (95)-WO ₃ (5)	70.83	27.37	1.80	100
TiO ₂ (90)-WO ₃ (10)	77.57	20.04	2.39	100
TiO ₂ (75)-WO ₃ (25)	72.95	20.89	6.16	100
TiO ₂ (50)-WO ₃ (50)	79.47	10.07	9.83	100
TiO ₂ (25)-WO ₃ (75)	76.83	6.33	16.84	100
100 % WO ₃	76.41	0	23.59	100

Table 4: Estimated by EDX analysis percent concentration (w/%) of O, Ti and W in deposited by spray-pyrolysis thin TiO₂-WO₃ layers**Tabela 4:** EDX-koncentracija (w/%) O, Ti in W v tankih TiO₂-WO₃ plasteh, nanešenih s pršilno pirolizo

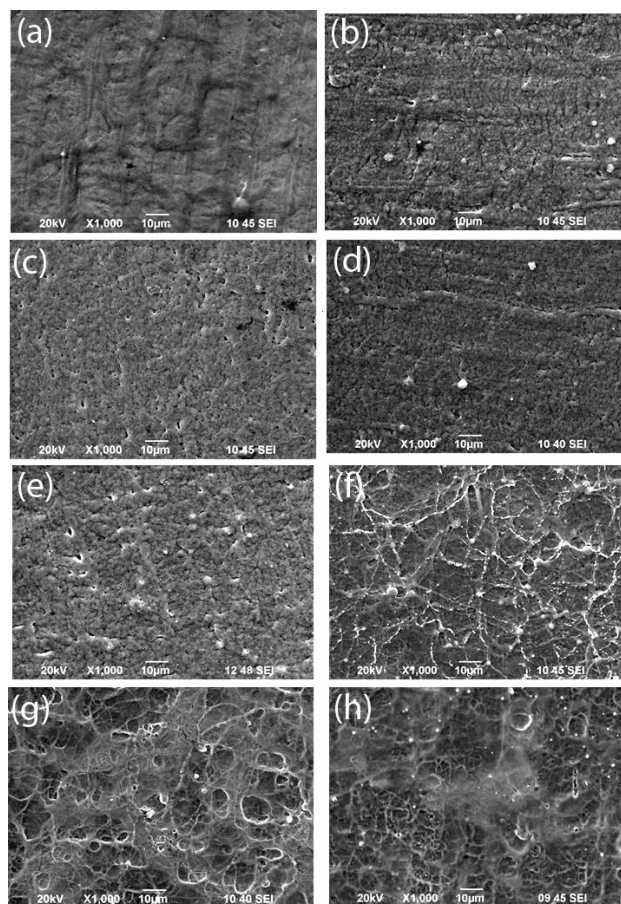
Sample	O w/%	Ti w/%	W w/%	Total
TiO ₂ (100)	57.86	42.14	0	100
TiO ₂ (99)-WO ₃ (1)	56.85	38.21	4.94	100
TiO ₂ (95)-WO ₃ (5)	40.83	47.23	11.94	100
TiO ₂ (90)-WO ₃ (10)	47.00	36.35	16.65	100
TiO ₂ (75)-WO ₃ (25)	35.36	30.32	34.32	100
TiO ₂ (50)-WO ₃ (50)	35.40	14.27	50.33	100
TiO ₂ (25)-WO ₃ (75)	26.56	6.55	66.89	100
WO ₃ (100)	21.99	0	78.01	100

It is seen from the obtained results, that at concentrations of WO₃ in the precursor lower than 10 %, its inclusion in the composite layers takes place. At the same time the content of co-deposited WO₃ and TiO₂ in the composite TiO₂-WO₃ thin films practically does not

correspond to the weight ratio of the two mixed precursor solutions (**Tables 3 and 4**). A specific deviation is observed, especially at the concentration interval of 1–10 % of mass fractions of WO₃ in the working solution. It is interesting to point that for the solution containing 5 % WO₃ both the weight and atomic percentages of co-deposited Ti are having their maximum along all the investigated samples and are even higher than in the case of the spray-pyrolysis deposited pure TiO₂, while the atomic percent of O has its minimum in this case.

The results of the SEM observations of the investigated TiO₂-WO₃ composite layers as well as pure TiO₂ and WO₃ layers at different magnifications are shown in **Figure 1**. It is seen from the obtained results that the surface structure of the pure TiO₂ layer is very smooth and compact, with no visible cracks (**Figure 1a**). The addition of WO₃ (H₂W₃O₁₂) to the working solution affected the structure of the obtained TiO₂-WO₃ composites and the layer surface morphology becomes well populated with irregularities, which can be associated with the irregular inclusion of WO₃ particles into the TiO₂ matrix (**Figures 1b to 1g**). At the low concentrations of WO₃ in the working solution there is a systematic appearance of macro-void formations. With increasing the content of WO₃ in the working solution and the content of the WO₃ in the composite layers, respectively, the number of elevations and depressions on the surface increases while the number of formed voids decreases. The surface of the composite coatings becomes lacy. Probably, this effect is due to the fast hydrolysis of the tungsten salts leaving holes behind them that create micron-sized concavities characterizing the "pure" WO₃ layers (**Figure 1h**). These results are fully consistent with the quantitative analysis of the surface topography and surface roughness obtained for the same systems using AFM.⁶²

As shown in **Figure 1**, the surfaces of the composite layers are decorated by agglomerated grains having a considerable surface roughness. Increasing the content of WO₃ in the TiO₂-WO₃ composites leads to the formation of numerous irregularities in their surface. The layers with a higher WO₃ content exhibit a rough surface texture with high 'mountains' and deep 'valleys' generated by the fusion of particles at the inter-particle contacts. As shown in⁶² there are differences in surface irregularity when forming the TiO₂-WO₃ composites. The surface roughness values increase significantly with an increase of the WO₃ content in the composite, reaching to 316 nm. The change of the surface roughness suggests that the small TiO₂ grains (with average diameter of about 4.5 nm) fill the voids and pores between the WO₃ agglomerates, promoting the surface flattening.

**Figure 1:** SEI images of samples: a) TiO₂(100), b) TiO₂(99)-WO₃(1), c) TiO₂(95)-WO₃(5), d) TiO₂(90)-WO₃(10), e) TiO₂(75)-WO₃(25), f) TiO₂(50)-WO₃(50), g) TiO₂(25)-WO₃(75), and h) WO₃(100).

Slika 1: SEI-posnetki vzorcev: a) TiO₂(100), b) TiO₂(99)-WO₃(1), c) TiO₂(95)-WO₃(5), d) TiO₂(90)-WO₃(10), e) TiO₂(75)-WO₃(25) (eII BEC posnetek), f) TiO₂(50)-WO₃(50) (fI in fIV – BEC posnetek; fIII: EDS-spekter in izračunane vrednosti v spodnji tabeli – Ti in W, dobljena v točki 3 – prikazani na Sliki 1 fII), g) TiO₂(25)-WO₃(75), in h) WO₃(100)

4.2 Mechanical characterization

In order to confirm the high adhesion of the formed coatings we performed adhesion tests with repeated

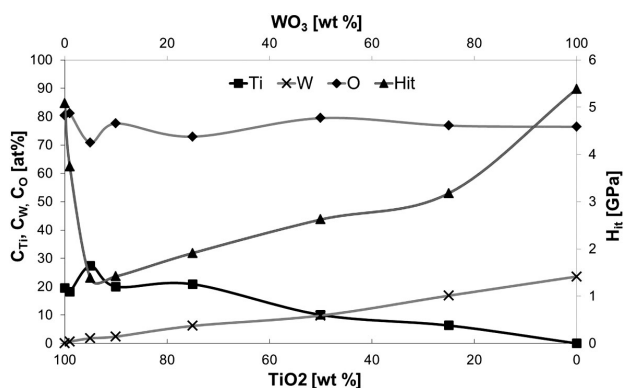
S. CHERNEVA et al.: NANO-INDENTATION INVESTIGATIONS OF THE MECHANICAL PROPERTIES OF THIN TiO_2 , WO_3 ...


Figure 2: Indentation hardness H_{IT} as a function of the concentration of Ti, W and O in the spray-pyrolysis-deposited TiO_2 - WO_3 layers, (at%)

Slika 2: Trdota vtiska H_{IT} v odvisnosti od koncentracije Ti, W in O v plasteh TiO_2 - WO_3 , nanešenih s pršilno pirolizo, (at%)

bending of coated foils at an angle of 180° (according EN ISO 2819-1994:2.9 "Bending test"). A good adhesion of the TiO_2 - WO_3 coatings to the SS substrate was found for all samples, and the attrition of coatings was negligible (less than 1 %). This observation ensures that during the indentation tests there is no separation of the coating from the substrate. This result gives us confidence in excluding the separation of the coating from the analysis of the mechanical properties.

As a result of the nano-indentation measurements, the load-displacement curves for all samples were obtained and analysed for a determination of the indentation modulus and hardness of just the foil coatings. **Figures 2 to 5** present the results from calculated indentation hardness and indentation modulus for all the eight samples at a load of approximately 1.89 mN and indentation depths below 250 nm (25 % of the average film thickness).

The two main factors that may influence the H_{IT} and E_{IT} of the analysed composite thin films are their chemical content and their surface morphology and structure. As shown in **Figure 1** as well as in **Tables 3** and **4**,

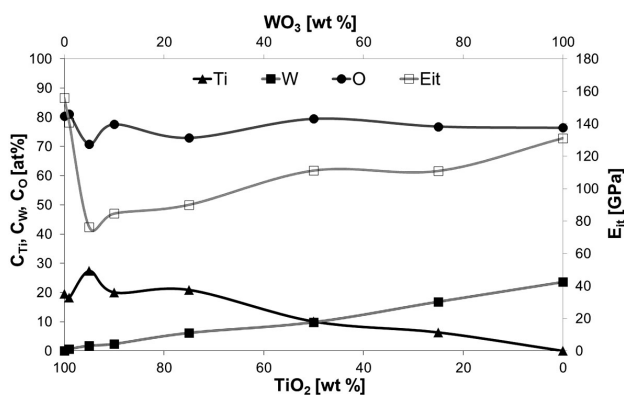


Figure 3: Indentation modulus E_{IT} as a function of the concentration of Ti, W and O in the spray-pyrolysis-deposited TiO_2 - WO_3 layers, (at%)

Slika 3: Modul vtiska E_{IT} v odvisnosti od koncentracije Ti, W in O v plasteh TiO_2 - WO_3 nanešenih s pršilno pirolizo, (at%)

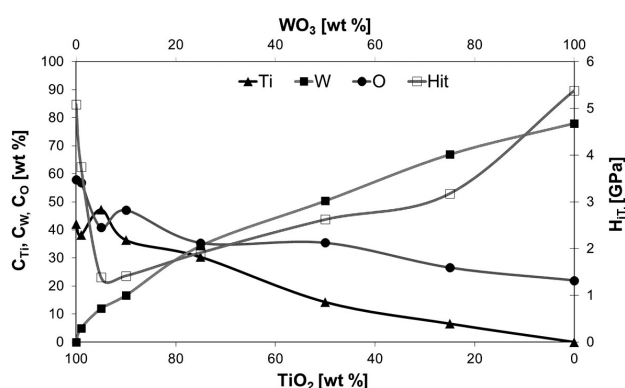


Figure 4: Indentation hardness H_{IT} as a function of Ti, W, and O content, (wt%)

Slika 4: Trdota vtiska H_{IT} v odvisnosti od vsebnosti Ti, W in O, (wt%)

the changes of the chemical content (the ratio between concentrations of TiO_2 and WO_3 phases) in the TiO_2 - WO_3 composite layer have a significant influence on the surface morphology, bulk structure, defects and porosity. This observation suggests that the change in the ratio between the concentrations of the two components and of their ingredients (O Ti, W) in the composite layer could have an important influence on the H_{IT} and E_{IT} values. This was the reason to investigate the influence of the change in the chemical content and the subsequent structural and phase changes in the spray-pyrolysis deposited TiO_2 - WO_3 layer on its mechanical characteristics.

First we consider the variation of the mechanical properties depending on the weight percent of the two precursors in the working solution. **Figures 2** and **4** show that the indentation hardness of the pure WO_3 and pure TiO_2 films is approximately of the same value. The slightly higher hardness of the pure WO_3 coating may be attributed to the observed less porosity. At small concentrations of WO_3 in the working solution (from 0 % to 5 %), there is a rapid drop in the indentation hardness of the obtained composite films. With a further increase of the WO_3 concentrations, the indentation hardness increases gradually to reach its maximum for the pure WO_3 layer. The behaviour of the indentation modulus is

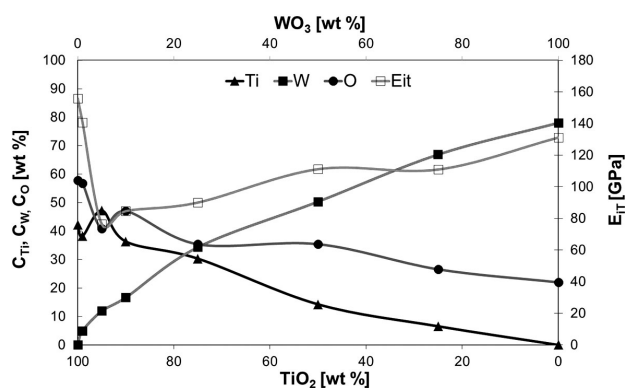


Figure 5: Indentation modulus E_{IT} as a function of Ti, W, and O content, (wt%)

Slika 5: Modul vtiska E_{IT} v odvisnosti od vsebnosti Ti, W in O, (wt%)

Table 5: Values of H_{IT} and E_{IT} at the characteristic points of the concentration ratio of TiO₂ and WO₃ precursors in the working solution, content of Ti and W in deposited layers, respectively**Tabela 5:** Vrednosti H_{IT} in E_{IT} pri značilnih točkah razmerja koncentracije TiO₂ in WO₃ osnov v delovni raztopini ter vsebnost Ti in W v nanješnih plasteh

Weight ratio of the TiO ₂ and WO ₃ precursors in the working solution	TiO ₂ 100 %	TiO ₂ 95 % WO ₃ 5 %	TiO ₂ 50 % WO ₃ 50 %	WO ₃ 100 %
Content (at%) of Ti and W in spray-pyrolysis deposited layers	Ti 19.56 W 0	Ti 27.37 (max) W 1.8 O 70.83 (min)	Ti 10.07 W 9.83 (approx. equal)	Ti 0 W 23.59
H_{IT} (GPa)	5.1	1.3 (min value)	2.7	5.4 (max value)
Standard deviation of H_{IT} (%)	7.8 %	11.99 %	16.68 %	16.3 %
E_{IT} (GPa)	155 (max value)	75 (min value)	110	133
Standard deviation of E_{IT} (%)	4.34 %	7.17 %	9.31 %	9.54 %

similar to that of the indentation hardness. When adding a small amount of WO₃ (from 0 % to 5 %) to the working solution, the indentation modulus of the composite films first decreases with increasing the content of WO₃ and reaches its minimum for sample TiO₂(95)-WO₃(5). With further increasing the concentrations of WO₃, the value of the indentation modulus increases gradually. However, in the case of pure WO₃ film the value of the indentation modulus is less than in the case of pure TiO₂ film.

The relation between the change of H_{IT} and E_{IT} and the chemical content of the investigated layers is also depicted in **Figures 2 to 5**. The results show that the H_{IT} and E_{IT} values of the TiO₂-WO₃ composite layer containing the maximum weight and atomic percent of Ti and minimum atomic percent of O are having the lowest values, as compared to those of the other composite as well as mono-component layers. In this case, the value of H_{IT} was four times lower in comparison with the hardness of the pure TiO₂ layer ($H_{IT}/TiO_2(100)$ 5.1 GPa vs. $H_{IT}/TiO_2(95)-WO_3(5)$ 1.3 GPa). It should be pointed out that the determined concentration of Ti in the deposited composite layer has its maximum value for sample TiO₂(95)-WO₃(5), even higher than the one determined for the spray-pyrolysis deposited nanosize 100 % ("pure") TiO₂ layer (27.4 % of amount fractions vs. 19.6 % of amount fractions of Ti). A remarkable property of the TiO₂(95)-WO₃(5) sample is observed from the Raman spectrum and is discussed in ⁶³. The conclusion is that the Raman spectra of the TiO₂(95)-WO₃(5) sample suggests the appearance of a tensile stress at the TiO₂-WO₃ interface. Such a tensile stress may decrease the hardness of the coating. In our case, the further increase of W percent concentration in the composite coatings has led to a practically proportional increase of H_{IT} . At higher concentrations (above 17 % of amount fractions) the increase of the H_{IT} value became more rapid.

When comparing the variation of H_{IT} with that of the Ti, W and O atomic concentrations in the studied layers, it can be concluded that the increase of the W concentration in the composite layer is monotonic, while that of Ti possesses a complex non-monotonic behaviour. With

the addition of WO₃ into the working solution, first the concentration of the Ti increases, reaching its maximum for TiO₂(95)-WO₃(5) sample. In the case of the working solution containing 10 % WO₃ precursor, the concentration of Ti in the deposited composite TiO₂-WO₃ layer starts to decrease, reaching ~11 % of amount fractions. Increasing the concentration of the WO₃ precursor (up to 25 %) leads to an increase of the concentration of W in the composite layers; however, this does not change proportionally the concentration of Ti. Furthermore, the values of H_{IT} continue to increase, indicating the dominant influence of the second component (WO₃) in the composite layer mechanical characteristics. This is also indicated by the values of H_{IT} at the approximately equal atomic concentration ratio of Ti and W – **Table 5**.

The values of H_{IT} and E_{IT} for the spray-pyrolysis deposited layers of TiO₂, WO₃ and TiO₂-WO₃ composites with weight ratio of the TiO₂ and WO₃ precursors 95:5 and 50:50 corresponding respectively to maximum concentration of Ti (27.5 % of amount fractions) and minimum concentration of O (70.83 % of amount fractions) and to the approximately the same content in % of the amount fractions of Ti and W (10.07:9.83 % of amount fractions) can be found in **Table 5**.

Considering the results discussed above, it can be concluded that the mechanical characteristics H_{IT} and E_{IT} mainly depend on the chemical content, structure and porosity of the investigated TiO₂-WO₃ composite layers. The comparison of the size changes in agglomerates building the layers shows that the amorphous "pure" TiO₂ layers (**Figure 2a**) are characterized by considerably higher H_{IT} and E_{IT} values than those of the composite TiO₂-WO₃ layers. The co-deposition of 0.6–2.4 % of amount fractions (5–17 % of mass fractions) W leads to a substantial increase of the porosity and the size of the agglomerates building the TiO₂-WO₃ layers that determine the dramatic decrease of H_{IT} and E_{IT} , according to the Hall-Petch relationship.⁶⁵ Increasing the concentration of the co-deposited W (WO₃) further, decreases the porosity of the layers, as well as the size of the agglomerates that build them, which leads to the increase of H_{IT} and E_{IT} .⁶² The latter values are close to the H_{IT} and E_{IT} measured for the spray-pyrolysis

deposited "pure" WO₃, which according to the SEM microphotographs is more likely to exhibit a crystal structure. Importantly, in all of the composite layers the values of H_{IT} and E_{IT} are lower than the one of the "pure" TiO₂ and WO₃ layers. Moreover, the obtained values are described by a dependency that has a minimum at low concentrations (1.5–2.5 % of amount fractions) of the co-deposited W, after which H_{IT} and E_{IT} increase with the concentration of W. This complex dependency suggests that along with the influence of the changes in the structure (the size of the crystallites that build the layers) other factors could have an influence on H_{IT} and E_{IT} when the concentration of co-deposited W (WO₃, respectively) increases in the composite layers. We can assume that the TiO₂ and WO₃ molecules interact in the TiO₂-WO₃ composite layer on an electron level. The reasons for making such an assumption are given in 62,66–68.

4.3 Further discussion

It is interesting to note that H_{IT} and E_{IT} drop coincides with the rise of the photoactivity of the corresponding TiO₂-WO₃ systems.⁶² After reaching the maximum values of the photocatalytic activity at 10 wt. % of WO₃, the drop of activity occurred with further increasing of the WO₃ content. The drop of photoactivity is followed by a simultaneous increase of the H_{IT} and E_{IT} factors. Obviously, materials properties that suits photocatalytic activities (well-developed surface area, porosity, surface defect, etc.) are a disadvantage for the mechanical characteristics of these coatings. Our previous investigations by XPS⁶² have shown that metals are in their main oxidation state, Ti⁴⁺ and W⁶⁺, but positive shift of the binding energy of Ti 2p by 0.5 eV is observed, pointing out that there is kind of interaction between TiO₂ and WO₃ phase. Furthermore, the Raman investigation reveals that TiO₂-WO₃ composites with up to 10 % of mass fractions of WO₃ are without free WO₃ phase that is incorporated within TiO₂ forming Ti_{1-x}W_xO₂ phase. Probably, such a structure leads to the disturbance of TiO₂ lattice, making it less resistant to the mechanical stress. Obviously, this increasing of the quantity of defects in the TiO₂-WO₃ composite phase and the increasing of the quantity of separately formed WO₃ phase (with increasing of WO₃ (H₂W₃O₁₂) in the working solution) surrounded by solitary TiO₂ particles can be another reason that will lead to an increase of the H_{IT} and E_{IT} of the deposited by spray-pyrolysis layers.

5 CONCLUSION

In present work it was shown that the mechanical properties of a deposited spray-pyrolysis composite's TiO₂-WO₃ layers strongly depend on the concentration of WO₃ (weight ratio between the two precursor solutions (TiO₂ colloidal solution and H₂W₃O₁₂), respectively) in the working solutions. For low concentrations

of the WO₃ (up to 10 %) in the working solution, the indentation hardness and modulus of the studied films decrease, due to the increase of the porosity and size of the building agglomerates. However, for higher concentrations of WO₃ (more than 10 %), the increase of H_{IT} and E_{IT} with the increase of the concentration of WO₃ can be attributed to the decrease of the size of the building agglomerates of the phase TiO₂-WO₃, as well as to filling of the concavities and pores between the separate WO₃ agglomerates with small-size TiO₂ grains that flatten the surface of the composite layer. The observed specific changes of H_{IT} and E_{IT} can also be associated with the interaction between the TiO₂ and the WO₃ in the TiO₂-WO₃ composites at the electron level. Moreover, it was found that increasing the defects in the TiO₂-WO₃ composite phase and increasing the quantity of separately formed WO₃ phases (with increasing of WO₃ (H₂W₃O₁₂) in the working solution) surrounded by solitary TiO₂ particles can be another reason leading to increasing of H_{IT} and E_{IT} of the spray-pyrolysis layers.

Acknowledgements

The authors gratefully acknowledge the financial support by the National Science Fund of Bulgaria under Projects: T 02-22 and DNTS/Germany 01/6; and Ministry of Education and Science of the Republic of Serbia – Project No. 172022.

6 REFERENCES

- I. V. Baklanova, V. N. Krasilnikov, L. A. Perelyaeva, O. I. Gyrdasova, *Theoretical and Experimental Chemistry*, 47 (2011), 215–218, doi:10.1007/s11237-011-9206-x
- W. Choi, *Catalysis Surveys from Asia*, 10 (2006), 16–28, doi:10.1007/s10563-006-9000-2
- U. Bach, D. Corr, D. Lupo, F. Pichot, M. Ryan, *Adv. Mater.*, 14 (2002), 845–848, doi:10.1002/1521-4095(20020605)
- P. I. Gouma, M. J. Mills, K. H. Sandhage, *J. Am. Ceram. Soc.*, 83 (2000), 1007–1009, doi:10.1111/j.1151-2916.2000.tb01320.x
- C. C. Oey, A. B. Djurišić, H. Wang., K. K. Y. Man, W. K. Chan, M. H. Xie, Y. H. Leung, A. Pandey, J.-M. Nunzi, P. C. Chui, *Nanotechnology*, 17 (2006), 706–713
- R. N. Grass, S. Tsantilis, S. E. Pratsinis, *AIChE Journal*, 52 (2006), 1318–1325, doi:10.1002/aic.10739
- L. Kao, T. Hsu, H. Lu, *J. Colloid Interf. Sci.*, 316 (2007), 160–167, doi:10.1016/j.jcis.2007.07.062
- X. Zhang, M. Zhou, L. Lei, *Appl. Catal. A- Gen.*, 282 (2005), 285–293, doi:10.1016/j.apcata.2004.12.022
- M. Kang, *Mater. Lett.*, 59 (2005), 3122–3127, doi:10.1016/j.matlet.2005.05.032
- X. Sui, Y. Chu, S. Xing, M. Yu, C. Liu, *Colloid. Surface A.*, 251 (2004), 103–107, doi:10.1016/j.colsurfa.2004.08.015
- K. Mori, K. Maki, S. Kawasaki, S. Yuan, H. Yamashita, *Chem. Eng. Sci.*, 63 (2008), 5066–5070, doi:10.1016/j.ces.2007.06.030
- C. Shifu, C. Lei, G. Shen, C. Gengyu, *Chem. Phys. Lett.*, 413 (2005), 404–409, doi:10.1016/j.cplett.2005.08.038
- T. Miyata, S. Tsukada, T. Minami, *Thin Solid Films*, 496 (2006), 136–140, doi:10.1016/j.tsf.2005.08.294
- W. Guo, Z. Lin, X. Wang, G. Song, *Microelectron. Eng.*, 66 (2003), 95–101, doi:10.1016/S0167-9317(03)00031-5

- ¹⁵ A. B. Haugen, I. Kumakiri, C. Simon, M. A. Einarsrud, J. Eur. Ceram. Soc., 31 (2011), 291–298, doi:10.1016/j.jeurceramsoc.2010.10.006
- ¹⁶ T. Novakovic, N. Radic, B. Grbic, D. Stoychev, P. Stefanov, T. Marinova, Mater. Sci. Forum, 555 (2007), 321–326
- ¹⁷ T. Novakovic, N. Radic, B. Grbic, V. Dondur, M. Mitric, D. Randjelovic, D. Stoychev, P. Stefanov, Appl. Surf. Sci., 255 (2008), 3049–3055, doi:10.1016/j.apsusc.2008.08.074
- ¹⁸ L. M. Bertus, A. Enesca, A. Duta, Thin Solid Films, 520 (2012), 4282–4290, doi:10.1016/j.tsf.2012.02.052
- ¹⁹ O. Sugiyama, M. Okuya, Sh. Koneko, J.Ceramic Soc.Japan, 117 (2009), 203–207, doi.org/10.2109/jcersj2.117.203
- ²⁰ J. M. Ortega, A. Martinez, D. Acosta, C. Magana, Sol. Energ. Mat. Sol., C. 90 (2006), 2471–2479, doi:10.1016/j.solma.2006.10.033
- ²¹ J. Dostanic, B. Grbic, N. Radic, P. Stefanov, Z. Saponjic, J. Buha, Chem. Eng. J., 180 (2012), 57–65, doi:10.1016/j.cej.2011.02.100
- ²² M. Maeda, T. Horikawa, MRS Proceedings (2013), mrsf12-1492-g07-07, doi:10.1557/opl.2013.220
- ²³ A. Fujishima, X. Zhang, D. A. Tryk, Surf. Sci. Rep., 63 (2008), 515–582, doi:10.1016/j.surfrep.2008.10.001
- ²⁴ M. Grätzel, Mod. Aspect. Electrochem., 15 (1983), 83–165
- ²⁵ P.V. Kamat, Chem. Rev., 93 (1993), 267–300, doi:10.1021/cr00017a013
- ²⁶ M. Machida, K. Norimoto, T. Kimura, J. Am. Ceram. Soc., 88 (2005), 95–100, doi:10.1111/j.1551-2916.2004.00006.x
- ²⁷ A. Markowska-Szczupaka, K. Ulfig, A.W. Morawski, Catal. Today, 169 (2011), 249–257, doi:10.1016/j.cattod.2010.11.055
- ²⁸ K. Sridharan, E. Jang, T. J. Park, Appl. Catal. B: Environ., 142–143 (2013), 718–728, doi:10.1016/j.apcatb.2013.05.077
- ²⁹ D. Chatterjee, S. Dasgupta, J. Photoch. Photobio., C 6 (2005), 186–205, doi:10.1016/j.jphotochemrev.2005.09.001
- ³⁰ J. Radjenovic, C. Sirtori, M. Petrovic, D. Barcelo, S. Malato, Appl. Catal. B: Environ., 89 (2009), 255–264, doi:10.1016/j.apcatb.2009.02.013
- ³¹ S. Chen, A. Wang, C. Dai, J. Benziger, Y. Lin, Chem.Eng.J., 249 (2014), 48–53, doi:10.1016/j.cej.2014.03.075
- ³² S. Stojadinovic, N. Radic, R. Vasilic, M. Petkovic, P. Stefanov, Lj. Zekovic, B. Grbic, Appl.Catal. B: Environ., 126 (2012), 334–341, doi:10.1016/j.apcatb.2012.07.031
- ³³ A. Kambur, G. Pozan, I. Boz, Appl.Catal. B, 115–116 (2012), 149–158, doi:10.1016/j.apcatb.2011.12.012
- ³⁴ M. A. Rauf, S. B. Bukallah, A. Hammadi, A. Sulaiman, F. Hammadi, Chem. Eng. J., 129 (2007), 167–172, doi:10.1016/j.cej.2006.10.031
- ³⁵ V. Puddu, R. Mokaya, G. Li Puma, Chem. Commun., 45 (2007), 4749–4751, doi:10.1039/B711559H
- ³⁶ O. Lorret, D. Francova, G. Waldner, N. Stelzer, Appl. Catal. B: Environ., 91 (2009), 39–46, doi:10.1016/j.apcatb.2009.05.005
- ³⁷ R. A. Carcel, I. Andronic, A. Duta, Mater. Charact., 70 (2012), 68–73, doi:10.1016/j.matchar.2012.04.021
- ³⁸ J. Georgieva, S. Armanyanov, E. Valova, Ts. Tsacheva, I. Poullos, J. Electroanal. Chem., 585 (2005), 35–43, doi:10.1016/j.elechem.2005.07.018
- ³⁹ E. Valova, J. Georgieva, S. Armanyanov, S. Sotiropoulos, A. Hubin, K. Baert, M. Raes, ECS Trans., 25 (2010), 13–24, doi:10.1149/13318500
- ⁴⁰ M. Ilieva, S. Ivanov, V. Tsakov, J. Appl. Electrochem., 38 (2008), 63–69, doi:10.1007/s10800-007-9399-9
- ⁴¹ M. Ilieva, A. Nakova, V. Tsakova, J.Appl.Electrochem., 42 (2012), 121–129, doi 10.1007/s10800-011-0378-9
- ⁴² A. Rey, P. Garcia-Munoz, M. D. Hernandez-Alonso, E. Mena, S. Garcia-Rodriguez, F. J. Beltran, Appl. Catal. B, 154–155 (2014), 274–284, doi:10.1016/j.apcatb.2014.02.035
- ⁴³ T. Tsatsuja, T. Tsatsuja, Y. Ohio, S. Satoh, R. Fujisama, Chem. Mater., 13 (2001), 2838–2842, doi:10.1021/cm010024k
- ⁴⁴ P. Nagootrakarwikat, Y. Ohio, R. Fujisawa, Phys.Chem., 5 (2003), 3234–3237
- ⁴⁵ R. Subavi, Electrochem.Comm., 5 (2000), 897–902, doi:10.1016/j.elecomm.2003.08.016
- ⁴⁶ Y. Takochushi, P. Nagootrakarwikat, T. Tsatsuja, Electrochim. Acta, 49 (2004), 2025–2029, doi:10.1016/j.electacta.2003.12.032
- ⁴⁷ R. Subavi, T. Shinohata, K. Mori, J.Electrochem.Soc., 102 (2005), B105–B110, doi:10.1149/1.1856912
- ⁴⁸ R. Subavi, T. Shinohata, K. Mori, Sci.Technol. Adv.Mater., 6 (2006), 501–507, doi:10.1016/j.stam.2005.01.003
- ⁴⁹ S. Li, Q. Wang, T. Chen, Z. Zhou, Y. Wang, J. Fu, Nanoscale Res. Lett., 7 (2012), 227–232, doi:10.1186/1556-276X-7-227
- ⁵⁰ T. Tsai, S. Chang, T. Hsueh, W. Weng, C. Hsue, B. Dai, Nanoscale Res. Lett., 6 (2011), 575–581, doi:10.1186/1556-276X-6-575
- ⁵¹ K. Hashimoto, I. Hiroshi, A. Fujisima, Jpn. J. Appl. Phys., 44 (2005), 8269–8285, doi:10.1143/JJAP.44.8269
- ⁵² B. Gambin, J. Ivanova, G. Nikolova, V. Valeva, In: Proc. 10-th Conference on Dynamical Systems. Theory and Applications, December 7–10 2009, Lodz, Poland, vol. 2, pp. 823–828
- ⁵³ W. Oliver, G. Pharr, J. Mater. Res., 19 (2004), 3–20, doi:10.1557/jmr.2004.19.1.3
- ⁵⁴ W. Oliver, G. Pharr, J. Mater. Res., 7 (1992), 1564–1583, doi:10.1557/jmr.1992.1564
- ⁵⁵ G.M. Pharr, A. Bolshakov, J. Mater. Res., 17 (2002), 2660–2671, doi:10.1557/JMR.2002.0386
- ⁵⁶ J. C. Hay, A. Bolshakov, G. M. Pharr, J. Mater. Res., 14 (1999), 2296–2305, doi:10.1557/JMR.1999.0306
- ⁵⁷ G. M. Pharr, W. C. Oliver, F. R. Brotzen, J. Mater. Res., 7 (1992), 613–617, doi:10.1557/JMR.1992.0613
- ⁵⁸ Agilent Nanoindenter G200 User's Guide, Part Number G2A-13192-1, Rev C, Agilent Technologies, Inc. 2012
- ⁵⁹ G. Pharr, J. Hay, ASM Handbook Volume 08: Mechanical Testing and Evaluation, ASM International. 2008, 231
- ⁶⁰ T. Novakovic, N. Radic, B. Grbic, T. Marinova, P. Stefanov, D. Stoychev, Catal. Commun., 9 (2008), 1111–1118, doi:10.1016/j.cattcom.2007.10.030
- ⁶¹ T. Rajh, A. Ostafin, O. I. Micic, D. M. Tiede, M.C.Thurnauer, J. Phys. Chem., 100 (1996), 4538–4545, doi:10.1021/jp952002p
- ⁶² B. Grbić, N. Radic, S. Stojadinović, R. Vasilic, Z. Dohčević-Mitrović, Z. Šaponjic, P. Stefanov, Surf. Coat. Technol., 258 (2014), 763–771, doi:10.1016/j.surfcoat.2014.07.082
- ⁶³ Agilent Nano Indenter G200 System Pre-Install Information Guide, Agilent Technologies, Inc. 2012
- ⁶⁴ M. Datcheva, S. Cherneva, D. Stoychev, R. Iankov, M. Stoycheva, Mater. Sci. Appl., 2 (2011), 1452–1464, doi:10.4236/msa.2011.210196
- ⁶⁵ W. Smith, J. Hashemi, Foundations of Materials Science and Engineering, 4th ed., McGraw-Hill, New York. 2006
- ⁶⁶ J. Georgieva, E. Valova, S. Armanyanov, N. Philippidis, I. Poullos, S. Sotiropoulos, J. Hazard. Mater., 211–212 (2012), 30–46
- ⁶⁷ C. Khare, K. Sliozberg, R. Meyer, A. Savan, W. Schuhmann, A. Ludwig, Int. J. Hydrogen Energy, 38 (2013), 15954–15964 doi:10.1016/j.ijhydene.2013.09.142
- ⁶⁸ G. Nikolova, Thermomechanical behaviour of thin multi-layered structures, Ph.D. Thesis, Institute of Mechanics – BAS, Sofia, Bulgaria, 2008

CORROSION DETERMINATION OF REINFORCEMENT USING
THE ELECTRICAL RESISTANCE METHODDOLOČANJE KOROZIJE PALICE V ARMIRANEM BETONU S
POMOČJO METODE ELEKTRIČNE UPORNOSTIMiroslav Brodňan¹, Peter Koteš¹, Jan Vaněrek², Rostislav Drochytka²¹University of Žilina, Faculty of Civil Engineering, Univerzitná 1, 010 26 Žilina, Slovakia²Brno University of Technology, Faculty of Civil Engineering, Veveří 95, 602 00 Brno, Czech Republic
brodnan@fstav.uniza.sk

Prejem rokopisa – received: 2015-07-12; sprejem za objavo – accepted for publication: 2016-01-19

doi:10.17222/mit.2015.217

The determination of reinforcement corrosion using the electrical resistance method of embedded bars in the concrete beams in laboratory conditions is described in this paper. For comparison, the achieved data from non-destructive measurements were compared to data from subsequent destructive tests when weight losses were recorded for each of the steel bars after their exposure time. Laboratory measurements of the reinforcements were realized particularly for verification of whether the electrical resistance method could be suitable for an in-situ corrosion-evaluation process. The next part of the research was focused on the corrosion simulation of the steel reinforcement in reinforced concrete. The effect of corrosion was simulated by a nonlinear numerical analysis with the program ATENA 3D using corrosion-rate data from a laboratory test.

Keywords: corrosion, steel, reinforcement, analysis, numerical modeling

V članku je opisano določanje korozije palic, vgrajenih v betonske stebre, v laboratorijskih pogojih z uporabo metode električne upornosti. Izvedena je bila primerjava podatkov iz neporušnih meritev s podatki iz porušitvenih testov, ko je bilo izmerjeno zmanjšanje teže vsake palice po določenem času. Laboratorijske meritve palic so bile izvedene predvsem za poskus, če je metoda električne upornosti primerna za oceno korozije in situ. Drugi del raziskave je bil usmerjen v simulacijo korozije jeklenih palic v armiranem betonu. Vpliv korozije je bil simuliran z nelinearno numerično analizo, s programom ATENA 3D, z uporabo korozijskih podatkov iz laboratorijskega preizkusa.

Ključne besede: korozija, jeklo, armature, analiza, numerično modeliranje

1 INTRODUCTION

Nowadays, the tendency in the branch of non-destructive or semi-destructive evaluation methods for the determination of a reinforcement's corrosion leads us to find such a suitable method that can precisely determine the actual state of reinforcement. In economic terms, as well as in terms of implementation, these methods are the most preferred.^{1,2} According to O. Klinghoffer et al., T. Jašniok and M. Jašniok et al., J. P. Broomfield and others, it is possible to prevent the further expansion of corrosion by an early localization of the endangered places and thus extend the lifetime of a construction.³⁻⁷ The corrosion of the reinforcement ordinarily causes a decrease in the adhesion between the reinforcement and concrete, volume changes (shrinkage, concrete creeping) unfavorably affecting the concrete. Finally, the reduction of the reinforcement cross-section impacts on the load-bearing capacity of the structure. For such a precise determination of the corrosion activity process of steel reinforcement, the methods such as the polarization methods, method of electrical resistance, method of half-cell potential, acoustic-emission method and others are applied.⁸⁻¹⁶ The development of non-destructive methods towards not only the methods of measurement by the method of half-cell potential, but also to other

methods (polarization method, method of electrical resistance etc.).

For the experimental work, the electrical measurement method (MER) was chosen due to good agreement of the achieved data with the real corrosion state of steel bars. Such a good correlation of the corrosion quantification was proved by the gravimetric method.^{17,18} For these methods, knowledge of the beginning electrical resistance of reinforcement or the continuing measurement of reinforcement are the critical aspects for further corrosion analysis. Because of the semi-destructive nature of the MER method, the access to uncovered reinforcement is an important restriction for its usage.

2 EXPERIMENTAL PART

2.1 Materials

2.1.1 Reinforced concrete test beams

The steel bars with 6 mm of its nominal size were chosen as the reinforcing bars (steel 10 216 grade according to ČSN 41 0216; ČSN 42 5512). Each reinforcement bar prior their usage was weighed, moreover the dimensional properties of the steel bar were recorded. Steel bars were then concreted into beams with dimensions of 50 mm × 50 mm × 340 mm with a uniform covering of 22 mm. In total, 41 of testing rein-

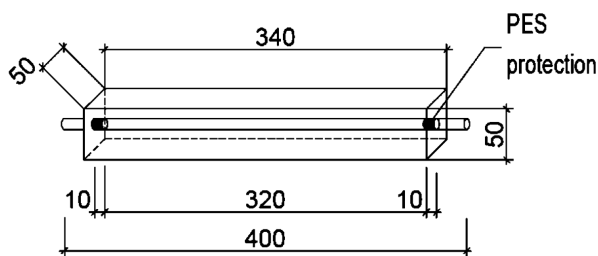


Figure 1: Dimensions of the test concrete sample with embedded steel bar

Slika 1: Dimenzije preizkusnega vzorca betona z vgrajeno jekleno palico

forced concrete beams were prepared using components of 400 kg of cement (CEM II/B – S 32,5); 1400 kg of aggregates (2–4 mm) and 225 L of water. To accelerate the migration of aggressive media to the steel reinforcement, the fine fraction of aggregates 0-2 mm was excluded. Another 14 reinforced concrete beams with reinforcement 10 216 were made to verify the changes of the electrical conductivity of reinforcement by the different moisture contents of the concrete. During the time of exposure to an aggressive environment, the overhang ends of the reinforcement bars were protected by the plug-polyethylene roller with Vaseline. The steel bars in the length of 10 mm in the concrete were coated with polyester paint for the elimination of possible resistances losses in this transition region. The scheme of the reinforced concrete beam is shown in **Figure 1**.

2.1.2 Short-term exposure of reinforced concrete beams

The prepared reinforced beams were exposed to cyclic effects of a chloride environment as recommended by RILEM AAC 7.2. It was an intermittent exposure of the beams to a 5 % water solution of NaCl, which were inserted up to 2/3 of its height for 16 h with a drying process for 8 h at 40 °C.

2.1.3 Steel samples

Measurement of individual samples (not embedded into concrete) of steel reinforcement by MER method. These samples of steel 10 505 grade (B 500 according to EN 10080; ČSN 42 0139) with diameters of (6, 8, 10, 12, 14, 16, 18, 20, 22, 25, 28, 32) mm with a uniform length of 2.0 m. The reason for using the MER method on the steel bars was to find out the meaningful ability of this method or to estimate the limitation of its usage.

2.2 Methods

2.2.1 Electrical resistance measuring method (MER)

Measuring the changes of electrical resistance of a metal sample is a method that can be applied for the non-destructive monitoring of the corrosion of steel reinforcement in concrete.¹⁹⁻²⁴ The principle of this method is based on the fundamental theory regarding the relation of electrical resistance change onto the cross-section size of each conductor, in following Equation (1):

$$R = \rho \cdot \frac{L}{A} \quad (\Omega) \quad (1)$$

where R is electrical resistance (Ω), ρ resistivity of electric conductor ($\Omega \text{ mm}^2 \text{ m}^{-1}$), (for steel $\rho = 0.098 - 0.15 \Omega \text{ mm}^2 \text{ m}^{-1}$ at temperature of 20 °C), L length of electric conductor (m), A cross-sectional area of conductor (m^2).

Each measuring of the electrical resistance of the steel sample was performed in both polarity of current flow, three measurements for each polarity were performed to minimize the effect of thermoelectric voltage. During the measurement, the temperature of the reinforcement was measured with a contact thermometer in order to eliminate the influence of different temperatures of the reinforcement on the electrical resistance value. The measured resistance was determined at a certain temperature and subsequently recalculated using Equation (2) for the resistance at 20 °C using a thermal resistance coefficient α for iron 6.2 (10^{-3} K^{-1}):

$$R_{20} = \frac{R}{1 + [0.0062 \cdot (t_x - 20)]} \quad (\Omega) \quad (2)$$

where t_x is temperature of reinforcement (°C), R_x measured resistance of reinforcement (Ω).

Measurements were undertaken in two different ways: 1) by measuring the electrical resistance using the digital ohmmeter (**Figure 2**) and 2) by measuring the electric current and voltage to calculate the resulting electrical resistance from these parallel measurements (**Figure 3**). In the case of using the ohmmeter equipment, the four-connections wiring was used in the range up to 2.00 m Ω at current of 3 A with a measurement sensitivity of 100 n Ω . For measurements using a set of

Digital Ohmmeter

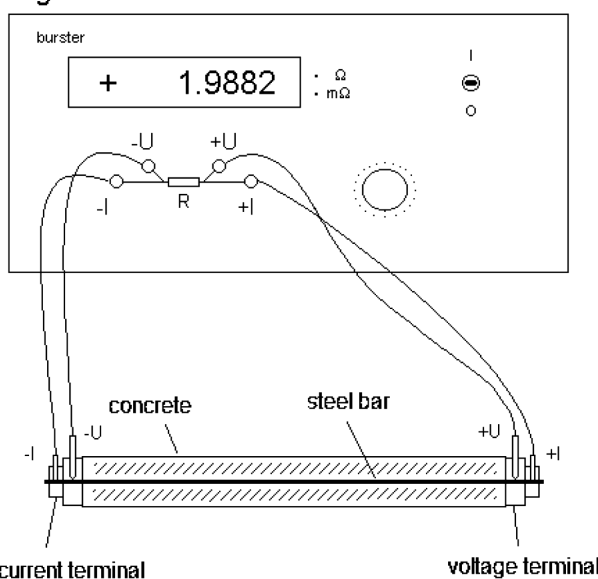


Figure 2: MER of embedded steel bars using digital ohmmeter

Slika 2: MER-vgrajene jeklene palice, izmerjen s pomočjo ohmetra



Figure 3: MER of embedded steel bars using a set of apparatus
Slika 3: MER-vgrajene jeklene palice, z uporabo sklopa naprav

apparatus, the millivoltmeter (range of 1 mV/10 mV), ampermeter (range of 2 A) and stabilized D.C. power supply were used.

From both MER methods the change of the electrical resistance value can represent the following data of corroded steel elements, in particular Equation (3):

- a) effective value of the cross-section reduction RCS, where

$$RCS = CS_0 \cdot \frac{\Delta R}{R_0} \text{ (mm}^2\text{)} \quad (3)$$

where CS_0 is initial cross section (mm^2), R_0 initial electrical resistance (Ω), ΔR difference between the electrical resistance measured at the beginning of measurement R_0 and R_t measured at the time and

- b) value of mass loss WL_c

$$WL_c = RCS \cdot L_A \cdot S_{IR} \text{ (g)} \quad (4)$$

where L_A is length of the active part of the sensor, S_{IR} specific weight of used iron bar.

2.2.2 Elemental analysis of steel and corrosive materials

Elemental analysis was carried out on selected steel bars (as a matrix) and on the corrosion products formed on their surfaces. Analysis was performed on the SEM

microscope using 20 kV voltage and an EDX probe for elemental analysis.

3 RESULTS

3.1 Influence of concrete moisture on the electrical resistance of steel bars

To prove whether the higher amount of concrete moisture content could partially influence its conductivity regarding the change of electrical current, the MER method of tested reinforcements in tested beams with different moisture content was performed. Measurements of electrical resistance were carried out on 14 pieces of reinforcement embedded in concrete beams, which have been continuously exposed to a humid environment, increasing its moisture content. Results of the electrical resistance deviation values are shown in **Table 1**. The values of moisture content of the concrete cover layer ranged from 3.4 % to 8.9 %.

3.2 Electrical resistance of steel bars with different diameter

The achieved values of electrical resistance measurements of steel samples with different diameters were compared to nominal values of the cross-sections of the steel bars (**Figure 4**). The measurement was realized on each reinforcement several times at different distances. Laboratory measurements of different diameters of

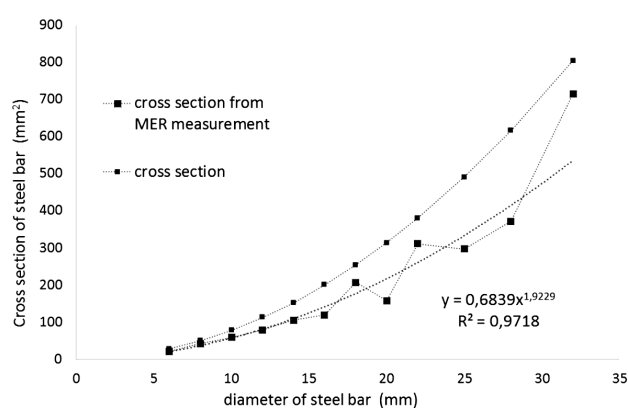


Figure 4: Changes of the cross-sections of steel bars
Slika 4: Spreminjanje preseka jeklenih palic

Table 1: Differences between values of electrical resistance with different moisture content of concrete

Tabela 1: Razlike med vrednostmi električne upornosti pri različni vsebnosti vlage v betonu

No.	Electrical resistance		No.	Electrical resistance		No.	Electrical resistance	
	Absolute difference (mΩ)	Relative difference (%)		Absolute difference (mΩ)	Relative difference (%)		Absolute difference (mΩ)	Relative difference (%)
1	0.13	2.4	6	0.13	2.5	11	0.11	2.2
2	0.07	1.4	7	0.11	2.0	12	0.10	2.0
3	0.08	1.6	8	0.09	1.7	13	0.11	2.0
4	0.13	2.5	9	0.16	3.1	14	0.09	1.7
5	0.13	2.4	10	0.09	1.7			

reinforcements were realized particularly for verification, whether there is the possibility and good correlation of its usage. Regarding the positive results, the method could be used for in-situ corrosion monitoring process.

3.3 Electrical resistance of reinforced steel bars

Figure 5a shows the changes in electrical resistance of the reinforcements in concrete, which were calculated from electrical data of the electrical voltmeter and the current. **Figure 5b** shows the changes in electrical resistance of the reinforcements, in which a digital ohmmeter was used for the measurement.

For some bars, evaluations of their weight losses were realized to verify the achieved values of weight losses WL_c calculated according to Equation (4), to those detected from built-in steel bars after exposure time. A comparison of both weights losses is listed in **Table 2**.

Moreover, elemental analyses of the steel and corrosive products were performed for the detailed specification of the used steel material (matrix). Further, the images specify the morphological manifestations of the created corrosive processes on the reinforcement surfaces (**Figure 6**) regarding the influence of the Cl^- ions in the exposure environment.

Table 3: Determined values of elemental analysis of the matrix of monitored steel reinforcements

Tabela 3: Elementna analiza preiskovanega jekla za ojačanje

Specimen number	Component contents (w/%)		
	Fe	Si	Mn
10	99.06	0.24 [*])	0.69
33	98.88	–	1.12

*: inclusions

Table 2: Detected values of weight losses in selected testing specimens and calculated weight losses WL_c determined by the MER method

Tabela 2: Izmerjene vrednosti zmanjšanja teže pri izbranih preizkusih vzorcev in izračunano zmanjšanje teže WL_c , določeno z MER-metodo

No.	Weight loss (Δm)	Bar diameter (d)	Bar length	S_{IR}	Corroded length	CS_0	R_t	R_0	ΔR	RCS	WL_c
	g	mm	mm	$g \cdot mm^{-3}$	mm	mm^2	$m\Omega$	$m\Omega$	$m\Omega$	mm^2	g
6	8.13	5.96	380	0.00739	320	27.90	1.95491	1.71854	0.23637	3.84	9.07
8	10.94	6.05		0.00741	319	28.75	2.16592	1.93429	0.23163	3.44	8.14
9	11.61	5.99		0.00728	321	28.18	2.07425	1.71940	0.35484	5.82	13.58
12	12.32	5.93		0.00742	320	27.62	2.03967	1.73674	0.30292	4.82	11.44
13	13.49	5.96		0.00733	321	27.90	2.09727	1.73019	0.36708	5.92	13.92
14	12.31	6.05		0.00743	322	28.75	2.22707	1.91870	0.30837	4.62	11.05
17	13.96	6.09		0.00704	319	29.13	2.09929	1.71212	0.38717	6.59	14.80
18	8.74	5.86		0.00763	321	26.97	1.95222	1.71118	0.24103	3.80	9.30
22	6.80	6.24		0.00696	321	30.58	2.09572	1.92223	0.17349	2.76	6.17
23	7.63	6.02		0.00714	318	28.46	1.96267	1.71653	0.24614	4.08	9.27
29	11.91	5.98		0.00731	323	28.09	2.08694	1.72167	0.36527	5.96	14.07
32	12.83	5.91		0.00777	321	27.43	2.27632	1.91798	0.35834	5.13	12.78
36	9.22	6.02		0.00718	319	28.46	2.01649	1.73438	0.28211	4.63	10.61
37	9.35	6.00		0.00728	321	28.27	2.03956	1.92749	0.11207	1.64	3.84
38	8.59	6.17		0.00708	317	29.90	2.13750	1.93679	0.20072	3.10	6.96
39	8.74	6.18		0.00707	321	30.00	2.17311	1.93828	0.23483	3.63	8.25

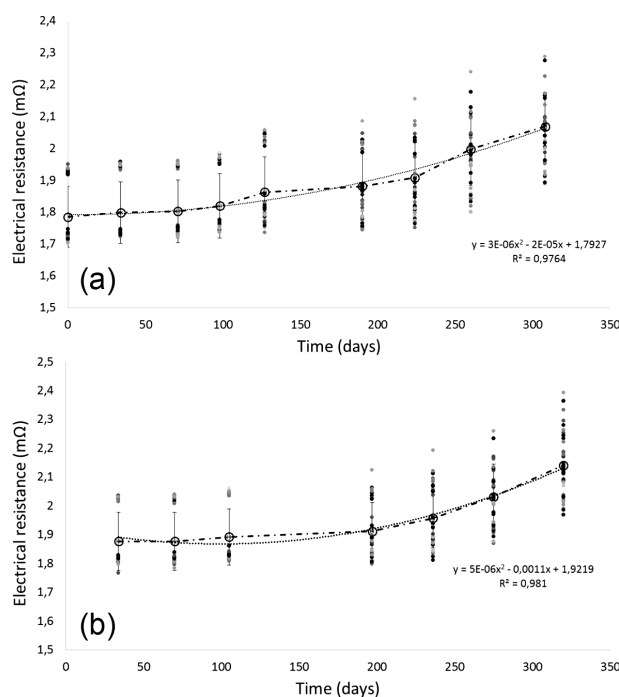


Figure 5: a) Scheme of changes of electrical resistance of steel bars embedded in concrete measured by the indirect method (current and voltage measurements), b) scheme of changes of electrical resistance of steel bars embedded in concrete measured by the direct method with ohmmeter

Slika 5: a) Prikaz spremembe električne upornosti jeklenih palic, vgrajenih v beton, izmerjene s posredno metodo (meritve tokov in napetosti), b) spreminjanje električne upornosti jeklenih palic, vgrajenih v beton, izmerjene z neposredno metodo z ohmmetrom

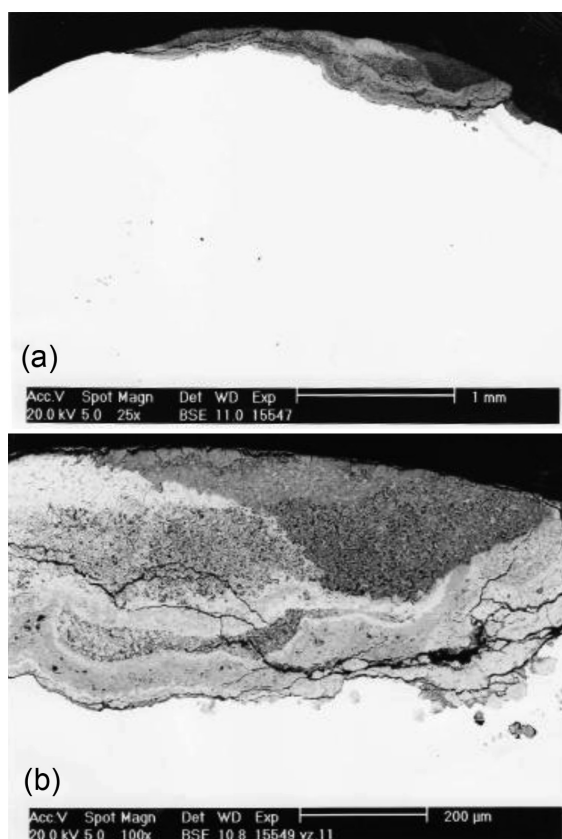


Figure 6: Detail of morphology of the corrosive processes on the surface of reinforcement: a) max. 25 \times , b) max. 100 \times

Slika 6: Detajl morfologije korozijskega procesa na površini palice za ojačanje, povečava: a) max. 25 \times , b) max. 100 \times

4 DISCUSSION

4.1 Influence of concrete moisture on the electrical resistance of steel bars

According to the achieved results, it can be concluded that the increased electrical conductivity of fully soaked concrete cover layer did not affect measured values of electrical resistance. For the in-situ application of the MER method, the moisture content of concrete has negligible influence on the performed measurements.

4.2 Measured electrical resistance of steel bars

The difference between values of the cutting cross-sections calculated from achieved electrical resistances measured on the uncovered steel bars reinforcement and designed cross-sections values of each bars was found, as shown in **Figure 4**. Due to these findings, the evaluation of the embedded steel reinforcement cannot be undertaken after a single measurement. Despite this fact, very significant correlations were found in the experimental after long-term exposure of reinforced concrete samples bars. The two methods of electrical resistance measurements were used for quantitative measurements of the steel corrosions, where a slight constant difference

between achieved values between these two methods were found. In terms of long-term monitoring of corrosion process, the electrical resistance changes of the average value of 15.9 % using the indirect method (resistance was calculated from voltage and current) and 14.0 % using measurements using ohmmeter equipment were found. In both cases, this change was obtained during the cyclic exposure to a corrosive environment for 308 d and 320 d, respectively.

5 INFLUENCE OF REINFORCEMENTS CORROSION ON THE CRACK WIDTH

The results from the experimental measurements were used for a numerical simulation of corrosion influence on cracking in concrete. The numerical modeling (with the program ATENA 3D) of the reinforcement corrosion confirms that already the small corrosion causes the formation of cracks within the cross-section near the reinforcement. With increasing corrosion, the cracks are going through the concrete cover to the surface of the member. So, it has a strong effect on reducing the remaining lifetime of structures not only due to Ultimate Limit States (ULS) of structure, but also due to Serviceability Limit States (SLS). The significance of the influence depends on the aggressiveness of environment. From this view, the most influenced elements are the members of bridges.

5.1 Experimental measurements

Corrosion has a great effect on the structure in terms of the ultimate limit state and serviceability limit state. Thus, the corrosion not only decreases the reinforcement cross-section area, thus decreasing the resistance, but it also increases the volume of the corrosive products (rust), giving rise to tensile and compressive stresses and then cracks, which are undesirable in terms of serviceability.²⁵⁻²⁷

Due to corrosion, cracks occurred in the bulk and on the surface of the specimens. The maximum measured

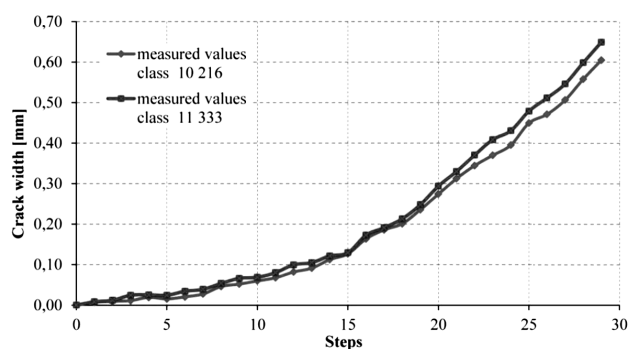


Figure 7: Average values of maximum crack width – measurements on surface

Slika 7: Povprečne vrednosti maksimalne širine razpoke – meritve na površini

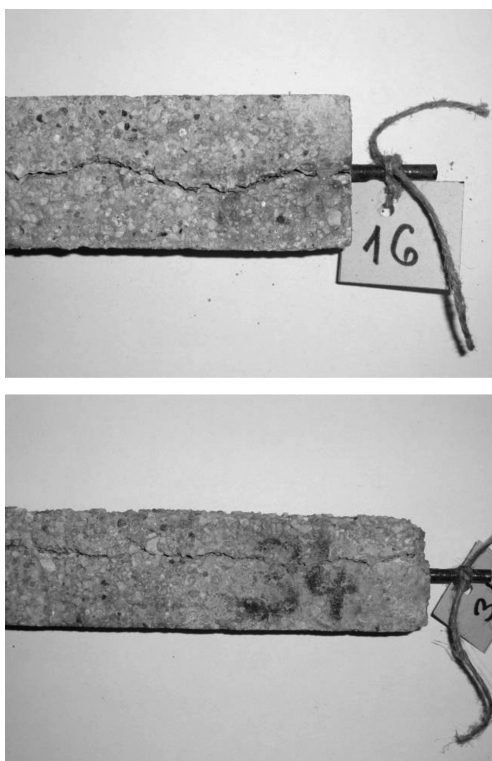


Figure 8: Photographs – crack on surface
Slika 8: Posnetka – razpoka na površini

crack width was 0.60 mm in the case of beams with steel class 10 216 and 0.65 mm in the case of tube class 11 333. The values from the experiment shown in **Figure 7** are the average values of the measurements. The marginal cracks on surface of some specimens are shown in **Figure 8**.

5.2 Numerical modeling of reinforcement corrosion

The influence of reinforcement corrosion was numerically modeled with the 3D software ATENA. Only the specimens (small beams) with smooth-faced reinforcement class 10 216 were modeled.

The reinforcement volume is decreasing with time, but the total volume, including the rust ring, is increasing (**Figure 7**). The software ATENA does not have the function "corrosion", it is necessary to use another way to model it. So, the total volume increasing due to corrosion was entered into the model as load using a shrink-

age function, but with the opposite value so as to cause an increase of the reinforcement volume. This load was evenly distributed within the cross-section and incrementally increases with load steps.

The reinforcement cross-section area is decreasing due to corrosion, while the volume of the corrosive products (rust) increases with percentage p .^{28,29} Due to this phenomenon, it was necessary to recalculate the reinforcement diameter $\phi(t)$ at time t and also the percentage loss of the cross-section area of the embedded reinforcement (**Figure 9**).

The total area of reinforcement at time t is calculated as:

$$A_{s1, total}(t) = A_{s1} \cdot (1 + p^*) \quad (\text{mm}^2) \quad (5)$$

$$A_{s1} = \frac{\pi \cdot \phi^2}{4} \quad (\text{mm}^2) \quad (6)$$

where A_{s1} is the reinforcement cross-section without corrosion, p^* is the percentage loss of reinforcement cross-section, whereas the experiment confirmed a 6 % increase of corrosion during the testing period, hence follows $p = 0.06$. The diameter $\phi(t)$ depending on time t was calculated from the Equation (7):

$$f(t) = \sqrt{\frac{\left(-A_{s1, total}(t) + \frac{\pi}{4} \phi^2 (1+p)\right) \cdot 4}{\pi \cdot p}} \quad (\text{mm}^2) \quad (7)$$

Subsequently, the percentage loss of reinforcement cross-section area was calculated in Equation (8):

$$p^* = \frac{A_{s1, total}(t)}{A_{s1}} - 1 \quad (-) \quad (8)$$

A material "3D Bilinear Steel Von Mises" was used for reinforcement class 10 216 modeling, and a material "3D Nonlinear Cementitious 2" was used for modeling concrete elements with strength $f_c = 25 \text{ MN m}^{-2}$. In the 3D version of ATENA, the crack width is evaluated in volume, not at an accurate point. The crack is propagating from inside out (to surface) and the maximum width is near reinforcement, not on the surface. Thus, to compare the relevant crack width on the surface, the concrete part of the specimen was divided into two parts – core and ring around core with a width of 3 mm (**Figure 10**). A contact between those two elements was considered as rigid. The reinforcement cross-section was

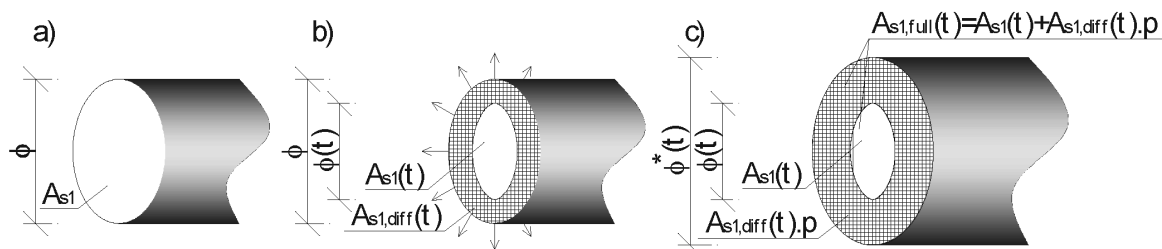


Figure 9: Change of the reinforcement cross-section area due to corrosion – theoretical approach
Slika 9: Spreminjanje površine preseka palice za ojačanje, zaradi korozije – teoretični približek

modeled as a hexagon with the same cross-section area as the original circle, because the 3D version of ATENA does not allow us to model circular cross-sections. The monitors for crack width were given as global for concrete ring macro elements and for all the three axes of the coordinate system (x,y,z) .

The next important part of the work was also modeling the contact between concrete and reinforcement. In the case of the 3D version of ATENA, the function "shrinkage" with the opposite value is applied for the whole volume of a given macro element. It means an increase of volume, not only in cross-section, but also in longitudinal direction. The increase of volume in the longitudinal direction also causes tension stresses in the longitudinal direction in concrete and subsequently cracks perpendicular to reinforcement. It is not a real state, so it is needed to model the contact, which transfers just the normal stresses in cross-section, but not the shear stresses between reinforcement and concrete. The material model "3D Interface" was used in ATENA. This model is used for contact modeling between the two different elements.

The interface material model "3D Interface" is based on the Mohr-Coulomb criterion with tension cut off. The constitutive relation for a general three-dimensional case is given in terms of tractions on interface planes and relative sliding and opening displacements, and it is given by Equation (9):

$$\begin{Bmatrix} \tau_1 \\ \tau_2 \\ \sigma \end{Bmatrix} = \begin{bmatrix} K_{tt} & 0 & 0 \\ 0 & K_{tt} & 0 \\ 0 & 0 & K_{nn} \end{bmatrix} \begin{Bmatrix} \Delta v_1 \\ \Delta v_2 \\ \Delta u \end{Bmatrix} \quad (\text{MPa}) \quad (9)$$

where τ is the shear stress in direction x and y , σ is the normal stress, Δv is the relatively displacement on surface, Δu is the relatively opening of contact, K_{tt} is the initial elastic shear stiffness, K_{nn} is the initial elastic normal stiffness.

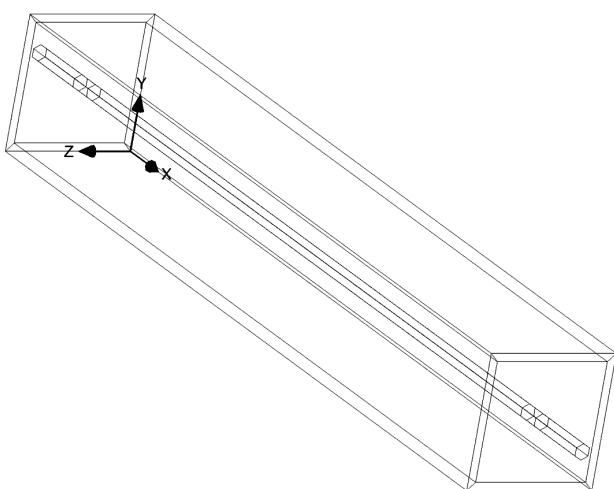


Figure 10: The 3D model in ATENA

Slika 10: 3D model ATENA

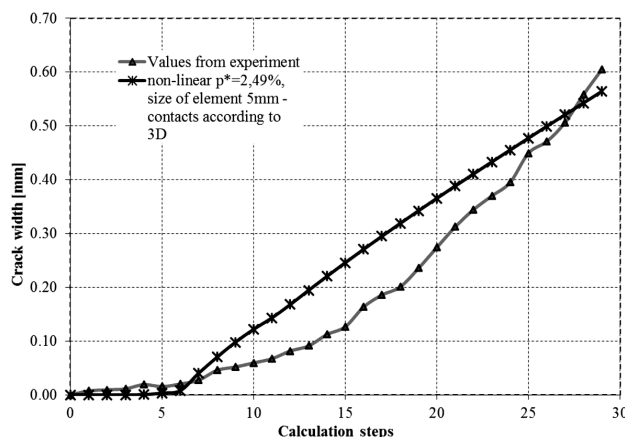


Figure 11: Comparison of crack width from experiment and numerical model

Slika 11: Primerjava širine razpoke iz eksperimenta in numeričnega modela

The initial failure surface corresponds to the Mohr-Coulomb condition with tension cut off:

$$|\tau| \leq c + \sigma \phi \quad \text{for } \sigma \leq f_t \quad (\text{MPa}) \quad (10)$$

$$\tau = 0 \quad \text{for } \sigma > f_t \quad (\text{MPa}) \quad (11)$$

where c is the cohesion, ϕ is the coefficient of friction, f_t is the tensile strength on surface.

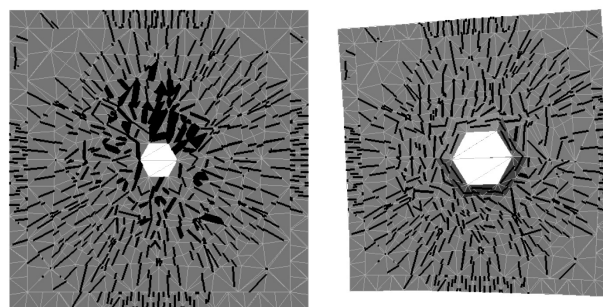
After stresses violate this condition, the surface collapses to a residual surface, which corresponds to dry friction.

The cohesion c is equal to surface stresses σ_{surf} and the value $c = 0$ was considered. Also, the coefficient of friction and tensile strength equal to zero were considered ($\phi = 0, f_t = 0$). The values of the initial elastic normal and shear stiffness are estimated from Equation (12):

$$K_{nn} = \frac{E}{t_1}, \quad K_{tt} = \frac{G}{t_1} \quad (\text{MN/m}^3) \quad (12)$$

where E is the minimal elastic modulus, G is the minimal shear modulus, t_1 is width of the interface zone.

The values $K_{nn} = 3.0 \cdot 10^6 \text{ MN/m}^3$ and $K_{tt} = 1.0 \cdot 10^3 \text{ MN/m}^3$ were considered to transfer the compressive stresses from reinforcement to concrete in



a) Plotting without deformation b) Plotting with deformation

Figure 12: Propagation of cracks from inside towards outside in the 3D model

Slika 12: Napredovanje razpok od znotraj navzven pri 3D modelu

the transverse direction and to ensure the slip between reinforcement and concrete in the longitudinal direction. It eliminates the creation of tensile stresses in the longitudinal direction.

The value $p^* = 2.488 \%$ was determined from Equation (8). This value best represents the measured values from the experiment (curves in **Figure 11**). The high consistency of the results can be seen in **Figure 11**.

The crack propagation and crack pattern in the middle cross-section are shown in **Figure 12**.

6 CONCLUSIONS

A great advantage of these methods is the fact that in the case when the reinforcements with known entrance electrical resistance are inserted into the structural element, we can relatively easily and inexpensively determine the status of other reinforcements, without the destructive interference with the concrete cover layer.

From the obtained results it is possible to conclude that this monitoring method is useful for the quantity corrosion reinforcement evaluation. The determination of the actual state of steel bars is a major criterion in the decision-making process for consequent reinforced-concrete structures redevelopment. The numerical modeling of reinforcement corrosion confirms that already the small corrosion, namely the small percentage of corroded surface causes the formation of cracks within the cross section near the reinforcement. The increase of corrosion products (rust) causes the connection of cracks from within to outside due to an increase of the radial tensile stresses. Those cracks weaken the bond between the concrete and the reinforcement and consecutive concrete cover dropping out.

In practice, it means that it is necessary to place greater emphasis on diagnostics in cases where the corrosion of the reinforcement was identified. Moreover, it means to verify the rate of concrete cover damage and the decrease of the bond. Based on the diagnostics and analysis, it is necessary to consider carefully whether it is possible to retain moderately damaged parts of concrete cover and repair them, or is it necessary to replace one by the new layer.

In conclusion, it is important to emphasize the need for a combination of different methods in monitoring the state of the steel reinforcement in terms of obtaining, if possible, the most comprehensive quantitative and qualitative information. Therefore, increasing knowledge related to the further development of research in this area is justified.

Acknowledgement

The research is supported by the Slovak Research and Development Agency under contract No. APVV-0106-11 and by Research Project No. 1/0566/15 of Slovak Grant Agency. The authors would like to

acknowledge the support of Internal Specific Research project of Brno University of Technology, No. FAST-S-14-2570 and financial support of GACR research project No. 14-25504S "Research of Behavior of Inorganic Matrix Composites Exposed to Extreme Conditions" of Czech Science Foundation.

REFERENCES

- ¹ V. M. Malhotra, N. J. Carino, *Nondestructive Testing of Concrete*, CRC Press LLC, USA 2004
- ² J. Hoła, J. Bień, L. Sadowski, K. Schabowicz, Non-destructive and semi-destructive diagnostics of concrete structures in assessment of their durability, *Bulletin of the Polish Academy of Sciences Technical Sciences*, 63 (2015) 1, 87–96, doi:10.1515/bpasts-2015-0010
- ³ FIB Bulletin 34: Model Code for Service Life Design. International Federation for Structural Concrete, Lausanne, 2006, 110
- ⁴ O. Klinghoffer, T. Frolund, E. Poulsen, Rebar corrosion rate measurements for service life estimates, ACI Fall Convention, Toronto, Canada, 2000
- ⁵ T. Jaśniok, M. Jaśniok, A. Zybura Studies on corrosion rate of reinforcement in reinforced concrete water tanks, *Ochrona przed korozją*, 56 (2013), 227–234
- ⁶ T. Jaśniok, M. Jaśniok, Electrochemical tests on corrosion of the reinforcement in reinforced concrete silos for cement, *Ochrona przed korozją*, 57 (2014), 225–229
- ⁷ J. P. Broomfield, *Corrosion of Steel in Concrete. Understanding, investigation and repair*, E&FN Spon London, 1997, 240
- ⁸ R. Polder, C. Andrade, B. Elsener, O. Vennesland, J. Gulikers, R. Weidert, M. Raupach, Test methods for on site measurement of resistivity of concrete, *RILEM, Materials and Structures*, 33 (2000), 603–611
- ⁹ V. Živica, Improved method of electrical resistance – a suitable technique for checking the state of concrete reinforcement. *Materials and Structures*, 26 (1993), 328–332
- ¹⁰ J. Rodríguez, L. M. Ortega, A. M. Garcia, On-site corrosion measurements in concrete structures. *Concrete repair*, November-December 1995, 27–30
- ¹¹ C. M. Hansson, Comments on electrochemical measurements of the rate of corrosion of steel in concrete, *Cement and concrete research*, 4 (1984), 574–584
- ¹² S. Feliú, C. Andrade, J. A. González, C. Alonso, A new method for in-situ measurement of electrical resistivity of reinforced concrete. *RILEM, Materials and Structures*, 29 (1996), 362–365
- ¹³ L. Sadowski, Methodology for assessing the probability of corrosion in concrete structures on the basis of half-cell potential and concrete resistivity measurements, *The Scientific World Journal*, 2013, doi:10.1155/2013/714501
- ¹⁴ ASTM C 876-91 Standard Test Method for Half-Cell Potentials of Uncoated Reinforcing Steel in Concrete, ASTM International, West Conshohocken, 1999
- ¹⁵ ASTM G59-97 Standard Test Method for Conducting Potentiodynamic Polarization Resistance Measurements, ASTM International, West Conshohocken, 2003
- ¹⁶ L. Pazdera, L. Topolar, M. Korenska, T. Vymazal, J. Smutny, V. Bilek, Monitoring early-age concrete with the acoustic-emission method and determining the change in the electrical properties, *Mater. Tehnol.*, 49 (2015) 5, 703–707, doi:10.17222/mit. 2014.112
- ¹⁷ R. Jambor, V. Živica, Monitoring of steel reinforcement corrosion in concrete by method of electrode potential and electrical resistance. *Building Journal*, VEDA Bratislava, 30 (1982), 563–586
- ¹⁸ V. Živica, Utilisation of electrical resistance method for the evaluation of the state of steel reinforcement in concrete and the rate of its corrosion, *Construction and Building Material*, 14 (2000), 351–358

- ¹⁹ M. Kouril, T. Prosek, B. Scheffel, Y. Degres, Corrosion monitoring in archives by the electrical resistance technique. *Journal of Cultural Heritage* 15 (2014), 99–103, doi:10.1016/j.culher.2013.04.002
- ²⁰ S. P. Karthick, S. Muralidharan, V. Saraswathy, K. Thangavel, Long-term relative performance of embedded sensor and surface mounted electrode for corrosion monitoring of steel in concrete structures. *Sensors and Actuators B: Chemical*, 192 (2014), 303–309
- ²¹ I. Martinez, C. Andrade, Examples of reinforcement corrosion monitoring by embedded sensors in concrete structures, *Cement & Concrete Composites*, 32 (2009), 545–554
- ²² C. Andrade, C. Alonso, Corrosion rate monitoring in the laboratory and on-site, *Construction and Building Materials*, 10 (1996), 315–328
- ²³ A. J. Garzon, J. Sanchez, C. Andrade, N. Rebolledo, E. Menéndez, J. Fullera, Modification of four point method to measure the concrete electrical resistivity in presence of reinforcing bars, *Cement and Concrete Composites*, 53 (2014), 249–257, doi:10.1016/j.cemconcomp.2014.07.013
- ²⁴ V. Živica, Utilisation of electrical resistance method for the evaluation of the state of steel reinforcement in concrete and the rate of its corrosion, *Construction and Building Material*, 14 (2000), 351–358
- ²⁵ J. Bilčík, L. Fillo, V. Benko, J. Halvoník, *Concrete Structures, Design by STN EN 1992-1-1*, STU Bratislava, 2008, 374
- ²⁶ V. Borzovič, J. Halvoník, *Flat Slab Reinforcement with Regard to the Distribution and Redistribution of Internal Forces*, Third international workshop Design of concrete structures using Eurocodes, Vienna, Grafische Zentrum HTU GmbH, 2012, 223–228
- ²⁷ K. Gajdošová, *Stress and Crack Width Control According to EN 1992*, Third international workshop Design of concrete structures using Eurocodes, Vienna, Grafische Zentrum HTU GmbH, 2012, 199–202
- ²⁸ P. Koteš, M. Brodňan, K. Šlopková, P. Kotula, Numerical modelling of reinforcement corrosion in reinforced concrete, *Journal Ochrana przed korozja*, 53 (2010) 6, 307–309
- ²⁹ P. Koteš, M. Brodňan, K. Šlopková, *Simulation of corrosion of reinforcement in reinforced concrete*. International RILEM Symposium on Concrete Modelling – CONMOD 08, CD, Delft – The Netherlands, 2008, [Edited by Erik Schlangen & Geert De Schutter, 2008], 761–766

EFFECT OF QUENCHING PARAMETERS ON THE MECHANICAL PROPERTIES OF THE 7A04 ALUMINIUM ALLOY

VPLIV PARAMETROV GAŠENJA NA MEHANSKE LASTNOSTI ALUMINIJEVE ZLITINE 7A04

Dequan Shi, Kaijiao Kang, Guili Gao

Harbin University of Science & Technology, Department of Materials Science & Engineering 150040 Harbin, China
shidequan2008@163.com*Prejem rokopisa – received: 2015-08-30; sprejem za objavo – accepted for publication: 2016-01-05*

doi:10.17222/mit.2015.267

The effects of quenching parameters, including the solid-solution temperature, water temperature of quenching, transfer time before quenching and delay time after quenching on the mechanical properties of the 7A04 aluminium alloy were studied. The experimental results showed that the mechanical properties are relatively stable when the solid-solution temperature is at 460–490 °C, but the over-burn will appear once the temperature exceeds 500 °C. When the water temperature of quenching and the transfer time before quenching are above 40 °C and 20 s, the strengths of the 7A04 alloy will drop remarkably. Before the delay time after quenching is 8 h, the strengths will drop gradually while the elongation will rise continuously. In the range of 8–24 h there is an opposite change of mechanical properties compared to the previous 8 h. Once it exceeds 24 h, the mechanical properties will become stable.

Keywords: quenching parameters, 7A04 aluminium alloy, mechanical properties, delay time, transfer time

Preučevani so bili vplivi parametrov gašenja, vključno s temperaturo raztopnega žarjenja, časa prehoda pred gašenjem in časa zadrževanja po gašenju, na mehanske lastnosti aluminijeve zlitine 7A04. Rezultati eksperimentov so pokazali, da so mehanske lastnosti relativno stabilne, če je temperatura raztopnega žarjenja med 460 °C–490 °C; zažgano pa je, ko temperatura preseže 500 °C. Ko je temperatura vode za gašenje nad 40 °C in čas prehoda pred gašenjem nad 20 s, se trdnosti zlitine 7A04 občutno zmanjšajo. Pri času zadrževanja do 8 h po gašenju, se trdnost stalno zmanjšuje, medtem ko se raztezek povečuje. V času od 8–24 h je ravno obratna sprememba mehanskih lastnosti, v primerjavi s predhodnimi pri 8 h. Ko čas preseže 24 h, mehanske lastnosti postanejo stabilne.

Ključne besede: parametri gašenja, aluminijeva zlitina 7A04, mehanske lastnosti, čas zadrževanja, čas prehoda

1 INTRODUCTION

7A04 is a high-strength aluminium alloy of the Al-Zn-Mg-Cu series. Due to the high strength and hardness, good corrosion resistance and wear resistance, it has become a key structural material in the aerospace field instead of the steels.^{1,2} Generally speaking, Al-Zn-Mg-Cu series aluminium alloys are produced by the method of electromagnetic semi-continuous casting,³ and then their properties were improved by the solution and aging treatment. Therefore, the heat-treatment parameters will directly affect the mechanical properties of the 7A04 aluminium alloy. At present, many experimental researches on optimizing the solution and aging treatment parameters had also been widely reported. For example, from the aspects of improving both the mechanical properties and the efficiency of heat treatment, A. L. Ning et al.⁴ studied the influences of loading the specimen at high temperature, rapid short-time progressive solution and high-temperature short-time aging on the microstructure and mechanical properties of 7A04 aluminium alloy, respectively. J. J. Liu et al.⁵ investigated the influence of the solid-solution conditions on the microstructure and resistivity of Al-Zn-Mg-Cu series alloy by in-situ resistivity measurement, optical microscopy,

scanning electron microscopy, transmission electron microscopy. O. N. Senkov et al.⁶ studied the effect of Sc additions on precipitation strengthening in a direct chill-cast Al-Zn-Mg-Cu alloy after natural and artificial aging. The microhardness, room-temperature mechanical properties, and phase composition of the alloys were determined after different steps of aging, and the strengthening mechanism was discussed. Y. Lin et al.⁷ studied the effect of non-isothermal cooling aging on the microstructure and mechanical properties of an Al-Zn-Mg-Cu alloy, and the tensile strength, yield strength and conductivity were increased 2.9 %, 8.1 % and 8.3 % compared to that of the T6 treatment, respectively. T. Marlaud et al.⁸ studied the influence of alloy composition and heat treatment on the precipitate composition. However, the effects of the quenching parameters on the microstructure and mechanical properties are rarely studied. Therefore, there is an urgent need to investigate how the quenching parameters affect the mechanical properties, which will further improve the mechanical properties and product quality of the 7A04 aluminium alloy.

In this study, the mechanical properties are measured using a CSS-44300 electronic universal testing machine, and the microstructures are observed by optical micro-

scopy. The effect of the solid-solution temperature, water temperature of quenching, transfer time before quenching and delay time after quenching on the mechanical properties of 7A04 aluminium alloy were studied, respectively, and the optimal quenching parameters were also obtained according to the experimental results.

2 EXPERIMENTAL PART

The experimental materials are hot-rolled 7A04 aluminium alloy plates with 12 mm thickness, and their chemical compositions are shown in **Table 1**.

Table 1: Chemical composition of 7A04 aluminium alloy, in mass fractions (w%)

Tabela 1: Kemijska sestava aluminijeve zlitine 7A04, v masnih odstotkih (w%)

Zn	Mg	Cu	Cr	Fe	Si	Mn	Ti
6.05	2.62	1.53	0.18	0.16	0.08	0.45	0.02

Because the 7A04 aluminium alloy is not online quenched during industrial production, it is very important to choose optimal quenching parameters. In this study, through independently altering the solid-solution temperature, the water temperature of quenching, transfer time before quenching and delay time after quenching, the effects of the quenching parameters on the mechanical properties of 7A04 aluminium alloy were investigated, respectively. If the solid-solution temperature was too high, the over-burn phenomenon in the microstructure of 7A04 aluminium alloy might appear. Therefore, the microstructure was observed by the OLYMPUS-GX71 optical microscopy when the solid-solution temperature was studied.

The hot-rolled 7A04 aluminium alloy plates were homogenized at $460 \pm 5^\circ\text{C}/24$ h, and the standard samples were prepared by horizontally cutting on the plates according to the GB/T228-2010 of China. The samples were heated to different temperatures in the salt bath furnace and the time of holding at temperature was 60 min. Then the samples were quenched according to the experimental design, and artificial aging treatment of $130 \pm 5^\circ\text{C}/24$ h was carried out. In order to study the effects of the quenching parameters on the mechanical properties, the following experiments were designed.

- 1) When the water temperature of quenching, transfer time before quenching and delay time after quenching were kept at 30°C , 20 s and 2 h, respectively, the solid-solution temperature was changed from 400°C to 510°C with the step of 10°C .
- 2) When the solid-solution temperature, transfer time before quenching and delay time after quenching were kept at 470°C , 20 s and 2 h, respectively, the water temperature of quenching was changed from 10°C to 80°C with a step of 10°C .
- 3) When the solid-solution temperature, water temperature of quenching and delay time after quenching

were kept at 470°C , 30°C and 1 h, respectively, the transfer time before quenching was changed at 5 s and from 10 s to 60 s with a step of 10 s.

- 4) When the solid-solution temperature, water temperature of quenching and transfer time before quenching were kept at 470°C , 30°C and 20 s, respectively, the delay time after quenching was set to be 1 h, 2 h, 4 h, 8 h, 16 h, 24 h, 48 h and 72 h.

3 RESULTS AND DISCUSSION

3.1 Effect of solid-solution temperature on the mechanical properties and microstructure

Figure 1 shows the change of the mechanical properties of the 7A04 alloy with solid-solution temperature. With the increase of the solid-solution temperature, the tensile strength and yield strength will first increase and then decrease, but the elongation will drop monotonically. Before the solid-solution temperature reaches up to 460°C , the tensile strength and yield strength will rapidly increase. Once the temperature excess 460°C , the increase rate will become very slow.

This can be explained as follows. In general, to improve the solid-solution temperature at a certain range is an effective means to improve the strength. When the temperature was increased, the rate of dissolving the second-phase particles will increase. As a result, it can promote the number of the strengthening precipitation phase, thus the tensile strength and yield strength will increase. However, the increase in the temperature will make the recrystallization grain grow up, which will result in the decrease of the strength.^{9,10} Therefore, when the temperature was reached to a certain value, the increase rate of the strength will become slow.

The mechanical properties were satisfied when the solid-solution temperature was kept at 460 – 490°C , which proves that there is a wide range of solid-solution temperatures for the 7A04 aluminium alloy. But when

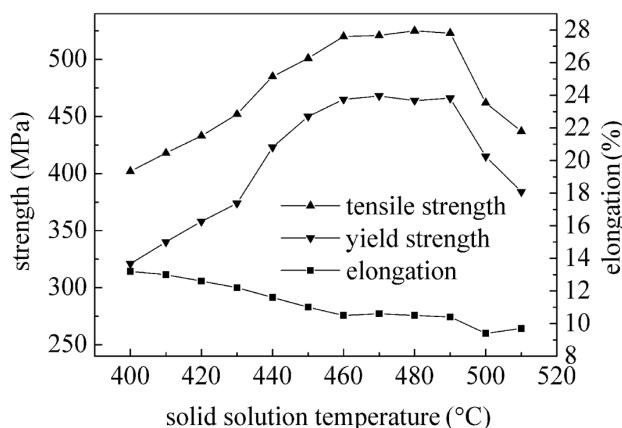


Figure 1: Mechanical properties changing with solution temperature
Slika 1: Spreminjanje mehanskih lastnosti v odvisnosti od temperature raztopnega žarjenja

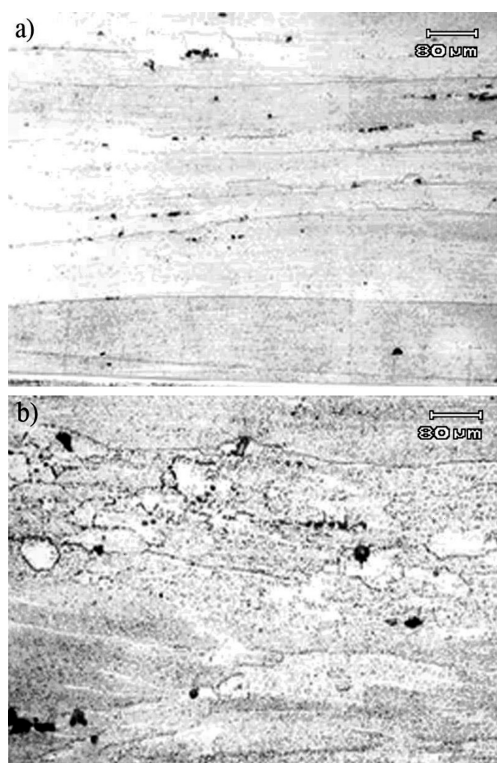


Figure 2: Microstructure at different solution temperatures: a) 470 °C, b) 500 °C

Slika 2: Mikrostruktura pri različnih temperaturah raztopnega žarjenja: a) 470 °C, b) 500 °C

the temperature is more than 500 °C, the tensile strength and yield strength will drop suddenly.

Figure 2 showed the microstructures at 470 °C and 500 °C, respectively. As shown in **Figure 2a**, the over-burn was not found in the microstructure. The partially recrystallized grains appear and they are elongated along the deformation direction. Some of the residual phase and the insoluble phase are broken, and they symmetrically arrange along the deformation direction. However, it can be seen from **Figure 2b** that the obvious over-burn

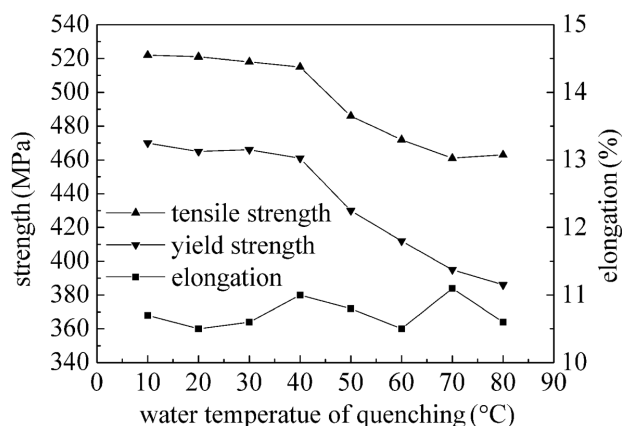


Figure 3: Mechanical properties changing with water temperature of quenching

Slika 3: Spreminjanje mehanskih lastnosti s temperaturo vode pri gašenju

and the complex re-melting grain boundaries appear. According to the relevant literature¹¹⁻¹³ the precipitated phases continuously distribute at the re-melting grain boundary. The evenly distributed fine precipitated phases inside the grains are the coherent GP zone and the small amount of transition phase. In addition, some of the large particles randomly distribute in the grain and/or the grain boundaries, and they are the main strengthening phase and the impurity phase.

3.2 Effect of water temperature of quenching on mechanical properties

The effect of the water temperature of quenching on the mechanical properties of the 7A04 aluminium alloy was shown in **Figure 3**. When the water temperature of quenching is below 40 °C, the tensile strength, yield strength and elongation are almost unchanged. However, when the water temperature is more than 40 °C, the tensile strength and yield strength decrease remarkably, while the elongation is found to have little change. This indicates that the 7A04 alloy is sensitive to the cooling rate.

The effect of the water temperature on the mechanical properties can be attributed to the cooling rate. It is well known that the precipitation sequence of the Al-Zn-Mg-Cu series alloy at the ageing treatment is super-saturation solid solution, GP zone, η' phase and η phase. So, the size, density and distribution of GP zone are very important for the forming of the η' phase. When the water temperature is below 40 °C, the cooling rate is large, and there is not enough time for the second phase to nucleate and precipitate at the grain boundary, which makes the concentration of solute atoms become higher. A lot of stable GP zones can form quickly. During ageing, many second phases can uniformly precipitate, and their sizes are not very different. So the strengthening effect is good, and the mechanical properties of 7A04 alloy are promoted. In contrast, when the water temperature increases and the cooling rate becomes small,

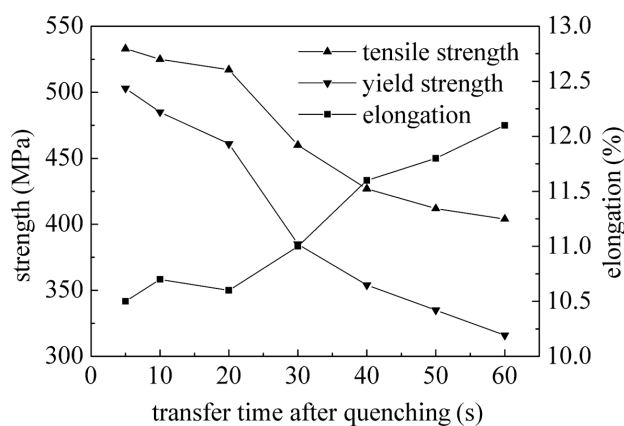


Figure 4: Mechanical properties changing with transfer time before quenching

Slika 4: Spreminjanje mehanskih lastnosti s časom prehoda pred gašenjem

there is enough time for the second phase to nucleate and precipitate at the grain boundary, and the formation of second phases will result in a decrease of the solute atom concentration at the grain boundary. During ageing, these second phases can continue to grow by absorbing the solute atoms near the grain boundary. So the GP zones will become few and instable. Therefore, the strengthening effect will become weak, and thus the mechanical properties of the 7A04 alloy will decrease.

Therefore, the water temperature of quenching should be kept below 40 °C. Actually, in order to avoid the quenching crack caused by the excessive stress, the cooling rate must be small. So, the water temperature must be high, which is contradictory to the requirement of a low water temperature due to improving the strength. Consequently, during practical production, the water temperature of quenching is as low as possible on the condition that the stress cracks do not occur.

3.3 Effect of transfer time before quenching on the mechanical properties

The effect of the transfer time before quenching on the mechanical properties of the 7A04 aluminium alloy was shown in **Figure 4**. When the transfer time before quenching is less than 20 s, a small effect can be found. But when the transfer time is more than 30 s, the tensile strength and yield strength will drop while the elongation will rise. So the transfer time should be kept within 20 s.

This can be explained as follows. Because of the additive Mn and Cr, the 7A04 aluminium alloy is sensitive to the quenching. Before the alloy was put into the water, it was cooled in the air, and the cooling rate is very small. When the transfer time was extended, there was plenty of time for the second phase to nucleate on the grain boundary and grow to a certain extent. According to the Ostwald ripening mechanism^{14,15} the second phase can absorb the solute atoms near the grain boundary and continue to grow during aging. It will lead to

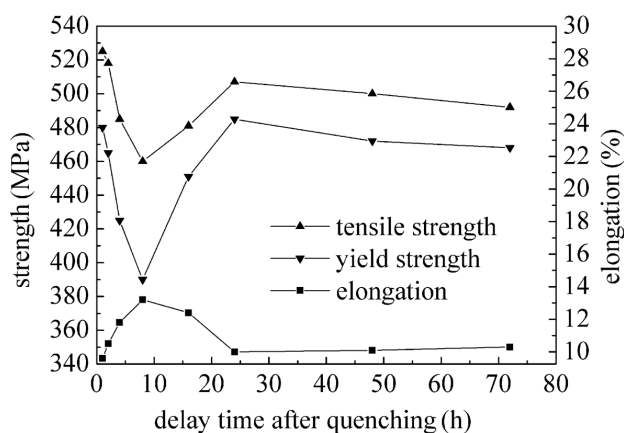


Figure 5: Mechanical properties changing with delay time after quenching

Slika 5: Spreminjanje mehanskih lastnosti s časom zadrževanja po gašenju

the poor area of solute atoms near the grain boundary, and make it difficult of the precipitation of a new second phase on the grain boundary. So the distribution of the precipitated phase on the grain boundary is discontinuous and their size difference becomes too big. On the other hand, the supersaturated vacancy concentration after quenching differs in different areas. During the cooling process, the vacancy will diffuse to the grain boundary, and it will cause a decrease of the vacancy concentration near the grain boundary. However, the vacancy away from the grain boundary has no space to diffuse, and thus the concentration is relatively higher. As a result, a concentration gradient was formed. When the transfer time is longer, more vacancies disappeared in the grain boundary. During the aging treatment the GP zone cannot appear in the area that is lower than the critical vacancy concentration, and thus a precipitation free zone will form.¹⁶⁻¹⁸ So, if the transfer time was extended, the width of the precipitation free zone would become large, and the mechanical properties of the alloy would be deteriorated.

3.4 Effect of delay time after quenching on the mechanical properties

Figure 5 shows the effect of the delay time after quenching on the mechanical properties of the 7A04 aluminium alloy, which indicated the tensile strength and yield strength is on the decline as a whole with the delay time. Within 8 h, the strengths drop gradually and the elongation rises continuously with the increase of the delay time. From 8 h to 24 h a rebound of the mechanical properties appears, and the strengths will rise and the elongation will drop. When the delay time is more than 24 h, the mechanical properties of 7A04 alloy are stable.

In fact, this obvious delay time effect began once the quenching was done, and it is related to the dissolution of the GP zone.¹⁹ Along with the extension of the delay time, a large number of partial poly groups will form, and thus the concentration of solute elements in solid solutions is greatly reduced. During the artificial aging, the GP zones that are less than the critical size will resolve back to the solid solution, and it will reduce the number of the precipitation strengthening phases. So, the strength of the alloy will reduce. But if the delay time continues to be extended, those GP zones that are less than the critical size are likely to grow up to the stable crystal nucleus. Therefore, the delay time effect became weak, and the mechanical properties of the alloy began to recover. Considering the practical production, the delay time after quenching is confined into 2 h. If there is not enough time, the artificial aging can be performed after the delay time of 24 h, which also can give ideal comprehensive performances.

4 CONCLUSIONS

1. In the range of 460–490 °C, the mechanical properties of the 7A04 alloy are relatively stable. When the

solid solution is higher than 500 °C, over-burn may appear.

- When the water temperature of quenching exceeds 40 °C or the transfer time before quenching is more than 20 s, the tensile strength and yield strength will drop remarkably while the elongation will rise.
- The tensile strength and yield strength will drop gradually while the elongation will rise continuously with the delay time after quenching before 8 h. At the range of 8–24 h there is an opposite change of mechanical properties compared to the previous 8 h. Once the delay time exceeds 24 h, the mechanical properties become stable.
- The optimal quenching parameters are as follows. The solid solution temperature is 460–490 °C, and the water temperature of quenching and the transfer time before quenching are below 40 °C and 20 s, respectively, and the delay time after quenching is below 2 h or above 24 h.

Acknowledgement

This research was financially supported by Foundation of Heilongjiang Educational Committee (12541107) and Natural Science Foundation of Heilongjiang Province (F201213).

5 REFERENCES

- M. Nakai, T. Eto, New aspect of development of high strength aluminum alloys for aerospace applications, *Mater. Sci. Eng., B*, 285 (2000) 1–2, 62–68, doi:10.1016/S0921-5093(00)00667-5
- D. Vojtěch, J. Šerák, O. Ekrt, Improving the casting properties of high-strength aluminium alloys, *Mater. Tehnol.*, 38 (2004) 1–2, 99–102
- Y. Zuo, J. Cui, Z. Zhao, H. Zhang, L. Li, Q. Zhu, Mechanism of grain refinement of an Al-Zn-Mg-Cu alloy prepared by low frequency electromagnetic casting, *J. Mater. Sci.*, 47 (2012) 14, 5501–5508, doi:10.1007/s10853-012-6441-z
- A. L. Ning, Z. Y. Liu, Q. C. Zheng, S. M. Zeng, Effects of progressive solution treatment on microstructure and mechanical properties of 7A04 aluminum alloy, *The Chinese Journal of Nonferrous Metals*, 14 (2004) 7, 1211–1216, doi:10.3321/j.issn:1004-0609.2004.07.028
- J. J. Liu, H.Y. Li, D. W. Li, Y. Wu, Application of novel physical picture based on artificial neural networks to predict microstructure evolution of Al-Zn-Mg-Cu alloy during solid solution process, *Trans. Nonferrous Met. Soc. China*, 25 (2015) 3, 944–953, doi:10.1016/S1003-6326(15)63683-4
- O. N. Senkov, S. V. Senkova, M. R. Shagiev, Effect of Sc on aging kinetics in a direct chill cast Al-Zn-Mg-Cu alloy, *Metall. Mater. Trans. A-Phys. Metall. Mater. Sci.*, 39 (2008) 5, 1034–1053, doi:10.1007/s11661-008-9485-6
- Y. Liu, D. M. Jiang, B. Q. Li, W. S. Yang, J. Hu, Effect of cooling aging on microstructure and mechanical properties of an Al-Zn-Mg-Cu alloy, *Mater. Des.*, 57 (2014) 5, 79–86, doi:10.1016/j.matdes.2013.12.024
- T. Marlaud, A. Deschamps, F. Bley, W. Lefebvre, B. Baroux, Influence of alloy composition and heat treatment on precipitate composition in Al-Zn-Mg-Cu alloys, *Acta Mater.*, 58 (2010) 1, 248–260, doi:10.1016/j.actamat.2009.09.003
- G. S. Wang, Z. H. Zhao, Y. H. Zhang, J. Z. Cui, Effects of solution treatment on microstructure and mechanical properties of Al-9.0Zn-2.8Mg-2.5Cu-0.12Zr-0.03Sc alloy, *Trans. Nonferrous Met. Soc. China*, 23 (2013) 9, 2537–2542, doi:10.1016/S1003-6326(13)62765-x
- O. N. Senkov, M. R. Shagiev, S. V. Senkova, D. B. Miracle, Precipitation of Al₃(Sc,Zr) particles in an Al-Zn-Mg-Cu-Sc-Zr alloy during conventional solution heat treatment and its effect on tensile properties, *Acta Mater.*, 56 (2008) 15, 3723–3738, doi:10.1016/j.actamat.2008.04.005
- M. Meng, Z. M. Zhang, J. M. Yu, X. K. Li, Effect of heat treatments on microstructure and properties of hot compression aluminum alloy 7A04, *Key Eng. Mater.*, 480–481 (2011), 433–436, doi:10.4028/www.scientific.net/KEM.480-481.433
- C. J. Yi, P. C. Zhai, L. Z. Dong, Q. H. Fu, Research on the strength improvement of 7A04 aluminum alloy, *Adv. Mater. Res.*, 488–489 (2012), 19–21, doi:10.4028/www.scientific.net/AMR.488-489.19
- V. V. Antipov, O. G. Senatorova, E. A. Tkachenko, R. O. Vakhromov, High-strength Al-Zn-Mg-Cu alloys and light Al-Li alloys, *Met. Sci. Heat Treat.*, 53 (2012) 9, 428–433, doi:10.1007/s11041-012-9410-x
- A. Baldan, Review progress in Ostwald ripening theories and their applications to nickel-base superalloys part I: Ostwald ripening theories, *J. Mater. Sci.*, 37 (2002) 11, 2171–2202, doi:10.1023/A:1015388912729
- T. Philippe, P. W. Voorhees, Ostwald ripening in multicomponent alloys, *Acta Mater.*, 61 (2013) 11, 4237–4244, doi:10.1016/j.actamat.2013.03.049
- J. D. Bernardin, I. Mudawar, Validation of the quench factor technique in predicting hardness in heat treatable aluminum alloys, *Int. J. Heat Mass Transf.*, 38 (1995) 5, 863–873, doi:10.1016/0017-9310(94)00204-9
- T. Ogura, S. Hirosawa, A. Cerezo, T. Sato, Atom probe tomography of nanoscale microstructures within precipitate free zones in Al-Zn-Mg(-Ag) alloy, *Acta Mater.*, 58 (2010) 17, 5714–5723, doi:10.1016/j.actamat.2010.06.046
- T. Ogura, S. Hirosawa, A. Hirose, T. Sato, Effects of microalloying tin and combined addition of silver and tin on the formation of precipitate free zones and mechanical properties in Al-Zn-Mg alloys, *Mater. Trans.*, 52 (2011) 5, 900–905, doi:10.2464/jilm.61.316
- P. A. Rometsch, Y. Zhang, S. Knight, Heat treatment of 7xxx series aluminum alloys-some recent developments, *Trans. Nonferrous Met. Soc. China*, 24 (2014) 7, 2003–2017, doi:10.1016/S1003-6326(14)63306-9

BIO-PLASTIC COMPOSITE SUBSTRATE MATERIAL BASED MICROSTRIP-FED PRINTED ANTENNA FOR WIRELESS COMMUNICATIONS

TISKANA ANTENA ZA BREŽIČNO KOMUNIKACIJO IZ BIOPLASTIČNEGA KOMPOZITA Z MIKROTRAKOM ZA NAPAJANJE

**Touhidul Alam^{2,3}, Mohammad Rashed Iqbal Faruque¹, Mohammed Shamsul Alam³,
Md. Moinul Islam¹, Md. Zulfiker Mahmud², Mohammad Tariqul Islam²**

¹Universiti Kebangsaan Malaysia, Space Science Center (ANGKASA), 43600UKM, Bangi, Selangor, Malaysia

²Universiti Kebangsaan Malaysia, Department of Electrical, Electronic and Systems Engineering, 43600UKM, Bangi, Selangor, Malaysia

³International Islamic University Chittagong, Department of Computer Science and Engineering, Chittagong, Bangladesh
touhid13@siswa.ukm.edu.my, tariqul@ukm.edu.my

Prejem rokopisa – received: 2015-09-02; sprejem za objavo – accepted for publication: 2015-01-06

doi:10.17222/mit.2015.271

This paper presents a printed bio-plastic wireless antenna to ensure biological compatibility between humans and wireless devices. The antenna has multiband characteristics, which can cover the GSM 1800, UMTS (1.92-2.17 GHz), LTE 40 frequency bands. The proposed antenna is incorporated with a circular slotted hexagonal radiator with a microstrip feed line and a rectangular slotted ground plane. The wireless mobile antenna has been designed and simulated using the commercially available electromagnetic (EM) simulation software CST Microwave Studio. The EM absorption rate of the proposed antenna has also been analysed with a human head phantom.

Keywords: antenna, bio-plastic material, electromagnetic absorption, wireless communication

Članek predstavlja brezžično anteno, tiskano iz bioplastike, za zagotavljanje biološke kompatibilnosti med človekom in brezžičnimi napravami. Antena dosega večpasovne karakteristike, ki lahko pokrijejo GSM 1800, UMTS (1.92-2.17 GHz) in LTE 40 frekvenčni pas. Predlagana antena je sestavljena iz šestoglatega sevalnika s krožno odprtino in z napajalnim trakom povezano štirioglato ozemljitveno ploščo. Brezžična antena je bila skonstruirana in simulirana s pomočjo komercialne elektromagnetne (EM) programske opreme za simulacijo CST Microwave Studio. EM absorpcijska hitrost predlagane antene je bila analizirana s pomočjo umetne človeške glave.

Ključne besede: antena, bioplastičen material, elektromagnetna absorpcija, brezžična komunikacija

1 INTRODUCTION

With the rapid development of science and technology, the mobile wireless industry has expanded very quickly over the last decades. Thereby, health concern regarding the use of mobile wireless devices near human body has been growing and given special consideration by researchers. Moreover, the development of an environment-friendly composite material technology has been promulgated around the world.

Several antennas have been developed for mobile wireless communication by conventional fossil petroleum-based material.¹⁻³ The electromagnetic absorption reduction of the wireless handset antenna has been analysed in many studies. C. Picher et al.⁴ proposed a slotted ground PIFA antenna for specific absorption analysis. A. Cabedo et al.⁵ proposed a handset antenna combining PIFA, slot and ground plane and analysed EM absorption value. A multi-standard wireless application has been made in ⁶.

The analysis of printed antenna on an organic multi-layers substrate has been developed in recent years. The

conventional fossil petroleum-based material is replaced by a bio-based composite substrate. M. H. Ullah and M. Islam⁷ proposed bio-based material for patch antenna design. He achieved 55.6 % of the impedance bandwidth at a lower frequency and 24 % of impedance bandwidth at the upper frequency band. However, the electromagnetic absorption analysis did not perform. A dual arm structured wireless antenna has been developed for mobile wireless applications, which covers the DCS, PCS, UMTS and WLAN (2.4GHz) frequency bands with an antenna size of 119×50 mm².⁸ Q. Rao and T. A. Denidni⁹ proposed an inverted L shaped antenna for DCS, PCS, and IMT tri-bands applications. S.-B. Chen et al.¹⁰ developed planar antennas for DCS 1800, PCS 1900, UMTS and WLAN applications. Here, the antenna dimensions are 65 mm² × 40 mm².

In this paper, an organic or bio plastic-based substrate antenna is proposed for mobile wireless communications and the electromagnetic absorption behaviour has been explored. Moreover, the proposed antenna paraded multi-band, which covers GSM 1800, UMTS 2100, WLAN 2400, WiMAX 2500, WiMAX 3600 and WLAN 5GHz.

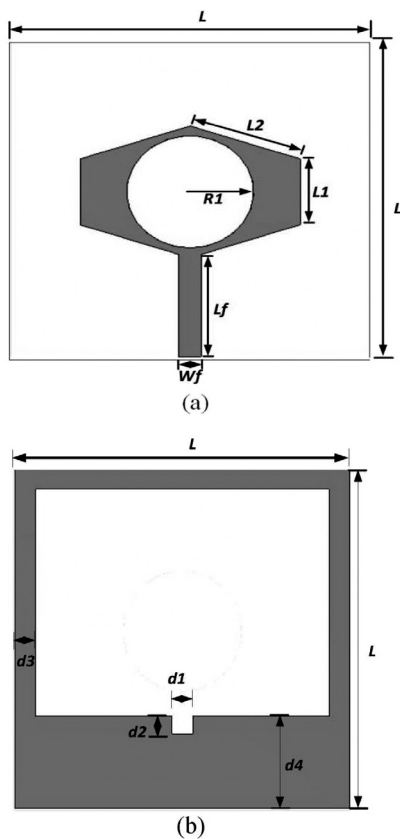


Figure 1: Geometry of the proposed antenna: a) top view, b) bottom view

Slika 1: Geometrija predlagane antene: a) pogled od zgoraj, b) pogled od spodaj

2 PROPOSED ANTENNA CONFIGURATION

The geometric layout of the proposed antenna is illustrated in **Figure 1**. It is seen from **Figure 1** that the antenna consists of a circular slotted hexagonal patch, which is connected with a 50Ω microstrip feed line. A rectangular slot was etched from the ground plane. The antenna design parameters are tabulated in **Table 1**. The proposed antenna is designed on a bio-plastic material (relative permittivity 12) substrate with dimensions of $48 \times 48 \times 1.95 \text{ mm}^3$.

Table 1: Antenna parameters

Tabela 1: Parametri antene

Parameter	Value (mm)	Parameter	Value (mm)
L	48	R	8.5
$L1$	10	$d1$	3
$L2$	15.55	$d2$	2.5
Lf	15.5	$d3$	5.83
Wf	3.10	$d4$	13.08

3 ANTENNA SUBSTRATE

The processing steps flowchart of the bio-plastic substrate material is presented in **Figure 2**. Habib et al.

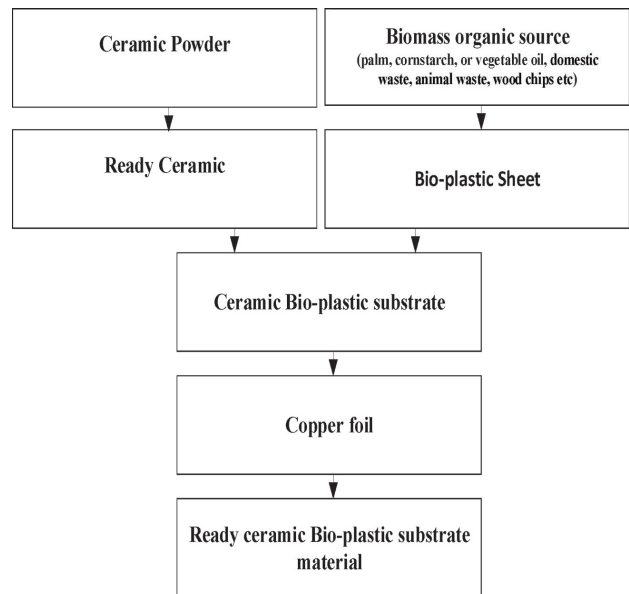


Figure 2: Flowchart of the manufacturing of bio-plastic substrate material

Slika 2: Potek izdelave podlage iz bio-plastike

proposed and analysed the antenna characteristics using bio-plastic substrate material. He also described the bio-plastics manufacturing procedures. The procedure begins with moulding ceramic powder and then mixing with polymeric binder preforming substances, such as cellulose. For sintering the ceramic powder the polymeric sponge method was used. Besides this, bio-plastic sheet is prepared from a biomass organic source, such as palm, corn starch, or vegetable oil. A three-layered sandwich structure of 59-ml (1.5-mm) thick ceramic, both surfaces covered by a 0.25-mm bio plastic, is pressed using a multi-press machine (RMP 210, Bungard Elektronik GmbH & Co).

4 RESULTS AND DISCUSSION

The proposed antenna was fabricated using bio-plastic material. The fabricated prototype of the proposed antenna is illustrated in **Figure 3**. The antenna performances were measured using a fabricated prototype. The reflection coefficient of the proposed antenna was measured using an Agilent N5227A performance network analyser. The measured and simulated reflection coefficient is presented in **Figure 4**. It is observed from **Figure 4** that the proposed antenna shows a measured -10dB impedance bandwidth of 620 MHz (1.6–2.22 GHz), 830 MHz (3.43–4.26GHz) and 1.17 GHz (4.8–5.97 GHz). It is seen from **Figure 4** that the measured resonance frequencies are nearly identical to the simulated one. Though there is a mismatch between the measured and simulated reflection coefficient, which is possibly attributed due to manufacturing tolerances and the imperfect soldering effect of the SMA connector. Moreover, surface current distribution at 1.8 GHz and 5.2 GHz

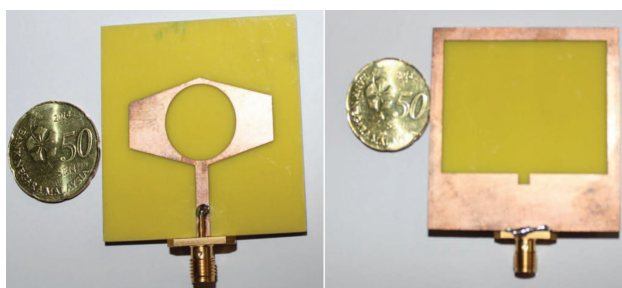


Figure 3: Fabricated antenna prototype
Slika 3: Izdelan prototip antene

is shown in **Figure 5** for the radiating behaviour of the antenna.

The radiation pattern of the proposed antenna was measured using the satimo near-field measurement system. **Figure 6** demonstrates the measured radiation pattern at (1.8, 2.0, 3.6, and 5.2) GHz. It is observed from **Figure 6** that the antenna shows a nearly omnidirectional radiation pattern, though cross polarization is high at higher frequency. Moreover, 3D radiation pattern is also presented for more visualization of the radiation

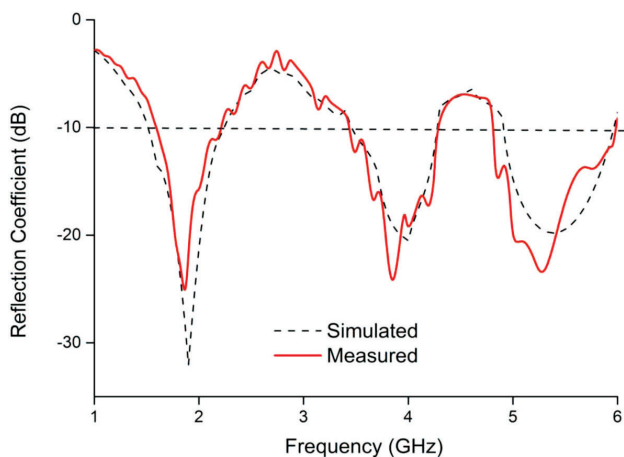


Figure 4: Simulated and measured reflection coefficient of the proposed antenna
Slika 4: Simuliran in izmerjen koeficient sevanja predlagane antene

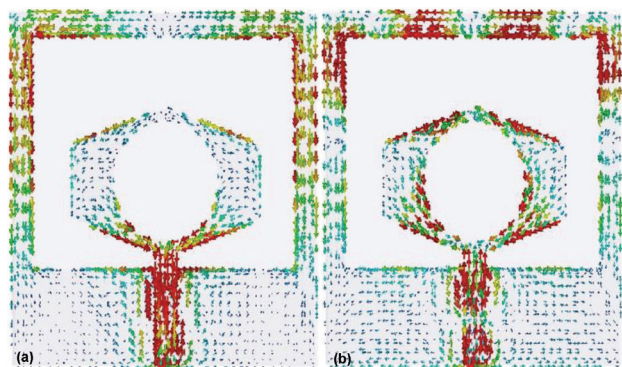


Figure 5: Surface current distribution of the proposed antenna:
a) 1.8 GHz and b) 5.2 GHz

Slika 5: Razporeditev toka na površini predlagane antene:
1,8 GHz in b) 5,2 GHz

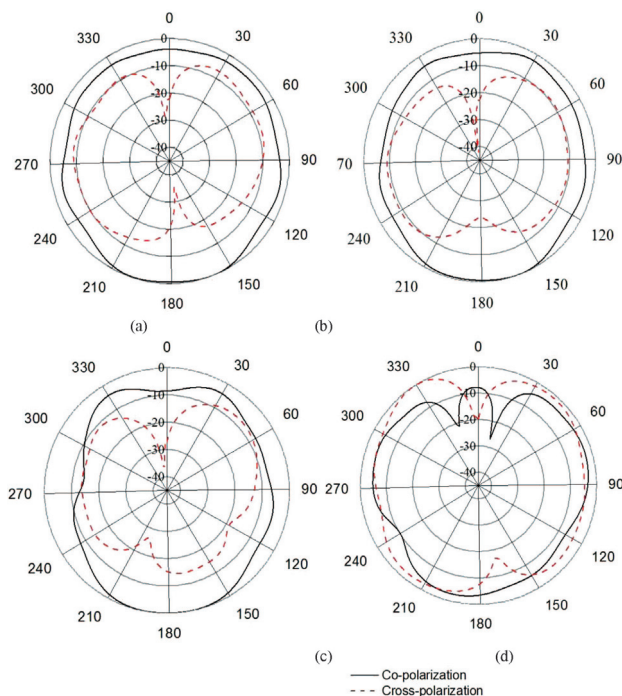


Figure 6: E-plane radiation pattern of the proposed antenna for frequency of: a) 1.8 GHz, b) 2.0 GHz, c) 3.6 GHz and d) 5.2 GHz

Slika 6: Sledi sevanja v E-ravnini pri predlagani anteni, pri frekvencah: a) 1,8 GHz, b) 2,0 GHz, c) 3,6 GHz in d) 5,2 GHz

phenomena, shown in **Figure 7**. The measured peak gain and radiation efficiency of the proposed antenna is presented in **Figure 8**. **Figure 8** shows that the maximum radiation efficiency of 86 % was obtained at 3.73 GHz. In addition, the maximum peak gain achieved at the lower band is 1.86 dB, at the middle band it is 4.38 dB and at the upper band it is 4.31 dB.

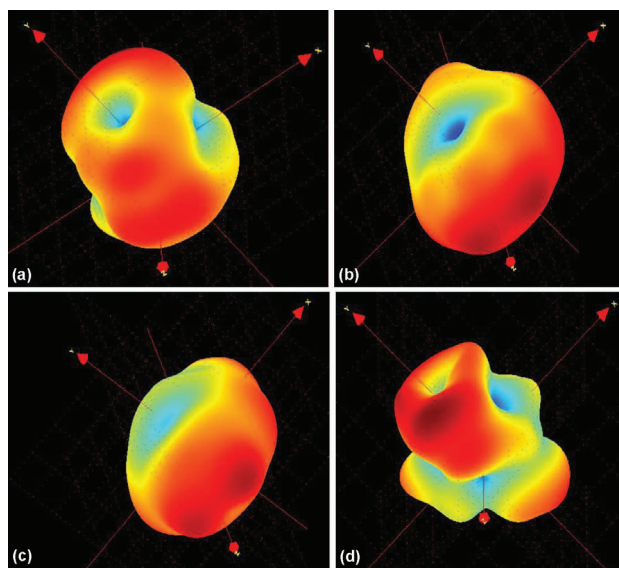


Figure 7: 3D radiation pattern of the proposed antenna for frequency of: a) 1.8 GHz, b) 2.0 GHz, c) 3.6 GHz and d) 5.2 GHz

Slika 7: 3D-sledi sevanja predlagane antene pri frekvencah: a) 1,8 GHz, b) 2,0 GHz c) 3,6 GHz in d) 5,2 GHz

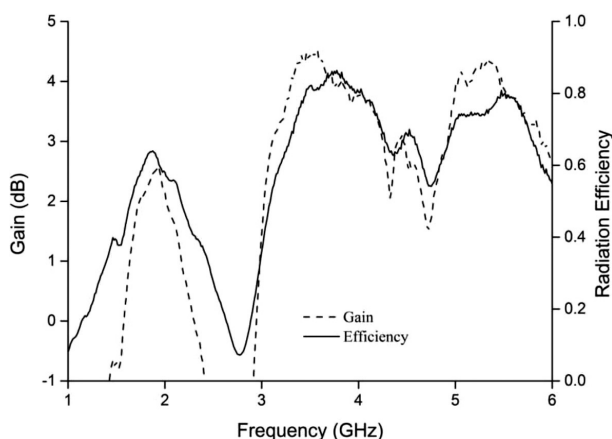


Figure 8: Radiation efficiency and gain of the proposed antenna
Slika 8: Učinkovitost sevanja in izkoristek pri predlagani anteni

5 EM ABSORPTION ANALYSIS

The specific absorption rate is defined by the power absorbed per mass of biological tissues and has units of watts per kilogram (W/kg). Currently, two international organizations have developed guidelines for limiting the exposure of electromagnetic radiation on human health. The EM absorption limit specified in IEEE C95.1:2005 is 1.6 W/kg in a 1 g averaging mass and 2 W/kg in a 10 g averaging mass of tissue, which is similar to the limit stated in the International Commission on Non-Ionizing Radiation Protection (ICNIRP) guideline.¹¹ To comply with the guidelines, the EM absorption values of the proposed antenna were analysed, and are listed in **Table 2**.

Table 2: SAR values of the proposed antenna

Tabela 2: SAR-vrednosti pri predlagani anteni

Frequency (GHz)	SAR 1 g (W/kg)	SAR 10 g (W/kg)
1.8	1.45	1.20
2.0	1.38	1.06

6 CONCLUSION

A new bio-plastic material based printed planar antenna is presented for GSM, UMTS, LTE band 40, WiMAX and WLAN wireless applications with accept-

able specific absorption rates and antenna performance, like impedance bandwidth, antenna gain, radiation pattern and radiation efficiency. The experimental results validate the simulated results. Therefore, the overall performances of the proposed antenna make it suitable for a wireless mobile application.

7 REFERENCES

- T. Alam, M. R. I. Faruque, M. T. Islam, Printed Circular Patch Wideband Antenna for Wireless Communication, *Informacije MIDEM*, 44 (2014) 3, 212–217
- K. S. Sultan, H. H. Abdullah, E. A. Abdallah, E. A. Hashish, Low-SAR, Miniaturized Printed Antenna for Mobile, ISM, and WLAN Services, *IEEE Antennas and Wireless Propagation Letters*, 12 (2013), 1106–1109, doi:10.1109/LAWP.2013.2280955
- A. H. Kusuma, A.-F. Sheta, I. M. Elshafiey, Z. Siddiqui, M. A. Alkanhal, S. Aldosari, et al., A new low SAR antenna structure for wireless handset applications, *Progress In Electromagnetics Research*, 112 (2011), 23–40, doi:10.2528/PIER10101802
- C. Picher, J. Anguera, A. Andújar, C. Puente, S. Kahng, Analysis of the human head interaction in handset antennas with slotted ground planes, *IEEE Antennas and Propagation Magazine*, 54 (2012) 2, 36–56, doi:10.1109/MAP.2012.6230717
- A. Cabedo, J. Anguera, C. Picher, M. Ribo, C. Puente, Multiband Handset Antenna Combining a PIFA, Slots, and Ground Plane Modes, *IEEE Transactions on Antennas and Propagation*, 57 (2009) 9, 2526–2533, doi: 10.1109/TAP.2009.2027039
- T. Alam, M. R. I. Faruque, M. T. Islam, N. Misran, Composite-material printed antenna for a multi-standard wireless application, *Mater. Tehnol.*, 49 (2015) 5, 745–749, doi:10.17222/mit.2014.132
- M. H. Ullah, M. Islam, Analysis of a ceramic filled bio-plastic composite sandwich structure, *Applied Physics Letters*, 103(2013), 223701, doi:10.1063/1.4833496
- D. Zhou, R. A. Abd-Alhameed, C. H. See, A. G. Alhaddad, P. S. Excell, Compact wideband balanced antenna for mobile handsets, *IET Microwaves, Antennas & Propagation*, 4 (2010) 5, 600–608, doi:10.1049/iet-map.2009.0153
- Q. Rao, T. A. Denidni, New broadband dual-printed inverted L-shaped monopole antenna for tri-band wireless applications, *Microwave and Optical technology letters*, 49 (2007) 2, 278–280, doi:10.1002/mop.22107
- S.-B. Chen, Y.-C. Jiao, W. Wang, F.-S. Zhang, Modified T-shaped planar monopole antennas for multiband operation, *Microwave Theory and Techniques*, *IEEE Transactions on*, 54 (2006) 8, 3267–3270, doi:10.1109/TMTT.2006.877811
- IEEE Standard for Safety Levels With Respect to Human Exposure to Radio Frequency Electromagnetic Fields, 3 kHz to 300 GHz, *IEEE Std C95.1-2005*, (2006), 0_1–238, doi:10.1109/IEEESTD.2010.5433227

THE GROWTH OF BETA PHASE IN THE
GAMMA-BRASS–COPPER DIFFUSION COUPLERAST BETA FAZE V DIFUZIJSKEM PARU GAMA MEDENINA –
BAKERAdhurim Hoxha¹, Dietrich Heger²¹Polytechnic University of Tirana, Department of Physics Engineering, Tirana, Albania²TU Bergakademie Freiberg, Institut für Werkstoffwissenschaft, Freiberg, Germany
hoxha_adhurim@yahoo.com

Prejem rokopisa – received: 2015-09-06; sprejem za objavo – accepted for publication: 2016-01-11

doi:10.17222/mit.2015.277

In this work we make a quantitative investigation of the growth of the β -phase in the γ -brass/copper diffusion couple. The diffusion couple was produced by electrolysis. The analysis of multiphase diffusion in the γ -brass/copper system was based on using the concentration-depth profiles provided by electron micro-beam analyzer. The growth constant of the β -phase for each of the used temperatures was calculated from the time dependency of the β -phase thickness. Using the Matano method it was possible to calculate the interdiffusion coefficient of Zn in the β -phase. The activation energy for the diffusion of Zn in the β -phase was also determined.

Keywords: γ -brass-copper system, growth of intermetallics, multiphase diffusion, interdiffusion coefficients, activation energy

V delu je prikazana kvantitativna preiskava rasti β -faze v difuzijskem paru γ -medenina-baker. Difuzijski par je bil izdelan z elektrolizo. Analiza difuzije v večfaznem difuzijskem sistemu γ -medenina-baker temelji na uporabi profilov koncentracija-globina, dobljenih z elektronskim mikroanalizatorjem. Konstanta rasti β -faze pri vsaki od uporabljenih temperatur je bila izračunana iz časovne odvisnosti debeline β -faze. Z uporabo Matano metode je bilo mogoče izračunati koeficiente nasprotnosmerne difuzije Zn v β -fazi. Določena je bila tudi aktivacijska energija za difuzijo Zn v β -fazi.

Ključne besede: system γ -medenina-baker, rast intermetalnih zlitin, difuzija v večfaznem sistemu, koeficienti nasprotnosmerne difuzije, aktivacijska energija

1 INTRODUCTION

The phenomenon of diffusion between two metallic species, which is followed by the formation of one or more intermetallics, is known as multiphase diffusion or interdiffusion.¹⁻³ Multiphase diffusion could be as well looked at as a chemical reaction between the original species, and this is why it can be referred to as chemical diffusion.¹

An experiment on multiphase diffusion consists in the study of a concentration-depth profile, known also as the diffusion profile, by examining a polished cross-section of the diffusion sample.⁴ This profile is most often established on a transverse section by electron-probe microanalysis (EPMA). The diffusion profile is then used to extract the corresponding diffusion coefficients by comparison with the corresponding solution of Fick's second law and the most common method used is the Matano method.^{1,2}

An experimental diffusion profile has the form of a series of curved segments, with concentration discontinuities at every interface. These concentration drops correspond to the intersection of an isotherm with the phase boundaries of the phase diagram. If the phase diagram of the selected system contains intermetallics, it is expected that the multiphase diffusion will give rise to the formation of these intermetallic layers.⁵ In practice,

certain phases are sometimes missing from the diffusion zone or the composition of the phases can differ from those indicated on the phase diagram. Sometimes, extra phases also appear.^{5,6} Although in most cases parabolic growth kinetics are observed, other kinetics can be observed as well.⁷

This paper originated from a study of multiphase diffusion in the Cu/Zn diffusion couple.⁸ Although many works have been carried out for multiphase diffusion on different binary systems, there are no systematic results found in the literature for this system. Referring to the Cu-Zn phase diagram⁹, there are four intermetallic phases, i.e., β -phase, γ -phase, δ -phase and ϵ -phase. So one can expect the formation of four stacked intermetallics in the diffusion zone.^{6,7} (It should be noted that unlike the other phases, δ -phase is stable over a limited temperature range going from 558 °C up to 700 °C.) One of the major difficulties in the investigation of the multiphase diffusion between copper and zinc is that there is a great difference in the melting temperatures of the diffusing species. So, for the growth of zinc-rich phases (γ - and ϵ -phase) low annealing temperatures must be used, while for the growth of the copper-rich phase (β -phase) higher temperatures are needed. Consequently, the problem cannot be solved by a simple combination of copper against zinc. In the experimental study mentioned above⁸, the β -phase was observed at a relatively high

A. HOXHA, D. HEGER: THE GROWTH OF BETA PHASE IN THE GAMMA-BRASS–COPPER DIFFUSION COUPLE

temperature (380 °C) and a relatively long annealing time (25 h) and it showed a reduced thickness. In order to have a well developed layer of the β -phase, longer annealing times are needed and this will result in an extended thickness of the fastest growing phase, γ -phase.⁸ So for the production of an infinite diffusion couple by a plating technique, the starting dimensions of the Cu and Zn samples must be considerable and this will limit the possibility of having a stable diffusion couple.¹⁰

In this work the diffusion couple was produced by electroplating copper in γ -brass. Annealing was performed in four different temperatures ranging from 500 °C to 650 °C and for each temperature we used six different annealing times, ranging from 1 h to 14 h. The concentration-depth profiles were determined by the use of EPMA. The presence of β -phase was detected by optical microscopy and EPMA. From the time dependency of the phase thickness, we have calculated the growth constant of the β -phase. Knowing the growth constant of β -phase and applying Matano analysis, we have calculated the interdiffusion coefficient of the fastest diffusing element, zinc.^{8,11} Using the Arrhenius relationship of the diffusion coefficient from temperature, we have calculated the activation energies for diffusion in β -phase.^{12,13}

2 MATERIALS AND EXPERIMENTAL PART

The base material was γ -brass and the melting of it was done in a middle-frequency induction furnace with a crucible. Casting took place in a cast-iron mould. The content of the produced γ -brass was investigated by

GDOES and X-Ray and the results are: 31.34 % of amount fractions of Cu and 68.52 % of amount fractions of Zn and 0.14 % of amount fractions of Fe.

γ -brass is a brittle intermetallic and prior to electrolysis the γ -brass sample was subject to a heat treatment at 650 °C for about 8 h. This was necessary for removing any residual stresses or internal stresses¹⁴ and thus facilitating the mechanical cut of the sample. After the heat treatment the homogeneity of the γ -brass sample was verified by EPMA.

The γ -brass samples were cut by a diamond cut-off wheel in plane cylindrical slices of 5 mm in thickness and nearly 30 mm in diameter. A fine grinding was sufficient for the copper atoms to be deposited in the γ -brass sample during the electrolysis. The used copper electrolyte contained 40 g/L copper and 160 g sulphuric acid (H₂SO₄). The temperature was 65 °C and the current was 0.2 A. The deposition process took place for about 30 h. By the light microscopy it was observed a deposited layer of copper with a thickness of more than 1 mm.

Annealing was carried out in thermal oven NABERTHERM Model L5 (30 °C–3000 °C). The temperatures were 500 °C, 550 °C, 600 °C and 650 °C and for each temperature there were used five to six different annealing times, ranging from 1 h to 14 h. Just after the annealing, each sample was cooled very quickly in cold water.

3 RESULTS AND DISCUSSION

After diffusion annealing the samples were polished perpendicularly to the diffusion zone and then they were

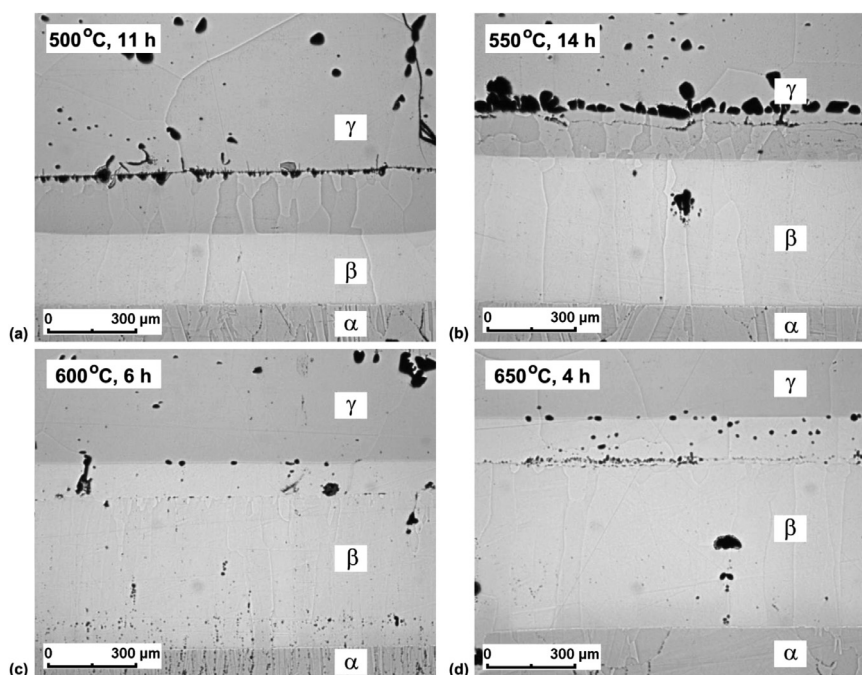


Figure 1: Optical micrographs of the diffusion zone at annealing temperature: a) 500 °C, b) 550 °C, c) 600 °C and d) 650 °C

Slika 1: Mikrostruktura difuzijskega področja pri temperaturi žarjenja: a) 500 °C, b) 550 °C, c) 600 °C in d) 650 °C

A. HOXHA, D. HEGER: THE GROWTH OF BETA PHASE IN THE GAMMA-BRASS-COPPER DIFFUSION COUPLE

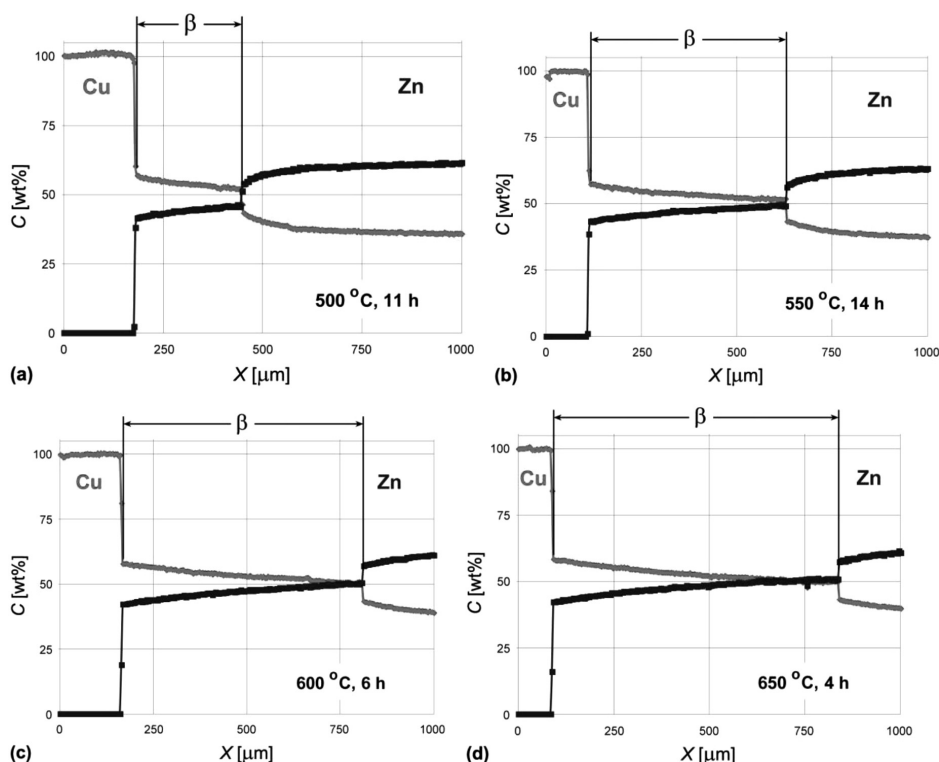


Figure 2: Concentration-depth profile across the diffusion zone at annealing temperature: a) 500 °C, b) 550 °C, c) 600 °C and d) 650 °C
Slika 2: Profil koncentracije v globino preko področja difuzije pri temperaturi žarjenja: a) 500 °C, b) 550 °C, c) 600 °C in d) 650 °C

investigated by light microscopy. **Figure 1** shows the typical optical micrographs of the diffusion zone for each of the annealing temperatures. From the micrographs shown one can see the presence of a well-defined layer of β -phase. The thickness of the β -phase is increasing with temperature, as well as with time (**Figure 1a–1d**). The presence of β -phase was detected by EPMA-WDX analysis.

The concentration-depth profiles across the diffusion zone were determined by the use of EPMA-WDX analysis, operated in step-scan-mode (20 kV, 100 nA, $\Delta x = 1 \mu\text{m}$). Depending on the thickness of the β -phase, the measurements were conducted for 600 up to 1200 data points. The concentration-depth profiles of the same

samples shown in the above optical micrographs are presented in **Figure 2**.

In β -phase field the concentration of Cu continuously increases while that of Zn continuously decreases. As shown in the optical micrographs, from the presented concentration-depth profiles one can easily see that β -phase is becoming thicker with increasing temperature (**Figure 2a–2d**), as well as with time.

In **Figure 3** we propose a schematic diagram that illustrates the presence of β -phase in the diffusion zone, according to Cu-Zn phase diagram. On the right-hand side of the selected concentration-depth profile, a 90° rotated phase diagram is zoomed out in the same scale. The β -phase field of the concentration-depth profile corresponds to that of the phase diagram. Below the same concentration-depth profile, an X-ray atomic map of the same sample is placed. This phase distribution image was provided by EPMA. (As we have already mentioned, the presence of β -phase in the diffusion zone was detected by EPMA-WDX analysis.)

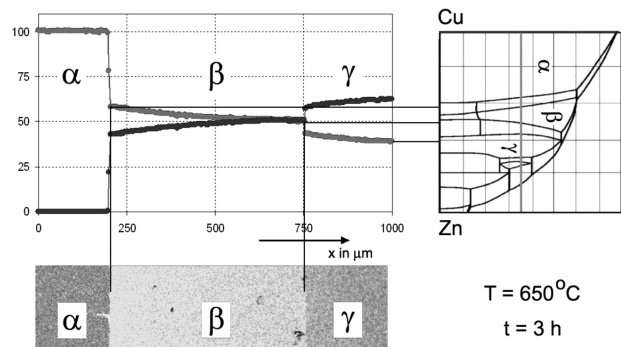


Figure 3: A schematic diagram illustrating the presence of β -phase in the diffusion zone.

Slika 3: Shematski diagram, ki kaže prisotnost β -faze v področju difuzije

3.1 Time dependency of the β -phase thickness

Figure 4 shows the plots of the square of the β -phase thickness versus diffusion time for each annealing temperature according to Equation (1):^{1,2}

$$X_i^2 = 2k_i t \quad (1)$$

where X is the thickness of the i -phase region, k_i is the phase growth constant and t is the diffusion time. The

A. HOXHA, D. HEGER: THE GROWTH OF BETA PHASE IN THE GAMMA-BRASS–COPPER DIFFUSION COUPLE

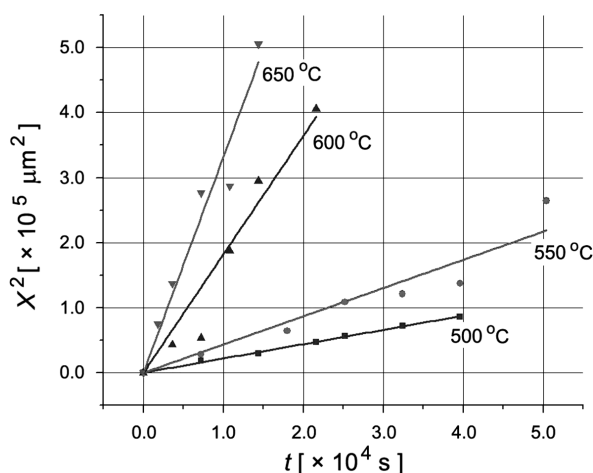


Figure 4: The plots of the square of the β -phase thickness versus diffusion time, for each temperature

Slika 4: Diagram kvadratov debeline β -faze pri navedenih temperaturah, v odvisnosti od časa difuzije

average layer thicknesses of the β -phase were measured directly in the EPMA concentration-depth profiles.

Parabolic growth and no incubation period were observed for all the temperatures used. It means that during the whole intermixing process local thermodynamic equilibrium is maintained and the layer growth is diffusion controlled.¹⁵

The growth constants for the β -phase, which were determined from the slope of the plots in **Figure 4**, are presented in **Table 1**.

Table 1: The growth constants for the β -phase at each temperature

Tabela 1: Konstante rasti β -faze pri navedeni temperaturi

Temperature (°C)	$k(\beta)$ (m^2/s)
500	1.10×10^{-12}
550	2.17×10^{-12}
600	9.11×10^{-12}
650	1.66×10^{-11}

From the values reported in **Table 1** we can see that the phase-growth constants are increasing with temperature. The phase-growth constants have a complex meaning and they depend on the diffusivity in the layers, as well as on the concentration gradients on both sides of the interface and on solubility limits of the phases.¹⁵

As with the diffusion coefficients, the temperature dependence of the phase growth constants follows an Arrhenius relationship.^{1,2}

$$k = k_0 \exp\left(-\frac{Q}{RT}\right) \quad (2)$$

Referring to Equation (2), from the slope and intercept of the plot of $\ln(k)$ versus $1/T$, shown in **Figure 5**, we have calculated the activation energy Q , for the growth of the β -phase and the constant k_0 for the β -phase. The calculated values are reported in **Table 2**.

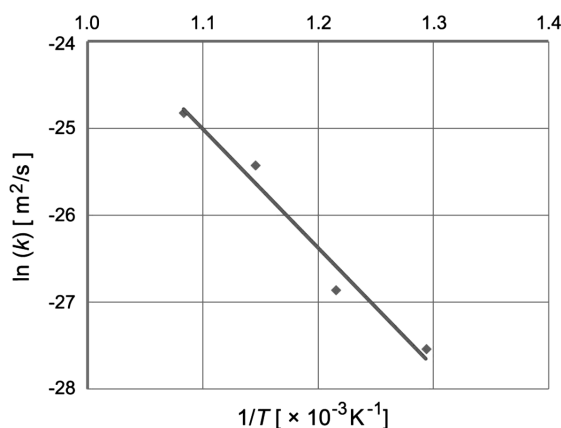


Figure 5: The plot of $\ln(k)$ versus $1/T$

Slika 5: Odvisnost med $\ln(k)$ in $1/T$

Table 2: The value of the activation energy for the growth of β -phase and that of the constant k_0

Tabela 2: Vrednost aktivacijske energije rasti β -faze in vrednost konstante k_0

Intermetallics	Q (J/mol)	k_0 (m^2/s)
β -phase	11.34×10^4	4.55×10^{-5}

3.2 The diffusion coefficients of Zn in the β -phase

The diffusion coefficient of the fastest diffusion element, which in the case of our system is zinc,⁸ was determined by employing the Matano method. The diffusion coefficients were calculated according to Equation (3):⁷

$$D_\beta = k_\beta \cdot \frac{1}{c_{\beta,\alpha} - c_{\beta,\gamma}} \cdot \frac{(c_{\beta,\gamma} - c_{\gamma,\beta}) \cdot (c_{\alpha,\beta} - c_{\beta,\alpha})}{(c_{\beta,\gamma} - c_{\gamma,\beta}) + (c_{\alpha,\beta} - c_{\beta,\alpha})} \quad (3)$$

The symbols used in Equation 3 were extracted from the corresponding concentration-depth profiles, as illustrated schematically in **Figure 6**. The calculated diffusion coefficients are reported in **Table 3**.

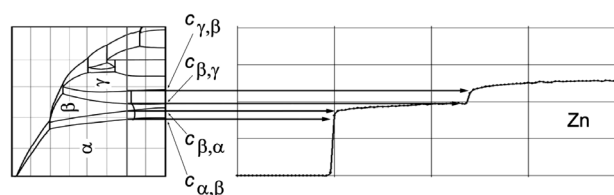


Figure 6: A schematic illustration of the meaning of the symbols used in Equation 3

Slika 6: Shematski prikaz pomena simbolov, uporabljenih v enačbi 3

Table 3: The diffusion coefficients of zinc in the β -phase

Tabela 3: Koeficienti difuzije cinka v β -fazi

Temperature (°C)	D_β^{Zn} (m^2/s)
500	8.47×10^{-13}
550	1.54×10^{-12}
600	3.30×10^{-12}
650	4.43×10^{-12}

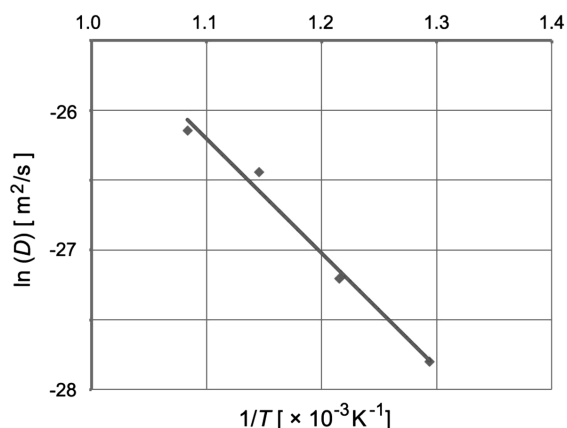


Figure 7: The plot of $\ln(D)$ versus $1/T$

Slika 7: Odvisnost med $\ln(D)$ in $1/T$

Table 4: The activation energy for the diffusion of zinc in β -phase and the corresponding frequency factor

Tabela 4: Aktivacijska energija za difuzijo cinka v β -fazi in odgovarjajoč frekvenčni faktor

Intermetallics	Q^{Zn}_{β} (J/mol)	D_0 (m ² /s)
β -phase	6.82×10^4	3.47×10^{-8}

3.3 The activation energy for the diffusion of zinc

The temperature dependence of the diffusion coefficients follows an Arrhenius relationship.^{1,2}

$$D = D_0 \exp\left(-\frac{Q}{RT}\right) \quad (4)$$

Table 4 shows the activation energy for the diffusion of zinc in β -phase Q^{Zn}_{β} , and the corresponding frequency factor D_0 , which are calculated respectively from the slope and intercept of the plot of $\ln(D)$ versus $1/T$ shown in **Figure 7**.

4 CONCLUSIONS

The γ -brass/copper diffusion couple produced by electrolysis can be used successfully in multiphase diffusion studies. After an isothermal diffusion annealing at four different temperatures, for five to six different annealing times, the growth of β -phase was observed in the diffusion zone. A single-phase domain was examined by light microscopy and the presence of β -phase was identified by EPMA-WDX analysis. The compositions of the β -phase did not differ from those indicated on the phase diagram.

The phase-growth constants for each temperature were determined by the time dependency of the β -phase thickness and the calculated values are presented in **Table 5**. Using the least-square fit to the experimental data a parabolic growth rate was observed. From the temperature dependency of the corresponding phase-growth constants, the activation energy characterizing the growth of β -phase was determined and its value is

$Q = 11.34 \times 10^4$ J/mol. (The corresponding constant is $k_0 = 4.55 \times 10^{-5}$ m²/s.)

Using the EPMA concentration-depth profiles and employing the Matano method, we have calculated the interdiffusion coefficients; these values are presented in **Table 5**. The activation energy of zinc in the β -phase was also determined and its calculated value is $Q^{Zn}_{\beta} = 6.82 \times 10^4$ J/mol. (The corresponding frequency factor is $D_0 = 3.47 \times 10^{-8}$ m²/s.)

Table 5: The growth constants for the β -phase and the diffusion coefficients of zinc in the β -phase

Tabela 5: Konstante rasti β -faze in difuzijski koeficienti cinka v β -fazi

Temperature (°C)	$k(\beta)$ (m ² /s)	D^{Zn}_{β} (m ² /s)
500	1.10×10^{-12}	8.47×10^{-13}
550	2.17×10^{-12}	1.54×10^{-12}
600	9.11×10^{-12}	3.30×10^{-12}
650	1.66×10^{-11}	4.43×10^{-12}

Acknowledgement

The experimental work presented in this paper has been carried out at the Institut für Werkstoffwissenschaft (Institute of Materials Science and Engineering), TU-Bergakademie Freiberg, Germany.

We are very grateful to the German Academic Exchange Service (DAAD), whose financial support made it possible.

5 REFERENCES

- J. Philibert, Atom Movement – Diffusion and Mass Transport in Solids, Les Editions de Physique, Les Ulis, Cedex A, France, 1991, 22
- H. Mehrer, Diffusion in Solids: Fundamentals, Methods, Materials, Diffusion Controlled Processes, 2nd Ed, Berlin Heidelberg, Springer, 2010, 161–166
- Th. Heumann, Diffusion in Metallen: Grundlagen, Theorie, Vorgänge in Reinetallen und Legierungen, Springer Berlin Heidelberg, 1992, 33, 131–207
- A. R. Allnatt, A. B. Lidiard, Atomic Transport in Solids, Cambridge University Press, 1993, 214–215
- E.M. Tanguet Njiokep, M. Salomon, H. Mehrer, Growth of intermetallic phases in the Al-Mg system, Defect Diffusion Forum, 194–199 (2001), 1581–1586
- J. Philibert, Interplay of Diffusion and Interface Processes in Multiphase Diffusion, Defect and Diffusion Forum, 95–98 (1993), 493–506
- V.I. Dybkov, The Growth Kinetics of Intermetallic Layers at the Interface of a Solid Metal and a Liquid Solder, J. Metals (JOM), 61 (2009) 1, 76–79
- A. Hoxha, H. Oettel, D. Heger, Calculation of the Interdiffusion Coefficient in the Cu-Zn Diffusion Couple, 7th International Conference of the Balkan Physical Union, AIP Conference Proceedings 1203 (2010), 591–595
- Massalski, T.B., Editor-in-Chief, Binary Alloy Phase Diagrams, ASM International, 1986, 981
- S. I. Fujikawa, Interdiffusion Between Aluminum and α -Brass, Defect and Diffusion Forum, 95–98 (1993), 611–617
- I. Stloukal, J. Cermak, Diffusion of zinc in two-phase Mg-Al alloy, Defect and Diffusion Forum, 263 (2007), 189–194

A. HOXHA, D. HEGER: THE GROWTH OF BETA PHASE IN THE GAMMA-BRASS–COPPER DIFFUSION COUPLE

- ¹² M. Oh, M.R. Notis, Growth kinetics of intermetallic phases in the Cu-Sn system at low temperatures, Abstr. Fifth Intern. Conf. on Diffusion in Materials DIMAT-2000, July 17–21, Paris, France, 2000, 72
- ¹³ S. Däbritz, V. Hoffmann, G. Sadowski, D. Bergner, Investigations of phase growth in the copper-tin system, Defect Diffusion Forum, 194–199 (2001), 1575–1580
- ¹⁴ H. Oettel, H. Schumman, Metallografie, Wiley-VCH Verlag GmbH & Co. KGaA, 15. Auflage, 2011, 482
- ¹⁵ W. Sprengel, M. Denking, H. Mehrer, Diffusion in Ordered Alloys (B.Fultz, R.W.Cahn, Gupta, eds.), TMS, 1993, 51–67

INVESTIGATION OF THE GEOMETRICAL ACCURACY AND THICKNESS DISTRIBUTION USING 3D LASER SCANNING OF AA2024-T3 SHEETS FORMED BY SPIF

PREISKAVA GEOMETRIJSKE NATANČNOSTI IN RAZPOREDITEV DEBELINE S TRIDIMENZIONALNIM LASERSKIM SKENIRANJEM PLOČEVINE IZ AA2024-T3, PREOBLIKOVANE S STOPNJUJOČIM PREOBLIKOVANJEM KOVINE

Halil Bayram^{1,2}, Nurullah Sinan Köksal³

¹Uludağ University, Department of Automotive Engineering, Bursa, Turkey

²Amasya University, Department of Automotive Engineering, Amasya, Turkey

³Celal Bayar University, Department of Mechanical Engineering, Manisa, Turkey
halilbayram@uludag.edu.tr

Prejem rokopisa – received: 2015-09-16; sprejem za objavo – accepted for publication: 2015-12-16

doi:10.17222/mit.2015.296

Incremental sheet forming (ISF) is developed in order to meet the increasing demand for sheet metal forming and because it is a more economical method. First of all, this method gains attention because it is a die-less method. Furthermore, process flexibility and higher formability are other advantages of this method. In this study, AA2024-T3 sheets with a determined geometry and parameters were formed using the ISF method. Among the forming process parameters, tool path, step size and lubrication parameters were changed. The tool diameter, feed rate, spindle speed, angle of the wall and the tool coating parameters were kept constant. The thickness distributions and geometrical accuracy of the processed samples with the three-dimensional laser scanning method were examined accurately. It is clear from the results that the tool path that spirals and always keeps in touch is more successful than the tool path that makes it an incremental process. ISF is preferable to die production for limited production runs because it is more economic and the processing time is short.

Keywords: incremental sheet forming, single point incremental sheet forming, aluminum alloy AA2024, laser scanning

Stopnjujoče preoblikovanje pločevine (angl. ISF) je bilo razvito z namenom zadovoljiti povpraševanje po različnem preoblikovanju pločevine na bolj ekonomičen način. Ta metoda vzbuja pozornost, ker gre za metodo brez orodja. Drugi dve prednosti te metode sta: fleksibilnost procesa in večja preoblikovalnost. V pričujoči študiji je bila pločevina iz AA2024-T3 preoblikovana z določeno geometrijo in parametri z uporabo metode ISF. Med postopkom preoblikovanja so bili spreminjani procesni parametri, kot je pot orodja, velikost koraka in parametri mazanja. Premer orodja, hitrost podajanja, hitrost vrtenja, naklon stene in parametri prekritja orodja, so bili konstantni. Razporeditev debelin in geometrijska natančnost izdelanih vzorcev so bili natančno preiskani s tridimenzionalnim laserskim skeniranjem. Rezultati so pokazali, da sta spiralna pot orodja in stalen stik bolj uspešna od poti orodja, ki dela postopoma. Pokazalo se je tudi, da je pri omejeni količini postopek ISF relativno bolj ekonomičen kot postopek z orodjem in tudi čas izdelave je krajši.

Ključne besede: stopnjujoče preoblikovanje pločevine, enočkovno stopnjujoče preoblikovanje pločevine, aluminijeva zlitina AA2024, lasersko skeniranje

1 INTRODUCTION

Incremental sheet forming (ISF), one of the new production procedures, is developed to form sheet metal without using die. This method has advantages of process flexibility, product independent tooling and higher formability. So, it aims to decrease both the prototyping time and the set-up costs of forming, especially for a small number of pieces. However, traditional sheet metal forming methods are too much dependent on the number of parts because of the time and cost. Especially in productions having a large number of products, these methods are preferred since the cost will be reduced for each part.¹⁻⁴ The production with ISF, which is also defined as die-less forming for limited parts suitable for the usage area is preferred.⁵ In sheet metal production,

factors such as the time, die and prototype costs become disadvantages for limited production.

It is essential in forming to keep the necessary strength minimum depending on the size, geometry and time of production and to form without any damage. Particularly in the part production special for the person and the place, quick and suitable solutions are found by using three-dimensional laser scanning.⁶

ISF can be applied to the specially designed machines and many computer numerical control (CNC) milling stands providing the opportunity of manufacturing. In addition, this method is categorized as single-point incremental sheet forming (SPIF) and two-point incremental sheet forming (TIPIF). SPIF is the simplest way as a system.^{4,7} They are named positive forming and negative forming, respectively. Whereas in the two-point incremental sheet forming, the tool starts to form from

H. BAYRAM, N. S. KÖKSAL: INVESTIGATION OF THE GEOMETRICAL ACCURACY AND THICKNESS ...

the center, it forms through the center in the single-point incremental sheet forming.⁸

The performance of the forming process is related to the geometry of tools. Hemisphere and ball forms are preferred in tools and their sizes are determined according to the given geometry. The head diameters of tools starts from 6 mm and can be up to 100 mm for large parts. The selection of the tool diameter is determined by looking at the lowest concave of the desired geometry. Besides, coating can be applied to tools in order to reduce the friction and prolong the life of the tool.^{8,9}

There is no standard part geometry to identify the maximum angle of the wall during forming. The forming limit and maximum inclination angle of the wall have been searched with frustum of cone studies without cracks.^{5,9} Feed rate, spindle speed, step size, tool diameter, lubrication, tool path and angle of wall are important parameters affecting ISF.^{10,11} The maximum angle of the wall has been investigated with two diameter, step-size and sheet-thickness parameters. This value is determined with the experimental solutions applied for different geometries.^{12,13}

Many studies have been conducted related to the forming and mechanic of various materials with the ISF method.^{14–17} The relation of the roughness on the surface of the material in ISF with the tool radius, step size and inclination angle of its parts has been searched numerically and experimentally.^{18,19}

The most common four parameters affecting the strength necessary for forming as desired without any damage during forming are the tool diameter, step size, right of the angle of part wall or wall and sheet metal thickness. Tool diameter has been examined in detail, because it is the contact area that stress is intensified generally.^{15,20–23}

Suitable selection of the tool and the lubrication in ISF is essential for the successful forming and a homogeneous surface quality. The effect of the tool and lubrication in steel, aluminum and titanium sheets on the quality of the surface treating was investigated with SEM and the measuring device for surface roughness.^{24,25}

The comparison of theoretical calculations and the suitability after forming depends on doing the measurements after the processing accurately. For this purpose, the three-dimensional laser scanning technique has been utilized in measurements. This method is one of the contactless test methods and it has a wide area of usage because it provides economic and reliable measurements. The stages of the measuring process are computerized as three-dimensional point clouds (in STL format) by scanning the samples with laser scanning. The point clouds are saved and combined, pierced, the spaces are filled, filtrated and three dimensional solid models of the samples are obtained. At the end, all the necessary measurements can be made over the solid model in a

computer environment and become comparable to the geometries.^{3,25,26}

In this study, the applicability of ISF to AA2024-T3 sheets, process performance and economic advantages have been investigated. The other aim of this study is prioritizing the process parameters in ISF. The samples were formed by changing the tool path, step size and lubrication parameters and the geometrical accuracy and thickness alterations and have been measured by the three-dimensional laser scanning method. The comparison of ISF with the die production method was made for this model and the optimum test parameters were determined.

2 MATERIALS AND METHODS

2.1 Materials

In the study, AA2024-T3 commercial products in 200 mm × 200 mm × 1 mm sizes were used. The chemical composition and mechanical properties of the material are given in **Tables 1** and **2**.²⁷

Table 1: Chemical composition of AA2024 sample (w/%)

Tabela 1: Kemijska sestava vzorca AA2024 (w/%)

Element	Cu	Mg	Mn	Fe	Ti	Zn	Si	Al
Standard	3.80-4.90	1.20-1.80	0.30-0.90	Max 0.50	Max 0.15	Max 0.25	Max 0.50	90.70-94.70
Measured	4.59	1.49	0.54	0.10	0.02	0.02	0.07	93.14

Table 2: Mechanical properties of AA2024-T3 sample²⁷

Tabela 2: Mehanske lastnosti vzorca AA2024-T3²⁷

Tensile strength (MPa)		Strain failure (%)	
Standard	Experimental	Standard	Experimental
455	480	22.80	18.75

The experimental data in **Tables 1** and **2** are values in accordance with the standards.

2.2 Method

Incremental sheet processes applied to the samples were made with the single-point incremental sheet forming method in a First MCW300 CNC milling stand. The processes were made after the measurement precision of the retainer die specially manufactured for this method was provided and the retainer die was tied to the stand. AA2024-T3 samples which were laser cut in a way to be tied to the die (200×200×1) mm were anchored with the help of 8 M10 bolts during forming to prevent the sliding.

An uncoated carbide tool with a 10 mm diameter was chosen for the tool, which is one of the important parameters in forming. The feed rate was kept constant at 1000 mm/min and the spindle speed at 500 min⁻¹ in all the tests. The tool path, step size and lubrication parameters were changed in the processes. All the performed parameters in this study are given in **Table 3**.

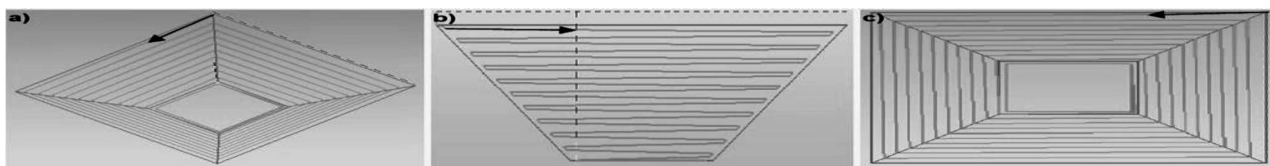


Figure 1: a) Perspective, b) side, c) top view of the tool path numbered 1

Slika 1: a) Perspektiva, b) stranski pogled, c) pogled iz vrha na pot orodja številka 1

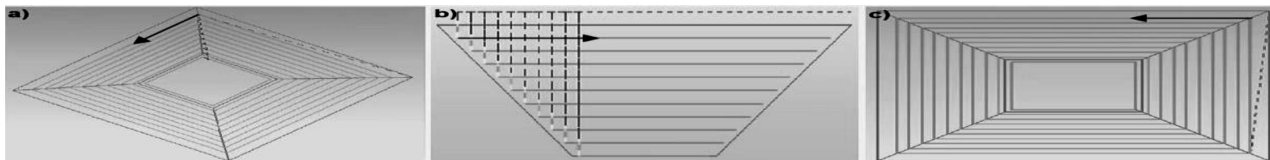


Figure 2: a) Perspective, b) side, c) top view of the tool path numbered 2

Slika 2: a) Perspektiva, b) stranski pogled, c) pogled z vrha na pot orodja številka 2

Table 3: All performed parameters

Tabela 3: Vsi uporabljeni parametri

Number of experiment	Number of tool path	Step size	Lubrication
1	1	0,2	A Lubricate
2			B Lubricate
3		0,5	A Lubricate
4			B Lubricate
5	2	0,2	A Lubricate
6			B Lubricate
7		0,5	A Lubricate
8			B Lubricate

Two different tool paths were designed using the NX Unigraphics CAM program. The first tool path does the step size as spirals and in this process the tool always keeps in contact with the sheet metal. The second one is the tool path always gives the step size from the same point after completing the whole circuit in a horizontal line. The perspective, side and top views of the 1st and 2nd tool paths are given in Figures 1 and 2 and again doing the same process incrementally. If during this

process the tool does not contact with the sheet metal continuously. The 0.2 mm, 0.3 mm, 0.5 and 0.7 mm values were tested for step sizes and the 0.2 mm and 0.5 mm step sizes were chosen.

Two different lube lubricates of which technical properties are given Table 4 were chosen for the lubrication in the application. The first one has been chosen as B lubricate emulsion, which is the machining coolant and the other one as the A lubricant.

Table 4: Technical properties of the used lubricants

Tabela 4: Lastnosti uporabljenih maziv

	A Lubricate	B Lubricate
Kinematic viscosity (40 °C, mm ² /s)	115-135	25-35

3 RESULTS

Solid models of the samples formed by the parameters determined with the incremental sheet forming were obtained by the method of three-dimensional laser scanning. Geometrical accuracies and thickness distributions of the solid models and the geometries that are

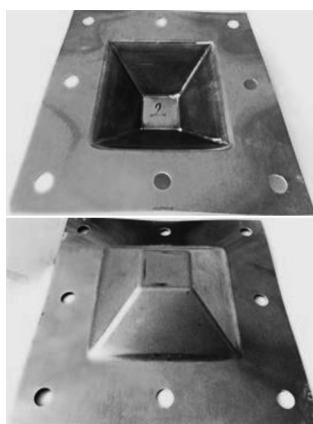


Figure 3: A lubricant, the views of the sample having 0.5 mm step size and 1st tool path parameters

Slika 3: Mazivo A, izgled vzorca s korakom 0,5 mm in poti orodja številka 1

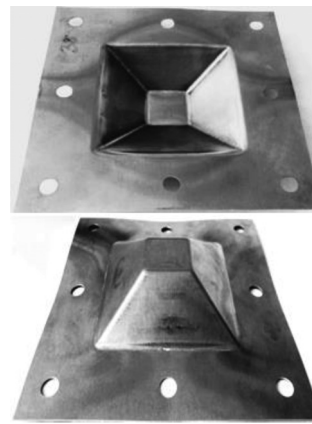


Figure 4: B lubricant, the views of the sample having 0.2 mm step size and 2nd tool path parameters

Slika 4: Mazivo B, izgled vzorca s korakom 0,2 mm in poti orodja številka 2

H. BAYRAM, N. S. KÖKSAL: INVESTIGATION OF THE GEOMETRICAL ACCURACY AND THICKNESS ...

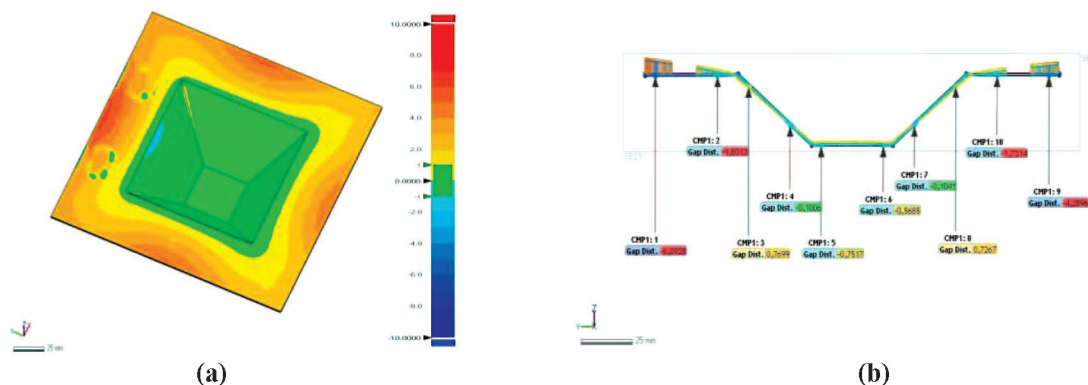


Figure 5: A lubricant, the results of geometric accuracy of the sample (a, b) having 0.5 mm step size and 1st tool path parameters
 Slika 5: Mazivo A, rezultati geometrijske natančnosti vzorca (a, b), pri koraku 0,5 mm in poti orodja številka 1

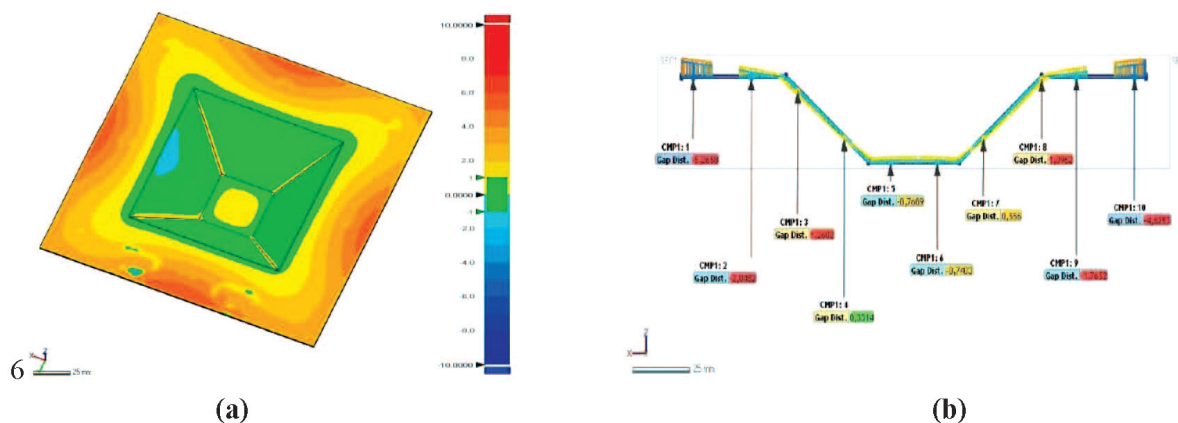


Figure 6: B lubricant the results of geometric accuracy of the sample (a, b) having 0.2 mm step size and 2nd tool path parameters
 Slika 6: Mazivo B, rezultati geometrijske natančnosti vzorca (a, b), pri koraku 0,2 mm in poti orodja številka 2

aimed to give to the samples were compared. Half of the part geometries were taken for the examination because they are symmetrical in this process. The views of the samples obtained after the forming process are given in Figures 3 and 4.

The thickness distribution of the samples after forming have been measured by sectioning the solid models obtained using thr CAD programs.

The values and measurement points of the samples having 0.5 mm step size and the 1st tool path parameter

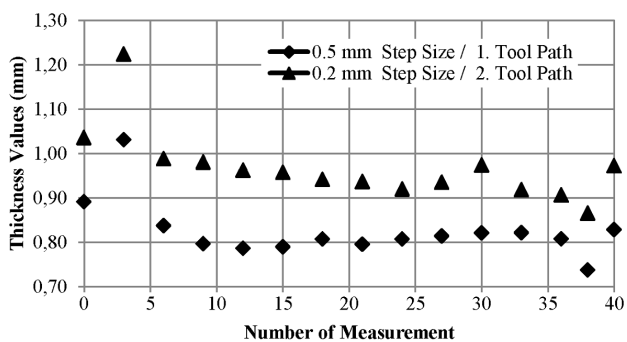


Figure 7: Graph shows measured thickness values of the inclined area (mm)

Slika 7: Grafičen prikaz izmerjene debeline na nagnjenem področju (mm)

Table 5: Measured thickness values of the inclined area (mm)

Tabela 5: Izmerjene vrednosti debeline na nagnjenem področju (mm)

Number of measurement	0.5 mm step size/ 1. tool path	0.2 mm step size/ 2. tool path	Number of measurement	0.5 mm step size/ 1. tool path	0.2 mm step size/ 2. tool path
1	0.8912	1.0358	21	0.8004	0.9425
2	0.9458	1.1493	22	0.7955	0.9370
3	1.0151	1.2310	23	0.8082	0.9484
4	1.0309	1.2242	24	0.8091	0.9585
5	0.9328	1.1046	25	0.8072	0.9198
6	0.8853	1.0143	26	0.8081	0.9474
7	0.8373	0.9885	27	0.8129	0.9402
8	0.8102	0.9704	28	0.8141	0.9351
9	0.8012	0.9787	29	0.8233	0.9368
10	0.7961	0.9806	30	0.8238	0.9352
11	0.7837	0.9598	31	0.8209	0.9742
12	0.7850	0.9579	32	0.8033	0.9304
13	0.7860	0.9624	33	0.8192	0.9290
14	0.7910	0.9540	34	0.8215	0.9181
15	0.7902	0.9489	35	0.8189	0.9032
16	0.7894	0.9577	36	0.8160	0.8998
17	0.7956	0.9558	37	0.8076	0.9064
18	0.7914	0.9362	38	0.7916	0.8967
19	0.8070	0.9413	39	0.7371	0.8656
20	0.7998	0.9417	40	0.8280	0.9723

and 0.2 mm step size and the 2nd tool path parameter among the samples formed are given in **Figures 5 and 6**. Comparative results of the measurements can be seen in **Figure 7**.

4 CONCLUSION

AA2024 materials formed in an acceptable way without being damaged by using incremental sheet forming. The effective parameters in this process are the lubricating fluid, the step size and the tool path. The type of tool, the feed rate and the number of revolution parameters were kept stable.

The A and B lubricants were used for the lubricating fluid, which is an effective parameter in forming. It was observed in the examination after processing that these two lubricating fluids were successful at the same rate.

Two different tool paths were used in the processes. It is clear that the tool path that is always in contact with the spirals is more successful than the tool path doing the progressive process. When the tool path which follows a spiral path and of which vertical steps enter from different points has been tried, different results could not be obtained. The first tool path has given better results in terms of geometrical accuracy and a homogeneous thickness distribution in the forming products. It was observed that the parameter having 0.5 mm step size displayed more geometrical accuracy and a more homogeneous distribution than the one with the 0.2 mm step size.

It was identified that the thickness alteration in the product showed a change suitable to the theoretical calculations by measuring accurately after ISF forming. In the results of the accurate measurement method 3D laser scanning, the alteration in the measured values in the middle of the product has been obtained at an acceptable level. The desired form with this method is the middle part of the sample and its sides need to be removed after the process. Therefore, it is not important that the alteration in the side values after forming is too much.

The economy of the method has been investigated in terms of die cost and labor cost, etc. Accordingly, the incremental sheet forming method is cheaper than the die production for the series of less than 500. However, if the number exceeds this value, the method loses its economic advantage. This method stands out in the private and less numbered productions.

The process has been carried out by applying very small strength compared to deep drawing and free from the size of the product in sheet forming. Correspondingly, it has been seen to stay in the safe area in the forming limit diagram (FLD) during forming.

Acknowledgement

This work has been carried out with the financial support from Celal Bayar University Scientific Research Projects Commission (2014-078).

6 REFERENCES

- 1 M. Benisa, B. Babic, A. Grbovic, Z. Stefanovic, Computer-Aided Modeling of the Rubber-Pad Forming Process, *Mater. Tehnol.*, 46 (2012) 5, 503–510
- 2 I. Cerro, E. Maidagan, J. Arana, A. Rivero, P. P. Rodriguez, Theoretical and experimental analysis of the dieless incremental sheet forming process, *Journal of Materials Processing Technology*, 177 (2006) 1, 404–408, doi:10.1016/j.jmatprotec.2006.04.078
- 3 G. Ambrogio, L. De Napoli, L. Filice, F. Gagliardi, M. Muzzupappa, Application of Incremental Forming process for high customized medical product manufacturing, *Journal of Materials Processing Technology*, 162 (2005), 156–162, doi:10.1016/j.jmatprotec.2005.02.148
- 4 G. Centeno, I. Bagudanch, A. J. Martínez-Donaire, M. L. García-Romeu, C. Vallellano, Critical analysis of necking and fracture limit strains and forming forces in single-point incremental forming, *Materials & Design*, 63 (2014), 20–29, doi:10.1016/j.matdes.2014.05.066
- 5 G. Hussain, G. Lin, N. Hayat, A new parameter and its effect on the formability in single point incremental forming: a fundamental investigation, *Journal of Mechanical Science and Technology*, 24 (2010) 8, 1617–1621, doi:10.1007/s12206-010-0514-1
- 6 K. Galanulis, Optical measuring technologies in sheet metal processing, *Advanced Materials Research*, 6 (2005), 19–34, doi:10.4028/www.scientific.net/AMR.6-8.19
- 7 M. J. Mirnia, B. M. Dariani, H. Vanhove, J. R. Dufloy, An investigation into thickness distribution in single point incremental forming using sequential limit analysis, *International Journal of Material Forming*, 7 (2014) 4, 469–477, doi:10.1007/s12289-013-1143-x
- 8 D. H. Nimbalkar, V. M. Nandedkar, Review of incremental forming of sheet metal components, *Journal of Engineering Research and Applications*, 3 (2013) 5, 39–51
- 9 D. Young, J. Jeswiet, Wall thickness variations in single-point incremental forming, *Proceedings of the Institution of Mechanical Engineers, Part B: Journal of Engineering Manufacture*, 218 (2004) 11, 1453–1459, doi:10.1243/0954405042418400
- 10 S. Kurra, S. P. Regalla, Experimental and numerical studies on formability of extra-deep drawing steel in incremental sheet metal forming, *Journal of Materials Research and Technology*, 3 (2014) 2, 158–171, doi:10.1016/j.jmrt.2014.03.009
- 11 S. B. Ehrif, M. Hrairi, Significant parameters for the surface roughness in incremental forming process, *Materials and Manufacturing Processes*, 29 (2014) 6, 697–703, doi:10.1080/10426914.2014.901519
- 12 R. Malhotra, A. Bhattacharya, A. Kumar, N. V. Reddy, J. Cao, A new methodology for multi-pass single point incremental forming with mixed toolpaths, *CIRP Annals-Manufacturing Technology*, 60 (2011) 1, 323–326, doi:10.1016/j.cirp.2011.03.145
- 13 J. C. LI, L. I. Chong, T. G. Zhou, Thickness distribution and mechanical property of sheet metal incremental forming based on numerical simulation, *Transactions of Nonferrous Metals Society of China*, 22 (2012), 54–60, doi:10.1016/S1003-6326(12)61683-5
- 14 M. S. Shim, J. J. Park, The formability of aluminum sheet in incremental forming, *Journal of Materials Processing Technology*, 113 (2001) 1, 654–658, doi:10.1007/BF03177368
- 15 K. Jackson, J. Allwood, The mechanics of incremental sheet forming, *Journal of Materials Processing Technology*, 209 (2009) 3, 1158–1174, doi:10.1016/j.jmatprotec.2008.03.025

H. BAYRAM, N. S. KÖKSAL: INVESTIGATION OF THE GEOMETRICAL ACCURACY AND THICKNESS ...

- ¹⁶ B. Lu, H. Ou, S. Q. Shi, H. Long, J. Chen, Titanium based cranial reconstruction using incremental sheet forming, *International Journal of Material Forming*, (2014), 1–10, doi:10.1007/s12289-014-1205-8
- ¹⁷ J. Park, J. Kim, N. Park, Y. Kim, Study of forming limit for rotational incremental sheet forming of magnesium alloy sheet, *Metallurgical and Materials Transactions A*, 41 (2010) 1, 97–105, doi:10.1007/s11661-009-0043-7
- ¹⁸ M. Durante, A. Formisano, A. Langella, Comparison between analytical and experimental roughness values of components created by incremental forming, *Journal of Materials Processing Technology*, 210 (2010) 14, 1934–1941, doi:10.1016/j.jmatprotec.2010.07.006
- ¹⁹ G. Hussain, L. Gao, N. Hayat, Forming parameters and forming defects in incremental forming of an aluminum sheet: correlation, empirical modeling, and optimization: part A, *Materials and Manufacturing Processes*, 26 (2011) 12, 1546–1553, doi:10.1080/10426914.2011.552017
- ²⁰ J. Dufloy, Y. Tunckol, A. Szekeres, P. Vanherck, Experimental study on force measurements for single point incremental forming, *Journal of Materials Processing Technology*, 189 (2007) 1, 65–72, doi:10.1016/j.jmatprotec.2007.01.005
- ²¹ M. Durante, A. Formisano, A. Langella, F. M. C. Minutolo, The influence of tool rotation on an incremental forming process, *Journal of Materials Processing Technology*, 209 (2009) 9, 4621–4626, doi:10.1016/j.jmatprotec.2008.11.028
- ²² P. A. F. Martins, N. Bay, M. Skjødt, M. B. Silva, Theory of single point incremental forming, *CIRP Annals-Manufacturing Technology*, 57 (2008) 1, 247–252, doi:10.1016/j.cirp.2008.03.047
- ²³ M. B. Silva, M. Skjødt, P. A. Martins, N. Bay, Revisiting the fundamentals of single point incremental forming by means of membrane analysis, *International Journal of Machine Tools and Manufacture*, 48 (2008) 1, 73–83, doi:10.1016/j.ijmactools.2007.07.004
- ²⁴ G. Hussain, N. Hayat, L. Gao, An experimental study on the effect of thinning band on the sheet formability in negative incremental forming, *International Journal of Machine Tools and Manufacture*, 48 (2008) 10, 1170–1178, doi:10.1016/j.jmatprotec.2008.03.025
- ²⁵ J. J. Park, Y. H. Kim, Fundamental studies on the incremental sheet metal forming technique, *Journal of Materials Processing Technology*, 140 (2003) 1, 447–453, doi:10.1016/S0924-0136(03)00768-4
- ²⁶ E. Malyer, The Influence of Toolpath Strategy on Geometric Accuracy in Incremental Forming, *Key Engineering Materials*, 554 (2013), 1351–1361, doi:www.scientific.net/KEM.554-557.1351
- ²⁷ S. A. Khodir, T. Shibayanagi, M. Naka, Microstructure and mechanical properties of friction stir welded AA2024-T3 aluminum alloy, *Materials Transactions*, 47 (2006) 1, 185–193, doi:10.2320/matertrans.47.185

FORMATION OF A CORROSION-RESISTANT ALUMINA COATING ON A 6061 ALUMINUM ALLOY USING A COMBINATION OF MICRO-ARC OXIDATION AND SEALING TREATMENTS

TVORBA KOROZIJSKO OBSTOJNE Al_2O_3 PREVLEKE NA ZLITINI ALUMINIJA 6061 S KOMBINACIJO OKSIDACIJE V MIKROOBLOKU IN POSTOPKA TESNJENJA

Ahmet Hilmi Paksoy, Faiz Muhaffel, Merve Koca, Ozge Gokce, Sanaz Mohammadzadeh, Huseyin Cimenoglu

Istanbul Technical University, Department of Metallurgical and Materials Engineering, 34469 Istanbul, Turkey
cimenoglu@itu.edu.tr

Prejem rokopisa – received: 2015-09-24; sprejem za objavo – accepted for publication: 2015-12-24

doi:10.17222/mit.2015.302

Micro-arc oxidation (MAO) is an attractive process for the fabrication of protective coatings on aluminum alloys used in many industrial applications, such as automotive, structural and aerospace. However, improvements in the corrosion resistance of aluminum alloys upon covering their surfaces with MAO coating may not be sufficient for extending the service life of the components utilized in harsh environments. In the present study, the MAO coating formed on a 6061 aluminum alloy was sealed using a stearic acid treatment. In the scope of the present study, the surface and cross-sectional microstructures and the phases of the MAO coatings were analyzed using scanning electron microscopy (SEM) and X-ray diffraction (XRD) techniques, respectively. The wettability and surface roughness of the samples were measured by goniometer and profilometer, respectively. The corrosion resistance was assessed by long-term immersion in 3.5 % of mass fractions NaCl solution. Finally, it is concluded that sealing of the MAO coating by stearic acid treatment significantly improved the corrosion resistance of the 6061 quality aluminum alloy as compared to the untreated state and the unsealed MAO state.

Keywords: aluminum alloy, micro-arc oxidation, ceramic coating, sealing, corrosion.

Oksidacija v mikroobloku (MAO) je zanimiv postopek za izdelavo zaščitnih nanosov na aluminijevih zlitinah, ki se jih uporablja v številnih industrijah, kot je avtomobilska, gradbeništvo in letalstvo. Vendar pa izboljšanje korozijske odpornosti aluminijevih zlitin po prekritju z MAO nanosom ni dovolj veliko za podaljšanje življenjskega doba komponent, ki se jih uporablja v kislinskih okoljih. V študiji je bila plast MAO, ki je nastala na zlitini aluminija 6061, zatesnjena z obdelavo s stearinsko kislino. V okviru te študije, so bile analizirane površine in mikrostrukture preseka in faze v MAO nanosu, s pomočjo elektronske vrstične mikroskopije (SEM) in z rentgensko difrakcijo (XRD). Omočljivost in hrapavost površine vzorcev sta bili izmerjeni z goniometrom in s profilometrom. Korozijska odpornost je bila določena z dolgotrajnim namakanjem v 3,5 % raztopini NaCl. Ugotovljeno je bilo, da tesnjenje MAO nanosa z obdelavo v stearinski kislini, močno izboljša korozijsko odpornost aluminijeve zlitine 6061 v primerjavi z neobdelanim stanjem ali z nezatesnjenim MAO.

Ključne besede: aluminijeva zlitina, oksidacija v mikroobloku, keramičen nanos, tesnjenje, korozija

1 INTRODUCTION

Aluminum alloys are the most commonly used weight-saving materials and preferred especially in the automotive, aerospace, military, marine and rail industries owing to their excellent mechanical properties, such as a high strength/weight ratio, resilience under static and dynamic loading, and good formability.^{1,2} Aluminum alloys are known for their good corrosion resistance due to the natural oxide film on their surface, consisting of oxyhydroxides (α -AlOOH, diaspore; γ -AlOOH, boehmite or pseudo-boehmite) or aluminum hydroxides ($Al(OH)_3$, gibbsite bayerite) with a thickness of 4–10 nm. The oxide film is formed at any temperature when the aluminum alloy contacts with air or an oxidizing medium.³⁻⁵ However, this natural oxide layer is not sufficiently protective against chloride-containing media.

The high solubility of the natural oxide film in the chloride ions containing media leads to severe corrosion after a relatively short service life.⁶ Chloride ions are greatly absorbed on the natural oxide film and cause deep ruptures into the surface.⁷ The generation of these ruptures and the dissolution of the oxide phases disrupt the film continuity and cause the propagation of corrosion. To overcome the corrosion-related problems, the interaction of the surface and corrosive environment must be disconnected. Therefore, the studies were concentrated on surface modification such as micro-arc oxidation (MAO), hard anodizing, physical vapor deposition (PVD), laser surface treatment, cold spraying (CS) and sol-gel.⁸⁻¹¹

MAO is a technique that can be used to fabricate ceramic coatings on the surface by the plasma-assisted electrochemical conversion of aluminum. The ceramic coating consists mainly of a multi-layer structure which

is comprised of a relatively dense polycrystalline layer of alpha-alumina (α - Al_2O_3) as the inner layer, and a more porous gamma-alumina (γ - Al_2O_3) layer as the outer layer. In the scope of wear and corrosion resistance, alumina coatings exhibit better surface properties than an aluminum substrate.¹² Although previous studies have shown that the MAO treatment remarkably enhances the corrosion resistance of the aluminum alloys, the corrosion protection of the coating may fail under highly concentrated corrosive media and/or longer periods of interaction between the corrosive media and the coating. Moreover, the MAO coatings have micro-pores on the surface and cracks due to the nature of the oxide-forming mechanism and the thermal stresses generated by rapid cooling. Unfortunately, corrosive media can move along the cavities of the alumina coating and reach the aluminum substrate, which causes the generation of corrosion under the coating.¹³⁻¹⁵

In this respect, a post-treatment is required to improve and extend the corrosion resistance of the MAO coating on an aluminum alloy. The sealing is a cost-effective and simple post-treatment that provides the closure of micro pores and micro cracks in order to hinder the migration of the corrosive media through the alumina coating.¹⁶⁻²⁰

The present study is aimed at improving the corrosion resistance of MAO formed alumina coating by a simple sealing post-treatment. The sealing treatment was performed by immersion in a hot stearic-acid-containing solution. After the microstructural and compositional analyses, the influence of the sealing treatment on the wettability and corrosion resistance of the MAO coating was investigated.

2 EXPERIMENTAL PART

The samples were cut to a size of 15 mm \times 15 mm from 6061 aluminum alloy and ground by SiC abrasive papers up to #2500. A 30-kW DC power supply with a stainless-steel container serving as the cathode was used in the MAO process. The samples treated in an electrolyte containing 20 g/L sodium aluminate (VWR International LLC) and 3 g/L potassium hydroxide (VWR International LLC) for 5 min with an applied voltage of 450 V in the positive half cycle and 60 V in the negative half cycle. The pulse frequency and duty cycle were 588 Hz and 60 %, respectively. During the process, the temperature of the electrolyte was below 30 °C using an external cooling system. After the MAO treatment, samples were washed with ethanol, distilled water and dried in air at room temperature. For the sealing treatment, the samples were immersed in an ethanol solution of 0.1 mol/L stearic acid at 65 °C for 1 h and then dried at 60 °C for 2 h. The untreated alloy, sealed alloy, MAO treated and sealed MAO treated samples will be coded as Al-6061, Al-6061+S, MAO, and MAO+S, respectively.

The surface morphology and cross-sectional microstructure of the MAO coating were examined with a

scanning electron microscope (SEM, Hitachi TM-1000). The phase composition of the MAO coating was identified by an X-ray diffractometer (XRD, Bruker D8 Advanced) using Cu- $K\alpha$ radiation ($\lambda = 0.154$ nm) at 40 kV and 30 mA with a scan range of 20–90°. Contact angle measurements were performed using a goniometer (KSV CAM 200). Distilled water was used for the test and the drop volume was 5 μL . Five measurements were performed for each sample at room temperature.

The samples were immersed in 3.5 % of mass fractions of NaCl solution for (2, 4, 6 and 14) d to evaluate the corrosion-resistant performance of the samples. The samples were removed from the 3.5 % of mass fractions of NaCl solution, cleaned in deionized water and subsequently in ethanol to remove the remaining NaCl residues and dried at ambient temperature. The samples were weighed using an electronic balance with an accuracy of 0.1 mg before and after the corrosion tests. The corrosion products were investigated using an energy-dispersive spectrometer (EDS, Oxford Instruments) in a Hitachi TM-1000 SEM. The corroded surfaces were observed by macro photography.

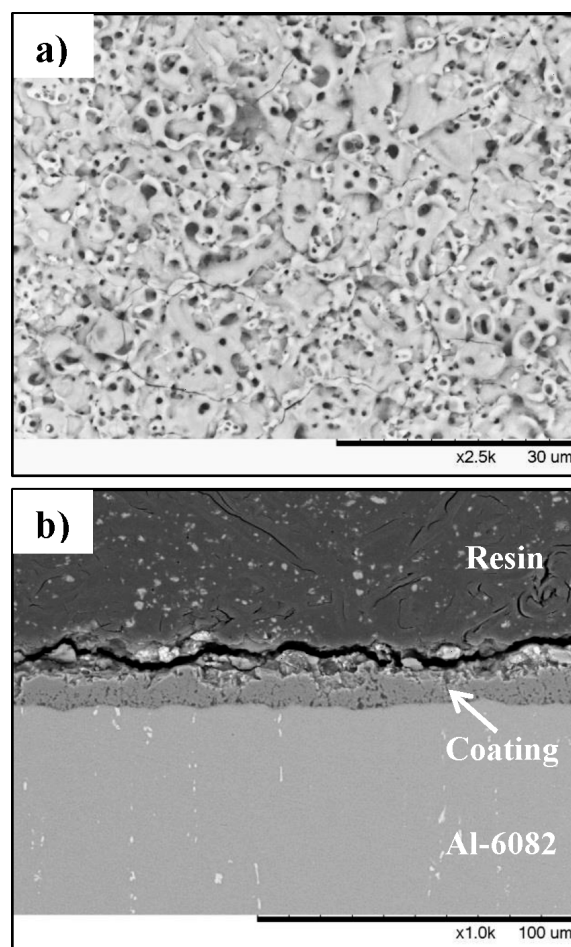


Figure 1: a) Surface and b) cross-sectional SEM images of the MAO sample

Slika 1: a) Površina in b) SEM-posnetek prečnega prereza vzorca MAO

3 RESULTS AND DISCUSSION

The surface and cross-section SEM micrograph of the MAO sample are shown in **Figure 1**. The coating showed the typical surface appearance of MAO process. The surface was covered with a coating containing spherical micro pores, micro cracks, crater-shaped structures as the result of the formation of discharge channels during the MAO process. Micro-cracking of the MAO coating is mainly associated with the thermal stress initiated during rapid solidification of the alumina melted in the discharge tunnel.²¹ The micro-pores were mainly ranged from about 1 μm to 3 μm in diameter. The thickness of the MAO coating was about 12 μm . Cross-section examinations revealed that the inner section of the MAO coating was denser than the outer section and showed a good bonding with the underlying substrate without any delamination and/or separation.

The XRD spectrum of the MAO-coated sample is presented in **Figure 2**. The MAO coating consisted of aluminum oxides in the form of α -alumina ($\alpha\text{-Al}_2\text{O}_3$) and γ -alumina ($\gamma\text{-Al}_2\text{O}_3$). The aluminum peak appeared due to the penetration of X-ray into the substrate. It is suggested that the outer sections of the MAO coating were primarily dominated by $\gamma\text{-Al}_2\text{O}_3$ owing to the higher cooling rate, while the inner section was mainly comprised of $\alpha\text{-Al}_2\text{O}_3$ as a result of more heat input gained during the MAO process.^{15,21}

In **Figure 3** contact angles measured on the as-received alloy (Al-6061), micro-arc oxidized alloy (MAO), sealed as-received alloy (Al-6061+S) and sealed MAO applied alloy (MAO+S) are presented. The as-received 6061 aluminum alloy and MAO samples exhibited low contact angles, as indicated by the high hydrophilicity and patelliform shape. The three times increase in the contact angle and the spherical shape of droplets showed that the stearic acid sealing treatment modified the surface to be more hydrophobic. Earlier studies have re-

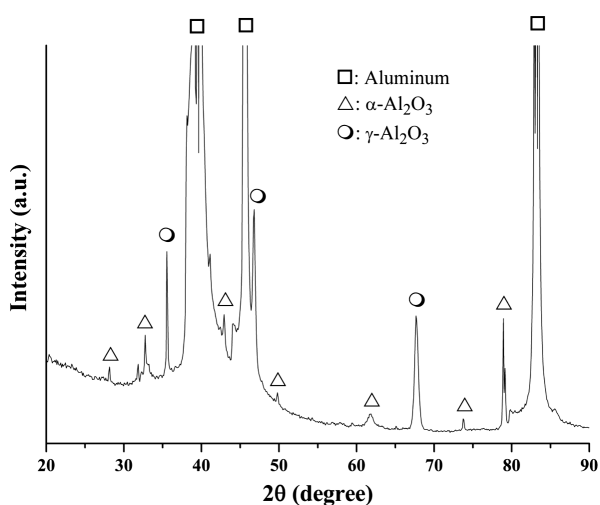


Figure 2: XRD spectrum of the MAO sample
Slika 2: Rentgenogram vzorca MAO

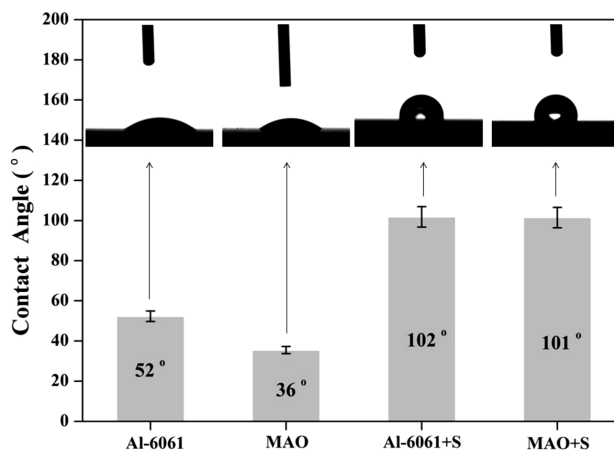


Figure 3: Contact-angle values of the samples and corresponding droplet images

Slika 3: Vrednosti kontaktnih kotov vzorcev in ustrezen posnetek kapljice

ported that hydrophobic surfaces provide relatively better corrosion protection in liquid media as compared to hydrophilic surfaces.²²⁻²⁴

The results of the corrosion tests are presented in **Figure 4** as the weight gain of the samples with respect to the immersion time in 3.5 % of mass fractions NaCl solution. As a general trend, the weight gain of the samples increased with an increasing duration time in the 3.5 % of mass fractions of NaCl solution and the highest weight gain values were obtained from the samples coded as Al-6061 and Al-6061+S after the immersion time of 14 d. In order to understand the reason for the weight gain, the Al-6061 sample immersed in the 3.5 % of mass fractions of NaCl solution was subjected to SEM examinations. As can be seen in **Figure 5**, the surroundings of the pits were enriched by chloride species, as reported previously.⁵

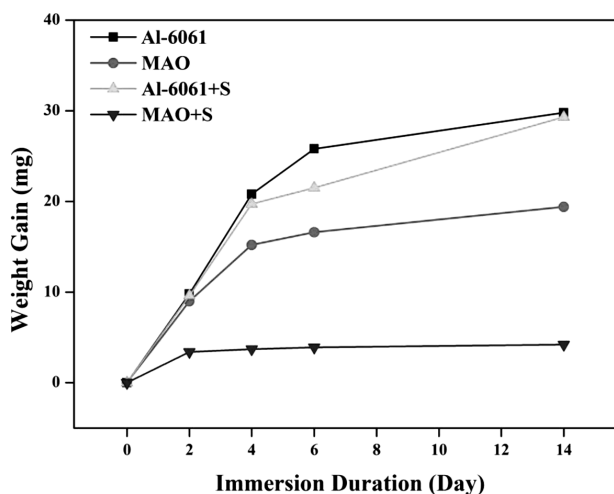


Figure 4: Corrosion weight gain – immersion duration plot of the samples

Slika 4: Pridobivanje teže zaradi korozije v odvisnosti od trajanja namakanja vzorcev

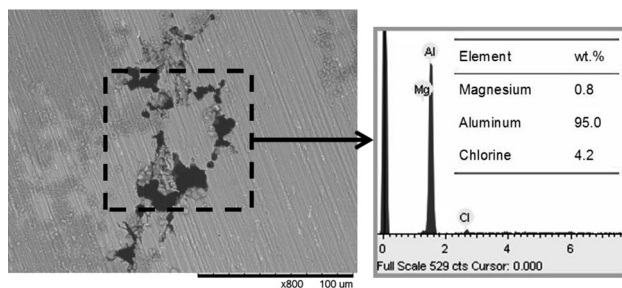
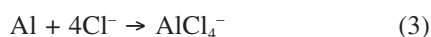


Figure 5: SEM micrograph and corresponding EDS analysis of Al-6061 sample after immersion in 3.5 % of mass fractions of NaCl solution for 14 days

Slika 5: SEM posnetek in ustrezna EDS analiza vzorca Al-6061 po namakanju 14 dni v raztopini 3,5 % NaCl

As the results of following reactions listed below, various pitting corrosion products such as complex aluminum chloride (AlCl_4^-), aluminum hydroxide ($\text{Al}(\text{OH})_3$) developed on the surface.⁵



Among the examined samples, lowest weight gain was measured for the MAO and MAO+S samples, indi-

cating the good corrosion-protection characteristics of MAO coatings. The sealing treatment enormously enhanced the corrosion resistance of the MAO coating so that the weight gain of the MAO+S sample was about five times lower than the MAO sample.

Macro images of the samples after immersion in 3.5 % of mass fractions of NaCl solution for different durations are depicted in **Figure 6**. Even after a short immersion duration in the corrosion media (2 d), the surface of the as-received 6061 aluminum sample turned to a dark color and contained many deep and wide pits. In general, the surface appearance of the sealed sample (Al-6061+S) exhibited similar features to that of the prior state of the corrosion test. The prolonged duration of the immersion also led the progress of corrosion on the surface of Al-6061+S sample completely. Unlike the Al-6061 and Al-6061+S samples, there was no severe pitting or deterioration as the indications of corrosion progress on the surfaces of MAO and MAO+S samples. Only a slight darkening and some small pits were observed on the surface of the MAO sample after 14 days of immersion in 3.5 % of mass fractions of NaCl solution.

It is obvious that the corrosive media were restricted to penetrate into the vicinities of the MAO coating by utilizing a stearic-acid -sealing treatment. Although the present approach showed a promising solution for corro-

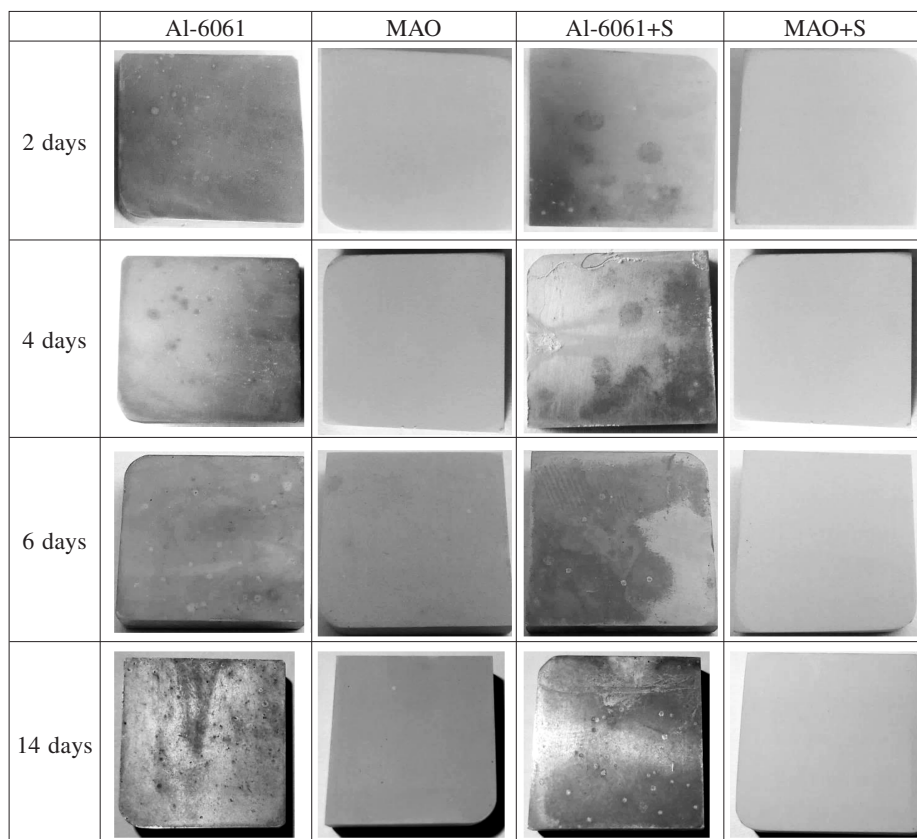


Figure 6: Macro images of the samples after immersion in 3.5 % of mass fractions of NaCl solution for different immersion times

Slika 6: Makroposnetek vzorca po različno dolgem namakanju v 3,5 % raztopini NaCl

sion protection of aluminum alloys, further studies are needed to be performed for understanding sealing mechanism and characterizing the modified MAO coating in more detailed.

4 CONCLUSIONS

The combination of MAO and sealing treatment with stearic acid was successfully applied to a 6061 aluminum alloy. The results demonstrated that when MAO or sealing treatments are separately applied the corrosion resistance of the examined aluminum alloy slightly improved. The sequential application of the MAO and the sealing treatment (MAO+S sample) provided the best corrosion resistance for the longest period (14 d) of immersion in 3.5 % of mass fractions of a NaCl solution.

5 REFERENCES

- 1 A. Polat, M. Avsar, F. Ozturk, Effects of the artificial-aging temperature and time on the mechanical properties and springback behaviour of AA6061, *Mater. Tehnol.*, 49 (2015), 487–493, doi:10.17222/mit.2013.154
- 2 W. S. Miller, L. Zhuang, J. Bottema, A. J. Wittebrood, P. De Smet, A. Haszler, A. Vierregge, Recent development in aluminium alloys for the automotive industry, *Materials Science and Engineering A*, 280 (2000), 37–49, doi:10.1016/S0921-5093(99)00653-X
- 3 A. Raveh, Z. K. Tsameret, E. Grossman, Surface characterization of thin layers of aluminium oxide, *Surface and Coatings Technology*, 88 (1997), doi:103–111, 10.1016/S0257-8972(95)02757-2
- 4 G. M. Scamans, N. Birbilis, R. G. Buchheit, Corrosion of Aluminum and its Alloys, *Shreir's Corrosion*, 2010, 1974–2010, doi:10.1016/B978-044452787-5.00095-0
- 5 C. Vargel, The Corrosion of Aluminium, 2004, doi:10.1016/B978-008044495-6/50011-2
- 6 A. Halap, M. Popovic, T. Radetic, V. Vascic, E. Romhanji, Influence of the thermo-mechanical treatment on the exfoliation and pitting corrosion of an AA5083-type alloy, *Mater. Tehnol.*, 48 (2014), 479–483
- 7 M. J. F. Gándara, Aluminium: The metal of choice, *Mater. Tehnol.*, 47 (2013), 261–265
- 8 Y. Bao, D. T. Gawne, J. Gao, T. Zhang, B. D. Cuenca, A. Alberdi, Thermal-spray deposition of enamel on aluminium alloys, *Surface and Coatings Technology*, 232 (2013), 150–158, doi:10.1016/j.surfcoat.2013.04.065
- 9 O. A. Gali, M. Shafiei, J. A. Hunter, A. R. Riahi, The tribological behavior of PVD coated work roll surfaces during rolling of aluminum, *Surface and Coatings Technology*, 260 (2014), 230–238, doi:10.1016/j.surfcoat.2014.06.071
- 10 D. K. Merl, I. Milošev, P. Panjan, F. Zupanič, Morphology and corrosion properties PVD Cr-N coatings deposited on aluminium alloys, *Mater. Tehnol.*, 45 (2011), 593–597
- 11 J. Tian, Z. Luo, S. Qi, X. Sun, Structure and antiwear behavior of micro-arc oxidized coatings on aluminum alloy, *Surface and Coatings Technology*, 154 (2002), 1–7, doi:10.1016/S0257-8972(01)01671-1
- 12 H. Ding, Z. Dai, S. C. Skuiry, D. Hui, Corrosion wear behaviors of micro-arc oxidation coating of Al₂O₃ on 2024Al in different aqueous environments at fretting contact, *Tribology International*, 43 (2010), 868–875, doi:10.1016/j.triboint.2009.12.022
- 13 R. C. Barik, J. A. Wharton, R. J. K. Wood, K. R. Stokes, R. L. Jones, Corrosion, erosion and erosion-corrosion performance of plasma electrolytic oxidation (PEO) deposited Al₂O₃ coatings, *Surface and Coatings Technology*, 199 (2005), 158–167, doi:10.1016/j.surfcoat.2004.09.038
- 14 L. Wen, Y. Wang, Y. Zhou, L. Guo, J. H. Ouyang, Microstructure and corrosion resistance of modified 2024 Al alloy using surface mechanical attrition treatment combined with microarc oxidation process, *Corrosion Science*, 53 (2011), 473–480, doi:10.1016/j.corsci.2010.09.061
- 15 O. Tazegul, F. Muhaffel, O. Meydanoglu, M. Baydogan, E. S. Kayali, H. Cimenoglu, Wear and corrosion characteristics of novel alumina coatings produced by micro arc oxidation on AZ91D magnesium alloy, *Surface and Coatings Technology*, 258 (2014), 168–173, doi:10.1016/j.surfcoat.2014.09.035
- 16 J. A. González, M. Morcillo, E. Escudero, V. López, E. Otero, Atmospheric corrosion of bare and anodized aluminium in a wide range of environmental conditions. Part I: Visual observations and gravimetric results, *Surface and Coatings Technology*, 153 (2002), 225–234, doi:10.1016/S0257-8972(01)01680-2
- 17 X. Yu, C. Cao, Electrochemical study of the corrosion behavior of Ce sealing of anodized 2024 aluminum alloy, *Thin Solid Films*, 423 (2003), 252–256, doi:10.1016/S0040-6090(02)01038-6
- 18 J. J. Suay, E. Giménez, T. Rodríguez, K. Habbib, J. J. Saura, Characterization of anodized and sealed aluminium by EIS, *Corrosion Science*, 45 (2003), 611–624, doi:10.1016/S0010-938X(02)00137-3
- 19 M. A. Chen, S. Y. Liu, J. M. Li, N. Cheng, X. M. Zhang, Improvement to corrosion resistance of MAO coated 2519 aluminum alloy by formation of polypropylene film on its surface, *Surface and Coatings Technology*, 232 (2013), 674–679, doi:10.1016/j.surfcoat.2013.06.073
- 20 X. Cui, X. Lin, C. Liu, R. Yang, X. Zheng, and M. Gong, Fabrication and corrosion resistance of a hydrophobic micro-arc oxidation coating on AZ31 Mg alloy, *Corrosion Science*, 90 (2015), 402–412, doi:10.1016/j.corsci.2014.10.041
- 21 T. Wei, F. Yan, J. Tian, Characterization and wear- and corrosion-resistance of microarc oxidation ceramic coatings on aluminum alloy, *Journal of Alloys and Compounds*, 389 (2005), 169–176, doi:10.1016/j.jallcom.2004.05.084
- 22 V. Bertola, M. Wang, Dynamic contact angle of dilute polymer solution drops impacting on a hydrophobic surface, *Colloids and Surfaces A*, 481 (2015), 600–608, doi:10.1016/j.colsurfa.2015.05.052
- 23 P. Wang, D. Zhang, R. Qiu, Y. Wan, J. Wu, Green approach to fabrication of a super-hydrophobic film on copper and the consequent corrosion resistance, *Corrosion Science*, 80 (2014), 366–373, doi:10.1016/j.corsci.2013.11.055
- 24 Z. Wang, Q. Li, Z. She, F. Chen, L. Li, X. Zhang, P. Zhang, Facile and fast fabrication of superhydrophobic surface on magnesium alloy, *Applied Surface Science*, 271 (2013), 182–192, doi:10.1016/j.apsusc.2013.01.158

CLASSIFICATION OF SURFACE DEFECTS ON STEEL SHEET USING CONVOLUTIONAL NEURAL NETWORKS

KLASIFIKACIJA POVRŠINSKIH NAPAK Z UPORABO KONVOLUCIJSKE NEVRONSKE MREŽE

Shiyang Zhou, Youping Chen, Dailin Zhang, Jingming Xie, Yunfei Zhou

Huazhong University of Science and Technology, School of Mechanical Science and Engineering, Wuhan, 430074, China
mnizhang@mail.hust.edu.cn

Prejem rokopisa – received: 2015-11-30; sprejem za objavo – accepted for publication: 2016-01-07

doi:10.17222/mit.2015.335

A convolutional neural network (CNN) is proposed to learn multiple useful feature representations for a classification from low level (raw pixels) to high level (object). Convolutional kernels are initialized by the learned filter kernels that come from sparse auto-encoders. Unlike some traditional methods, which divide the feature abstracting and classifier training into two separated processes, a discriminative feature vector and a single multi-class classifier of softmax regression are learned simultaneously during the training process. Based on the learned high-quality feature representation, the classification can be efficiently performed. A real-world case of surface defects on steel sheet, which evaluates the classification performance of the proposed method, is depicted in detail. The experimental results indicate that the proposed method is quite simple, effective and robustness for the classification of surface defects on hot-rolled steel sheet.

Keywords: convolutional neural networks, classification, surface defects, steel sheet, convolutional kernels, sparse auto-encoder

Konvolucijska nevronska mreža (CNN) je predlagana za učenje številnih koristnih predstavitev pri klasifikaciji od nizkega nivoja (grobe slikovne pike) do visokega nivoja (predmet). Konvolucijska jedra so inicializirana z naučenimi filtrirnimi jedri, ki izhajajo iz redkih samoenkoderjev. Različno od nekaterih klasičnih metod, ki delijo funkcijo abstrakcije in trening klasifikacije v dva ločena procesa, se vektor nediskriminativne funkcije v enostavnem večrazrednem klasifikatorju regresije softmax, uči hkrati med procesom treninga. Na osnovi naučene predstavitve z visoko kvalitetno funkcijo, se lahko klasifikacija učinkovito izvede. Primer iz resničnega sveta površinske napake na jekleni pločevini, ki ocenjujejo zmogljivost klasifikacije je prikazan v podrobnostih. Rezultati eksperimentov kažejo, da je predlagana metoda razmeroma preprosta, učinkovita in robustna pri klasifikaciji površinskih napak na vroče valjani jekleni pločevini.

Ključne besede: konvolucijske nevronske mreže, klasifikacija, površinske napake, jeklena pločevina, konvolucijska jedra, redki samoenkoder

1 INTRODUCTION

With the development of industrial automation, computer vision and machine learning, a machine-vision-based inspection system for surface defects of steel sheet has becoming more and more prevalent in the iron and steel industry. Classification accuracy is the main consideration in the inspection system, while a discriminative feature representation of surface defects is the foundation. How to extract a set of better feature representations and design the appropriate classifier for surface defects has been a hot research topic for many years.¹⁻⁸ A lot of methods about feature extraction and classification for image have been developed⁹⁻¹⁷. M. X. Chu et al.¹⁶ extracted features of geometry, gray, projection, texture and frequency-domain of defect in steel, then an enhanced twin support vector machine was adopted to realize the classification. A. Cord et al.¹² proposed a classification method of statistical learning based on a textural feature for defect of metallic surface. S. Ghorai⁷ derived a set of good-quality defect descriptors from wavelet feature set and applied support vector machine to the classification and detection of the defects. These traditional methods usually use hand-

crafted features, such as geometrical shape^{11,13,15,16}, grayscale^{1,13,16}, texture^{3,10-12}, local binary pattern⁸, wavelet transform^{4-7,9} or their combinations^{2,11,16}, followed by a trainable classifier, such as artificial neural networks^{9,11,14}, support vector machine^{6-8,13,15} and so on. They mainly include three stages: 1) Locating the position of surface defects (Detection). 2) Computing a large number of feature representations of surface defects. 3) Training a classifier via optimized feature vector and then predicting a new pattern by the trained classifier (Classification). Recently, computer vision has been disrupted by the use of convolutional neural networks (CNNs). CNNs have been shown to give incredible result and record-breaking performance on some challenging problems.¹⁸⁻²³ J. Masci et al.¹⁴ presented the max-pooling convolutional neural networks for the classification of steel defects. Z. Q. Zhao et al.²⁴ introduced the growing of convolutional neural networks for plant-leaf identification. K. Xu et al.¹⁵ exploited the unsupervised convolutional neural networks for vehicle-type classification. As the availability of large datasets, fast growth in computing power such as

availability of GPU and efficient algorithms such as dropout^{18,20}, CNNs have been widely used.^{24,25}

Although the traditional methods have achieved moderate results by means of some advanced features and classifiers, they have three main drawbacks: 1) manually designed features depend on powerful expert knowledge and complicated design method. 2) the design of features is done separately from the design of the classifier, so the designed features might not be the best for the classifier. 3) the design of features and classifier are varying for different tasks. In order to overcome the above shortcomings, the paper uses the CNNs to classify the surface defects of steel sheet, which can directly learn some better representative features from the labeled images of surface defects by supervised learning.

The rest of the paper is organized as follows: Section 2 describes the basic methodology. The experiments are discussed in Section 3. Finally, conclusions are drawn in Section 4. Throughout the paper, we denote scalars, vectors, matrices as the non-bold lower case letters, bold lower case letters, and non-bold upper case letters, respectively.

2 METHODOLOGY

CNNs can be considered as a special instance of artificial neural networks (ANNs), which are inspired by the concept of simple and complex cells in the biological visual cortex.²⁶ The visual cortex contains some cells that are only sensitive to a local receptive field.^{21,23} In contrast to traditional fully connected ANNs, neurons or units in CNNs are arranged for a squared feature map, and each neuron of the feature map in each layer is only sparsely connected to a small set of neurons in the previous layer. CNNs are an end-to-end auto-learning model with a minimal need for human design. It constructs a trainable architecture that combinations of feature extractor and classifier and operates on raw pixels of two-dimensional image directly. The extensive use of shared weight in CNNs can reduce the number of parameters. As is well

known, higher-level features are class-sensitive, whereas lower-level features are generic. Therefore, the high-level feature representations are more useful and critical for classification.²³ CNNs are good at extracting and forming the useful hierarchical feature representations from low level to high level. These discriminative feature representations can improve the classification performance.²⁸

2.1 Architecture of model

As shown in **Figure 1**, our model is a structure of 7 layers. A grayscale image of 40×40 is given as one channel input to the first convolutional layer with 20 filter kernels of 5×5 . The resulting 20 feature maps of 36×36 are then passed to the first max-pooling layer, which takes the maximum over 2×2 spatial regions with a stride of 2. The output is a set of 20 feature maps of 18×18 . They are followed by the second convolutional layer with 1000 filter kernels of 5×5 . The resulting 50 feature maps of 14×14 are then passed to the second max-pooling layer, which takes the maximum over 2×2 spatial regions with a stride of 2. The output is a set of 50 feature maps of 7×7 . They are followed by the third convolutional layer with 20,000 filter kernels of 4×4 . The resulting 400 feature maps of 4×4 are then concatenated into a 1D feature vector of 6400×1 . This feature vector is then fed into a classification layer that produces a 1D output vector of 8×1 , each element represents the confidence of each class. There are four different kinds of layer in the model as follows:

1) Input layer –

The input layer employs raw pixels of image directly.

2) Convolutional layer –

Convolutional layer achieves a two-dimensional convolution operation for previous feature maps. The activation of output feature maps is obtained by summing one or more convolutional responses that are passed through a pixel-wise activation function. Each convolutional layer has many filter kernels that generate some different

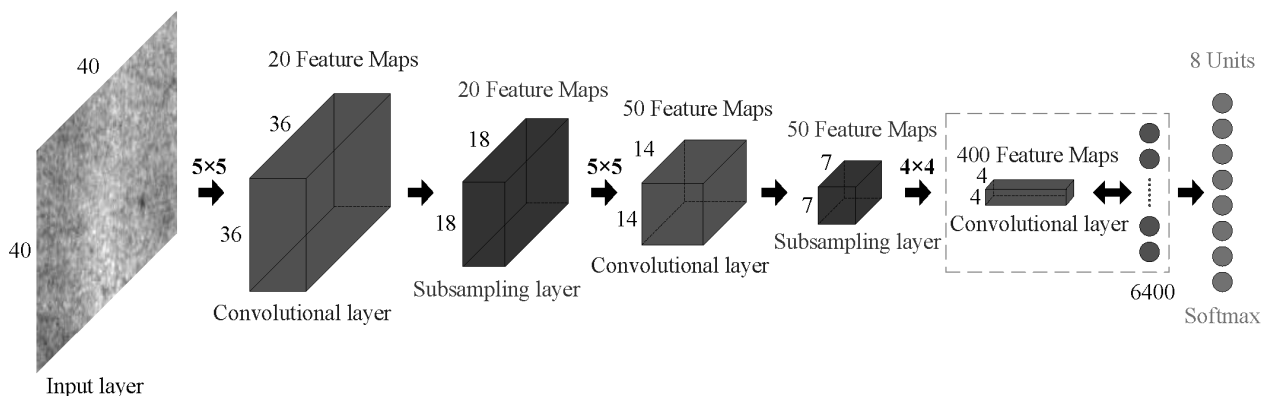


Figure 1: The schematic diagram of the architecture of the model. The width, height and depth of the block denote the width, height and numbers of feature maps, respectively. The number above the solid black arrow indicates the size of the convolutional filter kernel.

Slika 1: Shematski prikaz zgradbe modela. Širina, višina in globina bloka označujejo širino, višino in število funkcijskih zemljevidov. Številka nad črno puščico kaže velikost filtra konvolucijskega jedra.

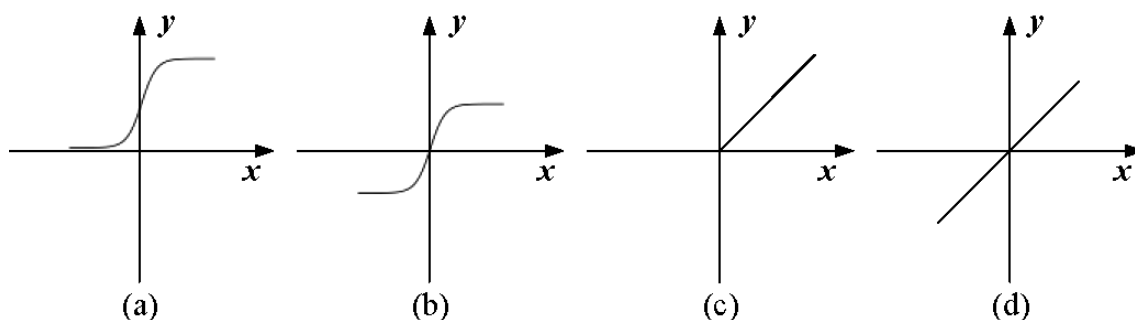


Figure 2: Four kinds of active function: a) sigmoid, b) hyperbolic tangent, c) ReLUs, d) LUs

Slika 2: Štiri vrste aktivnih funkcij: a) sigmoidna, b) hiperbolična tangenta, c) ReLUs, d) LUs

output feature maps, and different filter kernels can extract different feature representations, such as edges, crossings and corners.²⁸ As shown in **Figure 2**, there are many kinds of activation function, such as sigmoid, hyperbolic tangent and rectified linear units (ReLUs).¹⁸ ReLUs are only bound by their minimum value zero and can represent any non negative real value. At the same time, ReLUs have good sparsity properties, since having a zero activation value, as well as limiting the saturation of the output and diffusion of the gradient during the training process. Unlike the traditional CNNs²², the simplest activation function of linear units (LUs) is employed in our model. The derivative of LUs is one that can greatly reduce the calculation complexity.

3) Subsampling layer

A subsampling layer achieves a "pooling" operation, which is a form of dimensionality reduction and non-linearity. Feature pooling makes activation of a feature map less sensitive to the exact location of the pixel of an image and the specific structure of the model. Feature pooling allows feature representations of a higher layer to preserve the most critical feature information and reduce the computational burden without losing too much information.^{22,29} The output feature maps of the subsampling layer are given by a certain activation of the non-overlapping or overlapping square regions. There are some pooling methods, such as average-pooling, max-pooling and so on. In this paper, max-pooling is employed.

4) Classification layer

The classification layer employs softmax regression.²³ It produces a probability distribution over the output classes and ensures each output can be interpreted as the probability of a certain input belonging to a certain class. For a given unlabeled input image, the label of the maximum output corresponds to its class.

2.2 Learned filter kernel

The training of CNNs is a highly non-convex optimization problem, the initialization of weights largely affects the accuracy and convergence speed of the training.²¹ The initialization of weights by a sparse auto-encoder²³ tends to set the model in a better initial state

than random initialization, leading to impressive gain in the classification performance.²⁹⁻³¹ A sparse auto-encoder of three layers is utilized to learn lots of the filter kernels. A training set is generated by randomly sampling 5×5 image patches from the image of surface defects of steel sheet, and 24,000 patches are sampled in total. **Figure 3** shows some typical patterns that refer to the learned weights between the input layer and the middle layer. As we expected, the learned filter kernels mainly preserve the edges or corners at different positions and orientations; this is consistent with much prior work.^{26,30} The sparsity regularization in the auto-encoder is necessary for learning these edges or corners. With the purpose of not being stuck in local minima and speeding up convergence, the filter kernels of the convolutional layer in our model are initiated by these learned filter kernels.

2.3 Algorithm

There is a training dataset $[\mathbf{x}^{(m)}, \mathbf{y}^{(m)}]$ of N samples with c classes, $\mathbf{x}^{(m)} \in \mathbb{R}^d$, $\mathbf{y}^{(m)} \in \mathbb{R}^c$. The structure of fully connected ANNs of three layers is shown in **Figure 4**.

2.3.1 Back-propagation

1) Forward-propagation pass

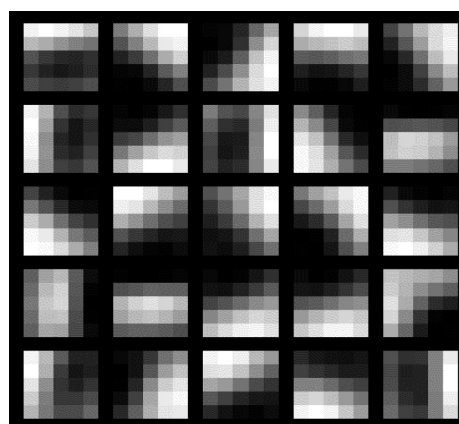


Figure 3: Visualization of the weights that were learned by a sparse auto-decoder of three layers

Slika 3: Vizualizacija uteži naučene z redkim samoenkoderjem treh plasti

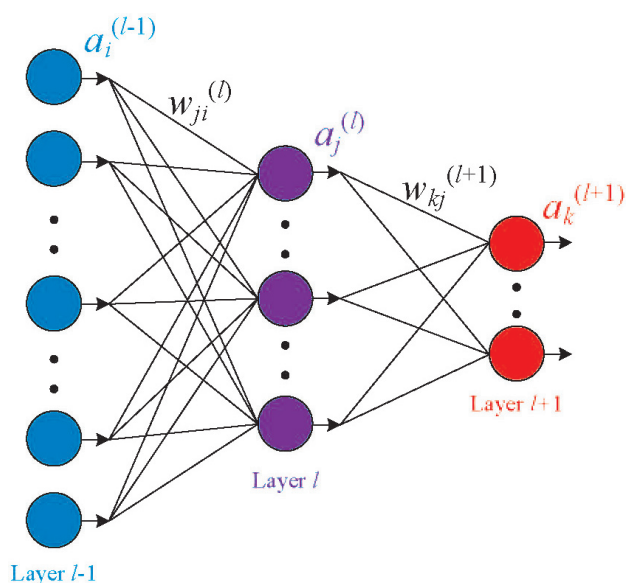


Figure 4: The structure of fully connected ANNs of three layers (bias not shown). There are n_{l-1} units (blue), n_l units (purple) and n_{l+1} units (red) in layer $l-1$, layer l and layer $l+1$ respectively, where, suppose layer $l+1$ is a classification layer. $w_{ji}^{(l)}$ and $w_{kj}^{(l+1)}$ denote the connection weight, $a_i^{(l-1)}$, $a_j^{(l)}$ and $a_k^{(l+1)}$ denote the output value of a unit.

Slika 4: Struktura povezane ANN na treh plasteh (razlika ni prikazana). Predstavljene so enote n_{l-1} (modro), n_l (vijolično) in n_{l+1} (rdeče) v plasti $l-1$, plasti l in plasti $l+1$, pri čemer je plast $l+1$ domnevno klasifikacijska plast. $w_{ji}^{(l)}$ in $w_{kj}^{(l+1)}$ označujejo uteži povezave, $a_i^{(l-1)}$, $a_j^{(l)}$ in $a_k^{(l+1)}$ označujejo izhodno vrednost enote.

For a single training sample, the forward-propagation step is given by the following Equations (1), (2), (3) and (4):

$$z_j^{(l)} = \sum_{i=1}^{n_{l-1}} w_{ji}^{(l)} a_i^{(l-1)} + b_j^{(l)} \quad (1)$$

$$a_j^{(l)} = f(z_j^{(l)}) \quad (2)$$

$$z_k^{(l+1)} = \sum_{j=1}^{n_l} w_{kj}^{(l+1)} a_j^{(l)} + b_k^{(l+1)} \quad (3)$$

$$a_k^{(l+1)} = \frac{\exp(z_k^{(l+1)})}{\sum_{k=1}^{n_{l+1}} \exp(z_k^{(l+1)})} \quad (4)$$

where, $f(\cdot)$ denotes the activation function of a unit, $b_j^{(l)}$ and $b_k^{(l+1)}$ denote the bias of the unit j in layer l and the unit k in layer $l+1$, respectively.

In order to take better advantage of the parallelism in matrix operations, a vectorization is employed. For N training samples, the vectorization form is given by the following Equations (5) and (6).

$$A^{(l)} = f(W^{(l)} A^{(l-1)} + B^{(l)}) \quad (5)$$

$$A^{(l+1)} = \exp(W^{(l+1)} A^{(l)} + B^{(l+1)}) / V \quad (6)$$

where, $A^{(l-1)}$, $A^{(l)}$, $A^{(l+1)}$, $W^{(l)}$, $W^{(l+1)}$, $B^{(l)}$ and $B^{(l+1)}$ are $n_{l-1} \times N$, $n_l \times N$, $n_{l+1} \times N$, $n_l \times n_{l-1}$, $n_{l+1} \times n_l$, $n_l \times N$, $n_{l+1} \times N$ matrices, respectively. Each column of bias matrix $B^{(l)}$ and $B^{(l+1)}$ is equal. For V of $n_{l+1} \times N$ matrix, each element in the same column equals l_2 norm of each column of $\exp(W^{(l+1)} A^{(l)} + B^{(l+1)})$, so $\exp(W^{(l+1)} A^{(l)} + B^{(l+1)}) / V$ represents division element-wish for two matrices.

2) Back-propagation pass

The data matrix X contains the entire training dataset by concatenating each training sample $\mathbf{x}^{(m)}$ to form the column of X , so X is a $d \times N$ matrix, the m -th column of X corresponds to the m -th training sample. Suppose the loss function is softmax regression, the overall loss function for N training samples is given by the Equation (7):

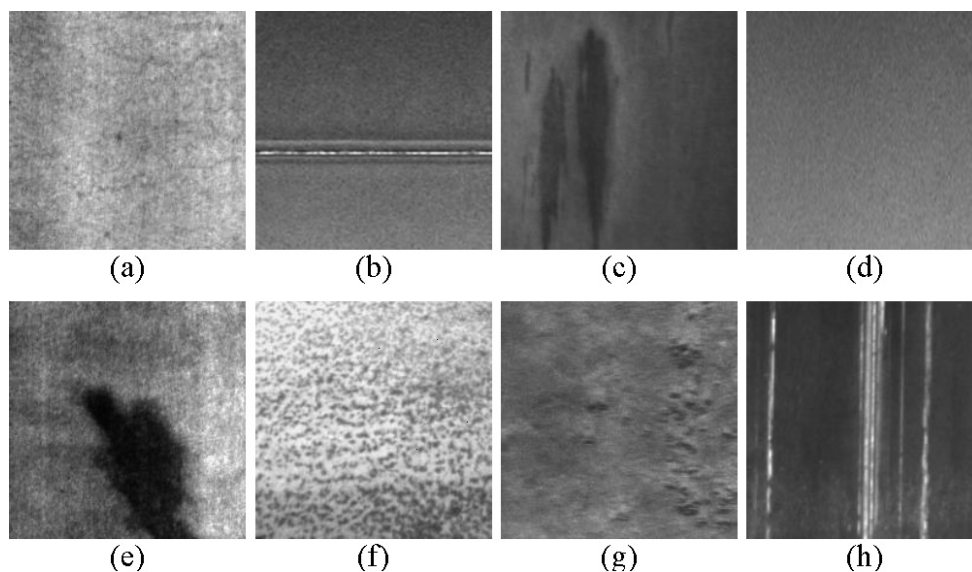


Figure 5: Sample images of surface defects of hot-rolled steel sheet: a) crazing, b) folding, c) inclusion, d) original, e) patch, f) pitted surface, g) rolled-in scale, h) scratch. Surface defects of steel sheet are different in direction, scale, etc.

Slika 5: Vzorčni posnetki površinskih napak na vroče valjani jekleni pločevini: a) mreža razpok, b) zavihek, c) vključek, d) original, e) nalepek, f) jamičasta površina, g) uvaljana škaja, h) raza. Površinske napake na jekleni pločevini se razlikujejo v smeri, luske in tako naprej.

$$J = \frac{1}{N} \|G \odot \ln f(X; \Theta)\|_F^2 + \frac{\lambda}{2} \|\Theta\|_F^2 \quad (7)$$

where, the operator \odot denotes the Hadamard produce operation (the component-wise multiplication), $\|\cdot\|_F$ denotes the *Frobenius*-norm, the first term is the error term, the second term is the regularization term that decreases the magnitude of weights and helps prevent overfitting of the model, λ is the weight decay (sparsity regularization) parameter that balances the relative importance of these two terms in the optimization process. The model parameters Θ (weights and biases) are changed in a direction that will reduce the value of the loss function. During the training process, the real outputs of the model are compared with the target output, and any difference is used for training the Θ throughout the network. Suppose the ground truth matrix (label matrix) G is a $c \times N$ matrix, the m -th column $g_m = [0, \dots, 1, \dots, 0]^T \in \mathbf{R}^c$ corresponds to the target output vector (label vector) of the m -th training sample, each column has only one non-zero element 1, the position of 1 indicates its class label. The optimization of J is usually non-convex and as large as the complex architecture of CNNs, which needs to be trained from thousands or millions of samples. Therefore, the minimization of J often uses a variant of stochastic gradient descent, which is called mini-batch stochastic gradient descent.³²

For each unit in each layer, we want to compute the sensitivity, which measures how much that unit is responsible for any error of output. Differentiating Equation (7), the sensitivity of the unit is given by the following Equations (8), (9) and (10):

$$\Delta^{(l+1)} = \frac{1}{N} (G - A^{(l+1)}) \quad (8)$$

$$\Delta^{(l)} = (W^{(l+1)})^T \Delta^{(l+1)} f'(Z^{(l)}) \quad (9)$$

$$\Delta^{(l-1)} = (W^{(l)})^T \Delta^{(l)} f'(Z^{(l-1)}) \quad (10)$$

The partial derivative of weight is given by the following Equations (11) and (12):

$$\Delta W^{(l+1)} = \Delta^{(l+1)} (A^{(l)})^T + \lambda W^{(l+1)} \quad (11)$$

$$\Delta W^{(l)} = \Delta^{(l)} (A^{(l-1)})^T + \lambda W^{(l)} \quad (12)$$

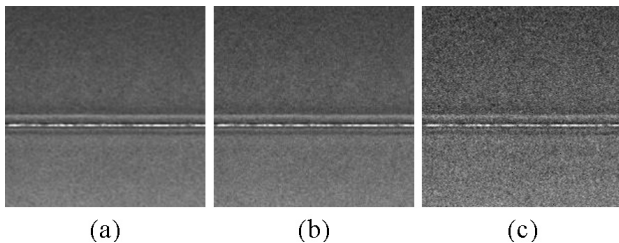


Figure 6: The same image of the sample is polluted by Gaussian noise with different values of SNR: a) SNR = 35 dB, b) SNR = 25 dB, c) SNR = 15 dB

Slika 6: Ista slika vzorca je onesnažena z Gaussovim hrupom, z različno vrednostjo SNR: a) SNR = 35 dB, b) SNR = 25 dB, c) SNR = 15 dB

where, $\Delta^{(l+1)}$, $\Delta^{(l)}$, $\Delta^{(l-1)}$, $\Delta W^{(l+1)}$ and $\Delta W^{(l)}$ are $n_{l+1} \times N$, $n_l \times N$, $n_{l-1} \times N$, $n_{l+1} \times n_l$, $n_l \times n_{l-1}$ matrix respectively.

Therefore, the weight update rule is given by the following Equations (13) and (14):^{27,32}

$$W^{(l)} = W^{(l)} - \eta \nabla W^{(l)} \quad (13)$$

$$W^{(l+1)} = W^{(l+1)} - \eta \nabla W^{(l+1)} \quad (14)$$

where, η is the learning rate.

2.3.2 Convolution and pooling

1) Convolution

Apply the filter kernel $w_{ji}^{(l)}$ for the previous feature map $a_i^{(l-1)}$ and then apply the activation function $f(\cdot)$, the output feature map is computed as follows:

$$a_j^{(l)} = f \left(\sum_{i \in M_j} a_i^{(l-1)} \cdot w_{ji}^{(l)} + b_j^{(l)} \right) \quad (15)$$

where, the operator $*$ denotes the two-dimensional convolution operation, M_j denotes the set of input feature map, $a_i^{(l-1)}$ and $a_j^{(l)}$ denote the i -th feature map of layer $l-1$, the j -th feature map of layer l , respectively, $b_j^{(l)}$ is the basis for the j -th feature map of layer l . Suppose the size of $a_i^{(l-1)}$ is $W \times H$, the size of $w_{ji}^{(l)}$ is $F \times F$, stride is F , so the size of $a_j^{(l)}$ is $(W-F+S)/S \times (H-F+S)/S$. Suppose the input feature maps \mathbf{I} is a 3D tensor of $H \times W \times m$, where H , W and m are the height, width and number of input feature maps respectively. The convolutional kernels \mathbf{K} is a 4D tensor of $F \times F \times m \times n$, where F is the size of the convolutional kernel and n is the number of output feature maps. We assume the convolution is performed with no padding zeros and the stride is equal to 1. Then, the output feature maps of a convolutional layer \mathbf{O} are given by the following Equation (16):

$$\mathbf{o}(x, y, j) = \sum_{i=1}^m \sum_{u=-F/2}^{F/2} \sum_{v=-F/2}^{F/2} \mathbf{I}(x-u, y-v, i) \mathbf{K}(u, v, i, j) \quad (16)$$

where, $j = 1, 2, \dots, n$, \mathbf{O} is a 3D tensor of $(H-F+1) \times (W-F+1) \times n$, which equals $\mathbf{I} * \mathbf{K}$.

2) Pooling

Let $a_k^{(l+1)}$ denotes the k -th feature map of layer $l+1$ and the size is $W \times H$, the size of the pooling region R is $r \times r$, the stride is S , the output feature map is given by the following Equation (17):

$$a_k^{(l+1)} = f \left(\frac{1}{n} \sum_{i \in M_k} \text{down}(a_i^{(l)}) + b_k^{(l+1)} \right) \quad (17)$$

where the operator $\text{down}(\cdot)$ denotes the down-sampling operation, M_k denotes the set of input feature map, $b_k^{(l+1)}$ is the basis for the k -th feature map of layer $l+1$. Therefore, the size of $a_k^{(l+1)}$ is $(W-r+S)/S \times (H-r+S)/S$.

3) Computing the gradients

Suppose layer $l-1$ is a subsampling layer, layer l is a convolutional layer, layer $l+1$ is a subsampling layer, $\delta_i^{(l-1)}$, $\delta_j^{(l)}$ and $\delta_k^{(l+1)}$ denote the sensitivity of the i -th

feature map of layer $l-1$, the j -th feature map of layer l , the k -th feature map of layer $l+1$, respectively.

$$\delta_j^{(l)} = \text{up}(\delta_k^{(l+1)})f'(z_j^{(l)}) \quad (18)$$

$$\delta_j^{(l-1)} = \sum_{j \in M_i} \delta_j^{(l)} \cdot w_{ji}^{(l)} \quad (19)$$

$$\nabla w_{ji}^{(l)} = a_i^{(l-1)} \circ \delta_j^{(l)} \quad (20)$$

where, the operator \circ denotes the two-dimensional correlation operation, the operator $\text{up}(\cdot)$ denotes the up-sampling operation, M_i denotes the set of connection of the i -th feature map of layer $l-1$ and some feature maps of layer l , $w_{ji}^{(l)}$ denotes filter kernel between the i -th feature map of layer $l-1$ and the j -th feature map of layer l .³³

After computing $\nabla w_{ji}^{(l)}$, the filter kernel $w_{ji}^{(l)}$ are updated by using gradient descent as follows:

$$w_{ji}^{(l)} = w_{ji}^{(l)} - \eta \nabla w_{ji}^{(l)} \quad (21)$$

where, η is the learning rate.

3 EXPERIMENTS

The classification performance of the proposed method was evaluated by using the practical surface defects of steel sheet.

3.1 Dataset of surface defects

In order to evaluate and certify the classification performance of our model, a dataset of surface defects was built from a hot-rolled steel sheet production line. As shown in **Figure 5**, the dataset of surface defects of hot-rolled steel sheet comprises seven kinds of typical surface defects (Crazing, Folding, Inclusion, Patch, Pitted Surface, Rolled-in Scale and Scratch) and one kind of zero surface defects (Original). There are 300 grayscale images per class and the size of each image is 200 pixels \times 200 pixels. Each pixel of the image represents the grayscale value in the range of (0, 255).

3.2 Data augmentation and preprocessing

To avoid over-fitting and lead to a better generalization ability, we artificially increased the size of the dataset.^{18,20} We used three affine transforms as follows: 1) Rescaling: scale each image from 200 \times 200 to 40 \times 40; 2) Rotation: rotate each 40 \times 40 image by 90°, 180°, 270° counterclockwise, respectively; 3) Flipping: flip each 40 \times 40 image for left and right, up and down, respectively. Therefore, there are 1800 samples for each class, 14400 samples for the whole dataset. As non-uniform brightness of image, each pixel of the image of 40 \times 40 was normalized to have zero mean and unit variance through the whole dataset. It is beneficial to improve the stability of training and increase the convergence speed.²⁹

3.3 Training details

We evaluated our model with different numbers of training samples, different sizes of image, different batch sizes, different epochs, different filter kernels and different activation functions on the aforementioned dataset. To evaluate the robustness against the failure of the image, additive Gaussian noise was added to the image, which simulated the failure behavior of the image. We corrupted 10 % of the random test samples from each class, every chosen image was added to Gaussian noise with three different values of signal-to-noise ratio (SNR), such as 35 dB, 25 dB and 15 dB. As shown in **Figure 6**, the same image of the sample is polluted by Gaussian noise with a different value of SNR.

All experiments were conducted using the open source VLFeat's MatConvNet library³⁴ in combination with NVIDIA's cuDNN library.³⁵ Training was done on a standard desktop with a NVIDIA GTX 970 GPU card with 4GB memory. To deal with random influence, we did every experiment 10 times. The filter kernels of the first convolutional layer were initialed with learned filter kernels by the sparse auto-encoder, the other filter kernels were all initialized by sampling from a standard normal distribution and the biases of the feature map were all initialized to zero. The model was optimized using mini-batch stochastic gradient descent over the whole training dataset with the following settings: a learning rate was initialized at 0.001 and decreased by 50 % every 50 epochs, the momentum was set to 0.9 and the parameter of the l_2 -norm weight decay was set to 0.0005.

3.4 Results

Some judicious techniques or tricks such as data augmentation, pre-training, and sparsity, enabled us to

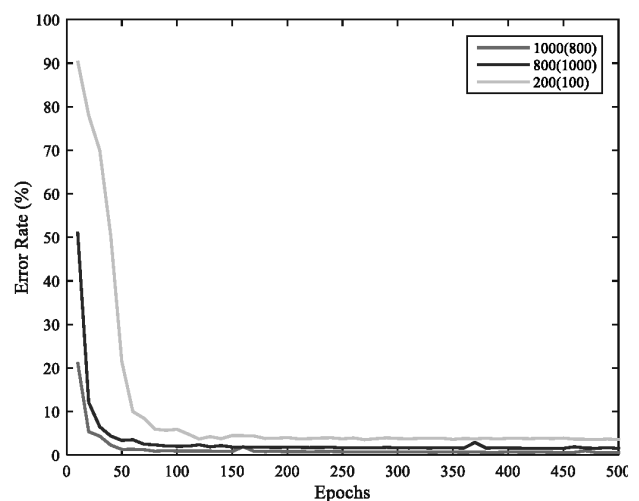


Figure 7: The classification error versus training samples and epochs, where the number enclosed in parenthesis is the test sample.

Slika 7: Napaka klasifikacije v odvisnosti od vzorca in trajanja, kjer je število v oklepaju preizkusni vzorec.

train a large model with a relatively small dataset. In **Figures 7** and **8**, the batch-sizes is 50. In **Figure 9**, **Tables 3** and **4**, the training samples, the test samples and the batch-sizes are 1000, 800, 50, respectively.

Table 1: The classification error versus batch sizes, train samples and epochs, the number enclosed in parenthesis is the test samples. The best result is in bold font.

Tabela 1: Klasifikacija napake v primerjavi z velikostjo serij, serijo vzorcev in časom trajanja, število v oklepaju je vzorčno. Najboljši rezultat je pisan krepko.

Batch Sizes	Train Samples	Epochs	Error Rate (%)	
			Train	Test
50	200 (100)	50	22.8250	21.5000
		100	1.2300	5.9250
		300	0	3.8250
		500	0	3.5750
	800 (1000)	50	1.8663	3.3734
		100	0.0025	2.0438
		300	0	1.6625
		500	0	1.5484
	1000 (800)	50	0.5675	1.3167
		100	0	0.9292
		300	0	0.7333
		500	0	0.6292
200	200 (100)	50	85.4550	89.7000
		100	73.9950	77.9750
		300	2.2000	6.2250
		500	0	4.4000
	800 (1000)	50	39.8975	40.4734
		100	4.5600	5.8750
		300	0.0800	2.1594
		500	0	1.8219
	1000(800)	50	9.7658	8.1167
		100	2.1042	2.7375
		300	0.0500	0.8708
		500	0.0192	0.8000

Table 2: The comparisons of classification error between learned and random filter kernel, the number enclosed in parenthesis is the test samples.

Tabela 2: Primerjave klasifikacij napak med naučenim in naključnim konvolucijskim filtrom, število v oklepajih je vzorčna vrednost.

Train Samples	Batch Sizes	Epochs	Kernel Type	Error Rate (%)	
				Train	Test
200 (100)	50	500	Learned	0	3.5750
			Random	0	9.3500
1000 (800)	50	500	Learned	0	0.6292
			Random	0	1.7917

As expected in **Table 1** and **Figure 7**, the more epochs and training samples, the lower the error we obtain. In addition, the marginal utility of epochs diminished at about 500, so we only use 500 epochs in the experiment. A smaller batch-size can improve the classification performance, but may cost more time. A moderate batch-size is used to smooth out the iteration and make better use of GPU. The model may bounce out of some local minima from perturbations of smaller batch-size. Therefore, a trade-off can be made between

precision and speed. Our model achieves approximately 99.9 % in the classification accuracy of the training and approximately 99 % in the classification accuracy of the test.

Table 3: The comparisons of classification error based on different activation functions, the name of activation function enclosed in parenthesis is used in the model.

Tabela 3: Primerjave kvalifikacijskih napak na podlagi različnih aktivacijskih funkcij, v oklepajih je navedba aktivacijske funkcije, ki je uporabljena pri modelu.

Method	Error Rate (%)
CNNs (Sigmoid)	12.8721
CNNs (Hyperbolic Tangent)	18.1129
CNNs (ReLU)	9.5018
Our Model (LUs)	0.6292

Table 4: The classification error versus Gaussian noise with different value of SNR

Tabela 4: Klasifikacija napak v primerjavi z Gaussovimi šumom z različno vrednostjo SNR

SNR (dB)	Error Rate (%)
35	0.9543
25	1.4092
15	5.7718

As shown in **Table 2** and **Figure 8**, the performance gap of the classification error of the test between learned and random filter kernels is approximately 5.8 % when the training samples are 200. When the training samples are 1000, the gap is approximately 1.2 %. It shows that unsupervised pre-training has a positive impact for classification performance, especially when the training samples are scarce. The learned filter kernels can substantially increase the classification result. Astonishingly, random filter kernels can also achieve decent

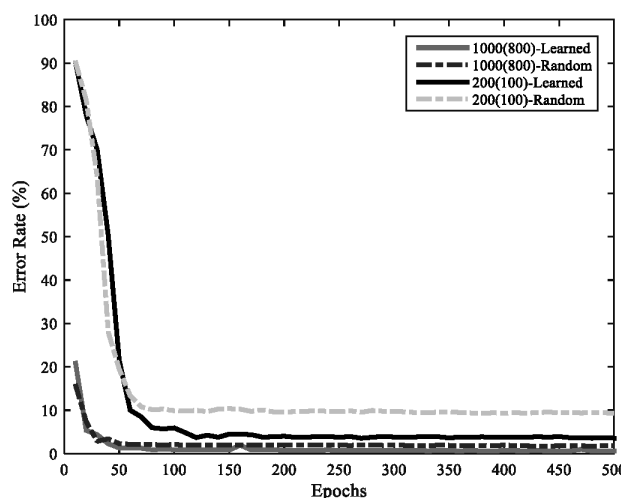


Figure 8: The comparison of classification error between learned and random filter kernels, where the number enclosed in parenthesis is the test samples.

Slika 8: Primerjava klasifikacije napak med naučenimi in naključnimi konvolucijskimi filtri, kjer je število v oklepajih vzorčno

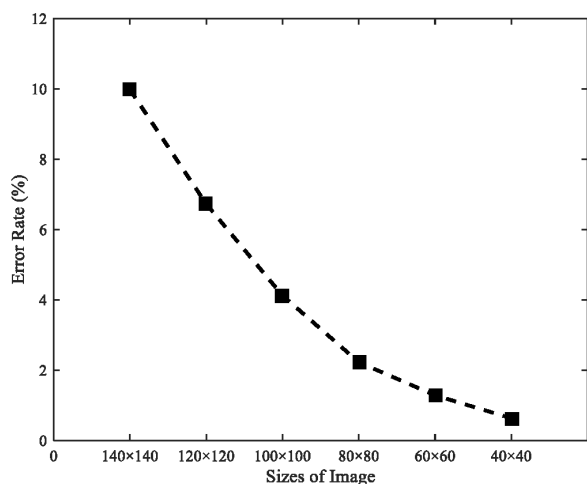


Figure 9: Results obtained in the experiments varying the sizes of image of sample. Slika 9: Rezultat, dobljen pri poizkusih z različnimi variacijami velikosti in posnetkov vzorca

performance, as long as the structure of the model is moderate.

For the certain CNNs, the classification performance varies with the size of the image. A larger size of image needs more training samples to avoid overfitting, a smaller size of image loses discriminative information of different classes of the image. As the structure of the model is fixed, these training samples are insufficient to learn so many parameters for a larger size of image, so it may be overfitting. Therefore, the classification error of a larger size of image is higher than a smaller size of image. As shown in **Figure 9**, the classification error of 40×40 is lower than 140×140 by approximately 9 %.

As shown in **Table 3**, our model with activation function of LUs is able to obtain a lower classification error than other activation functions.

As we can see from **Table 4**, although the classification error has increased with the value of SNR drops, our model achieves a moderate classification accuracy, so it can be concluded that the proposed method is robustness to failure of the image of the sample.

4 CONCLUSIONS

In the paper we present a simple model of CNNs to tackle the familiar task for the classification of surface defects of steel sheet. Unlike existing methods, our approach achieves the dual goal of extracting features and designing the classifier simultaneously. With experiments on the dataset of surface defects of steel sheet, we demonstrate our approach. The experimental results show that with a small dataset and a small model, our approach is able to achieve moderate accuracy in the classification of surface defects of steel sheet, the average classification accuracy can be up to 99 %. A user can select some parameters, such as the number of layers, the size of the image and so on, depending on the trade-off between classification performance and computational

load. Although the results have been demonstrated in hot-rolled steel sheet, it may be suitable for other textured material such as wood, paper, plastic and fabric. For future work, we will collect more kinds of surface defect for other kinds of steel sheet, such as cold-rolled sheet, silicon sheet, galvanized sheet, and develop an on-line inspection system for the surface defects of steel sheet for industrial application.

Acknowledgements

The authors would like to thank the editors and reviewers for their encouraging and constructive feedback. This work was supported by the Natural Science Foundation of China (51174151), and the Specialized Research Fund for the Key Science and Technology Innovation Plan of Hubei Province (2013AAA011).

5 REFERENCES

- 1 T. Piironen, O. Silven, M. Pietikäinen, T. Laitinen, E. Strömmer, Automated visual inspection of rolled metal surfaces, *Machine Vision and Applications*, 3 (1990) 4, 247–254, doi:10.1007/BF01211850
- 2 D. Brzakovic, N. Vujovic, Designing a defect classification system: A case study, *Pattern Recognition*, 29 (1996) 6, 1401–1419, doi:10.1016/S0963-8695(97)82095-6
- 3 D. M. Tsai, T. Y. Huang, Automated surface inspection for statistical textures, *Image and Vision Computing*, 21 (2003) 4, 307–323, doi:10.1016/S0262-8856(03)00007-6
- 4 X. L. Li, S. K. Tso, X. P. Guan, Q. Huang, Improving automatic detection of defects in castings by applying wavelet technique, *IEEE Transactions on Industrial Electronics*, 53 (2006) 6, 1927–1934, doi:10.1109/TIE.2006.885448
- 5 P. Caleb-Solly, J. E. Smith, Adaptive surface inspection via interactive evolution, *Image and Vision Computing*, 25 (2007) 7, 1058–1072, doi:10.1016/j.imavis.2006.04.023
- 6 X. W. Zhang, Y. Q. Ding, Y. Y. Lv, A. Y. Shi, R. Y. Liang, A vision inspection system for the surface defects of strongly reflected metal based on multi-class SVM, *Expert Systems with Applications*, 38 (2011) 5, 5930–5939, doi:10.1016/j.eswa.2010.11.030
- 7 S. Ghorai, A. Mukherjee, M. Gangadaran, P. K. Dutta, Automatic defect detection on hot-rolled flat steel products, *IEEE Transactions on Instrumentation and Measurement*, 62 (2013) 1, 612–621, doi:10.1109/TIM.2012.2218677
- 8 K. C. Song, Y. H. Yan, A noise robust method based on completed local binary patterns for hot-rolled steel strip surface defects, *Applied Surface Science*, 285 (2013) B, 858–864, doi:10.1016/j.apsusc.2013.09.002
- 9 C. S. Lee, C. H. Choi, J. Y. Choi, Y. K. Kim, S. H. Choi, Feature extraction algorithm based on adaptive wavelet packet for surface defect classification, *Proceedings of IEEE International Conference on Image Processing*, 1 (1996) 5, 673–676, doi:10.1109/ICIP.1996.560968
- 10 K. Wiltschi, A. Pinz, T. Lindeberg, An automatic assessment scheme for steel quality inspection, *Machine Vision and Applications*, 12 (2000) 3, 113–128, doi:10.1007/s001380050130
- 11 P. Caleb, M. Steuer, Classification of surface defects on hot rolled steel using adaptive learning methods, *Proceedings of IEEE International Conference on Knowledge-Based Intelligent Engineering Systems and Allied Technologies*, 1 (2000) 3, 103–108, doi:10.1109/KES.2000.885769

- ¹² A. Cord, F. Bach, D. Jeulin, Texture classification by statistical learning from morphological image processing: application to metallic surfaces, *Journal of Microscopy*, 239 (2010) 2, 159–166, doi:10.1111/j.1365-2818.2010.03365.x
- ¹³ H. J. Hu, Y. X. Li, M. F. Liu, W. H. Liang, Classification of defects in steel strip surface based on multiclass support vector machine, *Multimedia Tools and Applications*, 69 (2014) 1, 199–216, doi:10.1007/s11042-012-1248-0
- ¹⁴ J. Masci, U. Meier, D. Ciresan, J. Schmidhuber, G. Fricout, Steel defect classification with max-pooling convolutional neural networks, *IEEE International Joint Conference on Neural Networks*, (2012) 6, 1–6, doi:10.1109/IJCNN.2012.6252468
- ¹⁵ K. Xu, Y. H. Ai, X. Y. Wu, Application of multi-scale feature extraction to surface defect classification of hot-rolled steels, *International Journal of Minerals, Metallurgy, and Materials*, 20 (2013) 1, 37–41, doi:10.1007/s12613-013-0690-y
- ¹⁶ M. X. Chu., R. F. Gong, A. N. Wang, Strip steel surface defect classification method based on enhanced twin support vector machine, *ISIJ International*, 54 (2014) 1, 119–124, doi:10.2355/isijinternational.54.119
- ¹⁷ M. Kovacic, R. Jager, Modeling of occurrence of surface defects of C45 steel with genetic programming, *Mater. Tehnol.*, 49 (2015) 6, 857–863, doi:10.17222/mit.2013.304
- ¹⁸ A. Krizhevsky, I. Sutskever, G. E. Hinton, Imagenet classification with deep convolutional neural networks, *Advances in Neural Information Processing Systems*, 25 (2012), 1097–1105
- ¹⁹ J. Donahue, Y. Q. Jia, O. Vinyals, J. Hoffman, N. Zhang, E. Tzeng, T. Darrell, Decaf: a deep convolutional activation feature for generic visual recognition, *Proceedings of the 31st International Conference on Machine Learning*, 32 (2014), 647–655
- ²⁰ C. Szegedy, W. Liu, Y. Q. Jia, P. Sermanet, S. Reed, , D. Anguelov, D. Erhan, V. Vanhoucke, A. Rabinovich, Going deeper with convolutions, *IEEE International Conference on Computer Vision and Pattern Recognition*, (2015), 1–9, doi:10.1109/CVPR.2015.7298594
- ²¹ Y. LeCun, Y. Bengio, G. Hinton, Deep learning, *Nature*, 521 (2015) 7553, 436–444, doi:10.1038/nature14539
- ²² Y. LeCun, L. Bottou, Y. Bengio, P. Haffner, Gradient-based learning applied to document recognition, *Proceedings of IEEE*, 86 (1998) 11, 2278–2324, doi:10.1109/5.726791
- ²³ Y. Bengio, A. Courville, P. Vincent, Representation learning: a review and new perspectives, *IEEE Transactions on Pattern Analysis and Machine Intelligence* 35 (2013) 8, 1798–1828, doi:10.1109/TPAMI.2013.50.
- ²⁴ Z. Q. Zhao, B. J. Xie, Y. M. Cheung, X. D. Wu, Plant leaf identification via a growing convolution neural network with progressive sample learning, *Computer Vision – ACCV, 9004* (2014) 2, 348–361, doi:10.1007/978-3-319-16808-1_24
- ²⁵ Z. Dong, M. T. Pei, Y. He, T. Liu, Y. M. Dong, Y. D. Jia, Vehicle type classification using unsupervised convolutional neural network, *IEEE International Conference on Pattern Recognition*, (2014), 172–177, doi:10.1109/ICPR.2014.39
- ²⁶ B. A. Olshausen, D. J. Field, Emergence of simple-cell receptive field properties by learning a sparse code for natural images, *Nature*, 381 (1996), 607–609, doi:10.1038/381607a0
- ²⁷ D. E. Rumelhart, G. E. Hinton, R. J. Williams, Learning representations by back-propagating errors, *Nature*, 323 (1986), 533–536, doi:10.1038/323533a0
- ²⁸ M. D. Zeiler, R. Fergus, Visualizing and understanding convolutional networks, *Computer Vision – ECCV 8689* (2014) 1, 818–833, doi:10.1007/978-3-319-10590-1_53
- ²⁹ K. Jarrett, K. Kavukcuoglu, M. Ranzato, Y. LeCun, What is the best multi-stage architecture for object recognition, *IEEE International Conference on Computer Vision*, (2009), 2146–2153, doi:10.1109/ICCV.2009.5459469
- ³⁰ M. Ranzato, F. J. Huang, Y. L. Boureau, Y. LeCun, Unsupervised learning of invariant feature hierarchies with applications to object recognition, *IEEE International Conference on Computer Vision and Pattern Recognition*, (2007), 1–8, doi:10.1109/CVPR.2007.383157
- ³¹ D. Erhan, Y. Bengio, A. Courville, P. A. Manzagol, P. Vincent, S. Bengio, Why does unsupervised pre-training help deep learning, *Journal of Machine Learning Research*, 11 (2010), 625–660.
- ³² Y. Bengio, Practical recommendations for gradient-based training of deep architectures, *Neural Networks: Tricks of the Trade*, 7700 (2012), 437–478, doi:10.1007/978-3-642-35289-8_26
- ³³ J. Bouvrie, Notes on convolutional neural networks, MIT CBCL Tech Report, (2006), 38–44
- ³⁴ A. Vedaldi, K. Lenc, MatConvNet - convolutional neural networks for MATLAB, arXiv: 1412.4564 (2014)
- ³⁵ S. Chetlur, C. Woolley, P. Vandermersch, J. Cohen, J. Tran, B. Catanzaro, E. Shelhamer, cudnn: Efficient primitives for deep learning, (2014)

OPTIMIZATION OF THE MACHINING PARAMETERS FOR THE TURNING OF 15-5 PH STAINLESS STEELS USING THE TAGUCHI METHOD

UPORABA TAGUCHI METODE ZA OPTIMIZACIJO PARAMETROV OBDELAVE PRI STRUŽENJU NERJAVNEGA JEKLA 15-5 PH

Şerif Çetin¹, Turgay Kivak²

¹Düzce University, Institute of Science and Technology, Department of Manufacturing Engineering, 81620, Düzce, Turkey

²Düzce University, Faculty of Technology, Department of Manufacturing Engineering, 81620, Düzce, Turkey
turgaykivak@duzce.edu.tr

Prejem rokopisa – received: 2016-01-05; sprejem za objavo – accepted for publication: 2016-01-27

doi:10.17222/mit.2016.007

The present study investigated the effects of the control factors of cutting speed, feed rate and depth of cut on the response variables of cutting force (F_c) and surface roughness (R_a) in the dry turning of 15-5 PH martensitic stainless steel. Using PVD TiAlN-AlCrO- and CVD TiCN-Al₂O₃-TiN-coated carbide-cutting-tool inserts, a number of turning experiments were conducted via the L_{18} ($2^1 \times 3^3$) Taguchi mixed orthogonal array. The machining parameters were optimized using signal-to-noise ratio (S/N) and analysis of variance (ANOVA). Additionally, empirical models were created for predicting the F_c and R_a using multiple-regression analysis. The results indicated that depth of cut was the most significant cutting parameter affecting F_c , while the feed rate contributed the most to R_a . The developed quadratic regression model, showing a high determination coefficient of 0.981 for F_c and 0.988 for R_a , accurately explained the relationship between the response variable and the control factors.

Keywords: Taguchi method, turning, cutting force, surface roughness, 15-5 PH steel

Študija proučuje vplive kontrolnih faktorjev kot so: hitrost rezanja, hitrost podajanja in globina rezanja na spremenljivki odziva: silo rezanja (F_c) in hrapavost površine (R_a) pri suhem struženju martenzitega nerjavnega jekla 15-5 PH. Z uporabo PVD TiAlN-AlCrO- in CVD TiCN-Al₂O₃-TiN-nanosov na karbidnih vložkih za rezanje, so bili izvedeni številni preizkusi struženja s pomočjo mešane L_{18} ($2^1 \times 3^3$) Taguchi ortogonalne matrike. Parametri obdelave so bili optimirani z uporabo razmerja signala štima (S/N) in analizo variance (ANOVA). Dodatno so bili postavljeni empirični modeli za napovedovanje F_c in R_a z uporabo različnih regresijskih analiz. Rezultati so pokazali, da je globina reza najpomembnejši parameter rezanja, ki vpliva na F_c , medtem ko hitrost podajanja največ prispeva k R_a . Razviti kvadratni regresijski model, ki kaže določen visok koeficient 0,981 za F_c in 0,988 za R_a , natančno pojasni razmerje med spremenljivko odziva in kontrolnimi faktorji.

Ključne besede: Taguchi metoda, struženje, sila rezanja, hrapavost površine, jeklo 15-5 PH

1 INTRODUCTION

15-5 PH is a precipitation-hardened martensitic stainless steel that has the characteristics of high strength, good corrosion resistance, excellent weldability, low distortion and good mechanical properties at temperatures up to 600 °F (316 °C).¹⁻³ 15-5 PH stainless steel is widely used in the chemical, nuclear, aerospace, paper, food processing, petrochemical and general metalworking industries.⁴⁻⁵ Stainless steel is one of the materials that exhibits poor machinability. The greatest difficulty in the machining of these materials is poor surface quality and a short tool life.⁶ Especially after precipitation hardening, the increase in hardness and mechanical properties makes machinability even more difficult. However, only a few reports exist concerning the machining of precipitation-hardened martensitic stainless steel.

In the aviation and automotive sectors, the turning operation is one of the commonly used metal-cutting methods for industrial component manufacturing. In

industries where accuracy and measurement integrity are important, ways to improve the surface quality and lower the costs of lathed components have become perpetual subjects of investigation.⁷ Furthermore, surface roughness plays a significant role in the development and specification of the surface qualities of the produced components. When the surface-roughness value falls within the desired limits, it directly affects the material, energy and labor costs. In addition, a good surface quality provides significant improvements in the tribological properties, fatigue strength, corrosion resistance and aesthetic appearance of the finished product.⁸⁻¹⁰ One of the most important factors in production is energy consumption. The power consumed during machining is the factor that determines the energy consumption. Apart from the material factor (in terms of kW), the necessary power for the turning operation depends on the cutting depth, feed rate and cutting speed. Depending on the specific cutting resistance of the material with the other factors, the main cutting force (F_c) needed during machining is one of the most important parameters deter-

mining the power consumption for machining and consequently the energy cost.¹¹ There is a strong relation between the cutting force and the surface roughness, accuracy of the workpiece and tool wear.¹² There are a number of parameters, including cutting speed, feed, cutting depth and chip angle, that affect the cutting force and surface roughness.^{13–14} Suitable machining parameters must be determined in order to obtain low costs and high-quality products. For this purpose, several optimization methods and techniques are being used, one of which is the Taguchi experimental design method, which has been successfully applied in the solution of optimization problems.^{15–16}

D. P. Selvaraj et al.¹⁷ utilized the Taguchi method to define the optimal cutting parameters in the turning of two different grades of duplex stainless steel. The turning operations were carried out with TiC- and TiCN-coated carbide-cutting-tool inserts. The effects of cutting speed and feed rate on the cutting force, surface roughness and tool wear were analyzed and the results showed that the feed rate was the most significant parameter influencing the surface roughness and cutting force. The cutting speed was identified as the most significant parameter influencing the tool wear. C. Camposeco-Negrete¹⁸ conducted an experimental study to optimize machining parameters during the turning of AISI 6061 T6. The machining parameters were optimized using orthogonal array, *S/N* and ANOVA. The results showed that feed rate was the most dominant factor affecting the energy consumption and surface roughness. A. J. Makadia and J. I. Nanavati¹⁰ used response surface methodology (RSM) to determine the optimal cutting parameters for surface roughness in the turning of AISI 410 steel. The developed prediction model showed that the feed rate was the most significant factor on the surface roughness, followed by the tool nose radius. The surface roughness values were found to increase with increasing feed rate and to decrease with increasing tool nose radius. C. Ezilarasan et al.¹⁹ experimentally investigated and analyzed the machining parameters while turning Nimonic C-263 alloy, using Taguchi's experimental design. The cutting parameters considered were cutting speed, feed rate and depth of cut. The response variables of cutting force, tool wear and surface roughness were measured. Optimized cutting parameters were observed at 210 m/min cutting speed, 0.05 mm/r feed rate and 0.50 mm depth of cut. A. Haşçalık and U. Çaydaş²⁰ studied the turning operation of Ti-6Al-4V alloy and broadly examined the effects of cutting parameters on surface roughness and tool life by using the Taguchi method. An orthogonal array, *S/N* ratio, and ANOVA were employed to investigate the performance characteristics in the turning of commercial Ti-6Al-4V. The feed rate was found to be the most important factor on the surface roughness while cutting speed was the main factor that had a significant effect on tool life.

Upon examining studies in the literature, it can be seen that the Taguchi method has been successfully used in the optimization of machining parameters. On the other hand, the machinability of stainless steels is becoming a subject of perpetual investigation because of their wide usage and hard machinability characteristics. However, in recent years, very few studies have been conducted on the machinability of precipitation-hardened stainless, which, due to their excellent mechanical characteristics, are used especially in the aviation industry. Consequently, in this study, the aim was to optimize the machining parameters affecting the cutting force and surface roughness during the dry turning of 15-5 PH stainless steel using coated cementite-carbide tools. To this purpose, an experimental design employing a Taguchi L_{18} orthogonal array was created and analytical models were developed using regression analysis in order to estimate F_c and R_a . In addition, ANOVA was applied to determine the effect levels of the machining parameters.

2 EXPERIMENTAL PART

2.1 Machine tool and workpiece material

The experimental investigation was carried out using a Johnford TC 35 lathe with a maximum spindle speed of 3500 min⁻¹ and a 10-kW drive motor. The workpiece material used for experimentation was 15-5 precipitation-hardened (PH) martensitic stainless steel with a hardness of 42 HRC, in the form of round bars, 40 mm in diameter and 300 mm in length. The chemical composition and mechanical properties of the test samples are given in **Tables 1** and **2**, respectively. The precipitation-hardening treatment consisted of solutionizing at 1040 °C and air quenching, followed by a final tempering at 550 °C for 4 h (H1025 condition). The typical microstructures in the etched condition of the 15-5 PH stainless steel are shown in **Figure 1**. It can be clearly seen that the microstructure of the 15-5 PH precipi-

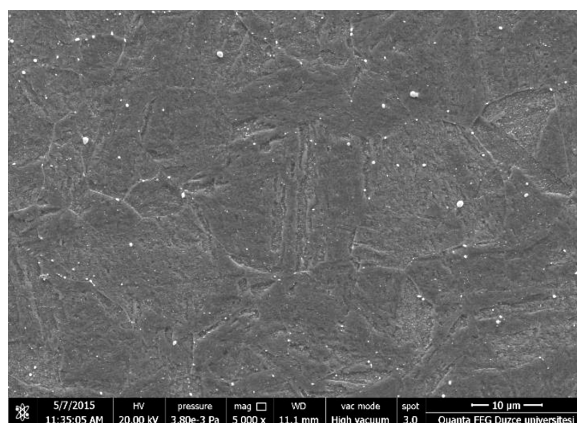


Figure 1: Microstructure of the precipitation-hardened 15-5 stainless steel

Slika 1: Mikrostruktura izločevalno utrjenega nerjavnega jekla 15-5

tation-hardened stainless steel shows lath martensite and fine carbides.

Table 1: Chemical composition of 15-5 PH martensitic stainless steel (w/%)

Tabela 1: Kemijska sestava martenzitnega nerjavnega jekla 15-5 PH (w/%)

Ni	Cu	Cr	C	Si	Mn	P	S	Nb	Ta
5.08	3.53	15.02	0.07	0.338	0.791	0.022	0.004	0.324	0.15

Table 2: Mechanical properties of 15-5 PH martensitic stainless steel

Tabela 2: Mehanske lastnosti martenzitnega nerjavnega jekla 15-5 PH

Tensile strength (MPa)	Yield strength (MPa)	Percentage elongation (%)	Hardness (HRC)
1202	1172	12	42

2.2 Cutting tools and holder

In the turning tests, commercially available PVD and CVD multilayer-coated carbide inserts (Sandvik Coromant – ISO CNMG 120408) were employed. The properties of the cutting tools and coating materials are given in **Table 3**. A right-hand style mechanical tool holder (ISO PSBNR 2525M12) was used for mounting the inserts. For each experimental parameter, a fresh cutting edge was utilized. The turning experiments were performed using two different cutting tools (PVD and CVD), three cutting speeds (150, 200, and 250) m/min and three feed rates (0.1, 0.2 and 0.3) mm/r.

Table 3: Properties of cutting tools and coating materials

Tabela 3: Lastnosti rezilnih orodij in nanosov

Coated method	Coated materials	Material quality of ISO (Grade)	Coating thickness (μm)	Hardness (HV)
PVD	TiAlN/AlCrO	GC1125	4	1640
CVD	TiCN/Al ₂ O ₃ /TiN	GC2015	5.5	1500

2.3 Cutting force measurement

During turning, the cutting force (F_c) was measured by using a three-component piezoelectric dynamometer (KISTLER – 9257B). The signals of F_c from the dynamometer were transmitted to a Kistler 5070-A multi-channel amplifier. Dynoware software was used for the data-acquisition system of the machine. The experimental setup and cutting force measurements are shown in **Figure 2**.

2.4 Surface-roughness measurement

The average surface roughness (R_a) of the workpiece was measured on a MAHR Perthometer M1 portable surface-roughness device. Cut-off and evaluation lengths for the surface roughness measurements were selected as 0.8 mm and 5.6 mm, respectively. Before the measurements of R_a , the measuring device was calibrated utiliz-

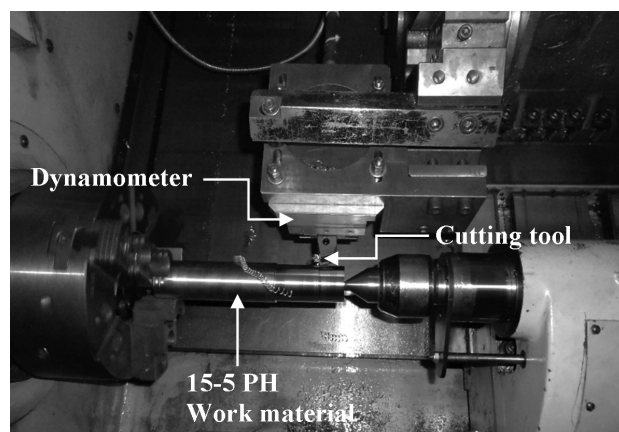


Figure 2: Experimental configuration for the measuring of cutting force

Slika 2: Eksperimentalni sestav za merjenje sile rezanja

ing a standard calibration specimen. The measurements were taken at three locations (120° apart) around the circumference of the workpieces in order to minimize the deviation, and the average values were reported. The surface roughness measurements are given in **Figure 3**.

2.5 Taguchi's design of experiments

Taguchi's Design of Experiments provides a simple, efficient and systematic approach for determining the optimum machining parameters in the manufacturing process.^{21,22} The Taguchi method significantly decreases the number of tests needed and increases the machining performance by using orthogonal arrays.^{23,24} For the realization of the experimental design, first of all, the control factors and their levels must be determined. In this study, the cutting tools (PVD and CVD), cutting speed (V), feed rate (f) and depth of cut (ap) were determined as the control factors. The cutting tool was designated in two levels, whereas the other control factors were in three levels. The control factors and their levels are indicated in **Table 4**.

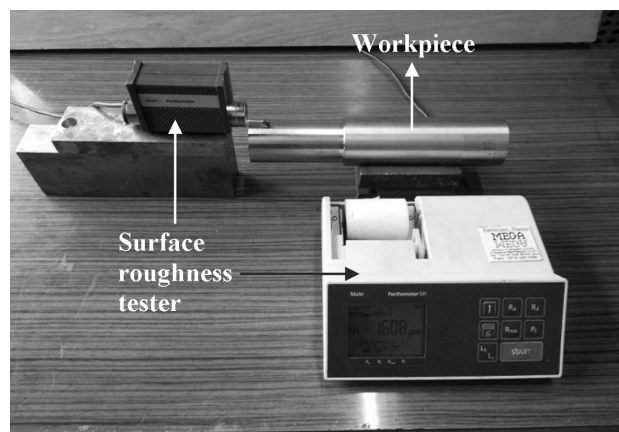


Figure 3: Surface-roughness measurement

Slika 3: Merjenje hrapavosti površine

Table 4: Control factors and their levels

Tabela 4: Kontrolni faktorji in njihovi nivoji

Control factors	Symbol	Level 1	Level 2	Level 3
Cutting tool	A	PVD	CVD	-
Cutting speed (m/min)	B	150	200	250
Feed rate (mm/r)	C	0.1	0.2	0.3
Depth of cut (mm)	D	0.5	1	1.5

The full-factorial experimental design required a large number of 54 (2¹×3³) tests, along with increased costs. Thus, Taguchi's experimental design was able to provide better results with fewer tests. For the specified control factors and their levels, L₁₈ was selected as the most suitable orthogonal array (**Table 4**). Consequently, the number of tests was decreased significantly and only 18 tests were made. The Taguchi method uses a loss function to determine the quality characteristics and the values of this loss function are also converted to a S/N ratio. In analyzing S/N ratios, three different quality characteristics are used: the "lower-the-better", the "higher-the-better" and the "nominal-the-best". Minimization of the F_c and R_a values was the main purpose of this study. For this reason, the "lower-the-better" quality characteristic was used for F_c and R_a.

"Lower is the better" characteristics (minimization):

$$S/N = -10 \lg \left[\frac{1}{n} \sum_{i=1}^n y_i^2 \right] \quad (1)$$

In the Equation (1), y_i is the observed data at the i-th experiment and n is the number of observations.

3 ANALYSIS AND DISCUSSION

3.1 Analysis of the S/N ratio and ANOVA results

The S/N ratio is defined as the ratio of the average for the standard deviation. This ratio is used to measure the deviation of quality characteristics from the desired value. In this study, F_c and R_a were specified as the quality characteristics. Lower F_c and R_a values are important from the point of view of energy consumption and product quality. Therefore, the "lower-the-better" equation was used for the calculation of the S/N ratio. The test results of the F_c and R_a and the corresponding S/N ratios are given in **Table 5**. The averages of the F_c and R_a values obtained from the experimental study were calculated as 447.67 N and 1.97 μm, respectively.

The S/N response table was used for the analysis of the effects of the control factors (Ct, V, f and ap) on the F_c and R_a. The S/N response table for F_c and R_a is given in **Table 6**. The highest S/N ratios in the table show the optimum levels. A graphical representation of variations in the S/N ratios depending on the F_c and R_a control factors is given in **Figures 4** and **5**. The optimum levels for F_c and R_a were determined as A2B3C1D1 and A2B2C1D1, respectively. Thus, the optimum cutting-force value was obtained at 250 m/min cutting speed, 0.1 mm/rev feed rate and 0.5 mm cutting depth using the

Table 5: Experimental results and S/N ratios values

Tabela 5: Rezultati eksperimentov in vrednosti razmerja S/N

Exp. No.	Control factors				Cutting force, F _c (N)	S/N ratio for F _c (dB)	Surface roughness, R _a (μm)	S/N ratio for R _a (dB)
	A Cutting tool (Ct)	B Cutting speed (V)	C Feed rate (f)	D Depth of cut (ap)				
1	PVD	150	0.1	0.5	195	-45.80	0.71	2.97
2	PVD	150	0.2	1.0	452	-53.10	1.99	-5.98
3	PVD	150	0.3	1.5	927	-59.34	3.97	-11.98
4	PVD	200	0.1	0.5	183	-45.25	0.42	7.54
5	PVD	200	0.2	1.0	460	-53.26	1.51	-3.58
6	PVD	200	0.3	1.5	912	-59.20	3.48	-10.83
7	PVD	250	0.1	1.0	308	-49.77	1.89	-5.53
8	PVD	250	0.2	1.5	627	-55.95	1.94	-5.76
9	PVD	250	0.3	0.5	357	-51.05	3.22	-10.16
10	CVD	150	0.1	1.5	411	-52.28	1.06	-0.51
11	CVD	150	0.2	0.5	273	-48.72	1.67	-4.44
12	CVD	150	0.3	1.0	656	-56.34	3.86	-11.73
13	CVD	200	0.1	1.0	277	-48.85	0.61	4.29
14	CVD	200	0.2	1.5	687	-56.74	1.53	-3.69
15	CVD	200	0.3	0.5	356	-51.03	3.08	-9.77
16	CVD	250	0.1	1.5	397	-51.98	0.57	4.88
17	CVD	250	0.2	0.5	268	-48.56	0.88	1.11
18	CVD	250	0.3	1.0	312	-49.88	3.12	-9.88

T_{Fc} (cutting force total mean value) = 447.67 N

T_{Fc-S/N} (cutting force S/N ratio total mean value) = -52.06 dB

T_{Ra} (surface roughness total mean value) = 1.97 μm

T_{Ra-S/N} (surface roughness S/N ratio total mean value) = -4.06 dB

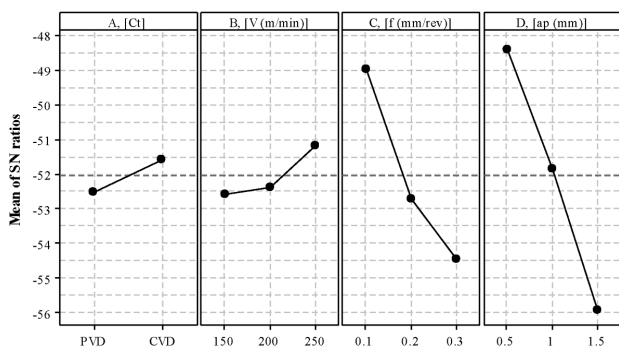


Figure 4: S/N graph for cutting force

Slika 4: S/N diagram za silo rezanja

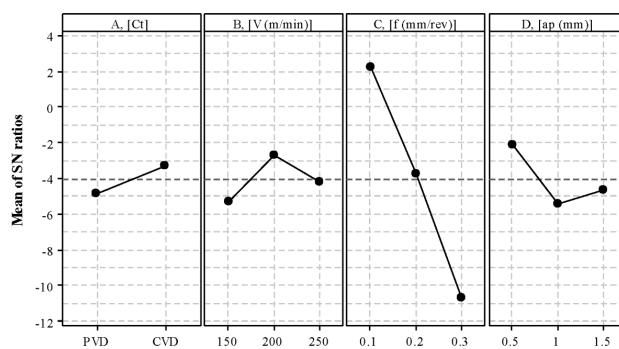


Figure 5: S/N graph for surface roughness

Slika 5: S/N diagram za hrapavost površine

Table 6: S/N response table for F_c and R_a control factors

Tabela 6: Tabela S/N odgovora za F_c in R_a kontrolna faktorja

Levels	Cutting force (F_c)				Surface roughness (R_a)			
	A	B	C	D	A	B	C	D
Level 1	-52.52	-52.60	-48.99	-48.40	-4.811	-5.276	2.275	-2.125
Level 2	-51.60	-52.39	-52.72	-51.87	-3.304	-2.675	-3.723	-5.400
Level 3	-	-51.20	-54.47	-55.91	-	-4.222	-10.724	-4.647
Delta	0.93	1.40	5.49	7.51	1.506	2.601	12.999	3.275

CVD-coated tool, whereas the optimum R_a was obtained at 200 m/min cutting speed, 0.1 mm/rev feed rate and 0.5 mm cutting depth, also by using the CVD-coated tool.

Table 7: Results of ANOVA for cutting force and surface roughness

Tabela 7: Rezultati ANOVA za silo rezanja in hrapavost površine

Variance source	Degree of freedom (DoF)	Sum of squares (SS)	Mean square (MS)	F ratio	Contribution rate (%)
F_c					
A	1	34148	34148	5.33	3.96
B	2	43599	21799	3.40	5.05
C	2	256557	128278	20.01	29.74
D	2	464230	232115	36.21	53.82
Error	10	64098	6410	-	7.43
Total	17	862632	-	-	100
R_a					
A	1	0.4214	0.4214	3.78	1.74
B	2	0.5862	0.2931	2.63	2.41
C	2	21.2808	10.6404	95.38	87.64
D	2	0.8777	0.4388	3.93	3.61
Error	10	1.1156	0.1116	-	4.59
Total	17	24.2816	-	-	100

ANOVA was used for the purpose of determining the effects of the control factors (Ct, V, f and ap) of the experimental design on F_c and R_a . The ANOVA analysis was performed with a 5 % significance level and 95 % confidence level. The ANOVA results for the F_c and R_a are shown in Table 7. In the determination of the significance levels of the control parameters, F ratio values were used, and from this, the contribution ratios of the machining parameters were calculated. The most effective factor on the F_c was revealed to be the depth of cut (factor D) with a 53.82 % contribution ratio, whereas on

the R_a , the most effective factor was the feed rate (factor C) with a contribution ratio of 87.64 %. Figure 6 shows the percentage contributions of the control factors on F_c and R_a . The error percentages were extremely low at 7.43 % and 4.59 %, respectively, for F_c and R_a .

3.2 Evaluation of the experimental results

The variations in the cutting forces obtained during the experimental study for precipitation-hardened 15-5 PH steel are given in the graphs of Figure 7. The cutting force exhibited a slight decrease with the increasing cutting speed. It is thought that the increasing cutting speed caused a decrease in the tool-chip contact area, resulting in a decrease in the cutting forces.²⁵ From the point of obtaining lower cutting force values, the CVD TiCN-Al₂O₃-TiN-coated tool showed some advantage over the PVD TiAlN-AlCrO-coated tool (Figure 7a). Cutting depth and feed rate had a significant effect on the cutting force (Figure 7b). Increase in the feed rate and

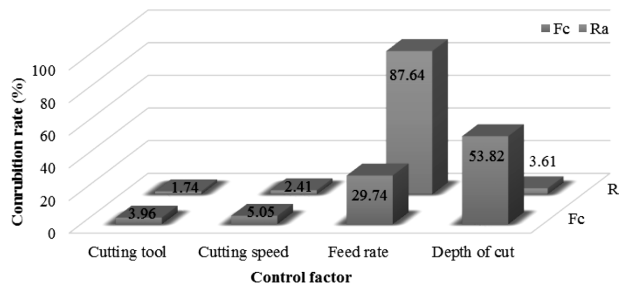


Figure 6: Percentage contribution of the control factors for cutting force and surface roughness

Slika 6: Prispevek kontrolnih faktorjev v odstotkih na silo rezanja in hrapavost površine

Š. ČETIN, T. KIVAK: OPTIMIZATION OF THE MACHINING PARAMETERS FOR THE TURNING ...

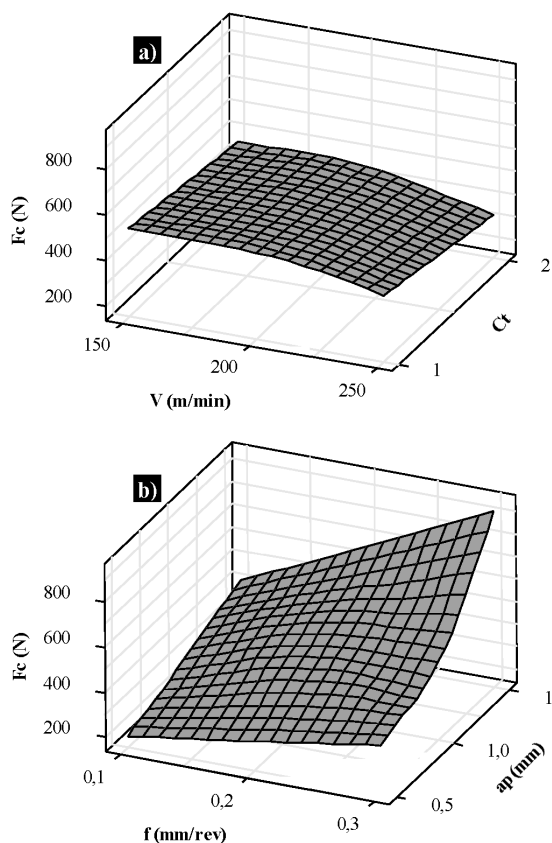


Figure 7: Effect of cutting parameters on cutting force: a) cutting speed and cutting tool, b) feed rate and depth of cut
Slika 7: Vpliv parametrov rezanja na silo rezanja: a) hitrost rezanja in rezilno orodje, b) hitrost podajanja in globina rezanja

depth of cut values increased the cutting force considerably. After precipitation hardening, the hardness of the material reached a value of 42 HRC and its resistance was increased against the penetration of the cutting tool. In addition to the increase in hardness, the martensite formation in the material structure following the heat treatment played an important role in the increasing cutting forces. Consequently, with the increase in F_c , the cutting depth was more effective than the feed rate.

The variations in surface roughness obtained in the experimental study for precipitation-hardened 15-5 PH steel are given in the graphs of **Figure 8**. Especially in the tests made with the CVD-coated tool, the R_a values decreased with increasing cutting speed. Although the application of different coatings had no effect on surface roughness, lower and R_a values were obtained with the CVD-coated tool. At a feed rate of 0.2 and 0.3 mm/r, increasing cutting depth caused the R_a values to increase (**Figure 8b**). Therefore, it is possible to say that among the parameters tested, the feed rate was the most effective parameter on the R_a . Since the R_a is a function of the feed rate, the increased values increased the R_a significantly. Moreover, the results of variance analysis also verified that feed rate, with a contribution rate of 87.64 %, was the most effective parameter on R_a . The cutting speed increasing in a way parallel to the cutting forces

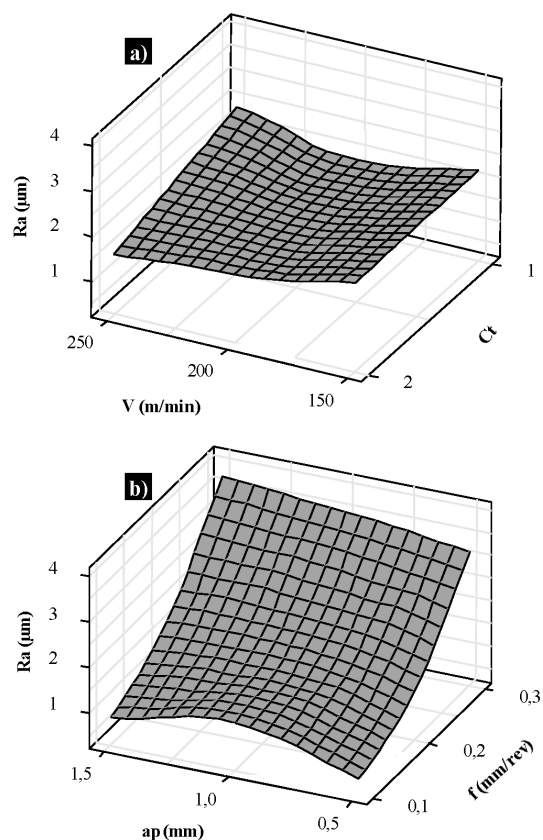


Figure 8: Effect of cutting parameters on surface roughness: a) cutting speed and cutting tool, b) feed rate and depth of cut
Slika 8: Vpliv parametrov rezanja na hrapavost površine: a) hitrost rezanja in rezilno orodje, b) hitrost podajanja in globina rezanja

caused a decrease in the R_a values. Furthermore, the increasing cutting depth, especially at higher feed rates, caused the R_a values to increase slightly. As was the case with the cutting forces, with the surface roughness, the CVD TiCN-Al₂O₃-TiN-coated tool also displayed some advantage over the PVD TiAlN-AlCrO-coated tool. This can be explained by the lower frictional coefficient of the TiN coating on the uppermost layer of the CVD coating.

3.3 Empirical models and prediction performance

For the purpose of defining the relationship between one dependent variable and one or more independent variables, regression analysis was used.²⁶ In this study, dependent variables were defined as F_c and R_a , whereas the independent variables were specified as the cutting tool, cutting speed, feed rate and cutting depth. Estimation equations for F_c and R_a were established for linear and quadratic regression models separately. The estimation equations obtained for the linear-regression model of F_c and R_a are given in Equations (2) and (3), whereas the estimation equations obtained for the quadratic regression model are given in Equations (4) and (5).

$$F_{c_i} = 113.667 - 871111Ct - 1.075V + 14575f + 388.167ap \quad (2)$$

$$\begin{aligned}
 R-Sq &= 89,93 \% \quad R-Sq(adj) = 86,83 \% \\
 Ra_1 &= -0.0297778 - 0.306Ct - \\
 &- 0.00272667V + 12.89f + 0.428667ap
 \end{aligned} \quad (3)$$

$$\begin{aligned}
 R-Sq &= 87,04 \% \quad R-Sq(adj) = 83,05 \% \\
 FC_q &= -1098.02 + 142.084Ct + 9.25331V + 4854.61f - \\
 &348.127ap - 0.857436CtV - 330.082Ctf + 47.4709Ctap - \\
 &0.0130256VV - 14.1955Vf - 0.699091Vap - \\
 &3055.32ff + 1174.87fap + 258.969apap
 \end{aligned} \quad (4)$$

$$\begin{aligned}
 R-Sq &= 98.11 \% \quad R-Sq(adj) = 91.97 \% \\
 Ra_q &= 2.20536 + 0.939478Ct + 0.0300324V + \\
 &+ 8.99345f - 3.17844ap - 0.00727744CtV - 2.5756Ctf + \\
 &+ 0.352393Ctap - 0.000113441VV - 0.0278727Vf - \\
 &- 0.00193455Vap - 61.1292ff + 1.41846fap + \\
 &+ 0.74574apap
 \end{aligned} \quad (5)$$

$$R-Sq = 98.79 \% \quad R-Sq(adj) = 94.87 \%$$

The correlation coefficient (R^2) of the equations obtained with the linear-regression model for F_c and R_a were calculated as 89.93 % and 87.04 %, respectively. These values were calculated for the quadratic regression model as 98.11 % and 98.79 %. When compared with

the linear-regression model, it can be seen that more accurate estimations can be made using the quadratic regression model. **Figure 9** gives the comparison of the Taguchi method with regression models for the estimation of F_c and R_a . From the figure it is clear that for both F_c and R_a , the closest values to the line were obtained with the quadratic regression model, followed by the values obtained by the Taguchi method and the linear regression model. Thus, it is possible to apply the quadratic regression model successfully for the estimation of F_c and R_a .

4 CONCLUSION

This study was focused on the optimization (via the Taguchi method) of machining parameters, which included cutting tool, cutting speed, feed rate and cutting depth affecting cutting force and surface roughness in the turning of 15-5 PH martensitic stainless steel. Analytical models were developed using regression analysis for the estimation of F_c and R_a . The results are summarized as follows:

The optimum levels of the control factors for minimizing F_c and R_a were defined by using signal-to-noise ratios. The optimum control factors for cutting force (A2B3C1D1) were determined as a CVD-coated cutting tool, a cutting speed of 250 m/min, a feed rate of 0.1 mm/r and a depth of cut of 0.5 mm, while the optimum control factors for surface roughness (A2B2C1D1) were determined as a CVD-coated cutting tool, a cutting speed of 200 m/min, a feed rate of 0.1 mm/r and a depth of cut of 0.5 mm.

The ANOVA analysis revealed that the depth of cut was the most dominant parameter on F_c with the contribution ratio of 53.82 %, and that the feed rate was the most dominant parameter on R_a with the contribution ratio of 87.64 %.

The R^2 values of the equations obtained by the linear-regression model for the cutting force and surface roughness were calculated as 89.93 % and 87.04 %, respectively. These values were found to be 98.11 % and 98.79 % for the quadratic regression model. The higher correlation coefficients showed that the models had a good estimation ability. Consequently, from the point of view of estimation performances, the best result was obtained with the quadratic regression model, followed by the Taguchi method and the linear regression model, accordingly.

From the point of view of obtaining lower cutting force and lower surface roughness, the CVD TiCN-Al₂O₃-TiN-coated tool exhibited some advantage over the PVD TiAlN-AlCrO-coated tool.

In conclusion, in the turning of precipitation-hardened 15-5 PH stainless steel, the Taguchi method can be used successfully to decrease energy consumption and to increase product quality.

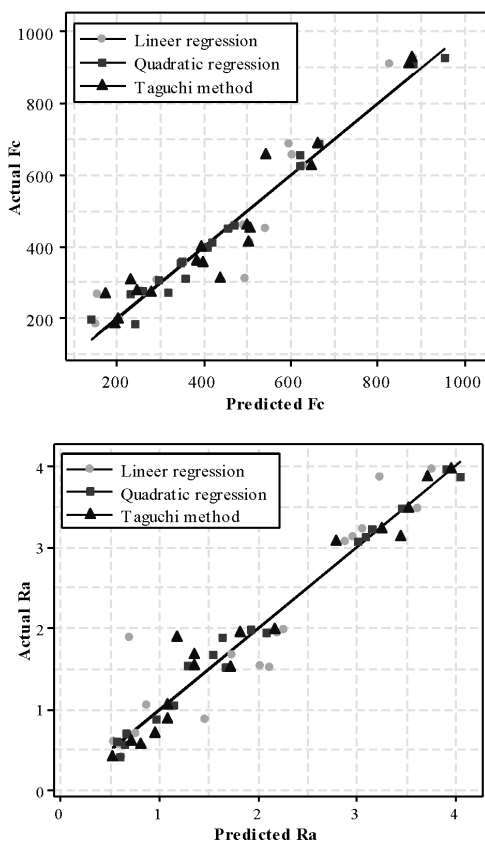


Figure 9: Comparisons of actual predicted values for: a) cutting force and b) surface roughness

Slika 9: Primerjave dobljenih-napovedanih vrednosti za: a) silo rezanja in b) hrapavost površine

Acknowledgment

The authors wish to place their sincere thanks to Düzce University Scientific Research Project Division for financial support for the Project No: BAP 2014.07.04.217

5 REFERENCES

- ¹ M. Aghaie-Khafri, F. Adhami, Hot deformation of 15-5 PH stainless steel, *Mater. Sci. Eng. A*, 527 (2010), 1052–1057, doi:10.1016/j.msea.2009.09.032
- ² A. Mondelin, F. Valiorgue, J. Rech, M. Coret, E. Feulvarch, Hybrid model for the prediction of residual stresses induced by 15-5PH steel turning, *Int. J. Mech. Sci.*, 58 (2012), 69–85, doi:10.1016/j.ijmecsci.2012.03.003
- ³ A. Kumar, Y. Balaji, N. Eswara, P. Rasad, G. Gouda, K. Tamilmani, Indigenous development and airworthiness certification of 15–5 PH precipitation hardenable stainless steel for aircraft applications, *Indian Academy of Sciences, Sadhana*, 38 (2013), 3–23
- ⁴ F. Danoix, J. Lacaze, A. Gibert, D. Mangelinck, K. Houmadaf, E. Andrieu, Effect of external stress on the Fe–Cr phase separation in 15-5 PH and Fe–15Cr–5Ni alloys, *Ultramicroscopy*, 132 (2013) 193–198, doi:10.1016/j.ultramic.2012.12.004
- ⁵ H. R. Habibi Bajguirani, The effect of ageing upon the microstructure and mechanical properties of type 15-5 PH stainless steel, *Mater. Sci. Eng. A*, 338 (2002), 142–159, doi:10.1016/S0921-5093(02)00062-X
- ⁶ H. Shao, L. Liu, H. L. Qu, Machinability study on 3%Co–12%Cr stainless steel in milling, *Wear*, 263 (2007), 736–744, doi:10.1016/j.wear.2007.01.074
- ⁷ M. Sarikaya, A. Güllü, Multi-response optimization of minimum quantity lubrication parameters using Taguchi-based grey relational analysis in turning of difficult-to-cut alloy Haynes 25, *J. Cleaner Prod.*, 91 (2015), 347–357, doi:10.1016/j.jclepro.2014.12.020
- ⁸ T. Kivak, Optimization of surface roughness and flank wear using the Taguchi method in milling of Hadfield steel with PVD and CVD coated inserts, *Measurement*, 50 (2014), 19–28, doi:10.1016/j.measurement.2013.12.017
- ⁹ M. A. Xavior, M. Adithan, Determining the influence of cutting fluids on tool wear and surface roughness during turning of AISI 304 austenitic stainless steel, *J. Mat. Process. Technol.*, 209 (2009), 900–909, doi:10.1016/j.jmatprotec.2008.02.068
- ¹⁰ A. J. Makadia, J. I. Nanavati, Optimisation of machining parameters for turning operations based on response surface methodology, *Measurement*, 46 (2013), 1521–1529, doi:10.1016/j.measurement.2012.11.026
- ¹¹ M. C. Çakır, Principles of modern metal cutting. Vipaş A.Ş, Bursa, Turkey, (2000), 350–390
- ¹² B. de Agustina, C. Bernal, A. M. Camacho, E. M. Rubio, Experimental Analysis of the Cutting Forces Obtained in Dry Turning Processes of UNS A97075 Aluminium Alloys, *Procedia Engineering*, 63 (2013), 694–699, The Manufacturing Engineering Society International Conference, MESIC 2013, doi:10.1016/j.proeng.2013.08.248
- ¹³ Y. Karpat, T. Özel, Multi-objective optimization for turning processes using neural network modeling and dynamic-neighborhood particle swarm optimization, *Int. J. Adv. Manuf. Technol.*, 35 (2008), 234–247, doi:10.1007/s00170-006-0719-8
- ¹⁴ A. Çiçek, T. Kivak, G. Samtaş, Y. Çay, Modelling of Thrust Forces in Drilling of AISI 316 Stainless Steel Using Artificial Neural Network and Multiple Regression Analysis, *Strojniški vestnik – Journal of Mechanical Engineering* 58 (7-8) (2012), 492–498, doi:10.5545/sv-jme.2011.297
- ¹⁵ İ. Asiltürk, S. Neşeli, Multi response optimisation of CNC turning parameters via Taguchi method-based response surface analysis, *Measurement* 45 (2012), 785–794, doi:10.1016/j.measurement.2011.12.004
- ¹⁶ M. Günay, E. Yücel, Application of Taguchi method for determining optimum surface roughness in turning of high-alloy white cast iron, *Measurement*, 46 (2013), 913–919, doi:10.1016/j.measurement.2012.10.013
- ¹⁷ D. P. Selvaraj, P. Chandramohan, M. Mohanraj, Optimization of surface roughness, cutting force and tool wear of nitrogen alloyed duplex stainless steel in a dry turning process using Taguchi method, *Measurement*, 49 (2014), 205–215, doi:10.1016/j.measurement.2013.11.037
- ¹⁸ C. Camposeco-Negrete, Optimization of cutting parameters for minimizing energy consumption in turning of AISI 6061 T6 using Taguchi methodology and ANOVA, *J. Cleaner Prod.*, 53 (2013), 195–203, doi:10.1016/j.jclepro.2013.03.049
- ¹⁹ C. Ezilarasan, V. S. Senthil Kumar, A. Velayudham, An experimental analysis and measurement of process performances in machining of nimonic C-263 super alloy, *Measurement*, 46 (2013), 185–199, doi:10.1016/j.measurement.2012.06.006
- ²⁰ A. Haşçalık, U. Çaydaş, Optimization of turning parameters for surface roughness and tool life based on the Taguchi method, *Int. J. Adv. Manuf. Technol.*, 38 (2008), 896–903, doi:10.1007/s00170-007-1147-0
- ²¹ U. Yalcin, A. D. Karaoglan, I. Korkut, Optimization of cutting parameters in face milling with neural networks and Taguchi based on cutting force, surface roughness and temperatures, *Int. J. Prod. Res.*, 51 (2013), 3404–3414, doi:10.1080/00207543.2013.774482
- ²² İ. Asiltürk, H. Akkuş, Determining the effect of cutting parameters on surface roughness in hard turning using the Taguchi method, *Measurement* 44 (2011), 1697–1704, doi:10.1016/j.measurement.2011.07.003
- ²³ Ş. Karabulut, Optimization of surface roughness and cutting force during AA7039/Al₂O₃ metal matrix composites milling using neural networks and Taguchi method, *Measurement* 66, (2015), 139–149, doi:10.1016/j.measurement.2015.01.027
- ²⁴ M. Sarikaya, Optimization of the surface roughness by applying the Taguchi technique for the turning of stainless steel under cooling conditions, *Materials and Technology*, 49 (6) (2015), 941–948, doi:10.17222/mit.2014.282
- ²⁵ A. Çiçek, F. Kara, T. Kivak, E. Ekici, Evaluation of machinability of hardened and cryo-treated AISI H13 hot work tool steel with ceramic inserts, *International Journal of Refractory Metals and Hard Materials*, 41 (2013), 461–469, doi:10.1016/j.ijrmhm.2013.06.004
- ²⁶ M. H. Cetin, B. Özcelik, E. Kuram, E. Demirbaş, Evaluation of vegetable based cutting fluids with extreme pressure and cutting parameters in turning of AISI 304L by Taguchi method, *J. Cleaner Prod.*, 19 (2011), 2049–2056, doi:10.1016/j.jclepro.2011.07.013

POWDER-METALLURGY PREPARATION OF NiTi SHAPE-MEMORY ALLOY USING MECHANICAL ALLOYING AND SPARK-PLASMA SINTERING

UPORABA METALURGIJE PRAHOV ZA PRIPRAVO NiTi ZLITINE S SPOMINOM S POMOČJO MEHANSKEGA LEGIRANJA IN SINTRANJA Z ISKRILNO PLAZMO

**Pavel Novák¹, Hynek Moravec¹, Vladimír Vojtěch¹, Anna Knaislová¹,
Andrea Školáková¹, Tomáš František Kubatík², Jaromír Kopeček³**

¹Institute of Chemical Technology, Department of Metals and Corrosion Engineering, Technická 5, 166 28 Prague 6, Czech Republic

²Institute of Plasma Physics AS CR, v.v.i., Za Slovankou 3, 182 00 Prague 8, Czech Republic

³Institute of Physics of the ASCR, v. v. i., Na Slovance 2, 182 21 Prague 8, Czech Republic
panovak@vscht.cz

Prejem rokopisa – received: 2016-01-13; sprejem za objavo – accepted for publication: 2016-02-02

doi:10.17222/mit.2016.011

In this work a combination of mechanical alloying and spark-plasma sintering was tested as a promising route for the preparation of a nanocrystalline NiTi shape-memory alloy. The mechanism of mechanical alloying was investigated. Results revealed that the Ti₂Ni phase forms preferentially, being followed by the NiTi phase (austenite B2 structure) and a small amount of Ni₃Ti. During spark-plasma sintering, only minor changes occurred in the phase composition, i.e., precipitation of the Ni₄Ti₃ phase and the partial transformation of NiTi to monoclinic martensite. The selected technology leads to a very high compression strength (approx. 2300 MPa), but also high brittleness.

Keywords: mechanical alloying, spark plasma sintering, NiTi, shape memory alloy

V delu je bila preizkušena kombinacija mehanskega legiranja in sintranja z iskrilno plazmo, ki predstavlja obetajoč način za pripravo nanokristalne NiTi spominske zlitine. Preiskovan je bil mehanizem mehanskega legiranja. Rezultati so odkrili, da se najprej tvori faza Ti₂Ni, ki ji sledi faza NiTi (avstenitna B2 struktura) in manjši delež Ni₃Ti. Med sintranjem z iskrilno plazmo se pojavijo le manjše razlike v sestavi faz, to je izločanje faze Ni₄Ti₃ in delna pretvorba NiTi v monoklinski martenzit. Izbrana tehnologija povzroči veliko tlačno trdnost (okoli 2300 MPa) in tudi veliko krhkost materiala.

Ključne besede: mehansko legiranje, sintranje z iskrilno plazmo, NiTi, zlitina z oblikovnim spominom

1 INTRODUCTION

The approximately equimolar Ni-Ti alloy, called nitinol, is the most widely used shape-memory alloy. The shape-memory effect in this alloy is connected with the transformation between high-temperature cubic austenite (B2 structure) and low-temperature monoclinic martensite (B19' structure).¹ Due to its exceptional properties, the NiTi alloy is applied in both medical (dental implants, stents, scaffolds)² and technical applications (actuators, robotics, etc.).³

As an alternative to conventional production methods for the NiTi alloy (vacuum induction melting and vacuum arc remelting), powder-metallurgy processes starting from pre-alloyed NiTi powder have been developed.⁴

An alternative powder-metallurgy process for the production of ceramics or intermetallics is reaction synthesis. In this process, the compressed mixture of elemental powders is transformed to intermetallic, thermally activated exothermic reactions. During the reactions, the heat is generated, which sustains and propagates the reaction through the body of the reactants. Therefore, the process is called self-propagating

high-temperature synthesis (SHS).⁵ Mechanical alloying is one of the techniques used for the production of nanostructured powders.⁶ Mechanical alloying is in fact high-energy ball milling. In this process, the high kinetic energy of balls causes the following phenomena: crushing of particles leading to the reduction of the particle size, local welding of particles by plastic deformation, friction forces and diffusion, structure refinement due to enormous plastic deformation and the formation of solid solutions and chemical compounds (intermetallics).⁶

Spark-plasma sintering (SPS) is the modern compaction method, which uses uniaxial pressing accompanied by the passage of the electric current through the sample. It causes rapid heating of the sample and discharges between powder particles that can cause local welding of the particles. Due to the high sintering rate during SPS this method is highly suitable for the compaction of nanocrystalline materials and phases with a lower thermal stability.⁶

In our previous paper⁶, we developed a novel mechanical alloying process that allows for the formation of intermetallics in a much shorter time than in previously published papers.⁷ In this work, this improved mecha-

nical-alloying process on NiTi shape-memory phase synthesis is studied. The combination of this process with spark-plasma sintering for the production of a NiTi shape memory alloy was tested.

2 EXPERIMENTAL PART

In this work, the material based on the NiTi shape memory phase was prepared from elemental powders by mechanical alloying and subsequent spark-plasma sintering (SPS) compaction. The mechanical alloying was carried out in a planetary ball mill (Retsch PM 100 CM) under the following conditions, optimized in our previous paper dealing with the synthesis of intermetallics:⁶

- milling duration: 15–360 min,
- change of rotation direction each 15 min,
- rotation speed: 400 min⁻¹,
- atmosphere: argon
- powder batch: 5 g
- ball-to-powder weight ratio: 70:1.

The powder mixtures for milling contained 54 % Ni and % Ti (by weight). This composition corresponds to the equimolar NiTi phase.⁸ Milled powders were examined by X-ray diffraction analysis (PANalytical X'Pert Pro diffractometer, Cu K_{α} radiation with the wavelength of 0.154060 nm) in order to identify the phase composition. The XRD patterns were evaluated using PANalytical HighScore software with the PDF-2 database. XRD patterns were also quantitatively processed using the Rietveld method. Metallographic samples were prepared from selected powders. The microstructure of powder samples was studied after etching by modified Kroll's reagent (10 mL HNO₃, 5 mL HF, 85 mL H₂O). Individual phases in the powders were identified on metallographic samples by chemical microanalysis using TESCAN VEGA 3 LMU scanning electron microscope equipped with OXFORD Instruments X-max EDS SDD 20 mm² detector (SEM-EDS).

Powder prepared under selected conditions (milling duration of 2 h) was compacted by SPS at the Institute of Plasma Physics AS CR. The weight of the batch for sintering was 5 g. Compaction was carried out using a Thermal Technology SPS 10-4 device using a pressure of 70 MPa for 5 min at various process temperatures with a heating rate of 300 K/min. The phase composition of the prepared compact samples was determined by XRD. The porosity of compact samples was studied on polished metallographic samples by image analysis using Lucia 4.8 image analyser. The mechanical properties of the SPS-consolidated material were tested in compression using LabTest 5.250SP1-VM universal loading machine (produced by LaborTech).

3 RESULTS

The dependence of phase composition of the powders obtained by mechanical alloying on process duration is

presented in **Figure 1**. During this experiment, a constant rotational velocity of 400 rpm and a ball-to-powder ratio of 70:1 were applied. After 15 min of mechanical alloying, a small amount of Ti₂Ni phase was formed. In addition to this phase, the obtained powder contained only unreacted initial powders of nickel and titanium. After prolongation of the mechanical alloying process to 30–60 min, the Ti₂Ni phase still dominated the phase composition and the NiTi phase arose in the XRD patterns. Residual nickel is still present in the powder mixture. Mechanical alloying for 120 min produced a powder composed of NiTi (austenite structure) and Ti₂Ni phases (**Figure 1**). When prolonging the mechanical alloying to 360 min, the Ti₂Ni still remains in the powder mixture and the new Fe₂Ti phase arises as a result of the contamination by milling in an iron-based vessel (**Figure 1**). Therefore, long-term milling cannot be recommended in this system and experimental setup.

The development of the microstructure of the powders during the milling process is shown in **Figure 2**. A short milling duration (15 min) results in the lamellar structure containing deformed nickel and titanium particles, which are mechanically bonded (**Figure 2a**). On the interface between these particles, the layers and/or fragmented particles of Ti₂Ni and traces of NiTi start to form. Prolonging the duration of milling to 30–45 leads to the disappearing of titanium particles (**Figure 2b**). The milling duration of 120 min creates the structure composed of NiTi matrix with dispersed Ti₂Ni particles (**Figure 2c**).

During spark-plasma sintering consolidation of the material, new phases precipitated from the mechanically

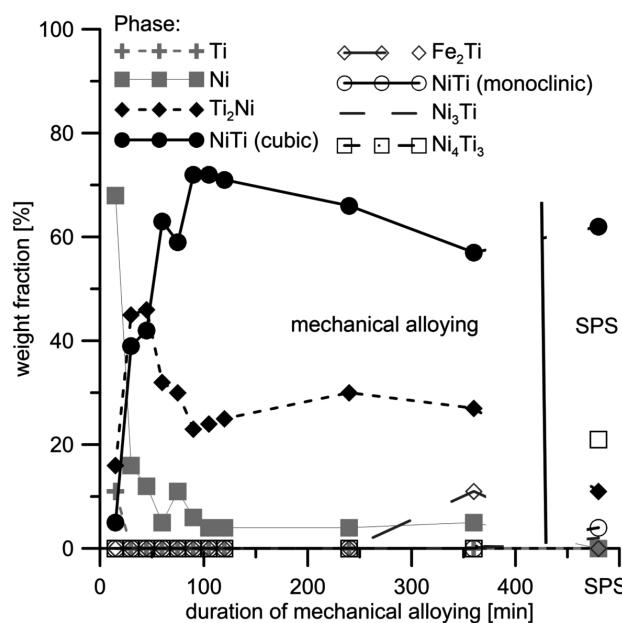


Figure 1: Amounts of phases in milled powders and SPS-consolidated sample (determined by XRD and Rietveld refinement)

Slika 1: Količine faz v mletem prahu in vzorcu, konsolidiranem z SPS (določeno z XRD in Rietveld metodo)

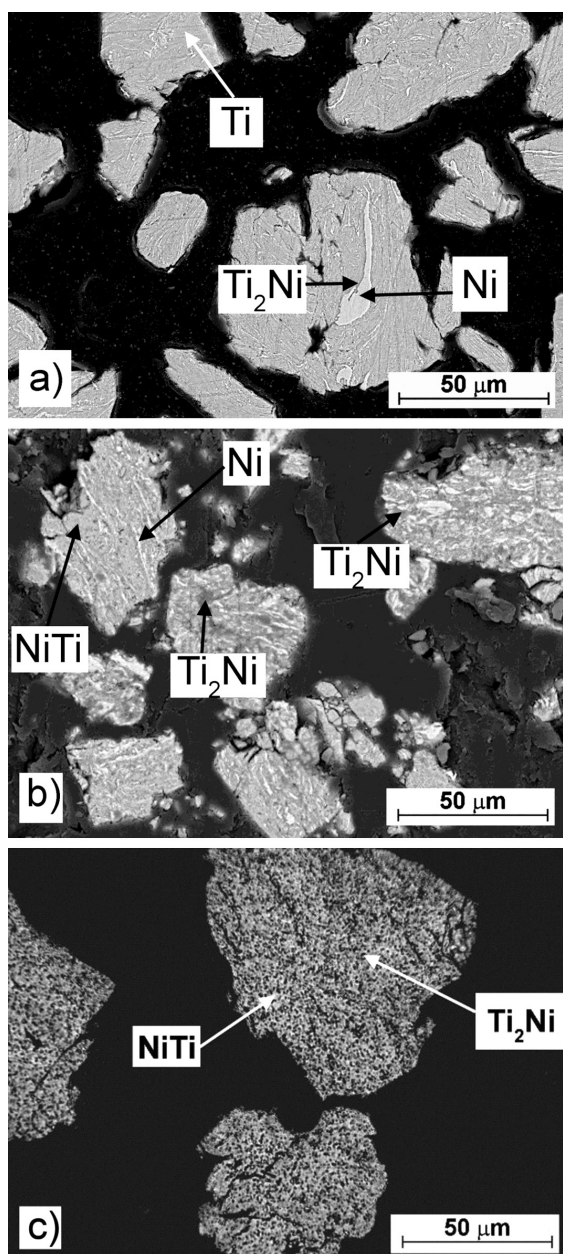


Figure 2: Microstructure of NiTi50 (in amount fractions, at%) alloy powder prepared by mechanical alloying for: a) 15 min, b) 45 min, c) 120 min

Slika 2: Mikrostruktura prahu zlitine NiTi50 (v volumskih deležih, at%), pripravljene z mehanskim legiranjem, a) 15 min, b) 45 min, c) 120 min

alloyed material, i.e., the Ni_4Ti_3 and Ni_3Ti intermetallic phases (**Figure 1**). Most probably, the Ni_4Ti_3 is a result of thermal exposure and compressive stress and Ni_3Ti originates from the reaction of residual nickel with NiTi phase. In addition, the NiTi phase was found in two crystal modifications: the monoclinic and B2 cubic phase. The product of spark-plasma sintering contains only a low amount of pores (below 1 vol. %, **Figure 3**).

The compressive strength of the mechanically alloyed and consolidated NiTi material reaches 2200 ± 90 MPa. However, the material exhibits almost brittle



Figure 3: Microstructure of the NiTi alloy prepared by mechanical alloying for 120 min and spark-plasma sintering at 900 °C with a heating rate of 300 °C min^{-1}

Slika 3: Mikrostruktura zlitine NiTi, pripravljene z mehanskim legiranjem 120 min in sintranjem z iskrilno plazmo pri 900 °C , s hitrostjo segrevanja 300 °C min^{-1}

behaviour (**Figure 4**), without the signs of the deformation-induced transformation of cubic austenite phase to monoclinic martensite. The reason probably lies in the strong deformation strengthening of the powder during milling. The material did not recover significantly during SPS consolidation due to the short time applied for sintering. Due to this fact, the material does not allow for plastic deformation during loading.

4 CONCLUSIONS

In this paper, the Ni-Ti phase evolution during ultra-high-energy short-term mechanical alloying was investi-

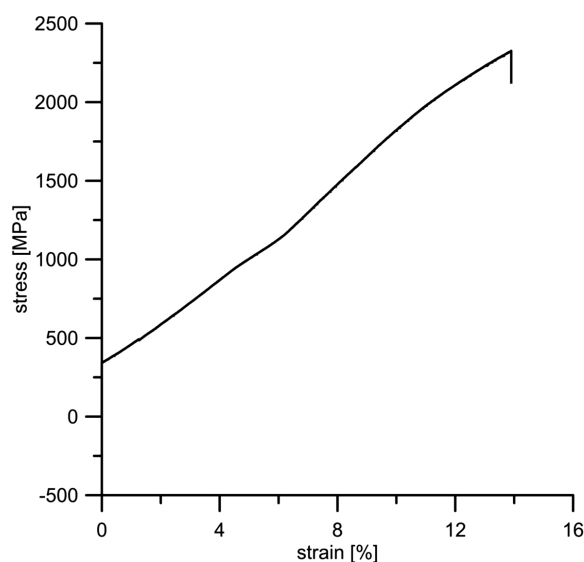


Figure 4: Stress-strain curve in compression of the NiTi alloy prepared by mechanical alloying for 120 min and spark-plasma sintering at 900 °C with a heating rate of 300 °C min^{-1}

Slika 4: Krivulja napetost-raztezek pri tlačnem preizkusu NiTi zlitine, pripravljene z mehanskim legiranjem 120 min in sintranjem z iskrilno plazmo pri 900 °C in hitrostjo segrevanja 300 °C min^{-1}

gated. In this technology, the Ti_2Ni phase forms preferentially, being followed by the NiTi shape-memory phase with an austenite (B2) structure. During spark-plasma sintering of the mechanically alloyed powder, the Ni_4Ti_3 , Ni_3Ti and monoclinic NiTi develop. Due to this fact, the formation of the undesirable Ti_2Ni phase cannot be avoided.

The samples achieve much higher mechanical properties than a NiTi alloy produced by conventional route, but they exhibit almost brittle behaviour. This can be caused by the change of deformation mechanism when going to nanoscale, or by trace contamination of the grain boundaries during the mechanical alloying process, lowering the cohesion of the grains.

Acknowledgement

This research was financially supported by the Czech Science Foundation, project No. 14-03044S.

5 REFERENCES

- ¹ M. Elahinia, M. Ahmadian, An enhanced SMA phenomenological model. Part I. The shortcomings of the existing models, *Smart Materials Structures*, 14 (2005), 1297–308, doi:10.1088/0964-1726/14/6/022
- ² D. Vojtěch, M. Voděrová, J. Kubásek, P. Novák, P. Šedá, A. Michalcová, J. Fojt, J. Hanuš, O. Mestek, Effects of short-time heat treatment and subsequent chemical surface treatment on the mechanical properties, low-cycle fatigue behavior and corrosion resistance of a Ni–Ti (50.9at.% Ni) biomedical alloy wire used for the manufacture of stents, *Materials Science and Engineering A*, 528 (2011), 1864–1876, doi:10.1016/j.msea.2010.10.043
- ³ M. Elahinia, H. Ashrafioun, Nonlinear control of a shape memory alloy actuated manipulator, *Journal of Vibration and Acoustics*, 124 (2002), 566–575, doi:10.1115/1.1501285
- ⁴ L. Krone, E. Schüller, M. Bram, O. Hamed, H.-P. Buchkremer, D. Stöver, Mechanical behaviour of NiTi parts prepared by powder metallurgical methods, *Materials Science and Engineering A*, 378 (2004), 185–190, doi:10.1016/j.msea.2003.10.345
- ⁵ P. Novák, A. Michalcová, J. Šerák, D. Vojtěch, T. Fabián, S. Randáková, F. Průša, V. Knotek, M. Novák, Preparation of Ti–Al–Si alloys by reactive sintering, *Journal of Alloys and Compounds*, 470 (2009), 123–126, doi:10.1016/j.jallcom.2008.02.046
- ⁶ P. Novák, T. Kubatík, J. Vystrčil, R. Hendrych, J. Kříž, J. Mlynár, D. Vojtěch, Powder metallurgy preparation of Al–Cu–Fe quasicrystals using mechanical alloying and Spark Plasma Sintering, *Intermetallics*, 52 (2014), 131–137, doi:10.1016/j.intermet.2014.04.003
- ⁷ T. Mousavi, F. Karimzadeh, M.H. Abbasi, Synthesis and characterization of nanocrystalline NiTi intermetallic by mechanical alloying, *Materials Science and Engineering A*, 487 (2008), 46–51, doi:10.1016/j.msea.2007.09.051
- ⁸ T. B. Massalski, *Binary Alloy Phase Diagrams*, ASM, Materials Park, 1990

LACUNARITY PROPERTIES OF NANOPHOTONIC MATERIALS
BASED ON POLY(METHYL METHACRYLATE) FOR CONTACT
LENSESRAZPOREDITEV PRAZNIN NANOFOTONIČNEGA MATERIALA
NA OSNOVI POLI(METIL METAKRILATA) ZA KONTAKTNE LEČEMarija Tomić¹, Božica Bojović², Dragomir Stamenković³, Ivana Mileusnić¹,
Djuro Koruga^{1,4}¹University of Belgrade, Faculty of Mechanical Engineering, Department of Biomedical Engineering, NanoLab,
Kraljice Marije 16, 11120 Belgrade, Serbia²University of Belgrade, Faculty of Mechanical Engineering, Department of Production Engineering,
Kraljice Marije 16, 11120 Belgrade, Serbia³Optix LLC, Oracka 13, 11070 Belgrade, Serbia⁴University for Peace established by the United Nations, Department of Biomedical Engineering and Nanomedicine,
ECPD, Terazije 41, 11000 Belgrade, Serbia
marija.m.tomic@gmail.com*Prejem rokopisa – received: 2016-01-17; sprejem za objavo – accepted for publication: 2016-02-05*

doi:10.17222/mit.2016.014

The aim was to develop new materials that would, after appropriate machining processes, improve the surface roughness and wettability of contact lenses. The samples used in this investigation were standard rigid gas-permeable (RGP) SOLEKO contact lenses, made of poly-MMA-co-siloxo silane methacrylate material (known under the commercial name SP40TM), and its modifications by adding three nanomaterials: fullerene C₆₀ (designated as SP40-A), fullerol C₆₀(OH)₂₄ (designated as SP40-B) and methformin hydroxylate fullerene C₆₀(OH)₁₂(OC₄N₅H₁₀)₁₂ (designated as SP40-C). Both atomic force microscopy (AFM) and magnetic force microscopy (MFM) were used to measure the topography and gradient of the magnetic field of the nanophotonic materials and the reference samples. According to the magnetic properties of all the materials yielded by MFM it can be concluded that adding fullerene and its derivatives certainly reduces the spectrum of the phase shifts angle by almost 50 %, which increases the paramagnetic characteristics of the nanophotonic material. The positive result of nanophotonic materials characterization is the fact that the roughness parameter values for all of these materials, are lower than those for the basic material. A surface lacunarity analysis, based on in-house procedures for determining the lacunarity value of contact lens surfaces, confirms the influence of surface topology on the tear film volume distribution and, consequently, the contact lens' surface lubrication. The presence of carbon nanomaterials, according to the surface roughness parameters, are improved for rigid gas-permeable (RGP) contact lenses made from nanophotonic polymer materials compared to those produced from the basic material.

Keywords: fullerenes, polymer materials, surface roughness, atomic force microscopy, magnetic force microscopy

Namen je bil razviti nov material, ki bi po ustrezni strojni obdelavi zmanjšal hrapavost površine in omočljivost kontaktnih leč. Vzorci, uporabljeni v tej raziskavi so bile standardne toge, za plin prepustne (RGP) SOLEKO kontaktne leče, narejene iz poli-MMA-ko-siloksi silan metakrilatnega materiala (s komercialnim imenom poznanega SP40TM) in njihove modifikacije z dodatkom treh nanomaterialov: fulerena C₆₀ (označenega kot SP40-A), fullerola C₆₀(OH)₂₄ (označenega z SP40-B) in metformin hidroksilat fulerena C₆₀(OH)₁₂(OC₄N₅H₁₀)₁₂ (označenega z SP40-C). Uporabljeni so bili: mikroskopija na atomsko silo (AFM), mikroskopija na magnetno silo (MFM) za merjenje topografije in gradient magnetnega polja nanofotonskih materialov in referenčnih vzorcev. Skladno z magnetnimi lastnostmi vseh materialov, dobljenih z MFM, je mogoče zaključiti, da dodajanje fulerenov in njegovih izpeljank, močno zmanjša spekter kotov faznega premika za skoraj 50 %, kar poveča paramagnetne značilnosti nanofotonskih materialov. Pozitivni rezultati karakterizacije nanofotonskih materialov so, da so vrednosti parametra hrapavosti pri vseh teh materialih nižje kot pri osnovnem materialu. Analiza površinske razporeditve praznin, na osnovi doma razvite tehnologije za določanje vrednosti razporeditve praznin na površini kontaktnih leč, je pokazala vpliv topologije površine na razporeditev plasti solz in posledično na mazanje površine kontaktnih leč. Prisotnost ogljikovih nanomaterialov je glede na parametre hrapavosti površine, izboljšala plinsko propustnost togih, za plin prepustnih (RGP) kontaktnih leč, izdelanih iz nanofotonskega polimernega materiala, v primerjavi s tistimi izdelanimi iz osnovnega materiala.

Ključne besede: fulereni, polimerni materiali, hrapavost površine, mikroskopija na atomsko silo, mikroskopija na magnetno silo

1 INTRODUCTION

The tear film is a liquid layer that covers the cornea and conjunctiva keeping the surface of the cornea smooth and making it optically clear. While blinking, the tear film lubricates the friction area between lids and ocular surface¹. The precorneal tear film thickness, which is related to dry eye and corneal integrity, is reported in range from 45 μm² to 3 μm.³⁻⁵ When a rigid

gas-permeable (RGP) contact lens is placed on the eye, the tear film is divided into two layers, the pre-lens and post-lens tear film. The importance of tear exchange behind an RGP contact lens remains an ongoing debate.⁶ Once a contact lens is inserted, the value of the precorneal tear film thickness doubles, resulting in a 2–5 μm thickness for pre and post lens tear films. Some authors⁷ determined the post lens tear film below 3 μm.

J. L. Creech et al.⁸ have concluded that tear film thickness is an important parameter that varies among individuals. The presence of any contact lens on the front surface of the eye influences and disturbs tear film stability. These changes in the tear film are caused by contact lens design, surface, material and applied solution for conditioning. The quality of a machined surface is determined by its roughness, which is described by the surface topography (i.e., the height differences between specific points of the surface), as well as by their exact position in regard to some reference area. The surface roughness of a contact lens has various implications, such as comfort, post lens tear film disruption and tear component deposition.

The aim is to test the response of a material's surface roughness quality to retain the tear film on the nano-level using a gliding-box method for lacunarity analysis. Surface lacunarity analysis is an innovative approach based on the work of B. Mandelbrot⁹, R. Voss¹⁰ and R. E. Plotnick¹¹. B. Mandelbrot introduced the term lacunarity from the Latin word 'lacuna', which is related to the English 'lake'.⁹ Lacunarity describes the degree of 'gappiness' of the fractal and is a complement to fractal dimension, because fractal dimension measures how much space is filled, whereas lacunarity measures how the fractal fills space. Intuitively, more and larger gaps give a higher lacunarity.¹² Although originally developed for further classification of fractals as a counterpart to the fractal dimension¹⁰, lacunarity application is more general, as presented and illustrated in R. E. Plotnick.¹¹ Lacunarity analysis is broadly applicable to many data sets used in natural sciences^{13,14}, as a very useful multi-scaled method for describing patterns of spatial dispersion. The fractal analysis can also be applied to biological samples such as microglia (the brain's immuno-inflammatory cell). This analysis may contribute significantly to the next steps forward in engineered tissues and 3D models in neuroscience.¹⁵

Taking these issues into account, the idea was to develop new contact lens materials that would, after an appropriate lathing and polishing process, improve the roughness parameters. There is a need for more precise measurements of the surface roughness as well as for detecting the physical properties of surfaces. To measure the topography and gradient of the magnetic field of nanophotonic materials, as well as of reference samples, both atomic force microscopy (AFM) and magnetic force microscopy (MFM) were used.

2 MATERIALS AND METHODS

2.1 Nanophotonic materials

New nanophotonic materials based on fullerene C₆₀ and its derivatives^{16–18} have been developed for the production of RGP contact lenses. Fullerenes and their derivatives show strong electron affinity, acting like 'radical sponges', and they easily enter addition reac-

tions with nucleophiles. One of the main disadvantages of fullerenes is their low solubility in water. In order to make them soluble, they have to be functionalized with polar groups such as –OH and –COOH. Of all the water-soluble fullerenes the most important are those with –OH groups attached, called fullerols or fullerlenols, (nano-C₆₀(OH)₂₄). These fullerene derivatives have shown promise as drug carriers to bypass the brain and ocular barriers and have been approved for use in nano-cosmetics, although fullerols have been found to be cytotoxic to HaCaT keratinocytes, a transformed epidermal human cell line and human dermal fibroblasts.¹⁹

The properties of C₆₀ can also be modified by its incorporation into polymers, making it a material that can be easily handled and produced. Combining both systems has led to a wide variety of new materials with appealing features based on the possibility of tuning their properties by modifying the chemical nature of the components or the chemical linkage between them.²⁰ The easiest method of incorporation of C₆₀ into a polymer is radical copolymerization, which can produce materials of widely varied fullerene content, but the degree of substitution of the fullerene is hard to control, and the structures are heterogeneous and hard to determine.²¹

The aforementioned nanomaterials were incorporated into the standard RGP SOLEKO™ material (Pontecorvo, Italy) known by the commercial name SP40™. This material belongs to the group of polymers known as poly-MMA-co-siloxy silane methacrylate, whose optical characteristics are given in **Table 1**. The polymerization was made separately on three samples by adding 1 g of each nanomaterial to the basic Soleko SP40™. Therefore, three new materials were produced, designated SP40-A (fullerene C₆₀), SP40-B (fullerol C₆₀(OH)₂₄) and SP40-C (methformin hydroxylate fullerene C₆₀(OH)₁₂(OC₄N₅H₁₀)₁₂). The percentage of nanomaterials in the solution was 0.33 % and although they were not completely dissolved in methylmethacrylate, the polymerization was homogeneous in all the samples. The fourth polymerization was conducted without nanomaterials so the regular Soleko SP40™ RGP material was used as a reference sample. The preparation of the samples was conducted at the Soleko, Italy laboratories. Each material was cut into a cylindrical sample of 12.8 mm diameter and 5.2 mm height. The samples were cut in a row from a rod produced by polymerization, providing optimal repeating. The contact lenses were manufactured by using a computer numerical control

Table 1: Optical characteristics of material SP40
Tabela 1: Optične značilnosti materiala SP40

Optical characteristics	Value	Test
Transmission in the visible part of the spectrum	>90 %	ISO 8599
Transmission in the UV part of the spectrum	<60 % (290–330 nm)	ISO 8599
Refractive index	1.472±0.003	ISO 9914

(CNC) lathe (Politech 1800 Aspheric-Toric) and polishing as a finishing process.

2.2 Atomic force microscopy and magnetic force microscopy

Both surfaces of the contact lens can be characterized by AFM, which allows the characterization of surface topography and surface roughness. AFM images are obtained by scanning a sharp probe across a surface while monitoring and compiling the tip-sample interactions to provide an image.²² The atomic force microscope used in this study was a JSPM-5200 (JEOL, Japan). MFM mode allows us to obtain the topography of the sample, but on the other hand provides information about the magnetic properties (magnetic gradient) of the material. In order to obtain both topography and magnetic gradient images, MFM operates in a so-called 'lift mode'.^{23,24} The lift mode or a two-pass technique is used to separate the effects of the magnetic and mechanical tip-sample forces.

The probe (cantilever) used in this study was produced by MikroMasch (Estonia) under the trade name NCS18/Co-Cr. The length of the cantilever is 230 μm , and a typical spring constant is 3.5 N/m. The tip curvature radius is 10 nm, but that is the radius of the uncoated tip. It is necessary to add a coating of ferromagnetic material to provide the magnetic field. This coating consists of a Co layer about 60 nm thick on the tip and backside of the probe. The Co coating is protected from oxidation by a 20-nm Cr layer. This leads to a total tip radius of 90 nm. All measurements were made at room temperature (around 23 $^{\circ}\text{C}$) under the atomic force microscope's glass bell to minimize the effects of temperature fluctuations. In phase imaging, the phase lag of the cantilever's oscillation relative to the drive signal is simultaneously monitored with topography data. Because the phase imaging highlights the edges and is not affected by large-scale height differences, it provides a clearer observation of the fine features, which can be obscured by rough topography.

The imaging area for RGP contact lenses was $2 \times 2 \mu\text{m}$, 256×256 pixels. Images obtained during the AFM/MFM scanning were analyzed using JEOL SPM Processing Software and WinSxM.²⁵ The parameters used for materials comparison are the height difference between the lowest and the highest point on the topography image (S_z) and the areal arithmetic mean deviation (S_a). Parameter S_a is calculated using Equation (1):²⁶

$$S_a = \frac{1}{S_0} \int_0^{x_{\max}} \int_0^{y_{\max}} |f(x, y) - Z_0| dx dy \quad (1)$$

where $f(x, y)$ is the function of surface asperities on the image in pixels denoted by (x, y) , S_0 is the image area and Z_0 is an average topography height. On the magnetic field gradient (phase images), relevant parameters are the maximum phase shift angle (α), minimum α and the entire spectrum of phase shift angles.

2.3 Lacunarity analysis

Based on the gliding box method proposed by R. Voss¹⁰ and R. E. Plotnick¹¹, the procedures for determining the lacunarity values of the contact lens surfaces were developed using Matlab software. All the necessary image processing was also performed in Matlab. First, the surface topography image was considered as a matrix filled by surface height in each pixel. Such a matrix represents an intensity image type with a grayscale map. Second, the maximum height is divided into 100 levels. Surface topography images are sliced on these levels by planes starting from the top and all the way down. For each section the pixels that belong to a surface are colored white and considered as binary 1. The rest of the surface image belongs to valleys, so they represent an empty space. Those pixels are colored black and are considered as binary 0.

This method considers the gliding box as a window systematically moving through the binary image. The gliding box could be moved either in a fixed scan or in an overlapping window sliding manner. Regardless of the sliding manner, the box mass value m is determined for each of the gliding boxes as a number of black pixels occupied by the gliding box. The gliding box size r is a variable and can take values of 2^n pixel length. According to R. E. Plotnick¹¹, lacunarity $L(r)$ is defined by Equation (2):

$$L(r) = \frac{M_2(r)}{M_1^2(r)} \quad (2)$$

where $M_1(r)$ and $M_2(r)$ are the first and second moments of the distribution of black pixels in the gliding box. The moments are defined by Equations (3) and (4):

$$M_1(r) = \sum_{m=1}^{r^2} m \cdot P(m, r) \quad (3)$$

$$M_2(r) = \sum_{m=1}^{r^2} m^2 \cdot P(m, r) \quad (4)$$

The probability $P(m, r)$ that the gliding box of size r contains m black pixels is defined by Equation (5):

$$P(m, r) = \frac{n(m, r)}{N(r)} \quad (5)$$

where $n(m, r)$ is the number of box size r with mass m , and $N(r)$ is the total number of boxes of size r .

If the calculated lacunarity $L(r)$ is plotted in a double logarithmic diagram then fractals will have straight-line plots, in other words, they have a similar appearance across scales. Otherwise, multi-fractals will have a different plot with few distinct areas, which means that they do not have a similar appearance across scales. The lacunarity plot for fractals can be fitted by a single line, but the multi-scaled object has to be fitted with several straight lines. Research done by R. E. Plotnick¹¹ offers double logarithmic plots for visual lacunarity distinction concerning either fractals or non-fractals. It provides

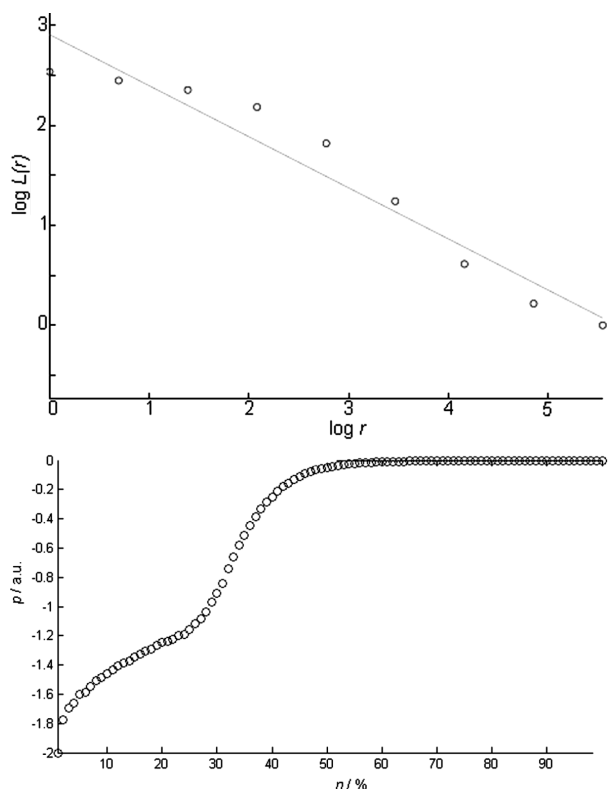


Figure 1: a) Plot of logarithms of $L(r)$ against r for arbitrary cutting level of the engineering surface and b) slope value p vs. cutting level n
Slika 1: a) Diagrama logaritmov $L(r)$ v odvisnosti od r za arbitrarno stopnjo rezanja inženirske površine in b) vrednosti naklona p v odvisnosti od nivoja n

visual information about the pixel entropy of the image representing the surface. The double logarithmic plot shown in **Figure 1** can serve as a basis for a comparison of different object plots.

The line slope as a numerical value p is suggested²² as a parameter that can be used for the AFM image lacunarity comparison. In the case of surface topography, particularly for binary images that are made by sectioning on levels of interest, the lacunarity double log plot (**Figure 1** (left)) can be used for a surface section comparison. However, the number p as a slope value for every section can serve as a parameter for the surface section characterization. Additionally, if parameter p is plotted for every section made by slicing the surface

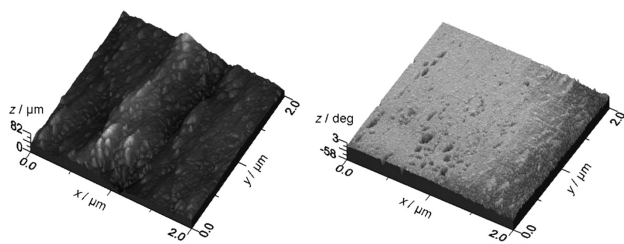


Figure 2: Average 3D topography image (left) and 3D magnetic force gradient (right) of basic material SP40

Slika 2: Posnetek povprečne 3D-topografije (levo) in 3D-gradient magnetne sile (desno) osnovnega materiala SP40

AFM image, then the diagram shown in **Figure 1** (right) can be considered as the AFM image lacunarity signature. The plots shown in **Figure 1** have been made according to Equation (6):

$$\lg L(r) = c + p \cdot \lg r \quad (6)$$

The diagram, which consists of three sloped curves, can be connected to randomly distributed surface asperities generated by the machining process, as demonstrated in the work by B. Bojovic et al.²⁷

Lacunarity analysis offers two types of p -diagrams, which were presented in our previously reported work. The first type represents p -diagrams with four line slopes and we labeled them as contorted p -diagrams. In contrast to them is a second type consisting of slanted p -diagrams with three line slopes. Images associated with a specific type of diagrams demonstrate similar surface topology. The contorted p -diagram is related to topology with distinctive high hills and the slanted p -diagram is designated by regularly distributed asperities.

3 RESULTS AND DISCUSSION

The average results for the topography and gradient of the magnetic field investigations into the 12 investigated samples are presented in **Figures 2** and **3**. Topography images are necessary to provide information about the surface roughness and to see whether there are any potential bumps on the surface that could cause damage to the cornea or make wearing the contact lens uncomfortable.

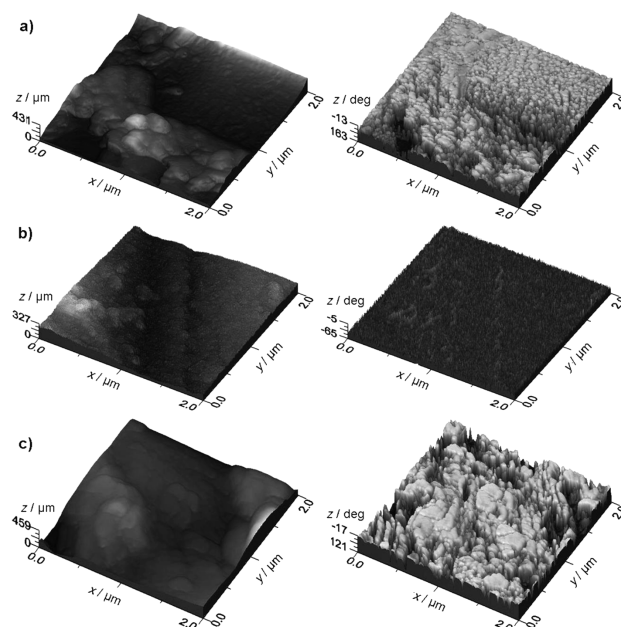


Figure 3: Average 3D topography image (left) and 3D magnetic force gradient (right) of nanophotonic materials a) SP40-A, b) SP40-B and c) SP40-C

Slika 3: Posnetek povprečne 3D-topografije (levo) in 3D-gradient magnetne sile (desno) nano fotonjskih materialov, a) SP40-A, b) SP40-B in c) SP40-C

As presented in D. Stamenkovic²⁸ all the materials possess topography that is smooth enough to fit the human eye. The maximum height difference of all materials can be seen on the topography of the basic material, and nanophotonic materials have smoother topographies. SP40 has the largest R_z value of 331.8 nm, which is much lower than the human tear film, as expected from commercially available materials. However, nanophotonic materials are proven to have much smaller height differences, where the second largest R_z of material SP40-C is 157.2 nm, which is more than half the R_z of SP40. The basic material has the largest surface roughness of 23.4 nm. The second largest is material SP40-A, and then material SP40-C with a surface roughness of 9.19 nm. It is interesting that material SP40-C, although it has the second largest R_z , has a smoother surface than material SP40-A.²⁸

The images of the gradient value of the magnetic field show that all materials have paramagnetic properties. The largest phase-shift angle difference is for the basic material, suggesting there are particles inside as impurities or that there are conglomerates of basic material with a higher density that have the largest differences in magnetic properties. Also, it can be seen that the basic material possesses the highest paramagnetic characteristics, with a minimum phase shift angle of -121.6° . However, a maximum phase shift of -10.8° shows a large variability in the paramagnetic properties. All nanophotonic materials show much smaller differences in the phase shift angles, which means that they have more consistent magnetic properties and density distributions (more homogenous). Also, it can be seen that nanophotonic materials tend to shift magnetic properties even more to paramagnetism, which is more strongly expressed in material SP40-A and material SP40-C.

3.1 Lacunarity analysis

For the contact lens lacunarity analysis, the topographic image of each material was recorded and imported to Matlab (Version R2013a, license number 853706) for further calculation. Four surfaces of four RGP contact lens materials were gathered. In order to make lacunarity perceptible for the integral contact lens surface, the parameter p is determined for every section made by slicing the AFM image.

The slanted form of p -diagrams can be seen in the case of the RGP contact lenses made of SP40 base materials (Figure 4). Topography images related to RGP materials group of diagrams demonstrate a similar surface topology (Figure 4). Consequently, the p -diagrams look alike and have similar line slopes through the levels. Only the p -diagram for the SP40-C material exhibits a line slope change in the range 20–32 % of maximum height. All p -diagrams reach asymptotic zero value after a certain level where materials become predominant, which is related to empty space in deep valleys. The

surfaces of all four RGP contact lens materials include large regions of material in the bottom half (20 %) of the maximum height, which makes the object very dense and the p -value obtains a constant value.

The frontal surface of a contact lens is in direct contact with the inner part of the upper eyelid. With each blink of the eye the upper eyelid covers the frontal surface with a tear film, thus filling in the gaps and smoothing the surface roughness. The surface of a contact lens with too many irregularities (high roughness) is undesirable because the tear film would not be sufficient to cover them, particularly at the end of the day when post lens tear film gets significantly thinner. According to the lacunarity analysis and observed line slope change in the range 20–32 % of maximum height, the nanophotonic lens surface made of SP40-C material exhibits a less desirable topography. However, by combining the surface maximal height with an unwanted elevations distribution, it could be concluded that they are significantly lower compared to the post lens tear film thickness.

From an optics (refraction) point of view, a surface with minor irregularities is not a disadvantage. Furthermore, 'over polished' surfaces have decreased wettability, which results in rapid 'breakage' of the tear film on the frontal surface of the lens. Besides aforementioned, 'over polished' surfaces have lower adhesion force which keeps the RGP lens in eye. Considering these specific requirements for functional behavior it could be concluded that nanophotonic lenses have an even more suitable topography compared to the conventional one.

Surface topography with deep valleys causes the contact lens to attract more proteins, lipids and other components of a tear film. These deposits have a negative effect on the optical characteristics of a contact lens, as well as on comfort. The results presented in the p -diagrams that is related to empty space in deep valleys indicate that all four RGP contact lens materials are appropriate for diminishing deposits.

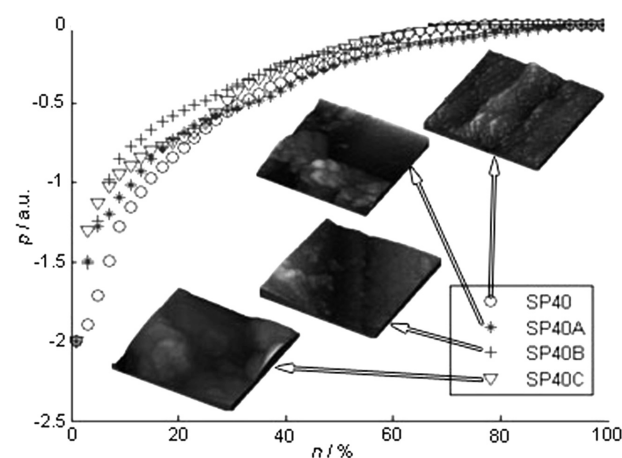


Figure 4: Plot of parameter p vs. cutting level n for RGP contact lens surface

Slika 4: Diagram parametra p v odvisnosti od nivoja rezanja n na površini RGP kontaktnih leč

4 CONCLUSION

The results presented here suggest the future commercialization of nanophotonic materials is affirmative. As suggested in D. Stamenkovic³⁰ the AFM method has shown that the quality of polished surfaces for all three nanophotonic materials completely satisfies the standards for the production of contact lenses since they have a smoother surface than SP40. The positive result is the fact that the roughness parameter values for all nanophotonic materials are lower than those for the basic material.³⁰

According to the magnetic properties of all the materials yielded by MFM it can be concluded that the basic material had very large phase shift angle differences, which are reduced by adding fullerene and its derivatives. The incorporation of these carbon nanomaterials caused the spectrum of phase shift angles to be reduced by almost 50 %. Also, although even the basic material has demonstrated paramagnetic properties it can be seen that adding carbon nanomaterials increases the paramagnetic characteristics of the material.

Topography images show that bumps significantly influence the surface lacunarity, because they embrace a great deal of lubricant volume. Therefore, the origins of the contorted *p*-diagram are bump-like entities. Considering the functional behavior of the contact lens surface, irregularities like bumps are unwanted, and thus this kind of contact surface cannot be considered acceptable. The surface lacunarity influences the tear film volume distribution and, consequently, the contact lens surface lubrication.

The surface lacunarity behavior can be related to the surface topology. The results of the surface lacunarity analysis confirm the sample surface state as belonging to an appropriate (slanted *p*-diagram) roughness concerning the tear film stability. Regarding the tribological behavior that depends on lacuna distribution on the surface, the RGP contact lenses made of three nanophotonic materials and machined in the usual manner are enhanced compared to commercially available ones. Those lacunas preserve a critical amount of tear film in the case of dry eye and therefore improve the lubrication process during RGP contact lens wearing.

Acknowledgements

This research was funded by the Ministry of Education, Science and Technological Development of the Republic of Serbia, through Project III45009. We would like to thank Soleko, Italy, for turning our initial ideas about new materials into a reality by producing them with us in their laboratories.

5 REFERENCES

- A. J. Bron, J. M. Tiffany, S. M. Gouveia, N. Yokoj, L. W. Voon, Functional aspects of the tear film lipid layer, *Exp. Eye Res.* 78 (2004) 3, 347, doi:10.1016/j.exer.2003.09.019
- J. I. Prydal, P. Arral, H. Woon, F.W. Campbell, Study of Precorneal Tear Film Thickness and Structure by Interferometry and Confocal Microscopy, *Invest. Ophthalmol. Vis. Sci.* 33 (1992) 6, 1996
- P. Smith, B. Fink, N. Fogt, K. Nichols, R. Hill, G. Wilson, The Thickness of the Human Precorneal Tear Film: Evidence from Reflection Spectra, *Invest. Ophthalmol. Vis. Sci.* 41 (2000) 11, 3348
- J. Wang, D. Fonn, T. L. Simpson, L. Jones, Precorneal and Pre- and Postlens Tear Film Thickness Measured Indirectly with Optical Coherence Tomography, *Invest. Ophthalmol. Vis. Sci.* 44 (2003) 6, 2524, doi:10.1167/iovs.02-0731
- K. Azartash, J. Kwan, J. R. Paugh, A. L. Nguyen, J. V. Jester, E. Gratton, Pre-corneal tear film thickness in humans measured with a novel technique, *Mol. Vis.* 17 (2011), 756
- A. Muntz, L. N. Subbaraman, L. Sorbara, L. Jones, Tear exchange and contact lenses: A review, *J. Optom.* 8 (2015) 1, 2, doi:10.1016/j.optom.2014.12.001
- J. J. Nichols, P. E. King-Smith, Thickness of the pre- and post-contact lens tear film measured in vivo by interferometry, *Invest. Ophthalmol. Vis. Sci.* 44 (2003) 1, 68, doi:10.1167/iovs.02-0377
- J. L. Creech, L. T. Do, I. Fatt, C. J. Radke, In vivo tear-film thickness determination and implications for tear-film stability, *Curr. Eye Res.* 17 (1998) 11, 1058–1066, doi:10.1076/ceyr.17.11.1058.5233
- B. Mandelbrot, *The Fractal Geometry of Nature*, W. H. Freeman and Co., New York, 1982
- R. Voss, *Random fractals: characterization and measurement, Scaling Phenomena in Disordered Systems*, Springer, 1986, 51–61
- R. E. Plotnick, R. H. Gardner, W. W. Hargrove, K. Prestegard, M. Perlmutter, Lacunarity analysis: A general technique for the analysis of spatial patterns, *Phys. Rev. E* 53 (1996) 5, 5461, doi:10.1103/PhysRevE.53.5461
- C. Allain, M. Cloitre, Characterizing the lacunarity of random and deterministic fractal sets, *Phys. Rev. A* 44 (1991) 6, 3552, doi:10.1103/PhysRevA.44.3552
- P. Borys, M. Krasowska, Z. J. Grzywna, M. B. A. Djamgoz, M. E. Mycielska, Lacunarity as a novel measure of cancer cells behavior, *Biosystems* 94 (2008) 3, 276, doi:10.1016/j.biosystems.2008.05.036
- S. Hoechstetter, U. Walz, N. Thinh, Adapting lacunarity techniques for gradient-based analyses of landscape surfaces, *Ecol. Complex.* 8 (2011) 3, 229, doi:10.1016/j.ecocom.2011.01.001
- A. Karperien, H. Jelinek, Fractal, multifractal, and lacunarity analysis of microglia in tissue engineering, *Front. Bioeng. Biotechnol.* 3 (2015) 51, 1, doi:10.3389/fbioe.2015.00051
- H. W. Kroto, J. R. Heath, S. C. O'Brien, R. F. Curl, R. E. Smalley, C₆₀: Buckminsterfullerene, *Nature* 318 (1985), 162, doi:10.1038/318162a0
- Dj. Koruga, S. Hameroff, J. Withers, R. Loutfy, M. Sundareshan, *Fullerene C60: History, Physics, Nanobiology, Nanotechnology*, Elsevier, Amsterdam, 1993
- M. S. Dresselhaus, G. Dresselhaus, P. C. Eklund, *Science of Fullerenes and Carbon Nanotubes*, Academic Press, Inc., New York, 1996
- P. Taroni, C. D'Andrea, G. Valentini, R. Cubeddu, D.N. Hu, J. E. Roberts, Fullerol in human lens and retinal pigment epithelial cells: time domain fluorescence spectroscopy and imaging, *Photochem. Photobiol. Sci.* 10 (2011), 904, doi:10.1039/c0pp00312c
- F. Giacalone, N. Martín, Fullerene polymers: synthesis and properties, *Chem. Rev.*, 106 (2006) 12, 5136, doi:10.1021/cr068389h
- W. T. Ford, T. Nishioka, S. C. McCleskey, T. H. Mourey, Structure and Radical Mechanism of Formation of Copolymers of C₆₀ with Styrene and with Methyl Methacrylate, *Macromolecules* 33 (2000) 7, 2413, doi:10.1021/ma991597+
- C. R. Blanchard, Atomic force microscopy, *Chem. Educator* 1 (1996) 5, 1, doi:10.1007/s00897960059a

- ²³ U. Hartmann, Magnetic force microscopy: Some remarks from micromagnetic point of view, *J. Appl. Phys.* 64 (1988) 3, 1561, doi:10.1063/1.341836
- ²⁴ U. Hartmann, Magnetic force microscopy, *Ann. Rev. Mater. Sci.* 29 (1999) 53, doi:10.1146/annurev.matsci.29.1.53
- ²⁵ JEOL SPM 5200, Instruction manual, 2005
- ²⁶ ISO 25178: Geometric Product Specifications (GPS) – Surface texture: areal-Part 2 (2013)
- ²⁷ B. Bojovic, M. Petrovic, Z. Miljkovic, B. Babic, L. Matija; Lubrication prediction in digital manufacturing, Proc. of the 6th Inter. Working Conference TQM, Belgrade, Serbia, 2011, 475
- ²⁸ D. Stamenkovic, Investigation and development of rigid gas permeable nanophotonic contact lenses based on poly (methyl methacrylate) and fullerene, PhD Thesis in Serbian, Faculty of Mechanical Engineering, University of Belgrade, 2012

MOLECULAR DYNAMICS SIMULATIONS OF PLASTIC
DEFORMATION OF METALLIC SURFACESSIMULACIJE PLASTIČNE DEFORMACIJE KOVINSKIH POVRŠIN
Z METODO MOLEKULARNE DINAMIKENuša Pukšič^{1,2}, Monika Jenko^{1,2}, Matjaž Godec¹¹Institute of Metals and Technology, Lepi pot 11, Ljubljana, Slovenia²Jožef Stefan International Postgraduate School, Jamova cesta 39, Ljubljana, Slovenia
nusa.puksic@imt.si*Prejem rokopisa – received: 2016-12-12; sprejem za objavo – accepted for publication: 2016-12-23*

doi:10.17222/mit.2016.334

An understanding of the physical properties of a wide array of geometries is important in the quest for ever smaller and more fine-tuned devices and their parts. Surfaces play a key role in the deformation of nano-scale systems. Molecular dynamics simulations of compressive and tensile deformation were performed on nickel and copper thin films with (111), (9 9 11) and (10 10 8) surface orientations at 10 K. The (9 9 11) and (10 10 8) surfaces are vicinal to (111) and consist of a series of equidistant monoatomic steps. All the cases exhibit a yield stress asymmetry, with the yield stress being higher in compression than in tension. The near-surface region is the first to plastically deform and dislocations nucleate at the surface. The influence of the surface is most pronounced for the cases of the (10 10 8) surfaces deformed in compression, where parallel stacking faults nucleate at the steps on the surfaces in both materials, overriding the primary slip systems.

Keywords: molecular dynamics (MD), metallic surfaces, thin films, deformation

Dobro razumevanje mehanskih lastnosti široke palete geometrij je pomembno pri izboljšavah vedno manjših in zahtevnejših naprav in njihovih delov. Površine igrajo pomembno vlogo pri deformaciji sistemov na nano-skali. Z metodo molekularne dinamike smo raziskali deformacijo (111), (9 9 11) in (10 10 8) orientiranih nikljevih in bakrovih tankih filmov ob raztezanju in krčenju pri temperaturi 10 K. Površini (9 9 11) in (10 10 8) sta sosednji nominalni površini (111) in sta sestavljeni iz ekvidistantnih stopnic. Vse površine imajo asimetrično mejo plastičnosti, ki je višja pri stiskanju kot pri raztezanju. Območja tik pod površino se najprej deformirajo in dislokacije izvirajo na površinah. Vpliv površine je najbolj izrazit za primera orientacije (10 10 8) pri stiskanju, ko se oba materiala deformirata s serijo vzporednih napak zloga, ki izvirajo iz stopnic na površinah in, ki nadomestijo primarne drsne sisteme.

Ključne besede: molekularna dinamika (MD), kovinske površine, tanki filmi, deformacija

1 INTRODUCTION

Experiments at the nanoscale can be very time consuming and costly, in addition, they often turn out ambiguous due to lack of constraint on the thin foils examined. Such experiments also require expensive equipment and sensors, which further motivates us to use atomistic simulations to better understand deformation mechanisms at the nanoscale. Molecular dynamics (MD) simulations can serve as an effective tool for analysing dislocation nucleation mechanisms in metallic materials.¹⁻⁴

Whereas the misorientation of adjacent grains determines the precise positioning of the atoms close to the boundaries, leading to diverse defect nucleation sites, the surface condition similarly influences the mechanical response of a material to external loads or deformation due to the relaxation of the topmost layers minimizing the surface energy and the adjacent free space into which the atoms can move.⁵⁻⁸

Vicinal surfaces, such as (10 10 8) and (9 9 11) investigated here, are produced by cutting a crystal close to a dense plane, and consist of terraces divided by equidistant monoatomic steps. When cutting or growing poly-

crystalline materials, such surfaces are unavoidable. As is the case with grain boundaries, the steps on the surface provide favourable nucleation sites for dislocations and stacking faults, key elements of plastic deformation. We show that deformation mechanisms in copper and nickel are influenced by the presence of steps at the surface.

2 EXPERIMENTAL PART

The simulations were performed on an array of substrates, with surface orientations (111), (9 9 11) and (10 10 8). The (9 9 11) and (10 10 8) surfaces are vicinal to (111) and consist of a series of equidistant monoatomic steps that have (001) and (-1-11) oriented microfacets, respectively.

Copper and nickel single crystal thin films of 10 nm thickness were simulated. The simulations of the tensile and compressive uniaxial deformations were performed at 10 K, applying engineering strain at a strain rate of $\pm 2.5\%$ /ps. The strain direction was perpendicular to the steps.

The boundaries of the simulation boxes were periodic in the *x* and *y* directions and fixed in the *z* direction.

In the z direction the simulated films were bound by a free surface at the top and by a layer of fixed atoms at the bottom to prevent the loss of atoms at the border of the simulation box and to simulate defect-free bulk. The thickness of this frozen layer was 1.2 nm. These atoms were fixed at the positions they had when equilibrated to 10 K and were remapped at every deformation of the simulation box. All the forces acting on these atoms were otherwise reset to zero.

In the y direction the size of the simulation box was subject to requirements for periodicity of the terraces and steps for vicinal surfaces. The number of steps and terraces included was 8.

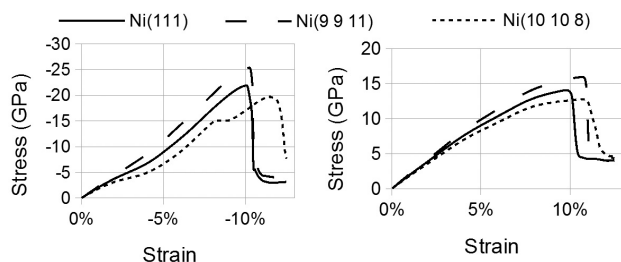
To simulate engineering compressive and tensile strains, the simulation box was deformed in the y direction in increments of 0.5 % with 200 fs periods of equilibration in-between, resulting in the overall strain rate of 2.5% /ps. The stress in the x direction was kept to zero.

The molecular dynamics simulations were carried out using the LAMMPS Molecular Dynamics Simulator⁹ and EAM potentials by Y. Mishin et al.¹⁰ OVITO¹¹ was used for visualization and analysis of the simulation data. Dislocation detection algorithm by A. Stukowski¹¹ implemented in OVITO was used in post-processing.

3 RESULTS

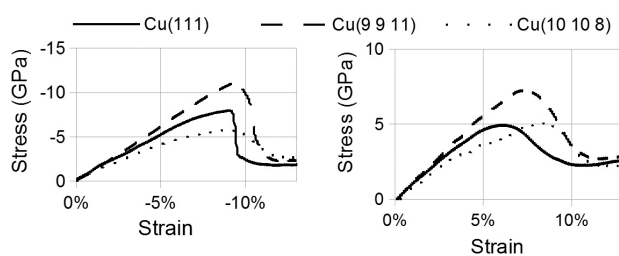
Deformation mechanisms of copper and nickel (111), (9 9 11) and (10 10 8) surfaces were investigated. Stress-strain curves are shown in **Figures 1** and **2**. As is expected from the direction of the strain, the Young modulus (expressed as the steepness of the stress-strain curve) is highest for the (9 9 11) surfaces and lowest for the (10 10 8) surfaces.

Yield stress is lower in copper than in nickel. Both materials exhibit the yield stress asymmetry, with yield stress being higher in compression than in tension. This is connected to the fact that the deformation mechanisms in compression and tension are not the same for any of the surfaces we investigated, although strict geometric analysis suggests otherwise: primary slip systems, namely $\{-111\}(0-11)$ and $\{1-11\}(-101)$, are the same for all the surfaces we investigated, with Schmidt factors of



(a) Nickel, compressive deformation (b) Nickel, tensile deformation
Figure 1: a) Stress-strain curves for nickel deformed in compression and b) in tension.

Slika 1: Diagrama napetost-raztezeka za nikelj; a) pri kompresiji, b) pri napetosti.



(a) Copper, compressive deformation (b) Copper, tensile deformation

Figure 2: a) Stress-strain curves for copper deformed in a) compression and b) in tension.

Slika 2: Diagrama napetost-raztezeka za baker: a) pri kompresiji, b) pri napetosti

0.408 for the (111) surface, 0.377 for (9 9 11) and 0.433 for (10 10 8).

In the case of Cu(111) surface deformed in tension, mostly stair-rod dislocations form throughout the bulk and are not limited to the near-surface region, while in compression, dislocations first nucleate at the surface as Schockley partials and no trailing partials detach from the surface.

In the case of Ni(111) surface deformed in tension, Schockley partial dislocations nucleate in the bulk, while in compression, Schockley partials nucleate at the surface and trailing partials detach from the surface.

For all the (9 9 11) surfaces, Schockley partial dislocation nucleate at the surface and trailing partials detach from the surface. Stair-rod dislocations form in Cu(9 9 11) and Ni(9 9 11) deformed in tension, **Figures 3b** and **3f**.

In the case of Cu(10 10 8) surface deformed in tension, **Figure 3a**, stair-rod dislocations nucleate at the surface, while in compression, **Figure 3c**, parallel stacking faults nucleate at the steps and grow into the bulk.

In the case of Ni(10 10 8) surface deformed in tension, **Figure 3e**, Schockley partial dislocation nucleate at the surface and in the near-surface region, while in compression, **Figure 3g**, parallel stacking faults nucleate at the steps and grow into the bulk.

4 DISCUSSION

We found two cases of easy glide where only one slip system is active: Cu(10 10 8) and Ni(10 10 8) surfaces deformed in compression, **Figures 3c** and **3g**. Schockley partial dislocations nucleate at all the steps on the surface and grow evenly into the bulk. The stress-strain curves have a small plateau in the region just before the peak of the curve is expected, more pronounced in the case of nickel, and the peak is moved to higher strains, **Figures 1a** and **2a**.

In the case of Cu(10 10 8) deformed in tension, **Figure 3a**, Schockley partial dislocations wrapped around stair-rod dislocations form, also nucleating at the steps on the surface. As the stair-rod dislocations only move with diffusion, which is limited at this temperature, the

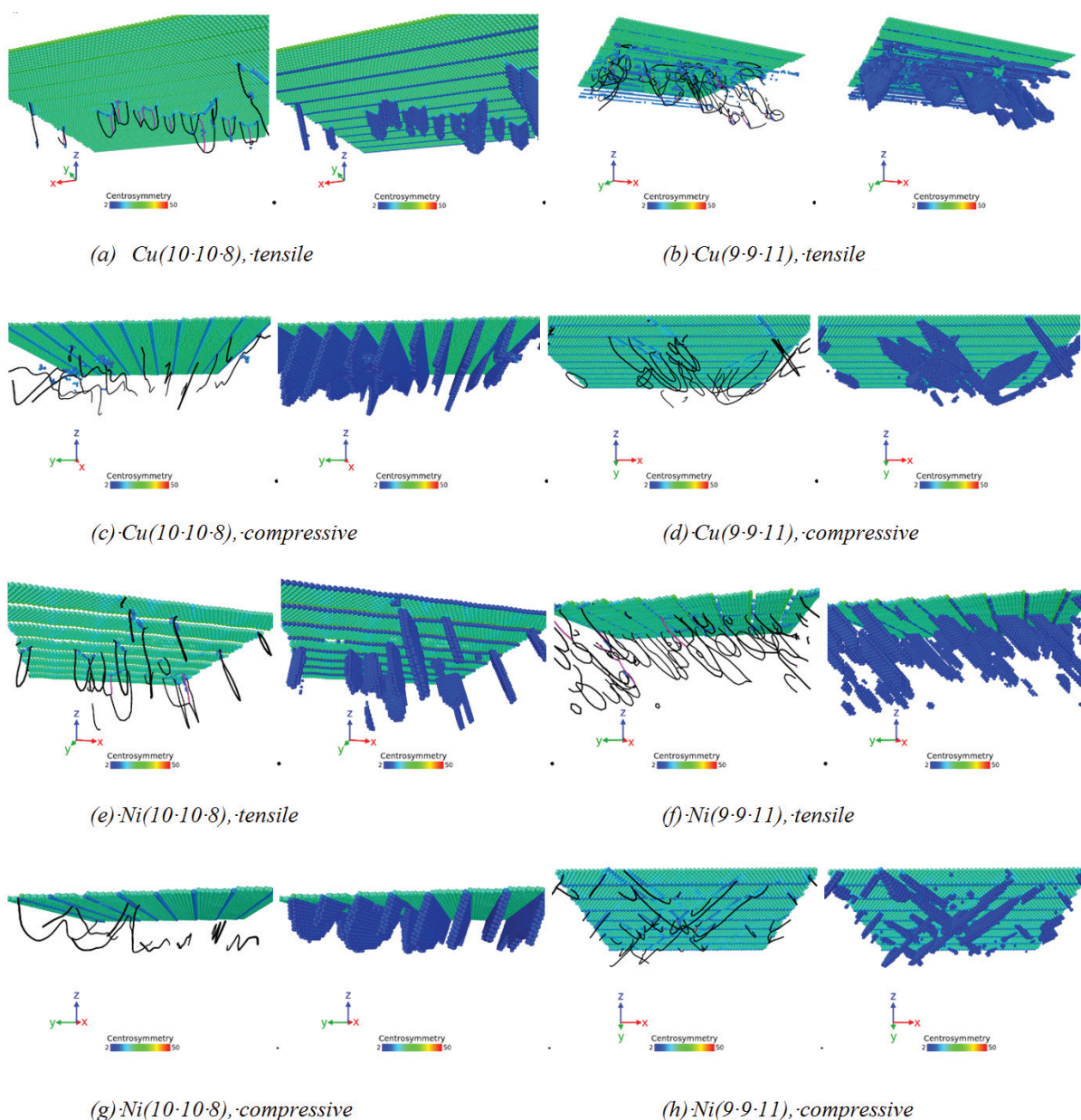


Figure 3: Dislocation nucleation in copper and nickel thin films deformed in tension and in compression. Two views are shown for each case: dislocations as lines (left) and atoms with centrosymmetry parameter $CS > 2$ (right). Black lines denote Shockley partial dislocations and pink lines denote stair-rod dislocations.

Slika 3: Začetki plastične deformacije v bakrovih in nikljevih stiskanih in raztezanih tankih filmih. Vsak primer prikazujeta dva pogleda: dislokacije označene s črtami (levo) in atomi s parametrom središčne simetrije $CS > 2$ (desno). Črne črte označujejo Shockleyeve delne dislokacije, roza črte pa Lomer-Cottrell stike.

effect on stress is the same as if only one slip system were active and the stress-strain curve exhibits a change in slope, **Figure 2b**.

A. Zimmerman et al.¹² studied Au(111) surfaces with single monoatomic steps at 0K and found that when the indenter came into physical contact with the step, the deformation mechanism beneath the indenter switched from dislocation emission from the surface to slip aligned with the step.

D. Shan et al.¹³ performed a similar study of nanoindentation on thin copper films and found that

when the indenter came into contact with the step, there was a significant difference in the strength of the first dislocation emission.

H. Lu and Y. Ni¹⁴ and H. Lu et al.¹⁵ investigated the effects of surface steps on nanoindentation in Al and found that the shear stress resulting from the step influences the choice of the active slip systems and lowers the threshold for plastic deformation.

Our analysis shows that it is not only the presence of steps that influences deformation mechanisms. While a switch to slip aligned with the steps occurs for the (10 10

8) surfaces deformed in compression for both materials we investigated, we found no such switch for the (9 9 11) surfaces.

The near-surface region is the first to plastically deform and dislocations nucleate at the surface, therefore the surfaces are softer than the bulk. We conclude that the stress inherent in the steps also lowered the threshold for plastic deformation in our systems.

5 CONCLUSIONS

Deformation mechanisms of copper and nickel thin films we investigated are more complex than geometric analysis would suggest. The surfaces are softer than the bulk, as the near-surface region is the first to plastically deform and dislocations nucleate at the surface. We conclude that the stress inherent in the steps lowered the threshold for plastic deformation in the thin films we investigated.

In tensile deformation in both materials, stair-rod dislocations nucleate at the surfaces and are not created by dislocation interactions.

The influence of the surface is most pronounced for the cases of the (10 10 8) surfaces deformed in compression, where parallel stacking faults nucleate at the steps on the surfaces in both materials, overriding the primary slip systems. The presence of the steps does not in itself influence the choice of slip systems. While a switch to slip aligned with the steps occurs for the (10 10 8) surfaces deformed in compression for both materials we investigated, we found no such switch for the (9 9 11) surfaces.

Acknowledgement

The authors acknowledge the financial support of the Slovenian Research Agency (ARRS).

6 REFERENCES

- ¹ P. Muller, Elastic effects on surface physics, *Surface Science Reports*, 54 (2004) 157–258, doi:10.1016/j.surfrep.2004.05.001
- ² Z. You, X. Li, L. Gui, Q. Lu, T. Zhu, H. Gao, L. Lu, Plastic anisotropy and associated deformation mechanisms in nanotwinned metals, *Acta Materialia*, 61 (2013) 217–227, doi:10.1016/j.actamat.2012.09.052
- ³ D. Huang, Q. Zhang, P. Qiao, Molecular dynamics evaluation of strain rate and size effects on mechanical properties of FCC nickel nanowires, *Computational Materials Science*, 50 (2011) 903–910, doi:10.1016/j.commatsci.2010.10.028
- ⁴ F. Ma, K.-W. Xu, P. K. Chu, Surface-induced structural transformation in nanowires, *Materials Science and Engineering: R: Reports*, 74 (2013) 173–209, doi:10.1016/j.mser.2013.05.001
- ⁵ D. Spearot, L. Capolungo, J. Qu, M. Cherkaoui, On the elastic tensile deformation of bicrystal interfaces in copper, *Computational Materials Science*, 42 (2008) 57–67, doi:10.1016/j.commatsci.2007.06.008
- ⁶ M. Chassagne, M. Legros, D. Rodney, Atomic-scale simulation of screw dislocation/coherent twin boundary interaction in Al, Au, Cu and Ni, *Acta Materialia*, 59 (2011) 1456–1463, doi:10.1016/j.actamat.2010.11.007
- ⁷ D. Bachurin, D. Weygand, P. Gumbsch, Dislocation–grain boundary interaction in textured thin metal films, *Acta Materialia*, 58 (2010) 5232–5241, doi:10.1016/j.actamat.2010.06.026
- ⁸ H. S. Park, K. Gall, J. A. Zimmerman, Deformation of FCC nanowires by twinning and slip, *Journal of the Mechanics and Physics of Solids*, 54 (2006) 1862–1881, doi:10.1016/j.jmps.2006.03.006
- ⁹ S. Plimpton, Fast Parallel Algorithms for Short-Range Molecular Dynamics, *Journal of Computational Physics*, (1995) 1–19, doi:10.1006/jcph.1995.1039, URL <http://lammps.sandia.gov/>
- ¹⁰ Y. Mishin, M. Mehl, D. Papaconstantopoulos, A. Voter, J. Kress, Structural stability and lattice defects in copper: Ab initio, tight-binding, and embedded-atom calculations, *Physical Review B*, 63 (2001) 224106, doi:10.1103/PhysRevB.63.224106
- ¹¹ A. Stukowski, Visualization and analysis of atomistic simulation data with OVITO—the Open Visualization Tool, *Modelling and Simulation in Materials Science and Engineering*, 18 (2010) 015012, doi:10.1088/0965-0393/18/1/015012
- ¹² J.A. Zimmerman, C. L. Kelchner, P. A. Klein, J. C. Hamilton, S. M. Foiles, Surface step effects on nanoindentation, *Phys. Rev. Lett.*, 87 (2001) 165507, doi:10.1103/PhysRevLett.87.165507
- ¹³ D. Shan, L. Yuan, B. Guo, Multiscale simulation of surface step effects on nanoindentation, *Materials Science and Engineering: A*, 412 (2005) 264–270, doi:10.1016/j.msea.2005.08.198
- ¹⁴ H. Lu, Y. Ni, Effect of surface step on nanoindentation of thin films by multiscale analysis, *Thin Solid Films*, 520 (2012) 4934–4940, doi:10.1016/j.tsf.2012.03.019
- ¹⁵ H. Lu, Y. Ni, J. Mei, J. Li, H. Wang, Anisotropic plastic deformation beneath surface step during nanoindentation of FCC Al by multiscale analysis, *Computational Materials Science*, 58 (2012), 192–200, doi:10.1016/j.commatsci.2012.01.026

THE INFLUENCE OF AN ISOTHERMAL ANNEALING PROCESS ON THE STRUCTURE AND MAGNETIC PROPERTIES OF THE BULK AMORPHOUS ALLOY FeCoBYMo

VPLIV IZOTERMNEGA ŽARJENJA NA STRUKTURO IN MAGNETNE LASTNOSTI MASIVNE AMORFNE ZLITINE FeCoBYMo

Paweł Pietrusiewicz¹, Marcin Nabiałek¹, Jacek Olszewski¹, Sabina Lesz²

¹Czestochowa University of Technology, Institute of Physics, 19 Armii Krajowej Av., 42-200 Czestochowa, Poland

²Silesian Technical University, Institute of Engineering Materials and Biomaterials, Konarskiego St. 18a, 44-100 Gliwice, Poland
pietrusiewicz@wip.pcz.pl, pawelpietrusiewicz@wp.pl

Prejem rokopisa – received: 2015-06-30; sprejem za objavo – accepted for publication: 2015-12-24

doi:10.17222/mit.2015.151

This paper presents the results of research into a bulk amorphous alloy based on Fe. Samples with the composition Fe₆₁Co₁₀Y₈Mo₁B₂₀ were prepared in the form of plates using an injection-casting method. The samples were then subjected to an isothermal annealing process (at less than the crystallization temperature) of 700 K for 1 h and 770 K for 3.5 h. The structures of the samples were investigated, both in the state after solidification and following the heat treatment, using X-ray diffraction (XRD) and Mössbauer spectroscopy. The results confirmed that the samples, both after solidification and after annealing, were amorphous. Magnetic measurements were carried out using a vibrating-sample magnetometer (VSM) with magnetic fields of up to 2 T. Based on these measurements, the effect of the isothermal annealing process on the magnetic properties was defined, including the saturation magnetization $\mu_0 M_s$ and coercive field H_c . Using the Kronmüller theory, the initial magnetization curves were analysed in the area of approach to ferromagnetic saturation. On the basis of this theory, the quantity and quality of the structural defects were defined; these defects play a critical role in the magnetization process in high magnetic fields. Following this study, the sample annealed at 770 K for 1 h was found to feature a relatively low coercive field and the higher value of magnetization saturation. Linear defects, the so-called quasidislocational dipoles, played the leading role in the process of magnetization of the test samples.

Keywords: bulk amorphous alloys, structure, soft magnetic properties, defects

Članek predstavlja rezultate raziskave masivne amorfne zlitine na osnovi Fe. Vzorci s sestavo Fe₆₁Co₁₀Y₈Mo₁B₂₀ so bili pripravljani v obliki plošč, s pomočjo tlačnega litja. Vzorci so bili izotermno žarjeni 1 h (pri temperaturi nižji od temperature kristalizacije) na 700 K in 3,5 h na 770 K. Preiskana je bila struktura vzorcev, v stanju po strjevanju in po toplotni obdelavi. Uporabljena je bila rentgenska difrakcija (XRD) in Mössbauerjeva spektroskopija. Rezultati so potrdili, da so bili vzorci po strjevanju in po žarjenju v amorfem stanju. Magnetne meritve so bile izvedene s pomočjo magnetometra z vibriranjem vzorca (VSM) v magnetnih poljih jakosti do 2 T. Na osnovi meritev je bil določen vpliv izotermnega žarjenja na magnetne lastnosti, vključno z nasičeno magnetizacijo $\mu_0 M_s$ in koercitivnim poljem H_c . Z uporabo Kronmüllerjeve teorije so bile analizirane začetne krivulje magnetizacije blizu področja feromagnetnega nasičenja. Na osnovi te teorije je bila določena količina in kakovost strukturnih napak; te napake igrajo ključno vlogo pri procesu magnetizacije v močnih magnetnih poljih. Na podlagi te študije je bilo ugotovljeno, da vzorci žarjeni 1 h kažejo relativno šibko koercitivno polje in visoko vrednost nasičene magnetizacije. Linearne napake, imenovane kvazi-dislokacijski dipoli, igrajo vodilno vlogo pri procesu magnetizacije preizkušanih vzorcev.

Ključne besede: masivne amorfne zlitine, struktura, mehko magnetne lastnosti, napake

1 INTRODUCTION

Amorphous soft magnetic materials are investigated in many research centres around the world. These materials are characterized by a low coercive field and high saturation magnetization.^{1–3} From a thermodynamic point of view, the structure of these materials is metastable. Nevertheless, such materials can be applied in devices such as electronic measuring and surveillance systems, magnetic wires, magnetic sensors, band-pass filters, magnetic shielding, energy-saving electric power transformers and other applications.^{4,5} During the past 20 years, intensive research has been conducted on amorphous alloy groups having a thickness or diameter exceeding 100 μm ; these are called bulk metallic glasses

(BMGs).^{6,7} These materials have good soft magnetic properties and a high mechanical strength.⁸

As mentioned previously, rapidly cooled amorphous materials are thermodynamically unstable; they exhibit instability in their physical properties with respect to time and temperature. In general, their thermodynamic stability can be improved by annealing for a specified time at appropriate temperatures.^{9–12}

As shown in the literature, the magnetic properties of amorphous alloys depend strongly on the annealing temperature.^{13–16} During the earlier sample production process, free volumes are created; annealing the samples at low temperatures leads to the diffusion of these free volumes to the surface of the material. Thus, the soft magnetic properties of these alloys can be improved

through the relaxation of internal stress, by annealing them at less than the crystallization temperature.¹⁷

The paper presents results of structural and magnetic studies concerning plate-shaped samples of the bulk amorphous alloy $\text{Fe}_{61}\text{Co}_{10}\text{Y}_8\text{Mo}_1\text{B}_{20}$. The investigated material was subjected to two-stage annealing processes, below the crystallization temperature.

2 EXPERIMENTAL PART

Samples of the composition $\text{Fe}_{61}\text{Co}_{10}\text{Y}_8\text{Mo}_1\text{B}_{20}$ were prepared in the form of plates using an injection-casting method. These amorphous plates featured the following dimensions: 10 mm width and 0.5 mm thickness. The component chemicals, used in the production process, were of high purity (~99.99 %). The ingots of alloy were melted in an electric arc furnace. The crystalline ingot and amorphous plate samples were prepared under a protective atmosphere of argon. The isothermal annealing of the material samples took place in a vacuum furnace, in order to prevent oxidation processes. Initially, a plate sample was annealed at 700 K for 1 h and then at 770 K for 3.5 h. The structure of the investigated material in the form of a plate, in the state following solidification and after annealing, was examined using a Bruker X-ray diffractometer (XRD) equipped with a copper lamp featuring a characteristic $\text{Cu-K}\alpha$ radiation of wavelength $\lambda = 0.154056$ nm. The XRD studies were performed within the angular range from 20° to 120° with a step of 0.01° and an exposure time of 7 s. In order to confirm the amorphous structure of the examined samples, Mössbauer spectra were recorded using a Polon spectrometer equipped with a ^{57}Co source with an intensity of 50 mCi.

Static hysteresis loops were obtained using a Lake-Shore vibrating-sample magnetometer (VSM) operating in a magnetic field of up to 2 T. On the basis of these measurements, the magnetization saturation ($\mu_0 M_s$) and coercive field (H_c) were determined, both for the heat-treated samples and in the state following solidification.

Analysis of the initial magnetization curve was performed in the area of the approach to ferromagnetic saturation, according to the Kronmüller theory.¹⁸ On the basis of this theory the authors specified the quantity and quality of structural defects playing a decisive role in the

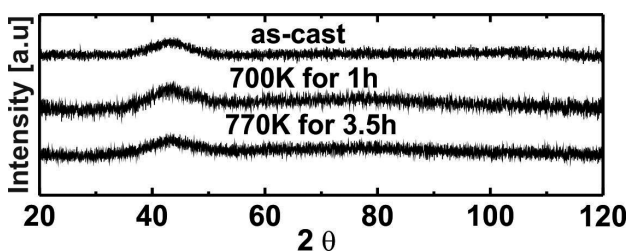


Figure 1: X-ray diffraction patterns for powdered as-quenched, annealed at 700 K/1h and 770 K/3.5h, plates

Slika 1: Rentgenogram zdrobljenih plošč, gašenih ter žarjenih 1 h na 700 K in 3,5 h na 770 K

process of magnetization under the influence of strong magnetic fields.

3 RESULTS AND DISCUSSION

Figure 1 shows the X-ray diffraction (XRD) patterns of the $\text{Fe}_{61}\text{Co}_{10}\text{Y}_8\text{Mo}_1\text{B}_{20}$ alloy in the states following solidification and after annealing at two different temperatures.

The X-ray diffraction patterns, shown in Figure 1, feature only one broad, blurred, maximum. This kind of maximum occurs for the samples in the state following solidification and after the isothermal annealing process. These patterns are typical for materials featuring an amorphous structure.

Figure 2 shows transmission Mössbauer spectra of the amorphous $\text{Fe}_{61}\text{Co}_{10}\text{Y}_8\text{Mo}_1\text{B}_{20}$ alloy plate samples in the state following solidification and after annealing firstly at a temperature of 700 K for 1 h and next at 770 K for 3.5 h. The spectra are expanded due to the disorder of the atomic structure and small asymmetries. The shapes of these spectra are typical for magnetic alloys having an amorphous structure.^{19,20}

Hyperfine field distributions $P(B)$, obtained from analysis of the Mössbauer spectra for all samples of the $\text{Fe}_{61}\text{Co}_{10}\text{Y}_8\text{Mo}_1\text{B}_{20}$ alloy (in the state following solidification and after annealing), are shown in Figure 3. These distributions are composed of two maxima. First, the lower maximum B_{eff} (of the average hyperfine field) is in the 10 T field, and the second peak lies higher in the 23 T field. It is assumed that the first low-field peak is associated with the nearest neighbourhoods of Fe and the local presence of Y.²¹ The second peak corresponds to the areas with less Fe, in which the ^{57}Fe are partly

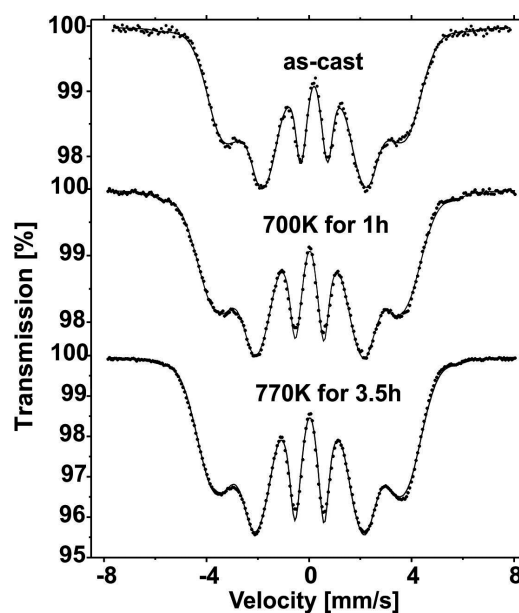


Figure 2: The transmission Mössbauer spectra for the investigated samples

Slika 2: Prenos Mössbauerjevega spektra preiskovanih vzorcev

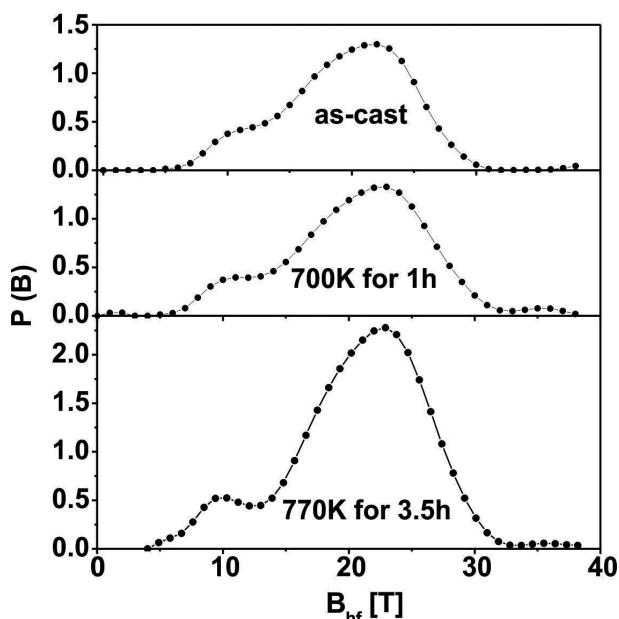


Figure 3: The hyperfine field distribution on the ^{57}Fe nuclei derived from analysis of the transmission Mössbauer spectra (Figure 2) for the investigated samples of $\text{Fe}_{61}\text{Co}_{10}\text{Y}_8\text{Mo}_1\text{B}_{20}$ alloy

Slika 3: Hiper drobna razporeditev polja na ^{57}Fe nukleusu, pridobljena iz analize prenosa Mössbauerjevega spektra (Slika 2) pri preiskovanih vzorcih zlitine $\text{Fe}_{61}\text{Co}_{10}\text{Y}_8\text{Mo}_1\text{B}_{20}$

surrounded by magnetic atoms (Co) and partly by non-magnetic atoms (B, Mo).

From an analysis of Figure 3, it can be concluded that post-production thermal treatment led to segregation and the emergence of areas more or less rich in iron. The data obtained from an analysis of the Mössbauer spectra are summarized in Table 1.

Figure 4 shows the static magnetic hysteresis loops for the samples in the state following solidification and after heat treatment at different temperatures. These hysteresis loops have a shape typical of materials with

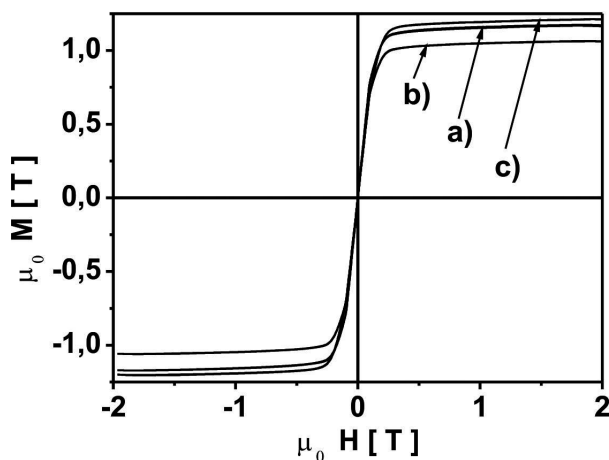


Figure 4: Static hysteresis loops measured for tested samples in the state following solidification (a), annealed at 700 K/1 h (b) and annealed at 770 K/3.5 h (c)

Slika 4: Statične histerezne zanke izmerjene na vzorcih v stanju po strjevanju (a), žarjeno 1 h na 700 K, (b) žarjeno 3,5 h na 770 K (c)

soft magnetic properties. The data obtained from analysis of the static hysteresis loops, such as the saturation magnetization ($\mu_0 M_s$) and the coercive field (H_c), are shown in Table 1.

Table 1: Data from analysis of the static hysteresis loops: $\mu_0 M_s$ – magnetization, H_c – coercivity and the value of the mean hyperfine field using the ^{57}Fe nuclei (B_{eff}) and the dispersion of the hyperfine field distributions of the amorphous phase (D_{am}).

Tabela 1: Podatki iz analize statične histerezne zanke: $\mu_0 M_s$ – magnetizacija, H_c – koercitivnost in vrednost glavnega hiper šibkega polja z uporabo ^{57}Fe nukleusov (B_{eff}) in disperzijo razporeditve hiper finega polja amorfne faze (D_{am}).

Sample	$\mu_0 M_s$	H_c	B_{eff} (T)	D_{am} (T)
as-cast	1.17	42	19.50(6)	5.13(8)
700	1.05	27	20.57(5)	5.78(5)
770	1.20	37	20.78(4)	5.50(5)

The initial magnetization curves were analysed according to the theory of the approach to ferromagnetic saturation proposed by H. Kronmüller and M. Fähnle¹⁸, A. Neuweiler et al.²² and M. Hirsher et al.²³ This theory facilitates the extraction of information about the sources of internal stresses occurring in the material, such as free volumes and quasi-dislocation dipoles.^{18,22} Inhomogeneities affect the internal stress of the structure and the process of magnetization in high magnetic fields. An analysis of the initial magnetization curves enabled the determination of the type of defects in the samples in a state following solidification and after isothermal annealing at the temperatures of 700 K and 770 K. Figure 5 shows a 'linear-fit' for the sample following solidification, fulfilling the law of the approach to ferromagnetic saturation (LAFS) as a function of $(\mu_0 H)^{-1}$ within magnetic fields ranging from $0.016 \text{ T} < \mu_0 H < 0.74 \text{ T}$. In contrast, for the sample after the isothermal

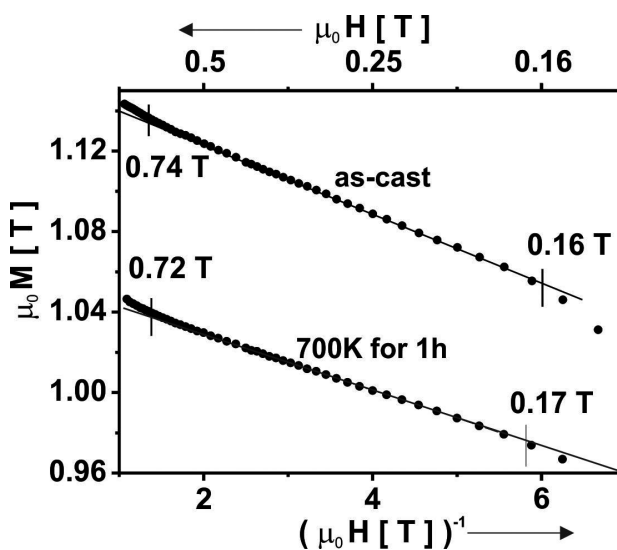


Figure 5: Magnetization as a function of $(\mu_0 H)^{-1}$ for a sample after solidification and annealed at 700 K for 1 h

Slika 5: Magnetizacija v odvisnosti od $(\mu_0 H)^{-1}$ za vzorec po strjevanju in žarjenem 1 h na 700 K

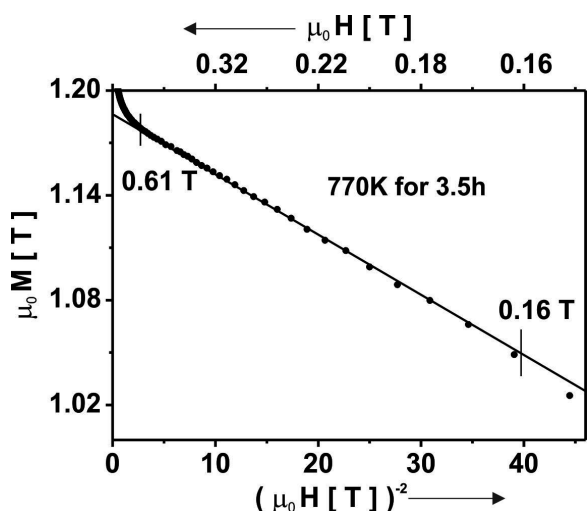


Figure 6: Magnetization as a function of $(\mu_0 H)^{-1}$ for a sample after annealing at 770K for 3.5h

Slika 6: Magnetizacija v odvisnosti od $(\mu_0 H)^{-1}$ pri vzorcu žarjenem 3,5 h na 770 K

annealing process, at a temperature of 700 K for 1 h the LAFS was fulfilled within the range of magnetic field of $0.017 \text{ T} < \mu_0 H < 0.72 \text{ T}$. This indicates that defects in the form of quasi-dislocational dipoles are playing a decisive role in the magnetization process (where the exchange distance l_H it is greater than the size of the dipole defect D_{dip} ($l_H > D_{\text{dip}}$)).^{18,22} For the sample annealed at 770 K for 3.5 h, the LAFS was fulfilled as a function of $(\mu_0 H)^{-2}$ (**Figure 6**) within the range from $0.16 \text{ T} < \mu_0 H < 0.61 \text{ T}$. In this case, the decisive role in the process of magnetization is played by quasi-dislocational dipoles, for which there is a relation $l_H < D_{\text{dip}}$.

At higher fields, where structural defects did not play a significant role in the magnetization process, the magnetization of the material occurs by means of the damping of thermally induced magnetic spin waves.

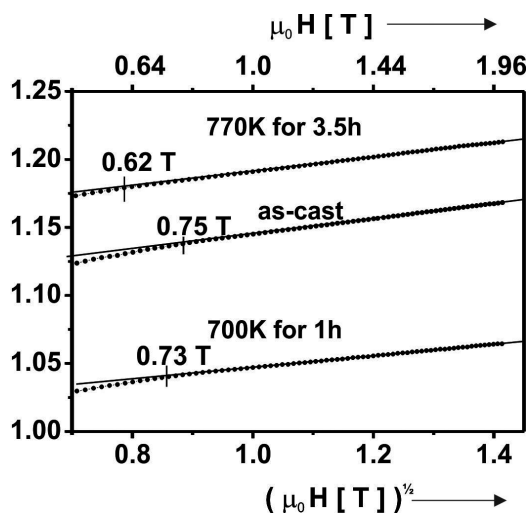


Figure 7: The Holstein-Primakoff para-process obtained for the investigated alloy

Slika 7: Holstein-Primakoff paraprocess pridobljen za preiskovano zlitino

Figure 7 shows the linear fit of the magnetization as a function of $(\mu_0 H)^{1/2}$, describing the Holstein-Primakoff paraprocess.²⁴ The following relationship was used in Equation (1):

$$b = 354 g \mu_0 \mu_B \left(\frac{1}{4\pi D_{\text{spf}}} \right)^{3/2} kT (g \mu_B)^{1/2} \quad (1)$$

where k – Boltzmann constant, μ_B – Bohr's magneton, g – gyromagnetic coefficient, calculated spin wave stiffness parameter (D_{spf}).²⁰ The calculated data, based on the theory of approach to ferromagnetic saturation, is summarized in **Table 2**.

Based on analysis of the data, presented in **Table 2**, and in the papers^{20,25,26}, it can be concluded that the sample that was thermally treated at 700 K for 1 h featured the most relaxed and homogeneous structure; this can also be seen through an analysis of the results of the magnetic and Mössbauer studies, presented in **Table 1**.

Table 2: Data obtained from analysis of the magnetization as a function of the magnetic field, as powers of $1/2$, 1, 2 and $1/2$. D_{spf} – spin wave stiffness parameter, A_{ex} – exchange constant, l_H – exchange length, N_{dip} – density of quasi-dislocational dipoles (1) as-cast state, (2) annealed 700 K, (3) annealed 770 K

Tabela 2: Podatki dobljeni iz analize magnetizacije, v odvisnosti od magnetnega polja, v pristojnosti $1/2$, 1, 2 in $1/2$. D_{spf} – parameter togosti spinskega vala, A_{ex} – izmenjalna konstanta, l_H – dolžina izmenjave, N_{dip} – gostota kvazi-dislokacijskih dipolov (1) lito stanje, (2) žarjeno na 700 K, (3) žarjeno na 770 K

lp	B ($10^{-2} \text{ T}^{1/2}$)	D_{spf} (10^{-2} meV nm ²)	A_{ex} (10^{-12} J m ⁻¹)	l_H (10^{-9} nm)	N_{dip} (10^{16} nm ⁻²)
1	5.657(6)	45.11(6)	1.71(3)	2.24(3)	19.93(3)
2	4.333(2)	53.84(2)	1.86(3)	2.38(3)	17.61(3)
3	5.415(2)	46.41(2)	1.80(2)	2.48(2)	16.24(2)

4 CONCLUSIONS

In the case of crystalline materials, it is well known that the structure is well described and can be characterised by one primitive cell featuring a certain number of atoms and angular translation. However, in the case of amorphous materials, their structure hitherto has not been completely characterised. In general, in the literature an amorphous structure is described as a metastable system of randomly distributed atoms. The first sign of changes in this structure is the process of nucleation of the crystalline grains, which results in a material consisting of two phases: the amorphous matrix and the fine crystalline grains. Of course, the results of the investigations concerning amorphous materials that have been subjected to an annealing process (below the crystallisation temperature) are presented in many papers. However, the description of the changes in the magnetic parameters is limited only to changes in the exchange interactions between the magnetic atoms.

In this paper, the "real" structure of an amorphous alloy in the as-quenched state, and after two stages of the

isothermal annealing, has been studied. An indirect method of investigation has been used, which relies on an analysis of the initial magnetization curves in the LAFS region.^{18,27} Currently, this is the only known method which facilitates a determination of the type and volume of the structural defects present in the amorphous materials. These defects are the source of the short-range structural defects and lead to non-collinear distributions of the magnetisation in their vicinity, which is directly reflected in the changes to the magnetisation curve.

It is well known that annealing results in structural relaxation. This can happen in two-ways: by conglomerating the free volumes to the linear defects or by releasing free volumes to the surface. Therefore, a two-stage annealing process was performed, at well-below the crystallisation temperature (at 700 K and 770 K). This resulted in structural relaxation through changes in the density and the local chemical composition, leading to a decrease in the number of centres of relaxation. It is shown in the literature^{14,28–31} that relaxations occur at the atomic level, where the pre-exponential factor in the Arrhenius law is in the order of 10^{-15} .

The investigated plate-shaped samples of the $\text{Fe}_{61}\text{Co}_{10}\text{Y}_8\text{Mo}_1\text{B}_{20}$ alloy in the state following solidification and after annealing at temperatures of 700 K and 770 K were found to feature an amorphous structure.

The magnetic studies showed that the annealing temperature has a significant impact on the changes in the magnetic properties. It was found that the sample annealed at 700 K for 1 h had the lowest coercive field, $H_c = 27$ A/m. In contrast, the sample that was heat-treated at 770 K for 3.5 h had the highest saturation magnetization.

The results of the Mössbauer studies and the analysis of the initial magnetization curve, in accordance with Kronmüller theory, showed that thermal treatment at a temperature of 700 K for 1 h caused the greatest homogenization of the structure of the samples. On the other hand, for the investigated alloy in the form of plates annealed at 700K for 1h, the decisive role in the process of magnetization is played by defects in the form of quasi-dislocational dipoles for which the relationship $l_H > D_{\text{dip}}$ is satisfied. For the plate samples that were annealed at 770 K for 3.5 h, the decisive role in the process of magnetization is played by quasi-dislocational dipoles for which there is a relationship $l_H < D_{\text{dip}}$.

5 REFERENCES

- P. Pietrusiewicz, M. Nabialek, M. Szota, K. Perduta, Microstructure and soft magnetic properties of $\text{Fe}_{61}\text{Co}_{10}\text{Y}_8\text{Me}_1\text{B}_{20}$ (where Me = W, Zr or Nb) amorphous alloys, *Archives of Metallurgy and Materials*, 57 (2013) 1, 265–270, doi:10.2478/v10172-012-0021-8
- P. Pietrusiewicz, M. Nabialek, M. Dośpiał, K. Gruszka, K. Bloch, J. Gondro, P. Brągiel, M. Szota, Z. Stradomski, Influence of production method on the magnetic parameters and structure of $\text{Fe}_{61}\text{Co}_{10}\text{Y}_8\text{Nb}_1\text{B}_{20}$ amorphous alloys in the as-quenched state, *Journal of Alloys and Compounds*, 615 (2014), S67–S70, doi:10.1016/j.jallcom.2014.03.028
- S. Lesz, M. Nabialek, R. Nowosielski, Structural, thermal and magnetic properties of Fe-Co-Ni-B-Si-Nb bulk amorphous alloy, *Mater. Technol.*, 49 (2015) 3, 409–412, doi:10.17222/mit.2014.108
- R. Hasegawa, Advances in amorphous and nanostructured materials, *Journal of Optoelectronics and Advanced Materials*, 6 (2004) 2, 503–510
- M. Vazquez, Soft magnetic wires, *Physica B*, 299 (2001) 3–4, 302–313, doi:10.1016/S0921-4526(01)00482-3
- W.H. Wang, C. Dong, C.H. Shek, Bulk metallic glasses, *Materials Science and Engineering R*, 44 (2004), 45–89, doi:10.1016/j.mser.2004.03.001
- C. Suryanarayana, A. Inoue, Iron-based bulk metallic glasses, *International Materials Reviews*, 58 (2013) 3, 131–166, doi:10.1179/1743280412Y.0000000007
- A. Inoue, B. L. Shen, A new Fe-based bulk glassy alloy with outstanding mechanical properties, *Advanced Materials*, 16 (2004) 23–24, 2189–2192, doi:10.1002/adma.200400301
- T. Sahoo, Influence of annealing environment on microstructure and magnetic properties of amorphous $\text{Co}_{75}\text{Fe}_5\text{Zr}_{10}\text{B}_{10}$ ribbons, *Journal of Alloys and Compounds*, 470 (2009) 1–2, 16–19, doi:10.1016/j.jallcom.2008.02.088
- M. Nabialek, Soft magnetic and microstructural investigation in Fe-based amorphous alloy *Journal of Alloys and Compounds*, 642 (2015), 98–103, doi:10.1016/j.jallcom.2015.03.250
- K. M. Gruszka, M. Nabialek, K. Bloch, J. Olszewski, Effect of heat treatment on the shape of the hyperfine field induction distributions and magnetic properties of amorphous soft magnetic $\text{Fe}_{62}\text{Co}_{10}\text{Y}_8\text{B}_{20}$ alloy, *Nukleonika*, 60 (2015) 1, 23–27, doi:10.1515/nuka-2015-0007
- K. Gruszka, M. Nabialek, K. Bloch, S. Walters, Analysis of the structure (XRD) and microstructure (TEM, SEM, AFM) of bulk amorphous and nanocrystalline alloys based on FeCoB, *International Journal of Materials Research (formerly Z. Metallkd.)*, 106 (2015) 7, 689–696, doi 10.3139/146.111226
- J. L. Fu, Z. J. Yan, Y. Xu, X. L. Fan, D.S. Xue, Effects of annealing temperature on structure and magnetic properties of amorphous $\text{Fe}_{61}\text{Co}_{27}\text{P}_{12}$ nanowire arrays, *Journal of Physics and Chemistry of Solids*, 68 (2007) 12, 2221–2226, doi:10.1016/j.jpcs.2007.06.023
- M. Nabialek, P. Pietrusiewicz, K. Bloch, M. Szota, An investigation into the effect of isothermal annealing on the structure (XRD), microstructure (SEM, TEM) and magnetic properties of amorphous ribbons and bulk amorphous plates, *International Journal of Materials Research (formerly Z. Metallkd.)*, 106 (2015) 7, 682–688, doi 10.3139/146.111231
- M. Coisson, S.N. Kane, P. Tiberto, F. Vinai, Influence of DC Joule-heating treatment on magnetoimpedance effect in amorphous $\text{Co}_{64}\text{Fe}_{21}\text{B}_{15}$ alloy, *Journal of Magnetism and Magnetic Materials*, 271 (2004), 312–317, doi:10.1016/j.jmmm.2003.09.038
- S. N. Kane, A. Gupta, S. D. Sarabhai, L. Kraus, Influence of Co content on structural and magnetic properties of $\text{Co}_x\text{Fe}_{84-x}\text{Nb}_7\text{B}_9$ alloys, *Journal of Magnetism and Magnetic Materials*, 254–255 (2003), 495–497, doi:10.1016/S0304-8853(02)00848-X
- S. N. Kane, A. Gupta, Zs. Gercsi, F. Mazaleyrat, L. K. Varga, Mössbauer and magnetic studies of $(\text{Fe}_{100-x}\text{Co}_x)_{62}\text{Nb}_8\text{B}_{30}$ ($X=0, 33, 50$) alloys, *Journal of Magnetism and Magnetic Materials*, 292 (2005), 447–452, doi:10.1016/j.jmmm.2004.11.314
- H. Kronmüller, M. Fähnle, *Micromagnetism and the microstructure of ferromagnetic solids*, Cambridge University Press, Cambridge 2003
- H. Oukris, H. Lassri, E. H. Sayouty, J. M. Greneche, Magnetic and Mössbauer studies of amorphous Fe–Al–Er–B ribbons, *Journal of Magnetism and Magnetic Materials*, 260 (2003) 1–2, 23–27, doi:10.1016/S0304-8853(02)00059-8
- M. Nabialek, P. Pietrusiewicz, K. Bloch, Influence of the production method of $\text{Fe}_{61}\text{Co}_{10}\text{Y}_8\text{W}_1\text{B}_{20}$ amorphous alloy on the resulting microstructure and hyperfine field distribution, *Journal of Alloys and Compounds*, 628 (2015), 424–428, doi:10.1016/j.jallcom.2014.12.136

P. PIETRUSIEWICZ et al.: THE INFLUENCE OF AN ISOTHERMAL ANNEALING PROCESS ON THE STRUCTURE ...

- ²¹ P. Gupta, A. Gupta, A. Shukla, Tapas Ganguli, A. K. Sinha, G. Principi, A. Maddalena, Structural evolution and the kinetics of Cu clustering in the amorphous phase of Fe-Cu-Nb-Si-B alloy, *Journal of Applied Physics*, 110 (2011) 3, 033537, doi:10.1063/1.3622325
- ²² A. Neuweiler, B. Hofmann, H. Kronmüller, Approach to magnetic saturation in nanocrystalline and amorphous Fe_{73.5}Cu₁Nb₃Si_{13.5}B₉, *Journal of Magnetism and Magnetic Materials*, 153 (1996), 28–34, doi:10.1016/0304-8853(95)00533-1
- ²³ M. Hirscher, R. Reisser, R. Würschum, H. E. Schaefer, H. H. Kronmüller, Magnetic after-effect and approach to ferromagnetic saturation in nanocrystalline iron, *Journal of Magnetism and Magnetic Materials*, 146 (1995), 117–122, doi:10.1016/0304-8853(94)01643-7
- ²⁴ T. Holstein, H. Primakoff, Field dependence of the intrinsic domain magnetization of a ferromagnet, *Physical Review*, 58 (1940), 1098–1113, doi:10.1103/PhysRev.58.1098
- ²⁵ N. Kaul, Magnetic properties of amorphous (Fe, Ni)₈₀B₂₀, (Fe, Ni)₈₀B₁₉Si₁, and (Fe, Ni)₈₀P₁₄B₆ alloys, *IEEE Transaction on Magnetics*, 17 (1981) 2, 1208–1215, doi:10.1109/TMAG.1981.1061194
- ²⁶ B.W. Corb, R.C. O’Handley, N.J. Grant, Chemical bonding, magnetic moments, and local symmetry in transition-metal—metalloid alloys, *Physical Review B*, 27 (1983), 636–641, doi:10.1103/PhysRevB.27.636
- ²⁷ K. Błoch, Magnetic properties of the suction-cast bulk amorphous alloy: (Fe_{0.61}Co_{0.10}Zr_{0.025}Hf_{0.025}Ti_{0.02}W_{0.02}B_{0.20})₉₆Y₄, *Journal of Magnetism and Magnetic Materials*, 390 (2015), 118–122, doi:10.1016/j.jmmm.2015.04.032
- ²⁸ M. Nabiałek, P. Pietrusiewicz, M. Dośpiał, M. Szota, J. Gondro, K. Gruszka, A. Dobrzańska-Danikiewicz, S. Walters, A. Bukowska, Influence of the cooling speed on the soft magnetic and mechanical properties of Fe₆₁Co₁₀Y₈W₁B₂₀ amorphous alloy, *Journal of Alloys and Compounds*, 615 (2014), S56–S60, doi:10.1016/j.jallcom.2013.12.236
- ²⁹ P. Pietrusiewicz, K. Błoch, J. Gondro, M. Nabiałek, M. Dośpiał, M. Szota, Magnetic relaxations in amorphous Fe₆₁Co₁₀Y₈Zr₁B₂₀ alloy, *Acta Physica Polonica A*, 126 (2014) 1, 106–107, doi:10.12693/APhysPolA.126.106
- ³⁰ K. Błoch, M. Nabiałek, P. Pietrusiewicz, J. Gondro, M. Dośpiał, M. Szota, K. Gruszka, Time and thermal stability of magnetic properties in Fe₆₁Co₁₀Y₈Nb₁B₂₀ bulk amorphous alloys, *Acta Physica Polonica A*, 126 (2014) 1, 108–109, doi:10.12693/APhysPolA.126.108
- ³¹ P. Pietrusiewicz, K. Błoch, M. Nabiałek, S. Walters, Influence of 1% addition of Nb and W on the relaxation process in classical Fe-based amorphous alloys, *Acta Physica Polonica A*, 127 (2015) 2, 397–399, doi:10.12693/APhysPolA.127.397

RHEOLOGICAL PROPERTIES OF FEEDSTOCKS AND THE STRUCTURE OF INJECTION MOULDERS FOR SINTERING COMPOSITE TOOL MATERIALS BASED ON MMCS

REOLOŠKE LASTNOSTI MEŠANIC IN STRUKTURA VBRIZGANIH REZKARJEV ZA SINTRANE KOMPOZITNE ORODNE MATERIALE NA OSNOVI MMCS

Klaudiusz Gołombek¹, Grzegorz Matula¹, Jarosław Mikula¹, Mirko Soković²

¹Silesian University of Technology, Institute of Engineering Materials and Biomaterials, Gliwice, Poland

²University of Ljubljana, Faculty of Mechanical Engineering, Ljubljana, Slovenia
klaudiusz.golombek@polsl.pl

Prejem rokopisa – received: 2015-10-20; sprejem za objavo – accepted for publication: 2015-12-24

doi:10.17222/mit.2015.318

New functional tool composite materials with a metallic matrix and reinforced with hard carbide phases have been developed. The effect of the polymer binder has been determined for the used moulding a mixture of hard carbide powders based on WC, TiC, (W, Ti)C, doped with VC, NbC and/or TaC and powders of a metallic matrix in the form of Co and/or Ni. The relevant type of polymer binder was selected, its optimum volume fraction was determined, the rheological properties of the polymer-powder slip were investigated along with thermal debinding conditions, i.e., atmosphere, time and temperature, as well as solvent debinding conditions, i.e., solving time and temperature and sintering conditions were matched. The structure and mechanical properties of the produced tool materials were examined, especially their resistance to abrasive wear, hardness and bending strength.

Keywords: composite tool materials, reinforced metal matrix, powder injection moulding (PIM)

Razvili smo nove funkcionalne kompozitne orodne materiale s kovinsko matrico, ojačane s trdimi karbidnimi fazami. Določili smo učinek polimernega veziva, uporabljenega za brizganje zmesi trdih prahov, na osnovi WC, TiC in (W,Ti) C, legirane z VC, NbC in/ali TaC, ter prahov kovinske matrice v obliki Co in/ali Ni. Izbrali smo ustrezno vrsto polimernega veziva in določili njegov optimalen volumski delež. Raziskali smo tudi reološke lastnosti sistema polimer-prah skupaj s pogoji termičnega razpada veziva, (atmosfera, čas in temperatura), kot tudi pogoje razgradnje topil (čas in temperatura raztapljanja) usklajeno s pogoji sintranja. Določili smo strukturo in mehanske lastnosti izdelanih orodnih materialov, zlasti odpornost proti abrazivni obrabi, trdoto in upogibno trdnost.

Ključne besede: kompozitni orodni materiali, ojačana kovinska matica, oblikovanje prahov z vbrizgavanjem

1 INTRODUCTION

Research institutes active in the field of tool materials for many years have been endeavouring to develop a "perfect" tool material possessing high ductility, resistance to dynamic loads and high abrasive-wear resistance. The manufacturing costs of engineering materials would be markedly lower if such a tool, often coated with protective coatings, had been developed with cost savings associated with machining, especially manufacturing downtimes and the necessary replacement of a worn tool. Even the high costs of investigations of properties and applications of modern tool materials and the related manufacturing costs do not constitute a barrier for the development of this field of research.

The use of injection moulding or the extrusion of sintered tool materials represents one of the modern directions of the research. Powder forming and sintering technologies offer unlimited opportunities for selecting the chemical composition of the tool composites produced. Classical powder metallurgy based on uniaxial pressing and sintering with potential isostatic pressing at

a high sintering temperature prevents the fabrication of tools with complicated shapes. The injection extrusion or forming techniques of a polymer-powder slip, undergoing rapid advancements, make it possible to produce relatively small parts with complicated shapes and a developed area, and also make it possible to produce materials not requiring plastic working or machining. The use of powder forming based on polymer binders, in particular injection moulding or extrusion, has become the subject of research in numerous research institutes and universities.

Moreover, our own research of high-speed steels manufactured by powder injection moulding and pressureless forming prove that the structure and wear resistance are similar with commercial high-speed steels, but with less ductility. In addition, the manufacturing technique employed, especially the debinding and sintering process carried out in protective atmospheres, permits the use of furnaces that are cheaper than vacuum furnaces, which is important in process lines. The monitoring and maintaining of a narrow range of sintering

temperature is undoubtedly a difficult aspect in industrial conditions. The use of modern, polymer-binder-based powder-forming technologies, in particular injection moulding, for preparing metal-matrix-reinforced tool composites creates a promising outlook for the fabrication of functional materials. WC, (W,Ti)C carbides doped with VC, NbC and/or TaC, frequently used as hard reinforcing phases of sintered carbides based on cobalt, especially in this configuration, were used for fabricating composite tool materials, as TiC phases, mainly VC, inhibit the growth of a WC carbide grain in sintering. Metal, constituting a matrix of sintered carbides, must exhibit a smaller affinity for carbon than a carbide metal, and in the liquid state it has to wet the carbide grains, interpenetrate the grains, filling in pores and exhibiting the limited solubility of carbide grains. Nickel and cobalt, often used as a matrix material, satisfy such conditions.¹⁻²² Some research groups propose to use cheaper compounds for the metal matrix such as Fe, but the sintering of WC carbides with a steel matrix causes the dissolving of this type of carbides and the precipitation of M_6C carbides with lower hardness.

The paper provides an overview of the fabricating of new Co- and/or Ni-based functional composite tool materials reinforced with hard carbide phases. The essence of the investigations concerns the application of a state-of-the-art polymer-powder slip forming technology for manufacturing composite tool materials in the form of sintered carbides ensuring high resistance to abrasive wear, corrosion and diffusion in the tools' working conditions.

2 EXPERIMENTAL PART

The experimental mixtures of powders used for manufacturing sintered carbides being the main component of the feedstock, as presented in **Table 1** and in **Figures 1 to 4**. The mixtures produced by Baildonit S.A. (CC1, CC2, CC3) come as a granulated product and feature a high flow rate and are intended mainly for

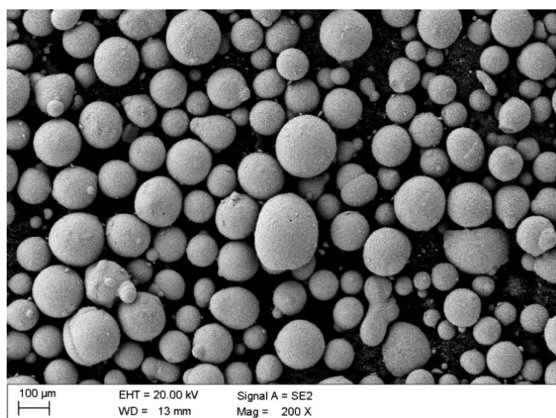


Figure 1: Morphology of CC1 granules
Slika 1: Morfologija CC1 granul

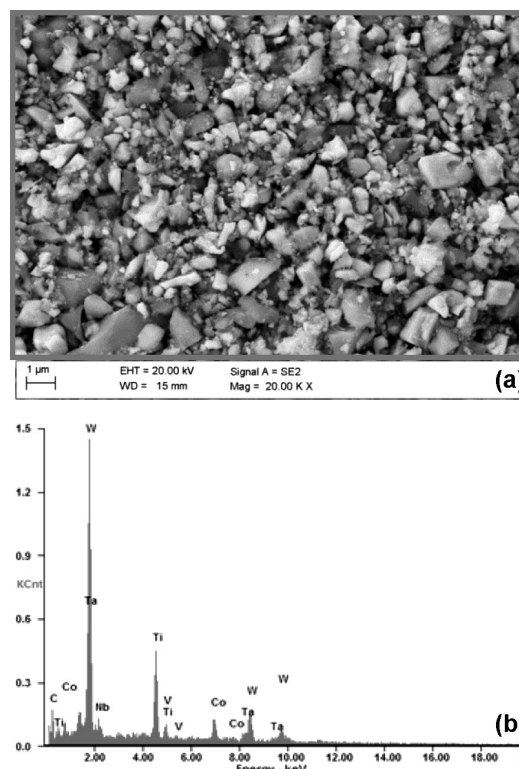


Figure 2: a) Morphology of CC1 powder, b) X-ray energy-dispersive plot of the area in **Figure 2a**

Slika 2: a) Morfologija prahu CC1, b) EDS-spekter področja označenega na Sliki 2a

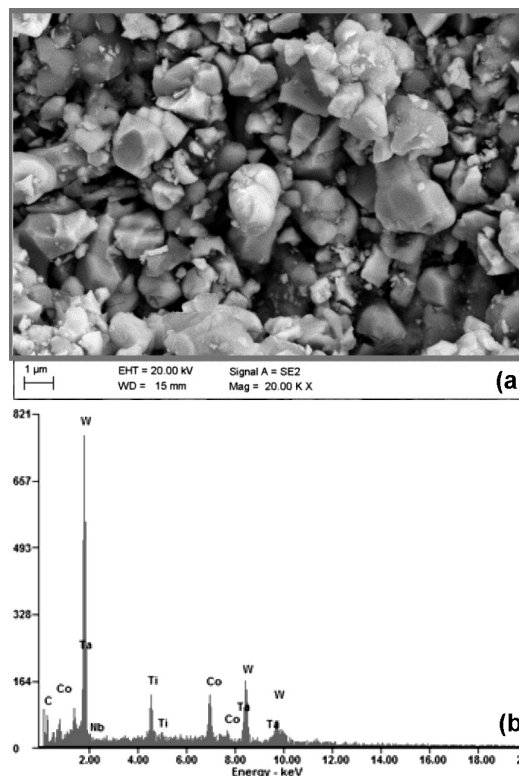


Figure 3: a) Morphology of CC2 powder, b) X-ray energy-dispersive plot of the area in **Figure 3a**

Slika 3: a) Morfologija prahu CC2, b) EDS-spekter področja označenega na Sliki 3a

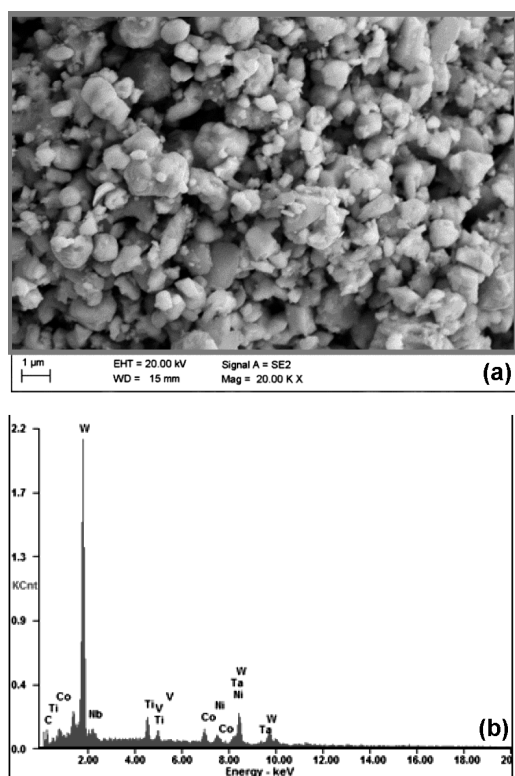


Figure 4: a) Morphology of CC3 powder, b) X-ray energy-dispersive plot the area in **Figure 4a**

Slika 4: a) Morfologija prahu CC2, b) EDS-spekter področja označenega na **Sliki 4a**

pressing shaped sections and then for sintering. The CC1, CC2, CC3 mixtures with a lubricant added exhibit the high compatibility required in moulding in a closed die. The mixture produced by Tetra Carbides-TC does not contain a lubricant.

Table 1: Applied mixture of carbides

Tabela 1: Uporabljena mešanica karbidov

Designation	Average particle size	Amount of components in volume fractions, %
CC1	2–3 μm	57WC, 20TiC, 14Ta(Nb)C, 9Co
CC2	2–3 μm	87WC, 5TiC, 8Co
TC Tetra Carbides	$d_{50} = 3.11\mu\text{m}$	33WC, 33TiC, 25TaC, 8NbC, Co
CC3	1–2 μm	69WC, 20 (TiC,TaC), 2VC, 5Co, 4Ni

The addition of a lubricant was considered when selecting a binder. Mixtures in the form of a granulated product make it possible to measure the powder grain size, hence only the average size of the powder grains given by the manufacturers is presented in **Table 1**. Grain size tests were made for the mixture of tetra carbides powders with a Malvern Mastersizer 2000 instrument for measuring the size of the particles with the laser-diffraction method.

A mixture of polypropylene (PP) and paraffin (PW) was used as a binder for producing the feedstock. The effect of the presence of stearic acid (SA), as a sur-

factant, on the feedstock viscosity was also examined. The feedstock was prepared with the Rheomex CTW100p instrument by Haake shown in **Figure 5** making it possible to record the torque of the vanes during the homogenisation of components. The fraction of the relevant components of the binder and powder is shown in **Table 2**. In order to cover the surface of the carbides with stearic acid (SA), carbide powders, stirred strongly for 30 min so that SA is distributed evenly across the surface of carbides, were added to the SA dissolved in ethanol. The mixture was then heated to 60 °C to evaporate the ethanol. The so-prepared carbide powders covered with the SA coating were next mixed with the main binder as PP and PW. Rheological tests were carried out in a capillary rheometer Rheoflax by ThermoHaake at 170 °C, 180 °C and 190 °C.

Table 2: Amount of components in all manufactured polymer-powder slurry in volume

Tabela 2: Volumski delež komponent v vseh proizvedenih kombinacijah gošče polimer-prah

Designation	Powder	PP, % in vol. frac.	PW, % in vol. frac.	SA, % in vol. frac.
CC160SA4	CC1	18	18	4
CC157SA2	CC1	20,5	20,5	2
CC154SA0	CC1	23	23	0
TC60SA4	Tetra Carbides	18	18	4
CC2	CC2	18	18	4
CC3	CC3	18	18	4

In order to prepare a homogenous mixture with a low viscosity enabling injection moulding or extrusion, carbide powders were covered with a thin layer of stearic acid, thus increasing their wettability when mixing with other binder components and to decrease a ready feedstock's viscosity.

The coagulation speed of 10 s⁻¹ to 10000 s⁻¹ was chosen during the investigations and the length and width of the capillary is, respectively, 30 mm and 1 mm. The melting point for the binders used was determined

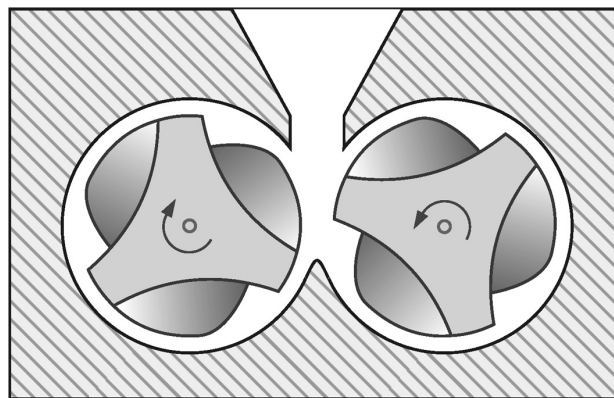


Figure 5: Scheme of Haake Rheomex CTW100p apparatus for the torque measurement and homogenization

Slika 5: Shema naprave Haake Rheomex CTW100p za merjenje navora in homogenizacijo

with differential scanning calorimetry (DSC) using a Perkin Elmer instrument, Diamond model, in order to determine the extrusion or injection moulding temperature of the prepared polymer-powder mixtures. The amount of heat can be recorded with the instrument and its software, presented as a peak chart as a heat effect of the process curve, while the area of the field underneath the peak equals the enthalpy of such a transformation.

The AB Machinery AB-400 piston injection moulder with a retractable mould heated to 150 °C was used for the injection moulding. The extruded sections were produced in the Rheomex CTW100p twin-screw extruder.

The structural observations of the examined composite tool materials were made with a LEICA MEF4A light microscope with the light field technique and the morphology of the powder grains and the structure of the materials produced was viewed with a scanning electron microscope ZEISS SUPRA 35 at the accelerating voltage of 20 kV using SE and BSE detection.

The bending strength of the injection moulders was measured with a ZWICK Z100 tensile testing machine fitted with an adapter for three-point bending. The test was made in line with PN ISO 3327: "Determination of bending strength".

3 RESULTS AND DISCUSSION

The results of the investigations into the grain size distribution of the tetra carbides powder ($d_{10} = 1.45 \mu\text{m}$, $d_{50} = 3.11 \mu\text{m}$ and $d_{90} = 7.36 \mu\text{m}$), and especially the values d_{10} and d_{90} , allow us to calculate the filling ratio of the injection-moulded section S_w according to the following dependence $S_w = 2.56 / (\log(d_{90}/d_{10}))$. The S_w value calculated is 3.64, which allows for the injection moulding of the powder examined. Powder with a S_w coefficient of 2 is the most recommended for injection moulding. It is not recommended to mould powder with a S_w coefficient of 7 with its powder grain size distribution characteristic being very narrow. The characteristic of the examined powder's grain size distribution is relatively broad, therefore, the pores forming between large grains may be filled by small particles. No grain size distributions tests and S_w coefficient calculations were made for the mixtures of powders manufactured by

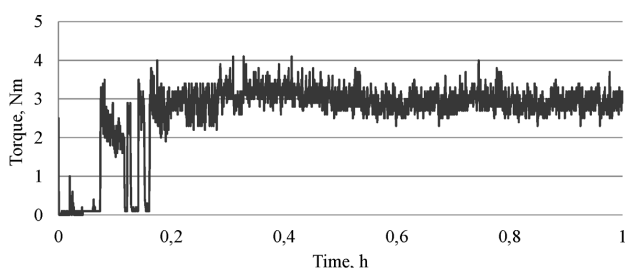


Figure 6: Torque measurements of feedstock based on PP and PW with 64 % amounts of CC1 mixture carbides

Slika 6: Meritve navora mešanice, ki temeljijo na PP in PW s 64 %-nim deležem zmesi karbidov CC1

Baldonit, as such powders are prepared as a granulated product and mainly intended for pressing.

It was determined according to tests of the torque tested during the homogenisation of powder mixtures with a binder that, irrespective of the powders used, their maximum fraction should not exceed 60 %. The tested torque of stirrers is considerably decreased by adding stearic acid.

Figure 6 shows a torque chart for a mixture of 64 % CC1 carbide with 13 % of paraffin and polypropylene in volume. The mixture was produced at 170 °C. The characteristic of the curve presenting the torque according to the feedstock mixing time is unstable, signifying an excessive fraction of carbide powders and inhomogeneous distribution of a binder in the matrix, despite a long homogenisation time. Besides, the curve does not show a falling tendency, despite long mixing, thus such a high content of powder cannot be used. In the case of a mixture with only 50 % content of carbides, the torque of the stirrers falls below 1 Nm after 20 min, proving the low viscosity of the polymer and powder mixture. A smooth and falling characteristic of the curve signifies the mixture's high homogeneity.

A 50 % content of carbides in the produced feedstock of the moulder or extruder ensures its low viscosity, but may cause numerous problems in the debinding of such a high fraction of a binder or may lead to the distortion of specimens during sintering as a result of high shrinkage of the sinter. Hence, a well-prepared feedstock should be characterised by a possibly high fraction of powder and relatively low viscosity enabling its formation. It has been concluded according to data from the literature and our own studies that the feedstock's viscosity is considerably reduced by applying a small amount of stearic acid as an active surfactant.

Table 3 shows the results of torque tests for the stirrers homogenising a polymer and powder slip for 1 h, containing 60 % of tetra carbides and a binder in the form of a paraffin (PW) and polypropylene (PP). The torque value is substantially decreased by using stearic acid (SA) covering the surface of the carbides (**Table 3**).

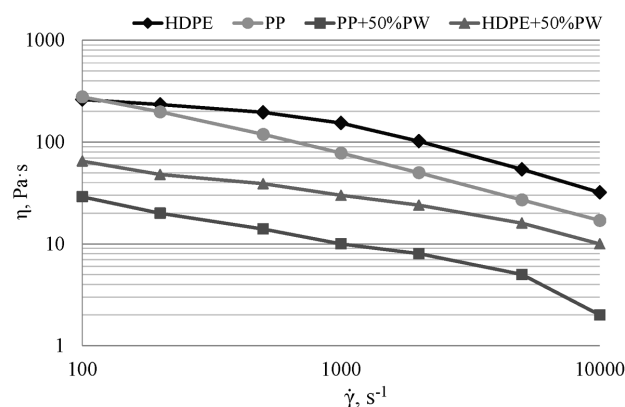


Figure 7: Influence of binder type on rheological behaviour at 170 °C
Slika 7: Vpliv vrste veziva na reološko obnašanje pri 170 °C

A low torque value of mixtures containing polypropylene (PP) and paraffin (PW) corresponds to a low viscosity. The torque is only negligibly reduced by increasing the content of stearic acid from 4 % to 8 %, hence its content in further investigations did not exceed 4 %.

Table 3: Torque measurements of feedstock based on PP, PW and SA with 60 % amounts of TC mixture carbides covered by SA

Tabela 3: Meritve navora mešanice, ki temeljijo na PP, PW in SA s 60 %-nim deležem TC zmesi karbidov, ki jih zajema SA

Time, min	Torque, Nm		
	0 % SA	4 % SA	8 % SA
5	12.20	2.20	1.80
10	7.30	5.90	1.40
15	5.50	1.80	1.30
20	6.00	1.70	1.20
25	5.20	2.10	1.20
30	4.90	1.90	1.20
35	5.50	1.80	1.10
40	5.20	1.60	1.20
45	4.90	1.60	1.10
50	4.90	1.60	1.10
55	5.50	1.50	1.00
60	4.70	1.40	1.10

The outcomes of the rheological tests indicate a smaller viscosity of a powder mixture with PP and PW in respect of a mixture containing High-Density Polyethylene (HDPE) instead of PP, and this is independent of the homogenisation rate. Viscosity is also considerably lowered by applying PW, as confirmed by the results of the rheological tests provided in **Figure 7**. In addition, paraffin allows us to use solvent debinding, expediting the rate of thermal debinding and this shortens the duration of the whole cycle. **Figure 8** presents the effect of the fraction of carbides coated and uncoated with stearic acid on the viscosity of the polymer and powder mixture. Polypropylene and paraffin are the main binder components, regardless the content of stearic acid.

Stearic acid improves the wettability of metallic and ceramic powders by covering their oxidized (polar) surface

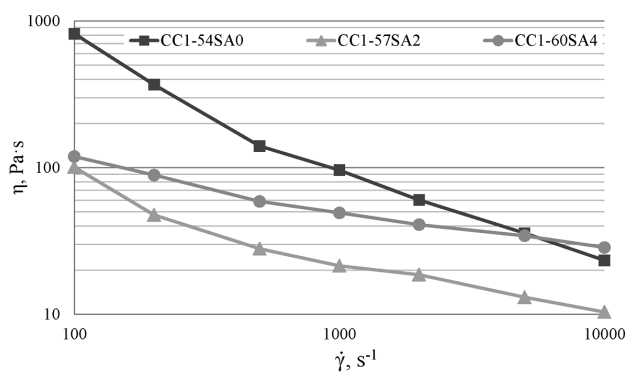


Figure 8: Influence of SA on rheological behaviour of binder and carbides CC1 type mixtures at 170 °C

Slika 8: Vpliv SA na reološko obnašanje veziva in zmesi karbidov CC1 pri 170 °C

that adsorbs the hydrophilic part of the chain as a result of the existing electrostatic forces between the powder and the wetting agent. The non-polar part of the chain should be mixed without limitations with other polymers present in the binder.

Apart from the decreasing viscosity, stearic acid acts as a lubricant in contact between the powder and the die surface or the surface of another particle. It also prevents powders from migrating during high-speed homogenisation. A process of migrating the powder inside the capillary or the destruction of the binder structure occurs most probably during the high-speed homogenisation of a mixture not containing stearic acid, presented in **Figure 8**. This is manifested by a strongly falling viscosity together with an increased homogenisation speed. The viscosity of mixtures containing stearic acid is not so much dependent on the homogenisation speed, hence the growing speed of homogenisation does not have such a strong effect on the structure of a homogenous mixture.

Considering the feedstock viscosity, the maximum applicable fraction of carbides uncoated with stearic acid is 50 %. If stearic acid is used for a mixture containing 50 % of carbides, the viscosity is greatly reduced and a higher volume fraction of carbides can be obtained. The maximum volume fraction of powders applicable in a mixture for injection moulding could be determined by investigating the technological properties of the polymer and the powder mixtures containing binder-carbides.

A test in a capillary rheometer could not have been made due to the excessive viscosity of the mixture containing 68 % of powder. Three polymer-powder mixtures are shown in the diagram. Two of them contain additionally SA, apart from the main binder components. It can be concluded by analysing the research outcomes that the content of stearic acid, similar to the tetra carbides, is strongly reducing the viscosity of the examined polymer-powder mixtures containing CC1 carbides. The mixture with the lowest content of powder and without SA possesses the highest viscosity. For the homogenisation speed of 5000 s⁻¹ and 10000 s⁻¹, the viscosity of

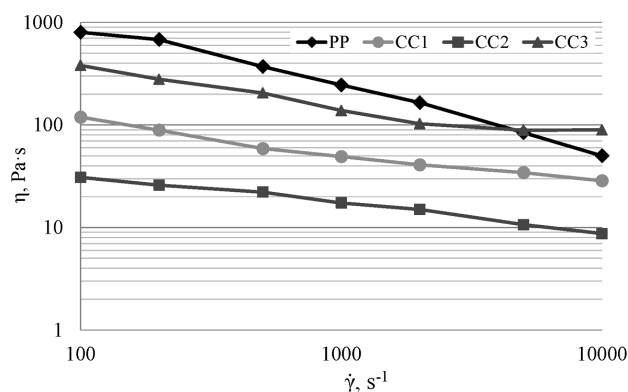


Figure 9: Influence of the type of carbides on rheological behaviour of the feedstock at 170 °C

Slika 9: Vpliv vrste karbidov na reološko obnašanje mešanice pri 170 °C

K. GOŁOMBEK et al.: RHEOLOGICAL PROPERTIES OF FEEDSTOCKS AND THE STRUCTURE ...

the CC154SA0 mixture is accordingly equal and lower than the viscosity of the CC160SA4 mixture. The CC157SA2 mixture has the lowest viscosity, irrespective the homogenisation speed. **Figure 9** shows the results of the viscosity tests according to the type of powder used. Regardless of the powder used, the content of the binder was 40 %, including 4 % of SA.

A mixture with tetra carbides powders applied has the highest viscosity. This is most likely connected with the fact that Baildonit's powder mixtures intended for pressing contain about 2 % of volume fraction of lubricant, most often paraffin, additionally increasing the wettability and reducing the viscosity. Mixtures designed for the industrial manufacturing of sintered carbides possess a high homogeneity and lubricant are tightly covering the surface of carbides. It is thus easier to prepare a polymer powder slip for injection moulding and the slip itself has better properties. Regardless of the mixture type, the viscosity is lower than 1000 Pa·s, hence each of the investigated mixtures is suitable for injection moulding. **Figure 10** compares the results of the viscosity tests for a mixture with tetra carbides applied with pure polypropylene. The viscosity of polypropylene, often used for injection moulding, is higher than the homogenisation speed by 100 s⁻¹ to 5000 s⁻¹, which confirms the earlier conclusion that a mixture with tetra carbides is suitable for injection or extrusion moulding.

Figure 11 presents the diagrams of dependency between stress and homogenisation speed for CC1S60SA4 and CC260SA4 mixtures. The stress is growing as the homogenisation speed grows. Higher stresses are present in a CC1S60SA4 material due to its higher viscosity.

The binder's melting point and debinding temperature start tests were made to determine an injection temperature. An injection temperature of 170 °C was determined according to such measurements. The results of the binder's melting point and crystallisation temperature tests, determined with Differential Scanning Calorimetry (DSC), are shown in **Table 4**. The melting point of polypropylene is 163 °C; however, when mixed with

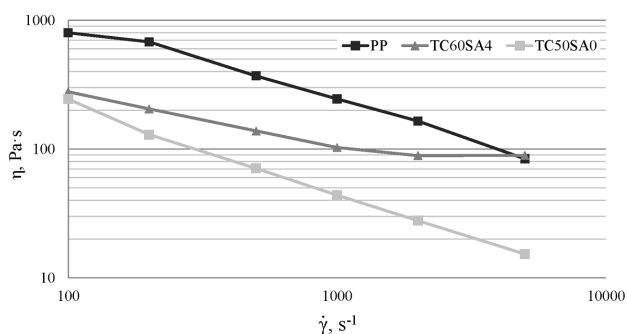


Figure 10: Comparison of feedstock viscosity including TC carbides with viscosity of polypropylene

Slika 10: Primerjava viskoznosti polnil za PIM, ki vključuje karbide TC z viskoznostjo polipropilena

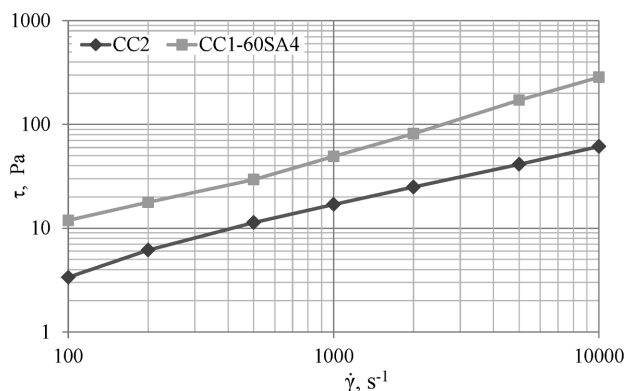


Figure 11: Flow curves of CC160SA4 and CC2 feedstock at 170 °C
Slika 11: Krivulje tečenja za CC160SA4 in CC2 polnilo pri 170 °C

paraffin in the same fraction, the melting point falls to 137 °C.

Table 4: Melting point and crystallization temperature of binder components and their mixture

Tabela 4: Tališče in temperatura kristalizacije komponent veziva in njihove zmesi

Material	Melting point (°C)	Crystallization temperature (°C)
HDPE	130	61
PP	163	108
PW	58.3	47.5
SA	73	62
HDPE/PW	$t_1 = 57.8; t_2 = 127$	$t_1 = 43; t_2 = 72$
PP/PW	$t_1 = 56.6; t_2 = 137$	$t_1 = 45; t_2 = 90$

Thermogravimetric analysis (TGA) for the polymers used, ready binders and ready polymer-powder mixtures were carried out to determine the start temperature of the thermal debinding and to select its cycle preceding sintering. The test results are provided in **Table 5**. The volume fraction of paraffin (PW) versus the main binder of 50 % was assumed. If the PW fraction is increased, the strength properties of the section moulded are deteriorated, while the increased fraction of PP or HDPE precludes the use of solvent debinding.

Table 5: Temperature of the start and finish of thermal debinding

Tabela 5: Temperatura začetka in končanja toplotnega odstranjevanja veziva

Polymer of mixture	Temperature of beginning of thermal debinding (°C)	Temperature of complete thermal debinding (°C)
HDPE	378	503
PP	320	480
PW	198	278
SA	204	286
HDPE/PW	234	497
PP/PW	215	446

An injection temperature cannot be higher than its value, especially considering the beginning of thermal debinding temperature, which is 217 °C. The thermal

debinding of paraffin, used as one of the binder components, may otherwise occur. The rate of mass loss changes at 287 °C, signifying the end of the paraffin debinding. The binder is subject to complete thermal debinding at 444 °C. The temperature of thermal debinding can be selected on the basis of thermogravimetric test results. Direct sintering is necessary due to the low properties of the sections after complete thermal debinding. High-temperature heaters often cannot be used for debinding due to degradation products deposited onto the heat chamber's surface. Debinding in a separate device should then be applied. The related necessity to transport the specimens after debinding into a high-temperature heater device forces us to use incomplete debinding, ensuring minimum mechanical properties, enabling the transport of the specimens. The maximum thermal debinding temperature should be about 420 °C when analysing the TGA curve.

A heating rate should be lowered at the temperature of 217 °C where the paraffin debinding starts, as sections' breaking may occur due to the growing pressure of gaseous products of debinding in pores.

The thermogravimetric tests of the polymer-powder CC260SA mixture were also performed. A thermal debinding cycle shown in **Figure 12** was selected based on the results of the tests. The rate of heating was chosen experimentally.

The heating rate in the thermogravimetric tests was 5 °C/min. Material defects such as cracks may occur during fast heating within the range of the binder's thermal debinding temperature. This is caused by a

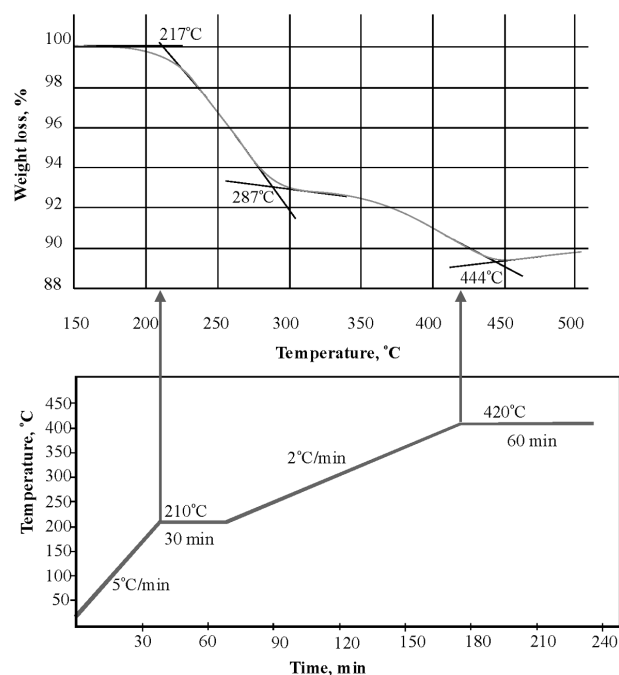


Figure 12: Thermal debinding cycle of CC1-60SA designed on the basis of TGA analysis

Slika 12: Cikel toplotnega odstranjevanja veziva pri CC160SA, zasnovan na podlagi TGA analize

growth in the pressure of gaseous products formed as a result of the thermal debinding. The heating rate was lowered to 2 °C/min. for this reason, and an isothermal interval was additionally used at 200 °C, i.e., the paraffin debinding start temperature. Another isothermal interval depends on several factors, such as the size of the heat chamber, the flow rate of the shielding gases or where a material must be transported into a chamber of another device for sintering. Where the transport of specimens is necessary, debinding should end at a temperature lower than this, resulting from a thermogravimetric curve. A thermal debinding cycle can be shortened by dissolving one of binder components, and no isothermal interval at 200 °C, corresponding to paraffin debinding, is needed for solvent debinding. A heating rate of feedstock can be, therefore, increased to the debinding temperature of PP or HDPE. The binder components such as PP or HDPE do not undergo solvent debinding, and their role is to maintain the formed specimens' shape to the maximum temperature possible.

If the thermal debinding of a binder is carried out at a temperature corresponding to the final temperature of PP or HDPE debinding determined on the thermogravimetric curve, this is linked to the complete degradation of a binder binding the powder particles, hence, such a heat cycle can take place only in a high-temperature

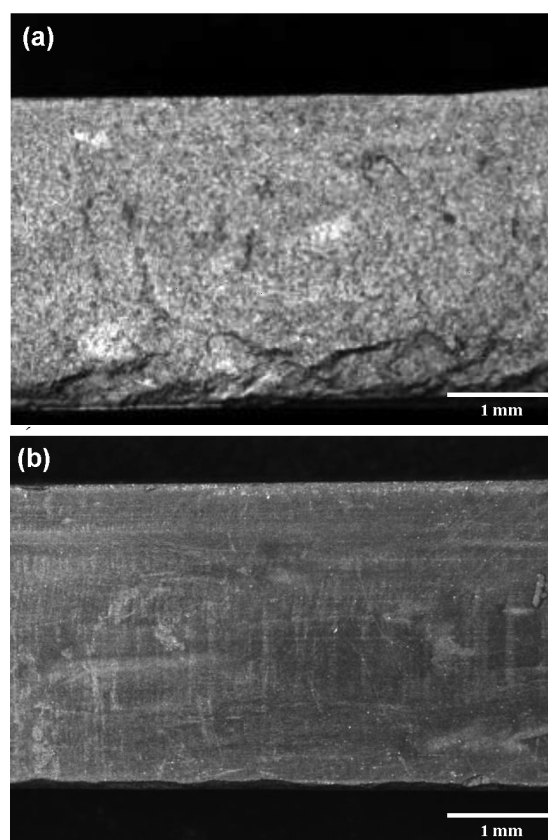


Figure 13: View of the fracture surface of injected CC2 materials: a), b)

Slika 13: Pogled na površini preloma injekcijsko brizganih CC2 materialov: a), b)

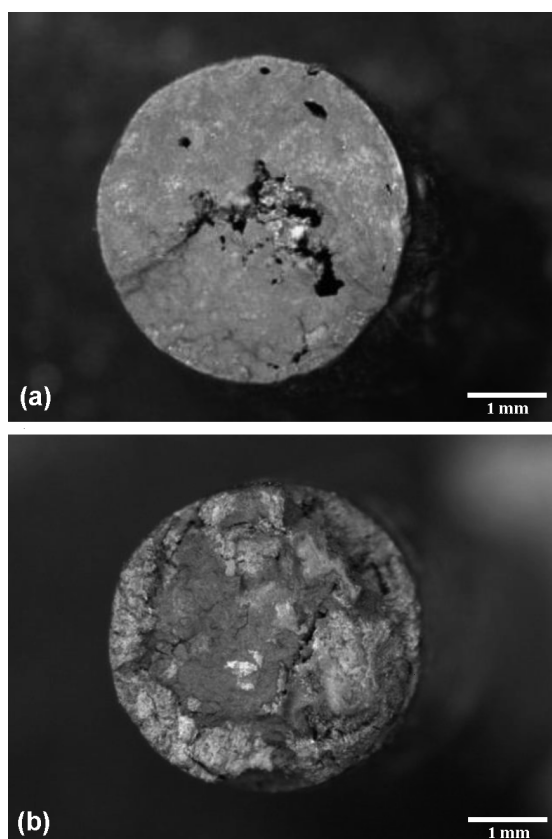


Figure 14: a) View of the fracture surface of CC160SA4 materials extruded at 140 °C, b) view of the fracture surface of extruded CC157SA2 materials at 170 °C

Slika 14: Pogled na prelomni ploskvi ekstrudiranih materialov: a) CC160SA4 pri 140 °C, b) CC157SA2 pri 170 °C

furnace permitting direct sintering after finished debinding.

Otherwise, it is very difficult and dangerous for the materials manufactured to transport specimens from low-temperature heating devices, designed mainly for thermal debinding, to the chambers of high-temperature devices, due to their low mechanical strength.

Injection-moulded materials exhibit the highest bending strength due to a higher moulding pressure and fewer pores. **Figure 13** shows the structure of the CC2S60SA4

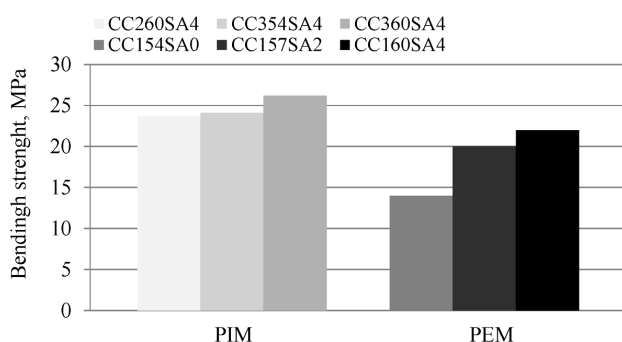


Figure 15: Bending strength of injected and extruded materials

Slika 15: Upogibna trdnost injekcijsko brizganih in ekstrudiranih materialov

material's fracture. No gas bubbles were identified in the material that may form during injection moulding and reduce the bending strength. Growing bending strength in the extruded specimens is linked to the presence of stearic acid covering the powder surface and enhancing the strength of the powder, i.e., binder bondage. The bending strength of the extruded specimens depends on the extrusion conditions. The fractures of the specimens extruded at 140 °C and 170 °C are given in **Figures 14a** and **14b**, respectively.

The results of the bending-strength tests from the injection moulded and extruded specimens are shown in **Figure 15**. The injection-moulded materials provide the highest resistance to bending due to the higher pressure and the formation of fewer pores.

4 CONCLUSION

The methods of injection moulding and extrusion of powders and sintering make it possible to fabricate small complex parts made of composite tool materials based on a cobalt or nickel-cobalt matrix, reinforced with hard carbide phases.

It was found based on the investigations conducted that the mixtures of carbide powders through injection extrusion or moulding can be produced by applying a binder in the form of paraffin or polyethylene. All the polymer-powder mixtures presented can be used for the injection moulding of powders or extrusion thereof and this is evidenced by the outcomes of the rheological tests presented. The fraction of powder in relation to powder in a slip can be increased by applying a surfactant such as stearic acid. Stearic acid is clearly reducing the viscosity of the investigated polymer-powder mixtures, hence its use is substantiated. The binder content in injection moulded or extruded materials should be as small as possible, enabling slip moulding only. Excessive binder content poses difficulties in degradation and causes a larger shrinkage and potential distortion in sintering. The results of the bending strength tests mainly depend on the conditions of moulding that should be selected so that the structure of the moulded specimens is uniform and does not exhibit any discontinuities. It is predicted that further investigations of such materials consisting of the selection of appropriate debinding and sintering conditions will make it possible to produce ready complex tool materials in the form of sintered carbides characterized by appropriate custom-made properties.

The application of the state-of-the-art powder moulding methods for producing composite tool materials reinforced with hard carbide phases is substantiated. The application of injection moulding or extrusion processes, opposite to casting processes and classical powder metallurgy, allows us to manufacture composite materials with complicated shapes and a developed geometry, including tool materials with a wide range of content of reinforcing

particles, without having to use additional procedures and sorting typical for casting materials.

4 REFERENCES

- ¹ G. Matula, L. A. Dobrzański, G. A. Herranz, A. Varez, B. Levenfeld, J. M. Torralba, Influence of binders on the structure and properties of high speed-steel HS6-5-2 type fabricated using pressureless forming and PIM methods, *Materials Science Forum*, 534–536 (2007) 1, 693–696, doi:10.4028/www.scientific.net/MSF.534-536.693
- ² G. Matula, L. A. Dobrzański, A. Varez, B. Levenfeld, J. M. Torralba, Comparison of structure and properties of the HS12-1-5-5 type high-speed steel fabricated using the pressureless forming and PIM methods, *Journal of Materials Processing Technology*, 162 (2005), 230–235, doi:10.1016/j.jmatprotec.2005.02.166
- ³ V. Leschynsky, M. Ignatev, H. Wiśniewska-Weinert, J. Borowski, T. Rybak, I. Dobrovnik, Forging tools modification with graphene-like solid lubricant nanoparticles, *Journal of Achievements in Materials and Manufacturing Engineering*, 43 (2010), 341–348, jamme.acmsse.h2.pl/papers_vol43_1/43137.pdf
- ⁴ H. Wiśniewska-Weinert, V. Leschynsky, M. Ignatev, J. Borowski, T. Wiśniewski, Innovative technology for fabrication of antiwear layers for forging tools, *Tribologia*, 239 (2011) 5, 239–248, t.tribologia.eu/trib/arttykul/2015-06-23-Tribo-11v42n5_p239_248.pdf
- ⁵ S. Zhao, X. Song, Ch. Wei, L. Zhang, X. Liu, J. Zhang, Effects of WC particle size on densification and properties of spark plasma sintered WC–Co cermet, *International Journal of Refractory Metals and Hard Materials*, 27 (2009) 6, 1014–1018, doi:10.1016/j.ijrmhm.2009.07.017
- ⁶ A. Eder, W. Lengauer, K. Dreyer, H. Van Den Berg, H.-W. Daub, D. Kassel, Phase formation during sintering of functionally graded hardmetals, *Plansee Seminar*, 2005
- ⁷ A. S. Bolokang, A comparison of the mechanically alloyed (V,W)C and (V,W)C–Co powders, *Journals of Alloys Compound*, 477 (2009) 1–2, 905–908, doi:10.1016/j.jallcom.2008.11.038
- ⁸ M. Rosso, Ceramic and metal matrix composites: Routes and properties, *Journal of Materials Processing Technology*, 175 (2006), 364–375, doi:10.1016/j.jmatprotec.2005.04.038
- ⁹ W. Acchar, C. Zollfrank, P. Greil, Microstructure and mechanical properties of WC-Co reinforced with NbC, *Materials Research*, 7 (2004) 3, 445–450, doi:10.1590/S1516-14392004000300012
- ¹⁰ H. O. Andrén, Microstructure development during sintering and heat-treatment of cemented carbides and cermets, *Materials Chemistry and Physics*, 67 (2001), 209–213, doi:10.1016/S0254-0584(00)00441-7
- ¹¹ R. M. German and A. Bose, *Injection Molding of Metals and Ceramics*, MPIF, Princeton, NJ, 1997
- ¹² R. M. German, Global research and development in powder injection moulding, *Powder Injection Moulding International*, 1 (2007) 2, 33–36
- ¹³ F. Petzoldt, Metal injection moulding in Europe: ten facts that you need to know, *Powder Injection Moulding International*, 1 (2007) 2, 23–28
- ¹⁴ H. Ye, X. Y. Liu, H. Hong, Fabrication of metal matrix composites by metal injection molding—A review, *Journal of Materials Processing Technology*, 200 (2008), 12–24, doi:10.1016/j.jmatprotec.2007.10.066
- ¹⁵ M. Wright, L. J. Hughes and S. H. Gressel, Rheological characterization of feedstocks for Metal Injection Molding, *Journal of Materials Engineering and Performance*, 3 (1994) 2, 300–306, doi:10.1007/BF02645856
- ¹⁶ J. A. Moore, B. P. Jarding, B. K. Lograsso and I. E. Anderson, Atmosphere control during debinding of powder injection molded parts, *Journal of Materials Engineering and Performance*, 4 (1995) 3, 275–282, doi:10.1007/BF02649064
- ¹⁷ T. Li, Q. Li, J. Y. H. Fuh, P. C. Yu, L. Lu, Two-material powder injection molding of functionally graded WC–Co components, *International Journal of Refractory Metals and Hard Materials*, 27 (2009), 95–100, doi:10.1016/j.ijrmhm.2008.04.005
- ¹⁸ A. Simchi, F. Petzoldt, Cosintering of Powder Injection Molding parts made from ultrafine WC-Co and 316L stainless steel powders for fabrication of novel composite structures, *Metallurgical and Materials Transactions A*, 41A (2010), 233–241, doi:10.1007/s11661-009-0045-5
- ¹⁹ L. A. Dobrzański, B. Tomiczek, M. Pawlyta, M. Król, Aluminium AlMg1SiCu matrix composite materials reinforced with halloysite particles, *Archives of Metallurgy and Materials*, (59) (2014), 335, doi:10.2478/amm-2014-0055
- ²⁰ M. Collin, S. Norgren, Hardness gradients in WC-Co created by local addition of Cr₃C₂, *Proceedings of the 16th International Plansee Seminar*, Reutte, (2005), 277–241
- ²¹ X. H. Qu, J. X. Gao, M. L. Qin, C. M. Lei, Application of a wax-based binder in PIM of WC–TiC–Co cemented carbides, *International Journal of Refractory Metals and Hard Materials*, 23 (2005), 273–277, doi:10.1016/j.ijrmhm.2005.04.006
- ²² M. Bram, M. Bitzer, H. P. Buchkremer, D. Stover, Phase transformation behavior of Hot Isostatically Pressed NiTi-X (X = Ag, Nb, W) alloys for functional engineering applications, *Journal of Materials Engineering and Performance*, 21 (2012) 12, 2071–2712, doi:10.1007/s11665-012-0375-0

GRAIN-REFINING ABILITY OF ULTRA-RAPID ANNEALING FOR
LOW-CARBON STEEL: SEVERE PLASTIC DEFORMATIONSPOSOBNOST UDROBNENJA ZRN PRI ZELO HITREM ŽARJENJU
MALOGLJIČNEGA JEKLA PO VELIKI PLASTIČNI
DEFORMACIJI**Mohammad Ali Mostafaei, Mohsen Kazeminezhad**Sharif University of Technology, Department of Materials Science and Engineering, Azadi Avenue, Tehran, Iran
mkazemi@sharif.edu*Prejem rokopisa – received: 2015-12-19; sprejem za objavo – accepted for publication: 2016-02-03*

doi:10.17222/mit.2015.350

To study the grain-refinement ability of ultra-rapid annealing (URA), heating rates from 0.3 °C/s up to 1200 °C/s with conventional annealing and URA in the intercritical temperature range were performed on severely deformed low-carbon steel. The results show that recrystallization in conventional annealing is completed below the critical temperature of A_{c1} without grain refinement. URA up to 730 °C at a heating rate of 200 °C/s causes grain refinement due to full interaction between the recrystallization and phase transformation. URAs up to 730 °C with heating rates of 600 °C/s and 1000 °C/s lead to partial grain refinement and no grain refinement, respectively. During annealing with a heating rate of 1200 °C/s, the temperature should reach 760 °C for the occurrence of recrystallization leading to grain refinement. The sample URAd at 600 °C/s up to 730 °C shows the maximum hardness due to fine grains being partially formed.

Keywords: conventional annealing, ultra-rapid annealing, interaction, severe plastic deformation

Za študij sposobnosti udrobnjenja zrn pri zelo hitrem žarjenju, so bile uporabljene hitrosti segrevanja od 0,3 °C/s do 1200 °C/s pri običajnem in zelo hitrem žarjenju v interkritisnem temperaturnem območju na močno deformiranem maloogljičnem jeklu. Rezultati kažejo, da je rekristalizacija pri konvencionalnem žarjenju zaključena pod kritično temperaturo A_{c1} brez udrobnjenja zrn. Zelo hitro žarjenje do 730 °C pri hitrosti ogrevanja 200 °C/s povzroči udrobnjenje zrn, zaradi polne interakcije med rekristalizacijo in fazno premeno. Zelo hitro žarjenje do 730 °C, s hitrostjo ogrevanja 600 °C/s in 1000 °C/s povzroči delno udrobnjenje zrn oz. udrobnjenja zrn ni. Med ogrevanjem s hitrostjo 1200 °C/s je potrebno doseči temperaturo 760 °C, da se pojavi rekristalizacija, ki povzroči udrobnitev zrn. Vzorec po zelo hitrem žarjenju z 600 °C/s do 730 °C kaže maksimalno trdoto zaradi delnega nastanka drobnih zrn.

Ključne besede: konvencionalno žarjenje, zelo hitro žarjenje, interakcija, močna plastična deformacija

1 INTRODUCTION

Conventional annealing of deformed steel with a slow heating rate (usually below 10 °C/s)¹ causes recovery and recrystallization to occur sequentially by subcritical temperature (below the critical temperature of A_{c1}).^{2,3} This annealing is followed by furnace soaking to complete the recrystallization.³ However, in low-carbon steel the grain refinement after conventional annealing needs to combine the steel's chemical composition and the annealing cycle.^{4,5} Also, the phase transformation during conventional annealing in the intercritical temperature range does not influence the grain refinement of deformed low-carbon steel.

On the other hand, ultra-rapid annealing (URA) of steels is a new method that leads to grain refinement in a very short time due to changes in the starting temperature of recrystallization.⁶⁻⁹ This condition provides the ability to control the microstructure by means of the simultaneous occurrence of recrystallization and phase transformation. URA shifts the start temperature of recrystallization to higher values near and above A_{c1} .^{3,7-15} So, in the intercritical temperature range, recrystalliza-

tion and phase transformation proceed concurrently and with a mutual "interaction". The intensity of the interaction depends of the amount of stored energy and determines the final microstructure of the steel.¹⁶⁻¹⁸ The heating rate controls the recrystallization start temperature and the amount of stored strain energy before the interaction. So, heating rate has a key role in controlling the microstructure and the grain refinement.

In this research, the effect of a slow heating rate (0.3 °C/s) up to a high heating rate (1200 °C/s) in the intercritical temperature range on the final microstructure of the severely deformed low-carbon steel is examined. The steel is subjected to severe plastic deformation to increase its stored strain energy before annealing.

2 EXPERIMENTAL PART

The low-carbon steel with 0.05 C, 0.2 Mn, 0.011 P, 0.007 S, 0.055 Al (all in w/%) in the form of a sheet with a thickness of 3 mm is used in this research. The as-received materials were normalized to obtain the spheroidized cementite. SPD was performed using two passes of constrained grooved pressing (CGP) on speci-

mens with a size of 80×50×3 mm in the sheet rolling direction. Each complete pass of CGP imposes an overall strain of 1.16, which contains four alternating stages of pressing grooving in dies and flattening dies. After the first two stages, the specimen is rotated 180° around the axis perpendicular to the sheet plane and then the two stages are repeated. The direction of the grooving dies is perpendicular to the rolling direction of the as-received sheet. Teflon layers were used as the lubricant between the samples and the dies. More details of the CGP method are given in ^{19,20}. For ultra-rapid annealing, the samples were machined from both sides up to a thickness of 1.8 mm, and then cut into specimens with a width of 14 mm.

The URA setup is based on resistance heating, which is provided by a high current transformer controlled by a digital control unit. A high current of about 5000 A passes through the sample and increases the temperature that is measured using a thermocouple finely spot welded to the center of the sample, and read with a high-speed data logger at a frequency of 3000. The data is concurrently transferred and saved to a PC, and the temperature-time diagram is drawn simultaneously during URA. Different heating rates were applied up to the desired sample temperature that was then immediately cooled after heating with a rate of about -700 °C/s with a high-speed spray of water and air.

Slow heating rate conventional annealing was carried out in a furnace with a heating rate of about 0.3 °C/s without any soaking time. At the desired temperature the samples were removed from the furnace and quenched as mentioned above.

After annealing, a hardness test was performed using 30 kg Vickers and then the samples were prepared for microstructural examinations, from thickness in the longitudinal direction.

3 RESULTS AND DISCUSSION

The microstructure of the as-received steel consists of ferrite grains (a mean grain size of about 80 µm) with dispersed carbide particles and was free of pearlite. After SPD, the mean grain size was reduced to about 30 µm, and particles were refined and highly dispersed at the grain boundaries and inside the grains (**Figure 1**).

The microstructure of the SPDed steel after conventional furnace annealing up to 730 °C (slightly above A_{c1}) is shown in **Figure 2**. Several experiments were done by annealing up to different temperatures showed that the A_{c1} temperature of the studied steel is about 720 °C and pearlite was observed after heating higher than 720 °C. The microstructure was recrystallized, the grains grew and some of the grains are marked with "A", grown to abnormal size. This shows that recrystallization started before the critical temperature of A_{c1} . **Figure 3** shows the microstructures of SPDed steel after subcritical conventional annealing up to the temperatures

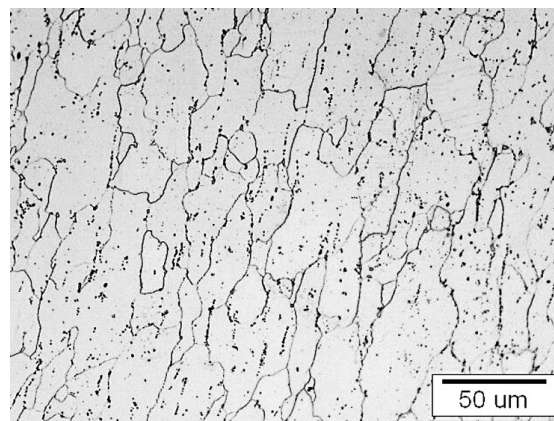


Figure 1: Microstructure of low-carbon steel after SPD
Slika 1: Mikrostruktura maloogljičnega jekla po SPD

of 500 °C and 650 °C. After heating up to 500 °C, the microstructure was similar to that of the SPDed sample and indicated that the recrystallization was not started. In the sample heated to 650 °C, the microstructure is fully recrystallized and the grain size is smaller than in **Figure 2**. This shows that the start and finish temperatures of the recrystallization during conventional annealing are much below the A_{c1} .

The microstructure of SPDed steel after URA with a heating rate of 200 °C/s up to 730 °C in **Figure 4** showed that URA produced grain refinement to an average grain size of 8 µm.

The scanning electron micrograph (SEM) in **Figure 4b** indicates the formation of pearlite massively dispersed at recrystallized ferrite grain boundaries. This suggests the full interaction of the ferrite recrystallization and the phase transformation. As the interaction occurs, the kinetics of recrystallization and transformation are increased.^{3,6,13,16,21} The austenite phase nucleates first at the deformed ferrite grain boundaries.²² On the other hand, austenite provides a preferred recrystal-

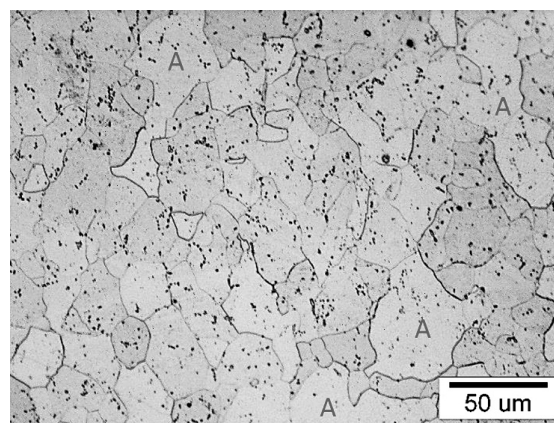


Figure 2: Microstructure of severely deformed steel by furnace annealing up to 730 °C with heating rate of 0.3 °C/s, abnormally grown grains are marked with A

Slika 2: Mikrostruktura močno deformiranega jekla po žarjenju v peči na 730 °C in s hitrostjo segrevanja 0,3 °C/s, neobičajno velika zrna so označena z A

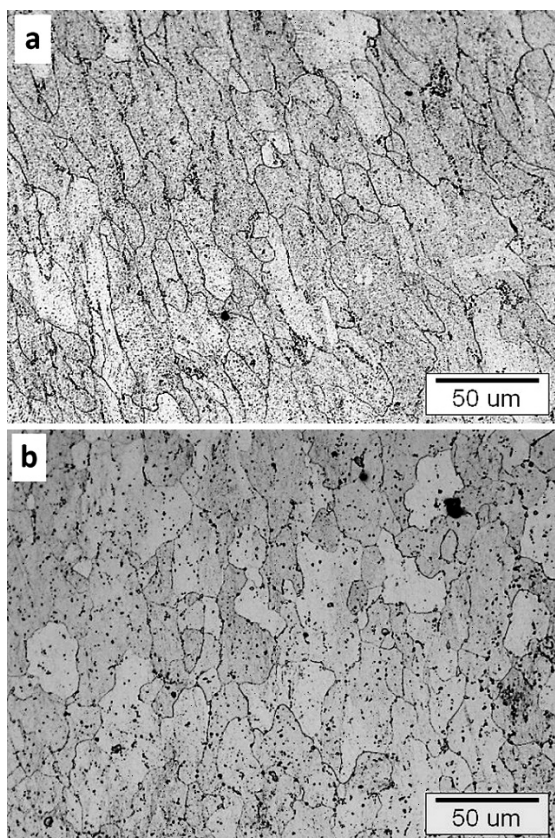


Figure 3: Microstructure of severely deformed steel after furnace annealing with a heating rate of 0.3 °C/s: a) 500 °C, and b) 650 °C
Slika 3: Mikrostruktura močno deformiranega jekla po žarjenju v peči s hitrostjo segrevanja 0,3 °C/s: a) 500 °C in b) 650 °C

lization nucleation site for the non-recrystallized ferrite. So, fine recrystallized ferrite grains are surrounded by austenite phases (which are transformed to pearlite during cooling) and their growth is inhibited and the microstructure with refined grains is formed. It should be noted that the transformation of austenite to pearlite during cooling was accelerated by the small size of the austenite grains.^{12,23,24}

URA with a heating rate of 600 °C/s up to 730 °C does not show a homogeneous grain refinement. This

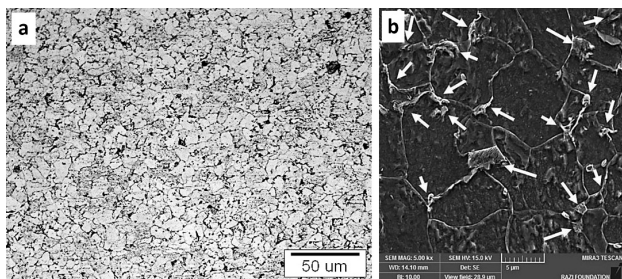


Figure 4: Microstructure of severely deformed steel after URA up to 730 °C with heating rate of 200 °C/s: a) optical microscopy image, and b) SEM image, arrows mark pearlites

Slika 4: Mikrostruktura močno deformiranega jekla po zelo hitrem žarjenju na 730 °C, s hitrostjo segrevanja 200 °C/s: a) posnetek s svetlobno mikroskopijo in b) SEM-posnetek, puščice označujejo perlitne

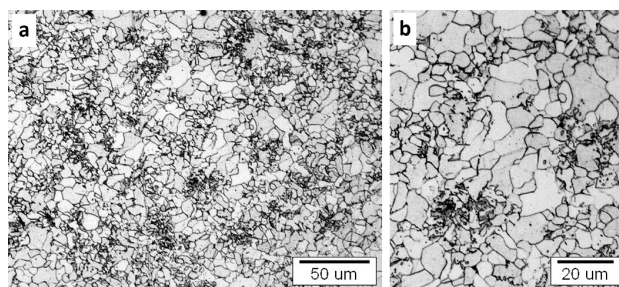


Figure 5: a) Microstructure of severely deformed steel after URA up to 730 °C with heating rate of 600 °C/s, b) higher magnification of a)
Slika 5: a) Mikrostruktura močno deformiranega jekla po zelo hitrem žarjenju do 730 °C s hitrostjo segrevanja 600 °C/s in b) večja povečava a)

microstructure (**Figure 5**) consists of two-sized grains of 10 μm and 2 μm. It can be seen that a partial grain refinement occurred due to incomplete recrystallization, and pearlite surrounded by the locally recrystallized ferrite grains were formed.

This shows a localized interaction. In comparison with the sample heated with 200 °C/s, the heating rate of 600 °C/s delays the start temperature of the recrystallization slightly above A_{c1} . During URA, austenite was formed and then recrystallization took place. In this situation the interaction between ferrite recrystallization and the formation of austenite is localized around recently formed austenite.

The microstructure shown in **Figure 6** is from the SPDed sample URA treated with heating at 1000 °C/s up to 730 °C and shows no recrystallization and the grain size of about 30 μm is similar to the grain size of the SPDed sample before URA. A very high heating rate of 1000 °C/s shifts the start temperature of the recrystallization higher than 730 °C. However, the transformation occurred and the pearlite phase was formed around the non-recrystallized ferrite grains (**Figure 6b**).

For the occurrence of recrystallization with a high heating rate, the peak temperature of URA should be increased in proportion to the heating rate. For example, from the microstructure in **Figure 7**, for URA with

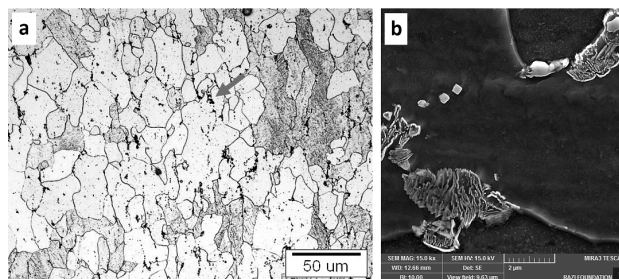


Figure 6: Microstructure of severely deformed steel after URA up to 730 °C with the heating rate of 1000 °C/s: a) optical microscopy image, b) SEM image of dark phases indicated by arrow in a)

Slika 6: Mikrostruktura močno deformiranega jekla po zelo hitrem žarjenju na 730 °C, s hitrostjo segrevanja 1000 °C/s: a) posnetek s svetlobno mikroskopijo in b) SEM-posnetek temnih faz v a), označeni so s puščico

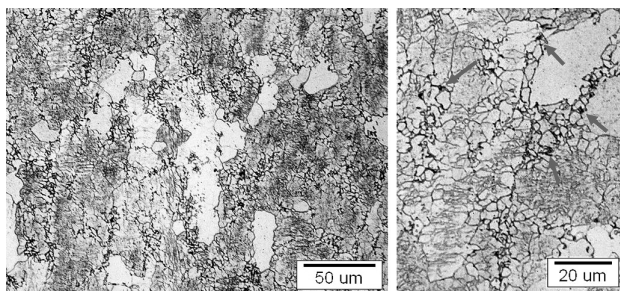


Figure 7: a) Microstructure of severely deformed steel after URA up to 760 °C with heating rate of 1200 °C/s, b) higher magnification of a), arrows marks the pearlite

Slika 7: a) Mikrostruktura močno deformiranega jekla po zelo hitrem žarjenju na 760 °C, s hitrostjo segrevanja 1200 °C/s, b) večja povečava a), puščice označujejo perlit

heating rate of 1200 °C/s up to 760 °C it is clear that there is the start of recrystallization.

In this condition, similar to **Figure 5**, transformation is started before recrystallization. During URA, the austenite phases were formed and then the recrystallization localized around them, causing the formation of the two-sized-grains microstructure with the sizes of 30 μm and 2 μm. The austenite transformed to pearlite during cooling is marked with arrows in **Figure 7b**.

The hardness of the specimens treated conventionally and with URA are shown in **Figure 8**.

The sample heated with 600 °C/s up to 730 °C has the highest hardness because of the partial formation of fine grains and the formation of pearlite in the microstructure. The composite-like microstructure of this sample is responsible for its high hardness. For a similar reason, the sample heated with 1200 °C/s up to 760 °C also has a relatively high value of hardness of about 183 HV.

The hardness of the conventionally annealed samples confirms the described microstructure. The sample annealed up to 550 °C has a similar hardness to that before annealing. This confirms the absence of recrystallization, as mentioned before. For the samples annealed up to 650 °C, the hardness is sharply reduced due to recrystallization.

4 CONCLUSIONS

The effect of the heating rate on the grain refinement is investigated with conventional annealing and ultra-rapid annealing for severely deformed low-carbon steel and the following conclusions can be drawn:

- In conventional annealing with a heating rate of 0.3 °C/s, recrystallization is completed below the critical temperature of A_{c1} , and the absence of grain refinement is confirmed with hardness values.
- URA with the heating rate of 200 °C/s up to 730 °C leads to full grain refinement due to the full interaction between ferrite recrystallization and austenite formation.
- At 730 °C, achieved with URA, the increasing of the heating rate to 600 °C/s causes a partial grain

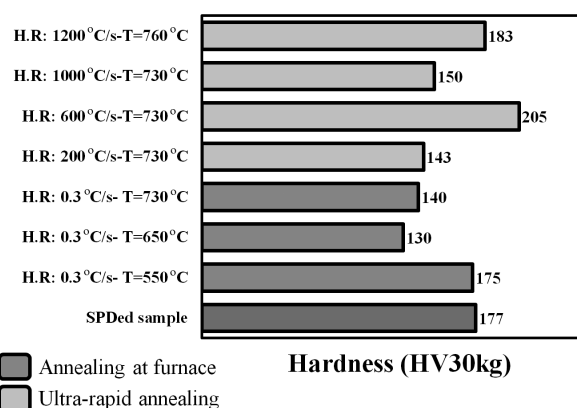


Figure 8: Hardness values of SPDED steel before annealing and after conventional and ultra-rapid annealing.

Slika 8: Vrednosti za trdoto SPD jekla pred žarjenjem in po konvencionalnem ter po zelo hitrem žarjenju

refinement due to localized interaction. The sample in this condition shows the maximum hardness value of 205 Hv.

- By increasing the heating rate to 1000 °C/s, no recrystallization occurs at the temperature of 730 °C.
- Temperature should be increased in proportion to the heating rate in order to start the recrystallization and the occurrence of grain refinement, such as those that occurred for the sample URAed with 1200 °C/s up to 760 °C.

Acknowledgement

The authors wish to thank the research board of Sharif University of Technology for the financial support and the provision of the research facilities used in this work.

5 REFERENCES

- ¹ Q. Meng, J. Li, H. Zheng, High-efficiency fast-heating annealing of a cold-rolled dual-phase steel, *Materials and Design*, 58 (2014), 194–197, doi:10.1016/j.matdes.2014.01.055
- ² A. Karmakar, D. Chakrabarti, Comparison between Conventional Annealing and Rapid-Transformation Annealing of Low-Carbon Steel, *International Journal of Metallurgical Engineering*, 2 (2013), 137–141, doi:10.5923/j.ijmee.20130202.04
- ³ P. Li, J. Li, Q. Meng, W. Hu, D. Xu, Effect of heating rate on ferrite recrystallization and austenite formation of cold-roll dual phase steel, *Journal of Alloys and Compounds*, 578 (2013), 320–327, doi:10.1016/j.jallcom.2013.05.226
- ⁴ H. Shi, Investigations of the effect of ultra-rapid heating on the softening of a cold rolled low-carbon steel, University of Wollongong, Wollongong 1990, 245 (PhD Thesis)
- ⁵ Z. Hou, Y. Xu, D. Wu, Recrystallization of ultra-low carbon steel sheet after ultra-rapid annealing, *Acta Metallurgica Sinica*, 48 (2012), 1057, doi:10.3724/SP.J.1037.2012.00115
- ⁶ C. Lesch, P. Álvarez, W. Bleck, J. Gil Sevillano, Rapid Transformation Annealing: a Novel Method for Grain Refinement of Cold-Rolled Low-Carbon Steels, *Metallurgical and Materials Transactions A*, 38 (2007), 1882–1890, doi:10.1007/s11661-006-9052-y

- ⁷ V. Massardier, A. Ngansop, D. Fabregue, J. Merlin, Identification of the parameters controlling the grain refinement of ultra-rapidly annealed low carbon Al-killed steels, *Materials Science and Engineering A*, 527 (2010), 5654–5663, doi:10.1016/j.msea.2010.05.024
- ⁸ R. Petrov, J. Sidor, W. Kaluba, L. Kestens, Grain Refinement of a Cold Rolled TRIP Assisted Steel after Ultra Short Annealing, *Materials Science Forum*, 715–716 (2012), 661–666, doi:10.4028/www.scientific.net/MSF.715-716.661
- ⁹ D. Muljono, M. Ferry, D. Dunne, Influence of heating rate on anisothermal recrystallization in low and ultra-low carbon steels, *Materials Science and Engineering A*, 303 (2001), 90–99, doi:10.1016/S0921-5093(00)01882-7
- ¹⁰ S.S. Gorelik, *Recrystallization in Metals and Alloys*, MIR Publisher, Moscow 1981, 92
- ¹¹ D. Xu, J. Li, Q. Meng, Y. Liu, P. Li, Effect of heating rate on microstructure and mechanical properties of TRIP-aided multiphase steel, *Journal of Alloys and Compounds*, 614 (2014), 94–101, doi:10.1016/j.jallcom.2014.06.075
- ¹² H. Azizi-Alizamini, M. Militzer, W. J. Poole, Austenite Formation in Plain Low-Carbon Steels, *Metallurgical and Materials Transactions A*, 42 (2011), 1544–1557, doi:10.1007/s11661-010-0551-5
- ¹³ C. Zheng, D. Raabe, Interaction between recrystallization and phase transformation during intercritical annealing in a cold-rolled dual-phase steel: A cellular automaton model, *Acta Materialia*, 61 (2013) 5504–5517, doi:10.1016/j.actamat.2013.05.040
- ¹⁴ J. Stockemer, P. Vanden Brande, P. Brande, Recrystallization of a cold-rolled low-carbon steel by cold-plasma-discharge rapid annealing, *Metallurgical and Materials Transactions A*, 34 (2003), 1341–1348, doi:10.1007/s11661-003-0245-3
- ¹⁵ J. Huang, W. J. Poole, M. Militzer, Austenite formation during intercritical annealing, *Metallurgical and Materials Transactions A*, 35 (2004), 3363–3375, doi:10.1007/s11661-004-0173-x
- ¹⁶ A. Karmakar, M. Ghosh, D. Chakrabarti, Cold-rolling and intercritical annealing of low-carbon steel: Effect of initial microstructure and heating-rate, *Materials Science and Engineering A*, 564 (2013), 389–399, doi:10.1016/j.msea.2012.11.109
- ¹⁷ R. R. Mohanty, O. a. Girina, N. M. Fonstein, Effect of heating rate on the austenite formation in low-carbon high-strength steels annealed in the intercritical region, *Metallurgical and Materials Transactions A*, 42 (2011), 3680–3690, doi:10.1007/s11661-011-0753-5
- ¹⁸ A. Chbihi, D. Barbier, L. Germain, A. Hazotte, M. Goune, Interactions between ferrite recrystallization and austenite formation in high-strength steels, *Journal of Materials Science*, 49 (2014), 3608–3621, doi:10.1007/s10853-014-8029-2
- ¹⁹ F. Khodabakhshi, M. Kazeminezhad, A. H. Kokabi, Constrained groove pressing of low carbon steel: Nano-structure and mechanical properties, *Materials Science and Engineering A*, 527 (2010), 4043–4049, doi:10.1016/j.msea.2010.03.005
- ²⁰ F. Khodabakhshi, M. Kazeminezhad, The effect of constrained groove pressing on grain size, dislocation density and electrical resistivity of low carbon steel, *Materials and Design*, 32 (2011), 3280–3286, doi:10.1016/j.matdes.2011.02.032
- ²¹ C. Lesch, W. Bleak, P. Alvarez, Grain refinement of cold rolled microalloyed steels by rapid transformation annealing, Luxembourg, 2006
- ²² N. Peranio, Y. Li, F. Roters, D. Raabe, Microstructure and texture evolution in dual-phase steels: Competition between recovery, recrystallization, and phase transformation, *Materials Science and Engineering A*, 527 (2010), 4161–4168, doi:10.1016/j.msea.2010.03.028
- ²³ E. Gutiérrez C., A. Salinas-Rodríguez, E. Nava-Vázquez, Effect of Fast Annealing on Microstructure and Mechanical Properties of Non-Oriented Al-Si Low C Electrical Steels, *Materials Science Forum*, 560 (2007), 29–34, doi:10.4028/www.scientific.net/MSF.560.29
- ²⁴ A. Karmakar, A. Karani, S. Patra, D. Chakrabarti, Development of Bimodal Ferrite-Grain Structures in Low-Carbon Steel Using Rapid Intercritical Annealing, *Metallurgical and Materials Transactions A*, 44 (2013), 2041–2052, doi:10.1007/s11661-012-1556-z

